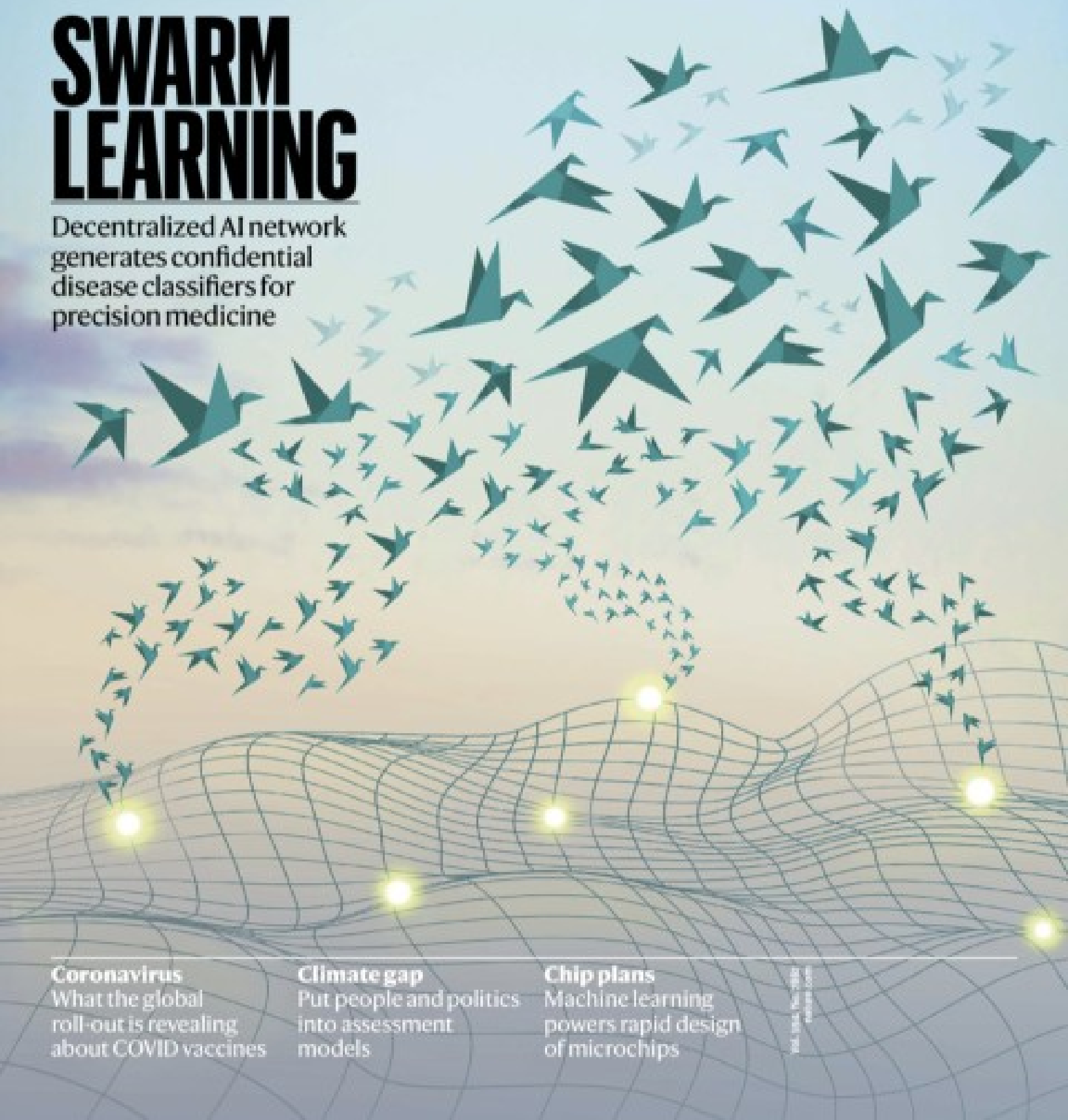


SWARM LEARNING

Decentralized AI network generates confidential disease classifiers for precision medicine



Coronavirus What the global roll-out is revealing about COVID vaccines

Climate gap Put people and politics into assessment models

Chip plans

Machine learning powers rapid design of microchips

Nature.2021.06.12

[Sat, 12 Jun 2021]

- [This Week](#)
- [News in Focus](#)
- [Books & Arts](#)
- [Opinion](#)
- [Work](#)
- [Research](#)

| [Next section](#) | [Main menu](#) |

Donation

| [Next section](#) | [Main menu](#) |

This Week

- **[Embrace the WHO's new naming system for coronavirus variants](#)** [09 June 2021]
Editorial • The World Health Organization's system should have come earlier. Now, media and policymakers need to get behind it.
- **[Google's AI approach to microchips is welcome — but needs care](#)** [09 June 2021]
Editorial • Artificial intelligence can help the electronics industry to speed up chip design. But the gains must be shared equitably.
- **[The replication crisis won't be solved with broad brushstrokes](#)** [08 June 2021]
World View • A cookie-cutter strategy to reform science will cause resentment, not improvement.
- **[A light touch changes the strength of a single atomic bond](#)** [07 June 2021]
Research Highlight • A technique that uses an electric field to tighten the bond between two atoms can allow a game of atomic pick-up-sticks.
- **[How fit can you get? These blood proteins hold a clue](#)** [04 June 2021]
Research Highlight • Scientists pinpoint almost 150 biomarkers linked to intrinsic cardiovascular fitness, and 100 linked to fitness gained from training.
- **[Complex, lab-made ‘cells’ react to change like the real thing](#)** [02 June 2021]
Research Highlight • Synthetic structures that grow artificial ‘organelles’ could provide insights into the operation of living cells.
- **[Elephants’ trunks are mighty suction machines](#)** [01 June 2021]
Research Highlight • The pachyderms can nab a treat lying nearly 5 centimetres away through sheer sucking power.
- **[More than one-third of heat deaths blamed on climate change](#)** [04 June 2021]

Research Highlight • Warming resulting from human activities accounts for a high percentage of heat-related deaths, especially in southern Asia and South America.

- **Pyramid made of dirt is world's oldest known war memorial** [27 May 2021]

Research Highlight • Grave goods suggest that some of the people whose bones are buried in the Syrian monument were charioteers.

- **The surprise hidden in the teeth of the ‘wandering meatloaf’** [02 June 2021]

Research Highlight • The teeth of a marine mollusc hold the mineral santabarbaraite, which has been found in no other living thing.

- EDITORIAL
- 09 June 2021

Embrace the WHO's new naming system for coronavirus variants

The World Health Organization's system should have come earlier. Now, media and policymakers need to get behind it.





•

[Download PDF](#)



Coronavirus variants will now be named using Greek letters. Credit: Shutterstock

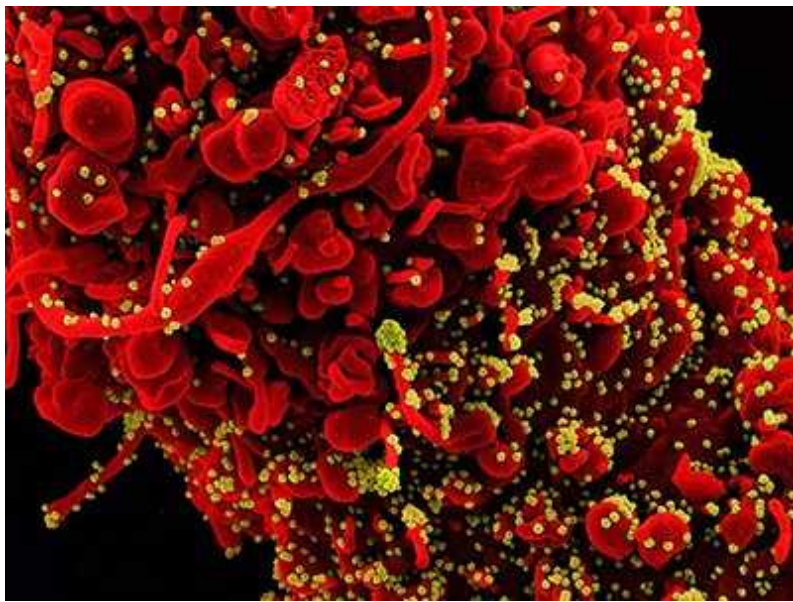
It has taken nearly six months, but the World Health Organization (WHO) last week announced the first iteration of its naming system for two kinds of coronavirus variant, to be used in public communications.

An expert committee advising the WHO recommended using the Greek alphabet to describe ‘variants of interest’ — which are coronavirus strains that lead to increased infections locally — as well as the more dangerous ‘variants of concern’.

The long-awaited system is intended for use by the media, policymakers and the public — and is published in *Nature Microbiology* ([F. Konings et al.](#), [Nature Microbiol. https://doi.org/10.1038/s41564-021-00932-w](https://doi.org/10.1038/s41564-021-00932-w); 2021). It should have come earlier, because its absence has fuelled the practice of naming variants after the places in which they were discovered — such as the ‘Kent variant’, which is otherwise known as B.1.1.7. Under the WHO’s new system, B.1.1.7 is also called Alpha. The B.1.617.2 lineage, first identified in India, is now called Delta.

The new system is both a more user-friendly alternative and designed to reduce the geographical stigma and discrimination that can come from associating a virus with a place. It's also important because, when countries are singled out by news organizations that have millions of readers and viewers, governments can become hesitant. They might delay collecting data on coronavirus strains, or announcing new variants, to avoid what they perceive as negative publicity or the risk of being blamed for creating a variant.

The new system does not change the alphanumeric nomenclature systems that researchers use. It also does not prevent the naming of a location where a virus variant has been identified, for example to indicate areas where variants are spreading. What it does do is provide an alternative to names that mean little to people outside research.



[Coronavirus variants get Greek names — but will scientists use them?](#)

At *Nature*, we will for now be using both the Greek letters and the nomenclature used by researchers, depending on the context, and will continue to avoid labelling variants by their geographical origin.

Nature's news team polled readers on [whether they would use the new system](#). Most of the 1,362 respondents indicated that they would — depending on the context. However, around 15% said they would continue

to use geographical descriptors. And more than a week after the WHO's announcement, some media organizations and prominent people are continuing to identify variants by geographical place names. That needs to end. The letters of the Greek alphabet are well known to international media and policymakers.

The WHO system's authors will be aware that theirs is a temporary solution. The WHO has already used 10 of its 24 letters to describe 6 variants of interest and 4 variants of concern that have been identified since December 2020. This means that a new naming system might need to be found.

Developing a naming system that is clear, intelligible and can work across cultures and languages is a complex process — which is one reason it has taken so long for the WHO's advisers to come up with its present solution. The World Meteorological Organization faces an analogous problem. It has a rotating list of 21 names for storms, such as Dolly and Omar. It also has a reserve list of all 24 Greek letters that it uses when the names in its standard list run out. But in March, it announced that it is retiring the Greek letters from its reserve list and adopting a new system of A–Z names, including Aidan and Zoe. The reason, it says, is that Greek letters can cause confusion when translated into other languages, and that some letters — such as eta and theta — sound alike and might be confused with each other.

The WHO's advisers need to keep working on the next iteration so that it is ready to be deployed when required, and they should consider alphabets from other languages. Their present solution, although not perfect, is a simple, straightforward alternative for variants that are otherwise being named after places. It will reduce the use of geographical origins as the default when referring to variants, and thus avoid an unintended stigma.

Nature **594**, 149 (2021)

doi: <https://doi.org/10.1038/d41586-021-01508-8>

Jobs from Nature Careers

-
-

- [All jobs](#)

○

- [Postdoctoral Fellow, Statistical Methodologies for Metabolomics Data Analysis](#)

[The University of British Columbia \(UBC\)](#)

[Vancouver, Canada](#)

[JOB POST](#)

- [Postdoctoral Fellow in River Dynamics](#)

[The University of British Columbia \(UBC\)](#)

[Vancouver, Canada](#)

[JOB POST](#)

- [PhD Student in Wnt signaling](#)

[German Cancer Research Center in the Helmholtz Association \(DKFZ\)](#)

[Heidelberg, Germany](#)

[JOB POST](#)

- [Postdoc \(all genders\), Department Detector Laboratory \(DTL\)](#)

[Helmholtz Centre for Heavy Ion Research GmbH \(GSI\)](#)

[Darmstadt, Germany](#)

[JOB POST](#)

[Download PDF](#)

Related Articles

- [SARS-CoV-2 Variants of Interest and Concern naming scheme conducive for global discourse](#)



- [Coronavirus variants get Greek names — but will scientists use them?](#)



- [The world needs a single naming system for coronavirus variants](#)

This article was downloaded by **calibre** from <https://www.nature.com/articles/d41586-021-01508-8>

| [Section menu](#) | [Main menu](#) |

- EDITORIAL
- 09 June 2021

Google's AI approach to microchips is welcome — but needs care

Artificial intelligence can help the electronics industry to speed up chip design. But the gains must be shared equitably.





•

[Download PDF](#)



A clean room in a microchip fabrication plant in Singapore. Credit: Lauryn Ishak/Bloomberg/Getty

One of the many consequences of the COVID-19 pandemic is a global shortage of the microchips that are essential to electronic devices. The factories that make these chips had to shut down for some of the pandemic, and are struggling to cope with an increase in demand. Some products could be delayed by months.

It's too early to know how the shortage will affect the industry in the long term, but the pandemic has focused attention on some key research questions — including how to make the manufacturing process more resilient to shocks and emergencies.

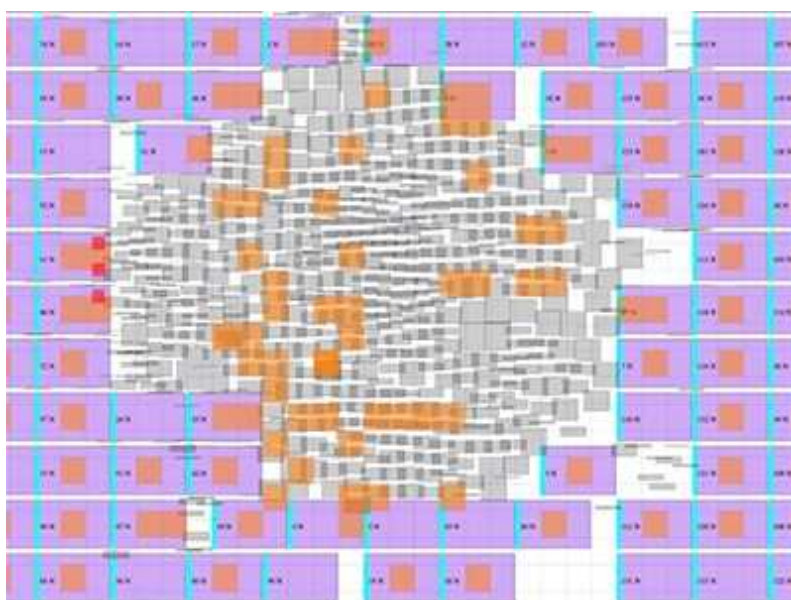
One well-known problem is that microchips are designed in just a handful of companies, including Samsung in South Korea and Intel, NVIDIA and Qualcomm in California. But not all these companies make the chips. Some do; others outsource the work to third parties. And around 80% of the chips are made in Asia ([*Nature Electron.* 4, 317; 2021](#)). The biggest manufacturer is the Taiwan Semiconductor Manufacturing Company (TSMC) in Hsinchu,

which is responsible for 28% of global capacity using current fabrication methods. Although this concentration has undoubtedly been of great benefit to the region, it has also contributed to the current restriction of supplies.

Signs of change are starting to emerge. China, the United States and some European countries are increasing investments in microchip research and development. Amazon, Google, Microsoft and other big US technology corporations are doing the same, with investments estimated at hundreds of millions of dollars. Spreading capability through more companies — and to more low- and middle-income countries — will help to make the industry more resilient.

Time-savers

Also of help is a report this week that researchers at Google have managed to greatly reduce the time needed to design microchips ([A. Mirhoseini et al. *Nature* 594, 207–212; 2021](#)). This is an important achievement and will be a huge help in speeding up the supply chain, but the technical expertise must be shared widely to make sure the ‘ecosystem’ of companies becomes genuinely global. And the industry must make sure that the time-saving techniques do not drive away people with the necessary core skills.

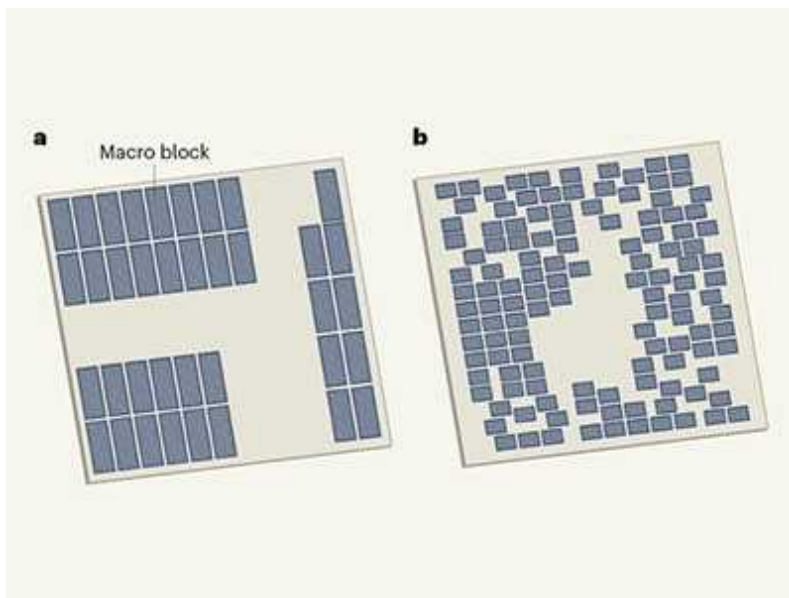


[Read the paper: A graph placement methodology for fast chip design](#)

Researchers and engineers continue to design and manufacture microchips with ever more processing power and complexity. In line with Moore's law — the principle that the number of transistors per chip doubles roughly every two years as transistors become smaller ([G. E. Moore *Electronics* 38, 114–117; 1965](#)) — the number of transistors per microchip has increased from a few thousand in the early 1970s to tens of billions today.

Although fabrication of the chips is largely automated, the design still relies on manual processes. Engineers and designers use computer-aided design software, but it can still take them weeks or months to work out how to fit all the components into the available space. Google's researchers have now shown that the process can be completed in less than a day by using artificial intelligence (AI).

Typically, the area of a microchip is of the order of tens to hundreds of millimetres square. That space needs to accommodate thousands of components, such as memory, logic and processing units, plus many kilometres of ultra-thin wire to connect these components together. One of the most challenging aspects of the design process is 'chip floorplanning'. This involves working out where best to place these components, in the same way that an architect designs a building's internal space such that it can accommodate all the required fixtures and fittings.



[AI system outperforms humans in designing floorplans for microchips](#)

Google's researchers used [10,000 chip floorplans to train their software](#). The software then worked out how to generate floorplans that used no more space, wire and electric power than did those designed by engineers. Miniaturization and low power are particularly important for the chips used in smartphones.

The AI-generated chips took less than six hours to design, and the method has already been used to design Google's tensor processing unit, or TPU, which is used mainly in the company's cloud-based machine-learning applications. More teams need to test the design software to make sure it is robust and can accommodate other data sets and chip types. If more groups can recreate its success, that will cement its place in the chip-design toolbox.

Now concentrate

More-accessible and more-efficient microchips will power the development of autonomous vehicles, 5G communications and AI — opportunities that should not be missed. But it's important to consider the wider implications of using automated design technologies, particularly the need for people with relevant skills and expertise, and for upskilling those who currently do the process manually.

Chip floorplanning — whether manual or automated — requires expertise in computing, electronic engineering and device physics. These skills take time to learn and are sorely needed in an industry that makes many other products besides microchips. It's crucial that the companies involved understand this, and take appropriate steps to meet their skills needs both locally and globally. Automation often fuels concerns about a reduction in jobs. In fact, maintaining momentum in the electronics industry will require people and companies with the foresight to create the next generation of microchips.

Nature **594**, 150 (2021)

doi: <https://doi.org/10.1038/d41586-021-01507-9>

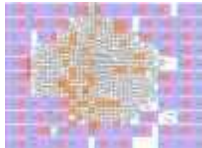
[Jobs from Nature Careers](#)

- - - [All jobs](#)
 - - [**Postdoctoral Fellow, Statistical Methodologies for Metabolomics Data Analysis**](#)
[The University of British Columbia \(UBC\)](#)
[Vancouver, Canada](#)
[JOB POST](#)
 - [**Postdoctoral Fellow in River Dynamics**](#)
[The University of British Columbia \(UBC\)](#)
[Vancouver, Canada](#)
[JOB POST](#)
 - [**PhD Student in Wnt signaling**](#)
[German Cancer Research Center in the Helmholtz Association \(DKFZ\)](#)
[Heidelberg, Germany](#)
[JOB POST](#)
 - [**Postdoc \(all genders\), Department Detector Laboratory \(DTL\)**](#)
[Helmholtz Centre for Heavy Ion Research GmbH \(GSI\)](#)
[Darmstadt, Germany](#)

JOB POST

[Download PDF](#)

Related Articles



- [Read the paper: A graph placement methodology for fast chip design](#)



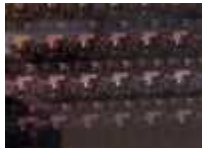
- [AI system outperforms humans in designing floorplans for microchips](#)



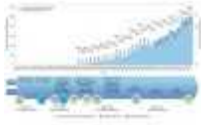
- [Am I arguing with a machine? AI debaters highlight need for transparency](#)



- [Don't ask if artificial intelligence is good or fair, ask how it shifts power](#)



- [Chips in a crisis](#)



- **The role of government policy in the building of a global semiconductor industry**

This article was downloaded by **calibre** from <https://www.nature.com/articles/d41586-021-01507-9>

| [Section menu](#) | [Main menu](#) |

- WORLD VIEW
- 08 June 2021

The replication crisis won't be solved with broad brushstrokes



A cookie-cutter strategy to reform science will cause resentment, not improvement.

- [David Peterson](#) 0

1. [David Peterson](#)

1. David Peterson is a postdoctoral researcher in sociology at the University of California, Los Angeles.

[View author publications](#)

You can also search for this author in [PubMed](#) [Google Scholar](#)





•

[Download PDF](#)

Alarm about a ‘replication crisis’ launched a wave of projects that aimed to quantitatively evaluate scientific reproducibility: statistical analyses, mass replications and surveys. Such efforts, collectively called metascience, have grown into a social movement advocating broad reforms: open-science mandates, preregistration of experiments and new incentives for careful research. It has drawn attention to the need for improvements, and caused rancour.

Philosophers, historians and sociologists no longer accept a single, unified definition of science. Instead, they document how scientists in different fields have developed unique practices of producing, communicating and evaluating evidence, guided loosely by a set of shared values. However, this diversity and underlying scholarship are often overlooked by metascience activists.

Over the past three years, Aaron Panofsky, a sociologist at the University of California, Los Angeles, and I have interviewed 60 senior biologists, chemists, geologists and physicists who are reviewing editors at *Science*, plus another 83 scientists seeking science-wide reforms. These highly recognized researchers saw growing interest in making science more open and robust — but also expressed scepticism.



Institutions can retool to make research more rigorous

Senior researchers bristled at the idea that their fields were in ‘crisis’, and suspected that activists were seeking recognition for themselves. A frustrated biologist argued that people running mass replication studies “were not motivated to find reproducibility” and benefited from finding it lacking. Others said metascientists dismissed replication work done to further a line of research rather than assess the state of the literature. Another saw data deposition as a frustrating, externally imposed mandate: “We’re already drowning in all the bureaucratic crap.”

Even those who acknowledged the potential value of reforms, such as those for data sharing, felt that there was no discussion about the costs. “If you add up all of the things that only take ten minutes, it’s a huge chunk of your day.”

Reformers counter that such complaints represent objections from a privileged elite, and point to perverse incentives, such as pressure to publish, that apply across academia. Marcus Munafò, a biological psychologist at the University of Bristol, UK, who co-founded the UK Reproducibility Network, hopes to change the system. He told me that science should move from a nineteenth-century “artisanal” practice towards one with structures to “audit or evaluate processes”. Brian Nosek, executive director of the Center for Open Science in Charlottesville, Virginia, feels progress has slowed because of “resistance” by people “doing quite well with the system as it is”.

I think that some reluctance does stem from entrenched interests. (It would be interesting to know whether early-career researchers would have answered differently.) But some is based on experience and knowledge. Many interviewees accepted the need for targeted improvements, but objected to blanket decrees. One physicist blamed data-deposition mandates on a bureaucracy that cannot distinguish differences in how scientific fields work. A plant biologist thought preregistration was appropriate for large, long-term experiments — such as clinical trials — but not short-term, iterative experiments such as hers, where each experiment depends on the previous one’s results.



The science institutions hiring integrity inspectors to vet their papers

Part of the problem is that many reformers come from a narrow swathe of academia. The authors of ‘A manifesto for reproducible science’, an influential perspective commissioned for the inaugural issue of *Nature Human Behaviour*, are predominantly from psychology, social and behavioural sciences ([M. R. Munafò et al. *Nature Hum. Behav.* 1, 0021; 2017](#)). Of the 39 authors introducing the widely adopted transparency and openness guidelines, most come from social sciences, and the rest are funders, employees at open-science institutes, editors of scientific journals and a science-policy scholar ([B. A. Nosek et al. *Science* 348, 1422–1425; 2015](#)).

The researchers we spoke to emphasized different norms across fields. A trained chemist who has also done research in biology explained that, although models in chemistry tend to have very high precision and very high reproducibility, “The reverse of that is true for biology.” This can lead to systematically different interpretations of failed replications, and evaluations of reproducibility. Are experiments poorly designed, or technically difficult?

My interviewees praised cases of overhaul that originated in the community they applied to. These included TERRINet, a program developed to coordinate research in robotics to code validation exercises in

seismography. In another much-lauded effort, thousands of cell biologists studying autophagy came together to standardize definitions and protocols ([D. J. Klionsky *Mol. Biol. Cell* 27, 733–738; 2015](#)).

If reformers want to make diverse scientific fields more robust, they need to demonstrate that they understand how specific fields operate before they push a set of practices about how science overall should operate. Rather than aligning practices with an overarching ideal, reformers should focus efforts on challenges in specific fields — for instance by working with scientific societies. Otherwise, efforts could be resisted as extensions of bureaucracy, rather than embraced as routes to more robust research.

Nature **594**, 151 (2021)

doi: <https://doi.org/10.1038/d41586-021-01509-7>

Editor's note: *Nature* journals have embraced practices to [promote robust practices and full, open reporting](#).

Competing Interests

The author declares no competing interests.

[Jobs from Nature Careers](#)

- - - [All jobs](#)
 - - [**Postdoctoral Fellow, Statistical Methodologies for Metabolomics Data Analysis**](#)

[The University of British Columbia \(UBC\)](#)

[Vancouver, Canada](#)

JOB POST

- **Postdoctoral Fellow in River Dynamics**

The University of British Columbia (UBC)

Vancouver, Canada

JOB POST

- **PhD Student in Wnt signaling**

German Cancer Research Center in the Helmholtz Association (DKFZ)

Heidelberg, Germany

JOB POST

- **Postdoc (all genders), Department Detector Laboratory (DTL)**

Helmholtz Centre for Heavy Ion Research GmbH (GSI)

Darmstadt, Germany

JOB POST

Download PDF

Related Articles



- **Raising research quality will require collective action**



- [Institutions can retool to make research more rigorous](#)



- [The science institutions hiring integrity inspectors to vet their papers](#)

This article was downloaded by **calibre** from <https://www.nature.com/articles/d41586-021-01509-7>

| [Section menu](#) | [Main menu](#) |



The sharp stylus of an atomic-force microscope (boxy structure) can be used to adjust the strength of an atomic bond. Credit: Jörg Kröger

Condensed-matter physics

07 June 2021

A light touch changes the strength of a single atomic bond

A technique that uses an electric field to tighten the bond between two atoms can allow a game of atomic pick-up-sticks.





•

The strength of a chemical bond between two atoms can be adjusted at will by applying an electric field, physicists have shown. Insights from that achievement might help in the design of future molecular-scale electronic devices.

Jörg Kröger at the Technical University of Ilmenau in Germany, Susanne Leitherer at Technical University of Denmark in Kongens Lyngby and their collaborators devised a method that harnesses an imaging device called an atomic-force microscope (AFM), which has a stylus for probing samples. The AFM stylus used by the researchers was fitted with a single gold atom at its tip.

The authors touched the tip to a single-atom-thick graphene sheet so that the gold atom and a carbon atom would form a covalent bond, in which electrons are shared between the two atoms. The team then applied an electric field between the surface and the AFM tip.

By varying the field's direction and strength, the researchers could either strengthen or weaken the gold–carbon bond. When they strengthened the bond enough and gently retracted the AFM tip, the graphene sheet pulled away from the surface to which it was attached.

[Phys. Rev. Lett. \(2021\)](#)

- [Condensed-matter physics](#)

This article was downloaded by **calibre** from <https://www.nature.com/articles/d41586-021-01479-w>

| [Section menu](#) | [Main menu](#) |



A suite of proteins in the blood could one day predict how much cardiovascular benefit a person will gain from a strenuous workout regime.
Credit: Lars Baron/Getty

Metabolism

04 June 2021

How fit can you get? These blood proteins hold a clue

Scientists pinpoint almost 150 biomarkers linked to intrinsic cardiovascular fitness, and 100 linked to fitness gained from training.





•

A person's fitness could one day be assessed by looking at a suite of telltale blood proteins — which could also predict the fitness the person could gain from working out.

As a step towards mapping fitness biomarkers, Robert Gerszten at Beth Israel Deaconess Medical Center in Boston, Massachusetts, and his colleagues sampled blood from more than 650 sedentary adults. The team also measured participants' maximum oxygen intake — an indicator of cardiometabolic health — before and after a 20-week exercise programme.

Analysis of some 5,000 blood proteins identified 147 linked with baseline oxygen-intake levels and 102 linked with improvements to oxygen intake

after the exercise programme. The proteins that were associated with fitness included enzymes that break down sugar and are known to surge in the blood after exercise; proteins linked to bone-building; and some with unknown relevance to exercise physiology.

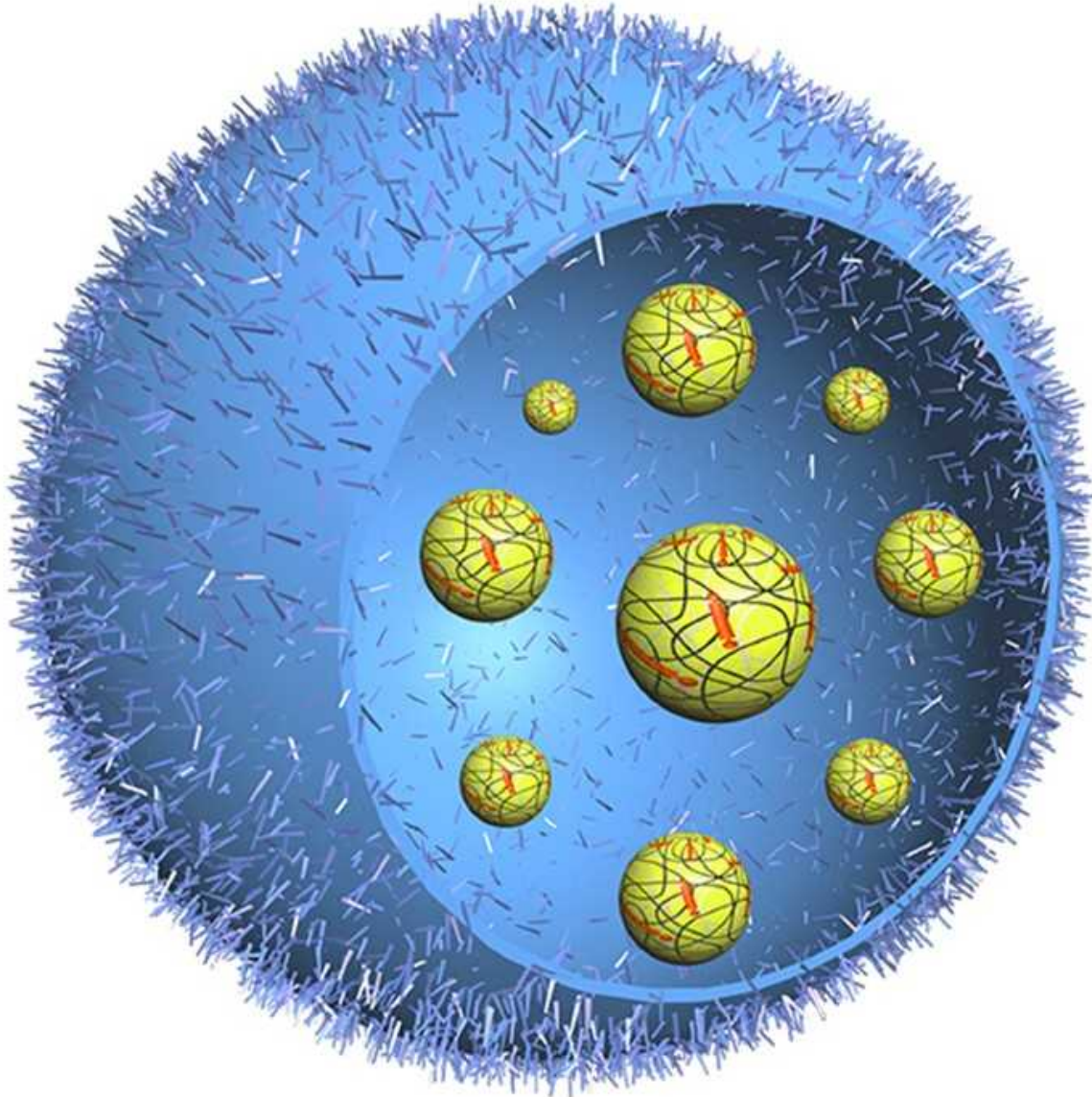
With better knowledge, the proteins that indicate the blood's oxygen-carrying capacity could serve as biomarkers for a person's fitness and future health risks, the authors say.

[Nature Metab. \(2021\)](#)

- [Metabolism](#)

This article was downloaded by **calibre** from <https://www.nature.com/articles/d41586-021-01476-z>

| [Section menu](#) | [Main menu](#) |



An artificial protocell with a protein skin (blue) holds self-contained liquid droplets that function like cellular organelles. Credit: Yan Qiao

Synthetic biology

02 June 2021

Complex, lab-made ‘cells’ react to change like the real thing

Synthetic structures that grow artificial ‘organelles’ could provide insights into the operation of living cells.





•

Artificial sacs made of proteins and stuffed with tiny liquid droplets resembling cellular substructures can respond to changes in their environment, not unlike living cells.

The simple models of living cells called protocells can help researchers to probe how the real thing processes information. Yan Qiao at the Chinese Academy of Sciences in Beijing, Yiyang Lin at Beijing University of Chemical Technology and their colleagues devised a protocell comprising a protein sac packed with internal ‘organelles’ made from a mixture of short, light-sensitive molecules and long, pH-sensitive polymers.

The organelles form at certain light and pH levels that prompt the components to intertwine into liquid spheres, which are well defined despite lacking membranes. Enzymes or strands of DNA can become concentrated inside the developing organelles, mimicking the build-up of such biomolecules inside cells.

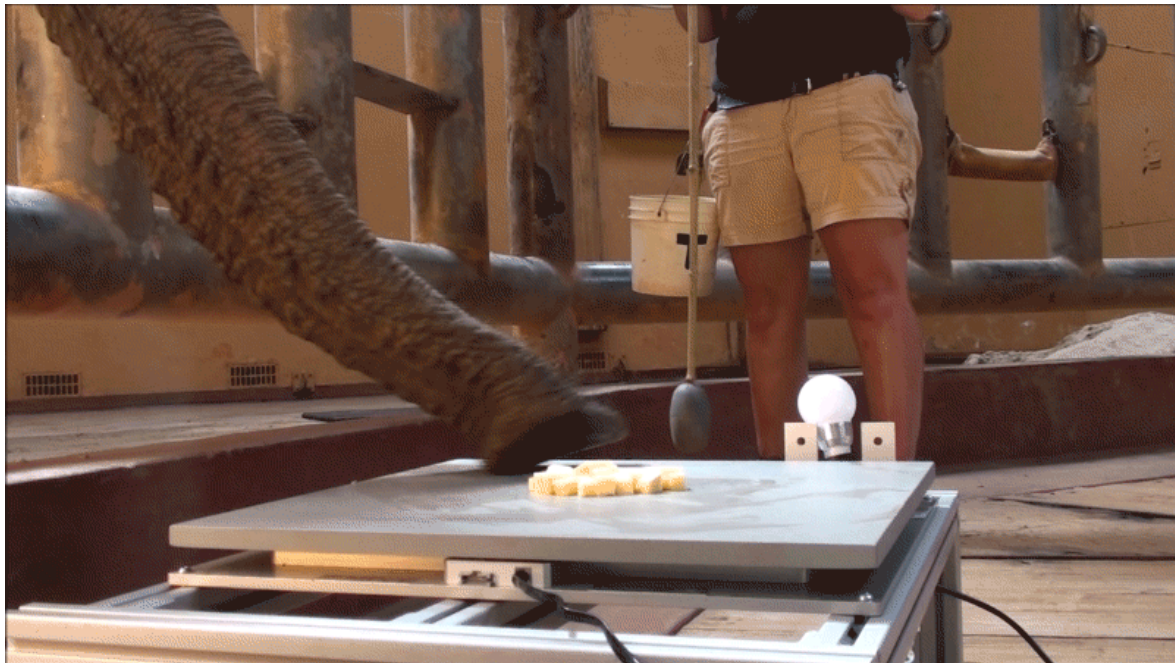
The protocells can process binary signals: organelles form if protocells are exposed to either lactose or oxygen, or to neither. But together, lactose and oxygen inhibit formation of organelles, and cause existing ones to unravel. This information-processing ability could allow scientists to program the protocells as if they were computer chips, to control chemical reactions.

[Sci. Adv. \(2021\)](#)

- [Synthetic biology](#)

This article was downloaded by **calibre** from <https://www.nature.com/articles/d41586-021-01477-y>.

| [Section menu](#) | [Main menu](#) |



An elephant hoovers up rutabaga cubes, which it will hold in its trunk before manoeuvring them into its mouth. Credit: Andrew Schulz, Jia Ning Wu

Animal behaviour

01 June 2021

Elephants' trunks are mighty suction machines

The pachyderms can nab a treat lying nearly 5 centimetres away through sheer sucking power.





•

The African elephant (*Loxodonta africana*) has more tricks up its trunk than heretofore suspected. Not only can it use the tips of its elegant nose like dexterous fingers, but it can also use its trunk to create a strong suction to hold items and pull them closer.

David Hu at the Georgia Institute of Technology in Atlanta and his colleagues observed zoo elephants as they used suction power to manipulate a variety of items. Elephants hoovered up rutabaga cubes, which the researchers note was accompanied by “a loud vacuuming sound”. They pulled tortilla chips close with the mighty force of their inhalations, which

the team calculated exceeded speeds of 150 metres per second, 30 times the speed of a human sneeze.

Mathematical modelling suggests that, thanks to their strong lungs and wide nostrils, elephants can procure tortilla chips from as far away as 4.6 centimetres through suction alone.

Most observations of animals using suction as a tool come from fish and other water-based species. The researchers hope their work will inspire roboticists.

[J. R. Soc. Interface \(2021\)](#)

- [Animal behaviour](#)

This article was downloaded by **calibre** from <https://www.nature.com/articles/d41586-021-01444-7>

| [Section menu](#) | [Main menu](#) |



A pedestrian seeks relief from searing temperatures in Spain, where a high proportion of heat-related deaths have been linked to climate change. Credit: SALAS/EPA-EFE/Shutterstock

Climate change

04 June 2021

More than one-third of heat deaths blamed on climate change

Warming resulting from human activities accounts for a high percentage of heat-related deaths, especially in southern Asia and South America.





•

Researchers have attributed 37% of deaths related to heat exposure around the world between 1991 and 2018 to global warming caused by humans.

Newly honed modelling techniques allow scientists to calculate global warming's contribution to weather events such as storms and droughts. To expand this approach to human health, Ana Maria Vicedo-Cabrera at the University of Bern, Antonio Gasparrini at the London School of Hygiene and Tropical Medicine and their colleagues collected temperature and mortality data during the warm season from 732 locations across 43 countries over a 28-year period.

The researchers calculated the death risk from extreme heat in each location. They also ran two climate simulations — one that factored in warming caused by greenhouse-gas emissions and one that didn't — and compared the deaths under each scenario.

The results show that 37% of the heat-related deaths could be attributed to rising temperatures induced by human activities. The combined toll from all assessed sites is roughly 9,700 deaths per year of the study, the authors estimate. The most affected areas included parts of southern Asia, southern Europe and central and South America.

[*Nature Clim. Change* \(2021\)](#)

- [Climate change](#)

This article was downloaded by **calibre** from <https://www.nature.com/articles/d41586-021-01475-0>

| [Section menu](#) | [Main menu](#) |



Human bones and military gear were carefully buried in Syria's White Monument. Credit: Euphrates Salvage Project

Archaeology

27 May 2021

Pyramid made of dirt is world's oldest known war memorial

Grave goods suggest that some of the people whose bones are buried in the Syrian monument were charioteers.





•

People living some 4,500 years ago in what is now Syria built what might be the world's first memorial to war dead.

Anne Porter at the University of Toronto in Canada and her colleagues re-analysed bones and artefacts found in a 22-metre-high artificial mound near the Euphrates River. The mound, called White Monument because the materials used in its construction cause it to glisten in sunlight, was used for rituals and burials for some 300 years until around 2450 BC. Then, between 2450 and 2300 BC, a series of horizontal steps were built over the original mound, turning it into a stepped pyramid that would have been visible over long distances.

The researchers found that the remains of at least 30 people, mostly male, were buried in the steps. The bodies seem to have been carefully interred along with earthen pellets that might have been fired on foes, as well as the skins and bones of donkey-like animals that were used to pull battle carts.

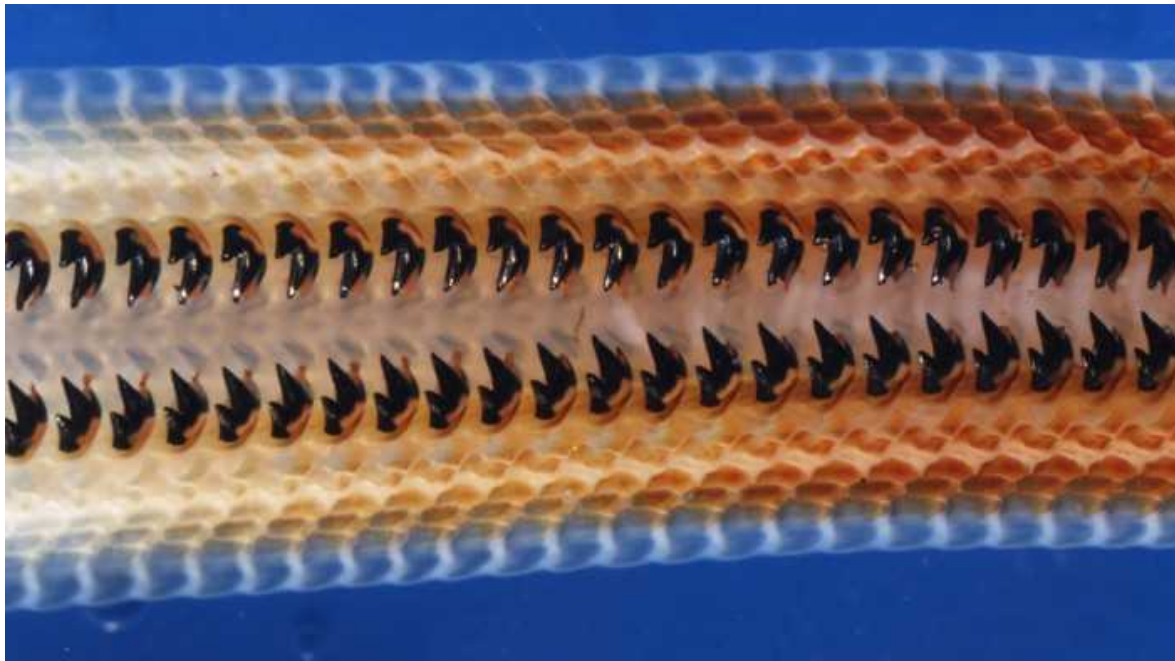
The burials suggest that the White Monument celebrated the community's warriors rather than serving as a mass grave for slain enemies, the authors say.

[Antiquity \(2021\)](#)

- [Archaeology](#)

This article was downloaded by **calibre** from <https://www.nature.com/articles/d41586-021-01443-8>

| [Section menu](#) | [Main menu](#) |



The teeth of *Cryptochiton stelleri* are among the hardest organic objects known in nature. Credit: Northwestern University

Biomaterials

02 June 2021

The surprise hidden in the teeth of the ‘wandering meatloaf’

The teeth of a marine mollusc hold the mineral santabarbaraite, which has been found in no other living thing.





•

The discovery of a rare iron mineral in the teeth of an alga-eating marine creature has inspired inks for 3D-printing strong, lightweight materials.

The coast-dwelling mollusc *Cryptochiton stelleri* has been dubbed the wandering meatloaf because of its large, oval, reddish-brown body, which can reach more than 30 centimetres long. However, the mollusc's modest exterior conceals several dozen rows of sharp teeth, which are among the hardest organic objects known in nature. The mollusc feeds by scraping these teeth along rocks covered in algae.



The bulky mollusc *Cryptochiton stelleri* has been nicknamed the ‘wandering meatloaf’. Credit: Jerry Kirkhart

Derk Joester at Northwestern University in Evanston, Illinois, and his colleagues analysed *C. stelleri* teeth using a range of advanced imaging techniques. Unexpectedly, they detected nanoparticles of santabarbaraite, an iron mineral that had previously been observed only in rocks. The researchers suggest that these particles could toughen the teeth without adding much weight.

The team then designed 3D-printing inks inspired by the composition of *C. stelleri* teeth. They used these inks to make strong, lightweight materials that vary in hardness and stiffness and might find applications in fields such as soft robotics.

[Proc. Natl Acad. Sci. USA \(2021\)](#)

- [Biomaterials](#)
-

This article was downloaded by **calibre** from <https://www.nature.com/articles/d41586-021-01478-x>

| [Section menu](#) | [Main menu](#) |

News in Focus

- **[COVID nasal spray, dark-matter map and a variant's rise](#)** [09 June 2021]
News Round-Up • The latest science news, in brief.
- **[Palaeontologists hope Biden will restore protections on fossil-rich US lands](#)** [28 May 2021]
News • Trump's shrinking of Utah's Bears Ears and Grand Staircase-Escalante reserves may be reversed — ensuring archaeological and fossil treasures are preserved for study.
- **[A complete human genome sequence is close: how scientists filled in the gaps](#)** [04 June 2021]
News • Researchers added 200 million DNA base pairs and 115 protein-coding genes — but they've yet to entirely sequence the Y chromosome.
- **[Elite US science academy expels astronomer Geoff Marcy following harassment complaints](#)** [27 May 2021]
News • This is the first time the National Academy of Sciences has kicked out a member for violating its amended code of conduct.
- **[Hundreds of gibberish papers still lurk in the scientific literature](#)** [27 May 2021]
News • The nonsensical computer-generated articles, spotted years after the problem was first seen, could lead to a wave of retractions.
- **[WHO approval of Chinese CoronaVac COVID vaccine will be crucial to curbing pandemic](#)** [04 June 2021]
News • CoronaVac is one of two Chinese vaccines already sustaining vaccination campaigns in more than 70 nations. Both should soon be much more widely available to low-income countries.
- **[Coronavirus variants get Greek names — but will scientists use them?](#)** [01 June 2021]
News • From Alpha to Omega, the labelling system aims to avoid confusion and stigmatization.
- **[The COVID vaccine pioneer behind southeast Asia's first mRNA shot](#)** [26 May 2021]

News Q&A • ChulaCov19 designer Kiat Ruxrungtham talks about his aim to make Thailand an mRNA vaccine hub, and the challenge of competing with bigger rivals.

- **Six months of COVID vaccines: what 1.7 billion doses have taught scientists** [04 June 2021]

News Feature • At a pivotal moment in the pandemic, Nature explores key questions about the vaccines that countries are racing to deliver while viral variants spread around the globe.

- **The four most urgent questions about long COVID** [09 June 2021]

News Feature • Scientists are starting to get insights into the lingering disorder that affects some people infected with SARS-CoV-2 — but many mysteries remain unsolved.

- NEWS ROUND-UP
- 09 June 2021

COVID nasal spray, dark-matter map and a variant's rise

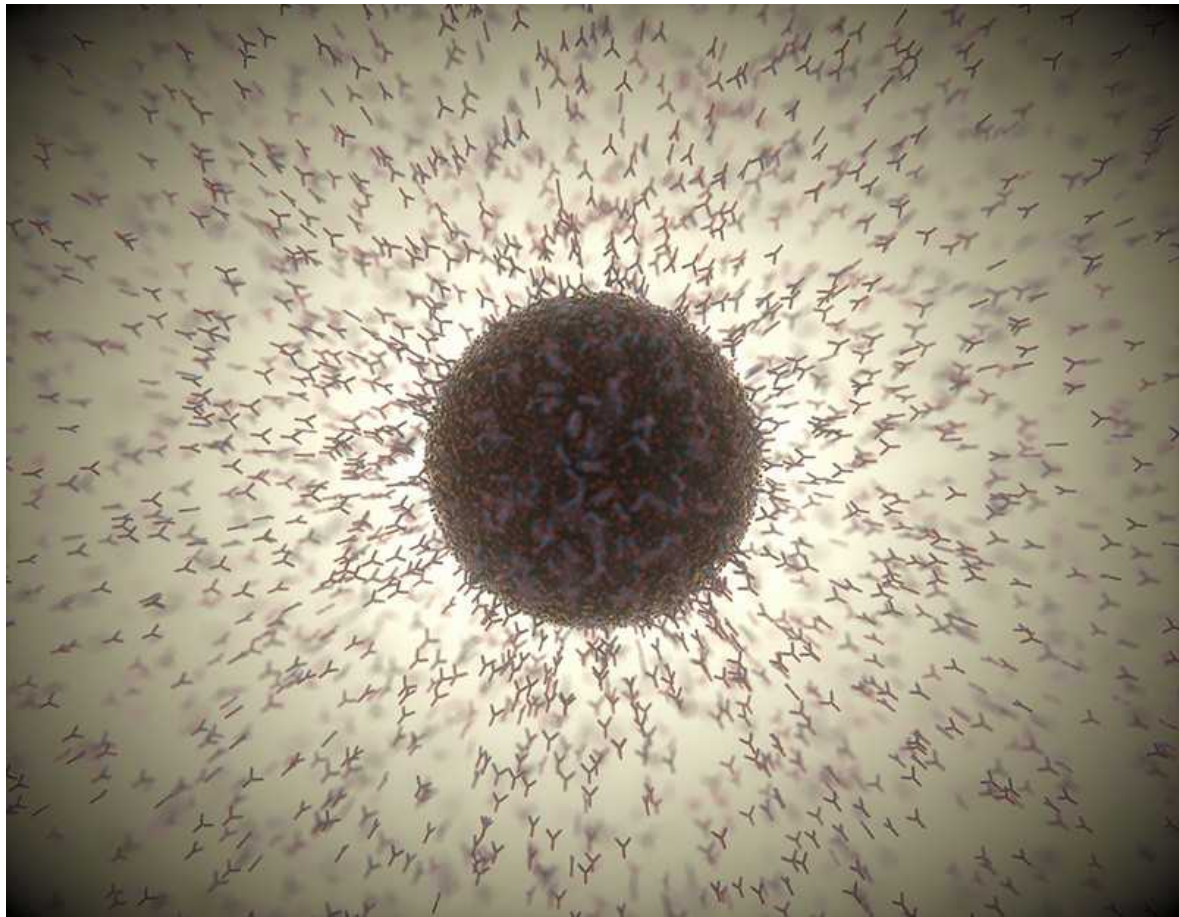
The latest science news, in brief.





•

[Download PDF](#)



Antibodies swarm a SARS-CoV-2 particle (artist's impression). A bioengineered antibody can block the virus from taking hold in the lungs of mice. Credit: KTSDesign/Science Photo Library

Antibody nasal spray could protect against COVID

A nasal spritz of a designer antibody offers strong protection against variants of the coronavirus SARS-CoV-2 in mice ([Z. Ku et al. *Nature* https://doi.org/gkctjj; 2021](#)).

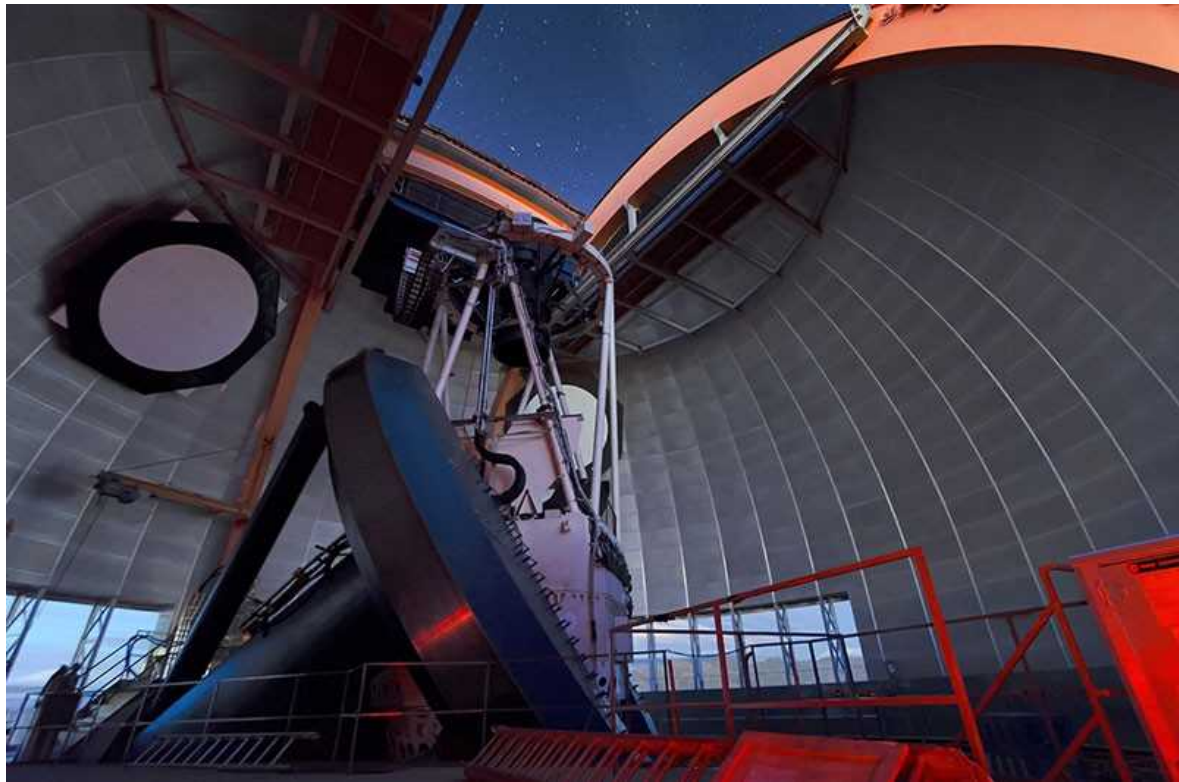
Since the early days of the pandemic, scientists have been developing antibodies as COVID-19 treatments. Today, several are in late-stage clinical trials, and a handful have been approved for emergency use.

Among doctors, however, antibody treatments have not been popular, says Zhiqiang An, an antibody engineer at the University of Texas Health Science Center at Houston. Those available are delivered intravenously rather than directly to the respiratory tract, where the virus is mainly found — so must be given in high doses.

An and his colleagues [engineered an antibody for delivery directly into the nose](#). They scanned an antibody library for those that could recognize a protein that SARS-CoV-2 uses to enter cells. Among the promising candidates were IgG antibodies.

The team stitched these IgG fragments to IgM antibodies, which act as first responders to many infections. The engineered IgMs had a much stronger ‘neutralizing’ effect on more than 20 variants of SARS-CoV-2 than did the IgGs alone. Squirted into the noses of mice six hours before or six hours after infection, the engineered IgMs sharply reduced the amount of virus in the rodents’ lungs two days after infection.

This work is a “big feat of engineering”, says Guy Gorochov, an immunologist at Sorbonne University in Paris. But he says there are open questions, such as how long the antibodies will linger in humans.



Inside the dome of the Víctor M. Blanco telescope, which surveyed the Southern Hemisphere sky between 2013 and 2019. Credit: CTIO/NOIRLab/NSF/AURA/D. Munizaga

The most detailed 3D map of the Universe ever made

A survey of the southern sky has reconstructed how mass is spread across space and time in the [biggest study of its kind](#).

The Dark Energy Survey (DES) collaboration observed the sky between 2013 and 2019 using a 570-megapixel camera at the Víctor M. Blanco telescope at the Cerro Tololo Inter-American Observatory in Chile. The survey covered one-quarter of the southern sky, and its exposures included 300 million galaxies ([N. Jeffrey et al. Mon. Not. R. Astron. Soc.](#) <https://doi.org/10.1093/mnras/stab1495; 2021>).

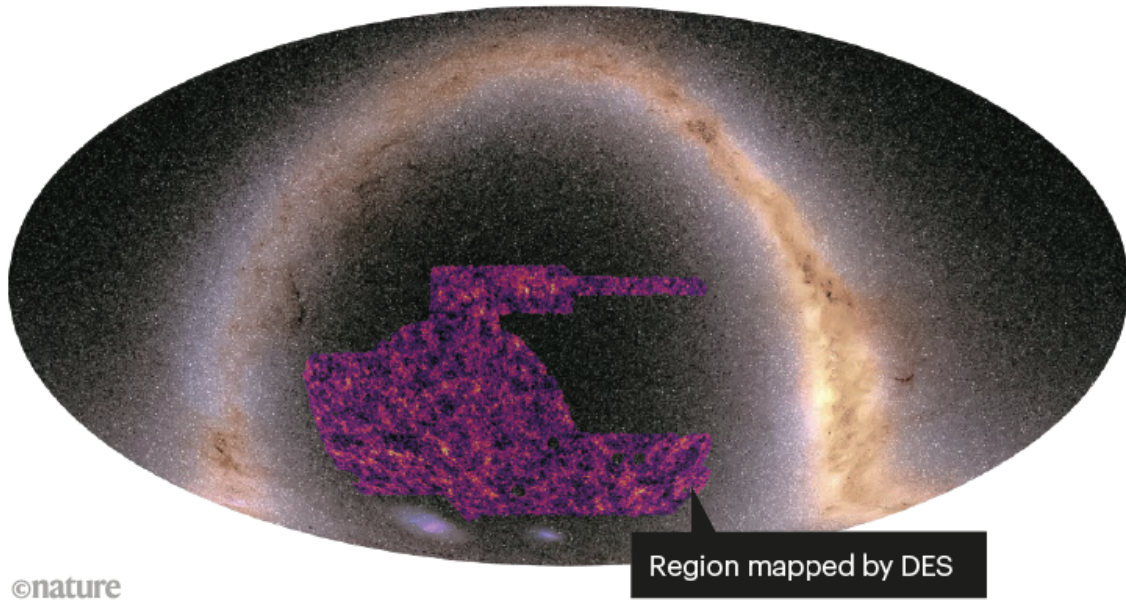
The resulting 3D cosmic map provides a record of the Universe's history. By tracking how galaxies spread out over time, researchers can measure the

forces at play. These include the gravitational pull of dark matter — the invisible stuff that constitutes some 80% of the Universe's mass — and dark energy, the mysterious force that seems to be pushing the Universe to accelerate its expansion.

The data provide striking evidence that dark energy has been constant throughout cosmic history. The DES team also found the Universe to be slightly smoother than expected — confirming findings that the collaboration first reported in 2017.

DARK-MATTER MAP

The Dark Energy Survey (DES) collaboration's detailed map of dark matter covers a large, tank-shaped area in the Southern Hemisphere sky.



Credit: N. Jeffrey/Dark Energy Survey collaboration

Increased contact fuelled gamma variant's rise

The coronavirus variant behind Brazil's ferocious second wave of COVID-19 emerged, in part, because of relaxed social distancing, according to an [analysis of viral sequences](#) from the outbreak's epicentre. In late 2020, researchers first spotted the P.1 variant — also called Gamma — in people who returned to Japan from Manaus in Brazil's Amazonas state.

To chart the rise of P.1, researchers sequenced the genomes of 250 SARS-CoV-2 samples collected from across Amazonas between March 2020 and January 2021, and conducted more-limited genetic testing on hundreds of samples.

They found that the prevalence of P.1 rose with breathtaking swiftness in Amazonas. There was no sign of the variant in samples from November 2020, but it accounted for nearly three-quarters of samples by mid-January 2021 ([F. G. Naveca et al. *Nature Med.* <https://doi.org/gj6w6j>; 2021](https://doi.org/gj6w6j)). The rise of P.1 coincided with reduced social distancing in Amazonas. This might have been linked to Christmas and New Year's holidays, as well as to municipal elections in November. The researchers think that these events, combined with the variant's heightened transmissibility, helped P.1 to flourish.

Nature **594**, 155 (2021)

doi: <https://doi.org/10.1038/d41586-021-01510-0>

Jobs from Nature Careers

- - - [All jobs](#)
 -
 - [**Postdoctoral Fellow, Statistical Methodologies for Metabolomics Data Analysis**](#)
[The University of British Columbia \(UBC\)](#)
[Vancouver, Canada](#)
[JOB POST](#)
- [**Postdoctoral Fellow in River Dynamics**](#)

The University of British Columbia (UBC)

Vancouver, Canada

JOB POST

▪ **PhD Student in Wnt signaling**

German Cancer Research Center in the Helmholtz Association (DKFZ)

Heidelberg, Germany

JOB POST

▪ **Postdoc (all genders), Department Detector Laboratory (DTL)**

Helmholtz Centre for Heavy Ion Research GmbH (GSI)

Darmstadt, Germany

JOB POST

Download PDF

This article was downloaded by **calibre** from <https://www.nature.com/articles/d41586-021-01510-0>

- NEWS
- 28 May 2021

Palaeontologists hope Biden will restore protections on fossil-rich US lands

Trump's shrinking of Utah's Bears Ears and Grand Staircase-Escalante reserves may be reversed — ensuring archaeological and fossil treasures are preserved for study.

- [Freda Kreier](#)
 1. Freda Kreier
[View author publications](#)

You can also search for this author in [PubMed](#) [Google Scholar](#)





•

[Download PDF](#)



Colourful rock layers deposited over many millions of years are an excellent source of fossils in Utah's Grand Staircase-Escalante National Monument. Credit: Shutterstock

When former US president Donald Trump announced his decision to [shrink protected areas](#) loaded with important fossils and artefacts in the southwest United States, many palaeontologists were appalled — and even helped launch a court case to restore the lands. Now, incumbent President Joe Biden is taking steps to review the decision, which many scientists hope will lead to a restoration of the original reserves.

In April, Biden sent Deb Haaland, the US Secretary of the Interior, to Utah to meet scientists, tribal leaders and officials. She is expected to soon make recommendations on whether to alter the reserves' current boundaries.



[Archaeologists uneasy as Trump shrinks Bears Ears monument lands](#)

The Department of the Interior declined to comment on when exactly the results will be made public, but in a statement after the trip Haaland said: “I look forward to sharing what I heard and saw with President Biden so he has the benefit of these perspectives as we chart a path forward on the stewardship of these incredible culturally rich places.”

Many, although not all, researchers are hoping that Haaland will argue for the Bears Ears and Grand Staircase–Escalante national monuments to be fully restored or even enlarged, saying that this will protect fossils and archaeological artefacts from looters and commercial interests.

‘Nowhere better on Earth’

“The Rocky Mountain West is one of the best places in the world to hunt for fossils,” says Joe Sertich, the curator of dinosaurs at the Denver Museum of Nature & Science in Colorado. “Given the resources that are still unexplored, I think there’s a really good case for restoring the original boundaries.”

He says that for the 90-million to 70-million-year-old ecosystems he studies from the Cretaceous period, “there’s nowhere else better on Earth” for fieldwork than Grand Staircase–Escalante. Fossils of relatives of *Tyrannosaurus rex* found here recently bolstered evidence that the animals

hunted in packs¹, and around 20 [new species](#) of dinosaur in total have come from here and Bears Ears, Sertich says.

Bears Ears preserves swathes of “critically important” fossil history from the Triassic period (252 million to 201 million years ago) and Cretaceous period (145 million to 66 million years ago) that is exposed in rocks nowhere else, adds Jessica Theodor, president of the Society of Vertebrate Paleontology (SVP), which is based in McLean, Virginia, and represents some 2,000 palaeontologists globally.

This is why researchers were alarmed when Trump cleaved a total of more than 8,000 square kilometres from the monuments in late 2017, shrinking Bears Ears by 85% and Grand Staircase–Escalante by almost half. This led the SVP to join a coalition of Native American and conservation groups to sue the Trump administration. The lawsuit has yet to be judged upon, but it may no longer be necessary if the cuts to the monuments are reversed.



Fossils are swaddled in protective plaster jackets at a dig in Grand Staircase-Escalante that yielded evidence some tyrannosaurs may have lived in groups.Credit: Dr Alan Titus/AP/Shutterstock

Fossil poaching risk

Trump's move opened up public land that was previously protected by its national monument status to ranching and resource extraction, including coal and uranium mining. The decision also removed certain protections that had been afforded to fossils, exposing invertebrate and plant fossils to risk of 'casual collection' according to [one report](#).

The rangers and resources afforded to national monuments make them better equipped than most public lands to guard fossil beds, and by removing land from the monuments, Trump made some sites vulnerable to looting. In 2018, *The Washington Post* reported that "extremely rare" vertebrate fossils from the Triassic period had been [removed from a fossil bed](#) now outside Bears Ears boundaries.

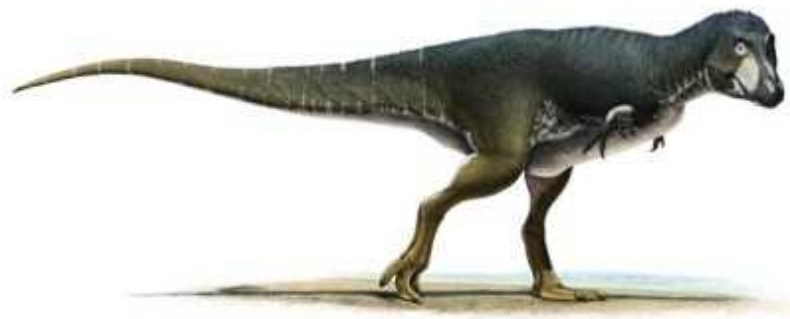
Kevin Madalena, an independent geologist who works on Indigenous land issues in the region, met with Haaland during her visit in April. He says that looting of cultural and fossil sites is an ongoing problem in the region and that areas excised from the monuments are at greater risk than areas still protected by national monument status. Given that fossils of dinosaurs such as *T. rex* routinely sell at auction for millions of dollars, scientists are concerned that, without adequate protection, important specimens could be lost to science.

Shrinking the monuments has also had other effects. Sertich, who has worked on fossil digs at Grand Staircase-Escalante for 17 years, says that he hasn't seen direct evidence of increased looting or vandalism, but has noticed more four-wheel-drive traffic.

Madalena, who is Jemez Pueblo, one of the tribes with cultural ties to the region, says the biggest threat could be from resource extraction. Mining and oil-drilling leases were expedited during the Trump administration, he says. "I was kind of staggered. It seemed like flame stacks doubled overnight."

Irreplaceable data on prehistory

But not all researchers agree that monument status is essential for protecting or advancing scientific research on public land. “We already have laws protecting fossils on federal lands,” says Brooks Britt, a palaeontologist at Brigham Young University in Provo, Utah, and a member of the Bears Ears National Monument Advisory Committee. “If things get too locked down, it can be difficult to do science,” he notes.



'King of gore' ruled before T. rex

Speaking outside his capacity as a council member, Britt says that research on public lands can be hindered by onerous restrictions and requirements for government permits, and that national monument status is not always necessary to safeguard fossil resources.

However, Theodor argues that the number of palaeontologists not in favour of restoring Bears Ears and Grand Staircase–Escalante to Obama-era boundaries are “vanishingly small”.

Researchers aren’t sure what the recommendations from Haaland — who is Laguna Pueblo, another tribe with ties here — will look like, but most expect that the review will call for at least a partial enlargement of the monument boundaries.

Former SVP president David Polly, a palaeontologist at Indiana University Bloomington, says he thinks it’s a “logical conclusion” for Grand Staircase–

Escalante. Madalena is also hopeful, adding “there’s irreplaceable data from past environments that needs to be preserved”.

Nature **594**, 157-158 (2021)

doi: <https://doi.org/10.1038/d41586-021-01445-6>

References

1. 1.

Titus, A. L. *et al.* *PeerJ* **9**, e11013 (2021).

[PubMed](#) [Article](#) [Google Scholar](#)

[Download references](#)

Jobs from Nature Careers

- - - [All jobs](#)
 - - **[Postdoctoral Fellow, Statistical Methodologies for Metabolomics Data Analysis](#)**
[The University of British Columbia \(UBC\)](#)
[Vancouver, Canada](#)
[JOB POST](#)
 - **[Postdoctoral Fellow in River Dynamics](#)**
[The University of British Columbia \(UBC\)](#)

[Vancouver, Canada](#)

[JOB POST](#)

- [PhD Student in Wnt signaling](#)

[German Cancer Research Center in the Helmholtz Association \(DKFZ\)](#)

[Heidelberg, Germany](#)

[JOB POST](#)

- [Postdoc \(all genders\), Department Detector Laboratory \(DTL\)](#)

[Helmholtz Centre for Heavy Ion Research GmbH \(GSI\)](#)

[Darmstadt, Germany](#)

[JOB POST](#)

[Download PDF](#)

Related Articles

-  ['King of gore' ruled before T. rex](#)
-  [Carnivorous-dinosaur auction reflects rise in private fossil sales](#)



- **Archaeologists uneasy as Trump shrinks Bears Ears monument lands**

This article was downloaded by **calibre** from <https://www.nature.com/articles/d41586-021-01445-6>

| [Section menu](#) | [Main menu](#) |

- NEWS
- 04 June 2021

A complete human genome sequence is close: how scientists filled in the gaps

Researchers added 200 million DNA base pairs and 115 protein-coding genes — but they've yet to entirely sequence the Y chromosome.

- [Sara Reardon](#)
 1. Sara Reardon
[View author publications](#)

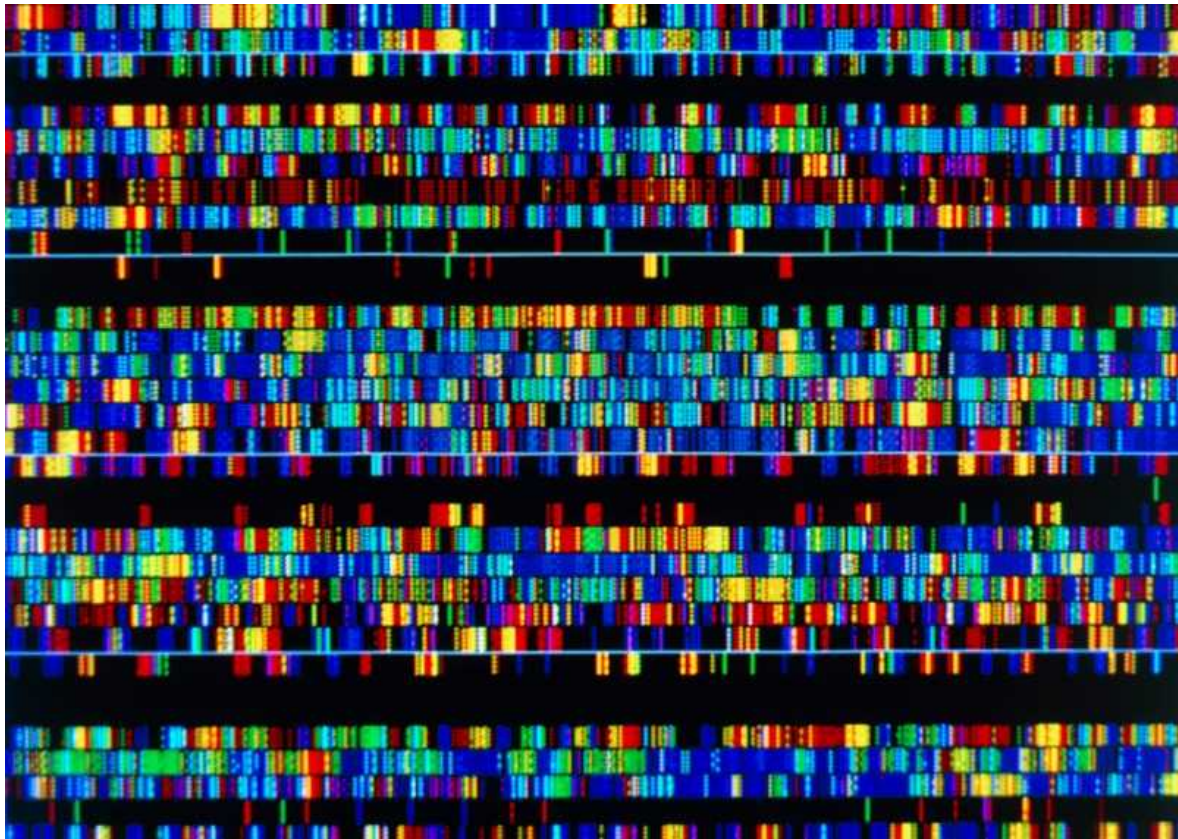
You can also search for this author in [PubMed](#) [Google Scholar](#)





•

[Download PDF](#)



Visualization of sections of the human genome sequence at the Wellcome Sanger Institute near Cambridge, UK. Credit: James King-Holmes/Science Photo Library

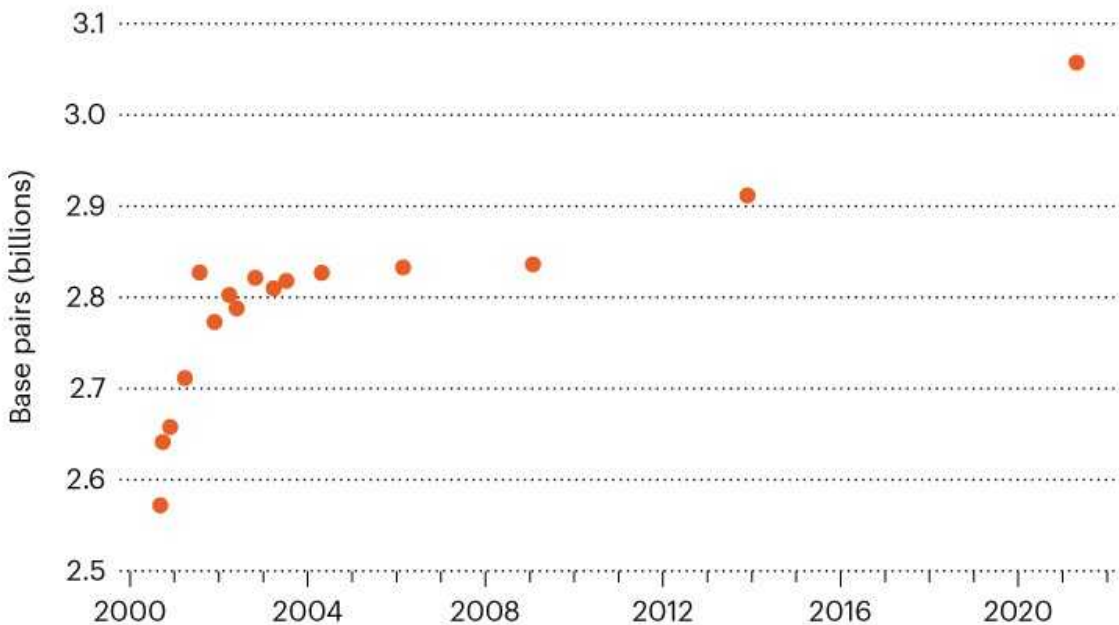
When the sequencing of the human genome was announced two decades ago by the Human Genome Project and biotech firm Celera Genomics, the sequence was not truly complete. About 15% was missing: technological limitations left researchers unable to work out how certain stretches of DNA fitted together, especially those where there were many repeating letters (or base pairs). Scientists [solved some of the puzzle over time](#), but the most recent human genome, which geneticists have used as a reference since 2013, still lacks 8% of the full sequence.

Now, researchers in the Telomere-to-Telomere (T2T) Consortium, an international collaboration that comprises around 30 institutions, have filled in those gaps. In a 27 May preprint¹ entitled ‘The complete sequence of a human genome’, genomics researcher Karen Miga at the University of California, Santa Cruz, and her colleagues report that they’ve sequenced the

remainder, in the process discovering about 115 new genes that code for proteins, for a total of 19,969.

COMPLETING THE HUMAN GENOME

Researchers have been filling in incompletely sequenced parts of the human reference genome for 20 years, and have now almost finished it, with 3.05 billion DNA base pairs.



“It’s exciting to have some resolution to the problem areas,” says Kim Pruitt, a bioinformatician at the US National Center for Biotechnology Information in Bethesda, Maryland, who calls the result a “significant milestone”.

New sequencing technology

The newly sequenced genome — dubbed T2T-CHM13 — adds nearly 200 million base pairs to the 2013 version of the human genome sequence.

This time, instead of taking DNA from a living person, the researchers used a cell line derived from what’s known as a complete hydatidiform mole, a type of tissue that forms in humans when a sperm inseminates an egg with

no nucleus. The resulting cell contains chromosomes only from the father, so the researchers don't have to distinguish between two sets of chromosomes from different people.

Miga says the feat probably wouldn't have been possible without new sequencing technology from Pacific Biosciences in Menlo Park, California, which uses lasers to scan long stretches of DNA isolated from cells — up to 20,000 base pairs at a time. Conventional sequencing methods read DNA in chunks of only a few hundred base pairs at a time, and researchers reassemble these stretches like puzzle pieces. The larger pieces are much easier to put together, because they are more likely to contain sequences that overlap.

T2T-CHM13 is not the last word on the human genome, however. The T2T team had trouble resolving a few regions on the chromosomes, and estimates that about 0.3% of the genome might contain errors. There are no gaps, but Miga says quality-control checks have proved difficult in those areas. And the sperm cell that formed the hydatidiform mole carried an X chromosome, so the researchers have not yet sequenced a Y chromosome, which typically triggers male biological development.

Hundreds of genomes to follow

T2T-CHM13 represents only one person's genome. But the T2T Consortium has teamed up with a group called the Human Pangenome Reference Consortium, which aims over the next 3 years to sequence more than 300 genomes from people all over the world. Miga says that the teams will be able to use T2T-CHM13 as a reference to understand which parts of the genome tend to differ between individuals. They also plan to sequence an entire genome that contains chromosomes from both parents, and Miga's group has been working on sequencing the Y chromosome, using the same new methods to help fill gaps.

Miga expects that genetics researchers will quickly find out whether any of the newly sequenced areas and possible genes are associated with human diseases. "When the human genome came out, we didn't have the tools poised and ready to go," she says, but information about the function of the

newly sequenced genes should come much faster now, because “we’ve built up a ton of resources”.

She hopes that future human genome sequences will cover everything, including the newly sequenced sections — not just the parts that are easy to read. This should be easier now that the reference genome has been completed and some of the technical snags have been worked out. “We need to reach a new standard in genomics where this isn’t special, but routine,” she says.

Nature **594**, 158-159 (2021)

doi: <https://doi.org/10.1038/d41586-021-01506-w>

References

1. 1.

Nurk, S. *et al.* Preprint at bioRxiv
<https://doi.org/10.1101/2021.05.26.445798> (2021).

[Download references](#)

Jobs from Nature Careers

- - - [All jobs](#)
 - - **Postdoctoral Fellow, Statistical Methodologies for Metabolomics Data Analysis**

[The University of British Columbia \(UBC\)](#)
[Vancouver, Canada](#)

JOB POST

- **Postdoctoral Fellow in River Dynamics**

The University of British Columbia (UBC)

Vancouver, Canada

JOB POST

- **PhD Student in Wnt signaling**

German Cancer Research Center in the Helmholtz Association (DKFZ)

Heidelberg, Germany

JOB POST

- **Postdoc (all genders), Department Detector Laboratory (DTL)**

Helmholtz Centre for Heavy Ion Research GmbH (GSI)

Darmstadt, Germany

JOB POST

Download PDF

Related Articles

-  **Human genomics: the genome finishers**

-  [New human gene tally reignites debate](#)
-  [How diplomacy helped to end the race to sequence the human genome](#)
-  [Twenty-five years of big biology](#)

This article was downloaded by **calibre** from <https://www.nature.com/articles/d41586-021-01506-w>

| [Section menu](#) | [Main menu](#) |

- NEWS
- 27 May 2021

Elite US science academy expels astronomer Geoff Marcy following harassment complaints

This is the first time the National Academy of Sciences has kicked out a member for violating its amended code of conduct.

- [Nidhi Subbaraman](#)

1. Nidhi Subbaraman
[View author publications](#)

You can also search for this author in [PubMed](#) [Google Scholar](#)





•

[Download PDF](#)



Geoffrey Marcy resigned in 2015 from the University of California, Berkeley, where an investigation had found him guilty of sexual harassment. Credit: Nikas Halle'n/AFP via Getty

The US National Academy of Sciences (NAS) has terminated astronomer Geoffrey Marcy's membership, in light of sexual-harassment complaints — the first time the respected group has expelled a member.

The action comes two years after the NAS [introduced a code of conduct](#) that would allow the organization to expel members “for the most egregious violations ... including for proven cases of sexual harassment”.



The US National Academy of Sciences can now kick out harassers. So why hasn't it?

The 158-year-old academy changed its by-laws following pressure from the scientific community and after the #MeToo movement, which highlighted pervasive workplace harassment and institutional failures to prevent it. In 2018, a report by the US National Academies of Sciences, Engineering, and Medicine warned that [sexual harassment is widespread in academic science](#).

Marcy, an exoplanet researcher, [resigned from his tenured position](#) at the University of California, Berkeley, in 2015, [after BuzzFeed News reported](#) that a university investigation had found that he had broken sexual-harassment policies in several cases over nearly a decade, until 2010.

Responding to his NAS expulsion, [Marcy told ScienceInsider](#) that he has been “completely out of organized academia for over 5 years”, and that he “always supported equal opportunity and success for women in academia and science”.

“My engaging and empathic style could surely be misinterpreted, which is my fault for poor communication,” he said. “I would never intentionally hurt anyone nor cause distress.” (Marcy did not respond to *Nature*’s request for comment.)

US science academy leaders approve plan to expel sexual harassers

Last September, *Nature* reported that despite the NAS's by-law amendment, [the organization was yet to expel any harassers](#), even though there were public reports of investigations and findings involving current members. NAS president Marcia McNutt told *Nature* at the time that the organization requires a complaint be filed before it can adjudicate on a member's status, and that no complaints had been filed.

That report prompted François-Xavier Coudert, a chemist at the French national research agency CNRS in Paris, to e-mail the organization and file complaints about four scientists, including Marcy, citing findings of inappropriate behaviour that had been reported in the press. "I found it was ridiculous as an argument for the academy to say, 'We have a policy, but no one is filing a complaint,'" says Coudert. He had previously posted about the *Nature* story on Twitter; McNutt replied, [urging him to take action](#).

"The NAS has chosen a policy that is very weak and that protects them in a way," says Coudert.

The academy has said in the past that it does not have the resources for formal investigations, outside of internal NAS business. The group relies on publicly documented investigations carried out by other organizations to begin inquiries into its members.

The NAS this week informed Coudert of Marcy's termination, which the chemist says is a preliminary step in the right direction.



Sexual harassment is rife in the sciences, finds landmark US study.

Membership of the highly selective NAS is regarded as a top honour in US science, burnishing the profile of elected members. It also confers a degree of influence — the group is regularly tapped by US agencies to offer scientific views on national affairs.

Seyda Ipek, a theoretical particle physicist at the University of California, Irvine, also submitted a complaint last September, including public details of harassment investigations and findings concerning Marcy. “It’s really important to not allow these people in these prestigious communities, because they are doing bad things for science,” says Ipek. She says she was surprised and angry to learn that scientists continued to collaborate with the astronomer, pointing out that manuscripts posted on the arXiv preprint server in the past six months [still listed Marcy](#) as a co-author. “Where is the justice for women pushed out of the field if people continue to work with him?”

Some of those papers point to Berkeley as Marcy’s affiliation. A Berkeley spokesperson says that Marcy is currently a retired professor at the university, and that University of California policy allows retirees to refer to themselves as emeritus faculty members at those institutions. They added that the university’s 2015 announcement of Marcy’s resignation was accurate at that time.

A spokesperson for the NAS confirmed that Marcy's membership had been rescinded as of 24 May. They did not say how many other members were under review as a result of sexual-harassment complaints.

Nature **594**, 159-160 (2021)

doi: <https://doi.org/10.1038/d41586-021-01461-6>

Jobs from Nature Careers

- - - [All jobs](#)
 -
 - [Postdoctoral Fellow, Statistical Methodologies for Metabolomics Data Analysis](#)
[The University of British Columbia \(UBC\)](#)
[Vancouver, Canada](#)
[JOB POST](#)
 - [Postdoctoral Fellow in River Dynamics](#)
[The University of British Columbia \(UBC\)](#)
[Vancouver, Canada](#)
[JOB POST](#)
 - [PhD Student in Wnt signaling](#)
[German Cancer Research Center in the Helmholtz Association \(DKFZ\)](#)

Heidelberg, Germany.

JOB POST

- [Postdoc \(all genders\), Department Detector Laboratory \(DTL\)](#)

[Helmholtz Centre for Heavy Ion Research GmbH \(GSI\)](#)

Darmstadt, Germany

JOB POST

[Download PDF](#)

Related Articles



- [The US National Academy of Sciences can now kick out harassers. So why hasn't it?](#)

- [US science academy leaders approve plan to expel sexual harassers](#)



- [Sexual harassment is rife in the sciences, finds landmark US study](#)



- [NIH's new sexual-harassment rules are still too weak, say critics](#)

This article was downloaded by **calibre** from <https://www.nature.com/articles/d41586-021-01461-6>

| [Section menu](#) | [Main menu](#) |

- NEWS
- 27 May 2021
- Clarification [28 May 2021](#)

Hundreds of gibberish papers still lurk in the scientific literature

The nonsensical computer-generated articles, spotted years after the problem was first seen, could lead to a wave of retractions.

- [Richard Van Noorden](#)
 1. Richard Van Noorden
[View author publications](#)

You can also search for this author in [PubMed](#) [Google Scholar](#)





•

[Download PDF](#)

Nonsensical research papers generated by a computer program are still popping up in the scientific literature many years after the problem was first seen, a study has revealed¹. Some publishers have told *Nature* they will take down the papers, which could result in more than 200 retractions.

The issue [began in 2005](#), when three PhD students created paper-generating software called SCIGen for “maximum amusement”, and to show that some conferences would accept meaningless papers. The program cobbles together words to generate research articles with random titles, text and

charts, easily spotted as gibberish by a human reader. It is free to download, and anyone can use it.

By 2012, computer scientist Cyril Labb   had found 85 fake SCIGen papers in conferences published by the Institute of Electrical and Electronic Engineers (IEEE); he went on to find [more than 120 fake SCIGen papers published by the IEEE and by Springer²](#). It was unclear who had generated the papers or why. The articles were subsequently retracted — or sometimes deleted — and Labb   [released a website](#) allowing anyone to upload a manuscript and check whether it seems to be a SCIGen invention. Springer also sponsored a PhD project to help spot SCIGen papers, which resulted in free software called [SciDetect](#). (Springer is now part of Springer Nature; *Nature*'s news team is editorially independent of its publisher.)



[The fight against fake-paper factories that churn out sham science](#)

Labb  , who works at the University of Grenoble Alpes in France, originally searched manuscripts for words typical of SCIGen's vocabulary. But he and another computer scientist, Guillaume Cabanac at the University of Toulouse, France, came up with a new idea: searching for key grammatical phrases characteristic of SCIGen's output. Last May, he and Cabanac searched for such phrases in millions of papers indexed in the Dimensions database.

After manually inspecting every hit, the researchers identified 243 nonsense articles created entirely or partly by SCIGen, they report in a study published on 26 May¹. These articles, published between 2008 and 2020, appeared in various journals, conference proceedings and preprint sites, and were mostly in the computer-science field. Some appeared in open-access journals; others were paywalled. Forty-six of them had already been retracted or deleted from the websites where they were first published.

Since last year, the researchers have added another 20 papers to their list, including gibberish articles created by MATHgen (software that generates mathematics papers) and the SBIR proposal generator (which creates nonsense grant proposals). Cabanac and Labbé have posted some of their findings on Twitter and the post-publication peer review website PubPeer, and they are releasing their [full results online](#).

CV padding

Most of the latest batch of SCIGen papers were authored by researchers from China (64%) or India (22%), although Labbé notes that the manuscripts could have been submitted in anyone's name without their knowledge. One author of several of the papers told Labbé and Cabanac that he'd submitted them as hoaxes. But other manuscripts appear to have been edited with genuine reference lists, suggesting that they might have been generated to inflate scientists' citation counts. "I think the vast majority are created to pad CVs in order to fulfil a need to publish papers," says Labbé.

The researchers found only two SCIGen papers that hadn't been retracted at IEEE — which is evaluating both of them — and one Springer paper that included a fragment of MATHgen text. But other publishers were caught out more badly. IOP Publishing, a subsidiary of the London-based Institute of Physics, says it retracted ten papers "as there was clear evidence they had been computer-generated" and is investigating why they weren't identified during peer review at the conference where they were accepted. "We have reasonable evidence to suggest that the peer review process for some of these papers was compromised," says Kim Eggleton, the publisher's integrity and inclusion manager.

The publishers who posted the most SCIGen content were Trans Tech Publications, a Swiss publisher, which published 57 SCIGen papers, Blue Eyes Intelligence Engineering and Sciences Publication (BEIESP), based in India, which had 54; and Atlantis Press, a French publisher that was acquired by Springer Nature this March, with 39. Both Trans Tech Publications and Atlantis told *Nature* that they were investigating and were in the process of retracting the articles, but a spokesperson for BEIESP said that it published only articles with original content that passed double-blind peer review and plagiarism checks.



[Hundreds of extreme self-citing scientists revealed in new database](#)

The popular SSRN preprint server, where papers are shared before peer review, had published 16 SCIGen articles, the study found. A spokesperson for SSRN said it was investigating the issue, and noted that it provided “limited screening” for its preprints (with “advanced screening” for health-care manuscripts).

Cabanac is concerned by the non-transparent way in which some publishers deal with such papers. The IEEE, for instance, has wiped some SCIGen papers off its website, but left formal retraction notices for others. Cabanac also notes that research papers — or earlier versions of them — sometimes disappear from the SSRN preprint server, without such changes being recorded.

An IEEE spokesperson said that its policy on removing a paper or leaving a retraction label was “contingent on the outcome of our evaluation”; SSRN did not respond to a question about its policies on retraction or deletion.

SCIgen papers are extremely rare: Labb   and Cabanac estimate from their screen that they make up a mere 75 papers per million in the computer-science literature. They are a far smaller problem than are, for instance, suspected [paper mills](#) — which create seemingly real research papers to order for academics — which Labb   and Cabanac have also helped to uncover.

But, says Labb  , the existence of these papers is an indication of the harmful effects of a ‘publish or perish’ culture, and an example of how nonsensical work can still make it into conference proceedings or journals. “You shouldn’t find these things in the literature,” he says.

Nature **594**, 160-161 (2021)

doi: <https://doi.org/10.1038/d41586-021-01436-7>

Updates & Corrections

- **Clarification 28 May 2021:** This article has been updated to clarify a statement from IOP Publishing.

References

1. 1.

Cabanac, G. & Labb  , C. *J. Assoc. Inf. Sci. Technol.*
<https://doi.org/10.1002/asi.24495> (2021).

[Article](#) [Google Scholar](#)

2. 2.

Labb  , C. & Labb  , D. *Scientometrics* **94**, 379–396 (2013)

[Article](#) [Google Scholar](#)

[Download references](#)

[Jobs from Nature Careers](#)

- - - [All jobs](#)
 - - **[Postdoctoral Fellow, Statistical Methodologies for Metabolomics Data Analysis](#)**
[The University of British Columbia \(UBC\)](#)
[Vancouver, Canada](#)
[JOB POST](#)
 - **[Postdoctoral Fellow in River Dynamics](#)**
[The University of British Columbia \(UBC\)](#)
[Vancouver, Canada](#)
[JOB POST](#)
 - **[PhD Student in Wnt signaling](#)**
[German Cancer Research Center in the Helmholtz Association \(DKFZ\)](#)
[Heidelberg, Germany](#)
[JOB POST](#)

▪ **Postdoc (all genders), Department Detector Laboratory (DTL)**

Helmholtz Centre for Heavy Ion Research GmbH (GSI).

Darmstadt, Germany.

JOB POST

[Download PDF](#)

Related Articles



- [The fight against fake-paper factories that churn out sham science](#)



- [Hundreds of extreme self-citing scientists revealed in new database](#)
- [Publishers withdraw more than 120 gibberish papers](#)
- [Computer conference welcomes gobbledegook paper](#)

This article was downloaded by **calibre** from <https://www.nature.com/articles/d41586-021-01436-7>

- NEWS
- 04 June 2021

WHO approval of Chinese CoronaVac COVID vaccine will be crucial to curbing pandemic

CoronaVac is one of two Chinese vaccines already sustaining vaccination campaigns in more than 70 nations. Both should soon be much more widely available to low-income countries.

- [Smriti Mallapaty](#)
 1. Smriti Mallapaty
[View author publications](#)

You can also search for this author in [PubMed](#) [Google Scholar](#)





•

[Download PDF](#)



China's CoronaVac COVID-19 vaccine is already in use in the Philippines, among many other countries. Credit: Ezra Acayan/Getty

The World Health Organization (WHO) has approved a second Chinese vaccine for emergency use. CoronaVac was found to be 51% effective at preventing COVID-19 in late-stage trials, and researchers say it will be key to curbing the pandemic.

This overall protection is lower than that provided by the seven other vaccines already listed by the WHO. But, importantly, trials suggest that CoronaVac — an inactivated-virus vaccine produced by Beijing-based company Sinovac — is 100% effective at preventing severe disease and death.

“CoronaVac will significantly contribute to the global fight against COVID-19 as a safe and moderately effective SARS-CoV-2 vaccine,” says Murat Akova, a clinical researcher in infectious diseases at Hacettepe University in Ankara.

Growing importance

CoronaVac's approval, on 1 June, came about a month after the WHO [listed another Chinese vaccine](#), made in Beijing by state-owned firm Sinopharm, which showed an efficacy of 79% against symptomatic disease. Both vaccines are already used widely around the world, and are driving China's massive internal immunization campaign.

CoronaVac is sustaining vaccination campaigns in more than 40 countries, such as Chile and Botswana. Globally, more than 600 million doses have been delivered. Sinopharm's vaccine has been approved in many more nations. But WHO emergency approval could now facilitate the further distribution of both vaccines to low-income countries, through the COVID-19 Vaccines Global Access (COVAX) initiative.



[China's COVID vaccines are going global — but questions remain](#)

A spokesperson for COVAX member Gavi, the Vaccine Alliance, in Geneva, Switzerland, says: "Gavi welcomes news that [CoronaVac] has been granted WHO Emergency Use Listing, as this means the world has yet another safe and effective tool in the fight against this pandemic."

The WHO's efficacy estimate of 51% was based on data from late-stage trials among health-care workers in Brazil, posted online as a preprint¹ in April. Of the 9,823 participants included in the analysis, 253 had COVID-19

— 85 in the vaccinated group and 168 among those who received the placebo. None of the vaccinated volunteers was hospitalized or died owing to COVID-19. Smaller, late-stage trials in Indonesia and Turkey have shown higher efficacies of up to 84%.

Preliminary findings from a post-trial study of 2.5 million people in Chile estimated that CoronaVac was 67% effective at preventing COVID-19, and 80% effective at preventing death from the disease, despite the presence of the Alpha (B.1.1.7) and Gamma (P.1) variants of the virus SARS-CoV-2.

Pandemic game changer

Preliminary results detailed at a press conference in Brazil on Tuesday, from a trial in the town of Serrana, suggest that CoronaVac could make a significant dent in the pandemic. The Butantan Institute in São Paulo conducted the study, in which almost the entire adult population of Serrana was vaccinated with CoronaVac. It found that the vaccine significantly reduced cases of COVID-19, hospitalizations and deaths.

The fact that CoronaVac can protect an entire town, despite nearly 40% of the population commuting daily to areas where the pandemic was raging, is “remarkable evidence” that this vaccine could be “a game changer in controlling the pandemic”, says trial leader Ricardo Palacios, medical director of clinical research at the Butantan Institute.

Both of the approved Chinese vaccines use established technology based on inactivated virus and can be stored at fridge temperatures, which makes them easy to distribute in resource-poor settings — but these kinds of COVID-19 vaccine seem to offer less protection against the disease than do mRNA vaccines, such as that made by pharmaceutical company Pfizer in New York City and biotechnology firm BioNTech in Mainz, Germany, and the one made by biotech company Moderna in Cambridge, Massachusetts.

Technology challenge

Researchers say this could be due to the technology itself. The vaccines use a killed version of SARS-CoV-2 to induce the human body to make

antibodies against many regions of the virus. But only some of these antibodies are effective at disabling the virus, says Gagandeep Kang, a virologist at the Christian Medical College in Vellore, India, who also advises the WHO on immunization.



Mix-and-match COVID vaccines trigger potent immune response

Other platforms induce more targeted responses against specific parts of the virus, which might be why they are more effective. The mRNA vaccines encode the ‘spike’ protein that SARS-CoV-2 uses to enter cells, so they trigger high numbers of antibodies that block that protein.

Most COVID-19 vaccines are given in two doses, and studies are under way to assess whether individuals will need to get booster shots after that. This question might be especially relevant for those who receive inactivated-virus vaccines such as CoronaVac and Sinopharm’s shot because they produce fewer antibodies, scientists say. But the priority for now should be to get as many people vaccinated with their first two doses as possible, says Kang.

The other vaccines that the WHO has approved for emergency use are the Moderna and Pfizer–BioNTech shots, as well as those made by Johnson & Johnson and the University of Oxford and AstraZeneca, and a version of the Oxford–AstraZeneca vaccine known as Covishield, which is produced by the Serum Institute of India in Pune.

doi: <https://doi.org/10.1038/d41586-021-01497-8>

References

1. 1.

Palacios, R. *et al.* Preprint at SSRN
<https://doi.org/10.2139/ssrn.3822780> (2021).

[Download references](#)

[**Jobs from Nature Careers**](#)

- - - [All jobs](#)
 -
 - **[Postdoctoral Fellow, Statistical Methodologies for Metabolomics Data Analysis](#)**
[The University of British Columbia \(UBC\)](#)
[Vancouver, Canada](#)
[JOB POST](#)
 - **[Postdoctoral Fellow in River Dynamics](#)**
[The University of British Columbia \(UBC\)](#)
[Vancouver, Canada](#)
[JOB POST](#)
 - **[PhD Student in Wnt signaling](#)**

German Cancer Research Center in the Helmholtz Association (DKFZ)

Heidelberg, Germany

JOB POST

- [Postdoc \(all genders\), Department Detector Laboratory \(DTL\)](#)

Helmholtz Centre for Heavy Ion Research GmbH (GSI)

Darmstadt, Germany

JOB POST

[Download PDF](#)

Related Articles

-  [China's COVID vaccines are going global — but questions remain](#)
-  [China's coronavirus vaccine shows military's growing role in medical research](#)
-  [China COVID vaccine reports mixed results — what does that mean for the pandemic?](#)

This article was downloaded by **calibre** from <https://www.nature.com/articles/d41586-021-01497-8>

| [Section menu](#) | [Main menu](#) |

- NEWS
- 01 June 2021

Coronavirus variants get Greek names — but will scientists use them?

From Alpha to Omega, the labelling system aims to avoid confusion and stigmatization.

- [Ewen Callaway](#)
 1. Ewen Callaway
[View author publications](#)

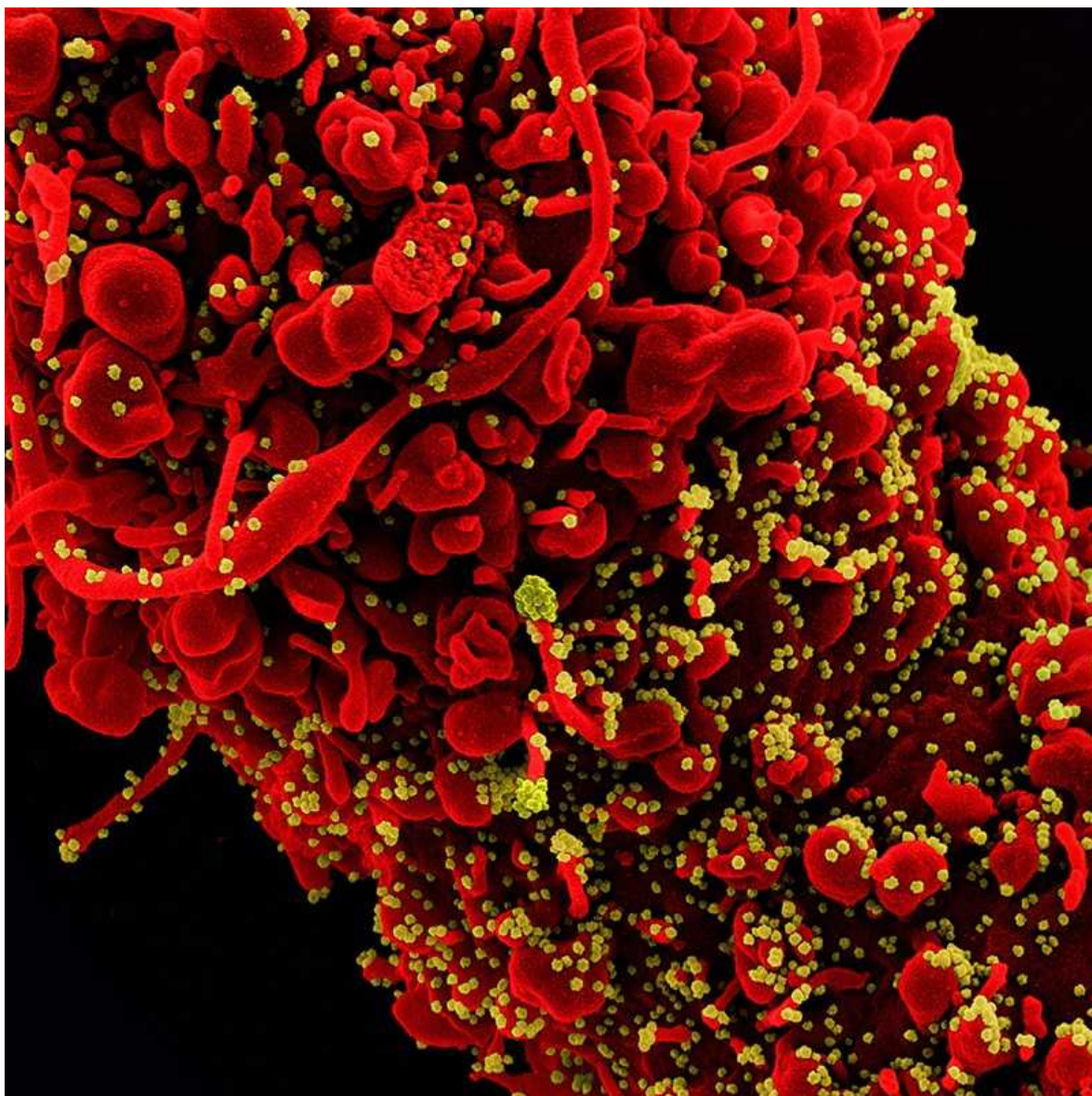
You can also search for this author in [PubMed](#) [Google Scholar](#)





•

[Download PDF](#)



Colourized scanning electron micrograph of a cell (red) infected with SARS-COV-2 virus particles (yellow). Credit: NIAID

When researchers in South Africa spotted a highly mutated strain of coronavirus driving the country's second wave in late 2020, they called it variant 501Y.V2. Naming schemes developed by other scientists have called it B.1.351, 20H/501Y.V2 and GH/501Y.V2. But many media outlets — and some scientists — describe the same virus as 'the South African variant'.

To quell such confusion and avoid geographical stigmas, everyone should now just call it 'Beta', according to a naming scheme announced on 31 May

by the World Health Organization (WHO) in Geneva and described in a forthcoming article in *Nature Microbiology*.

Variants of concern

WHO label	Pango lineage	GISAID clade	Nextstrain clade	Earliest documented samples	Date of designation
Alpha	B.1.1.7	GRY	20I/S:501Y.V1	UK, Sept 2020	Dec 2020
Beta	B.1.351	GH/501Y.V2	20H/S:501Y.V2	South Africa, May 2020	Dec 2020
Gamma P.1		GR/501Y.V3	20J/S:501Y.V3	Brazil, Nov 2020	Jan 2021
Delta	B.1.617.2	G/452R.V3	21A/S:478K	India, Oct 2020	May 2021

Source: [WHO](#)

The names, taken from the Greek alphabet (see ‘Variants of concern’), are not intended to replace scientific labels, but will serve as a handy shorthand for policymakers, the public and other non-experts who are increasingly losing track of different variant names.

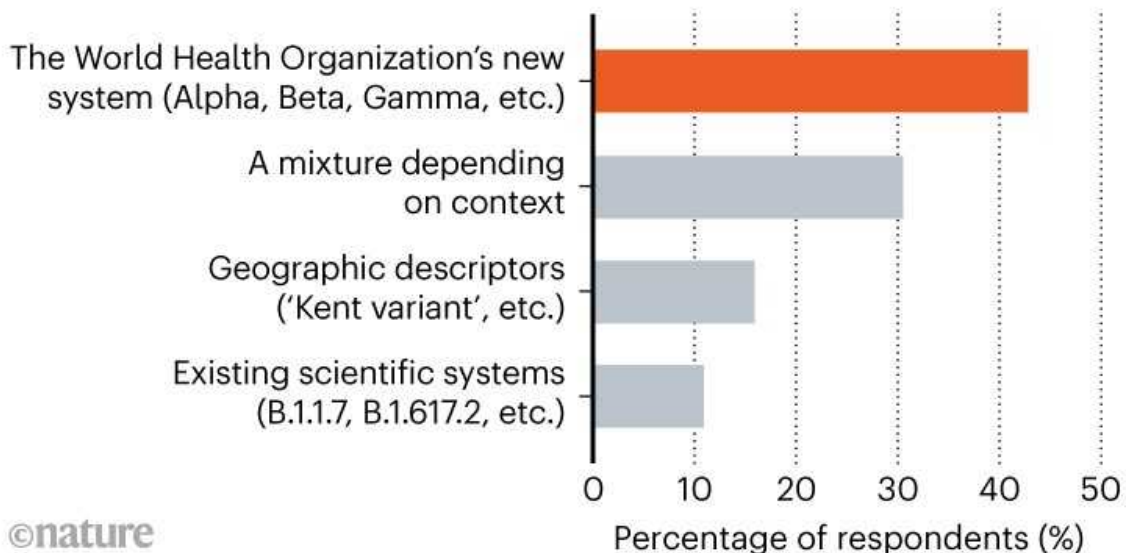
“It is a lot easier for a radio newsreader to say ‘Delta’ than bee-one-six-one-seven-two,” says Jeffrey Barrett, a statistical geneticist leading SARS-CoV-2-sequencing efforts at the Wellcome Sanger Institute in Hinxton, UK. “So I’m willing to give it a try to help it take off.”

“Let’s hope it sticks,” says Tulio de Oliveira, a bioinformatician and director of the KwaZulu-Natal Research Innovation and Sequencing Platform in Durban, South Africa, whose team identified the Beta variant. “I find the names quite simple and easy.”

The system could be especially useful in countries battling a number of variants, such as South Africa, where a variant found in the United Kingdom and known to scientists as B.1.1.7 — now called Alpha — is on the rise, and researchers such as de Oliveira are watching out for cases of the B.1.617.2 variant identified in India, now called Delta. “For a country like South Africa, to follow Beta and Alpha and keep a small eye on Delta, that will potentially be easier,” he says.

GREEK NAMING SYSTEM PREFERRED

Nature asked readers how they thought they would describe coronavirus variants in future. Of 1,362 respondents, most said they would use the new Greek naming system, or a mixture of names depending on context.



Confusion isn't the only reason to go with a simplified naming system, say advocates of the new system. Terms such as 'the South African variant' and 'the Indian variant' can stigmatize countries and their residents, and might even discourage nations from running surveillance for new variants. "The geographical names, we have to stop with that — really," says de Oliveira. He is aware of countries in Africa where health ministers have been reluctant to announce the discovery of new local variants because of concerns about being made pariahs.

"I can understand why people just call it 'the South African variant' — they don't mean anything by it," says Salim Abdool Karim, an epidemiologist at the Centre for the AIDS Program of Research in South Africa in Durban. "The problem is, if we allow it to continue, there are people who have an agenda and will use it."

Barrett intends to embrace the new naming system in media appearances, but he suspects geographical descriptors won't go away quickly. "The reason we use country names (which is problematic) is that it ties the variants to the story of the pandemic in a way that's easier to remember," he wrote in an e-mail to *Nature*. "The new system is still very anonymous and it will still be hard for the public to remember who's who."

In recent months, most scientists have settled on a single lineage-naming system that describes the evolutionary relationships between variants. With time, the WHO's naming system might gain the same currency among the general public, says Jeremy Kamil, a virologist at Louisiana State University Health in Shreveport. "If people use it, it will become the default."

Nature **594**, 162 (2021)

doi: <https://doi.org/10.1038/d41586-021-01483-0>

Jobs from Nature Careers

- - - [All jobs](#)
 -

- **Postdoctoral Fellow, Statistical Methodologies for Metabolomics Data Analysis**

The University of British Columbia (UBC)

Vancouver, Canada

JOB POST

- **Postdoctoral Fellow in River Dynamics**

The University of British Columbia (UBC)

Vancouver, Canada

JOB POST

- **PhD Student in Wnt signaling**

German Cancer Research Center in the Helmholtz Association (DKFZ)

Heidelberg, Germany

JOB POST

- **Postdoc (all genders), Department Detector Laboratory (DTL)**

Helmholtz Centre for Heavy Ion Research GmbH (GSI)

Darmstadt, Germany

JOB POST

Download PDF

Related Articles

-  [**‘A bloody mess’: Confusion reigns over naming of new COVID variants**](#)
- [**What the science says about lifting mask mandates**](#)
-  [**What scientists know about new, fast-spreading coronavirus variants**](#)

This article was downloaded by **calibre** from <https://www.nature.com/articles/d41586-021-01483-0>

| [Section menu](#) | [Main menu](#) |

- NEWS Q&A
- 26 May 2021

The COVID vaccine pioneer behind southeast Asia's first mRNA shot

ChulaCov19 designer Kiat Ruxrungtham talks about his aim to make Thailand an mRNA vaccine hub, and the challenge of competing with bigger rivals.

- [Smriti Mallapaty](#)
 1. Smriti Mallapaty
[View author publications](#)

You can also search for this author in [PubMed](#) [Google Scholar](#)





•

[Download PDF](#)



Kiat Ruxrungtham led the design of Thailand's ChulaCov19 mRNA vaccine. Credit: Diego Azubel/EPA-EFE/Shutterstock

Thailand is about to launch human trials of its first mRNA COVID-19 vaccine. If it is successful, the country could emerge as an important supplier of mRNA vaccines in Asia, making it a small but significant player in the dash to [adopt the new technology](#).

Last year saw the launch of the first viable vaccines that use messenger RNA to prompt an immune response, one developed by Pfizer in New York City and BioNTech in Mainz, Germany, and the other by Moderna in Cambridge, Massachusetts. These have proven [highly effective](#) against COVID-19, and have so far been given to hundreds of millions of people.

In Asia, home-grown mRNA vaccines are already undergoing trials in China, India and Japan. Thailand is a relative newcomer, but its efforts have increased in urgency as its neighbouring nations across south and southeast Asia suffer both vaccine shortages and [renewed COVID-19 surges](#). Thailand is now recording about 3,500 new infections a day — its biggest spike since the pandemic began.

Nature spoke to immunologist Kiat Ruxrungtham, founder of the Chula Vaccine Research Center at Chulalongkorn University in Bangkok, about his team's COVID-19 vaccine, called ChulaCov19.

What motivated you to develop your own vaccine?

During the H1N1 influenza pandemic in 2009–10, it took more than a year for Thailand to get vaccines. We wanted to develop and manufacture our own so that when a new pandemic hit, we wouldn't have to wait. We might be too late to fill the gap in the Thai market with our first-generation COVID-19 vaccine, but we have a chance to compete with second- and third-generation vaccines against emerging variants. Our goal is to produce enough to supply Thailand, and possibly also our neighbours, at an affordable price.

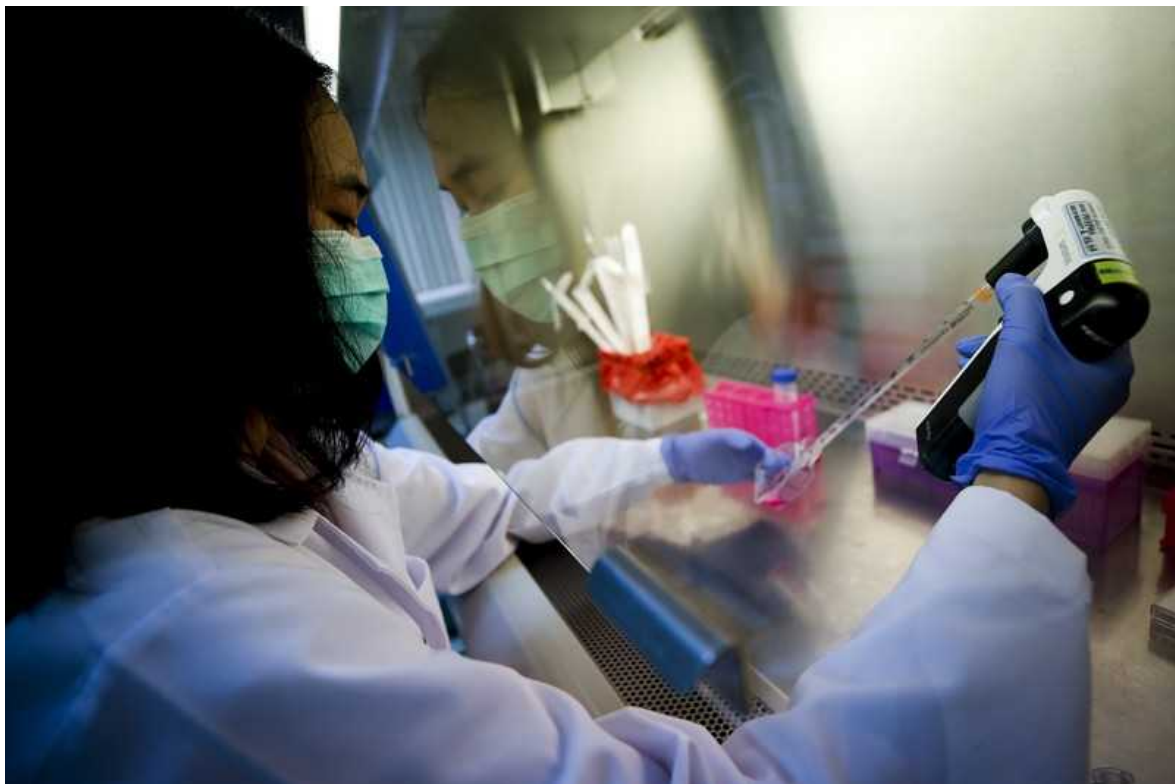
What inspired the shift to mRNA technology?

I founded my vaccine-research laboratory more than a decade ago and we have been developing vaccines against dengue fever, leptospirosis and cancer using many different technologies. In 2017, we invited the pioneer of mRNA technology, Drew Weissman at the University of Pennsylvania in Philadelphia, to speak at our annual forum. We then began working with Weissman on mRNA vaccines for allergies. But when the pandemic hit, we decided to focus on designing a COVID-19 vaccine instead.

The beauty of [mRNA vaccines](#) is that they are quicker to produce and can be made at large scales, which reduces their cost in the long run. These vaccines use small pieces of genetic material — mRNA — to tell cells to make specific viral proteins, such as the spike protein that SARS-CoV-2 uses to enter host cells. They can be developed rapidly using information about a virus's genomic sequence, which means that we don't need to wait until emerging variants enter Thailand to begin developing vaccines against them.

Tell me about your progress so far.

ChulaCov19 has shown promising results in unpublished preclinical studies in mouse and primate models. We plan to begin phase I clinical trials in people in June, and are already developing next-generation vaccines against the B.1.351 and B.1.1.7 variants of the virus. We are also keeping a close eye on B.1.617, which first emerged in India. We are happy to have come this far, but it has taken us more than a year to enter human clinical trials — almost a year behind major global pharmaceutical companies.



A technician at work at the Chula Vaccine Research Center of Chulalongkorn University in Bangkok. Credit: Diego Azubel/EPA-EFE/Shutterstock

What clinical trials are you planning?

The initial phase I trial will include some 100 people to figure out the appropriate dose for generating a good immune response. A US-based biotech company will probably produce the first batch but, by September, we plan to have the vaccines manufactured by the company BioNet-Asia in Bangkok. If the quality and results are comparable, then our locally

produced vaccines will hopefully gain the trust of the government and investors.

Once we pass this milestone, we plan to conduct phase II trials, testing the consistency of response in a few hundred volunteers, and then assessing the safety of the vaccine in some 5,000 individuals. To test efficacy, we will need to conduct phase III trials in tens of thousands of individuals.

How might you get approval for the vaccine without late-stage trials?

The World Health Organization, the US National Institutes of Health and several other organizations around the world are working to determine the level of neutralizing antibodies that a vaccine should induce to provide adequate protection. This '[correlate of protection](#)' could be used to assess efficacy without conducting late-stage trials, as is commonly done for new flu vaccines.

We have also asked colleagues in Singapore and Malaysia to send us blood samples from people vaccinated with the Pfizer–BioNTech vaccine, and we will collect samples from people in Thailand immunized with AstraZeneca's and Sinovac's vaccines. If the immune response generated by our vaccines is as good as or better than those induced by others, the Thai regulatory body might consider approving ChulaCov19 for emergency use without phase III trial results.

What have been the biggest challenges?

Funding has been a major obstacle. As we are an academic centre, the majority of support is from the government. We had interesting preclinical results as early as May 2020, but it took almost six months to get the funds to start human trials. It also took time to transfer the know-how for producing mRNA vaccines to a manufacturer in Thailand.

Would you benefit from COVID-19 vaccine patent waivers?

An agreement to [waive patent protections](#) for COVID-19 vaccines in low- and middle-income countries would be wonderful. It would allow us to use technologies that are currently unaffordable or inaccessible to us to make our vaccine even better and cheaper. But waiving patents is only the first step — you also need funding, local manufacturing capacity and access to crucial raw materials.

Nature **594**, 163 (2021)

doi: <https://doi.org/10.1038/d41586-021-01426-9>

This interview has been edited for length and clarity.

[Jobs from Nature Careers](#)

- - - [All jobs](#)
 -
 - [Postdoctoral Fellow, Statistical Methodologies for Metabolomics Data Analysis](#)

[The University of British Columbia \(UBC\)](#)
[Vancouver, Canada](#)

[JOB POST](#)
- [Postdoctoral Fellow in River Dynamics](#)

[The University of British Columbia \(UBC\)](#)

Vancouver, Canada

JOB POST

- **PhD Student in Wnt signaling**

German Cancer Research Center in the Helmholtz Association (DKFZ)

Heidelberg, Germany

JOB POST

- **Postdoc (all genders), Department Detector Laboratory (DTL)**

Helmholtz Centre for Heavy Ion Research GmbH (GSI)

Darmstadt, Germany

JOB POST

Download PDF

Related Articles



- **India's neighbours race to sequence genomes as COVID surges**



- **Can Cuba beat COVID with its homegrown vaccines?**



- **China's COVID vaccines are going global — but questions remain**

This article was downloaded by **calibre** from <https://www.nature.com/articles/d41586-021-01426-9>

| [Section menu](#) | [Main menu](#) |

- NEWS FEATURE
- 04 June 2021

Six months of COVID vaccines: what 1.7 billion doses have taught scientists

At a pivotal moment in the pandemic, *Nature* explores key questions about the vaccines that countries are racing to deliver while viral variants spread around the globe.

- [Heidi Ledford](#)
 1. Heidi Ledford
[View author publications](#)

You can also search for this author in [PubMed](#) [Google Scholar](#)





•



A campaign to vaccinate people against COVID-19 in Goma, Democratic Republic of the Congo, in May. Credit: Guerchom Ndebo/Getty

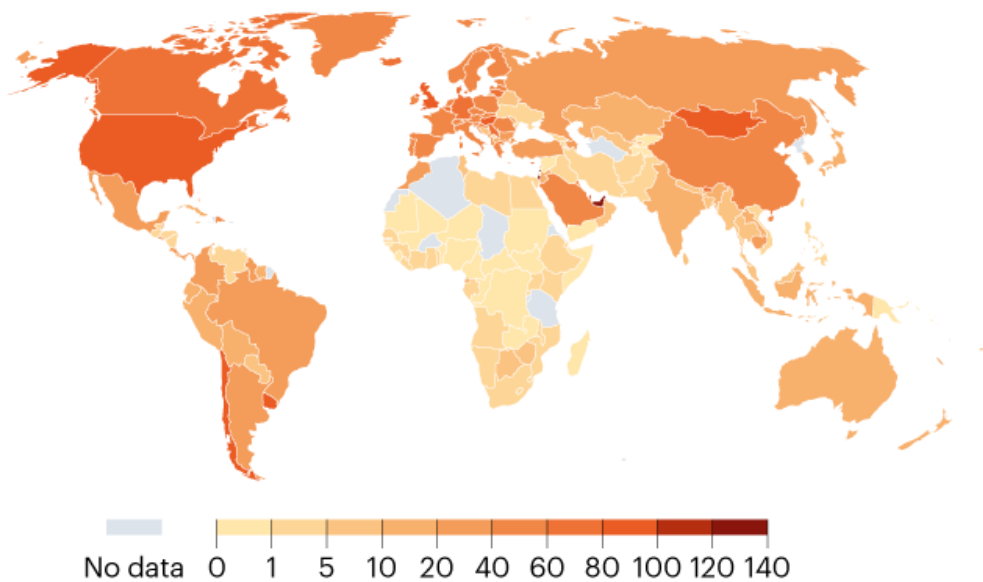
[Download PDF](#)

Over the past six months, hundreds of millions of people around the world have rushed to follow in the footsteps of a 90-year-old British woman named Margaret Keenan.

At 6:30 a.m. on 8 December 2020, Keenan became the first person to receive a COVID-19 vaccine as part of a mass vaccination effort. Her shot was the culmination of a frenzied effort to develop vaccines safely and in record time. Now, more than 1.7 billion doses later (see ‘Global doses’), researchers are sifting through the data to address lingering questions about how well the vaccines work — and how they might shape the course of the coronavirus pandemic that has already taken more than 3.5 million lives.

GLOBAL DOSES

Vaccine roll-outs are uneven across the world, as shown by the number of COVID-19 vaccine doses administered per 100 people in the total population*.



*Data as of 2 June 2021. Data don't reflect the number of people who have been vaccinated because some people have received two doses of a vaccine. Nature publications remain neutral with regard to contested jurisdictional claims in published maps.

©nature

Source: Our World in Data

“It’s absolutely astonishing that this has happened in such a short time — to me, it’s equivalent to putting a person on the Moon,” says paediatric infectious-disease specialist Cody Meissner at Tufts University School of Medicine and Tufts Children’s Hospital in Boston, Massachusetts. “This is going to change vaccinology forever.”

Nature looks at what lessons have emerged during the first six months of COVID-19 vaccinations, as well as what questions still linger. Overall, the

vaccine results have been extremely promising — even better than many had hoped — but researchers have concerns about emerging variants and the potential for immune responses to wane.

How well do the vaccines work in the real world?

Danish epidemiologist Ida Moustsen-Helms was excited in February when she first saw how well the Pfizer–BioNTech vaccine was working in health-care workers and residents of long-term care facilities, who were the first to receive it in Denmark. A clinical trial¹ in more than 40,000 people had already found the vaccine to be [95% effective in protecting recipients from symptomatic COVID-19](#). But Moustsen-Helms, who works at the Statens Serum Institut in Copenhagen, and her colleagues were among the first to test its effectiveness outside clinical trials, which can exclude some unhealthy individuals or those taking medicines that suppress immune responses.

The results² showed it was 64% effective in long-term-care residents with a median age of 84, and 90% effective in health-care workers — which struck Moustsen-Helms as good news, given that immune responses in older people can be muted. But some Danish politicians were upset by the relatively low effectiveness in older recipients. “People were saying ‘how can this be true?’” she says. “Sometimes they forget that when you look at a trial result, those individuals included in trials are very different from people in the real world.”

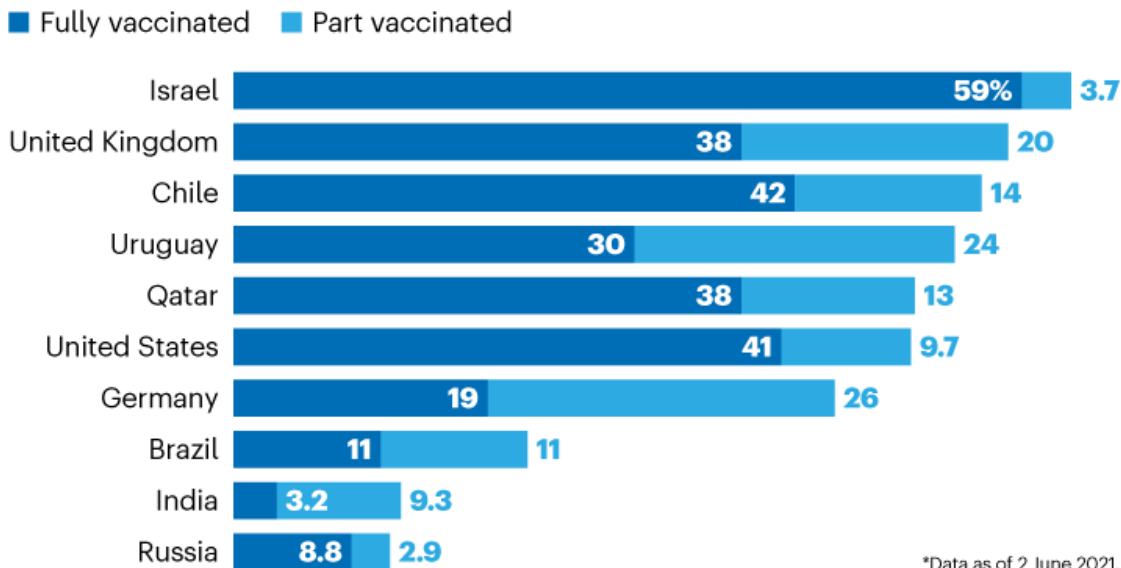


Five reasons why COVID herd immunity is probably impossible

Since then, real-world data have come in from several countries (see 'Vaccination variation'), and much of the news has continued to be positive about how well vaccines perform in the general population. A nationwide vaccination campaign in Israel found the Pfizer–BioNTech vaccine, co-developed by Pfizer in New York City and BioNTech in Mainz, Germany, to be 95% effective against SARS-CoV-2 infection seven days or more after the second dose³. The Gamaleya National Research Center of Epidemiology and Microbiology in Moscow and the Russian Direct Investment Fund announced that their Sputnik V vaccine has been [97% effective in almost 4 million people](#) in Russia. And last month, London-based Public Health England reported⁴ that the Pfizer–BioNTech and Oxford–AstraZeneca vaccines are both 85–90% effective in preventing symptomatic disease after two doses. It cautioned, however, that it had low statistical confidence in the result for the Oxford–AstraZeneca jab, developed by the University of Oxford, UK, and AstraZeneca in Cambridge, UK.

VACCINATION VARIATION

Some countries have vaccinated more than half of their populations, whereas many nations lag behind because of difficulties in obtaining doses*.



*Data as of 2 June 2021.

©nature

Source: Our World in Data

Among older adults who received the Pfizer–BioNTech vaccine, Israel has seen 94% protection from SARS-CoV-2 infection in people over 85 years old³. This is remarkably high for that age group, and considerably higher than Moustsen-Helms's result of 64%, possibly in part because long-term-care residents are prone to be in poor health. Similarly, a UK study found that the Pfizer–BioNTech and Oxford–AstraZeneca vaccines were both 80% effective at preventing COVID-19 hospitalizations in people aged 70 or older⁵. Studies are under way to see whether vaccine effectiveness can be boosted even more by [mixing and matching vaccines](#), and [early results have been promising](#). But the vaccines have already exceeded expectations, says Meissner, especially given how quickly they were developed — despite thorough safety testing in unusually large clinical trials — and the novel approaches they used. Some vaccines spend years in development, and still might not achieve this level of protection. “The efficacy of these vaccines is absolutely remarkable,” says Meissner.

At the other end of the age spectrum, Pfizer–BioNTech and Moderna in Cambridge, Massachusetts, have recently completed clinical trials of their vaccines in adolescents, showing 100% and [93% protection](#) in those aged 12–15 (ref. [6](#)) and 12–17, respectively. Real-world data are not yet available. Meissner, who is an external adviser on vaccines to the US Food and Drug Administration, questions whether children under 12 should get the vaccines before the shots have received full regulatory approval — rather than an emergency-use authorization.

How effective are the vaccines against variants?

Soon after the triumph of Keenan’s first dose, the world had a fresh reason to worry. A SARS-CoV-2 variant identified in the United Kingdom seemed to be spreading unusually fast; a different variant first identified in South Africa carried worrisome mutations in the [coronavirus spike protein that serves as the basis for most COVID-19 vaccines in use](#).

Since then, further ‘variants of concern’ have arrived in a steady parade, brandishing mutations that might boost the virus’s spread, or undermine the effectiveness of COVID-19 vaccines. “Uncontrolled outbreaks generate mutants,” says Jerome Kim, director-general of the International Vaccine Institute in Seoul.

Initial laboratory tests suggested that antibodies raised by the Pfizer–BioNTech vaccine were less effective against the B.1.351 variant identified in South Africa, but it was unclear how that would affect protection against disease. In May, [researchers in Qatar published reassuring data](#) showing that people who received two doses of the Pfizer–BioNTech vaccine were 75% less likely to develop COVID-19 from infection with B.1.351, and were almost completely protected from severe disease^{[7](#)}. “The big question right now is whether introduction of other variants could change the situation,” says study author and infectious-disease epidemiologist Laith Jamal Abu-Raddad at Weill Cornell Medicine–Qatar in Doha. “We are watching this on a daily basis, but we have optimism that maybe we have seen the worst.”



A health worker administers doses of the Oxford–AstraZeneca vaccine by the Amazon River in Brazil during a flood.Credit: Bruno Kelly/Reuters/Alamy

The Oxford–AstraZeneca vaccine did not fare as well in another test: in South Africa, a small clinical trial suggested that the vaccine did little to fend off infections of the B.1.351 variant that, by that point, was causing most infections there⁸. As a result, the South African government made the difficult decision to sell its doses and await a different vaccine. It is now rolling out the vaccine produced by Johnson & Johnson in New Brunswick, New Jersey, which in one clinical trial was 64% effective at blocking moderate to severe COVID-19 in South Africa at a time when B.1.351 constituted more than 94% of the infections in the trial⁹. And a vaccine made by Novavax in Gaithersburg, Maryland, which has not yet been authorized for emergency use, was 51% effective at preventing symptomatic COVID-19 among participants in South Africa who did not have HIV¹⁰.

But Shabir Madhi, an immunologist at the University of the Witwatersrand in Johannesburg and a lead investigator on trials of the vaccine in South

Africa, disagreed with the country's decision not to use the Oxford–AstraZeneca vaccine. There was still hope that it could protect against severe disease and death, he says — a possibility that was not tested in the trial, which enrolled mostly young participants with a low risk of severe disease. Madhi notes that a later study in hamsters¹¹ found that the vaccine prevented clinical disease caused by B.1.351.

The coronavirus SARS-CoV-2 has proved to be much more prone to mutations than researchers first thought, and more variants are emerging all the time. One variant of concern, called B.1.617.2, was first identified in India and is spreading rapidly in the United Kingdom, raising worries that it could be unusually transmissible. Public Health England has determined that two doses of either the Pfizer–BioNTech or the Oxford–AstraZeneca vaccines are 88% and 60% effective, respectively, at preventing symptomatic disease caused by this variant¹².

How long does protection against disease last?

Six months is not much time to collect data on how durable vaccine responses will be, but data could soon emerge from clinical-trial participants who had their first doses last July.

In the meantime, some researchers are looking to natural immunity as a guide. A study in more than 25,000 health-care workers in the United Kingdom found that a SARS-CoV-2 infection reduced the risk of catching the virus again by 84% for at least 7 months¹³. And Abu-Raddad says an unpublished study in Qatar is finding about 90% protection against reinfection as much as a year after a bout of SARS-CoV-2. “It seems to suggest that immunity is really strong against this virus,” he says. “I’m optimistic that vaccine immunity is going to last more than a few months and longer than a year, hopefully.”



What scientists know about new, fast-spreading coronavirus variants

But Mehul Suthar, a viral immunologist at Emory University in Atlanta, Georgia, is concerned that vaccine-induced immunity will not be as durable as immunity from natural infection. Suthar says that he and his collaborators have found that antibody levels declined faster in those who were vaccinated with the Moderna vaccine than in those who had been infected by SARS-CoV-2. Antibodies are not the only determinant of immunity, he says, but the results worry him. “I’m a little concerned that the vaccines weren’t as robust in generating more durable antibody responses,” Suthar says. “When you factor in variants, to me it’s clear that we’re going to need a booster.”

How soon that booster is needed could depend in part on the rate at which antibody levels decline — they could drop precipitously or plateau at a low level. One modelling study¹⁴ estimates that low levels of antibodies will be enough to offer significant protection against severe disease. But Pfizer chief executive Albert Bourla has said that he expects a booster to be needed in about 8–12 months after the second dose of the Pfizer–BioNTech vaccine.

On 19 May, the UK government announced that it had funded a study of 7 different COVID-19 vaccines given as boosters at least 10–12 weeks after the second dose of an initial vaccine. Early findings are expected in September — in time to inform a booster programme aimed at protecting the most vulnerable groups over the UK winter. The US National Institutes of

Health is also studying boosters in some study participants who received their first vaccine dose in an early clinical trial that began in March 2020.

Vaccine developers are now testing variant-specific boosters, too. Moderna has released preliminary results showing that a booster vaccine using a spike-protein sequence from the B.1.351 variant increased the concentration of antibodies that neutralize SARS-CoV-2, and particularly the B.1.351 variant^{[15](#)}.

Even if immunity does fade earlier than he hopes, Abu-Raddad is optimistic that it won't disappear entirely. "If I would make a bet right now, I would say that even when people start losing their immunity against infection, they will not lose immunity against severe infections," he says.

How much do vaccines block transmission?

Key clinical trials for currently authorized vaccines determined whether the inoculations could safely avert symptomatic disease in individuals. But blocking transmission of the virus is also crucial for ending a pandemic, and most of those clinical trials did not track asymptomatic infections that could fuel the virus's spread.

Researchers have been trying to fill this gap, and, so far, the data look promising. [Results announced by Johnson & Johnson](#) from clinical trials suggest that its vaccine is 74% effective against asymptomatic infections. Researchers studying deployment of the Pfizer–BioNTech vaccine in Israel have also reported that vaccination reduces the amount of virus found in infected individuals by up to 4.5-fold, suggesting that they could be less likely to shed that virus into the environment, where it might infect someone else^{[16](#)}.

And a study^{[17](#)} by Public Health England has found that even a single dose of either the Pfizer–BioNTech or Oxford–AstraZeneca vaccine reduced the spread of disease from infected individuals to household members by up to 50%. "It's likely that all the vaccines have some similar effect," says Michael Weekes, a viral immunologist at the University of Cambridge, UK. "Overall, it's quite an optimistic picture."

But, faced with incomplete data, these studies must often rely on inference to draw conclusions — assuming, for example, that lower viral load translates to reduced transmission, says Susan Little, an infectious-disease specialist at the University of California, San Diego. Little is an investigator on an ambitious trial spread across more than 30 higher-education institutions in the United States to determine how often vaccinated people infect others. The trial will randomize students so they either receive the Moderna vaccine or delay vaccination by four months. Researchers will test participants daily for infection; their close contacts will take coronavirus tests twice a week.



How to redesign COVID vaccines so they protect against variants

Little and her colleagues are looking for high-quality data to back up important decisions to come. “As people are starting to go back to work, at a policy level, should vaccination be required for schools, places of employment, public transport?” she asks. “Do vaccinated individuals need to wear masks or social distance?” On 13 May, the US Centers for Disease Control and Prevention [revised its guidelines on masking, saying that fully vaccinated people could go without masks in some public settings.](#)

But Little says widespread vaccine availability in the United States has left the study struggling to enrol participants. And the spread of viral variants could complicate the picture still more, says Kim. If vaccines are less able to decrease the viral load in individuals infected with a variant, they might also

be less able to block transmission, he cautions. “Transmission is a really hard one,” he says. “And an unknown variable here is how the variants will affect this.”

What have scientists learnt about safety?

The speed at which countries have rolled out COVID-19 vaccines is unparalleled — and the same can be said of the surveillance systems put in place to monitor vaccine safety.

Clinical trials of some vaccines involved more than 40,000 participants, and yielded few signs of side effects beyond those often seen after vaccination, including injection-site soreness, fever and nausea. “We generally say that no vaccine is 100% safe,” says Meissner. “But the safety of these vaccines is remarkable.”

Shortly after inoculations with the Pfizer–BioNTech vaccine began, a few regions [reported cases of a severe allergic reaction called anaphylaxis](#). But further study showed that the risk of this condition — which can be treated at the vaccination centre — is not much higher for the Moderna and Pfizer–BioNTech jabs than for other vaccines, says Meissner. For Pfizer–BioNTech, the risk is about 4.7 cases per 1 million doses¹⁸; the risk of anaphylaxis from any vaccination is estimated at 1.3 in a million.

More concerning has been the very rare occurrence of a blood-clotting syndrome in recipients of the Oxford–AstraZeneca and Johnson & Johnson vaccines. First reported in Europe and linked to vaccination with the Oxford–AstraZeneca vaccine, hallmarks of the syndrome include blood clots in unusual places — particularly in the brain and abdomen — coupled with depletion of clot-promoting cell fragments called platelets. The condition can be fatal, but regulators have repeatedly determined that the risk posed by COVID-19 is greater for many people than is the risk of developing the clotting syndrome. The European Medicines Agency has concluded that it occurs in about one in 100,000 vaccine recipients.

[Researchers are still racing to determine how the vaccine could cause the syndrome](#). But the subsequent US discovery of similar cases among

recipients of the Johnson & Johnson vaccine — although at a frequency of only about 3.5 per million people — has led to speculation that the condition might be linked to the disabled adenoviruses used in the vaccines to shuttle the coronavirus spike gene into cells.



Mix-and-match COVID vaccines trigger potent immune response

Since the syndrome was discovered, the United Kingdom has advised that people under the age of 40 receive a different vaccine, given their very low risk of complications from SARS-CoV-2 infection. The United States has resumed vaccinations with the Johnson & Johnson vaccine after pausing it in response to the reports. But in Denmark, the Oxford–AstraZeneca vaccine was discontinued in April, and those who have already received one dose have been advised to have an mRNA vaccine from Pfizer–BioNTech or Moderna as their second dose.

Meanwhile, surveys have suggested that the [debate over the safety of these vaccines was enough to damage public confidence in them](#). “What defines a safe vaccine?” says Meissner. “One out of a hundred thousand may seem very safe for one person; another person says ‘One in a million? What if that’s me?’”

Israel’s Ministry of Health is now evaluating a possible link between the Pfizer–BioNTech vaccine and reports of heart inflammation, a condition called myocarditis. So far, most cases have been mild and have occurred in men aged between 16 and 19.

What impact have the vaccines had on the course of the pandemic?

Several countries with high vaccination rates — including Israel and the United Kingdom — have seen precipitous declines in deaths and hospitalizations from COVID-19. Public Health England has calculated that the vaccines have saved 13,000 lives among those aged 60 and over⁴. The United Kingdom has fully vaccinated more than one-third of its population.

But these countries have conducted their vaccination campaigns while under strict social-distancing measures. Chile, by contrast, rolled back its distancing requirements early this year as it embarked on an aggressive vaccination campaign. By April, its intensive-care wards were overflowing with COVID-19 patients, despite the country having one of the world's highest vaccination rates.

Once vaccines have reached a wide swathe of the population, however, it might be possible to ease lockdowns and social-distancing restrictions. Israel's rates of infection, for example, have remained low after it gradually relaxed most restrictions once about half of its adult population had been vaccinated. Infections are also falling in the United States as the proportion of fully vaccinated adults there surpasses 40% (see 'Unequal protection').

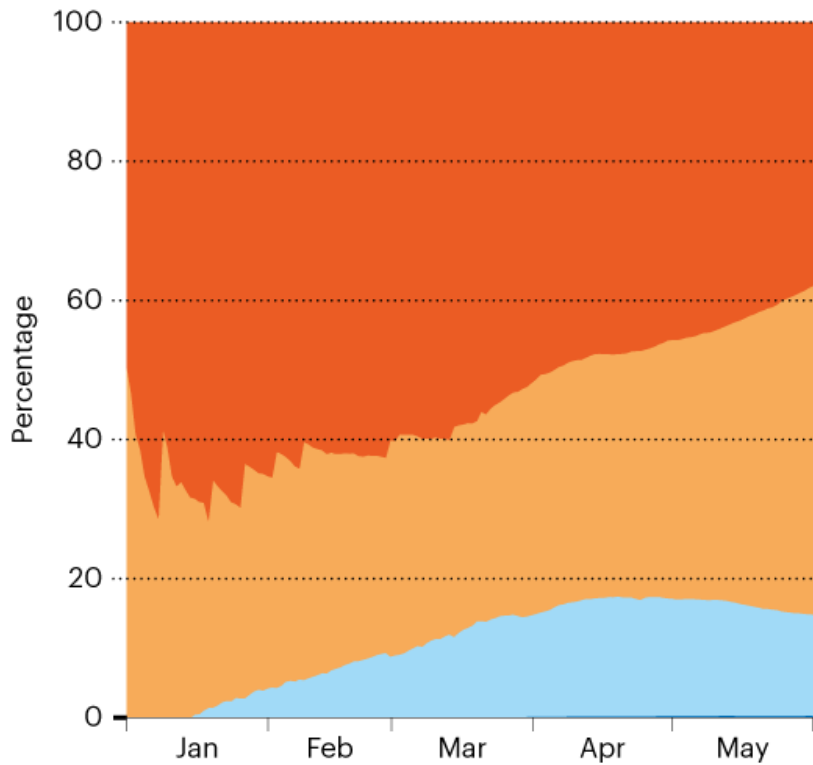
UNEQUAL PROTECTION

Wealthier nations have secured an inordinate share of vaccine supplies, as seen in a graph showing the proportion of doses administered since January 2021*.

- High income
- Upper middle income
- Lower middle income
- Low income

*Data as of 2 June 2021.

©nature



Source: Our World in Data

But the Seychelles, the most vaccinated country in the world (with a population of less than 100,000), experienced a surge in infections — although relatively few deaths — as it reached a level of more than 60% adult vaccination in early May.

For now, it's unclear what has driven that outbreak and whether coronavirus variants could be to blame, says Kim. But it pays to ease restrictions slowly, he says, even once a country has achieved a high level of vaccination. "It's probably wise to remember that every time we saw the numbers going down and we were relieved and relaxed, they came back again," says Kim. "That's the cautionary tale in all of this."

And for much of the world — particularly low- and middle-income countries — limited supplies mean that vaccines will probably have little impact on the course of the pandemic this year. Madhi says that he does not expect the current roll-out in South Africa to do much to protect it from the impending third surge there: by the time all people over the age of 60 have been offered their first dose at the end of June, he expects social distancing

and other measures to have already brought the country's burgeoning infection numbers down. And in India, a combination of low vaccination rates, aggressive variants and widespread social interaction are thought to have led to its [tragic and overwhelming COVID-19 outbreak](#).

Whereas some wealthy countries were able to pre-order large amounts of vaccine, many low- and middle-income countries have had to make do with less. The World Health Organization's target is to vaccinate 20% of the population in those countries by the end of this year. "This is not going to be the main exit strategy for them this year," says Mark Jit, an infectious-disease modeller at the London School of Hygiene & Tropical Medicine. "Maybe in 2022, when the supply is less constrained." Instead, such countries might need to rely heavily on social distancing, mask wearing and test-and-trace programmes.

And even in countries with higher vaccination rates, the once-glittering [hope of achieving herd immunity](#) — when enough immunity exists in the population to prevent disease spread — has faded, says Kim. "Now with widespread generation of these variants and continued uncontrolled outbreaks, that's looking less likely," he says. "And the impact of the pandemic will continue to be felt until vaccination can be accomplished not only in high-income but low- and middle-income countries."

Nature **594**, 164-167 (2021)

doi: <https://doi.org/10.1038/d41586-021-01505-x>

References

1. 1.

Polack, F. P. *et al.* *N. Engl. J. Med.* **383**, 2603–2615 (2020).

[PubMed](#) [Article](#) [Google Scholar](#)

2. 2.

Moustsen-Helms, I. R. *et al.* Preprint at medRxiv
<https://doi.org/10.1101/2021.03.08.21252200> (2021).

3. 3.

Haas, E. J. *et al.* *Lancet* **397**, 1819–1829 (2021).

[PubMed](#) [Article](#) [Google Scholar](#)

4. 4.

Public Health England. *COVID-19 Vaccine Surveillance Report Week 20* (PHE, 2021).

[Google Scholar](#)

5. 5.

Bernal, J. L. *et al.* *Br. Med. J.* **373**, n1088 (2021).

[Article](#) [Google Scholar](#)

6. 6.

Frenck, R. W. *et al.* *N. Engl. J. Med.*
<https://doi.org/10.1056/NEJMoa2107456> (2021).

[Article](#) [Google Scholar](#)

7. 7.

Abu-Raddad, L. J., Chemaitelly, H. & Butt, A. A. *N. Engl. J. Med.*
<https://doi.org/10.1056/NEJMc2104974> (2021).

[Article](#) [Google Scholar](#)

8. 8.

Madhi, S. A. *et al.* *N. Engl. J. Med.* **384**, 1885–1898 (2021).

[PubMed](#) [Article](#) [Google Scholar](#)

9. 9.

Sadoff, J. *et al.* *N. Engl. J. Med.* <https://doi.org/10.1056/NEJMoa2101544> (2021).

[Article](#) [Google Scholar](#)

10. 10.

Shinde, V. *et al.* *N. Engl. J. Med.* **384**, 1899–1909 (2021).

[PubMed](#) [Article](#) [Google Scholar](#)

11. 11.

Fischer, R. J. *et al.* Preprint at bioRxiv
<https://doi.org/10.1101/2021.03.11.435000> (2021).

12. 12.

Bernal, J. L. *et al.* Preprint at <https://go.nature.com/34rjcty> (2021).

13. 13.

Hall, V. J. *et al.* *Lancet* **397**, 1459–1469 (2021).

[PubMed](#) [Article](#) [Google Scholar](#)

14. 14.

Khoury, D. S. *et al.* *Nature Med.* <https://doi.org/10.1038/s41591-021-01377-8> (2021).

[Article](#) [Google Scholar](#)

15. 15.

Wu, K. *et al.* Preprint at medRxiv
<https://doi.org/10.1101/2021.05.05.21256716> (2021).

16. 16.

Levine-Tiefenbrun, M. *et al.* *Nature Med.* **27**, 790–792 (2021).

[PubMed](#) [Article](#) [Google Scholar](#)

17. 17.

Harris, R. J. *et al.* Preprint at <https://go.nature.com/3yyxtm3> (2021).

18. 18.

Shimabukuro, T. T., Cole, M. & Su, J. R. *J. Am. Med. Assoc.* **325**, 1101–1102 (2021).

[Article](#) [Google Scholar](#)

[Download references](#)

[Jobs from Nature Careers](#)

- - - [All jobs](#)
 - - [**Postdoctoral Fellow, Statistical Methodologies for Metabolomics Data Analysis**](#)
[The University of British Columbia \(UBC\)](#)
[Vancouver, Canada](#)
[JOB POST](#)

- **Postdoctoral Fellow in River Dynamics**

The University of British Columbia (UBC)

Vancouver, Canada

JOB POST

- **PhD Student in Wnt signaling**

German Cancer Research Center in the Helmholtz Association (DKFZ)

Heidelberg, Germany

JOB POST

- **Postdoc (all genders), Department Detector Laboratory (DTL)**

Helmholtz Centre for Heavy Ion Research GmbH (GSI)

Darmstadt, Germany

JOB POST

Download PDF

Related Articles

-  **Five reasons why COVID herd immunity is probably impossible**



- What scientists know about new, fast-spreading coronavirus variants



- How to redesign COVID vaccines so they protect against variants



- Mix-and-match COVID vaccines trigger potent immune response

This article was downloaded by **calibre** from <https://www.nature.com/articles/d41586-021-01505-x>

| [Section menu](#) | [Main menu](#) |

- NEWS FEATURE
- 09 June 2021

The four most urgent questions about long COVID

Scientists are starting to get insights into the lingering disorder that affects some people infected with SARS-CoV-2 — but many mysteries remain unsolved.

- [Michael Marshall](#) 0

1. Michael Marshall

1. Michael Marshall is a science writer based in Devon, UK.

[View author publications](#)

You can also search for this author in [PubMed](#) [Google Scholar](#)





•



Illustration by Acapulco Studio

[Download PDF](#)

When Claire Hastie fell ill in March of last year, she reacted the way she usually would to a minor ailment: she tried to ignore it. “It started off incredibly mild,” she says. “I would normally have paid no attention to it whatsoever.”

But within a week she was flattened. “I had just never felt ill in this way before. I felt like I had an elephant sitting on my chest.” At times, she became convinced she was going to die.

A single mother of three, Hastie “said what I thought might be my final words to the one child who happened to be walking past my bedroom door”. Although her condition is not quite as overwhelming one year on, she says, “I’ve never had a symptom-free day since.”

Hastie has what is now called [long COVID](#): a long-lasting disorder that arises following infection with SARS-CoV-2, the virus that causes COVID-19.

Surveys of thousands of people have revealed an extensive list of symptoms, such as fatigue, dry cough, shortness of breath, headaches and muscle aches. A team led by Athena Akrami, a neuroscientist at University College London who has long COVID, found 205 symptoms in a study of more than 3,500 people¹. By month 6, the most common were “fatigue, post-exertional malaise, and cognitive dysfunction”. These symptoms fluctuate, and people often go through phases of feeling better before relapsing².

In the first months of the pandemic, the idea that the virus might cause a chronic condition was overlooked in the desperate struggle to deal with acute cases. But Hastie soon realized that she was not alone in having a lingering form of the disease. In May 2020, she started a [Facebook group](#) for people with long COVID. Today, it has more than 40,000 members and works with research groups studying the condition — with Hastie sometimes appearing as a co-author of papers.

Meanwhile, long COVID has moved from a curiosity, dismissed by many, to a recognized public-health problem. In January, the World Health Organization revised its guidelines for COVID-19 treatment to include a recommendation that all patients should have access to follow-up care in case of long COVID.

Funding agencies are also paying attention. On 23 February, the US National Institutes of Health (NIH) announced that it would spend [US\\$1.15 billion over four years into research on long COVID](#), which it refers to as “post-

acute sequelae of COVID-19 (PASC)”. In the United Kingdom, the National Institute for Health Research (NIHR) announced in February that it was investing £18.5 million (US\$25.8 million) to fund four studies of long COVID — and the following month, it launched another round of funding worth £20 million. The UK BioBank plans to send self-testing kits to all its 500,000 participants, so that those with SARS-CoV-2 antibodies can be identified and invited for further studies.

As the number of confirmed COVID cases tops 170 million across the globe, millions of people might be experiencing persistent symptoms and searching for answers about their future health. Here, *Nature* looks at four of the biggest questions that scientists are investigating about the mysterious condition known as long COVID.

How many people get long COVID and who is most at risk?

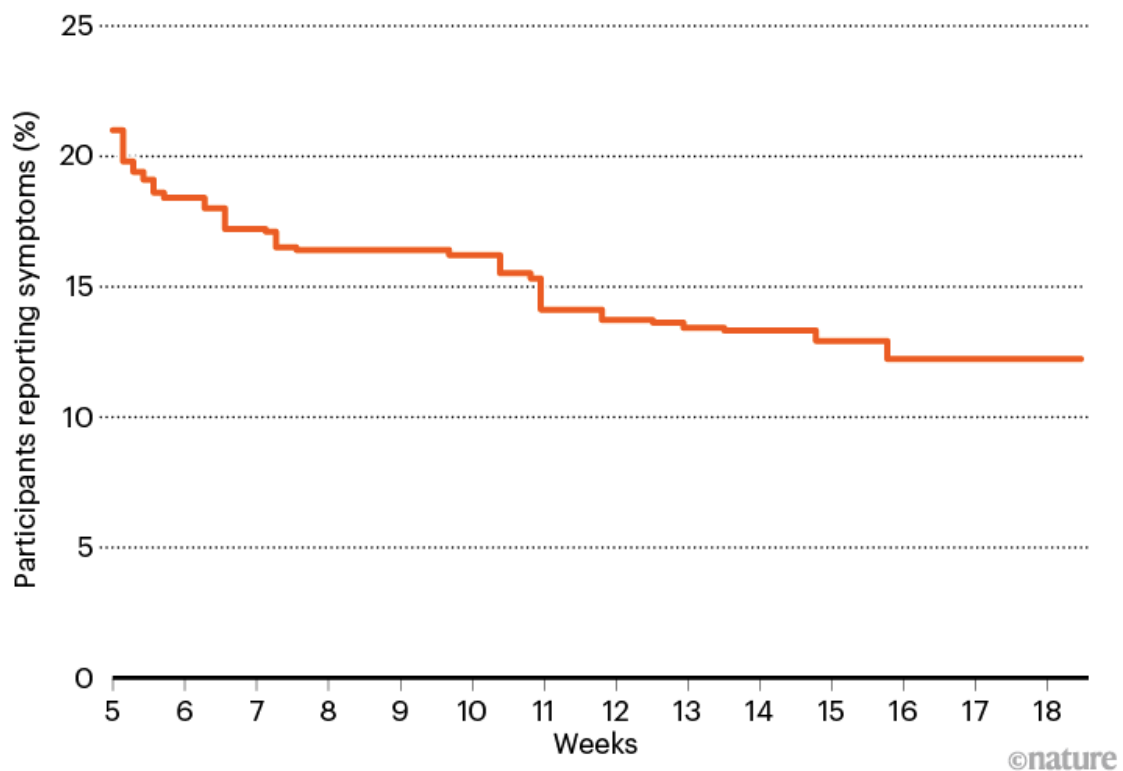
There is increasing clarity on the overall prevalence of long COVID, thanks to a series of surveys — but it is less certain who is most at risk, and why it affects only some.

Most of the early prevalence studies looked only at people who had been hospitalized with acute COVID-19. Ani Nalbandian, a cardiologist at Columbia University Irving Medical Center in New York, and her colleagues collated nine such studies for a review published on 22 March³. They found that between 32.6% and 87.4% of patients reported at least one symptom persisting after several months.

But most people with COVID-19 are never ill enough to be hospitalized. The best way to assess the prevalence of long COVID is to follow a representative group of people who have tested positive for the virus. The UK Office of National Statistics (ONS) has done just that, by following more than 20,000 people who have tested positive since April 2020 (see ‘Uncertain endpoint’). In [its most recent analyses](#), published on 1 April, the ONS found that 13.7% still reported symptoms after at least 12 weeks (there is no widely agreed definition of long COVID, but the ONS considers it to be COVID-19 symptoms that last more than 4 weeks).

UNCERTAIN ENDPOINT

The UK Office for National Statistics (ONS) tracked more than 20,000 people following a positive COVID-19 test, to determine how long their symptoms lasted. The ONS considers ‘long COVID’ to be the persistence of symptoms for more than four weeks.



Source: UK Office for National Statistics

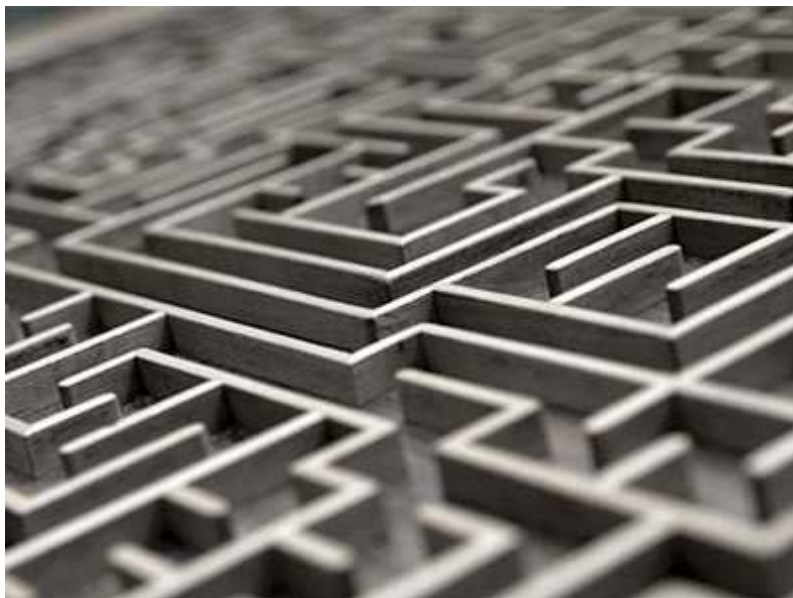
“I think that’s the best estimate so far,” says Akrami, who now splits her research time between her original focus, neuroscience, and work on long COVID.

In other words, more than one in 10 people who became infected with SARS-CoV-2 have gone on to get long COVID. If the UK prevalence is applicable elsewhere, that’s more than 16 million people worldwide.

The condition seems to be more common in women than in men. In another ONS analysis, 23% of women and 19% of men still had symptoms 5 weeks after infection. That is “striking”, says Rachael Evans, a clinician scientist at the University of Leicester, UK, and a member of the [Post-Hospitalisation COVID-19 study](#) (PHOSP-COVID). “If you’re male and get COVID, you’re

more likely to go to hospital and you're more likely to die. Yet if you survive, actually it's females that are much more likely to get the ongoing symptoms.”

There is also a distinctive age distribution. According to the ONS, long COVID is most common in middle-aged people: the prevalence was 25.6% at 5 weeks for those between 35 and 49 years old. It is less common in younger people and older people — although Evans says the latter finding is probably due to ‘survivor bias’, because so many old people who have had COVID-19 have died.



Scientists set out to connect the dots on long COVID

And although long COVID is rarer in younger people, that does not mean it is absent. Even for children aged 2–11, the ONS estimates that 9.8% of those who test positive for the virus still have symptoms after at least 5 weeks, reinforcing the suggestion from other studies that children can get long COVID⁴. Yet some medical professionals play down the idea, says Sammie Mcfarland, who founded the UK-based support group Long Covid Kids. “Long COVID in children isn’t believed. The symptoms are minimized.”

Nevertheless, age and sex are surprisingly powerful for identifying people at risk. A paper published in March presented a model that successfully

predicted whether a person would get long COVID using only their age, their sex and the number of symptoms reported in the first week⁵.

Still, many uncertainties remain. In particular, if about 10% of people infected with SARS-CoV-2 get long COVID — as the ONS data suggest — why those 10%?

What is the underlying biology of long COVID?

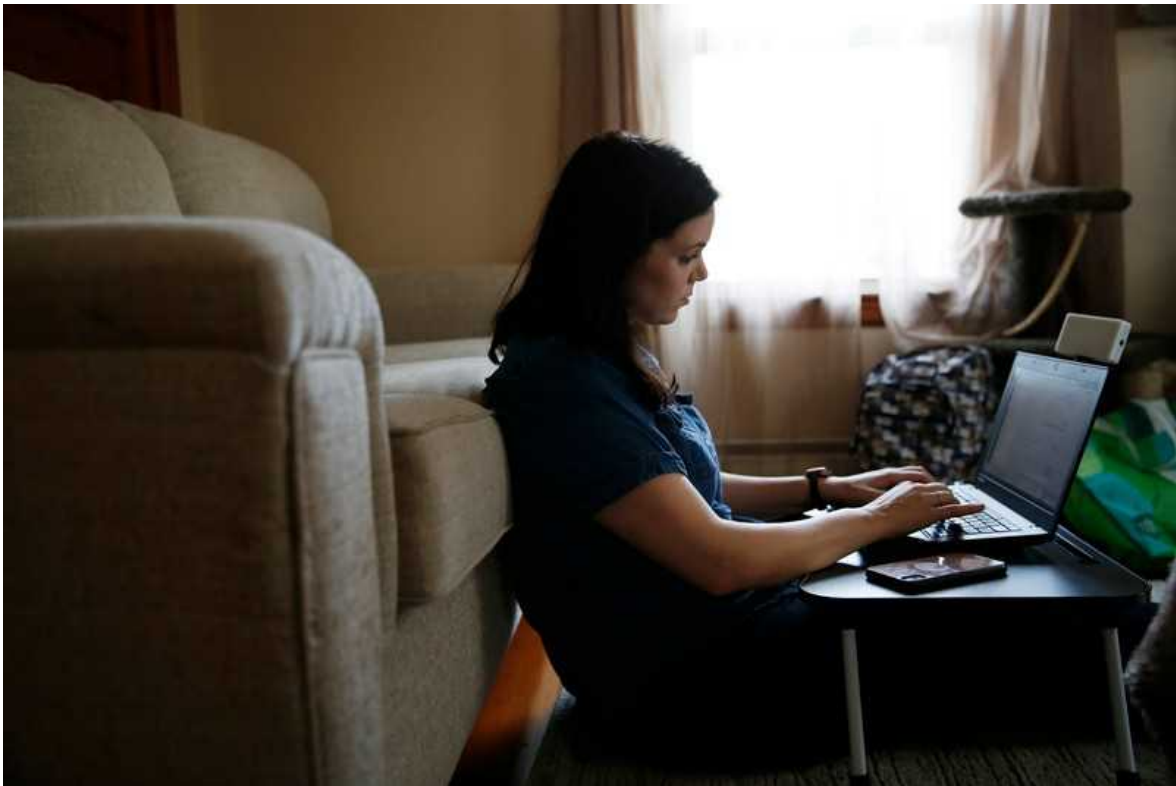
Although researchers have exhaustively surveyed the diverse symptoms of long COVID, no clear explanation for them exists. “We need people to be looking at the mechanisms,” says Hastie. This will not be easy: studies have shown that many people with long COVID have problems with multiple organs⁶, suggesting that it is a multisystem disorder.

It seems unlikely that the virus itself is still at work, says Evans. “Most of the studies have shown that after a few weeks you’ve pretty much cleared it, so I very much doubt it’s an infective consequence.”

However, there is evidence that fragments of the virus, such as protein molecules, can persist for months⁷, in which case they might disrupt the body in some way even if they cannot infect cells.

A further possibility is that long COVID is caused by the immune system going haywire and attacking the rest of the body. In other words, long COVID could be an autoimmune disease. “SARS-CoV-2 is like a nuclear bomb in terms of the immune system,” says Steven Deeks, a physician and infectious-disease researcher at the University of California, San Francisco. “It just blows everything up.” Some of those changes might linger — as has been seen in the aftermath of other viral infections (see ‘What is the relationship between long COVID and other post-infection syndromes?’).

Still, it is too early to say which hypothesis is correct, and it might be that each is true in different people: preliminary data suggest that long COVID could be several disorders lumped into one.



Symptoms such as fatigue and difficulty exercising are common in people with long COVID, and can persist for months after infection. Credit: Jessica Rinaldi/The Boston Globe/Getty

Some researchers are taking that next step, hoping to unpick the biology. PHOSP-COVID has recruited more than 1,000 UK patients and taken blood samples to look for evidence of inflammation, cardiovascular problems and other changes. Similarly, Deeks has helped to recruit almost 300 COVID-19 patients who have since been followed up every 4 months and have given blood and saliva samples. “We have a massive specimen bank,” says Deeks. “We’re looking at inflammatory outcomes, changes in the coagulation system, evidence that the virus persists.” The team has found altered levels of cytokines — molecules that help to regulate immune responses — in the blood of people who have had COVID-19, suggesting that the immune system is indeed out of balance, as well as protein markers suggesting neuronal dysfunction⁸.

A better understanding of the underlying biology will point the way to treatments and medications, says Evans. But it seems unlikely that there is a single, neat explanation for long COVID. Most researchers now suspect

several mechanisms are at work, so one person's long COVID might be profoundly different from another's. In October, a review published by the NIHR raised the possibility that long COVID symptoms "may be due to a number of different syndromes". "There is a story emerging," says Deeks. "There's not one clinical phenotype. There's different flavours, different clusters. They all may have different mechanisms." His group plans to use machine learning to work out how many types there are and how they differ.



The lasting misery of coronavirus long-haulers

Evans and her PHOSP-COVID colleagues have taken a stab at this, in a preprint posted on 25 March⁹. They studied 1,077 COVID-19 patients, recording symptoms including physical impairments, mental-health difficulties such as anxiety, and cognitive impairments in areas such as memory and language. The researchers also recorded basic information such as age and sex, and biochemical data such as levels of C-reactive protein — a measure of inflammation. The team then used a mathematical tool called cluster analysis to see whether there were identifiable groups of patients with similar profiles.

"We would think if you had a terrible acute lung injury and multi-organ failure, those would be the people that would have the ongoing pathology," says Evans. But the study found little relationship between the severity of the acute phase, or levels of organ damage, and the severity of long COVID.

The reality was more complicated. The analysis identified four clusters of long COVID patients whose symptoms were distinct. Three of the groups had mental-health and physical impairments to varying degrees, but few or no cognitive difficulties. The fourth cluster showed only moderate mental-health and physical impairments, but had pronounced cognitive problems.

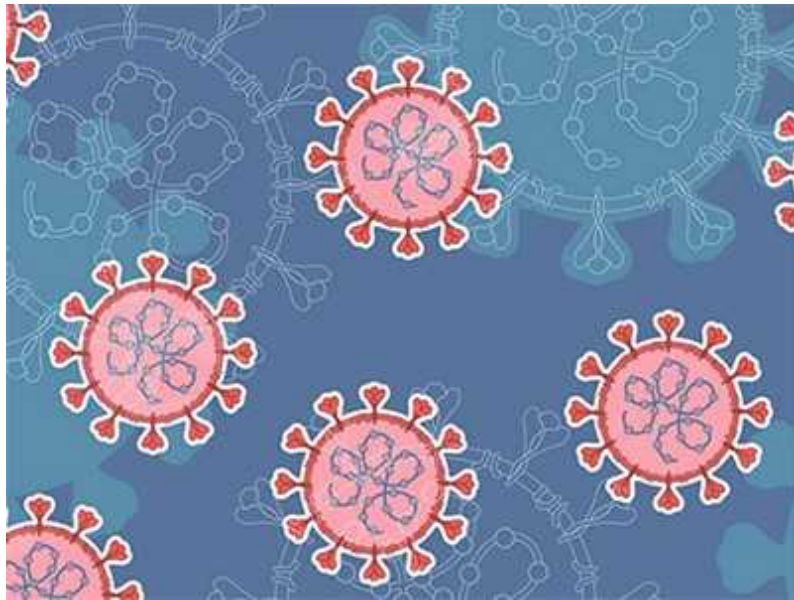
“Cognition was really quite separate, and we weren’t expecting that,” says Evans. She emphasizes that the study does not unpick the underlying mechanisms. “But it is definitely a first step.”

What is the relationship between long COVID and other post-infection syndromes?

Some scientists weren’t surprised by long COVID. Illnesses that linger after an infection have been reported in the scientific literature for 100 years, says Anthony Komaroff, an internal-medicine physician at Harvard Medical School in Boston, Massachusetts.

He noted that fact in March, during a webinar organised by MEAction, an organization based in Santa Monica, California, that works to raise awareness of myalgic encephalitis, also known as chronic fatigue syndrome (ME/CFS). People with this debilitating illness become exhausted after even mild activity, alongside experiencing other symptoms such as headaches. [Long dismissed by some medical professionals](#) because it had no clear biological underpinning, ME/CFS is often post-viral.

It isn’t uncommon for an infection to trigger long-lasting symptoms. One study of 253 people diagnosed with certain viral or bacterial infections found that after 6 months, 12% reported persistent symptoms including “disabling fatigue, musculoskeletal pain, neurocognitive difficulties, and mood disturbance”¹⁰. That percentage is strikingly similar to the long COVID prevalence observed in the United Kingdom by the ONS.



Long COVID's long R&D agenda

Some people with long COVID will probably meet the diagnostic criteria for ME/CFS, according to Komaroff and his colleague Lucinda Bateman, founder of the Bateman Horne Center in Salt Lake City, Utah, which specializes in treating ME/CFS¹¹. But there do seem to be differences: for instance, people with long COVID are more likely to report shortness of breath than are those with ME/CFS, Komaroff says. Furthermore, if long COVID does end up being subdivided into multiple syndromes, that will further complicate comparisons between it and ME/CFS.

“I’ve so far resisted saying long COVID is ME/CFS, because I really think it is an umbrella term and there are multiple things happening in this long COVID umbrella,” says Nisreen Alwan, a public-health researcher at the University of Southampton, UK. And Deeks speaks for many: “I think everybody needs to be a bit agnostic now, and not make too many assumptions, and not put all these different syndromes into the same bucket.” What many do agree on, however, is that the two conditions could productively be studied in tandem. “There should be a coalition,” says Alwan. Some researchers are already planning to collaborate. For instance, a major study called [DecodeME](#) aims to recruit 20,000 people to find genetic factors that contribute to ME/CFS — and Evans says PHOSP-COVID will be sharing data with it.

“I’m really hopeful that the silver lining will be, at the end of the day, we gain better insight into other post-viral problems,” says Akrami.

Hastie puts it more bluntly: “Let’s not waste a good crisis.”

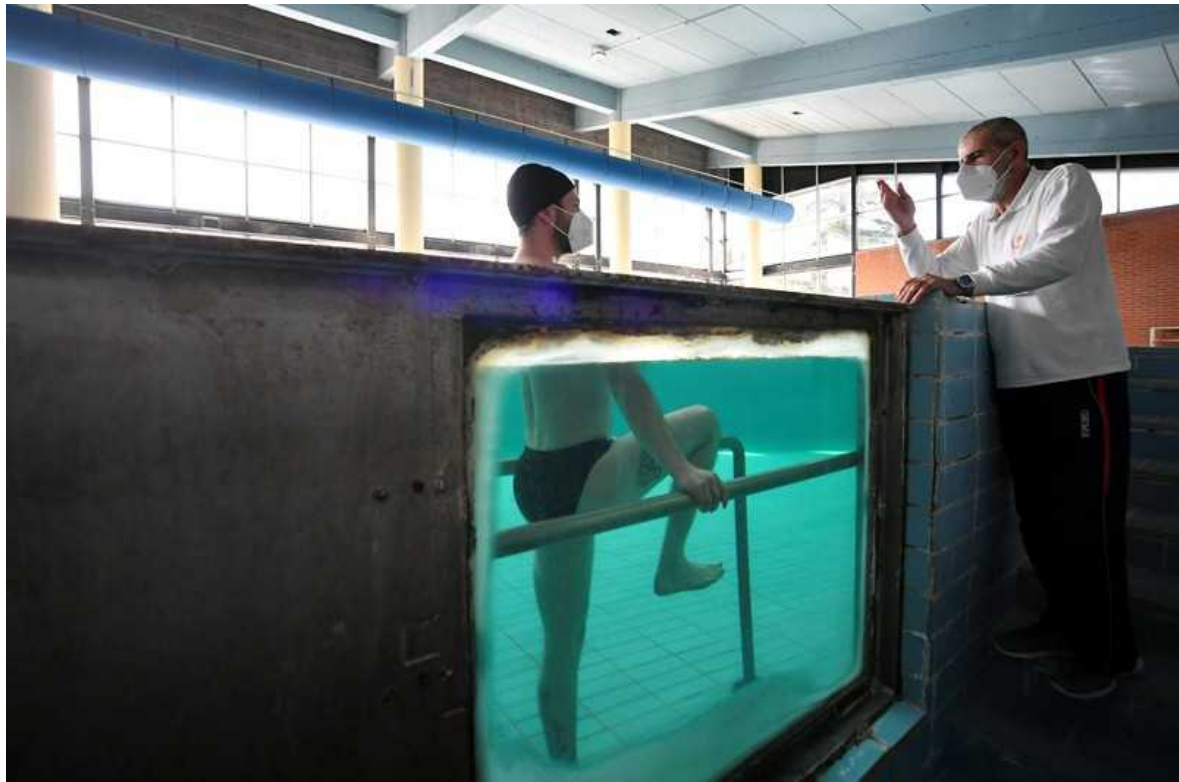
What can be done to help people with long COVID?

Right now, the options are fairly limited, because the disorder is so poorly understood.

Some countries are opening clinics for people with long COVID. In Germany, a company called MEDIAN has begun accepting people with long COVID at some of its private rehabilitation clinics. In England, the National Health Service has provided £10 million for a network of 69 clinics: these have started to assess and help people with the condition.

That is a welcome first step, says Hastie, but few evidence-based treatments exist. There is a growing consensus that multidisciplinary teams are needed, because long COVID affects so many parts of the body. “Every person on average has, like, 16 or 17 symptoms,” says Akrami. Often the clinics do not have such teams.

Much of the challenge will be social and political, because people with long COVID must rest, often for months at a time, and they need support while they do so. Their conditions “need to be recognized as a disability”, says Hastie.



People with long COVID are often left with respiratory difficulties, and some clinics are offering rehabilitation. Credit: Jennifer Lorenzini/Reuters

In terms of medicines, a handful are being tested. Biotechnology company PureTech Health in Boston, Massachusetts, announced in December that it was starting a clinical trial of deupirfenidone, an anti-fibrotic and anti-inflammatory agent that it has developed. Results are expected in the second half of 2021. In the United Kingdom, intensive-care specialist Charlotte Summers at the University of Cambridge and her colleagues have launched a study called [HEAL-COVID](#), which aims to prevent long COVID from taking hold. Participants who have been hospitalized with COVID-19 will be given one of two drugs after being discharged: apixaban, an anticoagulant that might reduce the risk of dangerous blood clots; and atorvastatin, an anti-inflammatory. In the United States, the NIH is funding a trial of existing drugs that people with mild COVID-19 can administer at home. Participants will be followed for 90 days to test the drugs' impact on longer-term symptoms.

Finally, there is the question of what part COVID-19 vaccines might play. Although many of them prevent death and severe illness, scientists do not

yet know whether they prevent long COVID.

What about the impact of vaccines in people who already have long COVID? A UK survey of more than 800 people with long COVID, which has not been peer reviewed, reported in May that 57% saw an overall improvement in their symptoms, 24% no change and 19% a deterioration after their first dose of vaccine¹². In April, Akrami's team launched a systematic survey to shed more light. “People need to get vaccinated to come out of the pandemic, but we need to first address their concern of whether the vaccine is going to help, or not harm, or [be] harmful.”

Similarly, Akiko Iwasaki, an immunobiologist at Yale University in New Haven, Connecticut, is recruiting people with long COVID who have not been vaccinated, so she and her colleagues can track how their bodies react to the vaccine. She hypothesizes that the vaccine might improve symptoms by eliminating any virus or viral remnants left in the body, or by rebalancing the immune system.

People with long COVID just want something that works. “How can we get better?” asks Hastie. “That’s what we want to know.”

Nature **594**, 168-170 (2021)

doi: <https://doi.org/10.1038/d41586-021-01511-z>

References

1. 1.

Davis, H. E. *et al.* Preprint at medRxiv
<https://doi.org/10.1101/2020.12.24.20248802> (2021).

2. 2.

Ziauddeen, N. *et al.* Preprint at medRxiv
<https://doi.org/10.1101/2021.03.21.21253968> (2021).

3. 3.

Nalbandian, A. *et al.* *Nature Med.* **27**, 601–615 (2021).

[PubMed](#) [Article](#) [Google Scholar](#)

4. 4.

Buonsenso, D. *et al.* *Acta Paediatr.* <https://doi.org/10.1111/apa.15870> (2021).

[Article](#) [Google Scholar](#)

5. 5.

Sudre, C. H. *et al.* *Nature Med.* **27**, 626–631 (2021).

[PubMed](#) [Article](#) [Google Scholar](#)

6. 6.

Ayoubkhani, D. *et al.* Preprint at medRxiv
<https://doi.org/10.1101/2021.01.15.21249885> (2021).

7. 7.

Gaebler, C. *et al.* *Nature* **591**, 639–644 (2021).

[PubMed](#) [Article](#) [Google Scholar](#)

8. 8.

Sun, B. *et al.* *Cells* **10**, 386 (2021).

[PubMed](#) [Article](#) [Google Scholar](#)

9. 9.

PHOSP-COVID Collaborative Group *et al.* Preprint at medRxiv
<https://doi.org/10.1101/2021.03.22.21254057> (2021).

10. 10.

Hickie, I. *et al.* *Br. Med. J.* **333**, 575 (2006).

[Article](#) [Google Scholar](#)

11. 11.

Komaroff, A. L. & Bateman, L. *Front. Med.* **7**, 606824 (2021).

[Article](#) [Google Scholar](#)

12. 12.

LongCOVIDSOS vaccine report. Available at go.nature.com/3yfqem2 (2021).

[Download references](#)

Jobs from Nature Careers

- - - [All jobs](#)
 -
 - **Postdoctoral Fellow, Statistical Methodologies for Metabolomics Data Analysis**
[The University of British Columbia \(UBC\)](#)
[Vancouver, Canada](#)
[JOB POST](#)
 - **Postdoctoral Fellow in River Dynamics**
[The University of British Columbia \(UBC\)](#)
[Vancouver, Canada](#)

JOB POST

- **PhD Student in Wnt signaling**

German Cancer Research Center in the Helmholtz Association (DKFZ)

Heidelberg, Germany

JOB POST

- **Postdoc (all genders), Department Detector Laboratory(DTL)**

Helmholtz Centre for Heavy Ion Research GmbH (GSI)

Darmstadt, Germany

JOB POST

Download PDF

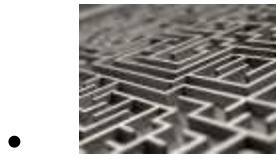
Related Articles



- **The lasting misery of coronavirus long-haulers**



- **Long COVID's long R&D agenda**



- **Scientists set out to connect the dots on long COVID**

This article was downloaded by **calibre** from <https://www.nature.com/articles/d41586-021-01511-z>

| [Section menu](#) | [Main menu](#) |

Books & Arts

- **[It takes a wood to raise a tree: a memoir](#)** [07 June 2021]
Book Review • An ecologist traces forests' support networks — and finds parallels in her own life.
- **[Managing the ‘dataome’, medical misogyny, and the problem with palm oil: Books in brief](#)** [09 June 2021]
Book Review • Andrew Robinson and Sara Abdulla review five of the week's best science picks.

- BOOK REVIEW
- 07 June 2021

It takes a wood to raise a tree: a memoir

An ecologist traces forests' support networks — and finds parallels in her own life.

- [Emma Marris](#) 0
- 1. [Emma Marris](#)

1. Emma Marris is an environmental writer who lives in Klamath Falls, Oregon.

[View author publications](#)

You can also search for this author in [PubMed](#) [Google Scholar](#)





•

[Download PDF](#)



Douglas firs in British Columbia, Canada: ‘mother trees’ help seedlings all around to flourish.Credit: Getty

Finding the Mother Tree: Discovering the Wisdom of the Forest Suzanne Simard Knopf (2021)

Growing up in the rainforests of the Pacific Northwest, I often grieved that their beauty — sky-high Douglas firs, rustling alders, sword ferns draped across the slopes — was born of a brutal battle for light, water and nutrients. So I thought.

In 1997, ecologist Suzanne Simard made the cover of *Nature* with the discovery of a subterranean lace of tree roots and fungal filaments, or hyphae, in British Columbia ([S. Simard et al. *Nature* 388, 579–582; 1997](#)). It was “a network as brilliant as a Persian rug”, she recalls in her memoir *Finding the Mother Tree* — a network through which multiple tree species were exchanging carbon. The trees were cooperating.

The discovery of this fungal network, or ‘wood wide web’, as it came to be known, upended a dominant scientific narrative — that competition is the

primary force shaping forests. Forest ecology is instead a much more nuanced dance, in which species sometimes fight and sometimes get along. This calls into question the way that most foresters manage trees. Clear-cutting, weeding and planting single species in well-spaced rows makes sense only if trees do best when they have all the resources they need to themselves.



Rediscovering the bush telegraph

Throughout her career, Simard has shown that, in fact, it takes a whole ‘village’ to raise a tree. Alders fix atmospheric nitrogen, which can then be used by pines and other tree species. Older, deeper-rooted trees bring up water from lower in the soil to shallow-rooted plants. Carbon, water, nutrients and information about threats and conditions are shared across the fungal-root network. When Douglas firs are infested with western spruce budworm (*Choristoneura occidentalis*), they alert pines to which they are connected through the wood wide web, and these respond by producing defence enzymes. In the middle of all this activity are the mother trees. The oldest, largest and most experienced, they subsidize the growth and flourishing of seedlings all around.

Simard creates her own complex network in this memoir, by weaving the story of these discoveries with vignettes from her past. The themes of her research — cooperation, the legacies that one generation leaves for the next,

the ways in which organisms react to and recover from stress and disease — are also themes in her own life. The network of friends, family and colleagues who support Simard, as a scientist and as a woman, is visible throughout: as central to the story as a forest's web of fungal filaments and delicate rootlets.

Simard's life story is, of course, unique, yet it has a striking universality. After working for a logging company, she moved into government service and then into academia, trying in each job to untangle the subterranean mysteries of the forest. She fought to have her ideas taken seriously in a male-dominated field. (There are shades of *Lab Girl*, by US geobiologist Hope Jahren, in her clear-eyed depictions of what she has to deal with behind the scenes — from being passed over for jobs for which she was the best candidate, to being called “Miss Birch” behind her back, a sound-alike for a much harsher epithet.) Simard found love, lost it, and found it again. She struggled, like so many scientists, to balance her research and her roles as a wife and mother. She faced mortality when diagnosed with cancer.



The thread-like roots of fungi are an essential element of a forest's ‘wood wide web’, through which trees exchange carbon, water, nutrients and information. Credit: Claire Welsh

Moving through life's highs and lows with her is rewarding because of these resonances, and because she comes across as the kind of person who usually doesn't write memoirs — shy and occasionally fearful, always earnest. It feels like a privilege to be let into her life.

The muddy, stressful and occasionally exhilarating experience of fieldwork shines through. "Jittery with adrenaline", while labelling seedlings in one field experiment, she describes feeling "as if I were about to parachute out of a plane, maybe land on Easter Island". Simard got her first morsel of proof for her theory in 1993, while kneeling on the forest floor holding a Geiger counter to detect the radioactive carbon-14 that she used to track carbon flows through plants and fungi. "I was enraptured, focused, immersed, and the breeze sifting through the crowns of my little birches and firs and cedars seemed to lift me clear up," she writes.

After publishing her *Nature* paper, Simard showed that trees direct more resources to their offspring than they do to unrelated seedlings. The finding suggests that trees maintain a level of control through the network that one might call intelligence. As she argues, plants seem to have agency. They perceive, relate and communicate, make decisions, learn and remember, she writes: "qualities we normally ascribe to sentience, wisdom". For Simard, that implies that they are due a certain respect.



[The community of trees](#)

She does not spell out the ethical implications, but the ideas raise fascinating moral questions. What responsibilities do we owe plants? Is logging or farming crops, to harvest and eat, cruel? What kinds of legal right might a tree have if we base our theories of rights on whether individuals, such as humans and chimpanzees, have intelligence or sentience?

It is tempting to ascribe the dominance of the ‘brutal competition’ narrative to the fact that ecology was dominated by men, and to find poetic power in the idea that a woman saw cooperation when her male colleagues couldn’t. But Simard tells a more complex tale. She struggled to see the truth in the soil and in her heart — and got there only because she was determined and intuitive.

Simard writes that big old trees are “mothering their children” by sending them, through the forest network, sugars, water, nutrients and information about threats. Reading this on page 5, I was sceptical. By the end I was convinced. The beauty of the forests of my youth turns out to be shaped, in a sense, by love.

Nature **594**, 171-172 (2021)

doi: <https://doi.org/10.1038/d41586-021-01512-y>

Competing Interests

The author declares no competing interests.

Jobs from Nature Careers

- - - [All jobs](#)
 - - [Postdoctoral Fellow, Statistical Methodologies for Metabolomics Data Analysis](#)

[The University of British Columbia \(UBC\)](#)

[Vancouver, Canada](#)

[JOB POST](#)

- [**Postdoctoral Fellow in River Dynamics**](#)

[The University of British Columbia \(UBC\)](#)

[Vancouver, Canada](#)

[JOB POST](#)

- [**PhD Student in Wnt signaling**](#)

[German Cancer Research Center in the Helmholtz Association \(DKFZ\)](#)

[Heidelberg, Germany](#)

[JOB POST](#)

- [**Postdoc \(all genders\), Department Detector Laboratory \(DTL\)**](#)

[Helmholtz Centre for Heavy Ion Research GmbH \(GSI\)](#)

[Darmstadt, Germany](#)

[JOB POST](#)

[Download PDF](#)

Related Articles

-  **Rediscovering the bush telegraph**
-  **No species is an island**
-  **The community of trees**
-  **In retrospect: The Lorax**

This article was downloaded by **calibre** from <https://www.nature.com/articles/d41586-021-01512-y>.

| [Section menu](#) | [Main menu](#) |

- BOOK REVIEW
- 09 June 2021

Managing the ‘dataome’, medical misogyny, and the problem with palm oil: Books in brief

Andrew Robinson and Sara Abdulla review five of the week’s best science picks.

- [Andrew Robinson](#) ⁰ &
- [Sara Abdulla](#)

1. [Andrew Robinson](#)

1. Andrew Robinson’s many books include *Lost Languages: The Enigma of the World’s Undeciphered Scripts* and *Einstein on the Run: How Britain Saved the World’s Greatest Scientist*. He is based in London.

[View author publications](#)

You can also search for this author in [PubMed](#) [Google Scholar](#)

2. Sara Abdulla

[View author publications](#)

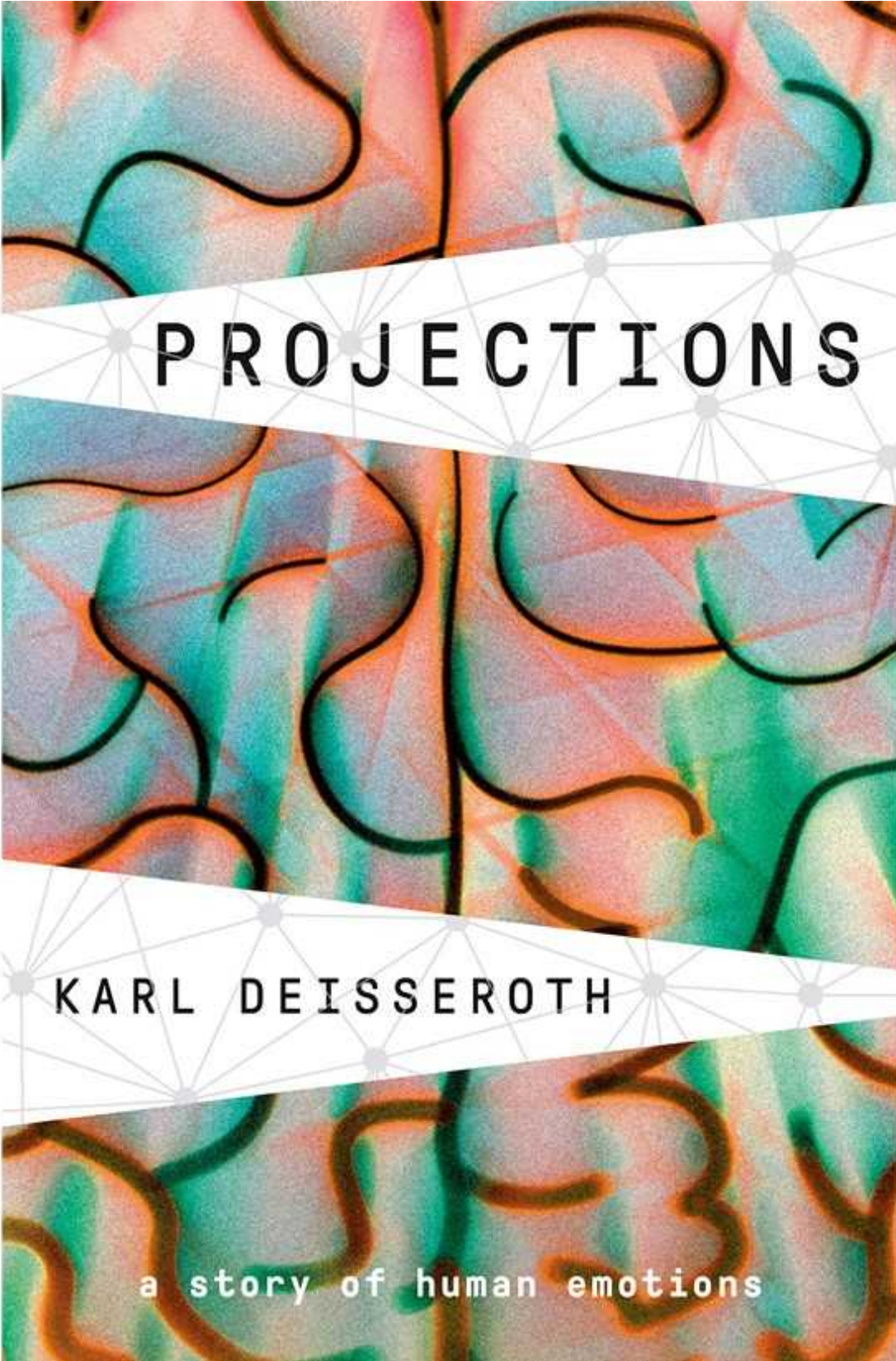
You can also search for this author in [PubMed](#) [Google Scholar](#)





•

[Download PDF](#)



PROJECTIONS

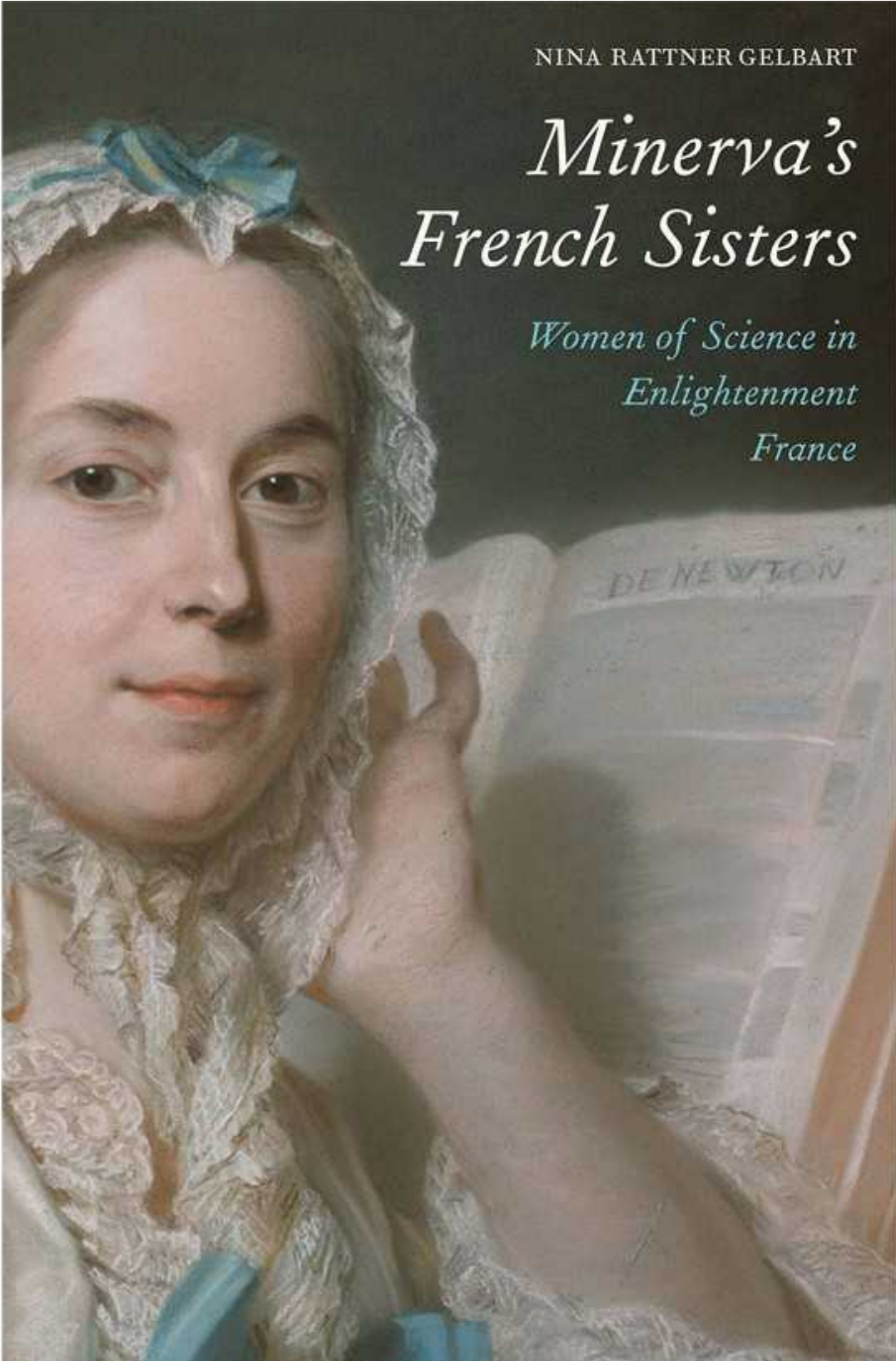
KARL DEISSEROTH

a story of human emotions

Projections

Karl Deisseroth *Random House* (2021)

“I still value literature as much as science in thinking about the mind,” writes bioengineer and psychiatrist Karl Deisseroth, co-inventor of optogenetics. His scintillating and moving analysis of the human brain and emotions, based on observations of his patients, proves he is not exaggerating. It is also a great read. Young Deisseroth was inspired to follow psychiatry by a chance encounter with a patient who abused him with novel words — including one resembling ‘telmetale’, a word invented by James Joyce.

A portrait painting of Sophie de Genlis, a French Enlightenment writer and educational reformer. She is shown from the chest up, wearing a white lace cap and a light-colored, ruffled lace-trimmed dress. Her right hand rests on an open book that is titled "DE NEWTON".

NINA RATTNER GELBART

Minerva's French Sisters

*Women of Science in
Enlightenment
France*

Minerva's French Sisters

Nina Rattner Gelbart *Yale Univ. Press* (2021)

Of the 72 scientific names engraved on the Eiffel Tower, none is female. Omissions include the six Enlightenment women dubbed “Minerva’s sisters” by historian Nina Gelbart in her pioneering, evocative rescue. Naturalist Jeanne Barret was the first woman to circumnavigate the world (disguised as a man); chemist Geneviève d’Arconville, the first person to suspect, long before Louis Pasteur, that putrefaction was caused by airborne agents. Others worked in mathematics, astronomy, mechanics, the physics of light, epistemology, botany and anatomy.

The Ascent of Information

Books, Bits, Genes,

Machines, and Life's

Unending Algorithm

Caleb Scharf

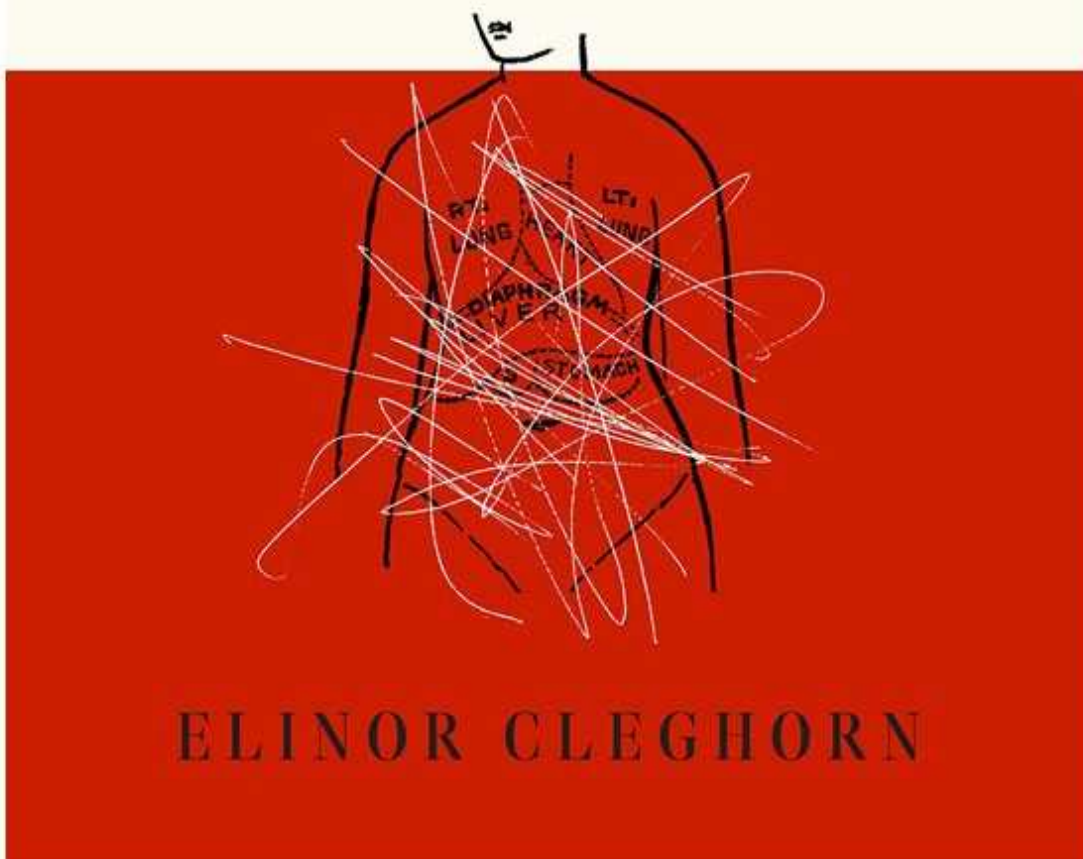
The Ascent of Information

Caleb Scharf *Riverhead* (2021)

In 1989, physicist John Wheeler coined “it from bit” to express his view that “all things physical are information-theoretic in origin”. Astronomer Caleb Scharf agrees in this demanding disquisition, drawing on archaeology, evolutionary biology, neuroscience, astrobiology, computer science and information theory. He coins “dataome” — modelled on ‘genome’ — defined as “all of the non-genetic data we carry externally and internally”. Data are the reason humans exist, he argues. So how can we stop our dataome from overwhelming us?

UNWELL WOMEN

MISDIAGNOSIS AND
MYTH IN A MAN-MADE WORLD



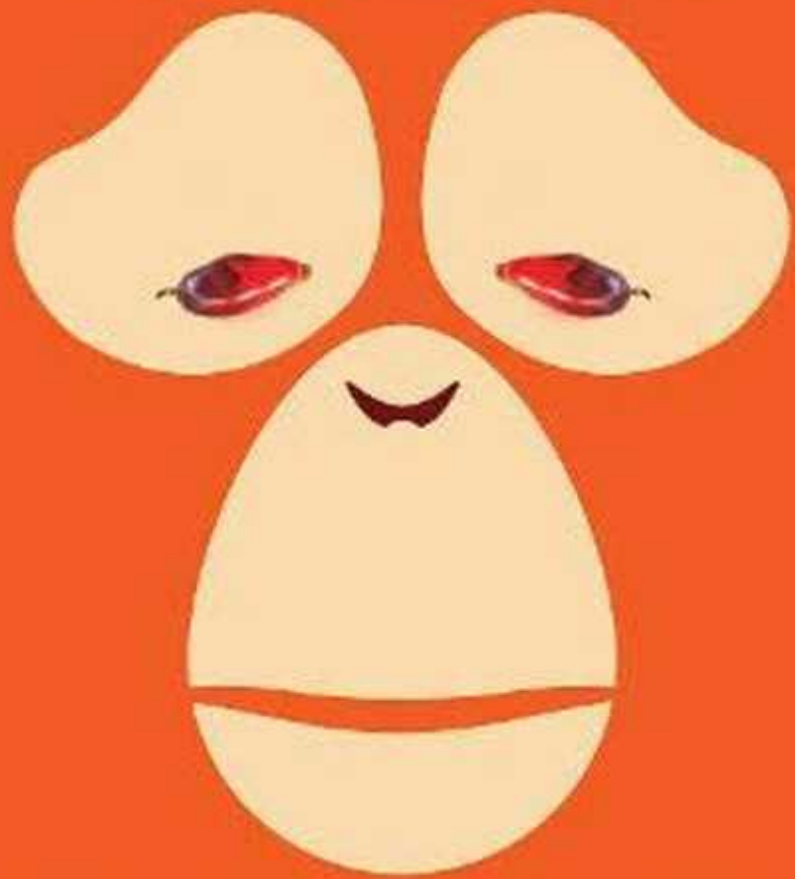
Unwell Women

Elinor Cleghorn *Dutton* (2021)

“Medicine has been complicit, for centuries, in the punishment, silencing and oppression of women,” argues this powerful history of misogyny and racism in health care. That male physicians once posited that women were too highly strung to be educated is the least of it. Elinor Cleghorn, a researcher in medical humanities, asks: how is it that many people still believe menstruation and menopause make women unsuited to power? She also draws on her own gruelling journey to be diagnosed with the autoimmune condition lupus.

Jocelyn C. Zuckerman

PLANET PALM



How Palm Oil Ended Up in Everything –
and Endangered the World

Planet Palm

Jocelyn C. Zuckerman *Hurst* (2021)

How did palm oil come to be in everything from toothpaste to bread, detergent and animal feed, asks journalist Jocelyn Zuckerman in her unflinching guide to a vast industry that threatens the ecosphere. Visiting deforested wastes in Liberia, wildfires in Sumatra and people living precarious lives in Guatemala, Zuckerman tells a tale of colonialism, stolen land, slave labour and globalization. Like salt, cotton and sugar, she writes, palm oil has “reshaped our economies and landscapes and reshuffled our geopolitics and health”.

Nature **594**, 172 (2021)

doi: <https://doi.org/10.1038/d41586-021-01513-x>

Competing Interests

The authors declare no competing interests.

Jobs from Nature Careers

- - - [All jobs](#)
 -
 - [**Postdoctoral Fellow, Statistical Methodologies for Metabolomics Data Analysis**](#)
[The University of British Columbia \(UBC\)](#)
[Vancouver, Canada](#)
[JOB POST](#)
- [**Postdoctoral Fellow in River Dynamics**](#)

The University of British Columbia (UBC)

Vancouver, Canada

JOB POST

▪ **PhD Student in Wnt signaling**

German Cancer Research Center in the Helmholtz Association (DKFZ)

Heidelberg, Germany

JOB POST

▪ **Postdoc (all genders), Department Detector Laboratory (DTL)**

Helmholtz Centre for Heavy Ion Research GmbH (GSI)

Darmstadt, Germany

JOB POST

Download PDF

This article was downloaded by **calibre** from <https://www.nature.com/articles/d41586-021-01513-x>

Opinion

- **Climate policy models need to get real about people — here's how** [08 June 2021]
Comment • To predict how society and political systems might actually respond to warming, upgrade integrated assessment models.
- **Scientists — be political in the good times, not just the bad** [08 June 2021]
Correspondence •
- **Indigenous lands: make Brazil stop mining to secure US deal** [08 June 2021]
Correspondence •
- **Diagnostic genomic laboratories should share their data** [08 June 2021]
Correspondence •
- **Chilean polymath Humberto Maturana remembered** [08 June 2021]
Correspondence •

- COMMENT
- 08 June 2021

Climate policy models need to get real about people — here's how

To predict how society and political systems might actually respond to warming, upgrade integrated assessment models.

- [Wei Peng](#)⁰,
- [Gokul Iyer](#)¹,
- [Valentina Bosetti](#)²,
- [Vaibhav Chaturvedi](#)³,
- [James Edmonds](#)⁴,
- [Allen A. Fawcett](#)⁵,
- [Stéphane Hallegatte](#)⁶,
- [David G. Victor](#)⁷,
- [Detlef van Vuuren](#)⁸ &
- [John Weyant](#)⁹

1. Wei Peng

1. Wei Peng is at the School of International Affairs and the Department of Civil and Environmental Engineering, Penn State University, Pennsylvania, USA.

[View author publications](#)

You can also search for this author in [PubMed](#) [Google Scholar](#)

2. Gokul Iyer

1. Gokul Iyer is at the Joint Global Change Research Institute, Pacific Northwest National Laboratory and University of Maryland, USA.

[View author publications](#)

You can also search for this author in [PubMed](#) [Google Scholar](#)

3. Valentina Bosetti

1. Valentina Bosetti is at Bocconi University and RFF–CMCC European Institute on Economics and the Environment in Milan, Italy.

[View author publications](#)

You can also search for this author in [PubMed](#) [Google Scholar](#)

4. Vaibhav Chaturvedi

1. Vaibhav Chaturvedi is at the Council on Energy, Environment and Water in New Delhi, India.

[View author publications](#)

You can also search for this author in [PubMed](#) [Google Scholar](#)

5. James Edmonds

1. James Edmonds is at the Joint Global Change Research Institute, Pacific Northwest National Laboratory and University of Maryland, USA.

[View author publications](#)

You can also search for this author in [PubMed](#) [Google Scholar](#)

6. Allen A. Fawcett

1. Allen A. Fawcett is at the Environmental Protection Agency in Washington DC, USA.

[View author publications](#)

You can also search for this author in [PubMed](#) [Google Scholar](#)

7. Stéphane Hallegatte

1. Stéphane Hallegatte is at the World Bank Group in Washington DC, USA.

[View author publications](#)

You can also search for this author in [PubMed](#) [Google Scholar](#)

8. [David G. Victor](#)

1. David G. Victor is at the University of California, San Diego, and the Brookings Institution in Washington DC, USA.

[View author publications](#)

You can also search for this author in [PubMed](#) [Google Scholar](#)

9. Detlef van Vuuren

1. Detlef van Vuuren is at PBL Netherlands Environmental Assessment Agency and Utrecht University, the Netherlands.

[View author publications](#)

You can also search for this author in [PubMed](#) [Google Scholar](#)

10. John Weyant

1. John Weyant is at the Department of Management Science and Engineering, Stanford University, USA.

[View author publications](#)

You can also search for this author in [PubMed](#) [Google Scholar](#)

-



•

[Download PDF](#)

Political support for decarbonizing the global economy is at an all-time high. The good news is that about two-thirds of carbon emissions come from countries that have committed to reach ‘net zero’ by mid-century — they aim to cut their greenhouse-gas outputs and capture as much as they emit¹. The bad news? The computer models that analysts use to assess routes to achieve such goals are missing a crucial factor: politics.

These ‘integrated assessment models’ (IAMs) combine insights from climate science and economics to estimate how industrial and agricultural processes

might be transformed to tackle global warming. They're encoded with knowledge about technologies, such as pollution-free power plants and the cost of electric vehicles. Thus IAMs enable researchers to probe, for example, how a carbon tax might induce big cuts in emissions², or how a drive to decarbonize the transport sector could shift investments towards greener fuels and electricity.

Yet the models are overly abstract. They don't characterize the difficult trade-offs that politicians face when they must respond to constituencies, or corporate leaders who must woo investors. In France, for example, a proposed increase to the fuel tax in 2018 was among the triggers of large protests. These saw the government backtrack on a key element of its climate policy. Fearing electoral consequences, many politicians around the world now shy away from carbon taxes and other market-based strategies. They instead rely heavily on regulatory instruments — such as fuel-economy standards — that make the cost of such policies less visible to the public and give politicians more control over who foots the bill³.



National COVID debts: climate change imperils countries' ability to repay

The story of politics isn't just one of conservatism and evasion. Support for action can change radically on the back of success. Current IAMs can't capture this dynamism either. Subsidies for wind and solar energy, for

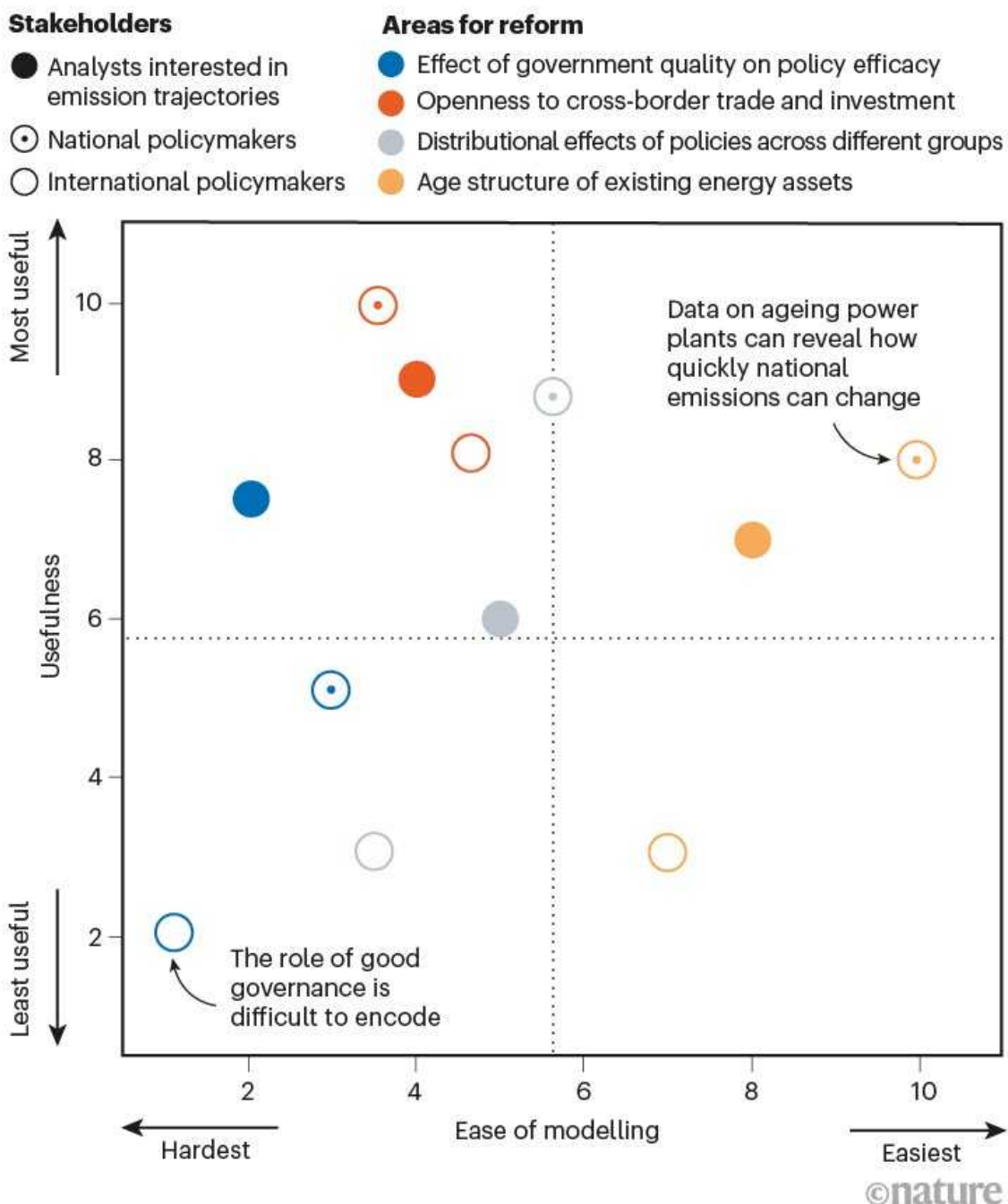
example, have sped up adoption, lowered costs and created industries that have tilted the landscape in favour of more investment in renewables.

To develop politically durable strategies, decision makers need to understand how climate policy creates winners and losers. This means moving IAMs away from jack-of-all-trades models and towards a suite of tailored ones, each tuned to a specific purpose and audience. A negotiator at the COP26 climate-change conference in Glasgow, UK, this November, for example, might want to understand how international trade policies affect global emissions. A national policymaker, however, might need to balance attempts to decarbonize transport infrastructure against election promises they have made to car-factory workers in their constituency.

As a first step, we — a group of political economists and IAM specialists — identified eight key areas in which insights from our disciplines can improve models' relevance for real-world policy and investment choices (see 'Eight political economy insights'). We also assessed numerous potential reforms (see 'How to improve models' and Supplementary information for a full list of 11 reforms), so that researchers can examine the trade-offs between making models tractable and making them more useful for real-world decisions.

HOW TO IMPROVE MODELS

The integrated assessment models used in climate science need improvement. They must better predict how policies to reduce emissions might influence industry, labour unions and voters — or vice versa. Updates to the models vary in how easy they are to implement, and how useful they will be to different stakeholders.



Source: Author analysis

Incentives and trade-offs

Similar to many economic tools developed decades ago, IAMs are built on an oversimplified logic: that people are rational optimizers of scarce resources. ‘Agents’ make decisions that maximize the benefits to a country or society². Price adjustments — for example, a carbon tax — or constraints on polluting technologies alter the agents’ incentives, yielding changes in behaviour that alter economies and emissions⁴.

In reality, human choice is a darker brew of misperception and missed opportunity, constrained by others’ decisions. Researchers in sociology, psychology and organizational behaviour have long studied human behaviours. They explore why people stick with old, familiar technologies even when new ones are much superior, for example. This kind of research can also explain why the passion of mass movements, such as the global climate-strike movement, Fridays for Future, is hard to understand based on just individual costs and benefits, yet it can have powerful effects on policy.

To get IAMs to reflect social realities and possibilities, one should look to the field of political economy. This studies how political institutions affect who gains and loses from a policy, which can have a big influence on the acceptability of said policy. Many of the political economy analyses needed are quantitative and, to varying degrees, readily adapted for use in IAMs. Indeed, some investigations have begun to pave the way. For example, they explore how political disagreements can raise the cost of decarbonization by delaying policy action⁵. Others look at how variations in the quality of governance affect the size and allocation of policy costs⁶. Yet others ask how perceptions of risk can make investors focus on the near term^{6,7}. This is bad news for climate policy, because most actions require a long-term plan over which the cost of new equipment can be paid off.

Eight political economy insights

Data improve models’ relevance to policy and investment choices.

- Access to capital can be constrained by risk-averse investors who fear unpredictable changes in policy, hampering low-carbon energy transitions.

- The design and type of a policy instrument, such as whether to subsidize green technologies or tax polluting industries, can be influenced by which interest groups are mobilized.
- Carbon lock-in and stranding of fossil-based energy assets might limit the degree to which emissions can deviate from their previous trajectory, without interventions that can weaken the power of incumbent polluters.
- Unequal costs and benefits of climate policies accrue to different economic, racial and religious groups, which can affect policies' moral and political acceptability.
- Public opinion might facilitate stronger action to tackle climate change.
- Confidence in political institutions or lack of it can influence the public's willingness to support actions that reduce emissions.
- Trade and investment policies can expand the markets for new green technology, leading to lower costs and more political support.
- Competence of government influences a state's ability to intervene in markets, make choices and alter the cost of deploying capital.

Model improvements

We distilled eight political-economy insights that align with important policy debates and can feasibly be included in IAMs. They range from quantifying the political impact of stranded fossil-fuel assets, to describing how the level of confidence in public institutions can influence public support for climate policies. We agreed on this list by conducting a wide survey of approaches, clustering and assessing them through a process of drafting, commenting and group deliberation (see Supplementary information).

In our analysis, we focused on three communities of policy-relevant decision makers that might find such insights useful. First, those who want better predictions about what might happen in the world as a whole, such as the future trajectory and impact of global emissions. This includes analysts who plan long-term adaptation strategies and need to know just how bad climate

change could get. Second, those that design international agreements. They seek diplomatic strategies that both maximize the curbing of global warming and have a chance, politically, of getting adopted. Third, those who design policy within countries. This group is pivotal to deep decarbonization, because its members turn aspirations for emission cuts into local reality.

Consider one of the central challenges in this era: reducing economic inequality. How that social goal is addressed could have profound moral and political impacts on climate policy. Decarbonization, for the most part, will be cheaper for those who have access to inexpensive capital, a disparity that is linked to many inequalities of income, race and opportunity.

Or consider the politics of deglobalization — in which institutions such as the World Trade Organization, anchored in the postwar ideal of open borders, are under threat. Understanding how far nationalism goes, and its consequences for the costs of clean-energy technologies, has become important to policymakers. The reality is that many of the revolutions that give hope for an affordable decarbonization, such as cheap solar cells and batteries, have seen their costs plummet thanks to global trade and investment⁸.



Climate mitigation and adaptation affects people's daily lives, and models need to better reflect that. Credit: Sia Kambou/AFP via Getty

Mindful of the opportunity to understand these patterns systematically, we identified concrete areas where improvements in the models would be valuable (see Supplementary information). For example, we looked at how the development of new theories⁹ of international trade helped to explain the direction and political stability of international trade policies. They showed how lowering tariffs could create local winners (and losers). That altered the coalitions in support of trade, investment and other hallmarks of globalization. This kind of thinking offers a sobering reminder that international policies can overreach, creating domestic backlash that reduces support for global collective action. With the right groundwork, similar concepts could be useful to the study of decarbonization in an era of deglobalization.

We considered coding changes great and small, from adding new factors and weights in functions or computing at different geographical and temporal resolutions, to including new data sets. For each, we evaluated how much the reform might add value for decision makers, and the feasibility of implementing it. The modelling feasibility also varies for decisions at different scales owing to data requirements and computational needs. (We also assessed our confidence in assigning those scores; see Supplementary information.)



Eight priorities for calculating the social cost of carbon

This approach identified priority areas where IAMs could be ripe for change: easy wins as well as harder ones worth the pain (see ‘How to improve models’ and Supplementary information). A potential reform relevant to national policymakers is to recode the models so that they reveal how decarbonization might disproportionately impose costs on low-income groups in a country. A reform valuable for international policymakers is to represent how openness to cross-border trade would lower the cost of key low-carbon technologies. This could, in turn, make it easier to build and hold together the political coalitions needed to advance climate policy.

We’re not the first to highlight the limitations of IAMs. A lot of people have called for more realism in climate models and have rightly questioned their overuse^{4,10}. But policymakers urgently need better tools. Our analysis shows that practical improvements to the models can add real value.

The road ahead

As analysts and researchers debate and test these ideas, two things are clear.

First, the right choices depend on the audience. IAM reforms are only worth the effort if they help decision makers. This is because big changes can often make it hard to identify which factors really drive outputs. Stakeholders should be consulted when problems are formulated and represented, not merely after the model development and results are completed.

Second, success will require fresh collaborations and funding. Reforming models will need teams of scholars who are anchored in the IAMs (with knowledge about what is feasible) and tethered to the social sciences (aware of what is important). We think these efforts should invest heavily in engaging political scientists and politically minded economists¹¹. This will require humility and flexibility from modellers, who must recognize that their framings will be seen, in other disciplines, as narrow and often uninviting.

Some of this work has begun. Europe is a promising place to test a new generation of IAMs. A huge continent-wide investment in decarbonized industrial policy is under way, under the banner of the European Green Deal. This will create new industries and new politics in the region and in key sectors, such as oil and gas. The continent is investing heavily in industries of the future, such as carbon capture and storage, and hydrogen and electricity (which is likely to be a winner with deep decarbonization).

This kind of collaboration is often seen in the natural sciences. Here, multi-authored papers are common and are reflected in the reward structure. Unfortunately, such an approach is riskier in many social sciences, including political science, particularly for junior scholars seeking promotion. Care will be needed to generate benefits that are seen as valuable within each field. Special mentoring for early-career academics will be needed to make sure that enthusiasm to work on the problem of the century doesn't distract them from what's needed to succeed professionally. Each discipline needs its own approach. Solutions are long overdue.

Nature **594**, 174-176 (2021)

doi: <https://doi.org/10.1038/d41586-021-01500-2>

The views expressed in this paper are those of the authors and do not necessarily represent the views or policies of their affiliations.

References

1. 1.

International Energy Agency. *Net Zero by 2050* (IEA, 2021).

[Google Scholar](#)

2. 2.

Clarke, L. *et al.* in *Climate Change 2014: Mitigation of Climate Change* (eds Edenhofer, O. *et al.*) Ch. 6 (Cambridge Univ. Press, 2014).

[Google Scholar](#)

3. 3.

Cullenward, D. & Victor, D. G. *Making Climate Policy Work* (Polity Press, 2020).

[Google Scholar](#)

4. 4.

Fisher-Vanden, K. & Weyant, J. *Annu. Rev. Resour. Econ.* **12**, 471–487 (2020).

[Article](#) [Google Scholar](#)

5. 5.

Jakob, M., Luderer, G., Steckel, J., Tavoni, M. & Monjon, S. *Clim. Change* **114**, 79–99 (2012).

[Article](#) [Google Scholar](#)

6. 6.

Iyer, G. C. *et al.* *Nature Clim. Change* **5**, 436–440 (2015).

[Article](#) [Google Scholar](#)

7. 7.

Battiston, S., Monasterolo, I., Riahi, K. & van Ruijven, B. J. *Science* **372**, 918–920 (2021).

[PubMed](#) [Article](#) [Google Scholar](#)

8. 8.

Nemet, G. F. *How Solar Energy Became Cheap* (Routledge, 2019).

[Google Scholar](#)

9. 9.

Melitz, M. J. *Econometrica* **71**, 1695–1725 (2003).

[Article](#) [Google Scholar](#)

10. 10.

Keppo, I. *et al. Environ. Res. Lett.* **16**, 053006 (2021).

[Article](#) [Google Scholar](#)

11. 11.

Keohane, R. O. *PS Political Sci. Politics* **48**, 19–26 (2015).

[Article](#) [Google Scholar](#)

[Download references](#)

Supplementary Information

1. [Explanations and Tables](#)

Competing Interests

The authors declare no competing interests.

[Jobs from Nature Careers](#)

- - - [All jobs](#)
 -
 -

Postdoctoral Fellow, Statistical Methodologies for Metabolomics Data Analysis

The University of British Columbia (UBC)

Vancouver, Canada

JOB POST

▪ Postdoctoral Fellow in River Dynamics

The University of British Columbia (UBC)

Vancouver, Canada

JOB POST

▪ PhD Student in Wnt signaling

German Cancer Research Center in the Helmholtz Association (DKFZ)

Heidelberg, Germany

JOB POST

▪ Postdoc (all genders), Department Detector Laboratory (DTL)

Helmholtz Centre for Heavy Ion Research GmbH (GSI)

Darmstadt, Germany

JOB POST

Download PDF

Related Articles

-  [National COVID debts: climate change imperils countries' ability to repay](#)
-  [Eight priorities for calculating the social cost of carbon](#)
-  [Net-zero emissions targets are vague: three ways to fix](#)
-  [Global warming will happen faster than we think](#)
-  [Beat protectionism and emissions at a stroke](#)

This article was downloaded by **calibre** from <https://www.nature.com/articles/d41586-021-01500-2>

- CORRESPONDENCE
- 08 June 2021

Scientists — be political in the good times, not just the bad

- [Jane Gregory](#) ✉
 1. [Jane Gregory](#)
 1. University of Cambridge, UK.

[View author publications](#)

You can also search for this author in [PubMed](#) [Google Scholar](#)





•

[Download PDF](#)

Your call for scientists to “get political” (*Nature* **592**, 660; 2021) echoes many similar injunctions during times of crisis. These have had limited effect. As Jon Beckwith and Franklin Huang argued years ago, “waiting for such crises will not do” (*Nature Biotechnol.* **23**, 1479–1480; 2005). For emergency interventions to be prompt and effective, scientists must be politically engaged all the time.

Even routine science is political. There is little going on in our intersected world that has nothing to do with science; in science, there is little going on

that does not have social or political aspects. Researchers should not confine their forays into politics to times when discovery itself stands to win or lose. They must use their authority to help society ([J. Gregory Sci. Mus. Group J. https://doi.org/gf87; 2016](https://doi.org/gf87)). A close-but-no-closer relationship might seem to offer freedom, but it removes scientists from arenas in which they could be influential.

The multiplicity of world views in politics can be unsettling, especially when these are nasty or ignorant. The solution is simple: get involved. This might mean adjusting your institutional machinery, communication skills and students' education. The more that creative and well-informed people contribute, the better prepared the world will be to manage the next crisis.

Nature **594**, 177 (2021)

doi: <https://doi.org/10.1038/d41586-021-01521-x>

Competing Interests

The author declares no competing interests.

Jobs from Nature Careers

- - - [All jobs](#)
 -
 - [**Postdoctoral Fellow, Statistical Methodologies for Metabolomics Data Analysis**](#)
 - [The University of British Columbia \(UBC\)](#)
 - [Vancouver, Canada](#)

- **Postdoctoral Fellow in River Dynamics**

The University of British Columbia (UBC)

Vancouver, Canada

JOB POST

- **PhD Student in Wnt signaling**

German Cancer Research Center in the Helmholtz Association (DKFZ)

Heidelberg, Germany

JOB POST

- **Postdoc (all genders), Department Detector Laboratory (DTL)**

Helmholtz Centre for Heavy Ion Research GmbH (GSI)

Darmstadt, Germany

JOB POST

Download PDF

Related Articles

- **See more letters to the editor**

- CORRESPONDENCE
- 08 June 2021

Indigenous lands: make Brazil stop mining to secure US deal

- [Glenn H. Shepard](#) 0

1. [Glenn H. Shepard](#)

1. Emílio Goeldi Museum, Belém do Para, Brazil.

[View author publications](#)

You can also search for this author in [PubMed](#) [Google Scholar](#)





•

[Download PDF](#)

Just before the global leaders' climate summit in April, Brazil's President Jair Bolsonaro promised the United States that he would reduce deforestation in the Amazon, hoping to secure a billion-dollar aid package. In my view, any such cash-for-conservation deal should be contingent on Bolsonaro withdrawing his February bid to legalize mining on Indigenous lands.

Bolsonaro has met with pro-mining Indigenous leaders in a crusade for economic development, despite evidence that mining in Brazil does not

bring lasting improvements to socio-economic indicators (see go.nature.com/2s6zknt; in Portuguese). Granting current requests for mining concessions would affect 30% of Brazil's Indigenous lands.

Heavily armed illegal gold miners are invading federally protected Indigenous lands with impunity, knowing that the president has their back. In a shoot-out last month with Yanomami Indigenous people in the state of Roraima, miners fired at community members and Federal Police agents.

Given Brazil's current economic devastation, the administration of US President Joe Biden is in a strong position to seek major concessions to secure the aid deal. High on that list should be stopping illegal incursions and reversing plans to legalize mining on Indigenous lands.

Nature **594**, 177 (2021)

doi: <https://doi.org/10.1038/d41586-021-01522-w>

Competing Interests

The author declares no competing interests.

Jobs from Nature Careers

- - - [All jobs](#)
 - - [Postdoctoral Fellow, Statistical Methodologies for Metabolomics Data Analysis](#)

[The University of British Columbia \(UBC\)](#)

[Vancouver, Canada](#)

[JOB POST](#)

- **Postdoctoral Fellow in River Dynamics**

The University of British Columbia (UBC)
Vancouver, Canada

JOB POST

- **PhD Student in Wnt signaling**

German Cancer Research Center in the Helmholtz Association (DKFZ)

Heidelberg, Germany

JOB POST

- **Postdoc (all genders), Department Detector Laboratory (DTL)**

Helmholtz Centre for Heavy Ion Research GmbH (GSI)

Darmstadt, Germany

JOB POST

Download PDF

Related Articles

- **See more letters to the editor**

This article was downloaded by **calibre** from <https://www.nature.com/articles/d41586-021-01522-w>

- CORRESPONDENCE
- 08 June 2021

Diagnostic genomic laboratories should share their data

- [Kok-Siong Poon](#) ORCID: <http://orcid.org/0000-0002-0873-2682>⁰
&
- [Evelyn Siew-Chuan Koay](#) ORCID: <http://orcid.org/0000-0001-6472-1462>¹

1. [Kok-Siong Poon](#)

1. National University Hospital, Singapore.

[View author publications](#)

You can also search for this author in [PubMed](#) [Google Scholar](#)

2. Evelyn Siew-Chuan Koay

1. National University of Singapore.

[View author publications](#)

You can also search for this author in [PubMed](#) [Google Scholar](#)





•

[Download PDF](#)

Getting diagnostic genomic laboratories — along with patients, clinicians and researchers — to share their data ethically could help to fix “the broken promise” that undermines human genome research (see [Nature 590, 198–201; 2021](#)). The promise was to make genomic data publicly accessible.

Laboratories that sequence DNA for diagnostic purposes hold information on patients’ clinical and phenotypic features alongside causal genomic findings (see [A. J. Gates et al. Nature 590, 212–215; 2021](#)). The benefits of sharing these data interpretations could extend far beyond the diagnostic

context — subject to patients' informed consent. They could create a giant resource for curated reference sequences and variants proved to be linked to disease.

The community has public repositories for data sharing, yet participation is low. Many laboratories prefer to maintain their own databases. This practice needs to change.

Now that sequencing of human genomes is routine, the number of variants of unknown significance has grown exponentially. Mostly considered neutral and non-actionable, these rare variants might still play a part in disease. Openly sharing genomic data and phenotypic details could provide insight into such unknowns.

Nature **594**, 177 (2021)

doi: <https://doi.org/10.1038/d41586-021-01523-9>

Competing Interests

The authors declare no competing interests.

Jobs from Nature Careers

- - - [All jobs](#)
 - - [**Postdoctoral Fellow, Statistical Methodologies for Metabolomics Data Analysis**](#)

[The University of British Columbia \(UBC\)](#)

[Vancouver, Canada](#)

[JOB POST](#)

- **Postdoctoral Fellow in River Dynamics**

The University of British Columbia (UBC)

Vancouver, Canada

JOB POST

- **PhD Student in Wnt signaling**

German Cancer Research Center in the Helmholtz Association (DKFZ)

Heidelberg, Germany

JOB POST

- **Postdoc (all genders), Department Detector Laboratory (DTL)**

Helmholtz Centre for Heavy Ion Research GmbH (GSI)

Darmstadt, Germany

JOB POST

Download PDF

Related Articles

- **See more letters to the editor**

- CORRESPONDENCE
- 08 June 2021

Chilean polymath Humberto Maturana remembered

- [Francisco J. Parada](#)⁰,
- [Alejandra Rossi](#)¹ &
- [Daniel Rojas-Líbano](#)²

1. [Francisco J. Parada](#)

1. Diego Portales University, Santiago, Chile.

[View author publications](#)

You can also search for this author in [PubMed](#) [Google Scholar](#)

2. Alejandra Rossi

1. Diego Portales University, Santiago, Chile.

[View author publications](#)

You can also search for this author in [PubMed](#) [Google Scholar](#)

3. Daniel Rojas-Líbano

1. Diego Portales University, Santiago, Chile.

[View author publications](#)

You can also search for this author in [PubMed](#) [Google Scholar](#)





•

[Download PDF](#)

As young Chilean neuroscientists, we have been profoundly influenced by the work of the Chilean polymath Humberto Maturana Romesín, who died last month aged 92.

As well as helping to lay the foundations of modern neuroscience (see [J. Y. Lettin et al. Proc. IRE 47, 1940–1951; 1959](#)), Maturana did pioneering and widely influential work on core issues in the biological, clinical and social sciences, philosophy and the humanities. His contributions to cybernetics — the science of communications and automatic control

systems in machines and living organisms — still permeate scientific, public and political discourse.

In the late 1960s, Maturana promoted biological materialism in cognitive science and epistemological pluralism in the biomedical sciences, both forerunners to today's thinking. In 1972, he — along with Francisco Varela and Ricardo Uribe — developed the transdisciplinary concept of autopoiesis, the self-generating and self-distinguishing biochemistry of living systems. This spawned important neuroscientific theories (see, for example, [E. Di Paolo *Topoi* 28, 9 \(2009\)](#); [M. Allen and K. J. Friston *Synthese* 195, 2459–2482; 2018](#)).

His later works centred on compassion and empathy and set the stage for social justice in Chile's current social and political context.

Nature **594**, 177 (2021)

doi: <https://doi.org/10.1038/d41586-021-01524-8>

Competing Interests

The authors declare no competing interests.

Jobs from Nature Careers

- - - [All jobs](#)
 - - [**Postdoctoral Fellow, Statistical Methodologies for Metabolomics Data Analysis**](#)
[The University of British Columbia \(UBC\)](#)
[Vancouver, Canada](#)

JOB POST

- **Postdoctoral Fellow in River Dynamics**

The University of British Columbia (UBC)

Vancouver, Canada

JOB POST

- **PhD Student in Wnt signaling**

German Cancer Research Center in the Helmholtz Association (DKFZ)

Heidelberg, Germany

JOB POST

- **Postdoc (all genders), Department Detector Laboratory (DTL)**

Helmholtz Centre for Heavy Ion Research GmbH (GSI)

Darmstadt, Germany

JOB POST

Download PDF

Related Articles

- **See more letters to the editor**

| [Section menu](#) | [Main menu](#) |

Work

- **How COVID changed schools outreach** [07 June 2021]
Career Feature • Since lockdowns closed classrooms and labs, scientists have devised online activities to inspire the next generation of researchers.
- **Education outreach can inspire the next generation of scientists** [04 June 2021]
Career Column • David Hiller finds that the joy of exploring maths and science with kids rivals his best days in the lab.
- **Fly me to the Moon** [07 June 2021]
Where I Work • Loredana Bessone instructs astronauts on living in space, walking on the Moon's surface and choosing rock samples for analysis.

- CAREER FEATURE
- 07 June 2021
- Correction [09 June 2021](#)

How COVID changed schools outreach

Since lockdowns closed classrooms and labs, scientists have devised online activities to inspire the next generation of researchers.

- [T. V. Padma](#) ⁰

1. T. V. Padma

1. T. V. Padma is a science journalist based in New Delhi, India.

[View author publications](#)

You can also search for this author in [PubMed](#) [Google Scholar](#)





•

[Find a new job](#)

[Download PDF](#)



Pre-COVID-19, the Max Planck Institute of Molecular Plant Physiology in Potsdam, Germany, hosted crop-technology demonstrations. Credit: MPI-MP, Lox und Bergmann

With a little help from potatoes, pencils, salt, wires and a battery, undergraduate science students at the Indian Institute for Science Education and Research in Pune embraced its newly digital school-outreach programme in September 2020.

Through video demonstrations by the students, school participants learnt about osmosis by seeing how potatoes shrank or expanded in an overnight saline bath. They discovered how to find the shortest path over round and curved surfaces, and how to make 2D projections of Earth's surface, using orange peel to simulate the globe.

Such common household items helped the institute's volunteer Science Nurture Programme to deliver on its mission to support disadvantaged children in their high-school science classes. Before the pandemic forced

events online, the programme, which started in 2014, had been running weekly lectures and offering participants visits to local science parks.

Meanwhile, more than 7,000 kilometres away in London, scientists at the Institute of Physics (IOP) took a similar tack, running a series of online video experiments for local primary-school pupils after the pandemic derailed plans to co-create an exhibition with pupils and their families.

The two institutions are far from alone in pivoting to digital schemes for their school-outreach programmes. Pandemic lockdowns around the world have created challenges for researchers who want to inspire the next generation of scientists. Closed laboratories have prevented them from hosting work-experience students, and emptied classrooms and museums have limited or barred opportunities to share stories and experiments in person.



[Meet the classroom collaborator](#)

Outreach organizers have been under particular pressure to adopt creative solutions because many programmes are targeted at groups that are under-represented in science, or at schools in deprived neighbourhoods. Students in many such schools have missed out on crucial lab experience because of closures, the challenges of home schooling and cancelled exams.

As happened with conference presenters and university lecturers' switch last year to virtual [sessions](#) and [classes](#), respectively, outreach organizers' adoption of digital formats was abrupt and unprecedented. But they have learnt that virtual outreach schemes can engage participants just as much as in-person activities can, can offer more flexibility and can also draw larger audiences.

Some outreach organizers are so pleased with the results of their digital programming that they expect to continue to offer hybrid activities that allow both in-person and virtual attendance.

Cancelled trips

Pre-pandemic, the Museum of Life in Rio de Janeiro, Brazil, offered outreach activities such as an 'Assemble your cell' workshop, in which primary-school pupils tried to assemble the organelles of a cell inside a plastic bag. For older pupils, the museum performed a play based on music and mathematics. But the two initiatives, along with a truck that took museum exhibits to remote areas, were halted in February 2020. In their place, the museum developed virtual exhibitions on *Aedes aegypti*, the mosquito that transmits dengue and Zika virus. Later this year, it is planning a vaccination-themed YouTube video series.

Some outreach programmes that involve competitions cancelled them last year so that schools could focus on missed lessons and coursework once they reopened. This is what happened with the South African Agency for Science and Technology Advancement's national science Olympiad, whose winners would normally get to attend London's International Youth Science Forum and the Australian National Youth Science Forum. This year, the agency has again cancelled those international trips for winners. But the organization is still running the project and awarding prizes such as laptops, tablets and school vouchers for lab equipment.



The Francis Crick Institute in London readied students to give science talks, pre-pandemic. Credit: Francis Crick Institute

The Max Planck Institute of Molecular Plant Physiology (MPI-MP) in Potsdam, Germany, is among organizations that found switching to a digital-outreach format, with videos on topics such as extracting DNA from plants, and online tours of the institution, has boosted participation. Before lockdowns were imposed, the MPI-MP had offered guided tours for high-school students that included garden visits to demonstrate plant-breeding techniques, gene heritability and crop technologies.

The online tours almost doubled the MPI-MP's website-engagement numbers last year, says spokesperson Ulrike Glaubitz, who notes that the institute's YouTube following has also risen this year. Glaubitz says that it is uncertain when in-person tours will resume.

Transitioning to an electronic format has also hugely boosted participation in an Indian government awards scheme that aims to spark students' interest in

science careers, and encourage creative thinking by setting up competitions among schools to find one million original scientific ideas.

Before the pandemic, the scheme, known as the INSPIRE Awards–MANAK (Million Minds Augmenting National Aspirations and Knowledge), had been drawing almost 400,000 competitors from across India. That shot up to more than 650,000 after the programme switched to video and radio offerings. Shortlisted students receive 10,000 rupees (US\$137), says spokesperson Sanjay Mishra at India’s Department of Science and Technology, which administers the scheme.



Why working as a travel guide or cruise lecturer can be an effective form of science outreach

Moving to a virtual format can offer more flexibility, according to Maite Ballesteros, who runs the Research Science Institute (RSI), a programme sponsored by the Center for Excellence in Education in McLean, Virginia. The RSI had offered a 5-week research internship for 80 students from the United States and elsewhere at the Massachusetts Institute of Technology in Cambridge. For now, that stint has been replaced by digital interactions that are almost boundless in their scope. “While we cannot do traditional bench science in a laboratory, we are no longer limited by distance or space,” Ballesteros says.

She says that the RSI’s offerings in mathematics, computer science and astronomy were not much affected by the new digital format. However,

some chemistry and biology experiments had to give way to data science. In 2020, for example, participants developed projects such as an algorithm that can be applied to complex systems in nuclear physics and computer science; analysis of protein data sets from mouse brains to understand a neurodegenerative disorder; and analysis of data on COVID-19 cases and deaths to understand the underlying social determinants. The programme now includes webinars, virtual classes and online guest lectures on natural sciences, maths and engineering.

Digital divides

The IOP's move to online educational outreach took creative manoeuvring, says public-engagement manager Toby Shannon-Smith, because participating pupils had varying degrees of Internet access. "We did not want to simply shift to an online format and carry on as if the world had not radically changed," he says. "We thought carefully about what we could offer families who were stuck at home and wanting to support their children to learn."

To bridge the digital divide, they e-mailed activity sheets to teachers to print out and send to children's homes. Participants then watched videos of experiments and games using cardboard or other recycled objects, including a watering can made from a milk container.

Carrying on in a digital format was also a challenge for the schools-engagement programme of the Kenya Medical Research Institute Wellcome Trust Research Programme (KWTRP), based in Kilifi. Pre-pandemic, the scheme typically engaged with about 4,000 students annually from 50 schools in the East African nation, and organized lab tours, science-career talks and an annual inter-school science quiz. There were also work-experience opportunities for final-year high-school students to gain technical or practical skills at the headquarters of the Kenya Medical Research Institute in Nairobi.

But all of this stopped in 2020. "Since many don't have access to the Internet [at home], and can only access it through school laptops, online

engagement was also not possible while schools were closed,” says Alun Davies, the KWTRP’s schools-engagement lead.

Kenyan schools reopened in January, and the KWTRP piloted online career sessions across ten schools in Kilifi. Davies says that groups of students have been gathering around computers to participate in the sessions, allowing them to engage with researchers in real time, and to view videos about careers related to health research.

To help plug the outreach gap, he says, one colleague developed materials to encourage participating primary schools to establish science clubs. Another colleague helped to produce animations and videos for pupils about COVID-19 vaccine research and contributing to biobanks.



[Collection: Science communication](#)

Uneven digital access guided decisions by Fun Lab, a physics programme of the American University in Cairo, around its online outreach offerings. Families without Internet access receive material on CDs, says Mohamed Soliman, science communication officer at the university’s physics department, and a TV channel run by Egypt’s education ministry broadcasts Fun Lab’s science shows, featuring a live audience of 40–50 socially distanced students.

The Francis Crick Institute, a biomedical research centre in London, modified its Primary Science Challenge, run in partnership with UK biomedical funding charity Wellcome and Regent High School, also in London. Primary-school pupils from that part of the city would ordinarily have worked with their teachers in a competition that culminated in giving science presentations at Regent's theatre. Last year, pupils took part in 'Science at Home' challenges instead. Participants could, for example, enter a competition to design a poster with a public-health message, or complete a science-related challenge set by a teacher, with the Crick awarding prizes to the best entries from each school. "Because of the COVID situation, the theatre event wasn't possible," says Clare Davy, education manager at the Crick. "We felt it was important to have a competition that anyone could take part in, so long as they could get a piece of paper. Many children in our schools can't access the Internet and don't have a lot of sciencey materials at home."

For students aged 16–17, the Crick turned to Google Classroom to adapt its work-experience opportunities, partnering with Centre of the Cell, a science-education centre based at Queen Mary University of London. Some students worked with the Crick's communications team to produce a video featuring interviews with Crick scientists about the pandemic. The adapted sessions also covered CV writing and interview techniques.

It is crucial, Davy says, to pique pupils' and students' interest in the scientific enterprise by engaging them in practical science. "That is such a motivator for science careers. If we can help to fill that gap, it would be great," she says.

Nature **594**, 289-291 (2021)

doi: <https://doi.org/10.1038/d41586-021-01517-7>

Updates & Corrections

- **Correction 09 June 2021:** An earlier version of this story overstated the numbers of people applying for the INSPIRE Awards-Manak. Also, a quote originally attributed to spokesperson Claire McLoughlin actually came from public-engagement manager Toby Shannon-Smith.

Jobs from Nature Careers

- - - [All jobs](#)
 - - [Postdoctoral Fellow, Statistical Methodologies for Metabolomics Data Analysis](#)
[The University of British Columbia \(UBC\)](#)
[Vancouver, Canada](#)
[JOB POST](#)
 - [Postdoctoral Fellow in River Dynamics](#)
[The University of British Columbia \(UBC\)](#)
[Vancouver, Canada](#)
[JOB POST](#)
 - [PhD Student in Wnt signaling](#)
[German Cancer Research Center in the Helmholtz Association \(DKFZ\)](#)
[Heidelberg, Germany](#)
[JOB POST](#)
 - [Postdoc \(all genders\), Department Detector Laboratory \(DTL\)](#)
[Helmholtz Centre for Heavy Ion Research GmbH \(GSI\)](#)

Darmstadt, Germany

JOB POST

Download PDF

Related Articles



- [Why working as a travel guide or cruise lecturer can be an effective form of science outreach](#)



- [Science diversified: Starting young](#)



- [Meet the classroom collaborator](#)



- [Collection: Science communication](#)

This article was downloaded by **calibre** from <https://www.nature.com/articles/d41586-021-01517-7>

- CAREER COLUMN
- 04 June 2021

Education outreach can inspire the next generation of scientists

David Hiller finds that the joy of exploring maths and science with kids rivals his best days in the lab.

- [David Hiller](#) ⁰

1. David Hiller

1. David Hiller is a research scientist in biochemistry and biophysics at Yale University in New Haven, Connecticut, and runs the science-education business Stempogo.

[View author publications](#)

You can also search for this author in [PubMed](#) [Google Scholar](#)





•

[Download PDF](#)



David Hiller ground cabbage leaves to explore pH with schoolchildren.Credit: Getty

It's April 2020, and I'm on a Zoom call, grinding cabbage leaves and exploring the concept of pH with more than 50 kids from across the United States. It's a bright spot during a difficult time at the start of the pandemic, and the activity fills me with much-needed joy.

It feels very far from the lab work that I'd focused on for the past 20 years, since graduating with a degree in chemistry from the California Institute of Technology in Pasadena. I'm now a research scientist at Yale School of Medicine in New Haven, Connecticut.

Many scientists find education outreach to be inspiring and rewarding, but it can be hard to find the time and resources to do it alongside research. How can we have good experiences, make a positive impact and still maintain our research?

I went from being too shy to speak in front of a group of students in 2005 to designing and leading an online outreach programme in 2020. I found that the joy of exploring maths and science with kids has rivalled my best days in the laboratory. The work's impact has been obvious — smiling, curious kids

and happy parents — and I enjoyed the intellectual challenge of creating activities for children.

Here's some advice for others who are interested in doing public-outreach work alongside their science.

Take advantage of existing opportunities

During my PhD programme, I focused on my own research and rarely considered public communication — but, after settling into my postdoctoral studies, I became more interested in sharing my love of science and nature with others. My first forays into outreach were built by someone else: I started mentoring students for the New Haven Science Fair, a two-day festival that aimed to help young people start hands-on experiments, in 2016, and I participated in one-day events such as the [Julia Robinson Mathematics Festival](#), which aims to achieve something similar in mathematics.

Even though the impact of these activities varied widely, seeing students light up when a scientist joined their classroom had me hooked. I remember walking into my five-year-old son's last day of preschool, where I'd volunteered to give science demonstrations, and seeing the children's favourite things from the year posted on the wall. When I saw that one child's favourite thing was "building rockets with Dr. Dave", my heart soared.



Collection: Science communication

Many universities have a list of available outreach opportunities through an education department or communications office, or directly in science departments. Science organizations such as the royal academies and the American Association for the Advancement of Science keep databases of programmes, including an increasing number of ‘science cafes’ (where scientists engage with the public in casual settings), and local governments often facilitate science fairs and reading programmes.

These programmes can usually take new volunteers, and you will often be able to start with small time commitments. This is a good way to try something new: I am a biochemist, but I loved helping students explore a logic puzzle about a pirate captain and crew (complete with pirate hats) at the Julia Robinson Mathematics Festival. At the same time, if a programme doesn’t inspire you, or you don’t think you’re having an impact, it’s okay to move on to something else.

Create events within existing frameworks

After my lab moved to Yale’s west campus in 2015, I created an outreach project with two graduate students to provide good opportunities for other graduate students and postdocs. We started an annual one-day festival to

showcase the breadth of science that occurs on the west campus, to show students that science can happen in gardens and art galleries — not just in biochemistry labs — so they could connect it to a field they already loved. And by tailoring our programme to our volunteers and resources, we hoped to maximize the value of our work to students and families in the surrounding school districts.

Early in our planning, we were directed to [Yale Pathways to Science](#), an umbrella organization that facilitates hundreds of outreach activities across campus. We took advantage of the logistical support provided by Pathways, such as help with advertising, registration, food and transportation, as well as their feedback on what content would benefit local students. This allowed the scientists who we recruited from campus, including biologists, chemists, art preservators and ecologists, to focus on what they did best and enjoyed most — creating engaging scientific experiences.

This was a valuable lesson: like science itself, the most success in science engagement often comes from building on the progress made by others. Even if no organization exists where you are, collaboration with other groups (especially if you've participated in their programmes before) can keep you from having to reinvent every logistical piece. Also, just like your research, keeping good records of what you did and whether it worked (and storing them in the cloud, so they can be easily shared) will help you to sustain and improve what you create.

Strike out on your own (if you're ready)

In 2016, a neighbour asked me whether I was interested in setting up an informal maths programme for our kids and their friends. I was excited to try it, and we started an after-school programme at our local primary school, for children aged five to eight.

We received logistical support from the school, such as classroom space and a way to market the class to students and parents, but we were wholly responsible for designing the programme.

We researched similar maths programmes — including [math circles](#), which are groups that focus on collaborative problem-solving — and built on what we had seen work in other contexts. We decided to create an environment, similar to that of a youth sports team, in which kids could work together to solve problems in different maths fields. We began by exploring logic, graph theory and topology with a group of curious students. In the process, I learnt as much maths as the students did.

The demand for this type of experience was high, and our first programme was oversubscribed. We quickly grew to multiple groups and, eventually, several schools. As the programme grew, we continually solicited feedback from parents about what worked and what didn't.

My colleagues involved in the programme and I enjoyed creating something that was equally rewarding for us and for students. Although it wasn't a perfectly smooth progression in building my own programme (I was turned down for one grant to expand the programme into lower-income schools), the overall success prompted me to devote more time to developing new activities. Two years after starting, I reduced my research load to give me time to start my own science and maths education business — which is how I found myself grinding those cabbage leaves on that Zoom call in April 2020.

Finding the time

It's important to recognize that support for outreach varies widely depending on your institution and the culture of your department or lab. Fortunately, both universities and funding agencies are placing increased emphasis on communicating science to the public, such as by including a version of 'broader impacts' in the funding criteria: both the US National Science Foundation and Marie Curie grants, delivered by the European Commission, now specifically mention outreach programmes.

Speaking about science to younger audiences also develops your communication skills, which will help the next time you give a talk, contribute to a grant application or write a paper. It might feel less challenging to describe your science to the professors on your dissertation

committee after you've figured out how to explain it to a group of nine year olds.

In my case, the support of my principal investigator and university allowed me to pursue my passion for outreach. As I developed new programmes, I created roles that had different commitments and skills to make sure anyone who was interested could find a good fit. Seeking that fit is key to feeling valued and having success in outreach. No one should feel guilty because they couldn't devote enough time to a project. Be clear and direct with yourself and anyone you're working with about the amount of time you're able to devote to outreach.

Outreach can be a meaningful component of your scientific career. Whether you are creating a programme from scratch or volunteering for something with a long history, participation should benefit both you and the public. That has been especially true for me, as the connections I've made have helped me through this past year.

Nature **594**, 291-292 (2021)

doi: <https://doi.org/10.1038/d41586-021-01518-6>

This is an article from the Nature Careers Community, a place for *Nature* readers to share their professional experiences and advice. [Guest posts are encouraged.](#)

Jobs from Nature Careers

- - - [All jobs](#)
 -
 - [**Postdoctoral Fellow, Statistical Methodologies for Metabolomics Data Analysis**](#)

[The University of British Columbia \(UBC\)](#)

[Vancouver, Canada](#)

[JOB POST](#)

- [Postdoctoral Fellow in River Dynamics](#)

[The University of British Columbia \(UBC\)](#)

[Vancouver, Canada](#)

[JOB POST](#)

- [PhD Student in Wnt signaling](#)

[German Cancer Research Center in the Helmholtz Association \(DKFZ\)](#)

[Heidelberg, Germany](#)

[JOB POST](#)

- [Postdoc \(all genders\), Department Detector Laboratory \(DTL\)](#)

[Helmholtz Centre for Heavy Ion Research GmbH \(GSI\)](#)

[Darmstadt, Germany](#)

[JOB POST](#)

[Download PDF](#)

Related Articles

-  **'All my art is curiosity-driven': the garden studio where art and physics collide**
-  **How the coronavirus pandemic is changing virtual science communication**
-  **The sourdough loaves that led two scientists to fame on The Great British Bake Off**

This article was downloaded by **calibre** from <https://www.nature.com/articles/d41586-021-01518-6>

| [Section menu](#) | [Main menu](#) |

- WHERE I WORK
- 07 June 2021

Fly me to the Moon

Loredana Bessone instructs astronauts on living in space, walking on the Moon's surface and choosing rock samples for analysis.

- [Virginia Gewin](#) ⁰

1. Virginia Gewin

1. Virginia Gewin is a freelance writer in Portland, Oregon.

[View author publications](#)

You can also search for this author in [PubMed](#) [Google Scholar](#)





•



Project leader Loredana Bessone facilitates the collection of lessons learned from the execution of a geological traverse.

Loredana Bessone heads the analogue field-testing and exploration-training unit at the European Space Agency in Cologne, Germany. Credits: A. Romeo/ESA

[Download PDF](#)

I have been training astronauts at the European Space Agency (ESA) since 1992, when I was a computer engineer teaching them about information technology. I gradually took on more types of training, and have helped to

design prospective human missions to Mars as well as missions to explore lunar caves.

This picture was taken in 2018 on Lanzarote, part of Spain's volcanic Canary Islands. There's little vegetation there, so it is a fantastic analogue for the Moon and Mars. We are debriefing here after a lunar simulation in which the astronauts learnt to identify and collect the most interesting rock samples for studying geological history. It was part of a three-week field course that the ESA introduced in 2016 that prepares astronauts for observing geological features.

We've done training sessions in the fjords of Norway; in the Bletterbach canyon in the Dolomites, in northeast Italy; and at the Nördlinger Ries impact crater site in southwest Germany. At sites such as these, astronauts learn how to select the best possible rock samples to take back to Earth. We have only 300 kilograms of rocks from the Moon, which are still being analysed. It's like gold to have these rocks for studying the origin of our Solar System.

Since 2011, I've also run a programme in which a team of up to six astronauts spends six days and nights isolated in caves on the Italian island of Sardinia, or in Slovenia. The astronauts are by themselves, and sometimes have to squeeze through narrow passages, but I follow them with safety instructors, a doctor and video operators to monitor their welfare. In space, the farther from Earth they go, the more responsible they are for their own safety.

Moon and Mars rocks offer a window into Earth's first billion years, of which we have only rare, localized records. We need astronauts to make the most of every chance to retrieve a chunk of Earth's history.

Nature **594**, 294 (2021)

doi: <https://doi.org/10.1038/d41586-021-01519-5>

Jobs from Nature Careers

- - - [All jobs](#)
 - - [**Postdoctoral Fellow, Statistical Methodologies for Metabolomics Data Analysis**](#)
[The University of British Columbia \(UBC\)](#)
[Vancouver, Canada](#)
[JOB POST](#)
 - [**Postdoctoral Fellow in River Dynamics**](#)
[The University of British Columbia \(UBC\)](#)
[Vancouver, Canada](#)
[JOB POST](#)
 - [**PhD Student in Wnt signaling**](#)
[German Cancer Research Center in the Helmholtz Association \(DKFZ\)](#)
[Heidelberg, Germany](#)
[JOB POST](#)
 - [**Postdoc \(all genders\), Department Detector Laboratory \(DTL\)**](#)
[Helmholtz Centre for Heavy Ion Research GmbH \(GSI\)](#)
[Darmstadt, Germany](#)

JOB POST

[Download PDF](#)

Related Articles



- [From high-altitude balloons to Moon missions](#)



- [Space pioneer](#)

This article was downloaded by **calibre** from <https://www.nature.com/articles/d41586-021-01519-5>

| [Section menu](#) | [Main menu](#) |

Research

- **[Activation of retinal neurons triggers tumour formation in cancer-prone mice](#)** [26 May 2021]

News & Views • Light-induced activation of neuronal cells in the retina stimulates the formation of optic-nerve tumours in cancer-prone mice, revealing a potential role of neuronal activity in cancer initiation.

- **[Squeezed light improves sensitivity of microscopy technique](#)** [09 June 2021]

News & Views • Vibrational signals from molecules can provide contrast in bioimaging techniques, but are difficult to detect. Light in a ‘squeezed’ quantum state has been used to reveal molecular vibrational signals previously obscured by noise.

- **[Ancient human faeces reveal gut microbes of the past](#)** [17 May 2021]

News & Views • Appreciation is growing of how our gut microbes shape health and disease. Now, a study of ancient human faeces sheds light on how microbial populations in the gut have changed during the past 2,000 years.

- **[AI system outperforms humans in designing floorplans for microchips](#)** [09 June 2021]

News & Views • A machine-learning system has been trained to place memory blocks in microchip designs. The system beats human experts at the task, and offers the promise of better, more-rapidly produced chip designs than are currently possible.

- **[Ancient seeds spill secrets about the evolution of flowering plants](#)** [26 May 2021]

News & Views • The origin and rapid diversification of flowering plants is a long-standing “abominable mystery”, as Charles Darwin put it. Part of the puzzle – the origin of the protective covering of flowering-plant seeds – is nearing resolution.

- **[Anisotropic satellite galaxy quenching modulated by black hole activity](#)** [09 June 2021]

Article • An analysis of archival data from the Sloan Digital Sky Survey finds that star-forming satellite galaxies are relatively more common along the minor axis of central galaxies owing to the effect of black hole feedback.

- **[Observation of first and second sound in a BKT superfluid](#)** [09 June 2021]

Article • First and second sound are experimentally observed in a two-dimensional superfluid, and the temperature-dependent sound speeds reveal the predicted jump in the superfluid density at the infinite-order Berezinskii–Kosterlitz–Thouless transition.

- [Experimental observation of non-Abelian topological charges and edge states](#) [09 June 2021]
Article • Non-Abelian topological charges and edge states in a PT-symmetric transmission line network are experimentally observed, and a non-Abelian quotient relation for the bulk–edge correspondence is found.
- [Quantum-enhanced nonlinear microscopy](#) [09 June 2021]
Article • A quantum microscope obtains signal-to-noise beyond the photodamage limits of conventional microscopy, revealing biological structures within cells that would not otherwise be resolved.
- [A graph placement methodology for fast chip design](#) [09 June 2021]
Article • Machine learning tools are used to greatly accelerate chip layout design, by posing chip floorplanning as a reinforcement learning problem and using neural networks to generate high-performance chip layouts.
- [Tomographic reconstruction of oxygen orbitals in lithium-rich battery materials](#) [09 June 2021]
Article • High-energy X-ray Compton measurements and first-principles modelling reveal how the electronic orbital responsible for the reversible anionic redox activity can be imaged and visualized, and its character and symmetry determined.
- [Phosphorus-mediated sp₂–sp₃ couplings for C–H fluoroalkylation of azines](#) [28 April 2021]
Article • Bench-stable fluoroalkylphosphine reagents are used to form C–CF₂X bonds in a one-pot process, reliably fluoroalkylating pyridine building blocks and drug and agrochemical intermediates.
- [Mesozoic cupules and the origin of the angiosperm second integument](#) [26 May 2021]
Article • Analysis of recurved cupules from a newly discovered Early Cretaceous silicified peat in Inner Mongolia, China and comparison with other potentially related Mesozoic plant fossils provides insight into the origins of angiosperms.
- [Evolutionary and biomedical insights from a marmoset diploid genome assembly](#) [28 April 2021]
Article • A trio-binning approach is used to produce a fully haplotype-resolved diploid genome assembly for the common marmoset, providing insight into the heterozygosity spectrum and the evolution of the sex-differentiation region.

- **Reconstruction of ancient microbial genomes from the human gut** [12 May 2021]
Article • Ancient microbiomes from palaeofaeces are more similar to non-industrialized than industrialized human gut microbiomes regardless of geography, but 39% of their de novo reconstructed genomes represent previously undescribed microbial species.
- **SARS-CoV-2 uses a multipronged strategy to impede host protein synthesis** [12 May 2021]
Article • RNA sequencing, ribosome profiling and metabolic labelling of newly synthesized RNA reveal the strategy used by SARS-CoV-2 to shut off cellular protein synthesis in the host and allow the translation of viral transcripts.
- **Multilevel proteomics reveals host perturbations by SARS-CoV-2 and SARS-CoV** [12 April 2021]
Article • Multi-omics profiling of effects of SARS-CoV-2 and SARS-CoV on A549, a lung-derived human cell line, produces a dataset enabling identification of common and virus-specific mechanisms of infection.
- **Adjuvanting a subunit COVID-19 vaccine to induce protective immunity** [19 April 2021]
Article • Trials in rhesus macaques show that a subunit vaccine against SARS-CoV-2, comprising the spike protein receptor-binding domain displayed on a nanoparticle protein scaffold, produces a robust protective response against the virus.
- **High-dimensional characterization of post-acute sequelae of COVID-19** [22 April 2021]
Article • Healthcare data from the US Department of Veterans Affairs are used to characterize the six-month incident sequelae of individuals who survive for at least thirty days after developing COVID-19.
- **Swarm Learning for decentralized and confidential clinical machine learning** [26 May 2021]
Article • Swarm Learning is a decentralized machine learning approach that outperforms classifiers developed at individual sites for COVID-19 and other diseases while preserving confidentiality and privacy.
- **PIK3CA and CCM mutations fuel cavernomas through a cancer-like mechanism** [28 April 2021]
Article • Aggressive cerebral cavernous malformations (CCMs) are found to grow through a three-hit cancer-like mechanism, involving gain of function of a gene that promotes vascular growth, and loss of function of genes that suppress it.
- **NF1 mutation drives neuronal activity-dependent initiation of optic glioma** [26 May 2021]

Article • Mouse models of NF1-associated optic pathway glioma show that tumour initiation and growth are driven by aberrantly high levels of NLGN3 shedding in the optic nerve in response to retinal neuron activity.

- **RNA transcripts stimulate homologous recombination by forming DR-loops** [12 May 2021]

Article • RNA transcripts stimulate homologous recombination through the formation of DR-loops, intermediate structures that contain both DNA–DNA and DNA–RNA hybrids.

- **Perovskite decomposition and missing crystal planes in HRTEM** [09 June 2021]

Matters Arising •

- **Reply to: Perovskite decomposition and missing crystal planes in HRTEM** [09 June 2021]

Matters Arising •

- NEWS AND VIEWS
- 26 May 2021

Activation of retinal neurons triggers tumour formation in cancer-prone mice

Light-induced activation of neuronal cells in the retina stimulates the formation of optic-nerve tumours in cancer-prone mice, revealing a potential role of neuronal activity in cancer initiation.

- [Varun Venkataramani](#)⁰ &
- [Frank Winkler](#)¹

1. Varun Venkataramani

1. Varun Venkataramani is in the Department of Neurology, University Hospital Heidelberg, at the German Cancer Research Center, 69120 Heidelberg, Germany, and in the Department of Functional Neuroanatomy, University Hospital Heidelberg.

[View author publications](#)

You can also search for this author in [PubMed](#) [Google Scholar](#)

2. [Frank Winkler](#)

1. Frank Winkler is in the Department of Neurology, University Hospital Heidelberg, and at the German Cancer Research Center, 69120 Heidelberg, Germany.

[View author publications](#)

You can also search for this author in [PubMed](#) [Google Scholar](#)

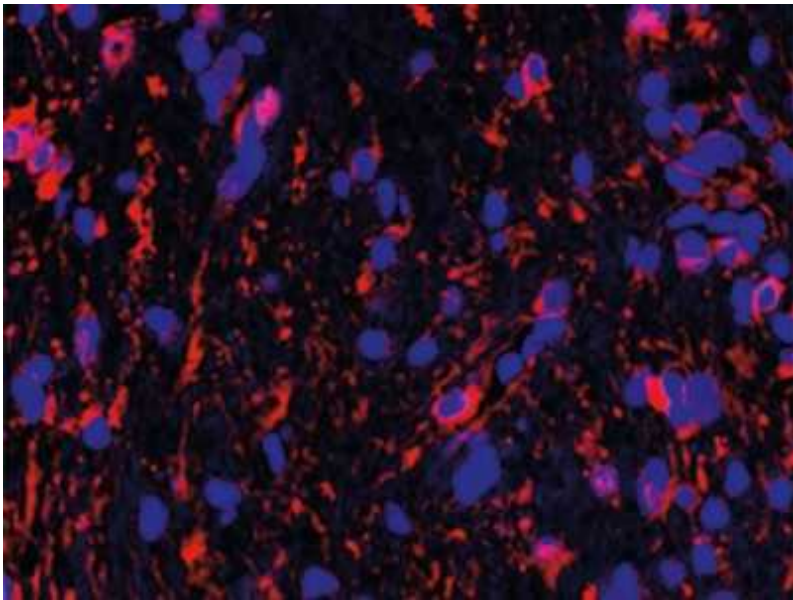
-



•

[Download PDF](#)

Cancer is not a disease involving uncontrolled division of isolated cells; rather, it is a condition in which various types of normal and malignant cells collaborate to drive tumour growth and dissemination. To the surprise of many, the nervous system — which includes neuronal cells and non-neuronal cells of the brain, spinal cord and nerves throughout the body — can also be involved in cancer progression. [Writing in Nature](#), Pan *et al.*¹ report that, in a mouse model of a rare disease that predisposes people to tumours along the optic nerve, light-induced neuronal activity is responsible not only for the growth of these tumours, but also for their initiation.



[Read the paper: NF1 mutation drives neuronal activity-dependent initiation of optic glioma](#)

Neurofibromatosis type 1 (NF1) affects one in about 3,000 people worldwide, and is caused by a mutation in the gene of the same name. Individuals with the *NF1* gene mutation are predisposed to early-childhood development of slow-growing (low-grade) tumours called gliomas along the optic pathway — the nervous pathway that includes the optic nerve and that carries visual information from the light-sensing cells of the retina to the brain.

The starting point for Pan and colleagues' study was a mouse model in which nearly all cells in the body carry the mutation in the mouse *Nf1* gene, but in which only the cells that transform into optic pathway gliomas (neural progenitor cells) lack a functional copy of the *Nf1* gene completely². Both of these conditions are a prerequisite for the development of optic pathway gliomas in mice at a young age (by about nine weeks)³, reflecting the situation in children and young adults with NF1, who can develop gliomas that show a lack of NF1 expression. Pan *et al.* used this relatively simple and controllable mouse model — called the *Nf1*–optical pathway glioma (*Nf1*^{OPG}) model — to address the exciting question of whether exposure to light, which increases neuronal activity in the optic pathway, triggers the formation of optic pathway gliomas.

The authors tested whether raising young *Nfl*^{OPG} mice in the dark from 6 to 12 weeks of age prevented the formation of optic pathway gliomas.

Remarkably, it did. Moreover, placing *Nfl*^{OPG} mice with already initiated tumours in darkness later in life (from 12 to 16 weeks) strongly reduced tumour growth. In line with these findings, artificial activation of neurons in the optic nerve, using a technique called optogenetics, drove increased growth of optic pathway gliomas in *Nfl*^{OPG} mice.

Next, the authors explored the molecular determinants behind the effects of visual experience on glioma growth (Fig. 1). In previous studies of another type of brain tumour (aggressive high-grade glioma), some researchers from the study by Pan *et al.* demonstrated that activated neurons secrete a protein called brain-derived neurotrophic factor and shed another protein, called neuroligin-3, that in turn stimulates glioma growth⁴. In Pan and colleagues' study, the team found that optogenetic stimulation of neurons in the retina increased the levels of both factors in the optic pathway, and that both proteins promoted the proliferation of low-grade glioma cells in culture. The role of neuroligin-3 in driving tumour growth in the *Nfl*^{OPG} model was then confirmed by demonstrating that its genetic loss from these mice, like light deprivation, reduced the incidence of glioma.

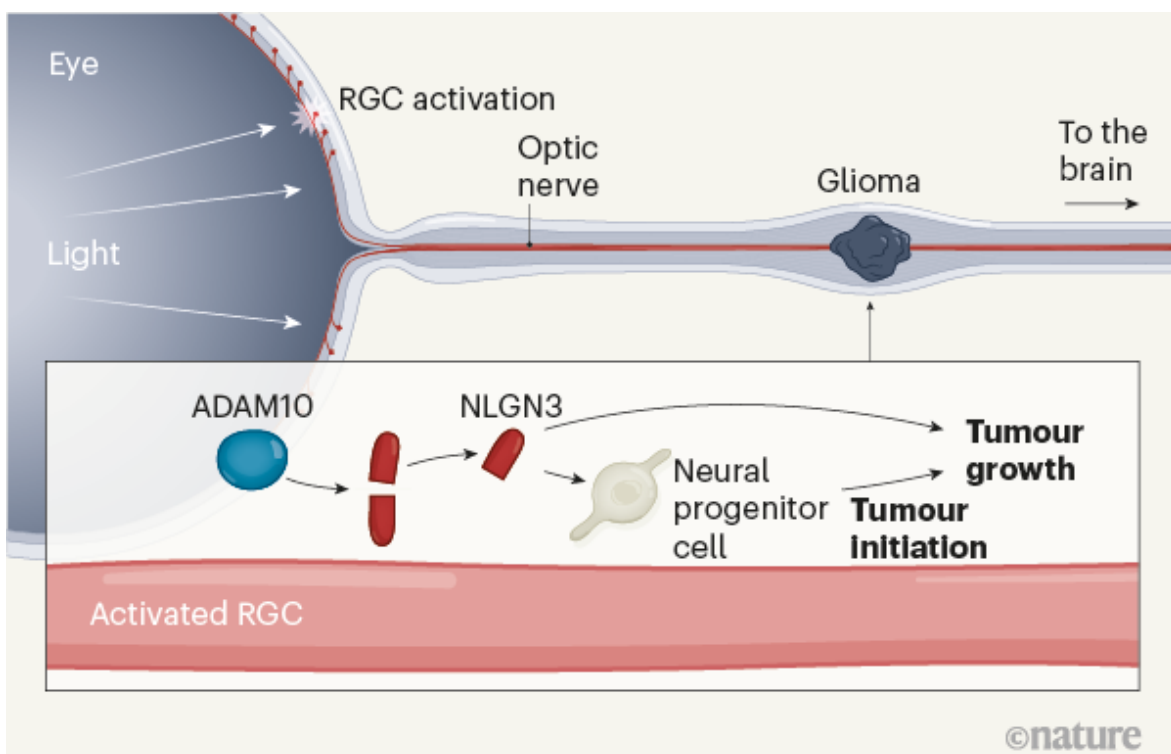
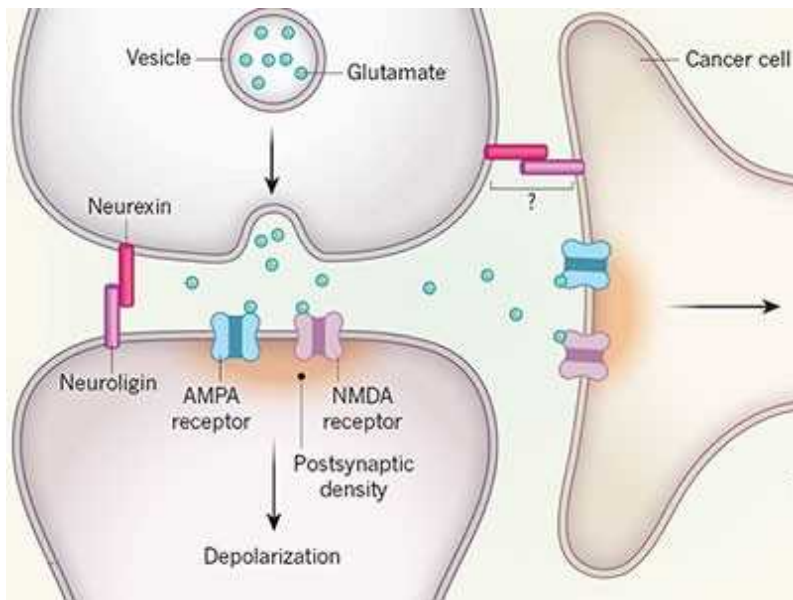


Figure 1 | Neuronal activity in the optic nerve of susceptible mice drives tumour formation. Neurofibromatosis type 1 (NF1) is a syndrome in which people are prone to developing certain types of cancer. Pan *et al.*¹ report that, in a genetically engineered mouse model of NF1, the light-induced activation of retinal ganglion cells (RGCs) is sufficient to induce the formation of tumours called gliomas of the optic nerve that contains a bundle of RGC projections carrying visual information to the brain. Compared with what happens in regular mice, activated RGCs in the model mice release more of the protein neuroligin-3 (NLGN3), which is cleaved from the cell membrane (not shown) by the enzyme ADAM10. NLGN3 promotes the transformation of neural progenitor cells into tumour cells, giving rise to optic pathway gliomas, and also stimulates the growth of these tumours.

Pan *et al.* also detected high levels of neuroligin-3 in tumour samples from humans with a type of low-grade glioma related to optic pathway gliomas, called pilocytic astrocytomas, although the level of expression varied between samples. Notably, tumour samples showing particularly high expression of neuroligin-3 also exhibited high expression of genes associated with the formation of synapses, the connections between neurons. This finding raises the question of whether neuron–glioma synapses that have been found in high-grade gliomas, where they boost tumour aggressiveness^{5,6}, are also present in NF1-related low-grade gliomas. This should be determined by future research.

Through further experiments, the authors demonstrate that greater amounts of neuroligin-3 are released by activated neurons in the optic pathway of *Nf1*^{OPG} mice than by activated neurons in the optic pathway of regular mice. This establishes a previously unknown mechanism by which the NF1 mutation can enable neuronal activity to initiate tumours and thus make people with NF1 susceptible to them. It will be interesting to learn whether this also applies to other tumour types that are typically associated with NF1, such as malignant peripheral nerve sheath tumours. A further question would be whether other cancer-predisposition syndromes involve similar mechanisms in which neuronal activity drives tumour formation and growth.



Dangerous liaisons as tumour cells form synapses with neurons

Building again on previous work on high-grade gliomas^{4,7}, the authors demonstrate that a drug that inhibits the enzyme that releases neuroligin-3 from neurons does so in the optic nerves of *Nf1*^{OPG} mice, too. Treating young *Nf1*^{OPG} mice with the drug prevented optic pathway glioma formation, mimicking the effects of light deprivation. Also like light deprivation, later treatment with the drug reduced the tumour size. This compound is already in clinical trials for high-grade gliomas (see this US trial run by the Pediatric Brain Tumor Consortium; go.nature.com/3w3mx44), and so its potential for preventing or treating NF1-related gliomas is intriguing.

The study by Pan and co-workers strengthens the idea that neuronal activity not only can drive the growth of tumours, but also can be crucial for cancer initiation — which has been previously suggested to be the case in cancers outside the central nervous system⁸. In prostate cancer and other cancers, progenitor cells from the brain can even home in on tumours, where they are instrumental in tumour development and growth⁹. Furthermore, in mice, removal of neurons that carry sensory information from the pancreas to the central nervous system prevented the formation of pancreatic tumours¹⁰. In mouse skin, tumours were found to preferentially originate in cell populations with particularly high neuronal innervation¹¹. Pan and

colleagues' study extends this link to the central nervous system, and to cancer-predisposition syndromes.

So, what are the clinical implications of this study? Should we tell individuals with NF1 to wear sunglasses or cover their eyes for a certain time? Or should we somehow aim to reduce the overall neuronal activity of individuals with brain tumours? Such 'strategies' would be problematic to implement, for many practical, not to mention ethical, reasons. However, current initiatives seeking to translate our understanding of the interactions between the nervous system and cancers support the use of pharmacological approaches that are targeted to specific molecular pathways¹². This study supports another such approach for individuals with NF1. It will be exciting to discover whether neuroscience-instructed cancer therapy will become a new pillar of treatment in oncology.

Nature **594**, 179-180 (2021)

doi: <https://doi.org/10.1038/d41586-021-01353-9>

References

1. 1.

Pan, Y. *et al.* Nature **594**, 277–282 (2021).

[Article](#) [Google Scholar](#)

2. 2.

Bajenaru, M. L. *et al.* Cancer Res. **63**, 8573–8577 (2003).

[PubMed](#) [Google Scholar](#)

3. 3.

Toonen, J. A., Ma, Y. & Gutmann, D. H. Neuro Oncol. **19**, 808–819 (2017).

[PubMed](#) [Google Scholar](#)

4. 4.

Venkatesh, H. S. *et al.* *Cell* **161**, 803–816 (2015).

[PubMed](#) [Article](#) [Google Scholar](#)

5. 5.

Venkataramani, V. *et al.* *Nature* **573**, 532–538 (2019).

[PubMed](#) [Article](#) [Google Scholar](#)

6. 6.

Venkatesh, H. S. *et al.* *Nature* **573**, 539–545 (2019).

[PubMed](#) [Article](#) [Google Scholar](#)

7. 7.

Venkatesh, H. S. *et al.* *Nature* **549**, 533–537 (2017).

[PubMed](#) [Article](#) [Google Scholar](#)

8. 8.

Magnon, C. *et al.* *Science* **341**, 1236361 (2013).

[PubMed](#) [Article](#) [Google Scholar](#)

9. 9.

Mauffrey, P. *et al.* *Nature* **569**, 672–678 (2019).

[PubMed](#) [Article](#) [Google Scholar](#)

10. 10.

Saloman, J. L. *et al.* *Proc. Natl Acad. Sci. USA* **113**, 3078–3083 (2016).

[PubMed](#) [Article](#) [Google Scholar](#)

11. 11.

Peterson, S. C. *et al.* *Cell Stem Cell* **16**, 400–412 (2015).

[PubMed](#) [Article](#) [Google Scholar](#)

12. 12.

Monje, M. *et al.* *Cell* **181**, 219–222 (2020).

[PubMed](#) [Article](#) [Google Scholar](#)

[Download references](#)

Competing Interests

The authors declare no competing interests.

[Jobs from Nature Careers](#)

- - - [All jobs](#)
 -
 - [Postdoctoral Fellow, Statistical Methodologies for Metabolomics Data Analysis](#)
 - [The University of British Columbia \(UBC\)](#)
 - [Vancouver, Canada](#)
 - [JOB POST](#)

- **Postdoctoral Fellow in River Dynamics**

The University of British Columbia (UBC)

Vancouver, Canada

JOB POST

- **PhD Student in Wnt signaling**

German Cancer Research Center in the Helmholtz Association (DKFZ)

Heidelberg, Germany

JOB POST

- **Postdoc (all genders), Department Detector Laboratory (DTL)**

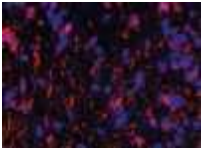
Helmholtz Centre for Heavy Ion Research GmbH (GSI)

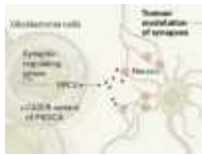
Darmstadt, Germany

JOB POST

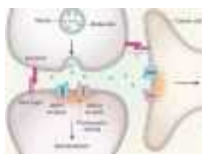
Download PDF

Related Articles

-  **Read the paper: NF1 mutation drives neuronal activity-dependent initiation of optic glioma**



- **Brain tumours manipulate neighbouring synapses**



- **Dangerous liaisons as tumour cells form synapses with neurons**
- **See all News & Views**

This article was downloaded by **calibre** from <https://www.nature.com/articles/d41586-021-01353-9>

- NEWS AND VIEWS
- 09 June 2021

Squeezed light improves sensitivity of microscopy technique

Vibrational signals from molecules can provide contrast in bioimaging techniques, but are difficult to detect. Light in a ‘squeezed’ quantum state has been used to reveal molecular vibrational signals previously obscured by noise.

- [Eric O. Potma](#) 0
 1. [Eric O. Potma](#)
 1. Eric O. Potma is in the Department of Chemistry, University of California, Irvine, Irvine, California 92617, USA.

[View author publications](#)

You can also search for this author in [PubMed](#) [Google Scholar](#)



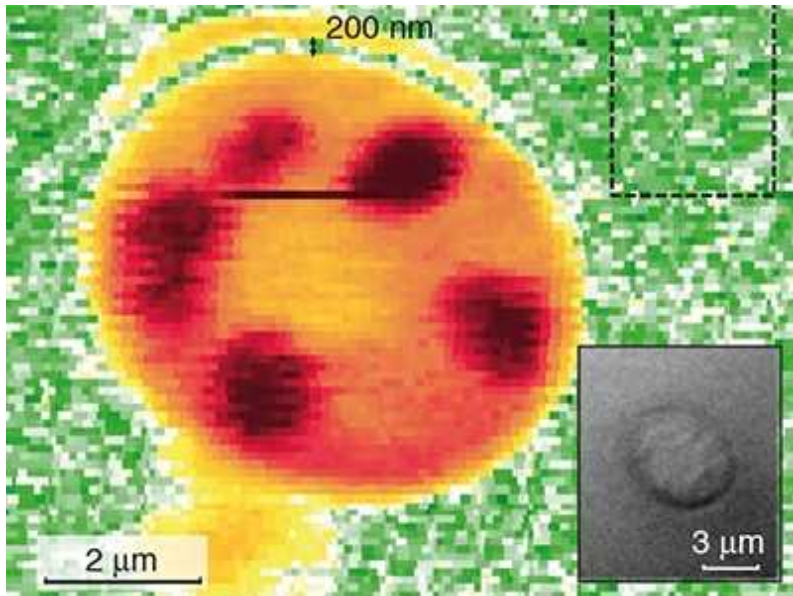


•

[Download PDF](#)

Much like fluorescence microscopy, stimulated Raman scattering (SRS) gain microscopy is an optical imaging method capable of generating high-resolution maps of biological tissues¹. The contrast in SRS images derives from the characteristic vibrations of the sample's molecules, which enable tissue imaging without the need to label samples with fluorescent dyes. SRS is gaining ground as a biomedical imaging tool, but the minimum molecular concentrations that it can detect are higher than those that can be detected using fluorescence microscopy, thus limiting its scope. Finding ways to fundamentally improve the detection sensitivity of this technique has been

challenging. [Writing in Nature](#), Casacio *et al.*² describe an approach for boosting sensitivity through quantum-enhanced suppression of noise in the SRS signal.



[Read the paper: Quantum-enhanced nonlinear microscopy](#)

SRS is based on a phenomenon called the Raman effect, which involves two photons: one known as the pump photon (of frequency ω_1), which interacts with a molecule; and another called the Stokes photon (of a lower frequency, ω_2), which is radiated by the molecule in response to its interaction with the pump photon. The frequency difference ($\omega_1 - \omega_2$) corresponds to the frequency of a particular vibrational mode of the molecule. Measurements of the wavelength of the Stokes photons can therefore be used to identify the molecule on the basis of its vibrational behaviour. However, the signal produced by the Raman effect is weak, giving rise to a long integration time (the period needed to collect a signal), which prevents it from being used for tissue imaging.

SRS cleverly overcomes the weakness of the Raman signal. Unlike the linear Raman effect described above, which uses one laser beam, SRS involves illuminating the sample with two laser-light fields: a pump field with frequency ω_1 and a Stokes field with frequency ω_2 . In SRS, the sample produces a stronger signal field than in the linear effect. Moreover, because

the signal field is produced in phase with the Stokes field, constructive interference occurs, greatly boosting the signal from the sample (Fig. 1). The amplified signal is therefore much stronger than the weak molecular signal produced by the linear effect.

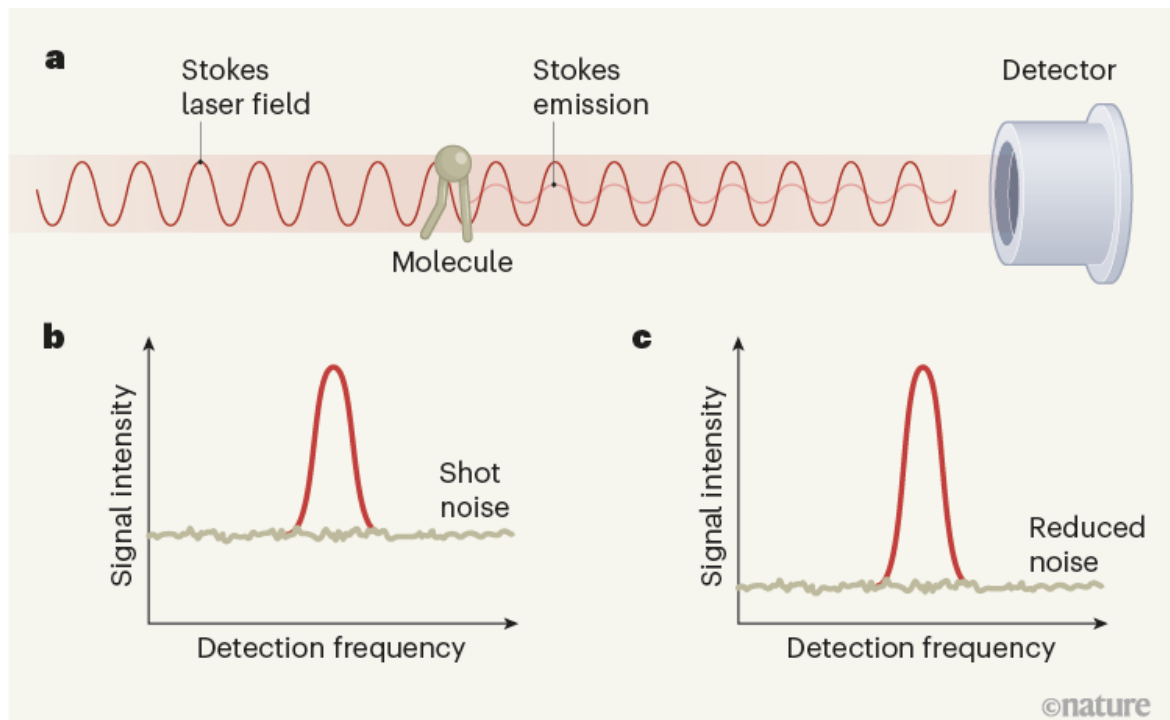
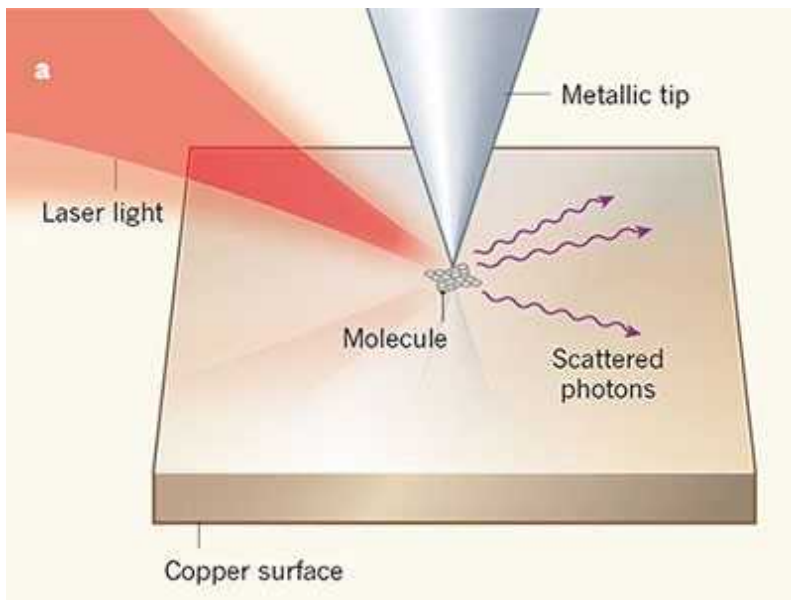


Figure 1 | Squeezed light reduces noise in stimulated Raman scattering (SRS) gain microscopy. **a**, In SRS gain microscopy, a sample is irradiated with laser light at a frequency (the pump frequency; not shown) that causes molecules to vibrate and emit light at a second frequency (the Stokes frequency), thus providing a weak optical signal. The sample is also irradiated with intense laser light at the Stokes frequency, boosting the emission from the molecule. The two Stokes fields — the emitted signal and the much stronger laser light — interfere constructively at the detector. **b**, This interference amplifies the signal, but a fundamental limit (the shot-noise limit) normally constrains the degree to which background noise can be suppressed. Some signals can therefore be lost in the noise. **c**, Casacio *et al.*² report that, when the photons in the Stokes laser beam are in a ‘squeezed’ quantum state, the background noise can be reduced below the shot-noise limit. The signal-to-noise ratio of the SRS signal is therefore increased.

The enhanced Raman signal enables fast imaging: in some cases, SRS imaging can be up to one million times faster than that achieved using linear Raman microscopy³. However, SRS signal detection is more complicated than in the linear effect, because the enhanced signal has to be distinguished from the towering background of the Stokes laser field. The ratio of the SRS signal to the laser background is typically of the order of 10^{-5} – 10^{-6} , necessitating special amplification techniques to retrieve the desired signal.

Any fluctuation in the background laser intensity makes it even more difficult to detect the SRS contribution⁴. Even when all other sources of noise — such as electronic noise from the detector — have been suppressed, random fluctuations in the laser background still impose a limit on the detection sensitivity. These fluctuations are called shot noise, and arise from the fact that the laser beam consists of discrete units of light (photons). Shot noise imposes a lower limit, known as the noise floor, on the amount of noise in SRS signals. The success of modern SRS microscopy has relied on the ability to reduce laser noise down to this limit. Nevertheless, weak signals remain buried beneath the noise floor, restricting the sensitivity of SRS microscopy and making it difficult to detect molecular targets at concentrations below 1 millimole per litre.

In principle, the SRS signal-to-noise ratio can be improved by increasing the number of photons in the laser beams. But there is a limit to the illumination dose that biological samples can tolerate without damage^{5,6}. SRS imaging studies usually operate at laser intensities just below the damage threshold, leaving little margin for improvement. And simple measures that increase the SRS signal strength relative to the noise floor, without introducing other complications, are hard to come by.



Snapshots of vibrating molecules

Casacio *et al.* improve SRS sensitivity in a radically different way. Instead of raising the signal, they lower the background noise, allowing smaller SRS signals to peak above the noise floor, like rocks exposed on a beach at low tide. To realize this idea, the detection limit set by shot noise has to be overcome, which can be accomplished when there are quantum correlations between the photons that make up the applied light beam^{7,8}. The use of such ‘non-classical’ light has been particularly successful in reducing shot noise in interferometry experiments, such as those used to detect gravitational waves⁹. The SRS process also depends on the interference between two light fields, suggesting that the use of non-classical light should translate well to SRS imaging.

The authors used a laser beam that is prepared in a ‘squeezed-amplitude state’. In this quantum state, the Stokes photons are no longer fully independent — which means that fluctuations in the number of photons in the beam no longer follow the statistical distribution observed in classical laser beams. By lowering the noise floor below the shot-noise limit, the researchers obtained a 35% improvement in the signal-to-noise ratio of SRS imaging, pushing down the minimum molecular concentration that could be detected by 14%. This improvement was achieved without increasing the intensity of the laser beams, thereby preserving the integrity of biological samples.

It should be noted that the currently reported improvements are modest, and the resulting performance is still below that of state-of-the-art SRS systems. Impressive noise reduction has been attained in other techniques by squeezing narrow-band laser light (see ref. 9, for example), but it might prove challenging to achieve similar reductions using the broadband laser beams that are needed for SRS. Moreover, the process of ‘squeezing’ light to produce correlations between photons adds an extra step to the already-complicated SRS imaging technique, and might deter users from adopting this noise-reduction approach.

Nevertheless, Casacio and colleagues’ work underlines the exciting possibilities of using quantum light in optical imaging techniques. Despite the challenges ahead, quantum light is likely to transform SRS microscopy for the better.

Nature **594**, 180-181 (2021)

doi: <https://doi.org/10.1038/d41586-021-01514-w>

References

1. 1.

Freudiger, C. W. *et al. Science* **322**, 1857–1861 (2008).

[PubMed](#) [Article](#) [Google Scholar](#)

2. 2.

Casacio, C. A. *et al. Nature* **594**, 201–206 (2021).

[Article](#) [Google Scholar](#)

3. 3.

Min, W., Freudiger, C. W., Lu, S. & Xie, X. S. *Annu. Rev. Phys. Chem.* **62**, 507–530 (2011).

[PubMed](#) [Article](#) [Google Scholar](#)

4. 4.

Audier, X., Heuke, S., Volz, P., Rimke, I. & Rigneault, H. *APL Photon.* **5**, 011101 (2020).

[Article](#) [Google Scholar](#)

5. 5.

Hopt, A. & Neher, E. *Biophys. J.* **80**, 2029–2036 (2001).

[PubMed](#) [Article](#) [Google Scholar](#)

6. 6.

Fischer, F. F. *et al.* *J. Biomed. Opt.* **13**, 1–8 (2008).

[Article](#) [Google Scholar](#)

7. 7.

Giovannetti, V., Lloyd, S. & Maccone, L. *Science* **306**, 1330–1336 (2004).

[PubMed](#) [Article](#) [Google Scholar](#)

8. 8.

Moreau, P.-A., Toninelli, E., Gregory, T. & Padgett, M. J. *Nature Rev. Phys.* **1**, 367–380 (2019).

[Article](#) [Google Scholar](#)

9. 9.

Aasi, J. *et al.* *Nature Photon.* **7**, 613–619 (2013).

[Article](#) [Google Scholar](#)

[Download references](#)

Competing Interests

The author declares no competing interests.

[Jobs from Nature Careers](#)

- - - [All jobs](#)
 -
 - [Postdoctoral Fellow, Statistical Methodologies for Metabolomics Data Analysis](#)
[The University of British Columbia \(UBC\)](#)
[Vancouver, Canada](#)
[JOB POST](#)
 - [Postdoctoral Fellow in River Dynamics](#)
[The University of British Columbia \(UBC\)](#)
[Vancouver, Canada](#)
[JOB POST](#)
 - [PhD Student in Wnt signaling](#)
[German Cancer Research Center in the Helmholtz Association \(DKFZ\)](#)
[Heidelberg, Germany](#)

JOB POST

- **Postdoc (all genders), Department Detector Laboratory (DTL)**

Helmholtz Centre for Heavy Ion Research GmbH (GSI)

Darmstadt, Germany

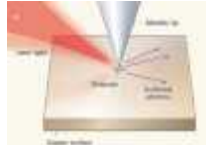
JOB POST

Download PDF

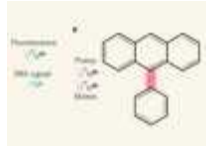
Related Articles



- [Read the paper: Quantum-enhanced nonlinear microscopy](#)



- [Snapshots of vibrating molecules](#)



- [A larger palette for biological imaging](#)

- [See all News & Views](#)

- NEWS AND VIEWS
- 17 May 2021

Ancient human faeces reveal gut microbes of the past

Appreciation is growing of how our gut microbes shape health and disease. Now, a study of ancient human faeces sheds light on how microbial populations in the gut have changed during the past 2,000 years.

- [Matthew R. Olm](#) ⁰ &
- [Justin L. Sonnenburg](#) ¹

1. [Matthew R. Olm](#)

1. Matthew R. Olm is in the Department of Microbiology and Immunology, Stanford University School of Medicine, Stanford, California 94305, USA.

[View author publications](#)

You can also search for this author in [PubMed](#) [Google Scholar](#)

2. [Justin L. Sonnenburg](#)

1. Justin L. Sonnenburg is in the Department of Microbiology and Immunology, Stanford University School of Medicine, Stanford, California 94305, USA; and at the Center for Human Microbiome Studies, Stanford University School of Medicine.

[View author publications](#)

You can also search for this author in [PubMed](#) [Google Scholar](#)



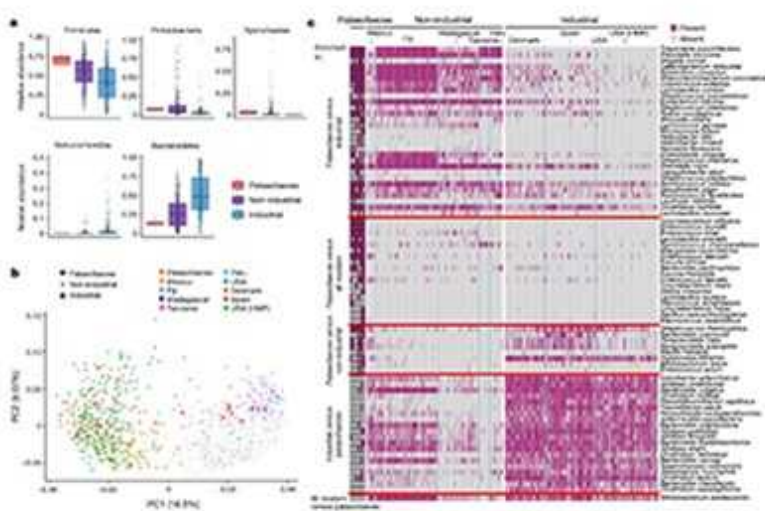


•

[Download PDF](#)

The microbial cells that inhabit the human gut, collectively called the gut microbiota or microbiome, have key influences on our metabolic and immune-system biology^{1,2}. Many microorganisms are passed down over the generations^{3,4}. However, the gut microbiota (tracked by analysing the microbial DNA in faeces) can be radically reshaped within days to months of certain events, such as immigration into a different country⁵ or antibiotic treatment⁶. Defining which microbes were once part of our evolutionary history and have since been lost might provide a key to understanding the relationship between microbes and human health. [Writing in Nature](#),

Wibowo *et al.*⁷ address this issue by turning to a microbial ‘time machine’: palaeofaeces. By using DNA sequencing to study the microbiomes of human stool samples that are 1,000–2,000 years old, this study provides valuable insights into gut microbes from a time before industrialization.



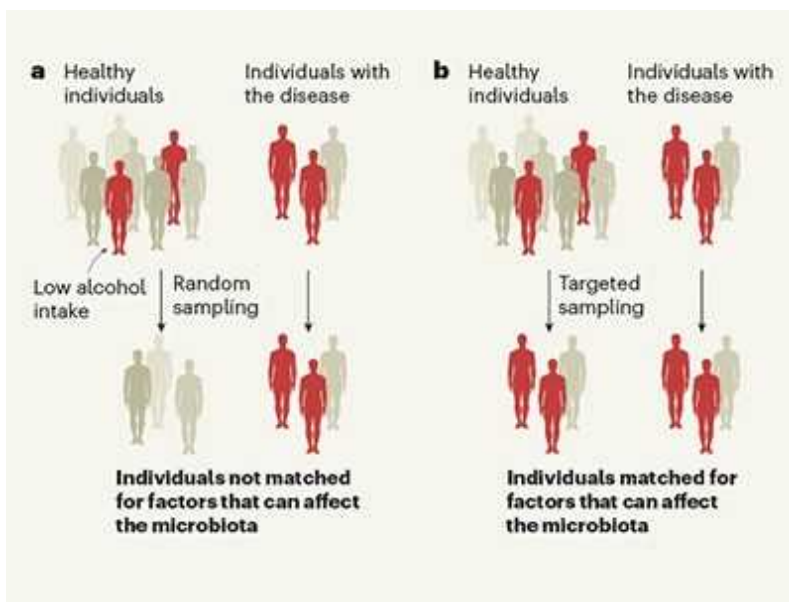
[Read the paper: Reconstruction of ancient microbial genomes from the human gut](#)

The human microbiome is a malleable component of our biology that adapts to specific circumstances, for example displaying seasonal variation corresponding to food availability⁸. Although this malleability offers a potential avenue for the treatment of human diseases linked to microbiota, it is also a vulnerability. Many aspects of industrialized life, such as antibiotic use and a fibre-deficient Western diet^{9,10}, have a negative effect on gut microbes.

Which core microbes and microbial functions from the pre-industrial microbiota were lost as societies became industrialized? Certain broad bacterial groups (referred to as ‘volatile and/or associated negatively with industrialized societies of humans’ (VANISH) taxa) are highly prevalent in present-day Indigenous populations living traditional lifestyles, but are rare or absent in industrialized populations¹⁰. There are also numerous bacterial taxa (referred to as ‘bloom or selected in societies of urbanization/modernization’ (BloSSUM) taxa) that have the opposite

pattern¹⁰. Whether present-day non-industrialized populations have microbiotas that are similar to those of humans who lived thousands of years ago has remained an open question, until now.

Wibowo *et al.* report DNA-sequencing analysis of 15 samples of palaeofaeces collected from the southwestern United States and Mexico. Seven of these samples were excluded for further study because of poor-quality DNA or evidence of soil contamination, or because the sample was found to come from a canine host. The age of the eight remaining samples was determined using carbon dating, and analysis of DNA damage revealed hallmarks that confirmed the antiquity of the material (ancient DNA has specific characteristics of degradation). The human origin of these samples was validated by microscopic analysis of dietary remains present in the palaeofaeces and by evidence of human mitochondrial DNA.



Identifying gut microbes that affect human health

The high quality of the data generated enabled the authors to detect known microbial species and to discover previously unknown microbes through the reconstruction of microbial genomes. A total of 181 of the 498 reconstructed microbial genomes were classified as gut derived and had extensive DNA damage, consistent with an ancient origin, and 39% of the ancient genomes offered evidence of being newly discovered species.

Wibowo and colleagues compared their data from the ancient gut samples with data from a collection of previously sequenced stool samples from present-day populations with industrialized and non-industrialized lifestyles. The species *Treponema succinifaciens*, a microbe in the Spirochaetaceae family shown to be lost from industrial populations⁸, was present in palaeofaeces, as were other VANISH taxa that were absent in industrialized samples and prevalent in non-industrialized samples. BloSSUM taxa, including the species *Akkermansia muciniphila* (which degrades human mucus), were more abundant in the industrialized samples than in the non-industrialized samples and the palaeofaeces. Together, these results support the idea that features of non-industrialized microbiomes are similar to the microbiomes of our human ancestors, and that industrialized populations have diverged from this microbial signature (Fig. 1).

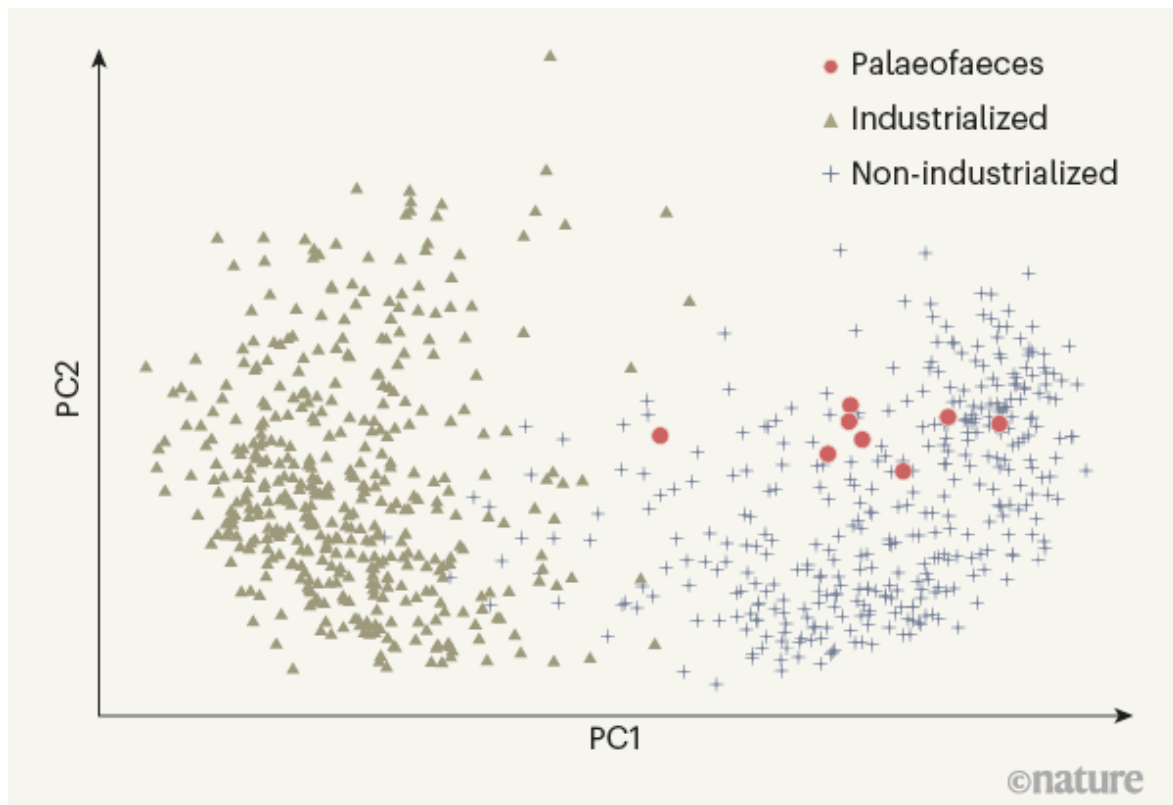


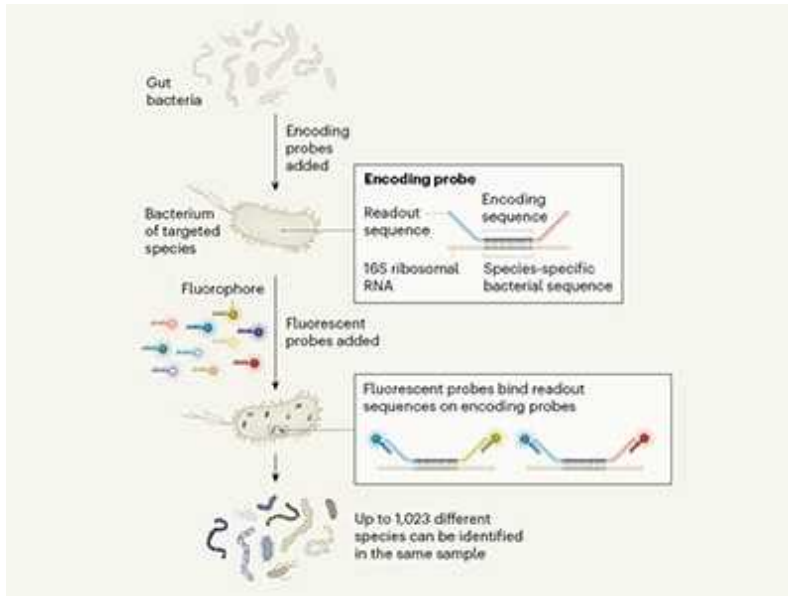
Figure 1 | A comparison of ancient and modern human gut microbes.

Wibowo *et al.*⁷ analysed the DNA of gut microbes found in 1,000–2,000-year-old human palaeofaeces, and compared this with the DNA of gut microbes in faecal samples from present-day individuals from industrialized and non-industrialized societies. The authors used a statistical method called

principal component analysis to compare the patterns of bacterial species present in the samples from each individual. This approach distributes data points corresponding to each individual's sample along two axes, termed PC1 and PC2. Samples that are more similar to each other are grouped more closely together on the graph. This analysis reveals that the samples of palaeofaeces are distributed among those from individuals living in non-industrialized societies, indicating a similarity of gut-microbe profiles between ancient humans and modern humans living traditional lifestyles — both of which are distinct from the microbial profile of people in industrialized societies. (Figure based on Fig. 1b of ref. 7.)

The authors moved beyond focusing on species identity: they compared the genes, and the predicted functions of the proteins encoded by those genes, for the microbes in palaeofaeces with those found in present-day samples. Both the industrialized and the non-industrialized present-day samples had a greater prevalence of antibiotic-resistance genes than did the palaeofaeces, a finding consistent with the ancient microbes being from before the era of antibiotic use. Palaeofaeces had a high prevalence of genes encoding proteins that can degrade the molecule chitin, a component of insect exoskeletons. This finding is consistent with human consumption of insects, known to be a component of ancestral diets. Insect ingestion was confirmed by the authors' microscopy analysis of material in the palaeofaeces. The authors report many genes that were particularly prevalent in industrialized samples, including those involved in the degradation of mucus in the human gut.

Wibowo and colleagues' study is a remarkable technical achievement. They were able to recover high-quality DNA from microbial organisms that lived thousands of years ago, probably because of the good preservation possible in the dry desert environment in which the samples were located. Multiple independent lines of evidence authenticated the sample age and the human origin of the faeces. Having these ancient DNA sequences available in the public domain will undoubtedly benefit scientists for years to come.



Bacterial species singled out from a diverse crowd

However, DNA-sequence-based analyses do have limitations when the results are not paired with validation by other types of laboratory experiment. Using computational tools to predict information about proteins encoded by DNA is an imperfect method under ideal conditions, and is particularly tricky when analysing gene functions for previously unknown organisms, such as those discovered in this study. Moreover, microbiomes are highly variable between individuals and between populations. Analyses of more palaeofaeces from a wider range of timescales and locations will be needed to better understand general and population-specific features of ancient human gut microbiomes.

The authors found notable differences in the composition and function of microbes in palaeofaeces compared with those of microbes in present-day faeces. The higher prevalence of mucus-degrading species and genes in industrialized microbiomes than in ancient and non-industrialized ones is probably driven by Western diets, which often lack sufficient dietary fibre to support once-numerous fibre-degrading microbial species^{11,12}. Given the links between the microbiome and the immune system, these differences might be connected to the rising rates of autoimmune, inflammatory and metabolic disorders in industrialized populations^{9,10}.

Wibowo and colleagues' work indicates that there are now two viable alternatives to time travel for understanding the composition of ancient microbiomes. Palaeofaeces enable the direct investigation of ancient microbiomes, but the sample age limits the further measurements and experiments that can be performed. Importantly, this study validates that present-day Indigenous populations living traditional lifestyles have similar microbiome compositions to those of ancient humans. It is essential to acknowledge that most of these present-day populations are marginalized, lead a vulnerable existence, and require exceptional protections to ensure they are not exploited. With ethically conducted research, these modern populations might open a window on our microbial past.

Nature **594**, 182-183 (2021)

doi: <https://doi.org/10.1038/d41586-021-01266-7>

References

1. 1.

Hooper, L. V., Littman, D. R. & Macpherson, A. J. *Science* **336**, 1268–1273 (2012).

[PubMed](#) [Article](#) [Google Scholar](#)

2. 2.

Karlsson, F., Tremaroli, V., Nielsen, J. & Bäckhed, F. *Diabetes* **62**, 3341–3349 (2013).

[PubMed](#) [Article](#) [Google Scholar](#)

3. 3.

Asnicar, F. *et al.* *mSystems* **2**, e00164-16 (2017).

[PubMed](#) [Article](#) [Google Scholar](#)

4. 4.

Moeller, A. H. *et al.* *Science* **353**, 380–382 (2016).

[PubMed](#) [Article](#) [Google Scholar](#)

5. 5.

Vangay, P. *et al.* *Cell* **175**, 962–972 (2018).

[PubMed](#) [Article](#) [Google Scholar](#)

6. 6.

Dethlefsen, L. & Relman, D. A. *Proc. Natl Acad. Sci. USA* **108**, 4554–4561 (2011).

[PubMed](#) [Article](#) [Google Scholar](#)

7. 7.

Wibowo, M. C. *et al.* *Nature* **594**, 234–239 (2021).

[Article](#) [Google Scholar](#)

8. 8.

Smits, S. A. *et al.* *Science* **357**, 802–806 (2017).

[PubMed](#) [Article](#) [Google Scholar](#)

9. 9.

Blaser, M. J. *Cell* **172**, 1173–1177 (2018).

[PubMed](#) [Article](#) [Google Scholar](#)

10. 10.

Sonnenburg, J. L. & Sonnenburg, E. D. *Science* **366**, eaaw9255 (2019).

[PubMed](#) [Article](#) [Google Scholar](#)

11. 11.

Makki, K., Deehan, E. C., Walter, J. & Bäckhed, F. *Cell Host Microbe* **23**, 705–715 (2018).

[PubMed](#) [Article](#) [Google Scholar](#)

12. 12.

Desai, M. S. *et al.* *Cell* **167**, 1339–1353 (2016).

[PubMed](#) [Article](#) [Google Scholar](#)

[Download references](#)

Competing Interests

The authors declare no competing interests.

[Jobs from Nature Careers](#)

- - - [All jobs](#)
 - - [Postdoctoral Fellow, Statistical Methodologies for Metabolomics Data Analysis](#)

[The University of British Columbia \(UBC\)](#)

[Vancouver, Canada](#)

[JOB POST](#)

- [Postdoctoral Fellow in River Dynamics](#)

[The University of British Columbia \(UBC\)](#)

[Vancouver, Canada](#)

[JOB POST](#)

▪ [**PhD Student in Wnt signaling**](#)

[German Cancer Research Center in the Helmholtz Association \(DKFZ\)](#)

[Heidelberg, Germany](#)

[JOB POST](#)

▪ [**Postdoc \(all genders\), Department Detector Laboratory \(DTL\)**](#)

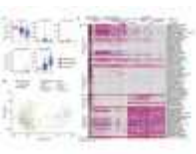
[Helmholtz Centre for Heavy Ion Research GmbH \(GSI\)](#)

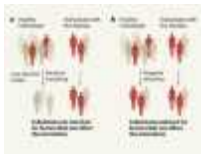
[Darmstadt, Germany](#)

[JOB POST](#)

[Download PDF](#)

Related Articles

-  [Read the paper: Reconstruction of ancient microbial genomes from the human gut](#)



- [Identifying gut microbes that affect human health](#)



- [Bacterial species singled out from a diverse crowd](#)
- [See all News & Views](#)

This article was downloaded by **calibre** from <https://www.nature.com/articles/d41586-021-01266-7>

| [Section menu](#) | [Main menu](#) |

- NEWS AND VIEWS
- 09 June 2021

AI system outperforms humans in designing floorplans for microchips

A machine-learning system has been trained to place memory blocks in microchip designs. The system beats human experts at the task, and offers the promise of better, more-rapidly produced chip designs than are currently possible.

- [Andrew B. Kahng](#) 0

1. [Andrew B. Kahng](#)

1. Andrew B. Kahng is in the Department of Computer Science and Engineering, and in the Department of Electrical and Computer Engineering, University of California, San Diego, La Jolla, California 92093, USA.

[View author publications](#)

You can also search for this author in [PubMed](#) [Google Scholar](#)



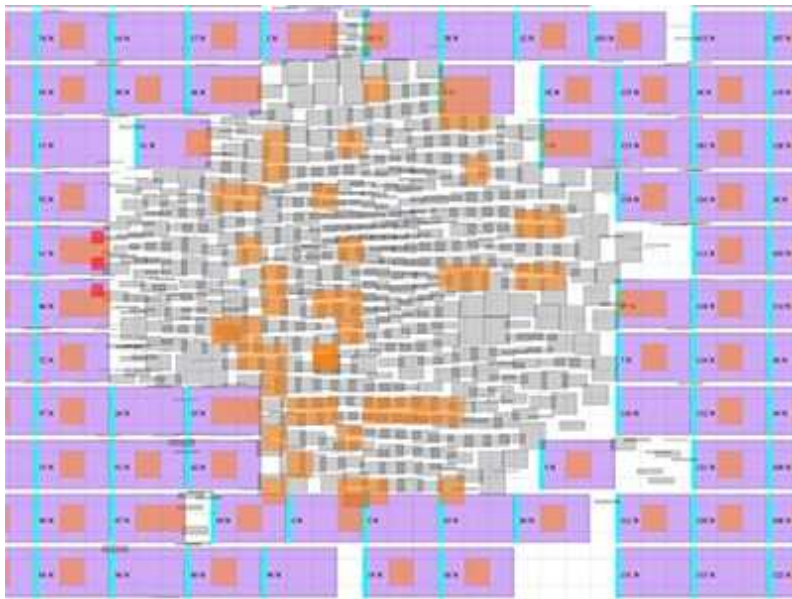


•

[Download PDF](#)

Success or failure in designing microchips depends heavily on steps known as floorplanning and placement. These steps determine where memory and logic elements are located on a chip. The locations, in turn, strongly affect whether the completed chip design can satisfy operational requirements such as processing speed and power efficiency. So far, the floorplanning task, in particular, has defied all attempts at automation. It is therefore performed iteratively and painstakingly, over weeks or months, by expert human engineers. But in [a paper in *Nature*](#), researchers from Google (Mirhoseini *et*

*al.*¹) report a machine-learning approach that achieves superior chip floorplanning in hours.

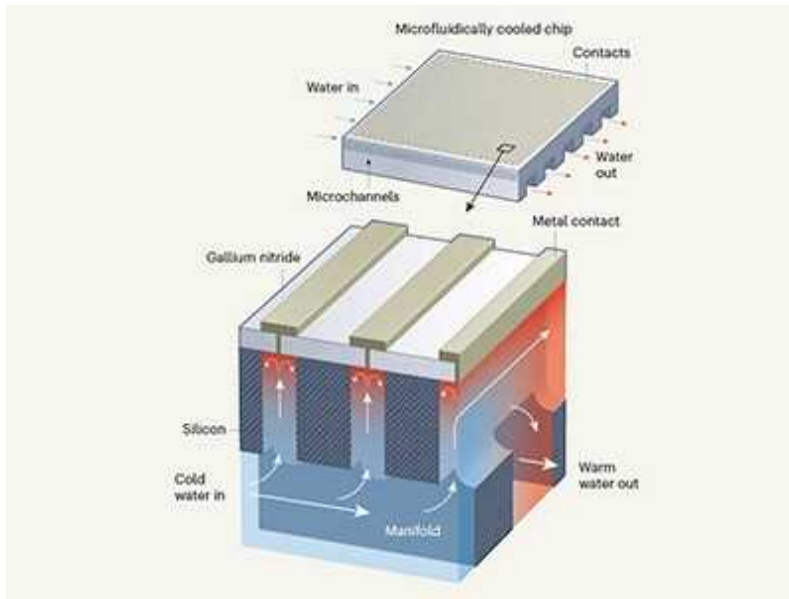


[Read the paper: A graph placement methodology for fast chip design](#)

Modern chips are a miracle of technology and economics, with billions of transistors laid out and interconnected on a piece of silicon the size of a fingernail. Each chip can contain tens of millions of logic gates, called standard cells, along with thousands of memory blocks, known as macro blocks, or macros. The cells and macro blocks are interconnected by tens of kilometres of wiring to achieve the designed functionality. Given this staggering complexity, the chip-design process itself is another miracle — in which the efforts of engineers, aided by specialized software tools, keep the complexity in check.

The locations of cells and macro blocks in the chip are crucial to the design outcome. Their placement determines the distances that wires must span, and thus affects whether the wiring can be successfully routed between components and how quickly signals can be transmitted between logic gates. Optimization of chip placement has been extensively studied for at least six decades^{2,3}. Seminal innovations in the mathematical field of applied optimization, such as a method known as simulated annealing⁴, have been motivated by the challenge of chip placement.

Because macro blocks can be thousands or even millions of times larger than standard cells, placing cells and blocks simultaneously is extremely challenging. Modern chip-design methods therefore place the macro blocks first, in a step called floorplanning. Standard cells are then placed in the remaining layout area. Just placing the macro blocks is incredibly complicated: Mirhoseini *et al.* estimate that the number of possible configurations (the state space) of macro blocks in the floorplanning problems solved in their study is about $10^{2,500}$. By comparison, the state space of the black and white stones used in the board game Go is just 10^{360} .



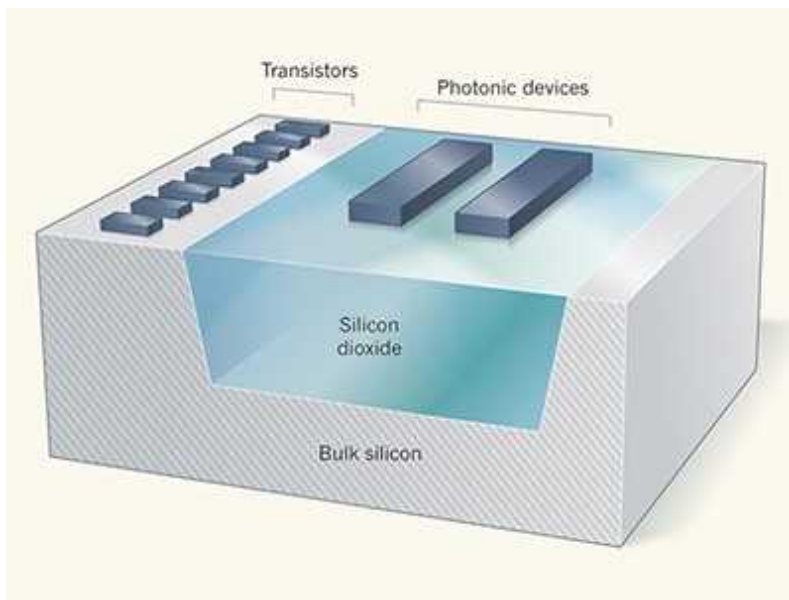
All-in-one design integrates microfluidic cooling into electronic chips

Viable floorplanning solutions must leave empty regions on the chip to achieve all of the subsequent steps — placement of the standard cells, routing of the wiring and maximizing of the chip's processing speed. However, the optimizations of logic circuitry inherent in these steps can increase the total area taken up by standard cells by 15% or more. Human engineers must therefore iteratively adjust their macro-block placements as the logic-circuit design evolves. Each of these iterations is carried out manually, and takes days or weeks.

The computer industry has famously been driven by Moore's law — the number of components per chip has roughly doubled every two years. This rate of advancement corresponds to an increase in the number of

components on a chip of about one per cent per week. The failure to automate floorplanning is therefore problematic — not only because of the associated time costs, but also because it limits the number of solutions that can be explored within chip-development schedules.

But everything changed on 22 April 2020. On that day, Mirhoseini *et al.* posted a preprint⁵ of the current paper to the online arXiv repository. It stated that “in under 6 hours, our method can generate placements that are superhuman or comparable” — that is, the method can outperform humans in a startlingly short period of time. Within days, numerous semiconductor-design companies, design-tool vendors and academic-research groups had launched efforts to understand and replicate the results.



Electronics and photonics united

Mirhoseini and colleagues trained a machine-learning ‘agent’ that can successfully place macro blocks, one by one, into a chip layout. This agent has a brain-inspired architecture known as a deep neural network, and is trained using a paradigm called reinforcement learning. At any given step of floorplanning, the trained agent assesses the ‘state’ of the chip being developed, including the partial floorplan that it has constructed so far, and then applies its learnt strategy to identify the best ‘action’ — that is, where to place the next macro block.

The technical details of this approach, such as how to represent the chip design and partial-floorplanning solutions, were developed with the overarching goal of finding a general, transferable solution to the macro-placement problem. In other words, the trained agent should succeed even when confronted with chip designs that it has not previously encountered, drawn from a wide range of applications and markets. The authors report that, when their agent is pre-trained on a set of 10,000 chip floorplans, it is already quite successful when used in a ‘one shot’ mode on a new design: with no more than six extra hours of fine-tuning steps, the agent can produce floorplans that are superior to those developed by human experts for existing chips. Moreover, the agent’s solutions are very different from those of trained human experts (Fig. 1).

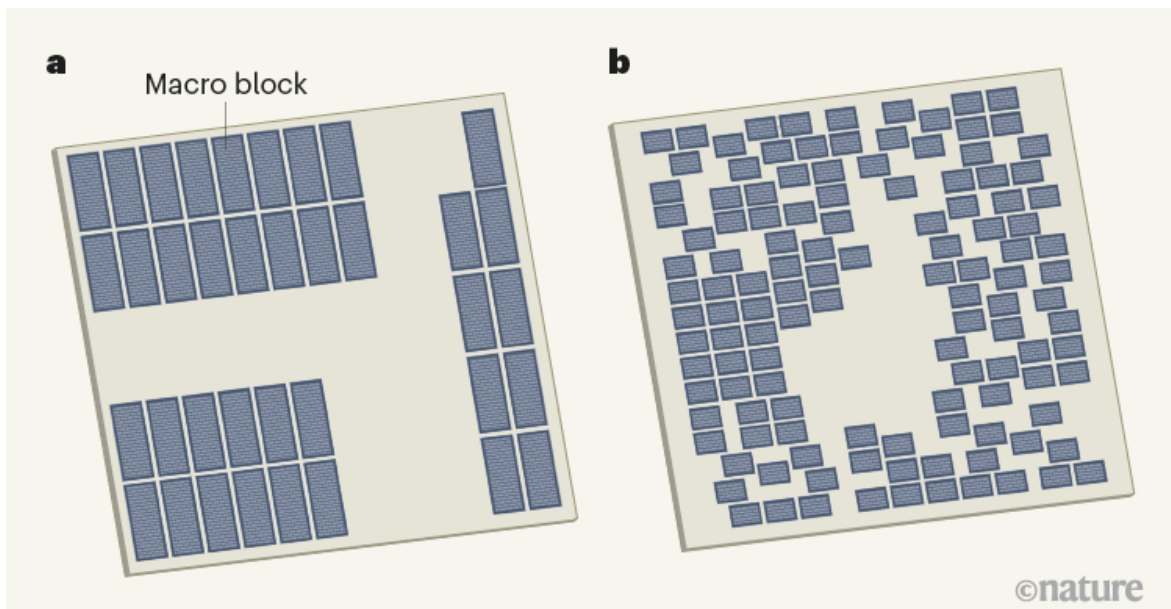


Figure 1 | Microchip floorplans designed by humans differ from those produced by a machine-learning system. An early step in microchip design is floorplanning — the placement of memory components called macro blocks on an empty layout canvas. Floorplanning is immensely complicated because of the vast number of potential configurations of macro blocks, and it involves multiple iterations as the logic-circuit design evolves. Each iteration is produced manually by human engineers, over days or weeks. **a**, This floorplan for a chip (the Ariane RISC-V processor⁸) is considered by human designers to be a good one. Its 37 macro blocks are close-packed in well-aligned rows and columns, leaving an uncluttered area

for placement of other components. **b**, Mirhoseini *et al.*¹ report a machine-learning agent that, in just a few hours, designs floorplans that outperform those designed by humans. This agent-produced arrangement is another implementation of the Ariane processor, and is very different from that shown in **a**. (Image in **b** adapted from Extended Data Fig. 4 of the paper¹.)

Arthur C. Clarke famously noted⁶ that “any sufficiently advanced technology is indistinguishable from magic”. To long-time practitioners in the fields of chip design and design automation, Mirhoseini and colleagues’ results can indeed seem magical. In the past year, experts worldwide have contemplated questions such as, ‘How is it that the agent can initially place each macro block in turn so effectively that the chosen placement is used in the final, manufactured chip design?’

The authors report that the agent places macro blocks sequentially, in decreasing order of size — which means that a block can be placed next even if it has no connections (physical or functional) to previously placed blocks. When blocks have the same size, the agent’s choice of the next block echoes the choices made by ‘cluster-growth’ methods⁷, which were previously developed in efforts to automate floorplan design, but were abandoned several decades ago. It will be fascinating to see whether the authors’ use of massive computation and deep learning reveal that chip designers took a wrong turn in giving up on sequential and cluster-growth methods.

Another much-debated question has been, ‘How does the agent’s choice of macro-block placements survive subsequent steps in the chip-design process?’ As mentioned earlier, human engineers must iteratively adjust their floorplans as the logic-circuit design evolves. The trained agent’s macro-block placements somehow evade such landmines in the design process, achieving superhuman outcomes for timing (ensuring that signals produced in the chip arrive at their destinations on time) and for the feasibility and efficiency with which wiring can be routed between components. Moreover, Mirhoseini and colleagues’ use of simple metrics as proxies for key parameters of the chip design works surprisingly well — it will be interesting to understand why these proxies are so successful. The authors’ intention to make their code available is invaluable in this light.

The development of methods for automated chip design that are better, faster and cheaper than current approaches will help to keep alive the ‘Moore’s law’ trajectory of chip technology. Indeed, for technical leaders and decision-makers in the chip industry, the most important revelation in Mirhoseini and colleagues’ paper might be that the authors’ floorplan solutions have been incorporated into the chip designs for Google’s next-generation artificial-intelligence processors. This means that the solutions are good enough for millions of copies to be printed on expensive, cutting-edge silicon wafers. We can therefore expect the semiconductor industry to redouble its interest in replicating the authors’ work, and to pursue a host of similar applications throughout the chip-design process.

Nature **594**, 183-185 (2021)

doi: <https://doi.org/10.1038/d41586-021-01515-9>

References

1. 1.

Mirhoseini, A. *et al. Nature* **594**, 207–212 (2021).

[Article](#) [Google Scholar](#)

2. 2.

Markov, I. L., Hu, J. & Kim, M.-C. *Proc. IEEE* **103**, 1985–2003 (2015).

[Article](#) [Google Scholar](#)

3. 3.

Kahng, A. B. *Proc. ACM/IEEE Int. Symp. Physical Design* 15–22 (2021).

4. 4.

Kirkpatrick, S., Gelatt, C. D. Jr & Vecchi, M. P. *Science* **220**, 671–680 (1983).

[PubMed](#) [Article](#) [Google Scholar](#)

5. 5.

Mirhoseini, A. *et al.* Preprint at <https://arxiv.org/abs/2004.10746> (2020).

6. 6.

Clarke, A. C. *Profiles of the Future: An Inquiry into the Limits of the Possible* 41 (Macmillan, 1973).

[Google Scholar](#)

7. 7.

Sait, S. M. & Youssef, H. *VLSI Physical Design Automation: Theory and Practice* Ch. 3, 90–95 (McGraw-Hill, 1995).

[Google Scholar](#)

8. 8.

Zaruba, F. & Benini, L. *IEEE Trans. Very Large Scale Integration* **27**, 2629–2640 (2019).

[Article](#) [Google Scholar](#)

[Download references](#)

Competing Interests

The author declares no competing interests.

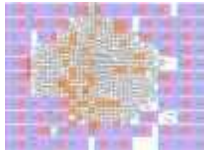
[Jobs from Nature Careers](#)

- - - [All jobs](#)
 - - [**Postdoctoral Fellow, Statistical Methodologies for Metabolomics Data Analysis**](#)
[The University of British Columbia \(UBC\)](#)
[Vancouver, Canada](#)
[JOB POST](#)
 - [**Postdoctoral Fellow in River Dynamics**](#)
[The University of British Columbia \(UBC\)](#)
[Vancouver, Canada](#)
[JOB POST](#)
 - [**PhD Student in Wnt signaling**](#)
[German Cancer Research Center in the Helmholtz Association \(DKFZ\)](#)
[Heidelberg, Germany](#)
[JOB POST](#)
 - [**Postdoc \(all genders\), Department Detector Laboratory \(DTL\)**](#)
[Helmholtz Centre for Heavy Ion Research GmbH \(GSI\)](#)
[Darmstadt, Germany](#)

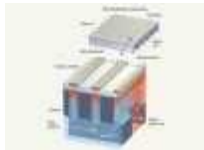
JOB POST

[Download PDF](#)

Related Articles



- [Read the paper: A graph placement methodology for fast chip design](#)



- [All-in-one design integrates microfluidic cooling into electronic chips](#)



- [Electronics and photonics united](#)
- [See all News & Views](#)

This article was downloaded by **calibre** from <https://www.nature.com/articles/d41586-021-01515-9>

- NEWS AND VIEWS
- 26 May 2021

Ancient seeds spill secrets about the evolution of flowering plants

The origin and rapid diversification of flowering plants is a long-standing “abominable mystery”, as Charles Darwin put it. Part of the puzzle – the origin of the protective covering of flowering-plant seeds – is nearing resolution.

- [Douglas E. Soltis](#) 0

1. [Douglas E. Soltis](#)

1. Douglas E. Soltis is at the Florida Museum of Natural History and in the Department of Biology, University of Florida, Gainesville, Florida 32611, USA.

[View author publications](#)

You can also search for this author in [PubMed](#) [Google Scholar](#)





•

[Download PDF](#)

One of the landmark events in evolution is the appearance of flowering plants, termed angiosperms. [Writing in Nature](#), Shi *et al.*¹ describe fossil evidence that sheds light on a long-standing mystery about seed evolution.



[Read the paper: Mesozoic cupules and the origin of the angiosperm second integument](#)

A number of botanical innovations accompanied the appearance of flowering plants and contributed to the organisms' rapid rise to worldwide dominance of terrestrial and many aquatic ecosystems. Such innovations include floral organs and a special nutritive tissue for the plant embryo — endosperm. In addition, flowering plants and another plant group, gymnosperms, produce seeds, which provide a protective layer around the developing embryo. This enabled seed plants to truly conquer the terrestrial environment, overtaking other land plants such as mosses and ferns, which do not produce seeds. Seeds have also had a central role in enabling human survival by providing an important food source.

Flowering plants arose from an ancestor in a the gymnosperms^{2,3}. The fossil record contains many clades of now-extinct gymnosperms, and it is not clear which group gave rise to the angiosperms, although it is definitely not one of the living groups of gymnosperms — plants such as conifers, ginkgo (*Ginkgo biloba*) or cycads^{2,3}.

All gymnosperms have just one protective layer, termed an integument, that surrounds their seeds, whereas flowering plants have two such layers. In a letter⁴ to the botanist J. D. Hooker, Charles Darwin described the origin of flowering plants as an “abominable mystery”. An enigma embedded in this

mystery is how the second (outer) protective layer evolved. The outer integument differs from the inner one in its developmental pathway and in the genetic control governing tissue-layer formation^{5,6}, and the two integuments are thus clearly very different from each other.

Shi and colleagues describe extremely well-preserved fossils of extinct seed plants. They use these remarkable newly described fossils, as well as other similar-looking fossils reported earlier², to build a tree of relationships between plants. Their effort places all of these fossils on the plant family tree at a position close to that of flowering plants — they are very close relatives of modern angiosperms, and, as such, might provide clues to their origin. The fossils of these ancient relatives of flowering plants show remarkable diversity in the shape of their reproductive structures.

Amazingly, these are not recently discovered fossil specimens; they were collected almost a century ago, deposited in museum collections and only recently unearthed for a second time (this time, from museum drawers by the authors), with their relevance for reconstructing the plant family tree now finally recognized.

These extinct plants had a cup-like structure, termed a cupule (Fig. 1), that surrounded the developing seed or seeds (each seed itself having just one integument, which typifies all gymnosperms, living and extinct). The role of these cupules is unknown, but they might have provided extra protection for the seed, or aided its dispersal.

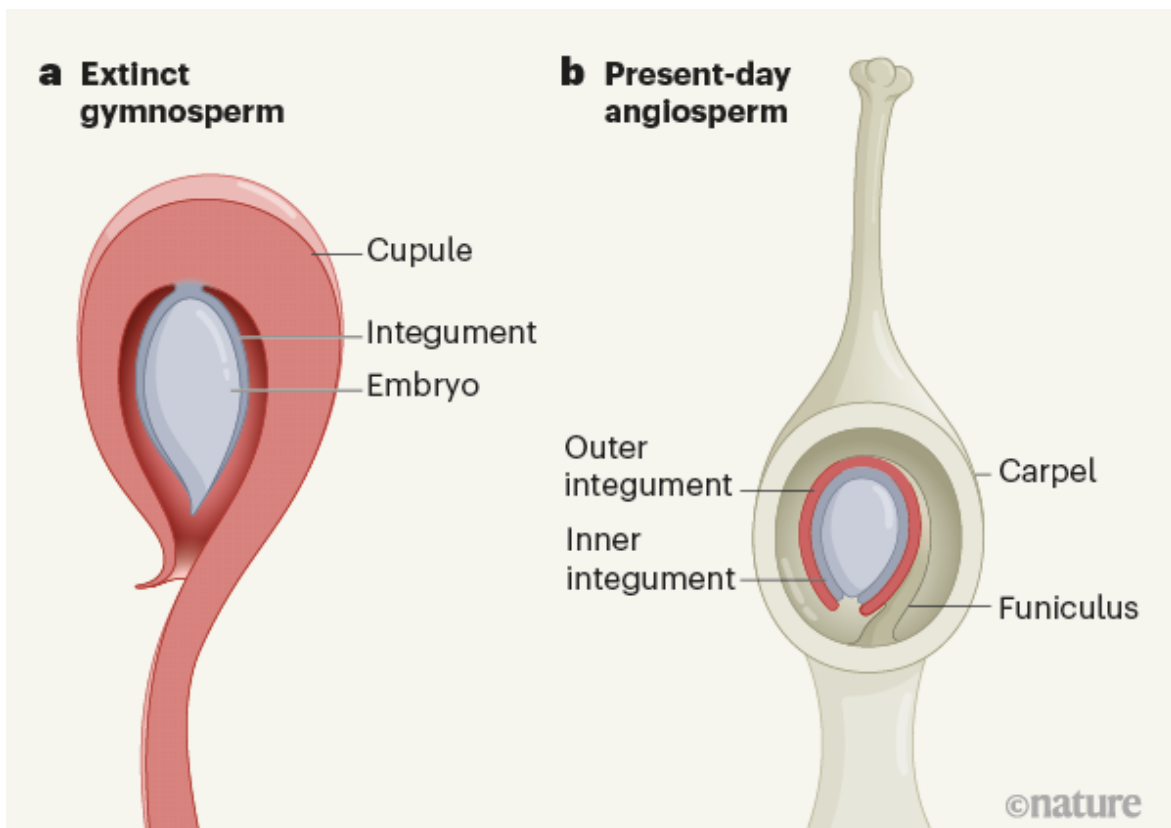


Figure 1 | Seed evolution. Shi *et al.*¹ present fossil evidence that sheds light on a long-standing mystery about the origin of the protective layer, termed the outer integument (or second integument), that surrounds the seeds of flowering plants (angiosperms). It is thought that flowering plants arose from now-extinct plants belonging to a group called the gymnosperms (living members of which include conifers). **a**, Gymnosperms have one integument that surrounds the embryo of a seed. A structure called the cupule, which might have provided protection or aided seed dispersal, formed the outer layer of ancient gymnosperm seeds. **b**, Flowering plants have inner and outer integuments. Shi and colleagues find that the cupule probably evolved to form the outer integument of flowering plants. Angiosperm seeds are connected to the carpel structure that surrounds them through a stalk called the funiculus. Shi and colleagues suggest that the funiculus evolved from the stalk of the gymnosperm cupule.

Might the cupule be the precursor to the outer protective layer unique to flowering-plant seeds? There is another twist (pun intended) to solving the mystery of angiosperm seeds. Flowering-plant seeds are also unusual in their overall structure — the top of the seed is bent back on the stalk that connects

it to the plant body⁵. Imagine if, instead of standing upright with your head well away from your toes (analogous to the ‘body plan’ of a seed of a living gymnosperm), you were bent over, with your head next to your toes (echoing the layout of a flowering-plant seed). Crucially, in these newly described fossils, the cupules, with the seed(s) they surround, are also bent back on themselves in a fashion remarkably like the distinctive ‘recurved’ seeds of flowering plants. Eureka!

Shi *et al.* describe fossils that date to only approximately 126 million years ago, a time by which, by most estimates, angiosperms were already on the scene³. So what is the big deal? Similar cupule-bearing fossils are much older — including *Caytonia*, a fossil gymnosperm whose discovery first raised the possibility that similar extinct plants with cupules and seeds were close relatives, or even ancestors, of flowering plants^{2,3}. They date to around 250 million years ago, long before most estimates of the time of origin of flowering plants^{7–9}. Collectively, the fossils described by Shi and co-authors, together with the earlier-reported fossils with cupules, paint a clear picture showing that the second integument is derived from the cupule of an extinct gymnosperm. Mystery solved.



Ancient plants escaped the end-Permian mass extinction

To be clear, the fossils described by Shi and colleagues do not correspond to the immediate ancestors of flowering plants; those fossils remain to be

found. Nonetheless, they provide previously missing crucial information about the origin of angiosperms. But more fossils are badly needed to clarify angiosperm origin further.

Although Shi and colleagues' work seems to have solved the riddle of the outer integument of angiosperm seeds, other mysteries remain. These include the origin of the protective covering (the ovary) that collectively surrounds all of the seeds in flowers and that ultimately gives rise to fruit, another structure that transformed our planet and is essential to human survival. The origin of special pollen-bearing structures termed stamens in flowering plants also requires clarification. Another evolutionary enigma concerns the endosperm, which is unique to flowering plants.

There has long been a romantic view that the fossils required to resolve these and other questions must be discovered by palaeontologists working in the field with rock hammers in hand. But, as Shi and colleagues' paper demonstrates, perhaps other key pieces to the fossil puzzle don't need to be unearthed. Instead, they might be hiding in plain sight in palaeobotanical collections around the world, waiting for an intrepid scientist to simply open the right cabinet drawer.

Nature **594**, 185–186 (2021)

doi: <https://doi.org/10.1038/d41586-021-01347-7>

References

1. 1.

Shi, G., Herrera, F., Herendeen, P. S., Clark, E. G. & Crane, P. R. *Nature* **594**, 223–226 (2021).

[Article](#) [Google Scholar](#)

2. 2.

Doyle, J. A. *Int. J. Plant Sci.* **169**, 816–843 (2008).

[Article](#) [Google Scholar](#)

3. 3.

Soltis, D. E. *et al.* *Phylogeny and Evolution of the Angiosperms* Revised & Updated Edn (Univ. Chicago Press, 2018).

[Google Scholar](#)

4. 4.

Darwin, F. & Seward, A. C. (eds) *More Letters of Charles Darwin* Vol. II (Murray, 1903).

[Google Scholar](#)

5. 5.

Endress, P. K. *Ann. Bot.* **107**, 1465–1489 (2011).

[PubMed](#) [Article](#) [Google Scholar](#)

6. 6.

Gasser, C. S. & Skinner, D. J. *Curr. Top. Dev. Biol.* **131**, 373–399 (2019).

[PubMed](#) [Article](#) [Google Scholar](#)

7. 7.

Barbacka, M. & Bóka, K. *Acta Palaeobot.* **40**, 85–111 (2000).

[Google Scholar](#)

8. 8.

Bomfleur, B. *et al.* *Int. J. Plant Sci.* **175**, 1062–1075 (2014).

[Article](#) [Google Scholar](#)

9. 9.

Taylor, T. N., Del Fueyo, G. M. & Taylor, E. L. *Am. J. Bot.* **81**, 666–677 (1994).

[Article](#) [Google Scholar](#)

[Download references](#)

Competing Interests

The author declares no competing interests.

[Jobs from Nature Careers](#)

- - - [All jobs](#)
 - - [Postdoctoral Fellow, Statistical Methodologies for Metabolomics Data Analysis](#)
[The University of British Columbia \(UBC\)](#)
[Vancouver, Canada](#)
[JOB POST](#)
 - [Postdoctoral Fellow in River Dynamics](#)
[The University of British Columbia \(UBC\)](#)
[Vancouver, Canada](#)
[JOB POST](#)

- **PhD Student in Wnt signaling**

German Cancer Research Center in the Helmholtz Association (DKFZ)

Heidelberg, Germany.

JOB POST

- **Postdoc (all genders), Department Detector Laboratory (DTL)**

Helmholtz Centre for Heavy Ion Research GmbH (GSI)

Darmstadt, Germany

JOB POST

Download PDF

Related Articles



- **Read the paper: Mesozoic cupules and the origin of the angiosperm second integument**



- **Ancient plants escaped the end-Permian mass extinction**



- **The family tree flowers**

- [**See all News & Views**](#)
-

This article was downloaded by **calibre** from <https://www.nature.com/articles/d41586-021-01347-7>

| [Section menu](#) | [Main menu](#) |

- Article
- [Published: 09 June 2021](#)

Anisotropic satellite galaxy quenching modulated by black hole activity

- [Ignacio Martín-Navarro](#) ORCID: [orcid.org/0000-0001-8494-0080^{1,2,3}](https://orcid.org/0000-0001-8494-0080),
- [Annalisa Pillepich³](#),
- [Dylan Nelson^{4,5}](#),
- [Vicente Rodriguez-Gomez](#) ORCID: [orcid.org/0000-0002-9495-0079⁶](https://orcid.org/0000-0002-9495-0079),
- [Martina Donnari³](#),
- [Lars Hernquist⁷](#) &
- [Volker Springel](#) ORCID: [orcid.org/0000-0001-5976-4599⁴](https://orcid.org/0000-0001-5976-4599)

Nature volume 594, pages 187–190 (2021) [Cite this article](#)

- 560 Accesses
- 169 Altmetric
- [Metrics details](#)

Subjects

- [Computational astrophysics](#)
- [Cosmology](#)
- [Galaxies and clusters](#)

Abstract

The evolution of satellite galaxies is shaped by their constant interaction with the circumgalactic medium surrounding central galaxies, which in turn may be affected by gas and energy ejected from the central supermassive black hole^{[1,2,3,4,5,6](#)}. The nature of such a coupling between black holes and galaxies is, however, much debated^{[7,8,9](#)} and observational evidence remains scarce^{[10,11](#)}. Here we report an analysis of archival data on 124,163 satellite galaxies in the potential wells of 29,631 dark matter halos with masses between 10^{12} and 10^{14} solar masses. We find that quenched satellite galaxies are relatively less frequent along the minor axis of their central galaxies. This observation might appear counterintuitive given that black hole activity is expected to eject mass and energy preferentially in the direction of the minor axis of the host galaxy. We show, however, that the observed anisotropic signal results precisely from the ejective nature of black hole feedback in massive halos, as outflows powered by active galactic nuclei clear out the circumgalactic medium, reducing the ram pressure and thus preserving star formation in satellite galaxies. This interpretation is supported by the IllustrisTNG suite of cosmological numerical simulations, even though the model's sub-grid implementation of black hole feedback is effectively isotropic^{[12](#)}.

Access options

Subscribe to Journal

Get full journal access for 1 year

\$199.00

only \$3.90 per issue

[Subscribe](#)

All prices are NET prices.

VAT will be added later in the checkout.

Tax calculation will be finalised during checkout.

Rent or Buy article

Get time limited or full article access on ReadCube.

from \$8.99

[Rent or Buy](#)

All prices are NET prices.

Additional access options:

- [Log in](#)
- [Access through your institution](#)
- [Learn about institutional subscriptions](#)

Fig. 1: Orientation of satellite galaxies around central galaxies.

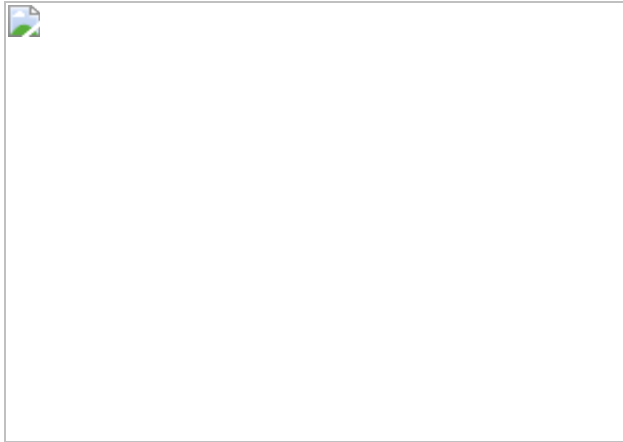


Fig. 2: Anisotropic distribution of quiescent satellite galaxies in SDSS.



Fig. 3: SDSS versus IllustrisTNG.

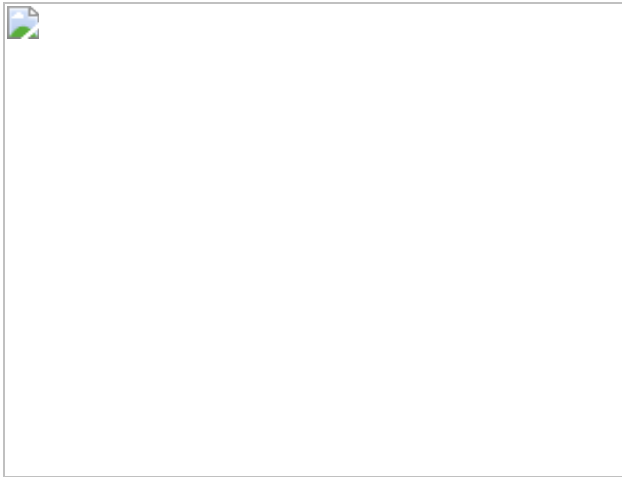
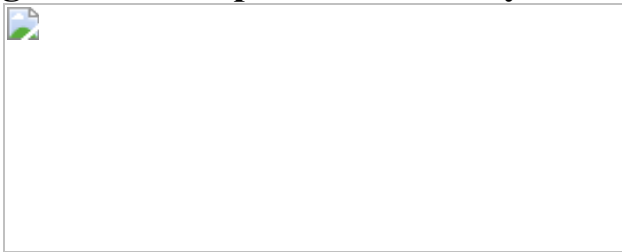


Fig. 4: Anisotropic CGM density in IllustrisTNG.



Data availability

All data used in this work are publicly available through the Sloan Digital Sky Survey and the Illustris and IllustrisTNG public data releases.

References

1. 1.

Cicone, C. et al. Massive molecular outflows and evidence for AGN feedback from CO observations. *Astron. Astrophys.* **562**, A21 (2014).

[Google Scholar](#)

2. 2.

Woo, J.-H., Bae, H.-J., Son, D. & Karouzos, M. The prevalence of gas outflows in type 2 AGNs. *Astrophys. J.* **817**, 108 (2016).

[ADS](#) [Google Scholar](#)

3. 3.

Pillepich, A. et al. Simulating galaxy formation with the IllustrisTNG model. *Mon. Not. R. Astron. Soc.* **473**, 4077–4106 (2018).

[ADS](#) [CAS](#) [Google Scholar](#)

4. 4.

Nelson, D. et al. First results from the TNG50 simulation: galactic outflows driven by supernovae and black hole feedback. *Mon. Not. R. Astron. Soc.* **490**, 3234–3261 (2019).

[ADS](#) [CAS](#) [Google Scholar](#)

5. 5.

Oppenheimer, B. D. et al. EAGLE and Illustris-TNG predictions for resolved eROSITA X-ray observations of the circumgalactic medium around normal galaxies. *Astrophys. J.* **893**, L24 (2020).

[ADS](#) [CAS](#) [Google Scholar](#)

6. 6.

Davies, J. J., Crain, R. A., Oppenheimer, B. D. & Schaye, J. The quenching and morphological evolution of central galaxies is facilitated by the feedback-driven expulsion of circumgalactic gas. *Mon. Not. R. Astron. Soc.* **491**, 4462–4480 (2020).

[ADS](#) [CAS](#) [Google Scholar](#)

7. 7.

Harrison, C. M. et al. AGN outflows and feedback twenty years on. *Nat. Astron.* **2**, 198–205 (2018).

[ADS](#) [Google Scholar](#)

8. 8.

Dashyan, G. et al. AGN-driven quenching of satellite galaxies. *Mon. Not. R. Astron. Soc.* **487**, 5889–5901 (2019).

[ADS](#) [CAS](#) [Google Scholar](#)

9. 9.

Veilleux, S., Maiolino, R., Bolatto, A. D. & Aalto, S. Cool outflows in galaxies and their implications. *Astron. Astrophys. Rev.* **28**, 2 (2020).

[ADS](#) [Google Scholar](#)

10. 10.

Cheung, E. et al. Suppressing star formation in quiescent galaxies with supermassive black hole winds. *Nature* **533**, 504–508 (2016).

[ADS](#) [CAS](#) [PubMed](#) [Google Scholar](#)

11. 11.

Martín-Navarro, I., Brodie, J. P., Romanowsky, A. J., Ruiz-Lara, T. & van de Ven, G. Black-hole-regulated star formation in massive galaxies. *Nature* **553**, 307–309 (2018).

[ADS](#) [PubMed](#) [Google Scholar](#)

12. 12.

Weinberger, R. et al. Simulating galaxy formation with black hole driven thermal and kinetic feedback. *Mon. Not. R. Astron. Soc.* **465**, 3291–3308 (2017).

[ADS](#) [CAS](#) [Google Scholar](#)

13. 13.

Tempel, E. et al. Flux- and volume-limited groups/clusters for the SDSS galaxies: catalogues and mass estimation. *Astron. Astrophys.* **566**, A1 (2014).

[Google Scholar](#)

14. 14.

Ahn, C. P. et al. The Tenth Data Release of the Sloan Digital Sky Survey: first spectroscopic data from the SDSS-III Apache Point Observatory Galactic Evolution Experiment. *Astrophys. J.* **211** (Suppl.), 17 (2014).

[Google Scholar](#)

15. 15.

Kauffmann, G. et al. Stellar masses and star formation histories for 10^5 galaxies from the Sloan Digital Sky Survey. *Mon. Not. R. Astron. Soc.* **341**, 33–53 (2003).

[ADS](#) [Google Scholar](#)

16. 16.

Brinchmann, J. et al. The physical properties of star-forming galaxies in the low-redshift Universe. *Mon. Not. R. Astron. Soc.* **351**, 1151–1179 (2004).

[ADS](#) [CAS](#) [Google Scholar](#)

17. 17.

Stoughton, C. et al. Sloan Digital Sky Survey: early data release. *Astron. J.* **123**, 485–548 (2002).

[ADS](#) [Google Scholar](#)

18. 18.

Nelson, D. et al. The IllustrisTNG simulations: public data release. *Comput. Astrophys. Cosmol.* **6**, 2 (2019).

[ADS](#) [Google Scholar](#)

19. 19.

Rodriguez-Gomez, V. et al. The optical morphologies of galaxies in the IllustrisTNG simulation: a comparison to Pan-STARRS observations. *Mon. Not. R. Astron. Soc.* **483**, 4140–4159 (2019).

[ADS](#) [CAS](#) [Google Scholar](#)

20. 20.

Donnari, M. et al. Quenched fractions in the IllustrisTNG simulations: comparison with observations and other theoretical models. Preprint at <https://arxiv.org/abs/2008.00004> (2020).

21. 21.

Fujita, Y. Pre-processing of galaxies before entering a cluster. *Publ. Astron. Soc. Jpn* **56**, 29–43 (2004).

[ADS](#) [Google Scholar](#)

22. 22.

Kauffmann, G., Li, C., Zhang, W. & Weinmann, S. A re-examination of galactic conformity and a comparison with semi-analytic models of galaxy formation. *Mon. Not. R. Astron. Soc.* **430**, 1447–1456 (2013).

[ADS](#) [Google Scholar](#)

23. 23.

Nelson, D. et al. The *illustris* simulation: public data release. *Astron. Comput.* **13**, 12–37 (2015).

[ADS](#) [Google Scholar](#)

24. 24.

Davé, R. et al. SIMBA: cosmological simulations with black hole growth and feedback. *Mon. Not. R. Astron. Soc.* **486**, 2827–2849 (2019).

[ADS](#) [Google Scholar](#)

25. 25.

McNamara, B. R. & Nulsen, P. E. J. Heating hot atmospheres with active galactic nuclei. *Annu. Rev. Astron. Astrophys.* **45**, 117–175 (2007).

[ADS](#) [Google Scholar](#)

26. 26.

Fabian, A. C. Observational evidence of active galactic nuclei feedback. *Annu. Rev. Astron. Astrophys.* **50**, 455–489 (2012).

[ADS](#) [CAS](#) [Google Scholar](#)

27. 27.

Gunn, J. E., Gott, I. & Richard, J. On the infall of matter into clusters of galaxies and some effects on their evolution. *Astrophys. J.* **176**, 1 (1972).

[ADS](#) [Google Scholar](#)

28. 28.

Yun, K. et al. Jellyfish galaxies with the IllustrisTNG simulations—I. Gas-stripping phenomena in the full cosmological context. *Mon. Not. R. Astron. Soc.* **483**, 1042–1066 (2019).

[ADS](#) [CAS](#) [Google Scholar](#)

29. 29.

Maiolino, R. et al. Star formation inside a galactic outflow. *Nature* **544**, 202–206 (2017).

[ADS](#) [CAS](#) [PubMed](#) [Google Scholar](#)

30. 30.

Navarro, J. F., Frenk, C. S. & White, S. D. M. The structure of cold dark matter halos. *Astrophys. J.* **462**, 563 (1996).

[ADS](#) [CAS](#) [Google Scholar](#)

31. 31.

Martín-Navarro, I., Burchett, J. N. & Mezcua, M. Quantifying the effect of black hole feedback from the central galaxy on the satellite populations of groups and clusters. *Astrophys. J.* **884**, L45 (2019).

[ADS](#) [Google Scholar](#)

32. 32.

de Vaucouleurs, G. Recherches sur les nebuleuses extragalactiques. *Ann. Astrophys.* **11**, 247 (1948).

[ADS](#) [Google Scholar](#)

33. 33.

Baes, M. et al. Efficient three-dimensional NLTE dust radiative transfer with SKIRT. *Astrophys. J.* **196** (Suppl.), 22 (2011).

[Google Scholar](#)

34. 34.

Camps, P., Baes, M. & Saftly, W. Using 3D Voronoi grids in radiative transfer simulations. *Astron. Astrophys.* **560**, A35 (2013).

[ADS](#) [Google Scholar](#)

35. 35.

Donnari, M. et al. The star formation activity of IllustrisTNG galaxies: main sequence, UVJ diagram, quenched fractions, and systematics. *Mon. Not. R. Astron. Soc.* **485**, 4817–4840 (2019).

[ADS](#) [CAS](#) [Google Scholar](#)

36. 36.

Nelson, D. et al. First results from the IllustrisTNG simulations: the galaxy colour bimodality. *Mon. Not. R. Astron. Soc.* **475**, 624–647 (2018).

[ADS](#) [CAS](#) [Google Scholar](#)

37. 37.

Huertas-Company, M. et al. The Hubble Sequence at $z \sim 0$ in the IllustrisTNG simulation with deep learning. *Mon. Not. R. Astron. Soc.* **489**, 1859–1879 (2019).

[ADS](#) [CAS](#) [Google Scholar](#)

38. 38.

Zanisi, L. et al. A deep learning approach to test the small-scale galaxy morphology and its relationship with star formation activity in hydrodynamical simulations. *Mon. Not. R. Astron. Soc.* **501**, 4359–4382 (2020).

[ADS](#) [Google Scholar](#)

39. 39.

Foreman-Mackey, D., Hogg, D. W., Lang, D. & Goodman, J. emcee: The MCMC hammer. *Publ. Astron. Soc. Pacif.* **125**, 306 (2013).

[ADS](#) [Google Scholar](#)

40. 40.

Simard, L., Mendel, J. T., Patton, D. R., Ellison, S. L. & McConnachie, A. W. A catalog of bulge+disk decompositions and updated photometry for 1.12 million galaxies in the Sloan Digital Sky Survey. *Astrophys. J.* **196** (Suppl.), 11 (2011).

[Google Scholar](#)

41. 41.

Martín-Navarro, I., Burchett, J. N. & Mezcua, M. Black hole feedback and the evolution of massive early-type galaxies. *Mon. Not. R. Astron. Soc.* **491**, 1311–1319 (2020).

[ADS](#) [Google Scholar](#)

42. 42.

van den Bosch, R. C. E. Unification of the fundamental plane and super massive black hole masses. *Astrophys. J.* **831**, 134 (2016).

[ADS](#) [Google Scholar](#)

43. 43.

Martín-Navarro, I., Brodie, J. P., van den Bosch, R. C. E., Romanowsky, A. J. & Forbes, D. A. Stellar populations across the black hole mass-velocity dispersion relation. *Astrophys. J.* **832**, L11 (2016).

[ADS](#) [Google Scholar](#)

44. 44.

Terrazas, B. A. et al. Quiescence correlates strongly with directly measured black hole mass in central galaxies. *Astrophys. J.* **830**, L12 (2016).

[ADS](#) [Google Scholar](#)

45. 45.

Terrazas, B. A., Bell, E. F., Woo, J. & Henriques, B. M. B. Supermassive black holes as the regulators of star formation in central galaxies. *Astrophys. J.* **844**, 170 (2017).

[ADS](#) [Google Scholar](#)

46. 46.

Terrazas, B. A. et al. The relationship between black hole mass and galaxy properties: Examining the black hole feedback model in IllustrisTNG. Preprint at <https://arxiv.org/abs/1906.02747> (2019).

47. 47.

Dullo, B. T., Bouquin, A. Y. K., Gil De Paz, A., Knapen, J. H. & Gorgas, J. The (black hole mass)-(color) relations for early- and late-type galaxies: red and blue sequences. Preprint at <https://arxiv.org/abs/2006.10128> (2020).

48. 48.

Li, Y. et al. Correlations between black holes and host galaxies in the Illustris and IllustrisTNG Simulations. *Astrophys. J.* **895**, 102 (2020).

[ADS](#) [CAS](#) [Google Scholar](#)

49. 49.

Donnari, M. et al. Quenched fractions in the IllustrisTNG simulations: the roles of AGN feedback, environment, and pre-processing. Preprint at <https://arxiv.org/abs/2008.00005> (2020).

50. 50.

Genel, S. et al. Introducing the Illustris project: the evolution of galaxy populations across cosmic time. *Mon. Not. R. Astron. Soc.* **445**, 175–200 (2014).

[ADS](#) [CAS](#) [Google Scholar](#)

51. 51.

Kauffmann, G. et al. The morphology and kinematics of the gaseous circumgalactic medium of Milky Way mass galaxies—II. Comparison of IllustrisTNG and Illustris simulation results. *Mon. Not. R. Astron. Soc.* **486**, 4686–4700 (2019).

[ADS](#) [CAS](#) [Google Scholar](#)

52. 52.

Lim, S. H. et al. Properties of the CGM and IGM: constraints on galaxy formation models from the Sunyaev-Zel'dovich effect. Preprint at <https://arxiv.org/abs/2007.11583> (2020).

53. 53.

Pillepich, A. et al. First results from the IllustrisTNG simulations: the stellar mass content of groups and clusters of galaxies. *Mon. Not. R. Astron. Soc.* **475**, 648–675 (2018).

[ADS](#) [CAS](#) [Google Scholar](#)

[Download references](#)

Acknowledgements

I.M.-N. acknowledges support from grant PID2019-107427GB-C32 from The Spanish Ministry of Science and Innovation and from the Marie Skłodowska-Curie Individual *SPanD* Fellowship 702607. A.P. and M.D. acknowledge support by the Deutsche Forschungsgemeinschaft (DFG, German Research Foundation) – Project-ID 138713538 – SFB 881 (“The Milky Way System”), subproject A01. We thank G. Pérez Díaz for helping with the design of the figures.

Author information

Affiliations

1. Instituto de Astrofísica de Canarias, La Laguna, Tenerife, Spain
Ignacio Martín-Navarro
2. Departamento de Astrofísica, Universidad de La Laguna, La Laguna, Tenerife, Spain
Ignacio Martín-Navarro
3. Max-Planck Institut für Astronomie, Heidelberg, Germany
Ignacio Martín-Navarro, Annalisa Pillepich & Martina Donnari
4. Max-Planck-Institut für Astrophysik, Garching, Germany
Dylan Nelson & Volker Springel
5. Universität Heidelberg, Zentrum für Astronomie, Institut für theoretische Astrophysik, Heidelberg, Germany
Dylan Nelson
6. Instituto de Radioastronomía y Astrofísica, Universidad Nacional Autónoma de México, Morelia, México
Vicente Rodriguez-Gomez

7. Harvard-Smithsonian Center for Astrophysics, Cambridge, MA, USA

Lars Hernquist

Authors

1. Ignacio Martín-Navarro

[View author publications](#)

You can also search for this author in [PubMed](#) [Google Scholar](#)

2. Annalisa Pillepich

[View author publications](#)

You can also search for this author in [PubMed](#) [Google Scholar](#)

3. Dylan Nelson

[View author publications](#)

You can also search for this author in [PubMed](#) [Google Scholar](#)

4. Vicente Rodriguez-Gomez

[View author publications](#)

You can also search for this author in [PubMed](#) [Google Scholar](#)

5. Martina Donnari

[View author publications](#)

You can also search for this author in [PubMed](#) [Google Scholar](#)

6. Lars Hernquist

[View author publications](#)

You can also search for this author in [PubMed](#) [Google Scholar](#)

7. Volker Springel

[View author publications](#)

You can also search for this author in [PubMed](#) [Google Scholar](#)

Contributions

I.M.-N. and A.P. developed the original idea and characterized the signal in the observed and simulated data. D.N. measured the gas mass density distribution in IllustrisTNG and contributed to the early development of the project. V.R.-G. generated the synthetic SDSS-like images based on IllustrisTNG data, and M.D. provided the information about the infalling time of satellites in IllustrisTNG. L.H. and V.S. contributed to the analysis and interpretation of the observed and simulated data. I.M.-N. and A.P. wrote the text, and all the co-authors contributed to refining and polishing the final manuscript.

Corresponding author

Correspondence to [Ignacio Martín-Navarro](#).

Ethics declarations

Competing interests

The authors declare no competing interests.

Additional information

Peer review information *Nature* thanks Claudia Cicone and the other, anonymous, reviewer(s) for their contribution to the peer review of this work. Peer reviewer reports are available.

Publisher's note Springer Nature remains neutral with regard to jurisdictional claims in published maps and institutional affiliations.

Extended data figures and tables

Extended Data Fig. 1 SDSS posterior distributions for the best-fitting description of the angular modulation of satellite quiescence.

We fit the observed data with a cosine function with three free parameters, the average quiescent fraction f_q , the amplitude of the modulation, and a re-scaling term for the expected error f . Posteriors are well behaved and allowed us to reject the null-hypothesis at a $\sim 6\sigma$ level. Blue solid vertical lines indicate the best-fitting values and the dashed lines indicate the 1σ confidence interval.

Extended Data Fig. 2 Sensitivity of the SDSS signal to PA uncertainties.

a, The fraction of SDSS quiescent galaxies as a function of the orientation based on the worst-fitting functional form (de Vaucouleurs versus exponential) according to the SDSS photometric pipeline. The stability of the signal demonstrates that our results are robust against the photometric fitting procedure. Error bars represent the best-fitting standard deviation, as described in the Methods. **b**, Coloured curves indicate the best-fitting solution for SDSS data obtained while randomly perturbing the PA of the central galaxy by ΔPA . For reference, black symbols and curves are the same as in Fig. 2. A clear modulation in the fraction of quiescent galaxies is observed even for $\Delta PA \approx 30$, which is an order of magnitude larger than the expected error on the individual PAs. **c, d**, The SDSS g -band images of galaxies best-fitted by a de Vaucouleurs (top row) and an exponential profile (bottom row), with the PA uncertainty indicated by the white-shaded area. The adopted PA is indicated in the top left corner of each image.

Extended Data Fig. 3 Test with randomized PAs.

a, The fraction of quiescent satellites in SDSS data after randomizing the PA of the central galaxies. As expected, no signal is recovered in this case. Error bars represent the best-fitting standard deviation, as described in the Methods. **b**, The posterior distributions for this test, where the modelled amplitude is consistent with no angular variation. Blue solid vertical lines

indicate the best-fitting values and the dashed lines indicate the 1σ confidence interval.

Extended Data Fig. 4 Characterization of the SDSS signal.

a, We show that the modulation in the observed signal is higher for satellites closer to the centre ($R_{\text{sat}} < 0.5R_{\text{vir}}$, orange symbols) than for those satellites in the outskirts ($R_{\text{sat}} < 0.5R_{\text{vir}}$, blue symbols). **b**, The signal is stronger for halos with more massive central galaxies ($\log M_{\text{cen}} > 11M_{\odot}$, orange symbols) compared to the signal observed in halos with less massive central galaxies ($\log M_{\text{cen}} < 11M_{\odot}$, blue symbols). **c**, Less massive satellites ($\log M_{\text{sat}} < 10.5M_{\odot}$, orange symbols) exhibit a larger variation than more massive ones ($\log M_{\text{sat}} > 10.5M_{\odot}$, blue symbols). **d**, The signal is also stronger in halos hosting more massive black holes in their centre (orange symbols), compared to those with relatively less-massive central black holes (blue symbols). Panels **e–h** are equivalent to panels **a–d** but without removing the offset between the different sub-samples.

Extended Data Fig. 5 Alternative metrics for the characterization of SDSS satellites' star-formation status.

a, b, The modulation observed in the average specific SFR (**a**) and distance from the star-formation main sequence (**b**) of SDSS satellites closely follows that shown by the fraction of quiescent satellites in Fig. 2. Regardless of the metric used to characterize the star-formation properties of satellite galaxies, there is a clear dependence on the orientation with respect to the central galaxy. Error bars indicate the 1σ uncertainty and yellow lines mark the location of the minor and major axes.

Extended Data Fig. 6 Additional trends with halo mass and distance in SDSS.

As in Fig. 2, black symbols represent the observed modulation on the SDSS data. The blue line indicates the change in the quiescent fraction that could be expected because of the average halo mass dependence on orientation,

which is much smaller than the reported one. Similarly, satellites along the minor axis are marginally closer to the central galaxy than along the major axis, leading to a negative and even weaker modulation, as shown by the red line. Error bars represent the best-fitting standard deviation, as described in the Methods.

Extended Data Fig. 7 Iso-quiescent fraction contours.

Similarly to Fig. 4, the contours of constant f_q are shown, but this time at three different levels: $f_q = \{0.36, 0.42, 0.48\}$. The background image corresponds to the IllustrisTNG gas over-density and the typical virial radius in the explored halo mass range is shown as a dashed grey circle, as in Fig. 4.

Extended Data Fig. 8 IllustrisTNG versus Illustris comparison.

Modulation in the fraction of quiescent galaxies for the IllustrisTNG (namely, TNG100, red symbols) and the original Illustris (blue symbols) simulations. Error bars represent the best-fitting standard deviation, as described in the Methods. The signal is shown in green for a sample of IllustrisTNG satellites with the same mass distribution as those in Illustris, to assess the possible effect of a mass bias between the two simulations. Both simulations probe a similar ~ 100 -Mpc comoving cosmological volume and thus share the same large-scale structure properties; the treatment of black hole growth and feedback is the most relevant difference between the two. However, it is clear that the amplitude of the modulation is much higher in IllustrisTNG (0.032 ± 0.004) than in Illustris (0.013 ± 0.007).

Extended Data Fig. 9 Quiescent versus star-forming central galaxies in IllustrisTNG and SDSS.

In **a**, at a fixed central stellar mass of $\sim \log M_{\text{cen}} = 10.5 M_\odot$, the modulation in the fraction of quiescent satellites in TNG100 is shown for star-forming (blue) and quiescent (orange) central galaxies. Although there are a limited number of satellites, the modulation in the signal appears to be stronger for

quiescent central galaxies than for star-forming ones. Since quiescentness in IllustrisTNG is a strong indication of an effective black hole feedback, the fact that the signal is stronger for quiescent galaxies is also an indication of the proposed AGN-related origin for the observed quenching directionality. The modulation in the fraction of quiescent satellites is shown for star-forming (blue) and quiescent (orange) central galaxies in **b** but this time for SDSS galaxies, again of $\log M_{\text{cen}} = 10.5 M_{\odot}$. The observed modulation is stronger for quiescent than for star-forming central galaxies as seen in IllustrisTNG. Solid lines and shaded areas indicate the best-fitting trends and 1σ confidence interval, respectively. Error bars represent the best-fitting standard deviation, as described in the Methods.

[Extended Data Fig. 10 Dependencies of the signal in IllustrisTNG.](#)

a, The fraction of quiescent satellites around central galaxies whose black holes have injected, relatively to their mass, more (red) and less (blue) total energy. **b**, Similarly, the same separation but in this case considering only the kinetic energy injected by the black holes. In both cases, the amplitude of the modulation is stronger when the total (**a**) and kinetic (**b**) energy released by the central black holes increase. Similar to Extended Data Fig. [4](#), panel **c** shows how the signal in IllustrisTNG depends on the relative mass of the central black hole, being stronger for more over-massive black hole galaxies. **d**, The observed signal in IllustrisTNG (red) and the de-projected signal (blue) using the underlying 3D satellite distribution. We note that in **d** we did not impose any cut in central stellar mass and therefore absolute values are different from the other panels. Error bars and shaded areas represent 1σ confidence intervals, and solid lines are the best-fitting solutions.

[Extended Data Fig. 11 Quenching directionality in IllustrisTNG.](#)

a, The number of TNG100 satellites in each orientation bin, depending on whether they are star-forming (blue symbols), quenched in their $z \approx 0$ host halo (green), were pre-processed and quenched in a different halo (orange),

or quenched as central galaxies (red). The last two groups (red and orange symbols) are sensitive to large-scale structure effects, but correspond only to a small fraction of the total satellite population. **b**, The fraction of quiescent satellites as a function of orientation is shown but only for those satellites that quenched in their $z \approx 0$ host halo (green symbols). The amplitude of this modulation mimics that measured for all IllustrisTNG satellites (grey-shaded area and black line).

Supplementary information

Peer Review File

Rights and permissions

Reprints and Permissions

About this article



Check for
updates

Cite this article

Martín-Navarro, I., Pillepich, A., Nelson, D. *et al.* Anisotropic satellite galaxy quenching modulated by black hole activity. *Nature* **594**, 187–190 (2021). <https://doi.org/10.1038/s41586-021-03545-9>

Download citation

- Received: 28 September 2020
- Accepted: 13 April 2021
- Published: 09 June 2021

- Issue Date: 10 June 2021
- DOI: <https://doi.org/10.1038/s41586-021-03545-9>

Comments

By submitting a comment you agree to abide by our [Terms](#) and [Community Guidelines](#). If you find something abusive or that does not comply with our terms or guidelines please flag it as inappropriate.

[Access through your institution](#)

[Change institution](#)

[Buy or subscribe](#)

Associated Content

[The great black hole clear-out](#)

- May Chiao

Nature Astronomy Research Highlight 10 Jun 2021

Advertisement

This article was downloaded by **calibre** from <https://www.nature.com/articles/s41586-021-03545-9>

- Article
- [Published: 09 June 2021](#)

Observation of first and second sound in a BKT superfluid

- [Panagiotis Christodoulou](#) ORCID: [orcid.org/0000-0001-7800-9484¹](#),
- [Maciej Gałka¹](#),
- [Nishant Dogra¹](#),
- [Raphael Lopes](#) ORCID: [orcid.org/0000-0003-3877-8478²](#),
- [Julian Schmitt](#) ORCID: [orcid.org/0000-0002-0002-3777¹](#) nAff³ &
- [Zoran Hadzibabic](#) ORCID: [orcid.org/0000-0002-0118-9285¹](#)

[Nature](#) volume **594**, pages 191–194 (2021) [Cite this article](#)

- 1246 Accesses
- 14 Altmetric
- [Metrics details](#)

Subjects

- [Phase transitions and critical phenomena](#)
- [Quantum fluids and solids](#)
- [Ultracold gases](#)

Abstract

Superfluidity in its various forms has been of interest since the observation of frictionless flow in liquid helium II^{1,2}. In three spatial dimensions it is

conceptually associated with the emergence of long-range order at a critical temperature. One of the hallmarks of superfluidity, as predicted by the two-fluid model^{3,4} and observed in both liquid helium⁵ and in ultracold atomic gases^{6,7}, is the existence of two kinds of sound excitation—the first and second sound. In two-dimensional systems, thermal fluctuations preclude long-range order^{8,9}; however, superfluidity nevertheless emerges at a non-zero critical temperature through the infinite-order Berezinskii–Kosterlitz–Thouless (BKT) transition^{10,11}, which is associated with a universal jump¹² in the superfluid density without any discontinuities in the thermodynamic properties of the fluid. BKT superfluids are also predicted to support two sounds, but so far this has not been observed experimentally. Here we observe first and second sound in a homogeneous two-dimensional atomic Bose gas, and use the two temperature-dependent sound speeds to determine the superfluid density of the gas^{13,14,15,16}. Our results agree with the predictions of BKT theory, including the prediction of a universal jump in the superfluid density at the critical temperature.

Access options

Subscribe to Journal

Get full journal access for 1 year

\$199.00

only \$3.90 per issue

[Subscribe](#)

All prices are NET prices.

VAT will be added later in the checkout.

Tax calculation will be finalised during checkout.

Rent or Buy article

Get time limited or full article access on ReadCube.

from \$8.99

[Rent or Buy](#)

All prices are NET prices.

Additional access options:

- [Log in](#)
- [Access through your institution](#)
- [Learn about institutional subscriptions](#)

Fig. 1: Sound excitations in a homogeneous two-dimensional Bose gas.

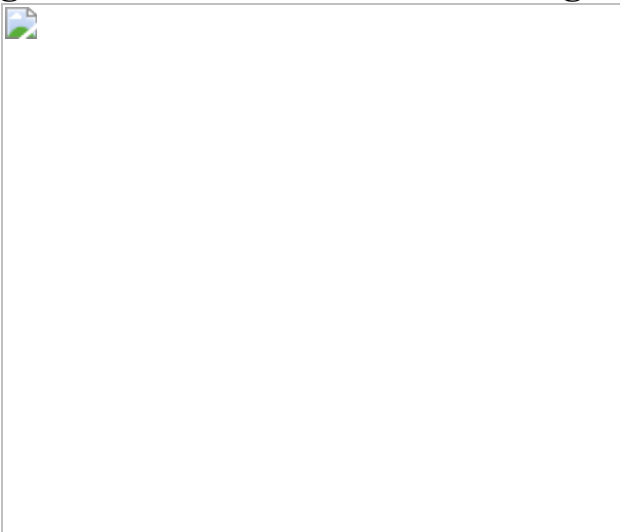


Fig. 2: First and second sound.

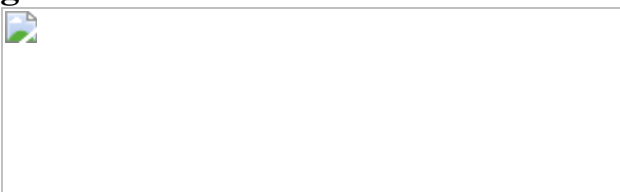
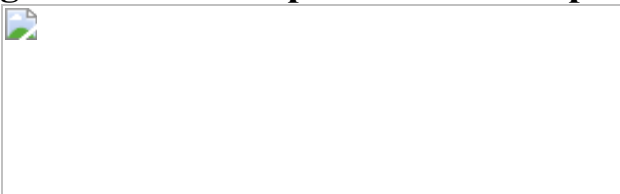


Fig. 3: The sound speeds and the superfluid density.



Data availability

The data that support the findings of this study are available in the Apollo repository (<https://doi.org/10.17863/CAM.66056>). Any additional information is available from the corresponding authors upon reasonable request. [Source data](#) are provided with this paper.

References

1. 1.

Kapitza, P. Viscosity of liquid helium below the λ -point. *Nature* **141**, 74 (1938).

[ADS](#) [CAS](#) [Google Scholar](#)

2. 2.

Allen, J. F. & Misener, A. D. Flow of liquid helium II. *Nature* **141**, 75 (1938).

[ADS](#) [CAS](#) [Google Scholar](#)

3. 3.

Tisza, L. Transport phenomena in helium II. *Nature* **141**, 913 (1938).

[ADS](#) [CAS](#) [Google Scholar](#)

4. 4.

Landau, L. Theory of the superfluidity of helium II. *Phys. Rev.* **60**, 356–358 (1941).

[ADS](#) [CAS](#) [MATH](#) [Google Scholar](#)

5. 5.

Peshkov, V. Second sound in helium II. *Sov. Phys. JETP* **11**, 580–584 (1960).

[Google Scholar](#)

6. 6.

Stamper-Kurn, D. M., Miesner, H.-J., Inouye, S. & Andrews, M. R. & Ketterle, W. Collisionless and hydrodynamic excitations of a Bose–Einstein condensate. *Phys. Rev. Lett.* **81**, 500–503 (1998).

[ADS](#) [CAS](#) [Google Scholar](#)

7. 7.

Sidorenkov, L. A. et al. Second sound and the superfluid fraction in a Fermi gas with resonant interactions. *Nature* **498**, 78–81 (2013).

[ADS](#) [CAS](#) [PubMed](#) [PubMed Central](#) [Google Scholar](#)

8. 8.

Hohenberg, P. C. Existence of long-range order in one and two dimensions. *Phys. Rev.* **158**, 383–386 (1967).

[ADS](#) [CAS](#) [Google Scholar](#)

9. 9.

Mermin, N. D. & Wagner, H. Absence of ferromagnetism or antiferromagnetism in one- or two-dimensional isotropic Heisenberg models. *Phys. Rev. Lett.* **17**, 1307 (1966).

[ADS](#) [Google Scholar](#)

10. 10.

Berezinskii, V. L. Destruction of long-range order in one-dimensional and two-dimensional systems possessing a continuous symmetry group. II. Quantum systems. *Sov. Phys. JETP* **34**, 610 (1971).

[ADS](#) [MathSciNet](#) [Google Scholar](#)

11. 11.

Kosterlitz, J. M. & Thouless, D. J. Ordering, metastability and phase transitions in twodimensional systems. *J. Phys. C* **6**, 1181–1203 (1973).

[ADS](#) [CAS](#) [Google Scholar](#)

12. 12.

Nelson, D. R. & Kosterlitz, J. M. Universal jump in the superfluid density of two-dimensional superfluids. *Phys. Rev. Lett.* **39**, 1201–1205 (1977).

[ADS](#) [CAS](#) [Google Scholar](#)

13. 13.

Prokof'ev, N., Ruebenacker, O. & Svistunov, B. Critical point of a weakly interacting two-dimensional Bose gas. *Phys. Rev. Lett.* **87**, 270402 (2001).

[PubMed](#) [PubMed Central](#) [Google Scholar](#)

14. 14.

Prokof'ev, N. & Svistunov, B. Two-dimensional weakly interacting Bose gas in the fluctuation region. *Phys. Rev. A* **66**, 043608 (2002).

[ADS](#) [Google Scholar](#)

15. 15.

Ozawa, T. & Stringari, S. Discontinuities in the first and second sound velocities at the Berezinskii–Kosterlitz–Thouless transition. *Phys. Rev. Lett.* **112**, 025302 (2014).

[ADS](#) [Google Scholar](#)

16. 16.

Ota, M. & Stringari, S. Second sound in a two-dimensional Bose gas: from the weakly to the strongly interacting regime. *Phys. Rev. A* **97**, 033604 (2018).

[ADS](#) [CAS](#) [Google Scholar](#)

17. 17.

Hu, H., Taylor, E., Liu, X.-J., Stringari, S. & Griffin, A. Second sound and the density response function in uniform superfluid atomic gases. *New J. Phys.* **12**, 043040 (2010).

[ADS](#) [Google Scholar](#)

18. 18.

Bishop, D. J. & Reppy, J. D. Study of the superfluid transition in two-dimensional ^4He films. *Phys. Rev. Lett.* **40**, 1727–1730 (1978).

[ADS](#) [CAS](#) [Google Scholar](#)

19. 19.

Hadzibabic, Z., Krüger, P., Cheneau, M., Battelier, B. & Dalibard, J. Berezinskii–Kosterlitz–Thouless crossover in a trapped atomic gas. *Nature* **441**, 1118–1121 (2006).

[ADS](#) [CAS](#) [PubMed](#) [PubMed Central](#) [Google Scholar](#)

20. 20.

Cladé, P., Ryu, C., Ramanathan, A., Helmerson, K. & Phillips, W. D. Observation of a 2D Bose gas: from thermal to quasicondensate to superfluid. *Phys. Rev. Lett.* **102**, 170401 (2009).

[ADS](#) [PubMed](#) [PubMed Central](#) [Google Scholar](#)

21. 21.

Tung, S., Lamporesi, G., Lobser, D., Xia, L. & Cornell, E. A. Observation of the presuperfluid regime in a two-dimensional Bose gas. *Phys. Rev. Lett.* **105**, 230408 (2010).

[ADS](#) [CAS](#) [PubMed](#) [PubMed Central](#) [Google Scholar](#)

22. 22.

Yefsah, T., Desbuquois, R., Chomaz, L., Günter, K. J. & Dalibard, J. Exploring the thermodynamics of a two-dimensional Bose gas. *Phys. Rev. Lett.* **107**, 130401 (2011).

[ADS](#) [PubMed](#) [PubMed Central](#) [Google Scholar](#)

23. 23.

Hung, C.-L., Zhang, X., Gemelke, N. & Chin, C. Observation of scale invariance and universality in two-dimensional Bose gases. *Nature* **470**, 236–239 (2011).

[ADS](#) [CAS](#) [PubMed](#) [PubMed Central](#) [Google Scholar](#)

24. 24.

Hadzibabic, Z. & Dalibard, J. Two-dimensional Bose fluids: an atomic physics perspective. *Riv. Nuovo Cimento* **34**, 389–434 (2011).

[CAS](#) [Google Scholar](#)

25. 25.

Desbuquois, R. et al. Superfluid behaviour of a two-dimensional Bose gas. *Nat. Phys.* **8**, 645–648 (2012).

[CAS](#) [Google Scholar](#)

26. 26.

Ha, L.-C. et al. Strongly interacting two-dimensional Bose gases. *Phys. Rev. Lett.* **110**, 145302 (2013).

[ADS](#) [PubMed](#) [PubMed Central](#) [Google Scholar](#)

27. 27.

Choi, J. Y., Seo, S. W. & Shin, Y. I. Observation of thermally activated vortex pairs in a quasi-2D Bose gas. *Phys. Rev. Lett.* **110**, 175302 (2013).

[ADS](#) [PubMed](#) [PubMed Central](#) [Google Scholar](#)

28. 28.

Chomaz, L. et al. Emergence of coherence via transverse condensation in a uniform quasi-two-dimensional Bose gas. *Nat. Commun.* **6**, 6162 (2015).

[ADS](#) [CAS](#) [PubMed](#) [PubMed Central](#) [Google Scholar](#)

29. 29.

Fletcher, R. J. et al. Connecting Berezinskii–Kosterlitz–Thouless and BEC phase transitions by tuning interactions in a trapped gas. *Phys. Rev. Lett.* **114**, 255302 (2015).

[ADS](#) [MathSciNet](#) [PubMed](#) [PubMed Central](#) [Google Scholar](#)

30. 30.

Murthy, P. A. et al. Observation of the Berezinskii–Kosterlitz–Thouless phase transition in an ultracold Fermi gas. *Phys. Rev. Lett.* **115**, 010401 (2015).

[ADS](#) [CAS](#) [PubMed](#) [PubMed Central](#) [Google Scholar](#)

31. 31.

Ville, J. L. et al. Sound propagation in a uniform superfluid two-dimensional Bose gas. *Phys. Rev. Lett.* **121**, 145301 (2018).

[ADS](#) [CAS](#) [PubMed](#) [PubMed Central](#) [Google Scholar](#)

32. 32.

Ota, M. et al. Collisionless sound in a uniform two-dimensional Bose gas. *Phys. Rev. Lett.* **121**, 145302 (2018).

[ADS](#) [CAS](#) [PubMed](#) [PubMed Central](#) [Google Scholar](#)

33. 33.

Cappellaro, A., Toigo, F. & Salasnich, L. Collisionless dynamics in two-dimensional bosonic gases. *Phys. Rev. A* **98**, 043605 (2018).

[ADS](#) [CAS](#) [Google Scholar](#)

34. 34.

Wu, Z., Zhang, S. & Zhai, H. Dynamic Kosterlitz–Thouless theory for two-dimensional ultracold atomic gases. *Phys. Rev. A* **102**, 043311 (2020).

[ADS](#) [CAS](#) [Google Scholar](#)

35. 35.

Bohlen, M. et al. Sound propagation and quantum-limited damping in a two-dimensional Fermi gas. *Phys. Rev. Lett.* **124**, 240403 (2020).

[ADS](#) [CAS](#) [PubMed](#) [PubMed Central](#) [Google Scholar](#)

36. 36.

Petrov, D. S., Holzmann, M. & Shlyapnikov, G. V. Bose–Einstein condensation in quasi-2D trapped gases. *Phys. Rev. Lett.* **84**, 2551–2555 (2000).

[ADS](#) [CAS](#) [PubMed](#) [PubMed Central](#) [Google Scholar](#)

37. 37.

Fletcher, R. J. et al. Elliptic flow in a strongly interacting normal Bose gas. *Phys. Rev. A* **98**, 011601 (2018).

[ADS](#) [CAS](#) [Google Scholar](#)

38. 38.

Navon, N., Gaunt, A. L., Smith, R. P. & Hadzibabic, Z. Emergence of a turbulent cascade in a quantum gas. *Nature* **539**, 72–75 (2016).

[ADS](#) [CAS](#) [PubMed](#) [PubMed Central](#) [Google Scholar](#)

39. 39.

Pitaevskii, L. & Stringari, S. *Bose–Einstein Condensation and Superfluidity* Ch. 7 (Oxford Univ. Press, 2016).

40. 40.

Hohenberg, P. C. & Martin, P. C. Superfluid dynamics in the hydrodynamic ($\omega\tau \ll 1$) and collisionless ($\omega\tau \gg 1$) domains. *Phys. Rev. Lett.* **12**, 69–71(1964).

[ADS](#) [Google Scholar](#)

41. 41.

Singh, V. P. & Mathey, L. Sound propagation in a two-dimensional Bose gas across the superfluid transition. *Phys. Rev. Res.* **2**, 023336 (2020).

[CAS](#) [Google Scholar](#)

42. 42.

Patel, P. B. et al. Universal sound diffusion in a strongly interacting Fermi gas. *Science* **370**, 1222–1226 (2020).

[ADS](#) [CAS](#) [PubMed](#) [PubMed Central](#) [Google Scholar](#)

43. 43.

Pilati, S., Giorgini, S. & Prokof'ev, N. Critical temperature of interacting Bose gases in two and three dimensions. *Phys. Rev. Lett.* **100**, 140405 (2008).

[ADS](#) [CAS](#) [PubMed](#) [PubMed Central](#) [Google Scholar](#)

44. 44.

Foster, C. J., Blakie, P. B. & Davis, M. J. Vortex pairing in two-dimensional Bose gases. *Phys. Rev. A* **81**, 023623 (2010).

[ADS](#) [Google Scholar](#)

45. 45.

Gawryluk, K. & Brewczyk, M. Signatures of a universal jump in the superfluid density of a two-dimensional Bose gas with a finite number of particles. *Phys. Rev. A* **99**, 033615 (2019).

[ADS](#) [CAS](#) [Google Scholar](#)

46. 46.

Lee, T. D. & Yang, C. N. Low-temperature behavior of a dilute Bose system of hard spheres. II. Nonequilibrium properties. *Phys. Rev.* **113**, 1406–1413 (1959).

[ADS](#) [MathSciNet](#) [MATH](#) [Google Scholar](#)

47. 47.

Pitaevskii, L. & Stringari, S. In *Universal Themes of Bose-Einstein Condensation* (eds Proukakis, N. P. et al.) 322–347 (Cambridge Univ. Press, 2017).

48. 48.

Eigen, C. et al. Observation of weak collapse in a Bose–Einstein condensate. *Phys. Rev. X* **6**, 041058 (2016).

[Google Scholar](#)

49. 49.

Campbell, R. L. D. et al. Efficient production of large ^{39}K Bose–Einstein condensates. *Phys. Rev. A* **82**, 063611 (2010).

[ADS](#) [Google Scholar](#)

50. 50.

Zaccanti, M. et al. Observation of an Efimov spectrum in an atomic system. *Nat. Phys.* **5**, 586 (2009).

[CAS](#) [Google Scholar](#)

51. 51.

Hohenberg, P. C. & Martin, P. C. Microscopic theory of superfluid helium. *Ann. Phys.* **34**, 291 (1965).

[ADS](#) [CAS](#) [Google Scholar](#)

52. 52.

Hu, H., Zou, P. & Liu, X.-J. Low-momentum dynamic structure factor of a strongly interacting Fermi gas at finite temperature: a two-fluid hydrodynamic description. *Phys. Rev. A* **97**, 023615 (2018).

[ADS](#) [CAS](#) [Google Scholar](#)

[Download references](#)

Acknowledgements

We thank J. Man for experimental assistance; and R. P. Smith, J. Dalibard, M. Zwierlein, R. J. Fletcher, T. A. Hilker, S. Nascimbene and T. Yefsah for discussions. This work was supported by the EPSRC (grant nos EP/N011759/1 and EP/P009565/1), ERC (QBox) and QuantERA (NAQUAS, EPSRC grant no. EP/R043396/1). J.S. acknowledges support from Churchill College (Cambridge), and Z.H. acknowledges support from the Royal Society Wolfson Fellowship.

Author information

Author notes

1. Julian Schmitt

Present address: Institut für Angewandte Physik, Universität Bonn, Bonn, Germany

Affiliations

1. Cavendish Laboratory, University of Cambridge, Cambridge, UK

Panagiotis Christodoulou, Maciej Gałka, Nishant Dogra, Julian Schmitt & Zoran Hadzibabic

2. Laboratoire Kastler Brossel, Collège de France, CNRS, ENS-PSL Research University, Sorbonne Université, Paris, France

Raphael Lopes

Authors

1. Panagiotis Christodoulou

[View author publications](#)

You can also search for this author in [PubMed](#) [Google Scholar](#)

2. Maciej Gałka

[View author publications](#)

You can also search for this author in [PubMed](#) [Google Scholar](#)

3. Nishant Dogra

[View author publications](#)

You can also search for this author in [PubMed](#) [Google Scholar](#)

4. Raphael Lopes

[View author publications](#)

You can also search for this author in [PubMed](#) [Google Scholar](#)

5. Julian Schmitt

[View author publications](#)

You can also search for this author in [PubMed](#) [Google Scholar](#)

6. Zoran Hadzibabic

[View author publications](#)

You can also search for this author in [PubMed](#) [Google Scholar](#)

Contributions

P.C. led the data acquisition and analysis. M.G. and J.S. contributed to the data acquisition. P.C., M.G., R.L. and J.S. contributed to the experimental setup. P.C., N.D. and J.S. produced the figures. Z.H. supervised the project. All authors contributed to the data analysis, interpretation of the results and writing of the manuscript.

Corresponding author

Correspondence to [Panagiotis Christodoulou](#).

Ethics declarations

Competing interests

The authors declare no competing interests.

Additional information

Peer review information *Nature* thanks the anonymous reviewers for their contribution to the peer review of this work.

Publisher's note Springer Nature remains neutral with regard to jurisdictional claims in published maps and institutional affiliations.

Source data

[Source Data Fig. 1](#)

[Source Data Fig. 2](#)

[Source Data Fig. 3](#)

Rights and permissions

[Reprints and Permissions](#)

About this article



Check for
updates

Cite this article

Christodoulou, P., Gałka, M., Dogra, N. *et al.* Observation of first and second sound in a BKT superfluid. *Nature* **594**, 191–194 (2021). <https://doi.org/10.1038/s41586-021-03537-9>

[Download citation](#)

- Received: 24 August 2020
- Accepted: 12 April 2021
- Published: 09 June 2021
- Issue Date: 10 June 2021
- DOI: <https://doi.org/10.1038/s41586-021-03537-9>

Comments

By submitting a comment you agree to abide by our [Terms](#) and [Community Guidelines](#). If you find something abusive or that does not comply with our terms or guidelines please flag it as inappropriate.

[Access through your institution](#)

[Change institution](#)

[Buy or subscribe](#)

Associated Content

[Second sound seen](#)

- Sandro Stringari

Nature Physics News & Views 09 Jun 2021

Advertisement

This article was downloaded by **calibre** from <https://www.nature.com/articles/s41586-021-03537-9>

| [Section menu](#) | [Main menu](#) |

- Article
- [Published: 09 June 2021](#)

Experimental observation of non-Abelian topological charges and edge states

- [Qinghua Guo](#)¹ na1,
- [Tianshu Jiang](#) [ORCID: orcid.org/0000-0002-0157-3877](#)¹ na1,
- [Ruo-Yang Zhang](#) [ORCID: orcid.org/0000-0002-3567-0499](#)¹ na1,
- [Lei Zhang](#) [ORCID: orcid.org/0000-0002-8634-8037](#)^{1,2,3},
- [Zhao-Qing Zhang](#)¹,
- [Biao Yang](#) [ORCID: orcid.org/0000-0002-5839-7261](#)^{1,4,5},
- [Shuang Zhang](#) [ORCID: orcid.org/0000-0003-4556-2333](#)^{6,7,8} &
- [C. T. Chan](#) [ORCID: orcid.org/0000-0002-9335-8110](#)¹

[Nature](#) volume 594, pages 195–200 (2021) [Cite this article](#)

- 1798 Accesses
- 12 Altmetric
- [Metrics details](#)

Subjects

- [Condensed-matter physics](#)
- [Optical physics](#)

Abstract

In the last few decades, topological phase^{1,2,3,4,5,6,7,8,9,10,11} has emerged as a new classification of matter states beyond the Ginzburg–Landau symmetry-breaking paradigm. The underlying global invariant is usually well characterized by integers, such as Chern numbers or winding numbers—the Abelian charges^{12,13,14,15}. Very recently, researchers proposed the notion of non-Abelian topological charges^{16,17,18,19}, which possess non-commutative and fruitful braiding structures with multiple (more than one) bandgaps tangled together. Here we experimentally observe the non-Abelian topological charges in a time-reversal and inversion-symmetric transmission line network. The quaternion-valued non-Abelian topological charges are clearly mapped onto an eigenstate-frame sphere. Moreover, we find a non-Abelian quotient relation that provides a global perspective on the distribution of edge/domain-wall states. Our work opens the door towards characterization and manipulation of non-Abelian topological charges, which may lead to interesting observables such as trajectory-dependent Dirac/Weyl node collisions in two-dimensional systems^{16,17,20}, admissible nodal line configurations in three dimensions^{16,19,20}, and may provide insight into certain strongly correlated phases of twisted bilayer graphene²¹.

Access options

Subscribe to Journal

Get full journal access for 1 year

\$199.00

only \$3.90 per issue

[Subscribe](#)

All prices are NET prices.

VAT will be added later in the checkout.

Tax calculation will be finalised during checkout.

Rent or Buy article

Get time limited or full article access on ReadCube.

from \$8.99

[Rent or Buy](#)

All prices are NET prices.

Additional access options:

- [Log in](#)
- [Access through your institution](#)
- [Learn about institutional subscriptions](#)

Fig. 1: Non-Abelian topological charges.

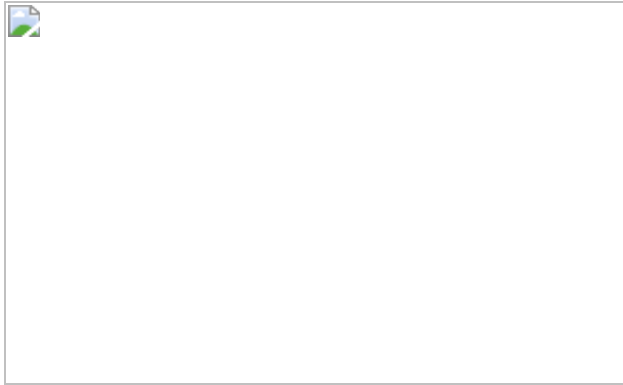


Fig. 2: Realizing non-Abelian topological charges in a tight-binding model.

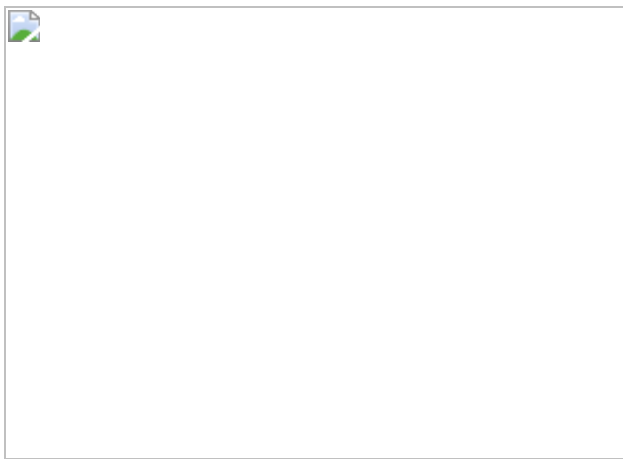


Fig. 3: Experimental characterization of non-Abelian topological charges and hard boundary edge states.

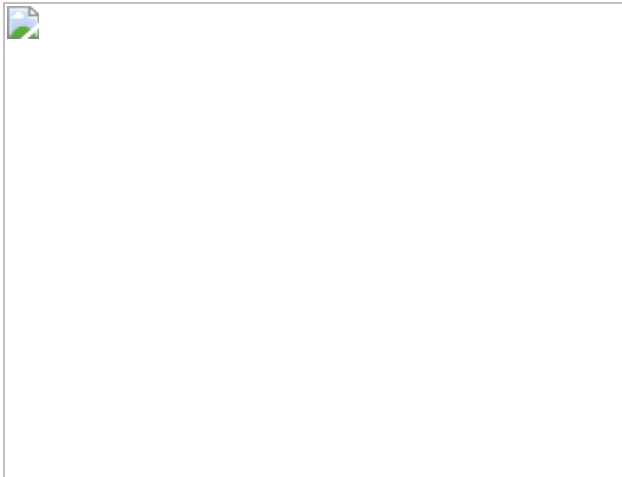


Fig. 4: Non-Abelian quotient relation.



Data availability

The data and code that support the findings of this study are available in DataSpace@HKUST at <https://doi.org/10.14711/dataset/5LXMUZ>.

References

1. 1.

Hasan, M. Z. & Kane, C. L. Topological insulators. *Rev. Mod. Phys.* **82**, 3045–3067 (2010).

[ADS](#) [CAS](#) [Article](#) [Google Scholar](#)

2. 2.

Qi, X.-L. & Zhang, S.-C. Topological insulators and superconductors. *Rev. Mod. Phys.* **83**, 1057–1110 (2011).

[ADS](#) [CAS](#) [Article](#) [Google Scholar](#)

3. 3.

Ando, Y. & Fu, L. Topological crystalline insulators and topological superconductors: from concepts to materials. *Annu. Rev. Condens. Matter Phys.* **6**, 361–381 (2015).

[ADS](#) [CAS](#) [Article](#) [Google Scholar](#)

4. 4.

Kruthoff, J., de Boer, J., van Wezel, J., Kane, C. L. & Slager, R.-J. Topological classification of crystalline insulators through band structure combinatorics. *Phys. Rev. X* **7**, 041069 (2017).

[Google Scholar](#)

5. 5.

Bradlyn, B. et al. Topological quantum chemistry. *Nature* **547**, 298–305 (2017).

[ADS](#) [CAS](#) [Article](#) [Google Scholar](#)

6. 6.

Armitage, N. P., Mele, E. J. & Vishwanath, A. Weyl and Dirac semimetals in three-dimensional solids. *Rev. Mod. Phys.* **90**, 015001 (2018).

[ADS](#) [MathSciNet](#) [CAS](#) [Article](#) [Google Scholar](#)

7. 7.

Ozawa, T. et al. Topological photonics. *Rev. Mod. Phys.* **91**, 015006 (2019).

[ADS](#) [MathSciNet](#) [CAS](#) [Article](#) [Google Scholar](#)

8. 8.

Ma, G., Xiao, M. & Chan, C. T. Topological phases in acoustic and mechanical systems. *Nat. Rev. Phys.* **1**, 281–294 (2019).

[Article](#) [Google Scholar](#)

9. 9.

Tang, F., Po, H. C., Vishwanath, A. & Wan, X. Comprehensive search for topological materials using symmetry indicators. *Nature* **566**, 486–489 (2019).

[ADS](#) [CAS](#) [Article](#) [Google Scholar](#)

10. 10.

Zhang, T. et al. Catalogue of topological electronic materials. *Nature* **566**, 475–479 (2019).

[ADS](#) [CAS](#) [Article](#) [Google Scholar](#)

11. 11.

Kim, M., Jacob, Z. & Rho, J. Recent advances in 2D, 3D and higher-order topological photonics. *Light Sci. Appl.* **9**, 130 (2020).

[ADS](#) [Article](#) [Google Scholar](#)

12. 12.

Schnyder, A. P., Ryu, S., Furusaki, A. & Ludwig, A. W. W. Classification of topological insulators and superconductors in three spatial dimensions. *Phys. Rev. B* **78**, 195125 (2008).

[ADS](#) [Article](#) [Google Scholar](#)

13. 13.

Kitaev, A. Periodic table for topological insulators and superconductors. *AIP Conf. Proc.* **1134**, 22–30 (2009).

[ADS](#) [CAS](#) [Article](#) [Google Scholar](#)

14. 14.

Ryu, S., Schnyder, A. P., Furusaki, A. & Ludwig, A. W. W. Topological insulators and superconductors: tenfold way and dimensional hierarchy. *New J. Phys.* **12**, 065010 (2010).

[ADS](#) [Article](#) [Google Scholar](#)

15. 15.

Chiu, C.-K., Teo, J. C. Y., Schnyder, A. P. & Ryu, S. Classification of topological quantum matter with symmetries. *Rev. Mod. Phys.* **88**, 035005 (2016).

[ADS](#) [Article](#) [Google Scholar](#)

16. 16.

Wu, Q., Soluyanov, A. A. & Bzdušek, T. Non-Abelian band topology in noninteracting metals. *Science* **365**, 1273–1277 (2019).

[MathSciNet](#) [CAS](#) [Article](#) [Google Scholar](#)

17. 17.

Ahn, J., Park, S. & Yang, B.-J. Failure of Nielsen–Ninomiya theorem and fragile topology in two-dimensional systems with space-time inversion symmetry: application to twisted bilayer graphene at magic angle. *Phys. Rev. X* **9**, 021013 (2019).

[CAS](#) [Google Scholar](#)

18. 18.

Tiwari, A. & Bzdušek, T. Non-Abelian topology of nodal-line rings in PT-symmetric systems. *Phys. Rev. B* **101**, 195130 (2020).

[ADS](#) [CAS](#) [Article](#) [Google Scholar](#)

19. 19.

Yang, E. et al. Observation of non-Abelian nodal links in photonics. *Phys. Rev. Lett.* **125**, 033901 (2020).

[ADS](#) [CAS](#) [Article](#) [Google Scholar](#)

20. 20.

Bouhon, A. et al. Non-Abelian reciprocal braiding of Weyl points and its manifestation in ZrTe. *Nat. Phys.* **16**, 1137–1143 (2020).

[CAS](#) [Article](#) [Google Scholar](#)

21. 21.

Kang, J. & Vafek, O. Non-Abelian Dirac node braiding and near-degeneracy of correlated phases at odd integer filling in magic-angle twisted bilayer graphene. *Phys. Rev. B* **102**, 035161 (2020).

[ADS](#) [CAS](#) [Article](#) [Google Scholar](#)

22. 22.

Jackiw, R. & Rebbi, C. Solitons with fermion number 1/2. *Phys. Rev. D* **13**, 3398–3409 (1976).

[ADS](#) [MathSciNet](#) [CAS](#) [Article](#) [Google Scholar](#)

23. 23.

Hatsugai, Y. Chern number and edge states in the integer quantum Hall effect. *Phys. Rev. Lett.* **71**, 3697–3700 (1993).

[ADS](#) [MathSciNet](#) [CAS](#) [Article](#) [Google Scholar](#)

24. 24.

Graf, G. M. & Porta, M. Bulk–edge correspondence for two-dimensional topological insulators. *Commun. Math. Phys.* **324**, 851–895 (2013).

[ADS](#) [MathSciNet](#) [Article](#) [Google Scholar](#)

25. 25.

Fang, C., Weng, H., Dai, X. & Fang, Z. Topological nodal line semimetals. *Chin. Phys. B* **25**, 117106 (2016).

[ADS](#) [Article](#) [Google Scholar](#)

26. 26.

Mermin, N. D. The topological theory of defects in ordered media. *Rev. Mod. Phys.* **51**, 591–648 (1979).

[ADS](#) [MathSciNet](#) [CAS](#) [Article](#) [Google Scholar](#)

27. 27.

Basener, W. F. *Topology and Its Applications* 255–256 (Wiley, 2006).

28. 28.

Jiang, T. et al. Experimental demonstration of angular momentum-dependent topological transport using a transmission line network. *Nat. Commun.* **10**, 434 (2019).

[ADS](#) [CAS](#) [Article](#) [Google Scholar](#)

29. 29.

Zhao, E. Topological circuits of inductors and capacitors. *Ann. Phys.* **399**, 289–313 (2018).

[ADS](#) [MathSciNet](#) [CAS](#) [Article](#) [Google Scholar](#)

30. 30.

Rechtsman, M. C. et al. Photonic Floquet topological insulators. *Nature* **496**, 196–200 (2013).

[ADS](#) [CAS](#) [Article](#) [Google Scholar](#)

31. 31.

Hafezi, M., Mittal, S., Fan, J., Migdall, A. & Taylor, J. M. Imaging topological edge states in silicon photonics. *Nat. Photon.* **7**, 1001–1005 (2013).

[ADS](#) [CAS](#) [Article](#) [Google Scholar](#)

32. 32.

Dutt, A. et al. A single photonic cavity with two independent physical synthetic dimensions. *Science* **367**, 59–64 (2020).

[ADS](#) [CAS](#) [Article](#) [Google Scholar](#)

33. 33.

Ke, Y. et al. Topological phase transitions and Thouless pumping of light in photonic waveguide arrays. *Laser Photonics Rev.* **10**, 1064 (2016).

[ADS](#) [Article](#) [Google Scholar](#)

34. 34.

Ünal, F. N., Bouhon, A. & Slager, R.-J. Topological Euler class as a dynamical observable in optical lattices. *Phys. Rev. Lett.* **125**, 053601 (2020).

[ADS](#) [MathSciNet](#) [Article](#) [Google Scholar](#)

[Download references](#)

Acknowledgements

This work is supported by the Hong Kong RGC (AoE/P-02/12, 16304717, 16310420) and the Hong Kong Scholars Program (XJ2019007). L.Z. acknowledges the National Natural Science Foundation of China (grant no. 12074230) and Shanxi Province 100-Plan Talent Program. S.Z. acknowledges support from the ERC Consolidator Grant (TOPOLOGICAL), the Royal Society and the Wolfson Foundation. C.T.C. thanks R. Cheng for making space available to construct the network.

Author information

Author notes

1. These authors contributed equally: Qinghua Guo, Tianshu Jiang, Ruo-Yang Zhang

Affiliations

1. Department of Physics and Institute for Advanced Study, The Hong Kong University of Science and Technology, Hong Kong, China

Qinghua Guo, Tianshu Jiang, Ruo-Yang Zhang, Lei Zhang, Zhao-Qing Zhang, Biao Yang & C. T. Chan

2. State Key Laboratory of Quantum Optics and Quantum Optics Devices, Institute of Laser Spectroscopy, Shanxi University, Taiyuan, China

Lei Zhang

3. Collaborative Innovation Center of Extreme Optics, Shanxi University, Taiyuan, China

Lei Zhang

4. College of Advanced Interdisciplinary Studies, National University of Defense Technology, Changsha, China

Biao Yang

5. Hunan Provincial Key Laboratory of Novel Nano-Optoelectronic Information Materials and Devices, National University of Defense Technology, Changsha, China

Biao Yang

6. School of Physics and Astronomy, University of Birmingham, Birmingham, UK

Shuang Zhang

7. Department of Physics, The University of Hong Kong, Hong Kong, China

Shuang Zhang

8. Department of Electrical and Electronic Engineering, The University of Hong Kong, Hong Kong, China

Shuang Zhang

Authors

1. Qinghua Guo

[View author publications](#)

You can also search for this author in [PubMed](#) [Google Scholar](#)

2. Tianshu Jiang
[View author publications](#)

You can also search for this author in [PubMed](#) [Google Scholar](#)

3. Ruo-Yang Zhang
[View author publications](#)

You can also search for this author in [PubMed](#) [Google Scholar](#)

4. Lei Zhang
[View author publications](#)

You can also search for this author in [PubMed](#) [Google Scholar](#)

5. Zhao-Qing Zhang
[View author publications](#)

You can also search for this author in [PubMed](#) [Google Scholar](#)

6. Biao Yang
[View author publications](#)

You can also search for this author in [PubMed](#) [Google Scholar](#)

7. Shuang Zhang
[View author publications](#)

You can also search for this author in [PubMed](#) [Google Scholar](#)

8. C. T. Chan
[View author publications](#)

You can also search for this author in [PubMed](#) [Google Scholar](#)

Contributions

Q.G., B.Y., S.Z. and C.T.C. conceived the idea; T.J. designed the transmission line network with input from Z.-Q.Z. and C.T.C.; Q.G. and

T.J. carried out all measurements; Q.G., T.J., R.-Y.Z., Z.-Q.Z., B.Y., S.Z. and C.T.C. developed and carried out the theoretical analysis; L.Z. participated in the analysis and discussion of the results. B.Y., S.Z. and C.T.C. supervised the whole project. Q.G., T.J., R.-Y.Z. and B.Y. wrote the manuscript and the Supplementary Information with input from all other authors.

Corresponding authors

Correspondence to [Biao Yang](#) or [Shuang Zhang](#) or [C. T. Chan](#).

Ethics declarations

Competing interests

The authors declare no competing interests.

Additional information

Peer review information *Nature* thanks Xiang Ni, Baile Zhang and the other, anonymous, reviewer(s) for their contribution to the peer review of this work. Peer reviewer reports are available.

Publisher's note Springer Nature remains neutral with regard to jurisdictional claims in published maps and institutional affiliations.

Supplementary information

[Supplementary Information](#)

This file contains Supplementary Text and Data, Supplementary Tables 1-3, Supplementary References and Supplementary Figures 1-25.

[Peer Review File](#)

Rights and permissions

[Reprints and Permissions](#)

About this article



Check for
updates

Cite this article

Guo, Q., Jiang, T., Zhang, RY. *et al.* Experimental observation of non-Abelian topological charges and edge states. *Nature* **594**, 195–200 (2021). <https://doi.org/10.1038/s41586-021-03521-3>

[Download citation](#)

- Received: 01 October 2020
- Accepted: 06 April 2021
- Published: 09 June 2021
- Issue Date: 10 June 2021
- DOI: <https://doi.org/10.1038/s41586-021-03521-3>

Comments

By submitting a comment you agree to abide by our [Terms](#) and [Community Guidelines](#). If you find something abusive or that does not comply with our terms or guidelines please flag it as inappropriate.

[Access through your institution](#)

[Change institution](#)

[Buy or subscribe](#)

Advertisement

This article was downloaded by **calibre** from <https://www.nature.com/articles/s41586-021-03521-3>

| [Section menu](#) | [Main menu](#) |

- Article
- [Published: 09 June 2021](#)

Quantum-enhanced nonlinear microscopy

- [Catxere A. Casacio¹](#),
- [Lars S. Madsen¹](#),
- [Alex Terrasson¹](#),
- [Muhammad Waleed¹](#),
- [Kai Barnscheidt](#) [ORCID: orcid.org/0000-0001-6783-7372²](#),
- [Boris Hage²](#),
- [Michael A. Taylor](#) [ORCID: orcid.org/0000-0003-4393-7760³](#) &
- [Warwick P. Bowen](#) [ORCID: orcid.org/0000-0001-8127-1715¹](#)

[Nature](#) volume **594**, pages 201–206 (2021) [Cite this article](#)

- 6694 Accesses
- 533 Altmetric
- [Metrics details](#)

Subjects

- [Multiphoton microscopy](#)
- [Quantum optics](#)

Abstract

The performance of light microscopes is limited by the stochastic nature of light, which exists in discrete packets of energy known as photons.

Randomness in the times that photons are detected introduces shot noise, which fundamentally constrains sensitivity, resolution and speed¹. Although the long-established solution to this problem is to increase the intensity of the illumination light, this is not always possible when investigating living systems, because bright lasers can severely disturb biological processes^{2,3,4}. Theory predicts that biological imaging may be improved without increasing light intensity by using quantum photon correlations^{1,5}. Here we experimentally show that quantum correlations allow a signal-to-noise ratio beyond the photodamage limit of conventional microscopy. Our microscope is a coherent Raman microscope that offers subwavelength resolution and incorporates bright quantum correlated illumination. The correlations allow imaging of molecular bonds within a cell with a 35 per cent improved signal-to-noise ratio compared with conventional microscopy, corresponding to a 14 per cent improvement in concentration sensitivity. This enables the observation of biological structures that would not otherwise be resolved. Coherent Raman microscopes allow highly selective biomolecular fingerprinting in unlabelled specimens^{6,7}, but photodamage is a major roadblock for many applications^{8,9}. By showing that the photodamage limit can be overcome, our work will enable order-of-magnitude improvements in the signal-to-noise ratio and the imaging speed.

Access options

Subscribe to Journal

Get full journal access for 1 year

\$199.00

only \$3.90 per issue

[Subscribe](#)

All prices are NET prices.

VAT will be added later in the checkout.

Tax calculation will be finalised during checkout.

Rent or Buy article

Get time limited or full article access on ReadCube.

from \$8.99

[Rent or Buy](#)

All prices are NET prices.

Additional access options:

- [Log in](#)
- [Access through your institution](#)
- [Learn about institutional subscriptions](#)

Fig. 1: Experimental setup.



Fig. 2: Quantifying photodamage.

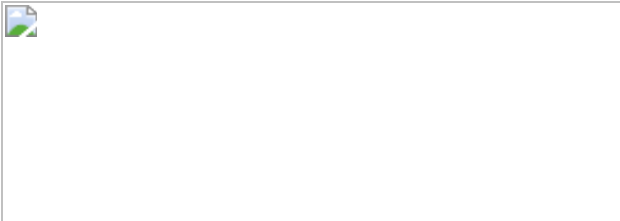


Fig. 3: Quantum-enhanced stimulated Raman microscopy.

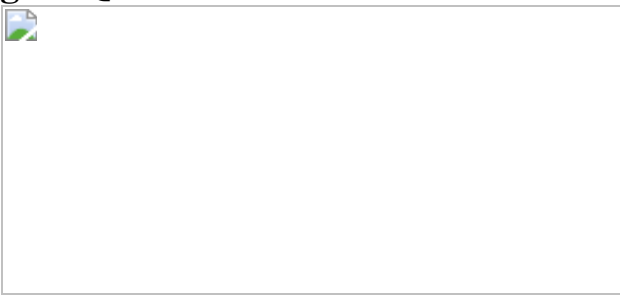
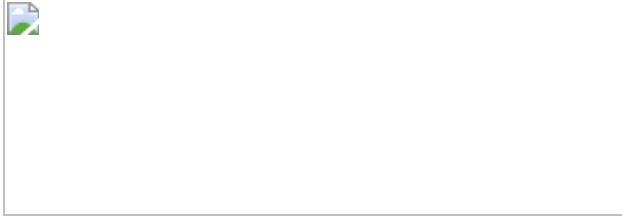


Fig. 4: Quantum-enhanced imaging.



Data availability

The data that support the findings of this study are included in the Supplementary Information. This includes data quantifying the detector design and performance (Supplementary Figs. 3–5); example power spectral densities of the stimulated Raman signal-to-noise ratio with and without squeezing (Supplementary Fig. 6); the raw measured power spectral densities of detector electronic noise, shot-noise and squeezing (Supplementary Fig. 7); experimental measurements of the squeezed variance and classical deamplification of the Stokes field as a function of the optical parametric amplifier pump power (Supplementary Fig. 9); the photocurrent power spectral density used to determine the concentration sensitivity when probing the CH aromatic stretch band in polystyrene (Supplementary Fig. 10); measurements of cell photodamage (Supplementary Fig. 11); and comparative cell images with and without quantum enhancement (Supplementary Fig. 12). Further data are available from the corresponding author upon reasonable request. [Source data](#) are provided with this paper.

References

1. 1.

Taylor, M. A. & Bowen, W. P. Quantum metrology and its application in biology. *Phys. Rep.* **615**, 1–59 (2016).

[ADS](#) [MathSciNet](#) [CAS](#) [Google Scholar](#)

2. 2.

Li, B., Wu, C., Wang, M., Charan, K. & Xu, C. An adaptive excitation source for high-speed multiphoton microscopy. *Nat. Methods* **17**, 163–166 (2020).

[CAS](#) [PubMed](#) [PubMed Central](#) [Google Scholar](#)

3. 3.

Wäldchen, S., Lehmann, J., Klein, T., Van De Linde, S. & Sauer, M. Light-induced cell damage in live-cell super-resolution microscopy. *Sci. Rep.* **5**, 15348 (2015).

[ADS](#) [PubMed](#) [PubMed Central](#) [Google Scholar](#)

4. 4.

Mauranyapin, N. P., Madsen, L. S., Taylor, M. A., Waleed, M. & Bowen, W. P. Evanescent single-molecule biosensing with quantum-limited precision. *Nat. Photon.* **11**, 477–481 (2017).

[CAS](#) [Google Scholar](#)

5. 5.

Slusher, R. E. Quantum optics in the '80s. *Opt. Photon. News* **1**, 27–30 (1990).

[ADS](#) [Google Scholar](#)

6. 6.

Cheng, J.-X. & Sunney Xie, X. Vibrational spectroscopic imaging of living systems: an emerging platform for biology and medicine. *Science* **350**, aaa8870 (2015).

[PubMed](#) [PubMed Central](#) [Google Scholar](#)

7. 7.

Wei, L. et al. Super-multiplex vibrational imaging. *Nature* **544**, 465–470 (2017).

[ADS](#) [CAS](#) [PubMed](#) [PubMed Central](#) [Google Scholar](#)

8. 8.

Camp, C. H. Jr & Cicerone, M. T. Chemically sensitive bioimaging with coherent Raman scattering. *Nat. Photon.* **9**, 295–305 (2015).

[ADS](#) [CAS](#) [Google Scholar](#)

9. 9.

Fu, Y., Wang, H., Shi, R. & Cheng, J.-X. Characterization of photodamage in coherent anti-Stokes Raman scattering microscopy. *Opt. Express* **14**, 3942–3951 (2006).

[ADS](#) [CAS](#) [PubMed](#) [PubMed Central](#) [Google Scholar](#)

10. 10.

Sigal, Y. M., Zhou, R. & Zhuang, X. Visualizing and discovering cellular structures with super-resolution microscopy. *Science* **361**, 880–887 (2018).

[ADS](#) [CAS](#) [PubMed](#) [PubMed Central](#) [Google Scholar](#)

11. 11.

Alex, M. et al. Applying systems-level spectral imaging and analysis to reveal the organelle interactome. *Nature* **546**, 162–167 (2017).

[Google Scholar](#)

12. 12.

Adam, Y. et al. Voltage imaging and optogenetics reveal behaviour-dependent changes in hippocampal dynamics. *Nature* **569**, 413–417

(2019).

[ADS](#) [CAS](#) [PubMed](#) [PubMed Central](#) [Google Scholar](#)

13. 13.

Schermelleh, L. et al. Super-resolution microscopy demystified. *Nat. Cell Biol.* **21**, 72–84 (2019).

[CAS](#) [PubMed](#) [PubMed Central](#) [Google Scholar](#)

14. 14.

Sewell, R. J., Napolitano, M., Behbood, N., Colangelo, G. & Mitchell, M. W. Certified quantum non-demolition measurement of a macroscopic material system. *Nat. Photon.* **7**, 517–520 (2013).

[ADS](#) [CAS](#) [Google Scholar](#)

15. 15.

Aasi, J. et al. Enhanced sensitivity of the LIGO gravitational wave detector by using squeezed states of light. *Nat. Photon.* **7**, 613–619 (2013).

[ADS](#) [CAS](#) [Google Scholar](#)

16. 16.

Giovannetti, V., Lloyd, S. & Maccone, L. Advances in quantum metrology. *Nat. Photon.* **5**, 222–229 (2011).

[ADS](#) [CAS](#) [Google Scholar](#)

17. 17.

Moreau, P.-A., Toninelli, E., Gregory, T. & Padgett, M. J. Imaging with quantum states of light. *Nat. Rev. Phys.* **1**, 367–380 (2019).

[Google Scholar](#)

18. 18.

Brida, G., Genovese, M. & Ruo Berchera, I. Experimental realization of sub-shot-noise quantum imaging. *Nat. Photon.* **4**, 227–230 (2010).

[ADS](#) [CAS](#) [Google Scholar](#)

19. 19.

Defienne, H., Reichert, M., Fleischer, J. W. & Faccio, D. Quantum image distillation. *Sci. Adv.* **5**, eaax0307 (2019).

[ADS](#) [PubMed](#) [PubMed Central](#) [Google Scholar](#)

20. 20.

Sabines-Chesterking, J. et al. Twin-beam sub-shot-noise raster-scanning microscope. *Opt. Express* **27**, 30810–30818 (2019).

[ADS](#) [CAS](#) [PubMed](#) [PubMed Central](#) [Google Scholar](#)

21. 21.

Samantaray, N., Ruo-Berchera, I., Meda, A. & Genovese, M. Realization of the first sub-shot-noise wide field microscope. *Light Sci. Appl.* **6**, e17005 (2017).

[ADS](#) [CAS](#) [PubMed](#) [PubMed Central](#) [Google Scholar](#)

22. 22.

Gregory, T., Moreau, P.-A., Toninelli, E. & Padgett, M. J. Imaging through noise with quantum illumination. *Sci. Adv.* **6**, eaay2652 (2020).

[ADS](#) [CAS](#) [PubMed](#) [PubMed Central](#) [Google Scholar](#)

23. 23.

Israel, Y., Rosen, S. & Silberberg, Y. Supersensitive polarization microscopy using NOON states of light. *Phys. Rev. Lett.* **112**, 103604 (2014).

[ADS](#) [PubMed](#) [PubMed Central](#) [Google Scholar](#)

24. 24.

Ono, T., Okamoto, R. & Takeuchi, S. An entanglement-enhanced microscope. *Nat. Commun.* **4**, 2426 (2013).

[ADS](#) [PubMed](#) [PubMed Central](#) [Google Scholar](#)

25. 25.

Lemos, G. B. et al. Quantum imaging with undetected photons. *Nature* **512**, 409–412 (2014).

[ADS](#) [CAS](#) [PubMed](#) [PubMed Central](#) [Google Scholar](#)

26. 26.

Kalashnikov, D. A., Paterova, A. V., Kulik, S. P. & Krivitsky, L. A. Infrared spectroscopy with visible light. *Nat. Photon.* **10**, 98–101 (2016).

[ADS](#) [CAS](#) [Google Scholar](#)

27. 27.

Paterova, A. V., Yang, H., An, C., Kalashnikov, D. A. & Krivitsky, L. A. Tunable optical coherence tomography in the infrared range using visible photons. *Quantum Sci. Technol.* **3**, 025008 (2018).

[ADS](#) [Google Scholar](#)

28. 28.

Zhang, L. et al. Spectral tracing of deuterium for imaging glucose metabolism. *Nat. Biomed. Eng.* **3**, 402–413 (2019).

[ADS](#) [CAS](#) [PubMed](#) [PubMed Central](#) [Google Scholar](#)

29. 29.

Tian, F. et al. Monitoring peripheral nerve degeneration in ALS by label-free stimulated Raman scattering imaging. *Nat. Commun.* **7**, 13283 (2016).

[ADS](#) [CAS](#) [PubMed](#) [PubMed Central](#) [Google Scholar](#)

30. 30.

Liu, B. et al. Label-free spectroscopic detection of membrane potential using stimulated Raman scattering. *Appl. Phys. Lett.* **106**, 173704 (2015).

[ADS](#) [Google Scholar](#)

31. 31.

Konstanze, T. et al. Phenazine production promotes antibiotic tolerance and metabolic heterogeneity in *Pseudomonas aeruginosa* biofilms. *Nat. Commun.* **10**, 762 (2019).

[Google Scholar](#)

32. 32.

Saar, B. G. et al. Video-rate molecular imaging in vivo with stimulated Raman scattering. *Science* **330**, 1368–1370 (2010).

[ADS](#) [CAS](#) [PubMed](#) [PubMed Central](#) [Google Scholar](#)

33. 33.

Freudiger, C. W. et al. Stimulated Raman scattering microscopy with a robust fibre laser source. *Nat. Photon.* **8**, 153–159 (2014).

[ADS](#) [CAS](#) [Google Scholar](#)

34. 34.

Freudiger, C. W. et al. Label-free biomedical imaging with high sensitivity by stimulated Raman scattering microscopy. *Science* **322**, 1857–1861 (2008).

[ADS](#) [CAS](#) [PubMed](#) [PubMed Central](#) [Google Scholar](#)

35. 35.

Pooser, R. C. & Lawrie, B. Plasmonic trace sensing below the photon shot noise limit. *ACS Photon.* **3**, 8–13 (2016).

[CAS](#) [Google Scholar](#)

36. 36.

Dowran, M., Kumar, A., Lawrie, B. J., Pooser, R. C. & Marino, A. M. Quantum-enhanced plasmonic sensing. *Optica* **5**, 628–633 (2018).

[ADS](#) [CAS](#) [Google Scholar](#)

37. 37.

Michael, A. et al. Biological measurement beyond the quantum limit. *Nat. Photon.* **7**, 229–233 (2013).

[Google Scholar](#)

38. 38.

Michael, A. et al. Subdiffraction-limited quantum imaging within a living cell. *Phys. Rev. X* **4**, 011017 (2014).

[Google Scholar](#)

39. 39.

Tenne, R. et al. Super-resolution enhancement by quantum image scanning microscopy. *Nat. Photon.* **13**, 116–122 (2019).

[ADS](#) [CAS](#) [Google Scholar](#)

40. 40.

Phan, N. M., Cheng, M. F., Bessarab, D. A. & Krivitsky, L. A. Interaction of fixed number of photons with retinal rod cells. *Phys. Rev. Lett.* **112**, 213601 (2014).

[ADS](#) [Google Scholar](#)

41. 41.

Choi, Y. et al. Shot-noise-limited two-color stimulated Raman scattering microscopy with a balanced detection scheme. *J. Phys. Chem. B* **124**, 2591–2599 (2020).

[CAS](#) [PubMed](#) [PubMed Central](#) [Google Scholar](#)

42. 42.

de Andrade, R. B. et al. Quantum-enhanced continuous-wave stimulated Raman spectroscopy. *Optica* **7**, 470–475 (2020).

[ADS](#) [Google Scholar](#)

43. 43.

Triginer Garces, G. et al. Quantum-enhanced stimulated emission detection for label-free microscopy. *Appl. Phys. Lett.* **117**, 024002 (2020).

[ADS](#) [CAS](#) [Google Scholar](#)

44. 44.

Okuno, M. et al. Quantitative CARS molecular fingerprinting of single living cells with the use of the maximum entropy method. *Angew. Chem.* **122**, 6925–6929 (2010).

[Google Scholar](#)

45. 45.

Kochan, K., Peng, H., Wood, B. R. & Haritos, V. S. Single cell assessment of yeast metabolic engineering for enhanced lipid production using Raman and AFM-IR imaging. *Biotechnol. Biofuels* **11**, 106 (2018).

[PubMed](#) [PubMed Central](#) [Google Scholar](#)

46. 46.

A Roadmap for Quantum Technologies in the UK 16 (UK Quantum Technologies Programme, 2015);
<https://epsrc.ukri.org/newsevents/pubs/quantumtechroadmap>

47. 47.

Vahlbruch, H., Mehmet, M., Danzmann, K. & Schnabel, R. Detection of 15 dB squeezed states of light and their application for the absolute calibration of photoelectric quantum efficiency. *Phys. Rev. Lett.* **117**, 110801 (2016).

[ADS](#) [PubMed](#) [PubMed Central](#) [Google Scholar](#)

48. 48.

Hoover, E. E. & Squier, J. A. Advances in multiphoton microscopy technology. *Nat. Photon.* **7**, 93–101 (2013).

[ADS](#) [CAS](#) [Google Scholar](#)

49. 49.

Zong, C. et al. Plasmon-enhanced stimulated Raman scattering microscopy with single-molecule detection sensitivity. *Nat. Commun.* **10**, 5318 (2019).

[ADS](#) [PubMed](#) [PubMed Central](#) [Google Scholar](#)

50. 50.

Michael, Y., Bello, L., Rosenbluh, M. & Pe'er, A. Squeezing-enhanced Raman spectroscopy. *npj Quantum Inf.* **5**, 81 (2019).

[ADS](#) [Google Scholar](#)

[Download references](#)

Acknowledgements

We acknowledge W. Wasserman for sourcing the yeast cells in trying circumstances, U. Hoff for contributions to the construction of the apparatus and APE GmbH for support related to the laser system. This work was supported primarily by the Air Force Office of Scientific Research (AFOSR) grant FA2386-14-1-4046. It was also supported by the Australian Research Council Centre of Excellence for Engineered Quantum Systems (EQUS, CE170100009). W.P.B. acknowledges the Australian Research Council Future Fellowship, FT140100650. M.A.T. acknowledges the Australian Research Council Discovery Early Career Research Award, DE190100641.

Author information

Affiliations

1. ARC Centre of Excellence for Engineered Quantum Systems, University of Queensland, St Lucia, Queensland, Australia

Catxere A. Casacio, Lars S. Madsen, Alex Terrasson, Muhammad Waleed & Warwick P. Bowen

2. Institut für Physik, Universität Rostock, Rostock, Germany

Kai Barnscheidt & Boris Hage

3. Australian Institute for Bioengineering and Nanotechnology, The University of Queensland, St Lucia, Queensland, Australia

Michael A. Taylor

Authors

1. Catxere A. Casacio

[View author publications](#)

You can also search for this author in [PubMed](#) [Google Scholar](#)

2. Lars S. Madsen

[View author publications](#)

You can also search for this author in [PubMed](#) [Google Scholar](#)

3. Alex Terrasson

[View author publications](#)

You can also search for this author in [PubMed](#) [Google Scholar](#)

4. Muhammad Waleed

[View author publications](#)

You can also search for this author in [PubMed](#) [Google Scholar](#)

5. Kai Barnscheidt

[View author publications](#)

You can also search for this author in [PubMed](#) [Google Scholar](#)

6. Boris Hage

[View author publications](#)

You can also search for this author in [PubMed](#) [Google Scholar](#)

7. Michael A. Taylor

[View author publications](#)

You can also search for this author in [PubMed](#) [Google Scholar](#)

8. Warwick P. Bowen

[View author publications](#)

You can also search for this author in [PubMed](#) [Google Scholar](#)

Contributions

C.A.C., A.T., L.S.M. and M.A.T. collected the data. C.A.C. and A.T. performed the data analysis. C.A.C., A.T. and L.S.M. constructed the experiment. M.W. constructed the microscope, with contributions from M.A.T. and L.S.M. K.B. and B.H. designed and built the photodetector used to observe the stimulated Raman signal. C.A.C., L.S.M., M.A.T. and W.P.B. designed the experiment. M.A.T. and W.P.B. conceived the idea. W.P.B., M.A.T., A.T. and C.A.C. wrote the manuscript with contributions from all authors. W.P.B. led the project with assistance from M.A.T. and L.S.M.

Corresponding author

Correspondence to [Warwick P. Bowen](#).

Ethics declarations

Competing interests

The authors declare no competing interests.

Additional information

Peer review information *Nature* thanks the anonymous reviewers for their contribution to the peer review of this work. Peer reviewer reports are available.

Publisher's note Springer Nature remains neutral with regard to jurisdictional claims in published maps and institutional affiliations.

Supplementary information

Supplementary Information

This file provides details about the theory, modelling, and experimental techniques used in the article.

Peer Review File

Source data

Source Data Fig. 2

Source Data Fig. 3

Rights and permissions

Reprints and Permissions

About this article



Check for
updates

Cite this article

Casacio, C.A., Madsen, L.S., Terrasson, A. *et al.* Quantum-enhanced nonlinear microscopy. *Nature* **594**, 201–206 (2021).
<https://doi.org/10.1038/s41586-021-03528-w>

[Download citation](#)

- Received: 31 March 2020
- Accepted: 09 April 2021
- Published: 09 June 2021
- Issue Date: 10 June 2021
- DOI: <https://doi.org/10.1038/s41586-021-03528-w>

Comments

By submitting a comment you agree to abide by our [Terms](#) and [Community Guidelines](#). If you find something abusive or that does not comply with our terms or guidelines please flag it as inappropriate.

[Access through your institution](#)

[Change institution](#)

[Buy or subscribe](#)

Associated Content

[Squeezed light improves sensitivity of microscopy technique](#)

- Eric O. Potma

Nature News & Views 09 Jun 2021

Advertisement

This article was downloaded by **calibre** from <https://www.nature.com/articles/s41586-021-03528-w>

| [Section menu](#) | [Main menu](#) |

- Article
- [Published: 09 June 2021](#)

A graph placement methodology for fast chip design

- [Azalia Mirhoseini](#) [ORCID: orcid.org/0000-0002-2440-0944](#)^{1 na1},
- [Anna Goldie](#) [ORCID: orcid.org/0000-0002-4887-6293](#)^{1,3 na1},
- [Mustafa Yazgan](#)²,
- [Joe Wenjie Jiang](#)¹,
- [Ebrahim Songhorl](#)¹,
- [Shen Wang](#)¹,
- [Young-Joon Lee](#)²,
- [Eric Johnson](#)¹,
- [Omkar Pathak](#)²,
- [Azade Nazi](#)¹,
- [Jiwoo Pak](#)²,
- [Andy Tong](#)²,
- [Kavya Srinivasa](#)²,
- [William Hang](#)³,
- [Emre Tuncer](#)²,
- [Quoc V. Le](#)¹,
- [James Laudon](#) [ORCID: orcid.org/0000-0003-1061-1780](#)¹,
- [Richard Ho](#)²,
- [Roger Carpenter](#)² &
- [Jeff Dean](#)¹

[Nature](#) volume **594**, pages 207–212 (2021) [Cite this article](#)

- 5330 Accesses

- 1 Citations
- 1262 Altmetric
- [Metrics details](#)

Subjects

- [Computational science](#)
- [Electrical and electronic engineering](#)

Abstract

Chip floorplanning is the engineering task of designing the physical layout of a computer chip. Despite five decades of research¹, chip floorplanning has defied automation, requiring months of intense effort by physical design engineers to produce manufacturable layouts. Here we present a deep reinforcement learning approach to chip floorplanning. In under six hours, our method automatically generates chip floorplans that are superior or comparable to those produced by humans in all key metrics, including power consumption, performance and chip area. To achieve this, we pose chip floorplanning as a reinforcement learning problem, and develop an edge-based graph convolutional neural network architecture capable of learning rich and transferable representations of the chip. As a result, our method utilizes past experience to become better and faster at solving new instances of the problem, allowing chip design to be performed by artificial agents with more experience than any human designer. Our method was used to design the next generation of Google's artificial intelligence (AI) accelerators, and has the potential to save thousands of hours of human effort for each new generation. Finally, we believe that more powerful AI-designed hardware will fuel advances in AI, creating a symbiotic relationship between the two fields.

Access options

Subscribe to Journal

Get full journal access for 1 year

\$199.00

only \$3.90 per issue

[Subscribe](#)

All prices are NET prices.

VAT will be added later in the checkout.

Tax calculation will be finalised during checkout.

Rent or Buy article

Get time limited or full article access on ReadCube.

from \$8.99

[Rent or Buy](#)

All prices are NET prices.

Additional access options:

- [Log in](#)
- [Access through your institution](#)
- [Learn about institutional subscriptions](#)

Fig. 1: Overview of our method and training regimen.

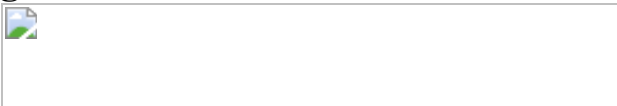


Fig. 2: Policy and value network architecture.

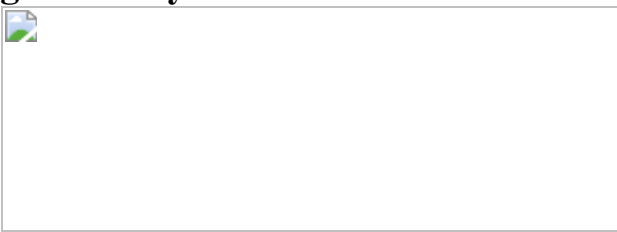


Fig. 3: Training from scratch versus fine-tuning for varying amounts of time.

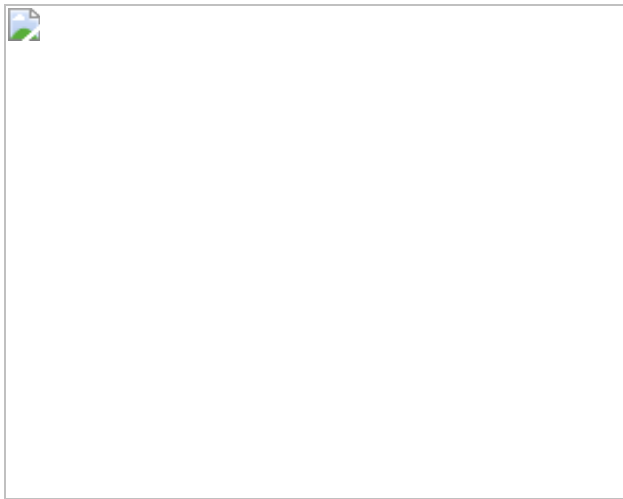


Fig. 4: Convergence plots on Ariane RISC-V CPU.

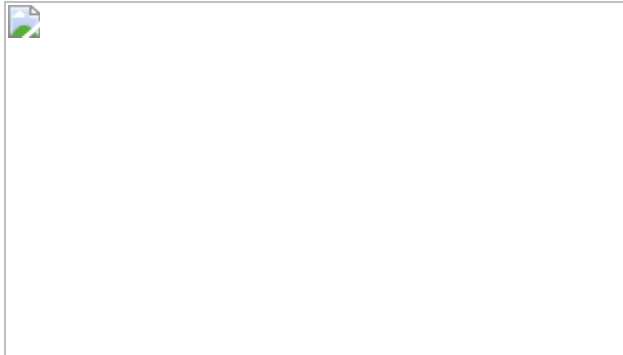


Fig. 5: Effect of pre-training dataset size.



Data availability

The data supporting the findings of this study are available within the paper and the Extended Data.

Code availability

The code used to generate these data is available from the corresponding authors upon reasonable request.

References

1. 1.

Markov, I. L., Hu, J. & Kim, M. Progress and challenges in VLSI placement research. *Proc. IEEE* **103**, 1985–2003 (2015).

[Article](#) [Google Scholar](#)

2. 2.

Tang, M. & Yao, X. A memetic algorithm for VLSI floorplanning. *IEEE Trans. Syst. Man Cybern. B* **37**, 62–69 (2007).

[Article](#) [Google Scholar](#)

3. 3.

Breuer, M. A. A class of min-cut placement algorithms. In *Proc. 14th Design Automation Conference (DAC 1977)* 284–290 (IEEE, 1977).

4. 4.

Fiduccia, C. M. & Mattheyses, R. M. A linear-time heuristic for improving network partitions. In *19th Design Automation Conference* 175–181 (IEEE, 1982).

5. 5.

Roy, J. A., Papa, D. A. & Markov, I. L. in *Modern Circuit Placement* (eds Nam, G.-J. & Cong, J. J.) 97–133 (Springer, 2007).

6. 6.

Kirkpatrick, S., Gelatt, C. D. & Vecchi, M. P. Optimization by simulated annealing. *Science* **220**, 671–680 (1983).

[ADS](#) [MathSciNet](#) [CAS](#) [Article](#) [Google Scholar](#)

7. 7.

Sechen, C. M. & Sangiovanni-Vincentelli, A. L. TimberWolf3.2: a new standard cell placement and global routing package. In *23rd ACM/IEEE Design Automation Conference* 432–439 (IEEE, 1986).

8. 8.

Sarrafzadeh, M., Wang, M. & Yang, X. in *Modern Placement Techniques* 57–89 (Springer, 2003).

9. 9.

Luo, T. & Pan, D. Z. DPlace2.0: a stable and efficient analytical placement based on diffusion. In *2008 Asia and South Pacific Design Automation Conference* 346–351 (IEEE, 2008).

10. 10.

Hu, B. & Marek-Sadowska, M. Multilevel fixed-point-addition-based VLSI placement. *IEEE Trans. Comput. Aided Des. Integrated Circ. Syst.* **24**, 1188–1203 (2005).

[Article](#) [Google Scholar](#)

11. 11.

Viswanathan, N., Pan, M. & Chu, C. in *Modern Circuit Placement* (eds Nam, G.-J. & Cong, J. J.) 193–228 (Springer, 2007).

12. 12.

Kim, M., Lee, D., Markov, I. L. & Sim, P. L. An effective placement algorithm. *IEEE Trans. Comput. Aided Des. Integrated Circ. Syst.* **31**,

50–60 (2012).

[Article](#) [Google Scholar](#)

13. 13.

Lu, J. et al. ePlace: electrostatics-based placement using fast Fourier transform and Nesterov’s Method. *ACM Trans. Des. Autom. Electron. Syst.* **20**, 17 (2015).

[ADS](#) [Article](#) [Google Scholar](#)

14. 14.

Cheng, C.-K., Kahng, A. B., Kang, I. & Wang, L. RePlAce: advancing solution quality and routability validation in global placement. *IEEE Trans. Comput. Aided Des. Integrated Circ. Syst.* **38**, 1717–1730 (2019).

[Article](#) [Google Scholar](#)

15. 15.

Silver, D. et al. Mastering the game of Go without human knowledge. *Nature* **550**, 354–359 (2017).

[ADS](#) [CAS](#) [Article](#) [Google Scholar](#)

16. 16.

Aslam, B., Amjad, F. & Zou, C. C. Optimal roadside units placement in urban areas for vehicular networks. In *2012 IEEE Symposium on Computers and Communications (ISCC)* 000423–000429 (IEEE, 2012).

17. 17.

Medlock, J. & Galvani, A. P. Optimizing influenza vaccine distribution. *Science* **325**, 1705–1708 (2009).

[ADS](#) [CAS](#) [Article](#) [Google Scholar](#)

18. 18.

Cherniak, C., Mokhtarzada, Z., Rodriguez-Esteban, R. & Changizi, K. Global optimization of cerebral cortex layout. *Proc. Natl Acad. Sci. USA* **101**, 1081–1086 (2004).

[ADS](#) [CAS](#) [Article](#) [Google Scholar](#)

19. 19.

Langford, J. & Zhang, T. The Epoch-Greedy algorithm for multi-armed bandits with side information. In *Advances in Neural Information Processing Systems* Vol. 20, 817–824 (2008).

20. 20.

Usunier, N., Synnaeve, G., Lin, Z. & Chintala, S. Episodic exploration for deep deterministic policies: an application to starcraft micromanagement tasks. In *Proc. International Conference on Learning Representations* (2017).

21. 21.

Bello, I., Pham, H., Le, Q. V., Norouzi, M. & Bengio, S. Neural combinatorial optimization with reinforcement learning. Preprint at <https://arxiv.org/abs/1611.09940> (2016).

22. 22.

Mirhoseini, A. et al. Device placement optimization with reinforcement learning. In *Proc. International Conference on Machine Learning* 2430–2439 (PMLR, 2017).

23. 23.

Mirhoseini, A. et al. A hierarchical model for device placement. In *Proc. International Conference on Learning Representations* (2018).

24. 24.

Schulman, J., Wolski, F., Dhariwal, P., Radford, A. & Klimov, O. Proximal policy optimization algorithms. Preprint at <https://arxiv.org/abs/1707.06347> (2017).

25. 25.

Obermeier, B., Ranke, H. & Johannes, F. M. Kraftwerk: a versatile placement approach. In *Proc. 2005 International Symposium on Physical Design* 242–244 (ACM, 2005).

26. 26.

Spindler, P., Schlichtmann, U. & Johannes, F. M. Kraftwerk2 – a fast force-directed quadratic placement approach using an accurate net model. *IEEE Trans. Comput. Aided Des. Integrated Circ. Syst.* **27**, 1398–1411 (2008).

[Article](#) [Google Scholar](#)

27. 27.

Viswanathan, N. et al. RQL: global placement via relaxed quadratic spreading and linearization. In *Proc. Design Automation Conference* 453–458 (ACM/IEEE, 2007).

28. 28.

Ioffe, S. & Szegedy, C. Batch normalization: accelerating deep network training by reducing internal covariate shift. In *Proc. 32nd International Conference on Machine Learning* 448–456 (JMLR, 2015).

29. 29.

Nair, V. & Hinton, G. E. Rectified linear units improve restricted Boltzmann machines. In *Proc. International Conference on Machine Learning* 807–814 (Omnipress, 2010).

30. 30.

Zaruba, F. & Benini, L. The cost of application-class processing: energy and performance analysis of a Linux-ready 1.7-GHz 64-Bit RISC-V core in 22-nm FDSOI technology. *IEEE Trans. Very Large Scale Integr. VLSI Syst.* **27**, 2629–2640 (2019).

[Article](#) [Google Scholar](#)

31. 31.

RePlAce software – the OpenROAD project <https://github.com/The-OpenROAD-Project/RePlAce> (2020).

32. 32.

Karypis, G. & Kumar, V. Hmetis: a hypergraph partitioning package <http://glaros.dtc.umn.edu/gkhome/metis/hmetis/overview> (1998).

33. 33.

Alpert, C. J., Hagen, L. W. & Kahng, A. B. A hybrid multilevel/genetic approach for circuit partitioning. In *Proc. APCCAS'96 – Asia Pacific Conference on 1012 Circuits and Systems* 298–301 (IEEE, 1996).

34. 34.

Caldwell, A. E., Kahng, A. B. & Markov, I. L. Improved algorithms for hypergraph 1014 bipartitioning. In *Proc. 2000 Design Automation Conference* 661–666 (IEEE, 2000).

35. 35.

Chen, H. et al. An algebraic multigrid solver for analytical placement with layout 1017 based clustering. In *Proc. 40th annual Design Automation Conference* 794–799 (ACM, 2003); 10.1145/775832.776034.

36. 36.

Alpert, C., Kahng, A., Nam, G.-J., Reda, S. & Villarrubia, P. A semi-persistent clustering technique for vlsi circuit placement. In *Proc. 2005 International Symposium on Physical Design*, 200–207 (ACM, 2005).

37. 37.

Fogaça, M., Kahng, A. B., Reis, R. & Wang, L. Finding placement-relevant clusters with fast modularity-based clustering. In *Proc. 24th Asia and South Pacific Design Automation Conference* 569–576 (ACM, 2019); <https://doi.org/10.1145/3287624.3287676>.

38. 38.

Fogaça, M. et al. On the superiority of modularity-based clustering for determining placement-relevant clusters. *Integration* **74**, 32–44 (2020).

[Article](#) [Google Scholar](#)

39. 39.

Kahng, A. B. Futures for partitioning in physical design (tutorial). In *Proc. 1998 International Symposium on Physical Design* 190–193 (ACM, 1998); <https://doi.org/10.1145/274535.274563>.

40. 40.

Shahookar, K. & Mazumder, P. VLSI cell placement techniques. *ACM Comput. Surv.* **23**, 143–220 (1991).

[Article](#) [Google Scholar](#)

41. 41.

Caldwell, A. E., Kahng, A. B., Mantik, S., Markov, I. L. & Zelikovsky, A. On wirelength estimations for row-based placement. *IEEE Trans. Comput. Aided Des. Integrated Circ. Syst.* **18**, 1265–1278 (1999).

[Article](#) [Google Scholar](#)

42. 42.

Kahng, A. B. & Xu, X. Accurate pseudo-constructive wirelength and congestion estimation. In *Proc. 2003 International Workshop on System-Level Interconnect Prediction* 61–68 (ACM, 2003); <https://doi.org/10.1145/639929.639942>.

43. 43.

Kahng, A. B. & Reda, S. A tale of two nets: studies of wirelength progression in physical design. In *Proc. 2006 International Workshop on System-Level Interconnect Prediction* |17–24 (ACM, 2006); <https://doi.org/10.1145/1117278.1117282>.

44. 44.

Kim, M.-C., Viswanathan, N., Alpert, C. J., Markov, I. L. & Ramji, S. MAPLE: Multilevel Adaptive Placement for Mixed-Size Designs. In *Proc. 2012 ACM International Symposium on International Symposium on Physical Design* 193–200 (ACM, 2012).

45. 45.

Nazi, A., Hang, W., Goldie, A., Ravi, S. & Mirhoseini, A. GAP: generalizable approximate graph partitioning framework. In *International Conference on Learning Representations Workshop* (2019).

46. 46.

Zhou, Y. et al. GDP: generalized device placement for dataflow graphs. Preprint at <https://arxiv.org/abs/1910.01578> (2019).

47. 47.

Zhang, M. & Chen, Y. Link prediction based on graph neural networks. In *Proc. International Conference on Neural Information*

Processing 5171–5181 (Curran Associates Inc., 2018).

48. 48.

Xie, Z. et al. RouteNet: routability prediction for mixed-size designs using convolutional neural network. In *2018 IEEE/ACM International Conference on Computer-Aided Design* (ICCAD) 1–8 (IEEE, 2018).

49. 49.

hMETIS – hypergraph and circuit partitioning manual
<http://glaros.dtc.umn.edu/gkhome/metis/hmetis/download>.

50. 50.

Dunlop, A. E. & Kernighan, B. W. A procedure for placement of standard-cell VLSI circuits. *IEEE Trans. Comput. Aided Des. Integrated Circ. Syst.* **4**, 92–98 (1985).

[Article](#) [Google Scholar](#)

51. 51.

Cheng C. K. & Kuh, E. S. Module placement based on resistive network optimization. *IEEE Trans. Comput. Aided Des. Integrated Circ. Syst.* **3**, 218–225 (1984).

[Article](#) [Google Scholar](#)

52. 52.

Tsay, R.-S., Kuh, E. & Hsu, C.-P. Proud: a fast sea-of-gates placement algorithm. In *Proc. Design Automation Conference 1988*, 318–323 (IEEE, 1988).

53. 53.

Agnihotri, A., Ono, S. & Madden, P. Recursive bisection placement: Feng Shui 5.0 implementation details. In *Proc. International*

Symposium on Physical Design 230–232 (ACM, 2005).

54. 54.

Alpert, C. et al. Analytical engines are unnecessary in top-down partitioning based placement. *VLSI Des.* **10**, 99–116 (2002).

[Article](#) [Google Scholar](#)

55. 55.

Kahng, A. B., Reda, S. & Wang, Q. Architecture and details of a high quality, large-scale analytical placer. In *IEEE/ACM International Conference on Computer-Aided Design* 2005 891–898 (IEEE, 2005).

56. 56.

Kahng, A. B. & Wang, Q. An analytic placer for mixed-size placement and timing-driven placement. In *IEEE/ACM International Conference on Computer Aided Design* 2004 565–572 (IEEE, 2004).

57. 57.

Kahng, A. B. & Wang, Q. Implementation and extensibility of an analytic placer. *IEEE Trans. Comput. Aided Des. Integrated Circ. Syst.* **24**, 734–747 (2005).

[Article](#) [Google Scholar](#)

58. 58.

Chen, T.-C., Jiang, Z.-W., Hsu, T.-C., Chen, H.-C. & Chang, Y.-W. A High-quality mixed-size analytical placer considering preplaced blocks and density constraints. In *Proc. 2006 IEEE/ACM International Conference on Computer-Aided Design* 187–192 (ACM, 2006).

59. 59.

Naylor, W., Donelly, R. & Sha, L. Non-linear optimization system and method for wire length and delay optimization for an automatic electric circuit placer. US Patent US6301693B1 (2001).

60. 60.

Chen, T., Jiang, Z., Hsu, T., Chen, H. & Chang, Y. NTUplace3: an analytical placer for large-scale mixed-size designs with preplaced blocks and density constraints. *IEEE Trans. Comput. Aided Des. Integrated Circ. Syst.* **27**, 1228–1240 (2008).

[Article](#) [Google Scholar](#)

61. 61.

Kim, M.-C. & Markov, I. L. ComPLx: a competitive primal-dual Lagrange optimization for global placement. In *Design Automation Conference 2012* 747–755 (ACM, 2012).

62. 62.

Brenner, U., Struzyna, M. & Vygen, J. BonnPlace: placement of leading-edge chips by advanced combinatorial algorithms. *Trans. Comp.-Aided Des. Integ. Cir. Sys.* **27**, 1607–1620 (2008).

[Article](#) [Google Scholar](#)

63. 63.

Lin, T., Chu, C., Shinnerl, J. R., Bustany, I. & Nedelchev, I. POLAR: placement based on novel rough legalization and refinement. In *Proc. International Conference on Computer-Aided Design* 357–362 (IEEE, 2013).

64. 64.

Lu, J. et al. ePlace-MS: electrostatics-based placement for mixed-size circuits. *IEEE Trans. Comput. Aided Des. Integrated Circ. Syst.* **34**, 685–698 (2015).

[Article](#) [Google Scholar](#)

65. 65.

Lu, J., Zhuang, H., Kang, I., Chen, P. & Cheng, C.-K. Eplace-3d: electrostatics based placement for 3d-ics. In *International Symposium on Physical Design* 11–18 (ACM, 2016).

66. 66.

Lin, Y. et al. DREAMPlace: deep learning toolkit-enabled GPU acceleration for modern VLSI placement. In *Design Automation Conference* 1–6 (ACM/IEEE, 2019).

67. 67.

Kahng, A. B. Machine learning applications in physical design: recent results and directions. In *Proc. 2018 International Symposium on Physical Design* 68–73 (ACM, 2018);
<https://doi.org/10.1145/3177540.3177554>.

68. 68.

Kahng, A. B. Reducing time and effort in ic implementation: a roadmap of challenges and solutions. In *Proc. 55th Annual Design Automation Conference* (ACM, 2018);
<https://doi.org/10.1145/3195970.3199854>.

69. 69.

Ajayi, T. et al. Toward an open-source digital flow: first learnings from the openroad project. In *Proc. 56th Annual Design Automation Conference 2019* (ACM, 2019);
<https://doi.org/10.1145/3316781.3326334>.

70. 70.

Huang, Y. et al. Routability-driven macro placement with embedded CNN-based prediction model. In *Design, Automation & Test in Europe*

Conference & Exhibition 180–185 (IEEE, 2019).

71. 71.

Khalil, E., Dai, H., Zhang, Y., Dilkina, B. & Song, L. Learning combinatorial optimization algorithms over graphs. *Adv. Neural Inf. Process Syst.* **30**, 6348–6358 (2017).

[Google Scholar](#)

72. 72.

Zoph, B. & Le, Q. V. Neural architecture search with reinforcement learning. In *Proc. International Conference on Learning Representations* (2017).

73. 73.

Addanki, R., Venkatakrishnan, S. B., Gupta, S., Mao, H. & Alizadeh, M. Learning generalizable device placement algorithms for distributed machine learning. *Adv. Neural Inf. Process Syst.* **32**, 3981–3991 (2019).

[Google Scholar](#)

74. 74.

Paliwal, A. et al. Reinforced genetic algorithm learning for optimizing computation graphs. In *Proc. International Conference on Learning Representations* (2020).

75. 75.

Zhou, Y. et al. Transferable graph optimizers for ML compilers. Preprint at <https://arxiv.org/abs/2010.12438> (2021).

76. 76.

Barrett, T. D., Clements, W. R., Foerster, J. N. & Lvovsky, A. I.
Exploratory combinatorial optimization with reinforcement learning.
Preprint at <https://arxiv.org/abs/1909.04063> (2020).

77. 77.

Kipf, T. N. & Welling, M. Semi-supervised classification with graph convolutional networks. Preprint at <https://arxiv.org/abs/1609.02907> (2016).

[Download references](#)

Acknowledgements

This project was a collaboration between Google Brain and the Google Chip Implementation and Infrastructure (CI2) Team. We thank M. Bellemare, C. Young, E. Chi, C. Stratakos, S. Roy, A. Yazdanbakhsh, N. Myung-Chul Kim, S. Agarwal, B. Li, S. Bae, A. Babu, M. Abadi, A. Salek, S. Bengio and D. Patterson for their help and support.

Author information

Author notes

1. These authors contributed equally: Azalia Mirhoseini, Anna Goldie

Affiliations

1. Google Research, Brain Team, Google, Mountain View, CA, USA

Azalia Mirhoseini, Anna Goldie, Joe Wenjie Jiang, Ebrahim Songhori, Shen Wang, Eric Johnson, Azade Nazi, Quoc V. Le, James Laudon & Jeff Dean

2. Google Chip Implementation and Infrastructure (CI2) Team, Google, Sunnyvale, CA, USA

Mustafa Yazgan, Young-Joon Lee, Omkar Pathak, Jiwoo Pak, Andy Tong, Kavya Srinivasa, Emre Tuncer, Richard Ho & Roger Carpenter

3. Computer Science Department, Stanford University, Stanford, CA, USA

Anna Goldie & William Hang

Authors

1. Azalia Mirhoseini

[View author publications](#)

You can also search for this author in [PubMed](#) [Google Scholar](#)

2. Anna Goldie

[View author publications](#)

You can also search for this author in [PubMed](#) [Google Scholar](#)

3. Mustafa Yazgan

[View author publications](#)

You can also search for this author in [PubMed](#) [Google Scholar](#)

4. Joe Wenjie Jiang

[View author publications](#)

You can also search for this author in [PubMed](#) [Google Scholar](#)

5. Ebrahim Songhori

[View author publications](#)

You can also search for this author in [PubMed](#) [Google Scholar](#)

6. Shen Wang

[View author publications](#)

You can also search for this author in [PubMed](#) [Google Scholar](#)

7. Young-Joon Lee

[View author publications](#)

You can also search for this author in [PubMed](#) [Google Scholar](#)

8. Eric Johnson

[View author publications](#)

You can also search for this author in [PubMed](#) [Google Scholar](#)

9. Omkar Pathak

[View author publications](#)

You can also search for this author in [PubMed](#) [Google Scholar](#)

10. Azade Nazi

[View author publications](#)

You can also search for this author in [PubMed](#) [Google Scholar](#)

11. Jiwoo Pak

[View author publications](#)

You can also search for this author in [PubMed](#) [Google Scholar](#)

12. Andy Tong

[View author publications](#)

You can also search for this author in [PubMed](#) [Google Scholar](#)

13. Kavya Srinivasa

[View author publications](#)

You can also search for this author in [PubMed](#) [Google Scholar](#)

14. William Hang

[View author publications](#)

You can also search for this author in [PubMed](#) [Google Scholar](#)

15. Emre Tuncer

[View author publications](#)

You can also search for this author in [PubMed](#) [Google Scholar](#)

16. Quoc V. Le

[View author publications](#)

You can also search for this author in [PubMed](#) [Google Scholar](#)

17. James Laudon

[View author publications](#)

You can also search for this author in [PubMed](#) [Google Scholar](#)

18. Richard Ho

[View author publications](#)

You can also search for this author in [PubMed](#) [Google Scholar](#)

19. Roger Carpenter

[View author publications](#)

You can also search for this author in [PubMed](#) [Google Scholar](#)

20. Jeff Dean

[View author publications](#)

You can also search for this author in [PubMed](#) [Google Scholar](#)

Contributions

A.G. and A.M. are co-first authors and the order of the names was determined by coin flip. M.Y., J.W.J., E.S., S.W. and Y.-J.L. were major contributors to this work. The following authors contributed to the overall evaluation and provided insights on physical design: E.J., O.P., A.N., J.P., A.T., K.S., W.H. and E.T. The following authors managed and advised on the project: Q.V.L., J.L., R.H., R.C. and J.D.

Corresponding authors

Correspondence to [Azalia Mirhoseini](#) or [Anna Goldie](#).

Ethics declarations

Competing interests

The following US patents are related to this work: ‘Generating integrated circuit floorplans using neural networks’ (granted as US10699043) and ‘Domain adaptive reinforcement learning approach to macro placement’ (filed).

Additional information

Peer review information *Nature* thanks Jakob Foerster and the other, anonymous, reviewer(s) for their contribution to the peer review of this work.

Publisher’s note Springer Nature remains neutral with regard to jurisdictional claims in published maps and institutional affiliations.

Extended data figures and tables

[Extended Data Fig. 1 Evaluation workflow for producing the results in Table 1.](#)

We allow each method access to the same clustered netlist hypergraph. We use the same hyperparameters (to the extent possible) in all the methods. Once the placement is completed by each method (this includes the legalization step for RePlAce), we snap the macros to the power grids, freeze the macro locations and use a commercial EDA tool to place the standard cells and report the final results.

Extended Data Fig. 2 Zero-shot performance of Edge-GNN versus GCN (graph convolutional neural network)⁷⁷.

The agent with an Edge-GNN architecture is more robust to over-fitting and yields higher-quality results, as measured by average zero-shot performance on the test blocks shown in Extended Data Fig. 1.

Extended Data Fig. 3 Generalization performance as a function of pre-training dataset size.

We pre-train the policy network on three different training datasets (the small dataset with 2 blocks is a subset of the medium one with 5 blocks, and the medium dataset is a subset of the large one with 20 blocks). For each policy, at various snapshots during pre-training we report its inference performance on an unseen test block. As the dataset size increases, both the quality of generated placements on the test block and the generalization performance of the policy improve. The policy trained on the largest dataset is most robust to over-fitting.

Extended Data Fig. 4 Visualization of Ariane placements.

Left, zero-shot placements from the pre-trained policy; right, placements from the fine-tuned policy. The zero-shot placements are generated at inference time on a previously unseen chip. The pre-trained policy network (with no fine-tuning) reserves a convex hull in the centre of the canvas in which standard cells can be placed, a behaviour that reduces wirelength and that emerges only after many hours of fine-tuning in the policy trained from scratch.

Extended Data Fig. 5 Visualization of a real TPU chip.

Human expert placements are shown on the left and results from our approach are shown on the right. The white area represents macros and the green area represents standard cells. The figures are intentionally blurred because the designs are proprietary. The wirelength for the human expert design is 57.07 m, whereas ours is 55.42 m. Furthermore, our method

achieves these results in 6 h, whereas the manual baseline took several weeks.

Extended Data Table 1 Hyperparameters used for fine-tuning the RL agent

[Full size table](#)

Extended Data Table 2 Hyperparameters used for the FD algorithm that places standard cell clusters

[Full size table](#)

Extended Data Table 3 Hyperparameters used to generate standard cell clusters with hMETIS³²

[Full size table](#)

Extended Data Table 4 Effect of different cost trade-offs on the post-PlaceOpt performance of Block 1 in Table 1

[Full size table](#)

Extended Data Table 5 Sensitivity of results to the choice of random seed, as measured on a Ariane RISC-V block

[Full size table](#)

Extended Data Table 6 Performance of our method compared to SA

[Full size table](#)

Rights and permissions

[Reprints and Permissions](#)

About this article



Check for
updates

Cite this article

Mirhoseini, A., Goldie, A., Yazgan, M. *et al.* A graph placement methodology for fast chip design. *Nature* **594**, 207–212 (2021).

<https://doi.org/10.1038/s41586-021-03544-w>

[Download citation](#)

- Received: 03 November 2020
- Accepted: 13 April 2021
- Published: 09 June 2021
- Issue Date: 10 June 2021
- DOI: <https://doi.org/10.1038/s41586-021-03544-w>

Further reading

- [AI system outperforms humans in designing floorplans for microchips](#)
 - Andrew B. Kahng

Nature (2021)

Comments

By submitting a comment you agree to abide by our [Terms](#) and [Community Guidelines](#). If you find something abusive or that does not comply with our terms or guidelines please flag it as inappropriate.

[Access through your institution](#)

[Change institution](#)

[Buy or subscribe](#)

Associated Content

AI system outperforms humans in designing floorplans for microchips

- Andrew B. Kahng

Nature News & Views 09 Jun 2021

Advertisement

This article was downloaded by **calibre** from <https://www.nature.com/articles/s41586-021-03544-w>

| [Section menu](#) | [Main menu](#) |

- Article
- [Published: 09 June 2021](#)

Tomographic reconstruction of oxygen orbitals in lithium-rich battery materials

- [Hasnain Hafiz](#) [ORCID: orcid.org/0000-0002-0202-794X](#)¹ nAff10,
- [Kosuke Suzuki](#) [ORCID: orcid.org/0000-0003-1711-0604](#)²,
- [Bernardo Barbiellini](#)^{3,4},
- [Naruki Tsuji](#)⁵,
- [Naoaki Yabuuchi](#) [ORCID: orcid.org/0000-0002-9404-5693](#)⁶,
- [Kentaro Yamamoto](#) [ORCID: orcid.org/0000-0002-8739-4246](#)⁷,
- [Yuki Orikasa](#) [ORCID: orcid.org/0000-0002-9869-9520](#)⁸,
- [Yoshiharu Uchimoto](#) [ORCID: orcid.org/0000-0002-1491-2647](#)⁷,
- [Yoshiharu Sakurai](#) [ORCID: orcid.org/0000-0001-7152-3261](#)⁵,
- [Hiroshi Sakurai](#)²,
- [Arun Bansil](#) ⁴ &
- [Venkatasubramanian Viswanathan](#) [ORCID: orcid.org/0000-0003-1060-5495](#)^{1,9}

[Nature](#) volume **594**, pages 213–216 (2021) [Cite this article](#)

- 2417 Accesses
- 91 Altmetric
- [Metrics details](#)

Subjects

- [Batteries](#)
- [Electronic properties and materials](#)

Abstract

The electrification of heavy-duty transport and aviation will require new strategies to increase the energy density of electrode materials^{1,2}. The use of anionic redox represents one possible approach to meeting this ambitious target. However, questions remain regarding the validity of the O²⁻/O⁻ oxygen redox paradigm, and alternative explanations for the origin of the anionic capacity have been proposed³, because the electronic orbitals associated with redox reactions cannot be measured by standard experiments. Here, using high-energy X-ray Compton measurements together with first-principles modelling, we show how the electronic orbital that lies at the heart of the reversible and stable anionic redox activity can be imaged and visualized, and its character and symmetry determined. We find that differential changes in the Compton profile with lithium-ion concentration are sensitive to the phase of the electronic wave function, and carry signatures of electrostatic and covalent bonding effects⁴. Our study not only provides a picture of the workings of a lithium-rich battery at the atomic scale, but also suggests pathways to improving existing battery materials and designing new ones.

Access options

Subscribe to Journal

Get full journal access for 1 year

\$199.00

only \$3.90 per issue

[Subscribe](#)

All prices are NET prices.
VAT will be added later in the checkout.
Tax calculation will be finalised during checkout.

Rent or Buy article

Get time limited or full article access on ReadCube.

from \$8.99

[Rent or Buy](#)

All prices are NET prices.

Additional access options:

- [Log in](#)
- [Access through your institution](#)
- [Learn about institutional subscriptions](#)

Fig. 1: Compton profile difference (CPD or ΔJ) of LTMO for lithium concentrations of $x = 0.8$ minus $x = 0.4$.



Fig. 2: PDOS of $\text{Li}_{0.4}\text{Ti}_{0.4}\text{Mn}_{0.4}\text{O}_2$ for the majority-spin electrons near the Fermi level.

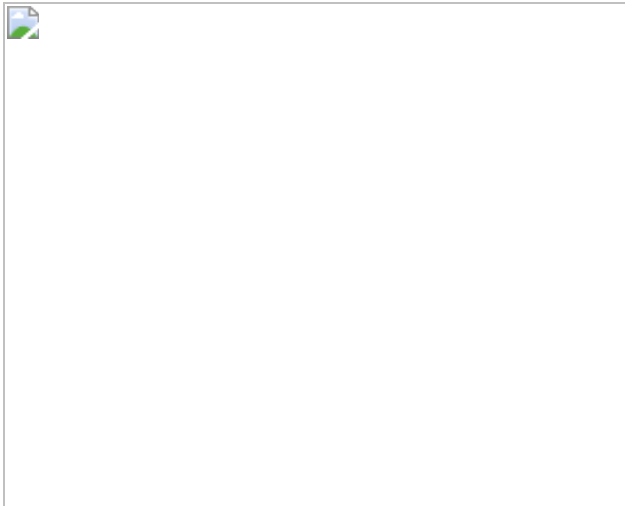
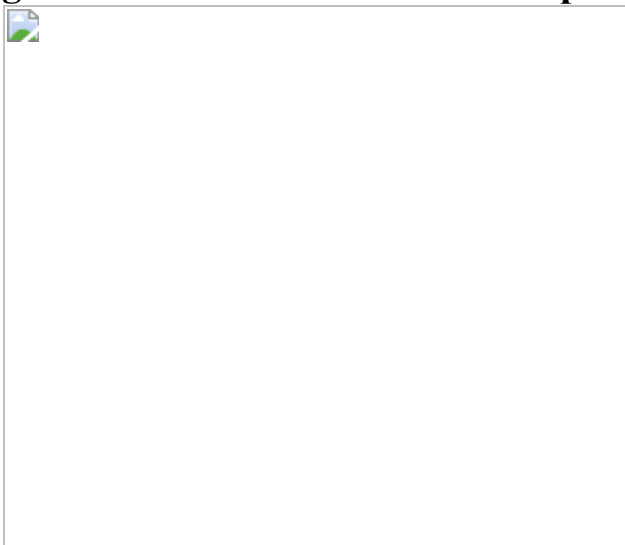


Fig. 3: Reconstructed 2D-EMD maps.



Data availability

The experimental data and theoretical simulations that support the findings of this study are available from the corresponding authors upon reasonable request.

References

1. 1.

Sripad, S. & Viswanathan, V. Performance metrics required of next-generation batteries to make a practical electric semi-truck. *ACS Energy Lett.* **2**, 1669–1673 (2017).

[CAS](#) [Google Scholar](#)

2. 2.

Viswanathan, V. & Knapp, B. M. Potential for electric aircraft. *Nat. Sustainability* **2**, 88–89 (2019).

[Google Scholar](#)

3. 3.

Radin, M. D., Vinckeviciute, J., Seshadri, R. & Van der Ven, A. Manganese oxidation as the origin of the anomalous capacity of Mn-containing Li-excess cathode materials. *Nat. Energy* **4**, 639–646 (2019).

[ADS](#) [CAS](#) [Google Scholar](#)

4. 4.

Suzuki, K. et al. Extracting the redox orbitals in Li battery materials with high-resolution x-ray Compton scattering spectroscopy. *Phys. Rev. Lett.* **114**, 087401 (2015).

[ADS](#) [CAS](#) [PubMed](#) [Google Scholar](#)

5. 5.

Krauskopf, T., Richter, F. H., Zeier, W. G. & Janek, J. Physicochemical concepts of the lithium metal anode in solid-state batteries. *Chem. Rev.* **120**, 7745–7794 (2020).

[CAS](#) [PubMed](#) [Google Scholar](#)

6. 6.

Salah, M. et al. Pure silicon thin-film anodes for lithium-ion batteries: a review. *J. Power Sources* **414**, 48–67 (2019).

[ADS](#) [CAS](#) [Google Scholar](#)

7. 7.

Jia, H. et al. Hierarchical porous silicon structures with extraordinary mechanical strength as high-performance lithium-ion battery anodes. *Nat. Commun.* **11**, 1474 (2020).

[ADS](#) [CAS](#) [PubMed](#) [PubMed Central](#) [Google Scholar](#)

8. 8.

Yabuuchi, N. et al. High-capacity electrode materials for rechargeable lithium batteries: Li₃NbO₄-based system with cation-disordered rocksalt structure. *Proc. Natl Acad. Sci. USA* **112**, 7650–7655 (2015).

[ADS](#) [CAS](#) [PubMed](#) [Google Scholar](#)

9. 9.

Seo, D.-H. et al. The structural and chemical origin of the oxygen redox activity in layered and cation-disordered Li-excess cathode materials. *Nat. Chem.* **8**, 692–697 (2016).

[CAS](#) [PubMed](#) [Google Scholar](#)

10. 10.

Yabuuchi, N. et al. Origin of stabilization and destabilization in solid-state redox reaction of oxide ions for lithium-ion batteries. *Nat. Commun.* **7**, 13814 (2016).

[ADS](#) [CAS](#) [PubMed](#) [PubMed Central](#) [Google Scholar](#)

11. 11.

Li, B. & Xia, D. Anionic redox in rechargeable lithium batteries. *Adv. Mater.* **29**, 1701054 (2017).

[Google Scholar](#)

12. 12.

Okubo, M. & Yamada, A. Molecular orbital principles of oxygen-redox battery electrodes. *ACS Appl. Mater. Interfaces* **9**, 36463–36472 (2017).

[CAS](#) [PubMed](#) [Google Scholar](#)

13. 13.

Assat, G. & Tarascon, J.-M. Fundamental understanding and practical challenges of anionic redox activity in Li-ion batteries. *Nat. Energy* **3**, 373–386 (2018).

[ADS](#) [CAS](#) [Google Scholar](#)

14. 14.

Clément, R., Lun, Z. & Ceder, G. Cation-disordered rocksalt transition metal oxides and oxyfluorides for high energy lithium-ion cathodes. *Energy Environ. Sci.* **13**, 345–373 (2020).

[Google Scholar](#)

15. 15.

Naylor, A. J. et al. Depth-dependent oxygen redox activity in lithium-rich layered oxide cathodes. *J. Mater. Chem. A Mater. Energy Sustain.* **7**, 25355–25368 (2019).

[CAS](#) [Google Scholar](#)

16. 16.

Li, M. et al. Cationic and anionic redox in lithium-ion based batteries. *Chem. Soc. Rev.* **49**, 1688–1705 (2020).

[CAS](#) [PubMed](#) [Google Scholar](#)

17. 17.

Xu, J. et al. Elucidating anionic oxygen activity in lithium-rich layered oxides. *Nat. Commun.* **9**, 947 (2018).

[ADS](#) [PubMed](#) [PubMed Central](#) [Google Scholar](#)

18. 18.

Mukai, K., Nonaka, T., Uyama, T. & Nishimura, Y. F. In situ X-ray Raman spectroscopy and magnetic susceptibility study on Li [Li_{0.15}Mn_{1.85}] O₄ oxygen anion redox reaction. *Chem. Commun.* **56**, 1701–1704 (2020).

[CAS](#) [Google Scholar](#)

19. 19.

Hong, J. et al. Metal–oxygen decoordination stabilizes anion redox in Li-rich oxides. *Nat. Mater.* **18**, 256–265 (2019).

[ADS](#) [CAS](#) [PubMed](#) [Google Scholar](#)

20. 20.

Tygesen, A. S., Chang, J. H., Vegge, T. & García-Lastra, J. M. Computational framework for a systematic investigation of anionic redox process in Li-rich compounds. *npj Comp. Mater.* **6**, 65 (2020).

[CAS](#) [Google Scholar](#)

21. 21.

Bhowmik, A. et al. A perspective on inverse design of battery interphases using multi-scale modelling, experiments and generative deep learning. *Energy Storage Materials* **21**, 446–456 (2019).

[Google Scholar](#)

22. 22.

Barbiellini, B. et al. Identifying a descriptor for *d*-orbital delocalization in cathodes of Li batteries based on x-ray Compton scattering. *Appl. Phys. Lett.* **109**, 073102 (2016).

[ADS](#) [Google Scholar](#)

23. 23.

Suzuki, K. et al. Non-destructive measurement of *in-operando* lithium concentration in batteries via X-ray Compton scattering. *J. Appl. Phys.* **119**, 025103 (2016).

[ADS](#) [Google Scholar](#)

24. 24.

Suzuki, K. et al. *In operando* quantitation of Li concentration for a commercial Li-ion rechargeable battery using high-energy X-ray Compton scattering. *J. Synchrotron Radiat.* **24**, 1006–1011 (2017).

[CAS](#) [PubMed](#) [Google Scholar](#)

25. 25.

Suzuki, K. et al. Dependency of the charge–discharge rate on lithium reaction distributions for a commercial lithium coin cell visualized by Compton scattering imaging. *Condensed Matter* **3**, 27 (2018).

[CAS](#) [Google Scholar](#)

26. 26.

Suzuki, K. et al. High-energy X-ray Compton scattering imaging of 18650-type lithium-ion battery cell. *Condensed Matter* **4**, 66 (2019).

[CAS](#) [Google Scholar](#)

27. 27.

Kaplan, I., Barbiellini, B. & Bansil, A. Compton scattering beyond the impulse approximation. *Phys. Rev. B* **68**, 235104 (2003).

[ADS](#) [Google Scholar](#)

28. 28.

Hafiz, H. et al. Visualizing redox orbitals and their potentials in advanced lithium-ion battery materials using high-resolution X-ray Compton scattering. *Sci. Adv.* **3**, e1700971 (2017).

[ADS](#) [PubMed](#) [PubMed Central](#) [Google Scholar](#)

29. 29.

Hafiz, H. et al. Identification of ferrimagnetic orbitals preventing spinel degradation by charge ordering in $\text{Li}_x\text{Mn}_2\text{O}_4$. *Phys. Rev. B* **100**, 205104 (2019).

[ADS](#) [CAS](#) [Google Scholar](#)

30. 30.

Sakurai, Y. et al. Imaging doped holes in a cuprate superconductor with high-resolution Compton scattering. *Science* **332**, 698–702 (2011).

[ADS](#) [CAS](#) [PubMed](#) [Google Scholar](#)

31. 31.

Schwarz, W. E. Measuring orbitals: provocation or reality? *Angew. Chem. Int. Edn* **45**, 1508–1517 (2006).

[CAS](#) [Google Scholar](#)

32. 32.

Cooper, M. et al. *X-ray Compton Scattering* (Oxford Univ. Press, 2004).

33. 33.

Isaacs, E. et al. Covalency of the hydrogen bond in ice: a direct x-ray measurement. *Phys. Rev. Lett.* **82**, 600 (1999).

[ADS](#) [CAS](#) [Google Scholar](#)

34. 34.

Eijt, S. W. H. et al. Electronic coupling of colloidal CdSe nanocrystals monitored by thin-film positron-electron momentum density methods. *Appl. Phys. Lett.* **94**, 091908 (2009).

[ADS](#) [Google Scholar](#)

35. 35.

Hoffmann, L., Shukla, A., Peter, M., Barbiellini, B. & Manuel, A. Linear and non-linear approaches to solve the inverse problem: applications to positron annihilation experiments. *Nucl. Instrum. Methods Phys. Res. A* **335**, 276–287 (1993).

[ADS](#) [CAS](#) [Google Scholar](#)

36. 36.

Hiraoka, N. et al. A new x-ray spectrometer for high-resolution Compton profile measurements at Spring-8. *J. Synchrotron Radiat.* **8**, 26–32 (2001).

[ADS](#) [CAS](#) [PubMed](#) [Google Scholar](#)

37. 37.

Itou, M. et al. Present status of the Cauchois-type Compton scattering spectrometer at Spring8. *Nucl. Instrum. Methods Phys. Res. A* **467–468**, 1109–1112 (2001).

[ADS](#) [Google Scholar](#)

38. 38.

Sakurai, Y. & Itou, M. A Cauchois-type X-ray spectrometer for momentum density studies on heavy-element materials. *J. Phys. Chem. Solids* **65**, 2061–2064 (2004).

[ADS](#) [CAS](#) [Google Scholar](#)

39. 39.

Kresse, G. & Joubert, D. From ultrasoft pseudopotentials to the projector augmented-wave method. *Phys. Rev. B* **59**, 1758–1775 (1999).

[ADS](#) [CAS](#) [Google Scholar](#)

40. 40.

Kresse, G. & Furthmuller, J. Efficiency of ab-initio total energy calculations for metals and semiconductors using a plane-wave basis set. *Comput. Mater. Sci.* **6**, 15–50 (1996).

[CAS](#) [Google Scholar](#)

41. 41.

Kresse, G. & Furthmuller, J. Efficient iterative schemes for ab initio total-energy calculations using a plane-wave basis set. *Phys. Rev. B* **54**, 11169–11186 (1996).

[ADS](#) [CAS](#) [Google Scholar](#)

42. 42.

Perdew, J. P., Burke, K. & Ernzerhof, M. Generalized gradient approximation made simple. *Phys. Rev. Lett.* **77**, 3865–3868 (1996).

[ADS](#) [CAS](#) [PubMed](#) [Google Scholar](#)

43. 43.

Sun, J., Ruzsinszky, A. & Perdew, J. P. Strongly constrained and appropriately normed semilocal density functional. *Phys. Rev. Lett.* **115**, 036402 (2015).

[ADS](#) [PubMed](#) [Google Scholar](#)

44. 44.

van de Walle, A. et al. Efficient stochastic generation of special quasirandom structures. *Calphad* **42**, 13–18 (2013).

[Google Scholar](#)

45. 45.

van de Walle, A., Asta, M. & Ceder, G. The alloy theoretic automated toolkit: a user guide. *Calphad* **26**, 539–553 (2002).

[Google Scholar](#)

46. 46.

Makkonen, I., Hakala, M. & Puska, M. Calculation of valence electron momentum densities using the projector augmented-wave method. *J. Phys. Chem. Solids* **66**, 1128–1135 (2005).

[ADS](#) [CAS](#) [Google Scholar](#)

47. 47.

Duncanson, W. E. & Coulson, C. A. Theoretical shape of the Compton profile for atoms from H to Ne. *Proc. Phys. Soc.* **57**, 190 (1945).

[ADS](#) [CAS](#) [Google Scholar](#)

48. 48.

Biggs, F., Mendelsohn, L. B. & Mann, J. B. Hartree-Fock Compton profiles for the elements. *Atomic Data Nucl. Data Tables* **16**, 201–309 (1975).

[ADS](#) [CAS](#) [Google Scholar](#)

49. 49.

Kaijser, P. & Smith, V. H. Jr Evaluation of momentum distributions and Compton profiles for atomic and molecular systems. *Adv. Quantum Chem.* **10**, 37–76 (1977).

[ADS](#) [CAS](#) [Google Scholar](#)

50. 50.

Weyrich, W., Pattison, P. & Williams, B. G. Fourier analysis of the Compton profile: atoms and molecules. *Chem. Phys.* **41**, 271–284 (1979).

[CAS](#) [Google Scholar](#)

51. 51.

Yu, M. & Trinkle, D. R. Accurate and efficient algorithm for Bader charge integration. *J. Chem. Phys.* **134**, 064111 (2011).

[ADS](#) [PubMed](#) [Google Scholar](#)

52. 52.

Maintz, S., Deringer, V. L., Tchougreeff, A. L., Dronskowsk, R. & Dronskowsk, R. LOBSTER: a tool to extract chemical bonding from plane-wave based DFT. *J. Comput. Chem.* **37**, 1030–1035 (2016).

[CAS](#) [PubMed](#) [PubMed Central](#) [Google Scholar](#)

[Download references](#)

Acknowledgements

We thank M. Radin for providing feedback on the manuscript; A. Terasaka (Gunma University) for technical support with the Compton scattering experiment; and M. Nakayama (Nagoya Institute of Technology) for sharing insights into COOP analysis. K.S. was supported by Japan Society for the Promotion of Science (JSPS) KAKENHI grants JP15K17873 and JP19K05519. Compton scattering experiments were performed with the approval of the Japan Synchrotron Radiation Research Institute (JASRI; proposals 2017A1122 and 2019B1668). The work at Northeastern University was supported by US Department of Energy (DOE), Office of Science, Basic Energy Sciences grant DE-FG02-07ER46352; and benefited from Northeastern University's Advanced Scientific Computation Center (ASCC), and the allocation of time at the National Energy Research Scientific Computing Center (NERSC)'s supercomputing center through DOE grant DE-AC02-05CH11231. The work at Carnegie Mellon University was supported by the Assistant Secretary for Energy Efficiency and Renewable Energy, Office of Vehicle Technologies of the US DOE through the Advanced Battery Materials Research (BMR) program under contract no. DE-EE0007810.

Author information

Author notes

1. Hasnain Hafiz

Present address: Theoretical Division, Los Alamos National Laboratory, Los Alamos, NM, USA

Affiliations

1. Department of Mechanical Engineering, Carnegie Mellon University, Pittsburgh, PA, USA

Hasnain Hafiz & Venkatasubramanian Viswanathan

2. Faculty of Science and Technology, Gunma University, Kiryu, Gunma, Japan

Kosuke Suzuki & Hiroshi Sakurai

3. Department of Physics, School of Engineering Science, LUT University, Lappeenranta, Finland

Bernardo Barbiellini

4. Department of Physics, Northeastern University, Boston, MA, USA

Bernardo Barbiellini & Arun Bansil

5. Japan Synchrotron Radiation Research Institute (JASRI), Sayo, Hyogo, Japan

Naruki Tsuji & Yoshiharu Sakurai

6. Department of Chemistry and Life Science, Yokohama National University, Yokohama, Kanagawa, Japan

Naoaki Yabuuchi

7. Graduate School of Human and Environmental Studies, Kyoto University, Sakyo-ku, Kyoto, Japan

Kentaro Yamamoto & Yoshiharu Uchimoto

8. Department of Applied Chemistry, Ritsumeikan University, Kusatsu, Shiga, Japan

Yuki Orikasa

9. Department of Physics, Carnegie Mellon University, Pittsburgh, PA, USA

Venkatasubramanian Viswanathan

Authors

1. Hasnain Hafiz

[View author publications](#)

You can also search for this author in [PubMed](#) [Google Scholar](#)

2. Kosuke Suzuki

[View author publications](#)

You can also search for this author in [PubMed](#) [Google Scholar](#)

3. Bernardo Barbiellini

[View author publications](#)

You can also search for this author in [PubMed](#) [Google Scholar](#)

4. Naruki Tsuji

[View author publications](#)

You can also search for this author in [PubMed](#) [Google Scholar](#)

5. Naoaki Yabuuchi

[View author publications](#)

You can also search for this author in [PubMed](#) [Google Scholar](#)

6. Kentaro Yamamoto

[View author publications](#)

You can also search for this author in [PubMed](#) [Google Scholar](#)

7. Yuki Orikasa

[View author publications](#)

You can also search for this author in [PubMed](#) [Google Scholar](#)

8. Yoshiharu Uchimoto

[View author publications](#)

You can also search for this author in [PubMed](#) [Google Scholar](#)

9. Yoshiharu Sakurai

[View author publications](#)

You can also search for this author in [PubMed](#) [Google Scholar](#)

10. Hiroshi Sakurai

[View author publications](#)

You can also search for this author in [PubMed](#) [Google Scholar](#)

11. Arun Bansil

[View author publications](#)

You can also search for this author in [PubMed](#) [Google Scholar](#)

12. Venkatasubramanian Viswanathan

[View author publications](#)

You can also search for this author in [PubMed](#) [Google Scholar](#)

Contributions

H.H. performed all of the theoretical simulations and analysed the data. K.S., H.S., N.T and Y.S. performed the X-ray Compton scattering experiment and data analyses. N.Y., K.Y., Y.O. and Y.U. synthesized and characterized the materials. H.H. and B.B. wrote the manuscript. V.V. and A.B. contributed to the theory and oversaw the research and writing of the manuscript. All authors were involved in revising the manuscript.

Corresponding authors

Correspondence to [Hasnain Hafiz](#) or [Arun Bansil](#) or [Venkatasubramanian Viswanathan](#).

Ethics declarations

Competing interests

The authors declare no competing interests.

Additional information

Peer review information *Nature* thanks B. L. Ahuja, Stephen Dugdale and the other, anonymous, reviewer(s) for their contribution to the peer review of this work.

Publisher's note Springer Nature remains neutral with regard to jurisdictional claims in published maps and institutional affiliations.

Extended data figures and tables

[Extended Data Fig. 1 Experimental valence Compton profiles of \$\text{Li}_x\text{Ti}_{0.4}\text{Mn}_{0.4}\text{O}_2\$ with different lithium concentrations.](#)

Lithium concentrations ranged from $x = 0$ to $x = 1.2$.

[Extended Data Fig. 2 Comparison of experimental CPDs in LTMO with theoretical models and fits.](#)

CPDs are denoted as ΔJ . The blue line shows the result of linear combination of atomic oxygen $2p$ orbitals; the cyan line represents the atomic lithium $2s$ orbitals; and the yellow line shows a model Coulomb repulsion profile for manganese $3d$ orbitals (see text). The experimental CPD is the difference in the Compton profiles for lithium concentrations of

$x = 0.8$ minus $x = 0.4$. The model Coulomb repulsion profile was obtained analytically to take into account the effects of localization of the atomic manganese $3d$ orbitals using normalized Slater-type orbitals. The inset shows manganese $3d$ Compton profiles for two different effective values of Z_{eff} . The fitting curve (red) and ΔJ are both normalized to one. The experimental error bars were obtained from a statistical analysis of the curves in Extended Data Fig. 1 and have a total length of 2σ .

Extended Data Fig. 3 Spin-dependent PDOS associated with manganese e_g , manganese t_{2g} and oxygen p orbitals in $\text{Li}_x\text{Ti}_{0.4}\text{Mn}_{0.4}\text{O}_2$ for lithium concentrations of $x = 0.4$ and $x = 0.8$.

a, $x = 0.4$. **b**, $x = 0.8$. The vertical dashed lines mark the Fermi energy (E_F). Up and down arrows indicate the contributions of spin-up and spin-down, respectively, to the PDOS.

Extended Data Fig. 4 COOP analysis between oxygen $2p$ and manganese $3d$ states for a lithium concentration of $x = 0.4$.

The vertical dashed line marks the Fermi energy (E_F). COOP analysis indicates an antibonding character (green shaded area) for localized oxygen $2p$ states right above the Fermi level, as shown in the PDOS in Fig. 2 and Extended Data Fig. 3a. Here, localized oxygen $2p$ holes point in the direction of a lithium-atom vacancy along the direction of the Li–O–Li axis.

Extended Data Fig. 5 Fourier transform, $B(r)$, of the CPD.

The reciprocal form factor $B(r)$ was computed for the CPD (black solid line), the fitted curve (red line) and the Coulomb profile (yellow line) shown in Extended Data Fig. 2. The $B(r)$ for experimental Coulomb profile (black dashed line) was obtained by subtracting the $B(r)$ of atomic oxygen $2p$ (blue line) from the experimental $B(r)$ (black solid line). Agreement between the fitted $B(r)$ (red line) and the experimental $B(r)$ (black solid line) was used to assess the goodness of fit of Extended Data Fig. 2.

Rights and permissions

[Reprints and Permissions](#)

About this article



Check for
updates

Cite this article

Hafiz, H., Suzuki, K., Barbiellini, B. *et al.* Tomographic reconstruction of oxygen orbitals in lithium-rich battery materials. *Nature* **594**, 213–216 (2021). <https://doi.org/10.1038/s41586-021-03509-z>

[Download citation](#)

- Received: 07 September 2020
- Accepted: 31 March 2021
- Published: 09 June 2021
- Issue Date: 10 June 2021
- DOI: <https://doi.org/10.1038/s41586-021-03509-z>

Comments

By submitting a comment you agree to abide by our [Terms](#) and [Community Guidelines](#). If you find something abusive or that does not comply with our terms or guidelines please flag it as inappropriate.

[Access through your institution](#)

[Change institution](#)

[Buy or subscribe](#)

Advertisement

This article was downloaded by **calibre** from <https://www.nature.com/articles/s41586-021-03509-z>

| [Section menu](#) | [Main menu](#) |

- Article
- [Published: 28 April 2021](#)

Phosphorus-mediated sp^2 – sp^3 couplings for C–H fluoroalkylation of azines

- [Xuan Zhang](#) [ORCID: orcid.org/0000-0002-7679-7963](#)¹ na1,
- [Kyle G. Nottingham](#)¹ na1,
- [Chirag Patel](#)¹,
- [Juan V. Alegre-Requena](#)¹,
- [Jeffrey N. Levy](#)¹,
- [Robert S. Paton](#) [ORCID: orcid.org/0000-0002-0104-4166](#)¹ &
- [Andrew McNally](#) [ORCID: orcid.org/0000-0002-8651-1631](#)¹

[Nature](#) volume **594**, pages 217–222 (2021) [Cite this article](#)

- 9540 Accesses
- 5 Altmetric
- [Metrics details](#)

Subjects

- [Synthetic chemistry methodology](#)

Abstract

Fluoroalkyl groups profoundly affect the physical properties of pharmaceuticals and influence almost all metrics associated with their pharmacokinetic and pharmacodynamic profile^{1,2,3,4}. Drug candidates increasingly contain trifluoromethyl (CF_3) and difluoromethyl (CF_2H) groups, and the same trend in agrochemical development shows that the effect of fluoroalkylation translates across human, insect and plant life^{5,6}. New fluoroalkylation reactions have undoubtedly stimulated this shift; however, methods that directly convert C–H bonds into C– CF_2X groups (where X is F or H) in complex drug-like molecules are rare^{7,8,9,10,11,12,13}. Pyridines are the most common aromatic heterocycles in pharmaceuticals¹⁴, but only one approach—via fluoroalkyl radicals—is viable for achieving pyridyl C–H fluoroalkylation in the elaborate structures encountered during drug development^{15,16,17}. Here we develop a set of bench-stable fluoroalkylphosphines that directly convert the C–H bonds in pyridine building blocks, drug-like fragments and pharmaceuticals into fluoroalkyl derivatives. No preinstalled functional groups or directing groups are required. The reaction tolerates a variety of sterically and electronically distinct pyridines, and is exclusively selective for the 4-position in most cases. The reaction proceeds through initial formation of phosphonium salts followed by sp^2 – sp^3 coupling of phosphorus ligands—an underdeveloped manifold for forming C–C bonds.

Access options

Subscribe to Journal

Get full journal access for 1 year

\$199.00

only \$3.90 per issue

[Subscribe](#)

All prices are NET prices.
VAT will be added later in the checkout.

Tax calculation will be finalised during checkout.

Rent or Buy article

Get time limited or full article access on ReadCube.

from \$8.99

[Rent or Buy](#)

All prices are NET prices.

Additional access options:

- [Log in](#)
- [Access through your institution](#)
- [Learn about institutional subscriptions](#)

Fig. 1: Importance of fluoroalkylated pyridines and methods in making C–CF₂X bonds (where X = F or H).

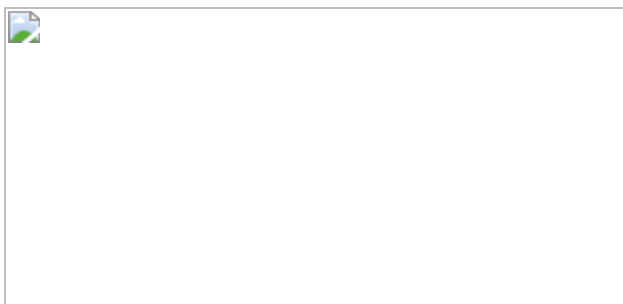


Fig. 2: Design and optimization of a phosphorus-mediated process for azine fluoroalkylation.

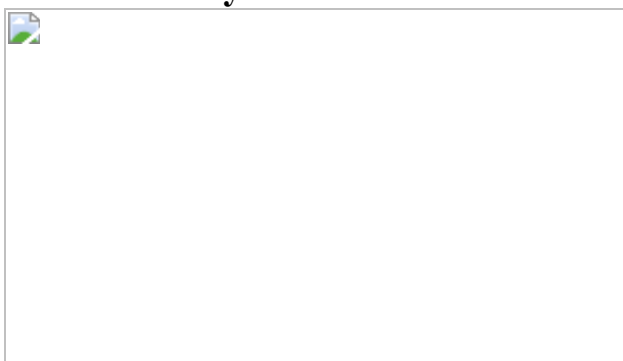


Fig. 3: Scope of building-block azines amenable to fluoroalkylation.

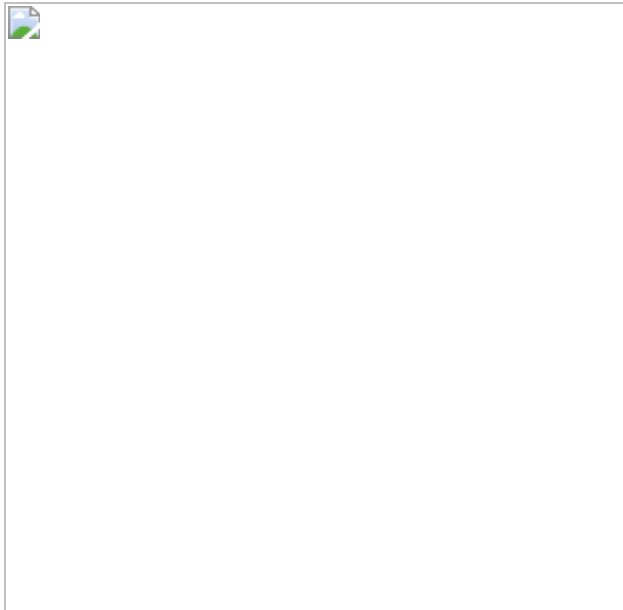
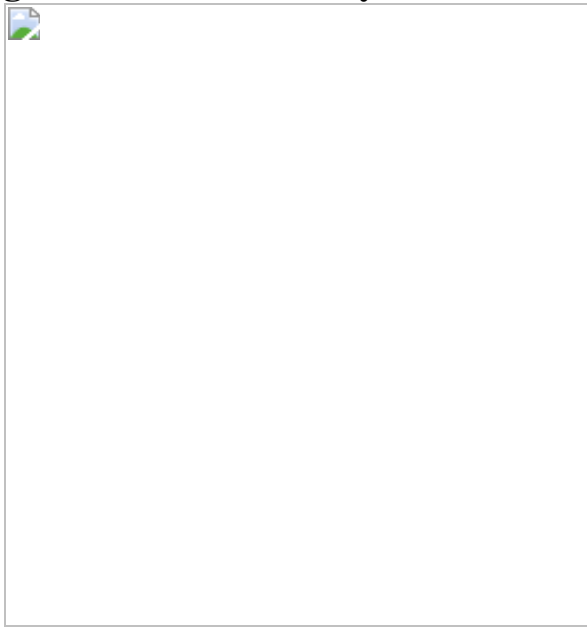


Fig. 4: Direct fluoroalkylation of complex azine-containing molecules.



Data availability

All data generated or analysed during this study are included in the published article (and its [Supplementary Information files](#)). The computational chemistry datasets generated and analysed here are available in Zenodo at <https://doi.org/10.5281/zenodo.4554587>.

Code availability

Computational chemistry datasets were analysed with Goodvibes version 3.0.0, available at Github (<https://github.com/bobbypaton/GoodVibes>) and Zenodo (<https://github.com/bobbypaton/GoodVibes>).

References

1. 1.

Müller, K., Faeh, C. & Diederich, F. Fluorine in pharmaceuticals: looking beyond intuition. *Science* **317**, 1881–1886 (2007).

[ADS](#) [Article](#) [Google Scholar](#)

2. 2.

Hagmann, W. K. The many roles for fluorine in medicinal chemistry. *J. Med. Chem.* **51**, 4359–4369 (2008).

[CAS](#) [Article](#) [Google Scholar](#)

3. 3.

Zhou, Y. et al. Next generation of fluorine-containing pharmaceuticals, compounds currently in phase II–III clinical trials of major pharmaceutical companies: new structural trends and therapeutic areas. *Chem. Rev.* **116**, 422–518 (2016).

[CAS](#) [Article](#) [Google Scholar](#)

4. 4.

Zafrani, Y. et al. Difluoromethyl bioisostere: examining the “lipophilic hydrogen bond donor” concept. *J. Med. Chem.* **60**, 797–804 (2017).

[CAS](#) [Article](#) [Google Scholar](#)

5. 5.

Jeschke, P. The unique role of fluorine in the design of active ingredients for modern crop protection. *ChemBioChem* **5**, 570–589 (2004).

[CAS](#) [Article](#) [Google Scholar](#)

6. 6.

Burriß, A. et al. The importance of trifluoromethyl pyridines in crop protection. *Pest Manag. Sci.* **74**, 1228–1238 (2018).

[CAS](#) [Article](#) [Google Scholar](#)

7. 7.

Alonso, C., Martínez de Marigorta, E., Rubiales, G. & Palacios, F. Carbon trifluoromethylation reactions of hydrocarbon derivatives and heteroarenes. *Chem. Rev.* **115**, 1847–1935 (2015).

[CAS](#) [Article](#) [Google Scholar](#)

8. 8.

Barata-Vallejo, S., Lantaño, B. & Postigo, A. Recent advances in trifluoromethylation reactions with electrophilic trifluoromethylating reagents. *Chem. Eur. J.* **20**, 16806–16829 (2014).

[CAS](#) [Article](#) [Google Scholar](#)

9. 9.

Yerien, D. E., Barata-Vallejo, S. & Postigo, A. Difluoromethylation reactions of organic compounds. *Chem. Eur. J.* **23**, 14676–14701 (2017).

[CAS](#) [Article](#) [Google Scholar](#)

10. 10.

Postigo, A. in *Late-Stage Fluorination of Bioactive Molecules and Biologically-Relevant Substrates* (ed. Postigo, A.) 243–285 (Elsevier, 2019).

11. 11.

Barata-Vallejo, S. & Postigo, A. Photocatalytic difluoromethylation reactions of aromatic compounds and aliphatic multiple C–C bonds. *Molecules* **24**, 4483 (2019).

[CAS](#) [Article](#) [Google Scholar](#)

12. 12.

Lemos, A., Lemaire, C. & Luxen, A. Progress in difluoroalkylation of organic substrates by visible light photoredox catalysis. *Adv. Synth. Catal.* **361**, 1500–1537 (2019).

[CAS](#) [Article](#) [Google Scholar](#)

13. 13.

Ye, F. et al. Aryl sulfonium salts for site-selective late-stage trifluoromethylation. *Angew. Chem. Int. Ed.* **58**, 14615–14619 (2019).

[CAS](#) [Article](#) [Google Scholar](#)

14. 14.

Vitaku, E., Smith, D. T. & Njardarson, J. T. Analysis of the structural diversity, substitution patterns, and frequency of nitrogen heterocycles among U.S. FDA approved pharmaceuticals. *J. Med. Chem.* **57**, 10257–10274 (2014).

[CAS](#) [Article](#) [Google Scholar](#)

15. 15.

Nagib, D. A. & MacMillan, D. W. C. Trifluoromethylation of arenes and heteroarenes by means of photoredox catalysis. *Nature* **480**, 224–228 (2011).

[ADS](#) [CAS](#) [Article](#) [Google Scholar](#)

16. 16.

Fujiwara, Y. et al. Practical and innate carbon-hydrogen functionalization of heterocycles. *Nature* **492**, 95–99 (2012).

[ADS](#) [CAS](#) [Article](#) [Google Scholar](#)

17. 17.

Beatty, J. W., Douglas, J. J., Cole, K. P. & Stephenson, C. R. J. A scalable and operationally simple radical trifluoromethylation. *Nat. Commun.* **6**, 7919 (2015).

[ADS](#) [Article](#) [Google Scholar](#)

18. 18.

Ekroos, M. & Sjögren, T. Structural basis for ligand promiscuity in cytochrome P450 3A4. *Proc. Natl Acad. Sci. USA* **103**, 13682–13687 (2006).

[ADS](#) [CAS](#) [Article](#) [Google Scholar](#)

19. 19.

Gibbs, M. A. & Hosea, N. A. Factors affecting the clinical development of cytochrome P450 3A substrates. *Clin. Pharmacokinet.* **42**, 969–984 (2003).

[CAS](#) [Article](#) [Google Scholar](#)

20. 20.

O’Hara, F., Blackmond, D. G. & Baran, P. S. Radical-based regioselective C–H functionalization of electron-deficient heteroarenes: scope, tunability, and predictability. *J. Am. Chem. Soc.* **135**, 12122–12134 (2013).

[Article](#) [Google Scholar](#)

21. 21.

Nagase, M., Kuninobu, Y. & Kanai, M. 4-Position-selective C–H perfluoroalkylation and perfluoroarylation of six-membered heteroaromatic compounds. *J. Am. Chem. Soc.* **138**, 6103–6106 (2016).

[CAS](#) [Article](#) [Google Scholar](#)

22. 22.

Finet, J.-P. *Ligand Coupling Reactions with Heteroatomic Compounds* 1st edn (Pergamon, 1998).

23. 23.

Uchida, Y., Onoue, K., Tada, N. & Nagao, F. Ligand coupling reaction on the phosphorus atom. *Tetrahedr. Lett.* **30**, 567–570 (1989).

[CAS](#) [Article](#) [Google Scholar](#)

24. 24.

Hilton, M. C. et al. Heterobiaryl synthesis by contractive C–C coupling via P(V) intermediates. *Science* **362**, 799–804 (2018).

[ADS](#) [CAS](#) [Article](#) [Google Scholar](#)

25. 25.

Boyle, B. T., Hilton, M. C. & McNally, A. Nonsymmetrical bis-azine biaryls from chloroazines: a strategy using phosphorus ligand-

coupling. *J. Am. Chem. Soc.* **141**, 15441–15449 (2019).

[CAS](#) [Article](#) [Google Scholar](#)

26. 26.

Krishnamurti, V., Barrett, C. & Prakash, G. K. S. Siladifluoromethylation and deoxo-trifluoromethylation of P^V-H compounds with TMSCF₃: route to P^V-CF₂⁻ transfer reagents and P-CF₃ compounds. *Org. Lett.* **21**, 1526–1529 (2019).

[CAS](#) [Article](#) [Google Scholar](#)

27. 27.

Anders, E. & Markus, F. Neue methode zur regiospezifischen substitution einiger reaktionsträcer N-heteroaromatischer ringsysteme. *Tetrahedr. Lett.* **28**, 2675–2676 (1987).

[CAS](#) [Article](#) [Google Scholar](#)

28. 28.

Hilton, M. C., Dolewski, R. D. & McNally, A. Selective functionalization of pyridines via heterocyclic phosphonium salts. *J. Am. Chem. Soc.* **138**, 13806–13809 (2016).

[CAS](#) [Article](#) [Google Scholar](#)

29. 29.

Fasano, V., LaFortune, J. H. W., Bayne, J. M., Ingleson, M. J. & Stephan, D. W. Air- and water-stable Lewis acids: synthesis and reactivity of P-trifluoromethyl electrophilic phosphonium cations. *Chem. Commun.* **54**, 662–665 (2018).

[CAS](#) [Article](#) [Google Scholar](#)

30. 30.

Barbe, G. & Charette, A. B. Highly chemoselective metal-free reduction of tertiary amides. *J. Am. Chem. Soc.* **130**, 18–19 (2008).

[CAS](#) [Article](#) [Google Scholar](#)

31. 31.

Fujimoto, H., Kodama, T., Yamanaka, M. & Tobisu, M. Phosphine-catalyzed intermolecular acylfluorination of alkynes via a P(V) intermediate. *J. Am. Chem. Soc.* **142**, 17323–17328 (2020).

[CAS](#) [Article](#) [Google Scholar](#)

32. 32.

Levy, J. N., Alegre-Requena, J. V., Liu, R., Paton, R. S. & McNally, A. Selective halogenation of pyridines using designed phosphine reagents. *J. Am. Chem. Soc.* **142**, 11295–11305 (2020).

[CAS](#) [Article](#) [Google Scholar](#)

33. 33.

Lim, S. & Radosevich, A. T. Round-trip oxidative addition, ligand metathesis, and reductive elimination in a P^{III}/P^V synthetic cycle. *J. Am. Chem. Soc.* **142**, 16188–16193 (2020).

[CAS](#) [Article](#) [Google Scholar](#)

34. 34.

Dolewski, R. D., Fricke, P. J. & McNally, A. Site-selective switching strategies to functionalize polyazines. *J. Am. Chem. Soc.* **140**, 8020–8026 (2018).

[CAS](#) [Article](#) [Google Scholar](#)

35. 35.

Ji, Y. et al. Innate C–H trifluoromethylation of heterocycles. *Proc. Natl Acad. Sci. USA* **108**, 14411–14415 (2011).

[ADS](#) [CAS](#) [Article](#) [Google Scholar](#)

36. 36.

Fujiwara, Y. et al. A new reagent for direct difluoromethylation. *J. Am. Chem. Soc.* **134**, 1494–1497 (2012).

[CAS](#) [Article](#) [Google Scholar](#)

[Download references](#)

Acknowledgements

This work was supported by the National Science Foundation (NSF) under grant number 1753087. We acknowledge the Rocky Mountain Advanced Computing Consortium (RMACC) Summit supercomputer, supported by the NSF (grants ACI-1532235 and ACI-1532236), and the Extreme Science and Engineering Discovery Environment (XSEDE) (allocations TG-CHE180056 and TG-CHE200033). We thank M. J. Gaunt for help in preparing the manuscript. We dedicate this paper to the memory of Robert M. Williams.

Author information

Author notes

1. These authors contributed equally: Xuan Zhang, Kyle G. Nottingham

Affiliations

1. Department of Chemistry, Colorado State University, Fort Collins, CO, USA

Xuan Zhang, Kyle G. Nottingham, Chirag Patel, Juan V. Alegre-Requena, Jeffrey N. Levy, Robert S. Paton & Andrew McNally

Authors

1. Xuan Zhang

[View author publications](#)

You can also search for this author in [PubMed](#) [Google Scholar](#)

2. Kyle G. Nottingham

[View author publications](#)

You can also search for this author in [PubMed](#) [Google Scholar](#)

3. Chirag Patel

[View author publications](#)

You can also search for this author in [PubMed](#) [Google Scholar](#)

4. Juan V. Alegre-Requena

[View author publications](#)

You can also search for this author in [PubMed](#) [Google Scholar](#)

5. Jeffrey N. Levy

[View author publications](#)

You can also search for this author in [PubMed](#) [Google Scholar](#)

6. Robert S. Paton

[View author publications](#)

You can also search for this author in [PubMed](#) [Google Scholar](#)

7. Andrew McNally

[View author publications](#)

You can also search for this author in [PubMed](#) [Google Scholar](#)

Contributions

X.Z., K.G.N., C.P. and J.N.L. carried out and analysed the experiments. A.M. directed the project. A.M., R.S.P. and K.G.N. wrote the manuscript. J.V.A.-R. and R.S.P. designed, carried out and analysed the computational experiments.

Corresponding authors

Correspondence to [Robert S. Paton](#) or [Andrew McNally](#).

Ethics declarations

Competing interests

A patent application based on the subject matter of this manuscript has been filed with the United States Patent and Trademark Office.

Additional information

Peer review information *Nature* thanks the anonymous reviewers for their contribution to the peer review of this work.

Publisher's note Springer Nature remains neutral with regard to jurisdictional claims in published maps and institutional affiliations.

Supplementary information

[Supplementary Information](#)

This file contains Supplementary Sections 1-18, including Supplementary Figures 1-18, Supplementary Tables 1-10 and ^1H , ^{13}C , ^{19}F , and ^{31}P Spectra data- see Contents page for details.

Rights and permissions

[Reprints and Permissions](#)

About this article



Check for
updates

Cite this article

Zhang, X., Nottingham, K.G., Patel, C. *et al.* Phosphorus-mediated sp^2 – sp^3 couplings for C–H fluoroalkylation of azines. *Nature* **594**, 217–222 (2021). <https://doi.org/10.1038/s41586-021-03567-3>

[Download citation](#)

- Received: 10 February 2021
- Accepted: 20 April 2021
- Published: 28 April 2021
- Issue Date: 10 June 2021
- DOI: <https://doi.org/10.1038/s41586-021-03567-3>

Comments

By submitting a comment you agree to abide by our [Terms](#) and [Community Guidelines](#). If you find something abusive or that does not comply with our terms or guidelines please flag it as inappropriate.

[Access through your institution](#)

[Change institution](#)

[Buy or subscribe](#)

Advertisement

This article was downloaded by **calibre** from <https://www.nature.com/articles/s41586-021-03567-3>

| [Section menu](#) | [Main menu](#) |

- Article
- [Published: 26 May 2021](#)

Mesozoic cupules and the origin of the angiosperm second integument

- [Gongle Shi](#) ORCID: [orcid.org/0000-0003-3374-6637¹](https://orcid.org/0000-0003-3374-6637),
- [Fabiany Herrera](#) ORCID: [orcid.org/0000-0002-2412-672X²](https://orcid.org/0000-0002-2412-672X),
- [Patrick S. Herendeen](#) ORCID: [orcid.org/0000-0003-2657-8671²](https://orcid.org/0000-0003-2657-8671),
- [Elizabeth G. Clark](#) ORCID: [orcid.org/0000-0003-4289-6370³](https://orcid.org/0000-0003-4289-6370) &
- [Peter R. Crane](#) ORCID: [orcid.org/0000-0003-4331-6948^{4,5}](https://orcid.org/0000-0003-4331-6948)

[Nature](#) volume 594, pages 223–226 (2021) [Cite this article](#)

- 3892 Accesses
- 211 Altmetric
- [Metrics details](#)

Subjects

- [Palaeontology](#)
- [Plant evolution](#)

Abstract

The second integument of the angiosperm ovule is unique among seed plants, with developmental genetics that are distinct from those of the inner integument¹. Understanding how the second integument should be compared to structures in other seed plants is therefore crucial to resolving the long-standing question of the origin of angiosperms^{2,3,4,5,6}. Attention

has focused on several extinct plants with recurved cupules that are reminiscent of the anatropous organization of the basic bitegmic ovules of angiosperms^{[1](#),^{[2](#)},^{[3](#)},^{[4](#)},^{[5](#)},^{[6](#)}}, but interpretations have been hampered by inadequate information on the relevant fossils. Here we describe abundant exceptionally well-preserved recurved cupules from a newly discovered silicified peat dating to the Early Cretaceous epoch (around 125.6 million years ago) in Inner Mongolia, China. The new material, combined with re-examination of potentially related fossils, indicates that the recurved cupules of several groups of Mesozoic plants are all fundamentally comparable, and that their structure is consistent with the recurved form and development of the second integument in the bitegmic anatropous ovules of angiosperms. Recognition of these angiosperm relatives (angiphytes) provides a partial answer to the question of angiosperm origins, will help to focus future work on seed plant phylogenetics and has important implications for ideas on the origin of the angiosperm carpel.

Access options

Subscribe to Journal

Get full journal access for 1 year

\$199.00

only \$3.90 per issue

[Subscribe](#)

All prices are NET prices.

VAT will be added later in the checkout.

Tax calculation will be finalised during checkout.

Rent or Buy article

Get time limited or full article access on ReadCube.

from \$8.99

[Rent or Buy](#)

All prices are NET prices.

Additional access options:

- [Log in](#)
- [Access through your institution](#)
- [Learn about institutional subscriptions](#)

Fig. 1: Recurved cupules of extinct seed plants; an angiosperm carpel; and the phylogenetic relationships of seed plants.

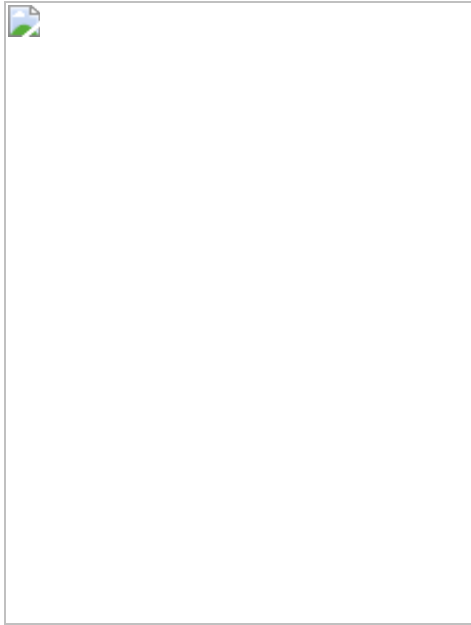
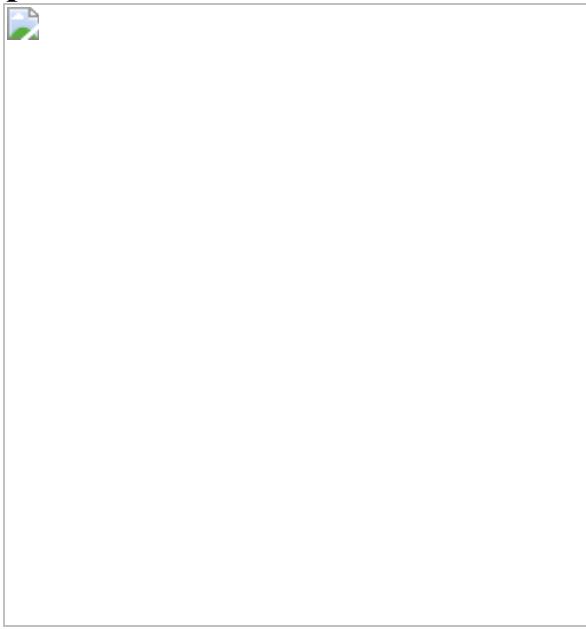


Fig. 2: Fossil cupules from the Early Cretaceous of Inner Mongolia, China.



Fig. 3: Three-dimensional reconstructions from segmented micro-computed tomography data, and scanning electron micrographs of cupules.



Data availability

The data matrix for phylogenetic analyses is provided in Supplementary Data 1. Computed tomography data have been deposited in Dryad at <https://doi.org/10.5061/dryad.5x69p8d2r>.

Code availability

The MrBayes commands for Bayesian analysis are included in the NEXUS formatted file in Supplementary Data [2](#).

References

1. 1.

Gasser, C. S. & Skinner, D. J. Development and evolution of the unique ovules of flowering plants. *Curr. Top. Dev. Biol.* **131**, 373–399 (2019).

[Article](#) [Google Scholar](#)

2. 2.

Gaussin, H. *Les Gymnospermes, Actuelles et Fossiles. Travaux du Laboratoire Forestier de Toulouse, Tome 2. Étud. Dendrol. Sect. 1*, Vol. 1 (1946).

3. 3.

Stebbins, G. L. *Flowering Plants: Evolution Above the Species Level* (Harvard Univ. Press, 1974).

4. 4.

Doyle, J. A. Origin of angiosperms. *Annu. Rev. Ecol. Syst.* **9**, 365–392 (1978).

[Article](#) [Google Scholar](#)

5. 5.

Crane, P. R. Phylogenetic analysis of seed plants and the origin of angiosperms. *Ann. Mo. Bot. Gard.* **72**, 716–793 (1985).

[Article](#) [Google Scholar](#)

6. 6.

Frohlich, M. W. & Chase, M. W. After a dozen years of progress the origin of angiosperms is still a great mystery. *Nature* **450**, 1184–1189 (2007).

[ADS](#) [CAS](#) [Article](#) [Google Scholar](#)

7. 7.

Harris, T. M. A new member of the Caytoniales. *New Phytol.* **32**, 97–113 (1933).

[Article](#) [Google Scholar](#)

8. 8.

Harris, T. M. *The Yorkshire Jurassic Flora, II. Caytoniales, Cycadales & Pteridosperms* (British Museum, Natural History, 1964).

9. 9.

Hilton, J. & Bateman, R. M. Pteridosperms are the backbone of seed-plant phylogeny. *J. Torrey Bot. Soc.* **133**, 119–168 (2006).

[Article](#) [Google Scholar](#)

10. 10.

Doyle, J. A. Integrating molecular phylogenetic and paleobotanical evidence on origin of the flower. *Int. J. Plant Sci.* **169**, 816–843 (2008).

[Article](#) [Google Scholar](#)

11. 11.

Rothwell, G. W. & Stockey, R. A. Phylogenetic diversification of Early Cretaceous seed plants: the compound seed cone of *Doylea tetrahedrasperma*. *Am. J. Bot.* **103**, 923–937 (2016).

[CAS](#) [Article](#) [Google Scholar](#)

12. 12.

Shi, G. et al. Diversity and homologies of corystosperm seed-bearing structures from the Early Cretaceous of Mongolia. *J. Syst. Palaeontology* **17**, 997–1029 (2019).

[Article](#) [Google Scholar](#)

13. 13.

Anderson, J. M. & Anderson, H. M. *Heyday of the Gymnosperms: Systematics and Biodiversity of the Late Triassic Molteno Fructifications* (Strelitzia, 2003).

14. 14.

Klavins, S. D., Taylor, T. N. & Taylor, E. L. Anatomy of *Umkomasia* (Corystospermales) from the Triassic of Antarctica. *Am. J. Bot.* **89**, 664–676 (2002).

[Article](#) [Google Scholar](#)

15. 15.

Axsmith, B. J., Taylor, E. L., Taylor, T. N. & Cuneo, N. R. New perspectives on the Mesozoic seed fern order Corystospermales based on attached organs from the Triassic of Antarctica. *Am. J. Bot.* **87**, 757–768 (2000).

[CAS](#) [Article](#) [Google Scholar](#)

16. 16.

Taylor, T. N., Del Fueyo, G. M. & Taylor, E. L. Permineralized seed fern cupules from the Triassic of Antarctica: implications for cupule and carpel evolution. *Am. J. Bot.* **81**, 666–677 (1994).

[Article](#) [Google Scholar](#)

17. 17.

Bomfleur, B. et al. Habit and ecology of the Petriellales, an unusual group of seed plants from the Triassic of Gondwana. *Int. J. Plant Sci.* **175**, 1062–1075 (2014).

[Article](#) [Google Scholar](#)

18. 18.

Taylor, T. N. & Archangelsky, S. The Cretaceous pteridosperms *Ruflorinia* and *Ktalenia* and implications on cupule and carpel evolution. *Am. J. Bot.* **72**, 1842–1853 (1985).

[Article](#) [Google Scholar](#)

19. 19.

Friis, E. M. & Crane, P. R. & Pedersen, K. R. *Geminispermum*, an Early Cretaceous (early–middle Albian) cupulate unit from the angiosperm-dominated Puddledock flora of eastern North America. *Acta Palaeobot.* **59**, 229–239 (2019).

[Article](#) [Google Scholar](#)

20. 20.

Barbacka, M. & Boka, K. A new Early Liassic Caytoniales fructification from Hungary. *Acta Palaeobot.* **40**, 85–111 (2000).

[Google Scholar](#)

21. 21.

Crane, P. R. in *Origin and Evolution of Gymnosperms* (ed. Beck, C. B.) 218–272 (Columbia Univ. Press, 1988).

22. 22.

Endress, P. K. Angiosperm ovules: diversity, development, evolution. *Ann. Bot.* **107**, 1465–1489 (2011).

[Article](#) [Google Scholar](#)

23. 23.

Doyle, J. A. & Donoghue, M. J. Phylogenies and angiosperm diversification. *Paleobiology* **19**, 141–167 (1993).

[Article](#) [Google Scholar](#)

24. 24.

Blomenkemper, P., Kerp, H., Abu Hamad, A., DiMichele, W. A. & Bomfleur, B. A hidden cradle of plant evolution in Permian tropical lowlands. *Science* **362**, 1414–1416 (2018).

[ADS](#) [CAS](#) [Article](#) [Google Scholar](#)

25. 25.

Deng, S. *Early Cretaceous Flora of Huolinhe Basin, Inner Mongolia, Northeast China* (Geological Publishing House, 1995).

26. 26.

Shi, G. et al. Age of the Huolinhe Formation in the Huolinhe Basin, eastern Inner Mongolia, China: evidence from U–Pb zircon dating and palynological assemblages. *J. Stratigr.* **45**, 69–81 (2021).

[Google Scholar](#)

27. 27.

Crane, P. R. & Herendeen, P. S. Bennettitales from the Grisethorpe Bed (Middle Jurassic) at Cayton Bay, Yorkshire, UK. *Am. J. Bot.* **96**, 284–295 (2009).

[Article](#) [Google Scholar](#)

28. 28.

Huang, D. *The Daohugou Biota* (Shanghai Scientific & Technical Publishers, 2016).

29. 29.

Galtier, J. & Phillips, T. L. in *Fossil Plants and Spores: Modern Techniques* (eds Jones, T. P. & Rowe, N. P.) 67–70 (Geological Society of London, 1999).

30. 30.

Friis, E. M. et al. Phase-contrast X-ray microtomography links Cretaceous seeds with Gnetales and Bennettitales. *Nature* **450**, 549–552 (2007).

[ADS](#) [CAS](#) [Article](#) [Google Scholar](#)

[Download references](#)

Acknowledgements

We thank B. Zhang, C. Dong, S. Yin, S. Hu, H. Jiang, Q. Li, W. Zhang and F. Lu for assistance with fieldwork in Inner Mongolia, China; R. Serbet and B. Atkinson for assistance with examination and the loan of *Petriellaea* specimens from the University of Kansas collections; X. Wang and F. Zheng for the loan of the *Caytonia* fossils from the Daohugou Bed in the collections of the Institute of Vertebrate Paleontology and Paleoanthropology, Chinese Academy of Sciences; Z.-X. Luo, A. I. Neander and C. Brodersen for assistance with micro-computed tomography (micro-CT) scanning; E.M. Friis, X. Xu and S. Donskaya for assistance in

processing micro-CT data; H. Wang, C. Zhang and M. Carvalho for assistance with phylogenetic analyses; and D. Yang for assistance with drawing. This work was supported by the Youth Innovation Promotion Association of the Chinese Academy of Sciences (2017359), the US National Science Foundation grant DEB-1748286, the Strategic Priority Research Program of the Chinese Academy of Sciences (XDB26000000), the National Natural Science Foundation of China (41790454) and the Oak Spring Garden Foundation.

Author information

Affiliations

1. State Key Laboratory of Palaeobiology and Stratigraphy, Nanjing Institute of Geology and Palaeontology and Center for Excellence in Life and Paleoenvironment, Chinese Academy of Sciences, Nanjing, China

Gongle Shi

2. Chicago Botanic Garden, Glencoe, IL, USA

Fabiany Herrera & Patrick S. Herendeen

3. Department of Biology, Duke University, Durham, NC, USA

Elizabeth G. Clark

4. Oak Spring Garden Foundation, Upperville, VA, USA

Peter R. Crane

5. Yale School of the Environment, Yale University, New Haven, CT, USA

Peter R. Crane

Authors

1. Goggle Shi

[View author publications](#)

You can also search for this author in [PubMed](#) [Google Scholar](#)

2. Fabiany Herrera

[View author publications](#)

You can also search for this author in [PubMed](#) [Google Scholar](#)

3. Patrick S. Herendeen

[View author publications](#)

You can also search for this author in [PubMed](#) [Google Scholar](#)

4. Elizabeth G. Clark

[View author publications](#)

You can also search for this author in [PubMed](#) [Google Scholar](#)

5. Peter R. Crane

[View author publications](#)

You can also search for this author in [PubMed](#) [Google Scholar](#)

Contributions

P.R.C. and G.S. designed the research. G.S., F.H., P.S.H. and P.R.C. discovered the new Early Cretaceous silicified peat and collected the palaeobotanical samples. G.S., F.H. and E.G.C. prepared the fossil material and processed the micro-CT data. G.S., F.H., P.S.H. and P.R.C. analysed the data. G.S. and P.R.C. wrote the manuscript, in discussion with F.H., P.S.H. and E.G.C. P.R.C supervised the research.

Corresponding author

Correspondence to [Goggle Shi](#).

Ethics declarations

Competing interests

The authors declare no competing interests.

Additional information

Peer review information *Nature* thanks William Friedman, Michael Frohlich and Douglas Soltis for their contribution to the peer review of this work. Peer reviewer reports are available.

Publisher's note Springer Nature remains neutral with regard to jurisdictional claims in published maps and institutional affiliations.

Extended data figures and tables

Extended Data Fig. 1 Fossil locality.

a, Map showing the location of the Zhahanaoer open-cast coal mine (indicated by a cupule) in Jarud Banner, eastern Inner Mongolia, China, and the Tevshiin Govi locality (left) in central Mongolia, where similar lignified cupules have been found¹². **b**, Stratigraphic section of the ‘lower coal-bearing member’ of the Huolinhe Formation at the margin of the Zhahanaoer coal mine showing the position of the silicified plant fossils (indicated by a cupule) and dated ash layer²⁶. **c**, Part of the outcrop showing the chert embedded in mudstones.

Extended Data Fig. 2 Fossil cupules and associated pollen from the Early Cretaceous of Inner Mongolia, China.

The small stems (**j, m**) and multiveined leaves (**k**) that occur with the cupules in the chert were probably produced by the same group of plants, but they remain to be linked conclusively. **a**, Individual seed-bearing unit that is attached to the axis of the cone in Fig. [1a](#). PB23663. **b**, Oblique

transverse section of cupule showing the attachment of one seed (right) to the pad of parenchyma tissue, and the vascular bundle (VB) with concentrically arranged xylem. PB23673. **c**, Longitudinal section of cupule. PB23674. **d**, Line drawing of **a** showing the stalked cupule (blue) and bract (green). **e**, Line drawing of **b** showing the cupule (blue), seeds (yellow) with a single integument (brown), pad of parenchyma tissue (grey) where one seed is attached, and concentrically arranged xylem (orange). **f**, Line drawing of **c**. Note that the micropyle of seed (yellow) is oriented towards the base of the cupule (blue) stalk. **g**, **h**, Three-dimensional reconstructions from segmented micro-CT data. **g**, Individual seed-bearing unit that is attached to the axis of the cone in Fig. 3a, showing the bract (green), stalked cupule (blue) and seed (brown). PB23672. **h**, Three-angled seed that is attached to the cupule in **g**. **i**, Longitudinal section of a seed, showing the bifid micropyle (arrows), the nucellus (n), detached inner cuticle of integument (ic) and megasporangium membrane (m). PB23675. **j**, Small stem with about 10 asymmetrical growth rings and well-developed pith (arrow). PB23676. **k**, Transverse section of a leaf showing nine longitudinal veins. PB23677. **l**, Bisaccate pollen grain adhering to the tip of nucellus within the integument. PB23678. **m**, Detail of secondary xylem of the small stem in **j**, showing uniseriate ray (arrow). Scale bars, 1 mm (**a–c**, **g**); 500 µm (**h–j**); 200 µm (**k**); 50 µm (**m**); 10 µm (**l**).

Extended Data Fig. 3 Details of vasculature at different levels in fossil cupules from the Early Cretaceous of Inner Mongolia, China.

The interpretative line drawings show the cupule (blue), xylem (orange) and poorly preserved phloem (dark blue). All sections are oriented in the same way as the vascular bundle in Fig. 2, with the upper side of each bundle towards the inner side of the cupule, and the lower side of each bundle towards the outer side of the cupule. **a**, Transverse section of the fused bract-cupule stalk complex (left) with line drawing (right), showing two median vascular bundles; the upper (adaxial) supplies the cupule and the lower (abaxial) supplies the bract. Note that in the two bundles the xylem (orange) is towards the centre of the complex relative to the spaces that indicate the former position of the phloem. PB23667. **b**, Detail of the upper vascular bundle in **a**. **c**, Transverse section of cupule stalk slightly distal to

a (left) with line drawing (right), showing two abutting vascular bundles with the xylem (orange) towards the outer side of the cupule relative to the space that indicates the former position of the phloem. PB23667. **d**, Detail of the two abutting vascular bundles in **c**. **e**, Transverse section of cupule stalk near the base of the cupule (left) with line drawing (right), showing two vascular bundles with flattened xylem. PB23669. **f**, Detail of the left vascular bundle in **e** showing xylem (orange) and poorly preserved phloem (dark blue). **g**, Transverse section of cupule stalk near the apex of the cupule (left) with line drawing (right), showing two vascular bundles with inverted V-shaped xylem. PB23670. **h**, Detail of the right vascular bundle in **g**. **i**, Transverse section of cupule stalk near the tip of its strongly curved distal portion (left) with line drawing (right). PB23671. **j**, Detail of the left vascular bundle in **i** showing the circular outline of the xylem (orange) and poorly preserved phloem (dark blue). Scale bars, 100 µm (**a, j**); 50 µm (**b, d, f, h**); 200 µm (**c, e**), 500 µm (**g, i**).

[Extended Data Fig. 4 Fossil cupules from the Early Cretaceous Tevshiin Govi Formation at the Tevshiin Govi locality in central Mongolia.](#)

Light micrographs with line drawings showing the bract (green), stalked cupules (blue) and the axis on which they are borne (brown). **a–f**, *Doylea mongolica* (*Umkomasia mongolica*)¹². **a**, Seed cone with lateral seed-bearing units loosely and helically arranged. PP56614. **b**, Line drawing of **a**. **c, e**, Upper (adaxial) (**c**) and lower (abaxial) (**e**) views of a lateral seed-bearing unit. PP55648. **d**, Line drawing of **c**. **f**, Line drawing of **e**. **g–j**, *Umkomasia corniculata*¹². Upper (adaxial) (**g**) and lower (abaxial) (**i**) views of a lateral seed-bearing unit. PP56628. **h**, Line drawing of **g**. **j**, Line drawing of **i**. **k–n**, *Umkomasia trilobata*¹². Upper (adaxial) (**k**) and lower (abaxial) (**m**) views of a lateral seed-bearing unit with a dorsiventrally flattened axis that bears the cupules. PP56684. **l**, Line drawing of **k**. **n**, Line drawing of **m**.

[Extended Data Fig. 5 Mesozoic seed plants with recurved cupules.](#)

a, *Umkomasia quadripartita* from the Late Triassic of South Africa; line drawing of the holotype. **b**, *Kannaskoppia vincularis* from the Late Triassic of South Africa; line drawing of the holotype. **c**, Reconstruction of *Umkomasia quadripartita*. **d**, Reconstruction of *Kannaskoppia vincularis*. The reconstructions in **a–d** are all based on a previous work¹³. **e**, Reconstruction of *Umkomasia resinosa* from the upper Middle or Upper Triassic of Antarctica¹⁴. **f**, Reconstruction of *Umkomasia uniramia* from the Late Triassic of Antarctica¹⁵. **g**, Reconstruction of a shoot bearing cupules of *Ktalenia circularis* and leaf of *Rusflorinia sierra* from the Early Cretaceous of Argentina¹⁸. **h**, Details of cupules of *Ktalenia circularis* that may contain one or two seeds¹⁸.

Extended Data Fig. 6 Fossil cupules and cupule stalks of *Caytonia* sp.

a–i, *Caytonia* sp. from the Middle Jurassic of Yorkshire, UK. **a**, **b**, Flattened cupule-bearing structures showing subopposite cupule stalks or attachment scars in two ranks that lack evidence of a bract subtending each cupule. **a**, PP60606. **b**, PP60607. **c–e**, Small, possibly aborted, cupules at pollination stage showing the distinct lips. **c**, PP60608. **d**, PP60609. **e**, Note the parallel grooves leading to the micropylar canals on the lip of the cupule. PP60610. **f**, Flattened seed removed from a cupule. PP60611. **g**, Fractured mature cupule showing seeds with the micropyles of the two on the left oriented towards the base of the cupule. PP60612. **h**, **i**, *Caytonia nathersti*⁸. **h**, Flattened cupule-bearing structure showing lateral cupules recurved towards the presumed upper (adaxial) surface. V.26661 (Natural History Museum, London). **i**, Portion of **h** showing the ridges on the presumed lower (abaxial) surface. **j–l**, *Caytonia* sp. from the Middle–Late Jurassic of Daohugou locality, eastern Inner Mongolia, China. **j**, **k**, Part and counterpart of a cupule containing eleven seeds arranged in two rows. See Fig. 3g for a three-dimensional reconstruction from segmented micro-CT data. B0441. **l**, Cupule showing the parallel grooves leading to the micropylar canals (arrow). B0440 (IVPP). Scale bars, 500 µm (**a**, **c–g**); 1 mm (**b**, **h–l**).

Extended Data Fig. 7 Permineralized cupules from the Triassic of Antarctica.

All specimens are deposited in the palaeobotanical collections of the University of Kansas. The interpretative line drawings show cupule (blue) and seed (yellow) with a single integument (brown). **a–k**, *Petriellaea triangulata*. **a**, Longitudinal section of empty seed-bearing structures. Note possible bract (arrow) fused to the cupule stalk. 10852A. **b**, Line drawing of **a** showing possible bract (stippled green). **c**, Transverse section of a cupule containing five seeds. Note the possible bract (arrow). 10025G. **d**, Line drawing of **c** showing the possible bract (stippled green). **e**, Transverse section of a cupule. 10023A. **f**, Line drawing of **e**. **g–j**, Detail of the vascular bundles of the cupule stalk, oriented in the same way as the vascular bundle in Fig. 2, Extended Data Fig. 3, with the upper side of each bundle towards the inner side of the cupule, and the lower side of each bundle towards the outer side of the cupule. 10025G. **h**, Line drawing of the vascular bundle in **g** showing the xylem (orange) that appears arranged in a circle in transverse section. **j**, Line drawing of the vascular bundle in **i** showing the xylem (orange). Note that in **g**, **i** there are no obvious sieve elements or space that may represent the former position of the phloem towards the outer side of the cupule (lower side of the image) relative to the xylem as originally interpreted¹⁶. **k**, Three-dimensional reconstruction from segmented micro-CT data showing three-angled seed in lateral and apical views. 10025G. **l–o**, *Umkomasia resinosa*. Transverse sections of cupules from the type material with interpretive line drawings. 11323. **l**, Cupule formed by the cupule stalk and two lateral flaps and containing two seeds. **m**, Line drawing of **l**. **n**, Cupule formed by the cupule stalk and flap and containing a single seed. **o**, Line drawing of **n**. Scale bars, 1 mm (**a**, **l**, **n**); 500 µm (**c**, **e**, **k**); 50 µm (**g–j**).

Extended Data Fig. 8 Interpretive diagrams of seed-bearing structures of Mesozoic plants with recurved cupules, with longitudinal sections of *Geminispermum virginicense* and an idealized angiosperm carpel.

The interpretative diagrams show the bract (green), the stalked cupules (blue) and the axis on which they are borne (red–brown), and seed consisting of the nucellus (yellow) with a single integument (brown). **a**, Fossil cupules from the Early Cretaceous of Inner Mongolia, China. The cupules are borne helically on a central axis, each cupule contains two seeds, and is subtended by a bract. **b**, *Doylea*^{11,12}. Each lateral seed-bearing unit consists of a bract subtending an axis that bifurcates into two cupule stalks; each cupule stalk bears one cupule that contains a single seed.

Individual cupules are not subtended by a bract. **c**, *Umkomasia trilobata*¹². Each lateral seed-bearing unit consists of a bract subtending a flattened axis that is divided distally into three flattened cupule stalks; each cupule stalk bears one cupule that contains a single seed. Individual cupules are not subtended by a bract. **d**, *Umkomasia resinosa*¹⁴. Cupules are borne helically on a branched elaborated axis and each cupule contains one or two seeds. The presence of a bract is not confirmed but the whole structure may have been borne in the axil of a bract or leaf. Individual cupules are not subtended by a bract. **e**, *Umkomasia quadripartita*¹³. The cupules are borne more or less decussately on an axis with two pairs of bracts near the base; each cupule contains a single seed. Individual cupules are not subtended by a bract. **f**, *Caytonia*^{7,8}. The cupules are subopposite in two ranks on an elaborated flattened axis; each cupule contains up to 30 seeds arranged in two or more rows. There are no bracts subtending individual cupules and the presence of a bract subtending the whole structure is not confirmed. **g**, *Petriella triangulata*¹⁶ and *Kannaskoppia vincularis*¹³. The cupules are probably borne helically (*P. triangulata*) or in two ranks (*K. vincularis*) on an axis; each cupule contains several seeds arranged in one row.

Interpretation in which individual cupules are not subtended by bract. **h**, Alternative interpretation of the seed-bearing structure of *P. triangulata*, in which each cupule is subtended by a bract as the Inner Mongolia cupules in **a**. **i**, *Umkomasia uniramia*¹⁵. Stalked cupules are borne in a whorl of four to eight at the tip of an axis bearing a pair of bracts, each cupule contains a single seed. **j**, **k**, *Geminispermum virginicense*¹⁹. **j**, A pair of recurved cupules face each other at the tip of an axis. **k**, Each cupule contains a single seed and is subtended by a bract. **l**, Angiosperm carpel with a bitegmic ovule curved in the same direction of the curvature of the enclosing carpel (syntropous)²², showing the carpel (green), funiculus and

second integument (blue), and inner integument (brown) and nucellus (yellow).

Extended Data Fig. 9 Phylogenetic relationships of seed plants based on parsimony, maximum likelihood and Bayesian analyses of a dataset for living and fossil seed plants.

See Supplementary Data 1 for the dataset. All trees are rooted with *Elkinsia*. As with all previous analyses of seed plant relationships^{5,9,10,30} support for most nodes is not strong. **a**, Strict consensus of 10 most parsimonious trees (221 steps. Consistency index (CI) = 0.5385; retention index (RI) = 0.7198) from an unconstrained parsimony analysis. Numbers at nodes above the lines are bootstrap values greater than 50%. **b–d**, Phylogenetic analyses with relationships among extant taxa constrained to be compatible to a molecular-backbone tree in which extant Gnetales and Pinaceae are sister taxa (GNE-PINE tree) ([Supplementary Information](#)). **b**, Strict consensus of the 45 most-parsimonious trees (236 steps, CI = 0.5042, RI = 0.6786) from a constrained parsimony analysis. Numbers at nodes above the lines are bootstrap values greater than 50%. **c**, Maximum likelihood tree inferred from a constrained analysis. Numbers at nodes above the lines are bootstrap values. **d**, The 50% majority-rule consensus from a constrained Bayesian analysis (Supplementary Data 2) with posterior probabilities indicated by numbers at the nodes. BEG is the abbreviation for the Bennettitales–Erdtmanithecales–Gnetales group³⁰. See [Supplementary Information](#) for details of characters, taxa, additional information, analyses and discussion.

Extended Data Fig. 10 Phylogenetic relationships of seed plants based on constrained parsimony.

Analyses are of the same dataset as the analyses in Extended Data Fig. 9, except for character 60: ovule-enclosing structures. The relationships among extant taxa are constrained to be compatible to a GNE-PINE molecular-backbone tree ([Supplementary Information](#)). Both trees are rooted with *Elkinsia*. Numbers at nodes above the lines are values of majority-rule consensus. **a**, The 50% majority-rule consensus of the 105

most-parsimonious trees (236 steps, CI = 0.5042, RI = 0.6759) from an analysis of the dataset in which the cupules of Triassic corystosperms, *Doylea* and the Inner Mongolia cupules are scored as ? for character 60. **b**, The 50% majority-rule consensus of the 345 most-parsimonious trees (238 steps, CI = 0.5042, RI = 0.6749) from an analysis of the dataset in which the cupules of Triassic corystosperms, *Doylea* and the Inner Mongolia cupules are scored as 7 (a new state) for character 60. Note that in both analyses the Bennettitales–Erdtmanithecales–Gnetales (BEG) group³⁰ (orange shading) is maintained, and *Caytonia* and glossopterids are resolved as the closest relatives of angiosperms, but the relationships of other angiophytes—Triassic corystosperms, Petriellales and *Doylea*, and the cupules from Inner Mongolia described here—are not well resolved in **a** but are resolved as a clade in **b**. See [Supplementary Information](#) for details of characters, taxa, additional information, analyses and discussion.

Supplementary information

[Supplementary Information](#)

This file contains details regarding the phylogenetic analyses.

[Reporting Summary](#)

[Supplementary Data 1](#)

Morphological matrix for phylogenetic analyses.

[Supplementary Data 2](#)

Morphological matrix with the MrBayes commands for constrained Bayesian analysis.

[.Peer Review File](#)

[Video 1](#)

Reconstructed slice data for specimen PB23667 showing longitudinal sections of a cupule containing two seeds.

Video 2

Three-dimensional reconstruction of a seed cone from segmented Micro-CT data for specimen PB23672.

Rights and permissions

[Reprints and Permissions](#)

About this article



Check for
updates

Cite this article

Shi, G., Herrera, F., Herendeen, P.S. *et al.* Mesozoic cupules and the origin of the angiosperm second integument. *Nature* **594**, 223–226 (2021).
<https://doi.org/10.1038/s41586-021-03598-w>

[Download citation](#)

- Received: 28 December 2020
- Accepted: 30 April 2021
- Published: 26 May 2021
- Issue Date: 10 June 2021
- DOI: <https://doi.org/10.1038/s41586-021-03598-w>

Comments

By submitting a comment you agree to abide by our [Terms](#) and [Community Guidelines](#). If you find something abusive or that does not comply with our terms or guidelines please flag it as inappropriate.

[Access through your institution](#)

[Change institution](#)

[Buy or subscribe](#)

Associated Content

[Ancient seeds spill secrets about the evolution of flowering plants](#)

- Douglas E. Soltis

Nature News & Views 26 May 2021

Advertisement

This article was downloaded by **calibre** from <https://www.nature.com/articles/s41586-021-03598-w>

Evolutionary and biomedical insights from a marmoset diploid genome assembly
[Download PDF](#)

- Article
- Open Access
- [Published: 28 April 2021](#)

Evolutionary and biomedical insights from a marmoset diploid genome assembly

- [Chentao Yang^{1,2}](#)^{na1},
- [Yang Zhou](#) ORCID: orcid.org/0000-0003-1247-5049¹^{na1},
- [Stephanie Marcus³](#)^{na1},
- [Giulio Formenti](#) ORCID: orcid.org/0000-0002-7554-5991^{3,4},
- [Lucie A. Bergeron²,](#)
- [Zhenzhen Song⁵,](#)
- [Xupeng Bi¹,](#)
- [Juraj Bergman](#) ORCID: orcid.org/0000-0002-9415-2747⁶,
- [Marjolaine Marie C. Rousselle⁶,](#)
- [Chengran Zhou](#) ORCID: orcid.org/0000-0002-9468-5973¹,
- [Long Zhou¹,](#)
- [Yuan Deng^{1,2},](#)
- [Miaoquan Fang¹,](#)
- [Duo Xie](#) ORCID: orcid.org/0000-0001-7010-3601¹,
- [Yuanyuan Zhu¹,](#)
- [Shangjin Tan¹,](#)
- [Jacquelyn Mountcastle](#) ORCID: orcid.org/0000-0003-1078-4905⁴,
- [Bettina Haase⁴,](#)
- [Jennifer Balacco⁴,](#)
- [Jonathan Wood⁷,](#)
- [William Chow⁷,](#)
- [Arang Rhee](#) ORCID: orcid.org/0000-0002-9809-8127⁸,
- [Martin Pippel](#) ORCID: orcid.org/0000-0002-8134-5929^{9,10},
- [Margaret M. Fabiszak](#) ORCID: orcid.org/0000-0002-2170-2170¹¹,

- [Sergey Koren](#) ORCID: orcid.org/0000-0002-1472-8962⁸,
- [Olivier Fedrigo](#) ORCID: orcid.org/0000-0002-6450-7551⁴,
- [Winrich A. Freiwald](#) ORCID: orcid.org/0000-0001-8456-5030^{11,12},
- [Kerstin Howe](#) ORCID: orcid.org/0000-0003-2237-513X⁷,
- [Huanming Yang](#)^{1,5,13,14},
- [Adam M. Phillippy](#) ORCID: orcid.org/0000-0003-2983-8934⁸,
- [Mikkel Heide Schierup](#) ORCID: orcid.org/0000-0002-5028-1790⁶,
- [Erich D. Jarvis](#) ORCID: orcid.org/0000-0001-8931-5049^{3,4,15} &
- [Guojie Zhang](#) ORCID: orcid.org/0000-0001-6860-1521^{2,16,17,18}

Nature volume 594, pages 227–233 (2021) [Cite this article](#)

- 8524 Accesses
- 128 Altmetric
- [Metrics details](#)

Subjects

- [Evolutionary genetics](#)
- [Experimental models of disease](#)
- [Genetics of the nervous system](#)
- [Genome informatics](#)
- [Genomics](#)

Abstract

The accurate and complete assembly of both haplotype sequences of a diploid organism is essential to understanding the role of variation in genome functions, phenotypes and diseases¹. Here, using a trio-binning approach, we present a high-quality, diploid reference genome, with both haplotypes assembled independently at the chromosome level, for the common marmoset (*Callithrix jacchus*), an primate model system that is widely used in biomedical research^{2,3}. The full spectrum of heterozygosity between the two haplotypes involves 1.36% of the genome—much higher than the 0.13% indicated by the standard estimation based on single-nucleotide heterozygosity alone. The de novo mutation rate is 0.43×10^{-8} per site per generation, and the paternal inherited genome acquired twice as many mutations as the maternal. Our diploid assembly enabled us to discover a recent expansion of the sex-differentiation region and unique evolutionary changes in the marmoset Y chromosome. In addition, we identified many genes with signatures of positive

selection that might have contributed to the evolution of *Callithrix* biological features. Brain-related genes were highly conserved between marmosets and humans, although several genes experienced lineage-specific copy number variations or diversifying selection, with implications for the use of marmosets as a model system.

[Download PDF](#)

Main

A diploid organism carries two haploid genomes with a range of variants, which make substantial contributions to phenotypic variation⁴. Phased haplotype assemblies can help to reveal the *cis*- and *trans*-acting variants on the two homologous genomes. However, most contemporary de novo genome-sequencing efforts produce a single mosaic reference genome derived from parts of both maternal and paternal alleles, with variations between homologous chromosomes normally being disregarded. As a consequence, these methods usually fail to assemble genomic regions with high heterogeneity, resulting in fragmented sequences. A few methods have been developed to produce partial haplotype-phased genome assemblies and showed power in using long sequencing reads to produce long haplotigs (haplotype-specific contigs)^{5,6}. However, producing an assembly that is completely phased at the chromosome level for both haplotypes of a diploid genome remains a challenge. Here, as part of the Vertebrate Genomes Project, we used a trio-binning approach^{7,8} to produce a chromosome-level, fully haplotype-resolved diploid genome assembly for the common marmoset, *C. jacchus*. This New World primate has been established as an animal model for a broad range of biomedical research such as neuroscience, stem cell biology and regenerative medicine^{2,3}. With our high-quality diploid assembly, we discovered new properties of heterozygosity on both autosomes and sex chromosomes of this primate species.

Diploid genome assembly

We generated 63×-coverage PacBio continuous long reads, 55× 10X Genomics Chromium linked-reads, 154× Bionano optical molecules, 105× chromosome conformation capture (Hi-C) reads from a captive male F₁ marmoset and 70× short-read sequences from the DNA of both parents (Supplementary Table 1, Supplementary Fig. 1). We used an updated version of TrioCanu^{7,8} to bin the PacBio long reads of the F₁ marmoset via *k*-mers of the parental short reads, and assembled each set into haploid-specific contigs, which were independently scaffolded with the 10X, Bionano and Hi-C data⁸ (Extended Data Fig. 1, Supplementary Fig. 2, Supplementary Tables 2, 3). The final contig and scaffold NG50 values after manually curation were 7.7 Mb and 146 Mb for the maternal assembly and 12.1 Mb and 136 Mb for the paternal

assembly, respectively. *k*-mer assessment indicated that the assemblies were fully phased (Extended Data Fig. 2a, Supplementary Figs. 3, 4). Each haploid genome includes 22 autosomes and each of the two sex chromosomes (X and Y), with 99.45% and 98.94% of the maternal and paternal alleles assigned to chromosomes, respectively. The assembled chromosome lengths showed a clear linear correlation with the estimated marmoset karyotype lengths^{8,9} (Extended Data Fig. 2b, Supplementary Note, Supplementary Tables 4, 5, Supplementary Fig. 5). Although marmosets show prevalent genetic chimerism between twins and triplets in utero¹⁰, the chimeric level of the F₁ male muscle sample used in this study was very low, as expected¹¹ (Extended Data Fig. 1d–g, Supplementary Fig. 6, Supplementary Tables 6, 7, Supplementary Note).

We estimated the single-base-pair accuracy rate to be 99.996% for the maternal assembly and 99.998% for the paternal assembly (Supplementary Note, Supplementary Fig. 7, Supplementary Tables 8, 9). About 93% and 88% of the gaps in the previously published marmoset reference genome cj3.2¹² were closed in our maternal and paternal assemblies, respectively, and both showed an increase of over 290-fold in contig N50, with 95.75% and 93.62% of the contigs being over 1 Mb, respectively (Extended Data Fig. 2c). Iso-Seq full-length transcriptome data also suggest a high completeness of our assembly (Supplementary Note, Supplementary Tables 10, 11). Comparison with two other recently released chromosome-level assemblies (cj1700 and cj2019) showed 16 large intra-chromosome-level structural variants (SVs) (larger than 1 Mb) and 3 inter-chromosomal SVs (Supplementary Tables 12, 13). PacBio long reads and 10X linked-reads confirmed that our assemblies were correct (Supplementary Figs. 8, 9, Supplementary Tables 12–14). However, these differences may also be due to the large structural polymorphisms.

Heterozygosity between parental genomes

In traditional genome-sequencing efforts, heterozygosity is normally estimated by mapping sequencing reads onto a mosaic reference genome, resulting in limited phase information of the heterozygous variants. Our assemblies enable us to directly compare the two parentally inherited genomes and identify the full spectrum of genetic variants between the parental alleles, including single nucleotide variations (SNVs), insertion and deletions (indels) and large SVs (Supplementary Fig. 10). We identified 3.47 million SNVs and around 232,000 short (maximum of 50 base pairs (bp)) indels across the whole genome (Fig. 1a), with 96.5% SNVs confirmed by short-read mapping. PCR experiments validated 99.6% and 95.2% randomly selected SNVs and short indels (Supplementary Note, Supplementary Tables 15–17), indicating that our diploid assembly enabled us to detect allelic variants with considerably high accuracy. We found a correlation between SNV rate and indel rate (Supplementary Fig. 11a), in

which both displayed a unimodal distribution across the genomes (Supplementary Figs. 11b, 12). Consistent with laboratory inbreeding, we observed 28 genomic regions with long runs of homozygosity (Fig. 2a), with the longest one spanning more than 10 Mb (Supplementary Fig. 13a). This pattern can also be detected in other marmoset samples with short-read resequencing data¹³ (Supplementary Fig. 13b, Supplementary Table 18), suggesting that captive marmosets are suffering a notable reduction of genetic diversity.

Fig. 1: Distribution of SNVs, small indels and SVs in a diploid marmoset genome.

 figure1

a, Heterozygosity landscape patterns between the two haploid marmoset genomes. Tracks from inside out (I–VI): distribution of runs of homozygosity (ROH) (>1 Mb), SNV density (window size, 500 kb; range, 0–0.85%), small indel (<50 bp) distribution (y axis, indel length), large indel density (≥ 50 bp; window size, 1 Mb; count, 0–9), CNV density (window size, 1 Mb; count, 0–9) and karyotype. The links in the

outermost circles denote differences in translocation events between maternal (inner) and paternal (outer) assemblies (VII). Triangles indicate locations of the de novo mutations in parental alleles. **b**, Schematic showing the proportion of parental sources of the de novo mutations.

[Full size image](#)

Fig. 2: Structures of sex chromosomes in marmosets and humans.



a, Alignment between the marmoset X and Y chromosome reveals a PAR of around 1 Mb in each chromosome. Dashed lines show the boundaries between the PAR and SDR. Alignment between the human and marmoset X chromosome also reveals different PABs between the two species, and an inversion near the marmoset PAB. Grey, PAR genes; orange, MSSDR genes; red, ancestral SDR genes. *ARSE* is also known as *ARSL*. **b**, Distribution of ampliconic genes in the marmoset (yellow) and human (purple) X chromosome. Green, genes that are ampliconic in both species. The copy number for each ampliconic gene is shown in parentheses. Asterisks indicate partial genes. Ampliconic genes with testis-specific expression are shown as the bottom half of the panel for each species. *IDS2* is also known as *IDSP1*.

[Full size image](#)

Heterozygous variation in regulatory or coding regions could result in allele-specific expression profiles or different products of the same genes from the two alleles¹⁴. We found that approximately 1.1% of SNVs and 0.58% of indels were located in protein-coding genes or regulatory regions. In particular, 8,144 SNVs caused non-synonymous substitutions and 274 indels caused frame-shifting mutations, which can produce allele-specific transcripts and proteins. This observation was validated by the Iso-Seq data, in which we detected that 2,537 genes produced transcripts with variation in open-reading frames from the parental alleles (Supplementary Fig. 14).

SVs contribute substantial genetic diversity with important evolutionary and medical implications. By comparing the two haploid genomes, we identified 11,663 SVs (larger than 50 bp), including 6,064 large indels, 27 inversions, 34 translocations, 5,514 copy number variations (CNVs) and 24 inverted translocations (Fig. 2a, Supplementary Table 19). We validated 95.7% of the large indels and 74.2% of the SVs with PacBio long reads, as well as 14 of 17 randomly selected large indels by PCR (Supplementary Fig. 15, Supplementary Table 20). By counting all types of variation between the two haploid genomes, we estimate the overall rate of heterozygosity on the autosomes of the sequenced individual to be around 1.36%.

Large heterogeneous SVs could cause a high incidence of chromosomally unbalanced gametes and thus are normally rare¹⁵. We found that 72% of SVs were shorter than 1.5 kb, with an average length of about 3.5 kb. The longest SV was a 304-kb inversion (Supplementary Fig. 16). We observed a higher density of LINE (L1) elements around the inversions ($P = 0.03752$, one-sided t -test). The indel peak at a length of 300 bp were enriched with Alu repeats (Supplementary Fig. 17a; $P = 2.2 \times 10^{-16}$, Chi-squared test, [Supplementary Note](#)). About 33% of the inversion variations between haplotypes were located between two inverted repeat sequences (Supplementary Fig. 17b), indicating that they were introduced by a repeat mechanism¹⁶. We detected and validated 58 genomic translocation events that differed between the two haplotypes, including 50 genes (Fig. 2a, Supplementary Table 21). About half of the affected genes were completely translocated from one allele to a different genomic location in the other allele. The mechanism driving such translocations remains to be elucidated.

De novo germline mutations

Germline mutations are the source of genetic diversity and the driving force of both evolution and genetic diseases¹⁷. However, finding de novo germline mutations is a challenging task, as in traditional assemblies less than half of the mutations can be phased to parental origin¹⁸. A fully diploid assembly enables us to use each parental haplotype independently as a reference to detect de novo mutations, and validate the loci detected independently from the two references as controls for false-positive calls

(Methods, [Supplementary Note](#)). We detected nine validated de novo mutations in this trio from the approximately 41% of callable sites in both maternal and paternal genomes (Fig. [1a](#), Supplementary Table [22](#)). The paternal-to-maternal ratio contribution of de novo mutations to the child was 2:1 (Fig. [1b](#)), which is lower than that in humans (4:1)^{[18](#)} but similar to the closely related owl monkey (2.1:1)^{[19](#)}. Our results suggest a mutation rate of 0.43×10^{-8} de novo mutations per site per generation for the marmoset. Using this estimated rate and the evolutionary branch length of marmoset substitutions inferred from whole-genome alignments^{[20](#)}, we estimated a divergence time between New World monkeys and humans at around 48.7 million years ago (Ma), which is close to what was estimated from data for the owl monkey^{[19](#)}.

New sex-differentiation region in the marmoset

On the basis of the sequencing depth of parental short reads on the F₁ male assembly ([Methods](#)), we identified X-linked sequences of around 147 Mb, with over 99% in a single X chromosome scaffold (Supplementary Table [23](#)). As the Y chromosome is enriched with repeat elements and segmental duplications, we de-collapsed unplaced and potential Y-linked scaffolds^{[21](#)} (Supplementary Fig. [18a](#)) then combined read-depth information and Hi-C interactions to identify final Y-linked sequences of 13.85 Mb (Supplementary Fig. [18b](#), Supplementary Table [24](#), Methods). This is smaller yet closer to the 20-Mb karyotype estimate^{[9](#)} and longer than that in other assemblies (Supplementary Table [25](#)).

Our diploid assembly resolved pseudoautosomal regions (PARs) of both the X and the Y chromosome, whereas most other male genomes result in collapsing PARs into one copy with mixed origin. This permits the precise identification of the pseudoautosomal boundary (PAB) in marmosets (Fig. [2a](#)). Marmoset PARs contain nine protein-coding genes, all of which are also found in the human PAR. However, an inversion was found between human and marmoset PARs, and it is likely to occur specifically in the marmoset lineage near its PAB (Fig. [2a](#), Supplementary Fig. [19](#)). In addition, downstream of this inversion in the X chromosome, we observed a genomic sequence spanning six human PAR orthologues that had become a new sex-differentiation region (SDR) in the marmoset (Fig. [2a](#)). Three genes in the region, *P2RY8Y*, *AKAP17AY* and *ZBEDY*, have been reported to be SDR-linked^{[22](#)}. We found that they were not collinear with the X chromosome, but were translocated to the middle of the Y chromosome (Fig. [2a](#), Extended Data Fig. [3](#), Supplementary Table [26](#)). All of the Y copies accumulated more mutations than their corresponding X copies (Supplementary Fig. [20](#)). Their X–Y genetic divergence was significantly higher than that of the PAR (one-sided *t*-test, $t = 5.7694$, $P = 1.468 \times 10^{-6}$) (Supplementary Table [27](#)), but significantly lower than that of the ancestral SDR (one-sided *t*-test,

$t = -8.9434$, $P = 3.319 \times 10^{-13}$) (Supplementary Fig. 21), suggesting that its recombination suppression began recently. These new SDR genes also showed a bias in expression in females; however, they were not significantly different from PAR or ancestral SDR genes (Supplementary Fig. 22).

We next applied two divergence-based methods to date the formation of the marmoset-specific SDR (MSSDR) (Supplementary Note, Supplementary Tables 28, 29). On the basis of the marmoset mutation rate estimated above, we inferred that the MSSDR formed at 5.23–9.41 Ma (Supplementary Tables 30, 31). Applying lower mutation rates of the closely related African green monkey (1.11×10^{-9} mutations per position per year (PPPY))²³ and the owl monkey (1.20×10^{-9} PPPY)²⁴, the formation of the MSSDR was dated at 6.67–12.97 Ma. All of these results indicate that the expansion of the SDR in the marmoset is an evolutionarily young event.

The translocation of the MSSDR on the Y chromosome makes the PAR of the marmoset the shortest among primates recorded so far²⁵. As X–Y recombination during male meiosis is limited to the PAR, this region is known to contain the highest per-site recombination rate in the genome²⁶ and an increased intensity of GC-biased gene conversion²⁷. Consistently, we observed a higher GC content in the marmoset PAR relative to the human PAR (one-sided t -test, $t = 3.1327$, $P = 0.0011$) (Supplementary Fig. 21). We also observed a 4.3-fold-higher rate of heterozygosity in the marmoset PAR (0.52%) compared to the average rate in autosomes (0.12%) (Supplementary Fig. 23), suggesting that more-intense recombination in the shorter marmoset PAR causes more mutations.

Ampliconic genes—genes with highly similar adjacent copies—are a notable and enigmatic feature of most sex chromosomes²⁸. They are often found specifically expressed in the testes and experience a very rapid turnover of copy number²⁹, leading to the hypothesis that ampliconic genes are involved in sexual antagonism²⁹. We detected 22 ampliconic genes on the marmoset X chromosome (Fig. 2b), of which 12 showed testes-restricted expression, at a proportion close to that in humans (40%). Six of the marmoset X-linked ampliconic genes were also present in the human X chromosome with overall similar duplication patterns, suggesting that they originated from a common ancestor (Fig. 2b, Supplementary Fig. 24). The marmoset Y chromosome also contains five multi-copy genes, of which two (*TSPY* and *RBMY*) are also ampliconic genes in the human Y chromosome³⁰. These results suggest that the sex-linked ampliconic genes have evolved under a very dynamic duplication process during primate evolution.

Rapid evolution of the marmoset Y chromosome

In contrast to the X chromosome, which maintained overall conserved synteny during primate evolution (Supplementary Fig. 25), we found that the Y chromosome experienced rapid structural changes. This is probably due to the accumulation of mutations as a consequence of Muller's ratchet effect³¹. We detected at least three large inversions and one large translocation involving genes between the male-specific region of the Y chromosome (MSY) in humans and marmosets. The human MSY contained 48 protein-coding genes and the marmoset MSY contained 46, but with different gene properties (Fig. 3a): Twenty-two human MSY genes were absent in the marmoset; of these, 15 of evolved during the evolution of the Hominoidea and the rest were ancestral gametologues that have become inactive or been lost in marmosets (Fig. 3a). Several MSY genes crucial for spermatogenic functions (for example, *HSFY1* and *VCY*) ([Supplementary Note](#)) have been lost in marmosets, or lost function owing to frame-shift mutations (for example, *USP9Y*) (Supplementary Fig. 26). The loss of these genes might be associated with the monogamous social structure of marmosets³², which potentially alleviates sperm competition. These findings indicate that although it has been claimed that the marmoset has similar patterns of spermatogenesis to humans³³, there are probably some key differences associated with these genes.

Fig. 3: Comparison of sex chromosomes across species.



a, Y-chromosome gene synteny between humans and marmosets. Lines between human and marmoset indicate one-to-one orthologues. Distance is not drawn to scale. The number of paralogues in unplaced de-collapsed Y-linked scaffolds are marked in parentheses. *ADT3* is also known as *SLC25A6*; *AC007244.1* is ENSG00000286265 under Ensembl release 98. **b**, Six evolutionary strata found in marmoset sex

chromosomes. The colour of the links between X and Y gametologues indicates the pairwise dS value. *THOC2X-Y* was not included in any strata because it is a very recently emerged gametologue pair formed via duplication. **c**, Correlation between pairwise dS and X-chromosome position for 14 X–Y SDR gametologues outside the marmoset PAR. Each point represents one gametologue.

[Full size image](#)

By contrast, the marmoset MSY only contains two genes that are absent in humans—*ARSHY* and *THOC2Y*. *THOC2Y* was thought to be lost early in the eutherian common ancestor and exhibits a high rate of synonymous substitutions (dS value) with its gametologue in marsupials³⁴. However, we found that the marmoset *THOC2Y* has a very low dS value (dS = 0.0502) with its X-linked gametologue, suggesting that it is not the ancestral gene but a marmoset-specific MSY gene that has recently been duplicated from its X-chromosome counterpart (Supplementary Fig. 27a). In humans, *THOC2* is widely expressed in many tissues and interacts with *XPO4*³⁵ which mediates the import of SOX2 and SRY proteins. In the marmoset, both *THOC2X* and *THOC2Y* have become testis-specific genes (tissue specificity index (Tau) > 0.8) (Supplementary Fig. 27b). The remaining MSY genes are present in both species, but some show CNVs (Fig. 3a, Supplementary Fig. 28).

Of the 46 marmoset MSY genes, 18 have their gametologues on the X chromosome (Fig. 3b), and their pairwise dS values between X and Y increased with their distance to the PAB on the X chromosome (Pearson's $r = 0.8342$, $P = 0.0002$) (Fig. 3c, Supplementary Table 27), as in humans³⁶. According to the sequence divergence as well as the phylogeny, we inferred the presence of six evolutionary strata in marmoset sex chromosomes, which we named from the oldest to the youngest, S1 to S6 (Fig. 3b). S1–S4 are shared with humans^{22,36} (Supplementary Fig. 29), suggesting an ancient origin. S5 of the marmoset contained one gametologue pair, *ARSHX-Y*, which has a low pairwise dS value (0.0605) close to that of gametologues in the MSSDR (Supplementary Table 27). In addition, the X copy of the marmoset is clustered with its Y copy instead of the X copies of other primates (Supplementary Fig. 30), suggesting that this stratum formed specifically in New World monkeys. S6 contained six pairs of gametologues, all residing in the MSSDR. The pairwise dS values of S6 gametologues are much lower than those of the ancestral gametologues (Fig. 3b). Notably, three gametologues (*DHRSX-Y*, *ASMTX-Y* and *CD99X-Y*) in S6 display the highest ratio of pairwise non-synonymous to synonymous substitutions rates (dN/dS value) among all gametologues (Supplementary Table 27). Of them, *CD99X* and *CD99Y* show tissue-specific expression in ovary and testis, respectively (Supplementary Table 32). These features imply a strong directional selection link to sex differentiation on these genes once they were translocated from the PAR in the marmoset.

Genetic basis of marmoset biological traits

As a representative species of Callitrichidae, the marmoset has many notable biological traits, such as small body size³⁷, twinning^{12,38}, exudate feeding³⁹ and maintaining bone density during ageing owing to reduced levels of gonadal oestrogen (thus marmosets do not suffer from age-related osteoporosis^{40,41}). To further expand our knowledge on the evolution of these biological features, we scanned for and identified 204 positively selected genes (PSGs) in the marmoset genome and 38 PSGs in the common ancestor of New World monkeys (Supplementary Tables 33–35). We have manually checked these PSGs to avoid potential artefacts due to alignment errors or the differences in sequencing and annotation methods across genomes, although we cannot fully rule out the possibility that the differences in quality between the compared assemblies could have affected some of these results. Among these genes, we found two that may be linked to manifesting diminutive size. Mutations of *ZDHC13* (PSG in marmosets) in mice causes post-translational lipid modification, resulting in weight loss and reduced bone mineral density⁴². *FGFR1* (PSG in New World monkeys) regulates a feedback signal to control the rate of differentiation of osteoblasts⁴³, and mutations cause autosomal dominant skeletal disorder⁴⁴. (Supplementary Fig. 31).

Marmosets exhibit several unique reproductive adaptations³⁷, which include sharing a common placental circulation with siblings⁴⁵ and the suppression of reproduction in nondominant females⁴⁶. Previous studies have identified several candidate genes that might be related to these traits^{12,38}. We found three marmoset PSGs (*PCSK6*, *NR1D1* and *TGIF1*) that might also contribute to their reproductive adaptation. *PCSK6* is expressed in numerous ovarian cell types and *PCSK6*-mutant mice exhibit progressive loss of ovarian function and formation of ovarian pathology⁴⁷. *NR1D1* is a circadian clock gene and might interact with the gonadotropin-releasing hormone signalling pathway⁴⁸. Knockout of this gene in mice reduces fertility⁴⁹. *TGIF1* is a repressor and reversibly modulates members of the TGF-β/SMAD signalling pathway, which has an important role in reproductive processes, including follicular activation, ovarian follicle development and oocyte maturation⁵⁰.

We found three marmoset PSGs (*BCL2L14*, *HOMER3* and *CHADL*) involved in osteoclastogenesis and bone metabolism. *BCL2L14* encodes a member of an anti-apoptotic family of proteins, which are known to suppress the functions of osteoclasts⁵¹. *HOMER3* participates in osteoclastogenesis and bone metabolism. Deletion of this gene markedly decreased tibia bone density, resulting in bone erosion in mice⁵². *CHADL* encodes a collagen-associated small leucine-rich protein and may influence the differentiation of chondrocytes by acting on its cellular

microenvironment⁵³. Further experiments are needed to investigate the potential roles of the positively selected substitutions in specialized bone metabolism in marmosets.

Captive marmosets in laboratories are intermittently plagued by gastrointestinal disorders⁵⁴, which may result from dietary differences in captivity versus the wild⁵⁵. Wild marmosets feed on gums as one of their primary food sources, to acquire energy and minerals³⁹. Compared to captive marmosets, the gut microbiome of wild marmosets is more enriched with *Bifidobacterium*⁵⁶. This probiotic bacterium may function to assist the digestion of gum⁵⁷. We found that *PTGS1*, which mediates the gastrointestinal inflammatory reaction, was under positive selection in the marmoset. Expression of this gene is higher in the intestinal mucosa of obese rats than rats of a normal weight^{58,59}, but its expression is reduced to normal levels when rats are fed with *Bifidobacterium*⁵⁹. It seems that *PTGS1* may have a role in the gastrointestinal function of marmosets, which might be regulated by their exudivore diet through the probiotic bacteria.

Genomic insights for biomedical research

Marmosets are becoming widely used as primate biomedical models in the neurosciences². Here, we compared 2,533 genes related to brain development and neurodegenerative diseases, and found that the majority are highly conserved between marmosets and humans in both sequence and copy numbers (Supplementary Fig. 32). However, we detected 24 genes that show CNVs and 8 genes that are under diversification selection between the two species. These may be associated with differences in the brain between humans and marmosets (Supplementary Fig. 33, Supplementary Tables 36, 37, [Supplementary Note](#)).

Pathogenic effects of mutations are highly dependent on their genomic context^{60,61}. We therefore scanned the marmoset genome for human pathogenic sites that cause or increase the risk of nervous system diseases. Notably, four genes in marmosets include substitutions that encode amino acids that are pathogenic in humans: *APOE*^{C130R}, *GBA*^{N227S}, *SNCA*^{A53T} and *PAH*^{R176Q} (Supplementary Figs. 34–36, Supplementary Table 38). All of them are fixed in the 12 marmoset individuals with genomic data¹³. Comparison with other primates suggests that the *GBA* and *PAH* genomic contexts are unique to the marmoset (Supplementary Figs. 35, 36). The presence of these two marmoset genes encoding amino acids that are pathogenic in humans suggests that this species might have evolved specific mechanisms to compensate for their pathogenic effects, and highlights the critical need to consider variation in the genomic context when using marmosets as models in human disease research.

Benefits of a diploid assembly

The ultimate goal of creating a reference genome assembly is to produce a gapless, chromosome-level assembly with all sequences fully phased into haplotypes. Several previous efforts have been made towards this goal using the information of a pedigree and/or long reads^{5,6}. Our findings demonstrate the power of using a trio-binning approach, in combination with long-read sequencing^{7,8}, to produce a diploid genome with the two parental haplotypes assembled independently. This method captures the full range of heterozygous variations at high rates of accuracy between the two alleles, resulting in a rate of heterozygosity that is 10 times higher than that found in most genomic studies that use only heterozygous SNVs. Our diploid assembly includes sequences that are more complete for both sex chromosomes—a particular challenge in the case of the Y chromosome with its densely repetitive elements. Whenever trio samples are available, this sequencing and assembly strategy offers the means to generate high-quality, phased reference genomes for a range of species, especially those with high rates of heterozygosity.

Methods

Sample collection, processing and sequencing

Samples were collected at an AAALAC-accredited facility from an F₁ male marmoset (3 months old) at The Rockefeller University, under USDA- and IACUC-approved protocols. The quadriceps muscle was dissected, collected and flash-frozen in liquid nitrogen immediately after euthasol administration; we extracted genomic DNA from the muscle sample. This DNA was used for Bionano optical mapping, PacBio library preparation and SMRT sequencing, 10X Genomics linked-read sequencing, Arima Hi-C library preparation and Illumina sequencing. We collected blood samples from both parents of the F₁ male (mother, 3 years 10 months; father, 3 years 7 months) for Illumina sequencing by shaving the area (thigh for saphenous vein and tail for lateral tail vein), applying 2% lidocaine jelly, prepping the vein with alcohol and collecting less than 2 ml blood per sample (1× sample for male and female) via intravenous blood draw into EDTA tubes.

For annotation purposes, we collected more than 18 tissues from the brother of the F₁ male. Blood was collected from the saphenous vein pre-mortem using the method described above. All additional tissues were dissected, collected and flash-frozen in liquid nitrogen or powdered dry ice immediately after euthasol administration; the brain and testes were dissected at first and all tissues were dissected and frozen within a 30-min period post-mortem. RNA integrity numbers (RINs) for all tissues used for PacBio SMRT sequencing and Iso-Seq analysis ('Sample processing and sequencing' in [Supplementary Note](#)) were high, ranging from 8.2 (lung) to 9.9 (cerebellum). We

performed Mashmap quality control analyses of sequencing reads to rule out any potential contamination or poor sequencing before assembling (Supplementary Fig. 1).

Sample size, randomization and blinding

We aim to use parental SNVs to determine and phase the two haplotype genomes of the offspring, thus the sample size for genome sequencing is three. Bioinformatic analyses were performed with all available data. Randomization for genome and transcriptome sequencing is not applied in this study. For SNV and indel PCR validation, variation sites were randomly selected by the Linux command ‘sort –R’. Blinding was not necessary for genome and transcriptome sequencing or PCR validation of genetic variation. The study aims to identify the genetic differences inherited from parental genomes, so only the DNA sample of the F₁ individual was used for PCR validation.

Genome assembly

We combined the previously developed trio-binning approach⁷ and further advanced the Vertebrate Genomes Project (VGP) assembly pipeline⁸ for scaffolding, to generate the haplotype-phased marmoset assembly (Supplementary Fig. 2). In the first step, we used TrioCanu (v.1.8+287) to bin PacBio long reads of the F₁ male into maternal and paternal haplotypes using haplotype-specific 21-mer markers generated from the Illumina short reads of the mother and father. After binning, TrioCanu independently generated contigs for each haplotype (haplotigs). From here on, the maternal and paternal haplotigs underwent the same steps independently. Separately, we assembled the mitochondrial genome with the mitoVGP pipeline (v.2.2)⁶² and added it to the haplotigs to keep any raw mitochondrial reads from being mapped to nuclear sequences, which would result in lower sequence quality after polishing. We used Arrow from SMRT Link (v.6.0.0.47841) to improve base-calling accuracy and purge_dups (v.1.0.0)⁶³ in an adapted trio mode to remove overlaps at the ends of contigs. The resulting polished, purged haplotigs were scaffolded in three stages: first, we used the 10X linked-reads in two rounds of Scaff10X (v.4.1.0) (<https://github.com/wtsi-hpag/Scaff10X>) to generate the primary scaffolds; second, we generated Bionano cmaps and used Bionano Solve (v.3.2.1_04122018)⁶⁴ for hybrid scaffolding and to break mis-assemblies; third, we used Salsa2 (v2.2)⁶⁵ to generate chromosome-level scaffolds using the molecular contact information from Hi-C linked reads. Finally, we performed a second round of Arrow polishing on the maternal and paternal scaffolds with the binned long reads. During this round of polishing, gaps between contigs were closed by the gap-filling function of Arrow. The parental haplotypes were then combined in a single assembly and underwent two rounds of short-read polishing using Long Ranger (v.2.2.2)⁶⁶ for short-read alignment and

freebayes (v.1.3.1)⁶⁷ for polishing ([Supplementary Note](#)). After splitting the scaffolds by haplotype and removing the mitochondrial genome from each assembly, the two assemblies (named mCalJac1.mat and mCalJac1.pat) underwent manual curation using the gEVAL tool⁶⁸, in particular to correct structural assembly errors. In the abbreviated name, m is mammal; CalJac is the abbreviated Latin species name; 1 is the first VGP assembly of this species; and mat and pat are maternal and paternal haplotypes, respectively.

Identification of sex-linked sequences and additional Y-chromosome assembly

To identify X-linked and Y-linked sequences in mCalJac1 (GCA_011100555.1), we mapped parental short reads to the assembly with BWA ALN (v.0.7.12)⁶⁹. Coverage was extracted with SAMTools (v.1.2) and normalized by the peak coverage. In the identification of X-linked sequences, the normalized female-versus-male (F/M) coverage ratio was calculated and plotted in a 5-kb window, and scaffolds with a F/M coverage ratio within the range 1.5 to 2.5 were identified as X-linked. In Y-linked sequence identification, the normalized F/M coverage ratio was calculated and plotted in a 2-kb window and scaffolds with a F/M coverage ratio within a 0.0 to 0.3 range were identified as Y-linked. We further manually examined large scaffolds in the maternal and paternal assemblies and included the Y chromosome Super_scaffold_pat_24. This scaffold was missing in the 0.3 cut-off condition because the first 1-Mb sequence shows an equal pattern of female and male coverage as the PAR.

In these previous steps, only Y-linked sequences of around 6 Mb were identified, about 14 Mb smaller than the expected 20-Mb size based on karyotyping. As sex chromosomes are notoriously difficult to assemble, and no primate has had a complete Y chromosome sequenced, to determine whether we missed any Y-chromosomal sequences, we performed additional assembly steps. We used Hi-C interaction information to call back potential Y-linked contigs that were filtered by our strict filtering on the basis of low female read depths. Arima Hi-C reads were mapped to mCalJac1 and the Hi-C interaction matrix was generated by HiCPro (v.2.10.0)⁷⁰. At 10-kb resolution, we extracted the interaction strength of every unplaced scaffold to each autosome, X or Y chromosome. Unplaced scaffolds with more than five interaction strength values to both autosomes/X and Super_scaffold_pat_24 were selected, and the interaction strength with the autosomes/X and the interaction strength with Y was compared for each scaffold by two-sided Wilcoxon rank-sum test. With a false discovery rate (FDR)-corrected *P* value cut-off of 0.01, we further identified 17 scaffolds that show a significantly higher interaction with Super_scaffold_pat_24 than with other chromosomes, and considered them putative Y-linked scaffolds. To validate this result, we collected sequences of bacterial artificial chromosome mapped to the

marmoset Y chromosome from NCBI and mapped them to mCalJac1 with minimap2. Almost all BAC sequences mapped to the eight Y-linked scaffolds were identified by the sequencing depth method. One, BAC AC279170.1, was previously missed, but can now be mapped to pat_scaffold_39_arrow_ctg1, which was identified by the Hi-C method. Thus, the dataset identified by the Hi-C method complements the dataset identified by the sequencing depth method. Combining these two datasets, a total of 25 potential Y-linked scaffolds (around 14.13 Mb) were identified from mCalJac1 (Supplementary Table 39).

Next, we mapped the PacBio raw reads to the assembly and found that some of the potentially Y-linked scaffolds had regions of considerably high coverage compared to autosomes and X chromosomes, indicative of collapsed sequences, which would cause the artificially high level of Hi-C interaction and introduce false-positive Y-linked sequences. To de-collapse these regions, we used the Segmental Duplication Assembler (SDA)²¹ and mapped the SDA-assembled contigs to their original scaffolds with minimap2 to remove potential assembly artefacts. To replace the original collapsed sequence in the assembly with the most plausible candidate de-collapsed sequence, we applied ‘the longest rule’: start with the de-collapsed sequence in the SDA output that has the longest stretch mapping back to the original scaffold, then select the second sequence with the longest match that does not overlap the previous one, and so on. Once all the non-overlapping de-collapsed sequences with the longest matches were selected, we filled in the gaps using the original scaffold as a backbone, and left 1,000 ‘N’s (gap indicating unknown nucleotides in the assembly) between each contig.

To further exclude false positives from the de-collapsed Y dataset, we refiltered the sequences with the sex-differential depth ratio and the Hi-C interaction criteria as mentioned above (Supplementary Table 24). However, as only the uniquely mapped reads were used in calculating the Hi-C interaction between unplaced scaffolds and autosomes/X/Y, our results underestimate Y-chromosomal DNA, including many de-collapsed Y scaffolds with multiple copies that might still be missed.

Detection of SNPs, indels and SVs using whole-haplotype genome alignment

To call heterozygous sites between the two haploid sequences, independent of the GenomeScope calculation, we first performed a Mummer (v.3.23) alignment with the parameters of ‘nucmer -maxmatch -l 100 -c 500’. Because our assemblies span most repetitive sequences, repeat-masking treatment was not necessary before conducting the Mummer alignment. A series of custom scripts (<https://github.com/comery/marmoset>) identified and sorted our SNPs and indels in the alignments. We used svmu (v.0.4-alpha)⁷¹, Assemblytics (v.1.2)⁷², and SyRi (v.1.0)⁷³,

to detect SVs from Mummer alignment. After several test rounds, we found that svmu reported more accurate large indels, and Assemblytics detected CNVs, particularly tandem repeats, whereas SyRi detected other SVs well. We used these three methods and combined the results as confident SVs. We used default parameters for svmu, Assemblytics, and recommended nucmer alignment for SyRi (<https://schneebergerlab.github.io/syri/>).

To generate a high-quality SV dataset, we manually checked all inversions and translocations with the following steps: (1) clip 300 bp of upstream/downstream flanking sequence of each break point between the two haplotypes, blast against local PacBio reads with threshold identity >96% and aligned length >550 bp, and require the SV region where the maternal and paternal sequences aligned to have high similarity (>90%); (2) if (1) failed, then check the 10X linked-read count between a 5-kb flanking region; (3) if any break point is not supported by 10X linked-reads, check the Hi-C heat map of this region; if it shows an inversion or translocation pattern on heat map or an ambiguous situation, then remove it.

To evaluate the accuracy of SV detection, we searched the binned PacBio reads around the break points of both maternal and paternal assemblies for all indels in chromosome 1. We looked for one of the following three features to determine the indel as accurate: (1) at least one single PacBio long read from each haplotype that spans the entire indel region with the variation found in each haplotype; (2) overlapping PacBio reads that span the two break points; or (3) manually validated PacBio read alignment by the Integrative Genomics Viewer (IGV)⁷⁴. Finally, we found that 95.7% of indels are correct when considering the breakage location; however, 74.2% are accurate when considering both boundary and location.

Estimation of sequencing error and polishing error

To calculate sequencing errors and polishing errors, we established a confident SNP set as a criterion. We used three individual approaches to detect SNPs between two haplotypes: (1) retrieved heterozygous sites from the Mummer alignment between the maternal and paternal haplotypes excluding the sex chromosomes (setA, containing 3.48 million SNVs); (2) GATK pipeline based on mapping of 10X linked-reads from the F₁ offspring (setB); and (3) SAMTools (v.1.8) mpileup followed by bcftools also based on 10X linked-reads mapping (setC). Then, a raw SNP dataset was generated by a two-step procedure: first taking the intersection of setB and setC to generate Set1 (3.72 million SNVs), followed by taking the union of setA and Set1 to get Set2 (3.77 million SNVs). We then took these two sets and selected among them to a high-quality 3.58-million SNP Set3 (Supplementary Fig. 10) with the following criteria applied: (1) 10X linked-read depth lower than 10; (2) filter out sites that do not align to the two haplotype assemblies; (3) filter out sites that we could not call a typical haplotype on

the basis of much less than 50% nucleotide distribution ($\pi > 0.4$ and the third highest depth > 5 , in which π is calculated as: $\backslash(\backslash(pi = 2\backslash times (AT + AC + AG + TC + TG + CG) / (\backslash rm{Totaldepth}) \backslash times (\backslash rm{Totaldepth} - 1)))$)

and A , T , C and G represent the sequencing depth of base A, T, C and G for each site. For example, a distribution of ‘A:20; T:20; C:14; G:0’ indicates a complex condition. We also collected the mapping information from raw PacBio reads and corrected PacBio reads. This allowed us to establish an evidence chain of how the bases in each haplotype changed during assembling and polishing, which allowed us to classify different error types. We classified 195,751 sequencing error sites and 180,712 polishing error sites. The sequencing and polishing error rates were estimated to be 3.41×10^{-5} and 3.66×10^{-5} , respectively. We further validated the variants with PCR experiments ([Supplementary Note](#)).

Mutation rate analysis

The 10X linked-reads of the F_1 offspring and the parents’ short reads were mapped to each genome assembly independently (paternal and maternal assemblies). Duplicate reads and reads that mapped to more than one region were removed. Variants were called using GATK4 HaplotypeCaller in base-pair resolution mode, calling each single site of the genome. Two independent joint genotypes were produced: one for the three individuals (mother, father and F_1 offspring) mapped to the maternal assembly and one for the three individuals mapped to the paternal assembly. We identified a maternal candidate de novo mutation as a site for which the parents were homozygous for the reference (0/0) and the offspring was heterozygous (0/1) when mapped to the paternal genome. For validation, such a candidate site would be expected to have the parents homozygous for the alternative (1/1), and the offspring heterozygous (0/1) when mapped to the maternal genome. Similarly, a paternal candidate de novo mutation was identified as a site for which the parents were homozygous for the reference (0/0), and the offspring was heterozygous (0/1) when mapped to the maternal genome. Here, again, those candidates were validated if they also appeared in the parents as homozygous for the alternative (1/1), and in the offspring heterozygous (0/1) when mapped to the paternal genome. Additional filters were applied for sites, genotype quality, read depth and number of alternative alleles in the parents and allelic balance in the offspring ([Supplementary Note](#)). Finally, we removed any potential sites with sequencing errors, polishing errors or assigning errors, as well as sites that failed the PCR validation. To calculate a rate, we computed the number of callable sites in each genome as the number of sites for which both parents were homozygous for the reference and all individuals passed the depth coverage between half and two times the average depth for each individual, number of alternative alleles allowed, and genotype quality filters. We corrected those callable sites by a negative rate factor, alpha (α), which is the percentage of callable sites that would be filtered away by our site filters

(following a known distribution) and the allelic balance filter (which corresponds to the number of sites for which one parent was homozygous for the reference allele, the other parent was homozygous for the alternative allele, and the offspring would be heterozygous, but the reads supporting each allele would be outside our allelic balance filter). The mutation rate was calculated as:

$$\$\$ \mu = \frac{\text{Mutations}_{\text{maternal}} + \text{Mutations}_{\text{paternal}}}{\text{Callability}_{\text{maternal}} \times (1 - \alpha_{\text{maternal}}) + \text{Callability}_{\text{paternal}} \times (1 - \alpha_{\text{paternal}})} . \$\$$$

Confirmation of the order of Y-linked sequences

Marmoset Y-chromosome-specific BAC end reads²² were obtained from the NCBI trace archive and mapped to Y-linked sequences with BWA MEM. Only the primary alignment was kept for each read. BAC location on the Y chromosome from a previous report²² was also obtained and visualized in a dot plot to confirm the order of the Y-linked sequences in mCalJac1. To confirm the MSSDR translocation in the Y chromosome, we further checked PacBio and 10X linked-reads support at the flanking break point of the MSSDR of the Y chromosome.

Detection of PSGs

We used the BLAST reciprocal best hits (RBH) method ([Supplementary Note](#)) to identify high-confidence one-to-one orthologous genes among species, including three other New World monkeys (white-faced capuchin (*Cebus capucinus*), Ma's night monkey (*Aotus nancymaae*) and black-capped squirrel monkey (*Saimiri boliviensis*)); three old world primates (human (*Homo sapiens*), macaque (*Macaca mulatta*) and chimpanzee (*Pan troglodytes*)); and three outgroups (treeshrew (*Tupaia glis*), mouse (*Mus musculus*) and cow (*Bos taurus*)). The marmoset was set as foreground when detecting marmoset-specific PSGs, whereas the New World monkeys were set as foreground when detecting New World monkey-specific PSGs. A total of 13,995 one-to-one orthologous genes were identified. To minimize the effect of gene annotation, we retrieved the corresponding coding sequences that shared the same isoform with human. These genes were used as an input dataset to conduct multiple sequence alignment using PRANK (v.170427)⁷⁵ and guidance (v.2.02)⁷⁶ to improve the alignment. The positive selection sites within a specific lineage were detected by branch-site model in PAML (v.4.9i)⁷⁷. Genes with an FDR-adjusted *P* value of less than 0.05 were treated as candidates for positive selection. To minimize effects of assembly and alignment, we filtered candidate PSGs if (1) the positively selected site has gaps in more than two species; (2) the positively selected sites had more than two non-synonymous substitution forms (ignoring outgroup), and (3) the flanking region

(± 10 amino acids) showed over-alignment across species. We also performed a manual check for all individual PSGs to avoid any other false-positive caused by annotation or alignment. Finally, we used read mapping to check the PSG sites to avoid sequencing errors. After filtering, the numbers of PSGs with high confidence detected in marmosets and New World monkeys were 204 and 38, respectively.

Scan for pathogenic or risky mutations in marmosets

Mutation information was obtained from ClinVar (https://ftp.ncbi.nlm.nih.gov/pub/clinvar/tab_delimited/variant_summary.txt.gz, on 30 June 2020) and mutations that were designated to be pathogenic or risky were extracted. Nervous-system-related mutations were extracted with the following keywords: adrenoleukodystrophy, Alzheimer, amyotrophic lateral sclerosis, Angelman, ataxia telangiectasia, Charcot-Marie-Tooth, Cockayne, deafness, Duchenne muscular dystrophy, epilepsy, fragile X syndrome, Friedreich ataxia, Gaucher, Huntington, Lesch-Nyhan syndrome, maple syrup urine disease, Menkes syndrome, myotonic dystrophy, narcolepsy, neurofibromatosis, Niemann-Pick disease, Parkinson disease, phenylketonuria, Refsum disease, Rett syndrome, spinal muscular, spinocerebellar ataxia, Tangier disease, Tay-Sachs disease, tuberous sclerosis, Von Hippel-Lindau syndrome, Wilson disease. Related protein sequences of humans and marmosets were extracted and aligned with PRANK and targeted amino acid sites were scanned to determine whether the human pathogenic or risky mutation is in the marmoset. The genomic coordinates of related codons were extracted to check the alignment of the 12 marmoset individuals with whole-genome-sequencing data. Alignment was visualized and manually examined with Jalview (v.2.11.1.0)⁷⁸.

Reporting summary

Further information on research design is available in the [Nature Research Reporting Summary](#) linked to this paper.

Data availability

Raw sequencing data for the marmoset trio is available under the GenomeArk github (https://vgp.github.io/genomeark/Callithrix_jacchus/). Curatorial information and data mappings to maternal and paternal assemblies are available on the genome evaluation browser, gEVAL (https://vgp-geval.sanger.ac.uk/all_genomes.html). The maternal, paternal, and combined (paternal autosomes and Y chromosome + maternal X chromosome + mitochondrial) assemblies, as well as PacBio Iso-Seq data for annotation, are available under the NCBI BioProject [PRJNA560230](#). The genome assemblies have also been deposited at the CNGB Sequence Archive (CNSA) of the China National GeneBank Database (CNGBdb) with accession numbers CNP0001310 and CNP0001311.

Code availability

The assembly pipeline is available at <https://github.com/VGP/vgp-assembly>; see Supplementary Tables [2](#), [3](#) for the full list of tools used, versions and availability. Workflows and applets built for the VGP are available at DNAexus (<https://www.dnanexus.com/>). Custom scripts are available at <https://github.com/comery/marmoset> and <https://github.com/gf777/misc/tree/master/marmoset%20Y>.

References

1. 1.

Aleman, F. The necessity of diploid genome sequencing to unravel the genetic component of complex phenotypes. *Front. Genet.* **8**, 148 (2017).

[PubMed](#) [PubMed Central](#) [Article](#) [CAS](#) [Google Scholar](#)

2. 2.

Okano, H., Hikishima, K., Iriki, A. & Sasaki, E. The common marmoset as a novel animal model system for biomedical and neuroscience research applications. *Semin. Fetal Neonatal Med.* **17**, 336–340 (2012).

[PubMed](#) [Article](#) [Google Scholar](#)

3. 3.

Kishi, N., Sato, K., Sasaki, E. & Okano, H. Common marmoset as a new model animal for neuroscience research and genome editing technology. *Dev. Growth Differ.* **56**, 53–62 (2014).

[CAS](#) [PubMed](#) [Article](#) [PubMed Central](#) [Google Scholar](#)

4. 4.

Wood, A. R. et al. Allelic heterogeneity and more detailed analyses of known loci explain additional phenotypic variation and reveal complex patterns of association. *Hum. Mol. Genet.* **20**, 4082–4092 (2011).

[CAS](#) [PubMed](#) [PubMed Central](#) [Article](#) [Google Scholar](#)

5. 5.

Chin, C.-S. et al. Phased diploid genome assembly with single-molecule real-time sequencing. *Nat. Methods* **13**, 1050–1054 (2016).

[CAS](#) [PubMed](#) [PubMed Central](#) [Article](#) [Google Scholar](#)

6. 6.

Weisenfeld, N. I., Kumar, V., Shah, P., Church, D. M. & Jaffe, D. B. Direct determination of diploid genome sequences. *Genome Res.* **27**, 757–767 (2017).

[CAS](#) [PubMed](#) [PubMed Central](#) [Article](#) [Google Scholar](#)

7. 7.

Koren, S. et al. De novo assembly of haplotype-resolved genomes with trio binning. *Nat. Biotechnol.* **36**, 1174–1182 (2018).

[CAS](#) [Article](#) [Google Scholar](#)

8. 8.

Rhie, A. et al. Towards complete and error-free genome assemblies of all vertebrate species. *Nature* <https://doi.org/10.1038/s41586-021-03451-0> (2021).

9. 9.

Sherlock, J. K., Griffin, D. K., Delhanty, J. D. A. & Parrington, J. M. Homologies between human and marmoset (*Callithrix jacchus*) chromosomes revealed by comparative chromosome painting. *Genomics* **33**, 214–219 (1996).

[CAS](#) [PubMed](#) [Article](#) [PubMed Central](#) [Google Scholar](#)

10. 10.

Benirschke, K., Anderson, J. M. & Brownhill, L. E. Marrow chimerism in marmosets. *Science* **138**, 513–515 (1962).

[CAS](#) [PubMed](#) [Article](#) [ADS](#) [PubMed Central](#) [Google Scholar](#)

11. 11.

Sweeney, C., Ward, J. & Vallender, E. J. Naturally occurring, physiologically normal, primate chimeras. *Chimerism* **3**, 43–44 (2012).

[PubMed](#) [PubMed Central](#) [Article](#) [Google Scholar](#)

12. 12.

The Marmoset Genome Sequencing and Analysis Consortium. The common marmoset genome provides insight into primate biology and evolution. *Nat. Genet.* **46**, 850–857 (2014).

[PubMed Central](#) [Article](#) [CAS](#) [Google Scholar](#)

13. 13.

Sato, K. et al. Resequencing of the common marmoset genome improves genome assemblies and gene-coding sequence analysis. *Sci. Rep.* **5**, 16894 (2015).

[CAS](#) [PubMed](#) [PubMed Central](#) [Article](#) [ADS](#) [Google Scholar](#)

14. 14.

Nembaware, V., Wolfe, K. H., Bettoni, F., Kelso, J. & Seoighe, C. Allele-specific transcript isoforms in human. *FEBS Lett.* **577**, 233–238 (2004).

[CAS](#) [PubMed](#) [Article](#) [PubMed Central](#) [Google Scholar](#)

15. 15.

Anton, E., Blanco, J. & Vidal, F. Meiotic behavior of three D;G Robertsonian translocations: segregation and interchromosomal effect. *J. Hum. Genet.* **55**, 541–545 (2010).

[PubMed](#) [Article](#) [PubMed Central](#) [Google Scholar](#)

16. 16.

Stankiewicz, P. & Lupski, J. R. Genome architecture, rearrangements and genomic disorders. *Trends Genet.* **18**, 74–82 (2002).

[CAS](#) [PubMed](#) [Article](#) [PubMed Central](#) [Google Scholar](#)

17. 17.

Acuna-Hidalgo, R., Veltman, J. A. & Hoischen, A. New insights into the generation and role of de novo mutations in health and disease. *Genome Biol.* **17**, 241 (2016).

[PubMed](#) [PubMed Central](#) [Article](#) [CAS](#) [Google Scholar](#)

18. 18.

Goldmann, J. M. et al. Parent-of-origin-specific signatures of de novo mutations. *Nat. Genet.* **48**, 935–939 (2016).

[CAS](#) [Article](#) [Google Scholar](#)

19. 19.

Chintalapati, M. & Moorjani, P. Evolution of the mutation rate across primates. *Curr. Opin. Genet. Dev.* **62**, 58–64 (2020).

[CAS](#) [PubMed](#) [Article](#) [PubMed Central](#) [Google Scholar](#)

20. 20.

Zoonomia Consortium. A comparative genomics multitool for scientific discovery and conservation. *Nature* **587**, 240–245 (2020).

[CAS](#) [Article](#) [ADS](#) [Google Scholar](#)

21. 21.

Vollger, M. R. et al. Long-read sequence and assembly of segmental duplications. *Nat. Methods* **16**, 88–94 (2019).

[CAS](#) [PubMed](#) [Article](#) [PubMed Central](#) [Google Scholar](#)

22. 22.

Bellott, D. W. et al. Mammalian Y chromosomes retain widely expressed dosage-sensitive regulators. *Nature* **508**, 494–499 (2014).

[CAS](#) [PubMed](#) [PubMed Central](#) [Article](#) [ADS](#) [Google Scholar](#)

23. 23.

Pfeifer, S. P. Direct estimate of the spontaneous germ line mutation rate in African green monkeys. *Evolution* **71**, 2858–2870 (2017).

[CAS](#) [PubMed](#) [Article](#) [PubMed Central](#) [Google Scholar](#)

24. 24.

Thomas, G. W. C. et al. Reproductive longevity predicts mutation rates in primates. *Curr. Biol.* **28**, 3193–3197 (2018).

[CAS](#) [PubMed](#) [PubMed Central](#) [Article](#) [Google Scholar](#)

25. 25.

Raudsepp, T. & Chowdhary, B. P. The eutherian pseudoautosomal region. *Cytogenet. Genome Res.* **147**, 81–94 (2015).

[PubMed](#) [Article](#) [CAS](#) [PubMed Central](#) [Google Scholar](#)

26. 26.

Hinch, A. G., Altemose, N., Noor, N., Donnelly, P. & Myers, S. R. Recombination in the human pseudoautosomal region PAR1. *PLoS Genet.* **10**, e1004503 (2014).

[PubMed](#) [PubMed Central](#) [Article](#) [CAS](#) [Google Scholar](#)

27. 27.

Holmquist, G. P. Chromosome bands, their chromatin flavors, and their functional features. *Am. J. Hum. Genet.* **51**, 17–37 (1992).

[CAS](#) [PubMed](#) [PubMed Central](#) [Google Scholar](#)

28. 28.

Hughes, J. F. & Page, D. C. The biology and evolution of mammalian Y chromosomes. *Annu. Rev. Genet.* **49**, 507–527 (2015).

[CAS](#) [PubMed](#) [Article](#) [PubMed Central](#) [Google Scholar](#)

29. 29.

Mueller, J. L. et al. Independent specialization of the human and mouse X chromosomes for the male germ line. *Nat. Genet.* **45**, 1083–1087 (2013).

[CAS](#) [PubMed](#) [PubMed Central](#) [Article](#) [Google Scholar](#)

30. 30.

Lucotte, E. A. et al. Dynamic copy number evolution of X- and Y-linked ampliconic genes in human populations. *Genetics* **209**, 907–920 (2018).

[CAS](#) [PubMed](#) [PubMed Central](#) [Article](#) [Google Scholar](#)

31. 31.

Bachtrog, D. A dynamic view of sex chromosome evolution. *Curr. Opin. Genet. Dev.* **16**, 578–585 (2006).

[CAS](#) [PubMed](#) [Article](#) [PubMed Central](#) [Google Scholar](#)

32. 32.

Wahab, F., Drummer, C. & Behr, R. Marmosets. *Curr. Biol.* **25**, R780–R782 (2015).

[CAS](#) [PubMed](#) [Article](#) [PubMed Central](#) [Google Scholar](#)

33. 33.

Millar, M. R., Sharpe, R. M., Weinbauer, G. F., Fraser, H. M. & Saunders, P. T. Marmoset spermatogenesis: organizational similarities to the human. *Int. J. Androl.* **23**, 266–277 (2000).

[CAS](#) [PubMed](#) [Article](#) [PubMed Central](#) [Google Scholar](#)

34. 34.

Cortez, D. et al. Origins and functional evolution of Y chromosomes across mammals. *Nature* **508**, 488–493 (2014).

[CAS](#) [PubMed](#) [Article](#) [ADS](#) [PubMed Central](#) [Google Scholar](#)

35. 35.

Havugimana, P. C. et al. A census of human soluble protein complexes. *Cell* **150**, 1068–1081 (2012).

[CAS](#) [PubMed](#) [PubMed Central](#) [Article](#) [Google Scholar](#)

36. 36.

Lahn, B. T. & Page, D. C. Four evolutionary strata on the human X chromosome. *Science* **286**, 964–967 (1999).

[CAS](#) [PubMed](#) [Article](#) [PubMed Central](#) [Google Scholar](#)

37. 37.

Abbott, D. H., Barnett, D. K., Colman, R. J., Yamamoto, M. E. & Schultz-Darken, N. J. Aspects of common marmoset basic biology and life history important for biomedical research. *Comp. Med.* **53**, 339–350 (2003).

[CAS](#) [PubMed](#) [PubMed Central](#) [Google Scholar](#)

38. 38.

Harris, R. A. et al. Evolutionary genetics and implications of small size and twinning in callitrichine primates. *Proc. Natl Acad. Sci. USA* **111**, 1467–1472 (2014).

[CAS](#) [PubMed](#) [Article](#) [ADS](#) [PubMed Central](#) [Google Scholar](#)

39. 39.

Power, M. L. in *The Evolution of Exudativory in Primates* 25–44 (Springer, 2010).

40. 40.

Colman, R. J. Absence of estrogen depletion bone loss in female common marmosets. *J. Bone Miner. Res.* **12**, S342 (1997)

[ADS](#) [Google Scholar](#)

41. 41.

Binkley, N. et al. Zoledronate prevents the development of absolute osteopenia following ovariectomy in adult rhesus monkeys. *J. Bone Miner. Res.* **13**, 1775–1782 (1998).

[CAS](#) [PubMed](#) [Article](#) [PubMed Central](#) [Google Scholar](#)

42. 42.

Saleem, A. N. et al. Mice with alopecia, osteoporosis, and systemic amyloidosis due to mutation in *Zdhhc13*, a gene coding for palmitoyl acyltransferase. *PLoS Genet.* **6**, e1000985 (2010).

[PubMed](#) [PubMed Central](#) [Article](#) [CAS](#) [Google Scholar](#)

43. 43.

Iseki, S., Wilkie, A. O. & Morriss-Kay, G. M. Fgfr1 and Fgfr2 have distinct differentiation- and proliferation-related roles in the developing mouse skull vault. *Development* **126**, 5611–5620 (1999).

[CAS](#) [PubMed](#) [Article](#) [PubMed Central](#) [Google Scholar](#)

44. 44.

White, K. E. et al. Mutations that cause osteoglophonic dysplasia define novel roles for FGFR1 in bone elongation. *Am. J. Hum. Genet.* **76**, 361–367 (2005).

[CAS](#) [PubMed](#) [Article](#) [PubMed Central](#) [Google Scholar](#)

45. 45.

Moore, H. D. M., Gems, S. & Hearn, J. P. Early implantation stages in the marmoset monkey (*Callithrix jacchus*). *Am. J. Anat.* **172**, 265–278 (1985).

[CAS](#) [PubMed](#) [Article](#) [PubMed Central](#) [Google Scholar](#)

46. 46.

Saltzman, W., Schultz-Darken, N. J., Severin, J. M. & Abbott, D. H. Escape from social suppression of sexual behavior and of ovulation in female common marmosets. *Ann. NY Acad. Sci.* **807**, 567–570 (1997).

[CAS](#) [PubMed](#) [Article](#) [ADS](#) [PubMed Central](#) [Google Scholar](#)

47. 47.

Mujoomdar, M. L., Hogan, L. M., Parlow, A. F. & Nachtigal, M. W. *Pcsk6* mutant mice exhibit progressive loss of ovarian function, altered gene expression, and formation of ovarian pathology. *Reproduction* **141**, 343–355 (2011).

[CAS](#) [PubMed](#) [Article](#) [PubMed Central](#) [Google Scholar](#)

48. 48.

Cho, H. et al. Regulation of circadian behaviour and metabolism by REV-ERB- α and REV-ERB- β . *Nature* **485**, 123–127 (2012).

[CAS](#) [PubMed](#) [PubMed Central](#) [Article](#) [ADS](#) [Google Scholar](#)

49. 49.

Chomez, P. et al. Increased cell death and delayed development in the cerebellum of mice lacking the rev-erbA(alpha) orphan receptor. *Development* **127**, 1489–1498 (2000).

[CAS](#) [PubMed](#) [Article](#) [PubMed Central](#) [Google Scholar](#)

50. 50.

Zhang, Z. et al. *TGIF1* and *SF1* polymorphisms are associated with litter size in Small Tail Han sheep. *Reprod. Domest. Anim.* **55**, 1145–1153 (2020).

[CAS](#) [PubMed](#) [PubMed Central](#) [Article](#) [Google Scholar](#)

51. 51.

Lagasse, E. & Weissman, I. L. Enforced expression of Bcl-2 in monocytes rescues macrophages and partially reverses osteopetrosis in *op/op* mice. *Cell* **89**, 1021–1031 (1997).

[CAS](#) [PubMed](#) [Article](#) [PubMed Central](#) [Google Scholar](#)

52. 52.

Son, A. et al. Homer2 and Homer3 modulate RANKL-induced NFATc1 signaling in osteoclastogenesis and bone metabolism. *J. Endocrinol.* **242**, 241–249 (2019).

[CAS](#) [PubMed](#) [Article](#) [PubMed Central](#) [Google Scholar](#)

53. 53.

Tillgren, V., Ho, J. C. S., Önnerfjord, P. & Kalamajski, S. The novel small leucine-rich protein chondroadherin-like (CHADL) is expressed in cartilage and modulates chondrocyte differentiation. *J. Biol. Chem.* **290**, 918–925 (2015).

[CAS](#) [PubMed](#) [Article](#) [PubMed Central](#) [Google Scholar](#)

54. 54.

Ludlage, E. & Mansfield, K. Clinical care and diseases of the common marmoset (*Callithrix jacchus*). *Comp. Med.* **53**, 369–382 (2003).

[CAS](#) [PubMed](#) [PubMed Central](#) [Google Scholar](#)

55. 55.

Bailey, M. T. & Coe, C. L. Intestinal microbial patterns of the common marmoset and rhesus macaque. *Comp. Biochem. Physiol. A*. **133**, 379–388 (2002).

[Article](#) [Google Scholar](#)

56. 56.

Malukiewicz, J. et al. The gut microbiome of exudivorous wild and captive marmosets. Preprint at <https://doi.org/10.1101/708255> (2020).

57. 57.

Turroni, F. et al. Glycan utilization and cross-feeding activities by Bifidobacteria. *Trends Microbiol.* **26**, 339–350 (2018).

[CAS](#) [PubMed](#) [Article](#) [PubMed Central](#) [Google Scholar](#)

58. 58.

Wiśniewski, J. R., Friedrich, A., Keller, T., Mann, M. & Koepsell, H. The impact of high-fat diet on metabolism and immune defense in small intestine mucosa. *J. Proteome Res.* **14**, 353–365 (2015).

[PubMed](#) [Article](#) [CAS](#) [PubMed Central](#) [Google Scholar](#)

59. 59.

Plaza-Díaz, J. et al. *Adamdec1*, *Ednrb* and *Ptgs1/Cox1*, inflammation genes upregulated in the intestinal mucosa of obese rats, are downregulated by three probiotic strains. *Sci. Rep.* **7**, 1939 (2017).

[PubMed](#) [PubMed Central](#) [Article](#) [ADS](#) [CAS](#) [Google Scholar](#)

60. 60.

Jordan, D. M. et al. Identification of *cis*-suppression of human disease mutations by comparative genomics. *Nature* **524**, 225–229 (2015).

[CAS](#) [PubMed](#) [PubMed Central](#) [Article](#) [Google Scholar](#)

61. 61.

Storz, J. F. Compensatory mutations and epistasis for protein function. *Curr. Opin. Struct. Biol.* **50**, 18–25 (2018).

[CAS](#) [PubMed](#) [Article](#) [PubMed Central](#) [Google Scholar](#)

62. 62.

Formenti, G. et al. Complete vertebrate mitogenomes reveal widespread gene duplications and repeats. Preprint at <https://doi.org/10.1101/2020.06.30.177956> (2020).

63. 63.

Guan, D. et al. Identifying and removing haplotypic duplication in primary genome assemblies. *Bioinformatics* **36**, 2896–2898 (2020).

[CAS](#) [PubMed](#) [PubMed Central](#) [Article](#) [Google Scholar](#)

64. 64.

Lam, E. T. et al. Genome mapping on nanochannel arrays for structural variation analysis and sequence assembly. *Nat. Biotechnol.* **30**, 771–776 (2012).

[CAS](#) [PubMed](#) [Article](#) [PubMed Central](#) [Google Scholar](#)

65. 65.

Ghurye, J. et al. Integrating Hi-C links with assembly graphs for chromosome-scale assembly. *PLOS Comput. Biol.* **15**, e1007273 (2019).

[CAS](#) [PubMed](#) [PubMed Central](#) [Article](#) [Google Scholar](#)

66. 66.

Bishara, A. et al. Read clouds uncover variation in complex regions of the human genome. *Genome Res.* **25**, 1570–1580 (2015).

[CAS](#) [PubMed](#) [PubMed Central](#) [Article](#) [Google Scholar](#)

67. 67.

Garrison, E. & Marth, G. Haplotype-based variant detection from short-read sequencing. Preprint at <https://arxiv.org/abs/1207.3907> (2012).

68. 68.

Chow, W. et al. gEVAL - a web-based browser for evaluating genome assemblies. *Bioinformatics* **32**, 2508–2510 (2016).

[CAS](#) [PubMed](#) [PubMed Central](#) [Article](#) [Google Scholar](#)

69. 69.

Li, H. & Durbin, R. Fast and accurate short read alignment with Burrows–Wheeler transform. *Bioinformatics* **25**, 1754–1760 (2009).

[CAS](#) [PubMed](#) [PubMed Central](#) [Article](#) [Google Scholar](#)

70. 70.

Servant, N. et al. HiC-Pro: an optimized and flexible pipeline for Hi-C data processing. *Genome Biol.* **16**, 259 (2015).

[PubMed](#) [PubMed Central](#) [Article](#) [CAS](#) [Google Scholar](#)

71. 71.

Chakraborty, M., Emerson, J. J., Macdonald, S. J. & Long, A. D. Structural variants exhibit widespread allelic heterogeneity and shape variation in complex traits. *Nat. Commun.* **10**, 4872 (2019).

[PubMed](#) [PubMed Central](#) [Article](#) [ADS](#) [CAS](#) [Google Scholar](#)

72. 72.

Nattestad, M. & Schatz, M. C. Assemblytics: a web analytics tool for the detection of variants from an assembly. *Bioinformatics* **32**, 3021–3023 (2016).

[CAS](#) [PubMed](#) [PubMed Central](#) [Article](#) [Google Scholar](#)

73. 73.

Goel, M., Sun, H., Jiao, W. B. & Schneeberger, K. SyRI: finding genomic rearrangements and local sequence differences from whole-genome assemblies. *Genome Biol.* **20**, 277 (2019).

[PubMed](#) [PubMed Central](#) [Article](#) [Google Scholar](#)

74. 74.

Robinson, J. T. et al. Integrative genomics viewer. *Nat. Biotechnol.* **29**, 24–26 (2011).

[CAS](#) [Article](#) [PubMed](#) [PubMed Central](#) [Google Scholar](#)

75. 75.

Löytynoja, A. Phylogeny-aware alignment with PRANK. *Methods Mol. Biol.* **1079**, 155–170 (2014).

[PubMed](#) [Article](#) [PubMed Central](#) [Google Scholar](#)

76. 76.

Sela, I., Ashkenazy, H., Katoh, K. & Pupko, T. GUIDANCE2: accurate detection of unreliable alignment regions accounting for the uncertainty of multiple parameters. *Nucleic Acids Res.* **43**, W7–W14 (2015).

[CAS](#) [PubMed](#) [PubMed Central](#) [Article](#) [Google Scholar](#)

77. 77.

Yang, Z. PAML 4: phylogenetic analysis by maximum likelihood. *Mol. Biol. Evol.* **24**, 1586–1591 (2007).

[CAS](#) [PubMed](#) [PubMed Central](#) [Article](#) [Google Scholar](#)

78. 78.

Waterhouse, A. M., Procter, J. B., Martin, D. M., Clamp, M. & Barton, G. J. Jalview Version 2—a multiple sequence alignment editor and analysis workbench. *Bioinformatics* **25**, 1189–1191 (2009).

[CAS](#) [PubMed](#) [PubMed Central](#) [Article](#) [Google Scholar](#)

[Download references](#)

Acknowledgements

This work was supported by the Strategic Priority Research Program of the Chinese Academy of Sciences (XDB31020000); the National Key R&D Program of China (MOST) grant 2018YFC1406901; the International Partnership Program of the Chinese Academy of Sciences (no. 152453KYSB20170002); the Carlsberg Foundation (CF16-0663); the Villum Foundation (no. 25900) to G.Z.; Howard Hughes Medical Institute and Rockefeller University start-up funds to E.D.J.; the Intramural Research Program of the National Human Genome Research Institute, the National Institutes of Health (NIH) (A.R., A.M.P. and S.K.); the Korea Health Technology R&D Project through the Korea Health Industry Development Institute HI17C2098 (A.R.); the NIH National Institute of General Medical Sciences (no. T32GM007739) and an NIH National Institute of Mental

Health F30 (no. MH112351) (M.M.F.); and the Guangdong Provincial Academician Workstation of BGI Synthetic Genomics (no. 2017B090904014) (H.Y.).

Author information

Author notes

1. These authors contributed equally: Chentao Yang, Yang Zhou, Stephanie Marcus

Affiliations

1. BGI-Shenzhen, Shenzhen, China

Chentao Yang, Yang Zhou, Xupeng Bi, Chengran Zhou, Long Zhou, Yuan Deng, Miaoquan Fang, Duo Xie, Yuanzhen Zhu, Shangjin Tan & Huanming Yang

2. Villum Centre for Biodiversity Genomics, Section for Ecology and Evolution, Department of Biology, University of Copenhagen, Copenhagen, Denmark

Chentao Yang, Lucie A. Bergeron, Yuan Deng & Guojie Zhang

3. Laboratory of Neurogenetics of Language, The Rockefeller University, New York, NY, USA

Stephanie Marcus, Giulio Formenti & Erich D. Jarvis

4. Vertebrate Genome Laboratory, The Rockefeller University, New York, NY, USA

Giulio Formenti, Jacquelyn Mountcastle, Bettina Haase, Jennifer Balacco, Olivier Fedrigo & Erich D. Jarvis

5. University of the Chinese Academy of Sciences, Beijing, China

Zhenzhen Song & Huanming Yang

6. Bioinformatics Research Centre, Aarhus University, Aarhus, Denmark

Juraj Bergman, Marjolaine Marie C. Rousselle & Mikkel Heide Schierup

7. Wellcome Sanger Institute, Hinxton, UK

Jonathan Wood, William Chow & Kerstin Howe

8. Genome Informatics Section, Computational and Statistical Genomics Branch, National Human Genome Research Institute, National Institutes of Health, Bethesda, MD, USA

Arang Rie, Sergey Koren & Adam M. Phillippy

9. Max Planck Institute of Molecular Cell Biology and Genetics, Dresden, Germany

Martin Pippel

10. Center for Systems Biology, Dresden, Germany

Martin Pippel

11. Laboratory of Neural Systems, The Rockefeller University, New York, NY, USA

Margaret M. Fabiszak & Winrich A. Freiwald

12. Center for Brains, Minds and Machines (CBMM), The Rockefeller University, New York, NY, USA

Winrich A. Freiwald

13. James D. Watson Institute of Genome Sciences, Hangzhou, China

Huanming Yang

14. Guangdong Provincial Academician Workstation of BGI Synthetic Genomics, BGI-Shenzhen, Shenzhen, China

Huanming Yang

15. Howard Hughes Medical Institute, Chevy Chase, MD, USA

Erich D. Jarvis

16. State Key Laboratory of Genetic Resources and Evolution, Kunming Institute of Zoology, Chinese Academy of Sciences, Kunming, China

Guojie Zhang

17. China National GeneBank, BGI-Shenzhen, Shenzhen, China

Guojie Zhang

18. Center for Excellence in Animal Evolution and Genetics, Chinese Academy of Sciences, Kunming, China

Guojie Zhang

Authors

1. Chentao Yang

[View author publications](#)

You can also search for this author in [PubMed](#) [Google Scholar](#)

2. Yang Zhou

[View author publications](#)

You can also search for this author in [PubMed](#) [Google Scholar](#)

3. Stephanie Marcus

[View author publications](#)

You can also search for this author in [PubMed](#) [Google Scholar](#)

4. Giulio Formenti

[View author publications](#)

You can also search for this author in [PubMed](#) [Google Scholar](#)

5. Lucie A. Bergeron

[View author publications](#)

You can also search for this author in [PubMed](#) [Google Scholar](#)

6. Zhenzhen Song

[View author publications](#)

You can also search for this author in [PubMed](#) [Google Scholar](#)

7. Xupeng Bi

[View author publications](#)

You can also search for this author in [PubMed](#) [Google Scholar](#)

8. Juraj Bergman

[View author publications](#)

You can also search for this author in [PubMed](#) [Google Scholar](#)

9. Marjolaine Marie C. Rousselle

[View author publications](#)

You can also search for this author in [PubMed](#) [Google Scholar](#)

10. Chengran Zhou

[View author publications](#)

You can also search for this author in [PubMed](#) [Google Scholar](#)

11. Long Zhou

[View author publications](#)

You can also search for this author in [PubMed](#) [Google Scholar](#)

12. Yuan Deng

[View author publications](#)

You can also search for this author in [PubMed](#) [Google Scholar](#)

13. Miaoquan Fang

[View author publications](#)

You can also search for this author in [PubMed](#) [Google Scholar](#)

14. Duo Xie

[View author publications](#)

You can also search for this author in [PubMed](#) [Google Scholar](#)

15. Yuanzhen Zhu

[View author publications](#)

You can also search for this author in [PubMed](#) [Google Scholar](#)

16. Shangjin Tan

[View author publications](#)

You can also search for this author in [PubMed](#) [Google Scholar](#)

17. Jacquelyn Mountcastle

[View author publications](#)

You can also search for this author in [PubMed](#) [Google Scholar](#)

18. Bettina Haase

[View author publications](#)

You can also search for this author in [PubMed](#) [Google Scholar](#)

19. Jennifer Balacco

[View author publications](#)

You can also search for this author in [PubMed](#) [Google Scholar](#)

20. Jonathan Wood

[View author publications](#)

You can also search for this author in [PubMed](#) [Google Scholar](#)

21. William Chow

[View author publications](#)

You can also search for this author in [PubMed](#) [Google Scholar](#)

22. Arang Rhie

[View author publications](#)

You can also search for this author in [PubMed](#) [Google Scholar](#)

23. Martin Pippel

[View author publications](#)

You can also search for this author in [PubMed](#) [Google Scholar](#)

24. Margaret M. Fabiszak

[View author publications](#)

You can also search for this author in [PubMed](#) [Google Scholar](#)

25. Sergey Koren

[View author publications](#)

You can also search for this author in [PubMed](#) [Google Scholar](#)

26. Olivier Fedrigo

[View author publications](#)

You can also search for this author in [PubMed](#) [Google Scholar](#)

27. Winrich A. Freiwald

[View author publications](#)

You can also search for this author in [PubMed](#) [Google Scholar](#)

28. Kerstin Howe

[View author publications](#)

You can also search for this author in [PubMed](#) [Google Scholar](#)

29. Huanming Yang

[View author publications](#)

You can also search for this author in [PubMed](#) [Google Scholar](#)

30. Adam M. Phillippy

[View author publications](#)

You can also search for this author in [PubMed](#) [Google Scholar](#)

31. Mikkel Heide Schierup

[View author publications](#)

You can also search for this author in [PubMed](#) [Google Scholar](#)

32. Erich D. Jarvis

[View author publications](#)

You can also search for this author in [PubMed](#) [Google Scholar](#)

33. Guojie Zhang

[View author publications](#)

You can also search for this author in [PubMed](#) [Google Scholar](#)

Contributions

G.Z. and E.D.J. initiated and designed the project. S.M., J.M., B.H., J. Balacco, M.M.F., O.F., W.A.F. and H.Y. coordinated and performed sample collection and sequencing. S.M., G.F., J.W., W.C., K.H., A.R., M.P., A.M.P., S.K., Y. Zhou, X.B., Z.S. and G.Z. performed genome assembling, curation and evaluation. C.Y., Y. Zhou, S.M. and G.F. performed the chimeric analysis. C.Y., L.A.B., X.B., C.Z. and G.Z. performed genetic diversity

analysis. L.A.B. and G.Z. calculated mutation rates. C.Y. and S.T. performed experimental validation. Y. Zhou, L.Z., J. Bergman, M.M.C.R., G.Z. and M.H.S. performed analysis of sex chromosomes. C.Y., Y. Zhou, Y.D., M.F., C.Z., D.X. and Y. Zhu. performed positive-selection analysis. Y. Zhou, Z.S. and G.Z. performed brain- and disease-related analysis. G.Z., E.D.J., M.H.S, C.Y., Y. Zhou, S.M., L.A.B., J. Bergman, M.M.C.R., G.F., X.B. and Z.S. wrote the manuscript.

Corresponding author

Correspondence to [Guojie Zhang](#).

Ethics declarations

Competing interests

The authors declare no competing interests.

Additional information

Peer review information *Nature* thanks Joanna Malukiewicz, Vagheesh Narasimhan and the other, anonymous, reviewer(s) for their contribution to the peer review of this work.

Publisher's note Springer Nature remains neutral with regard to jurisdictional claims in published maps and institutional affiliations.

Extended data figures and tables

[Extended Data Fig. 1 GenomeScope analyses.](#)

a, GenomeScope (v.1.0) profile for 31-mers collected from the F₁ 10X linked-reads using Meryl (<https://github.com/marbl/meryl>) (following GEM (gel-bead in emulsion) barcode trimming). Heterozygosity estimated at a maximum of 0.287%. Read error rate estimated at a maximum of 0.435%.

Genome haploid length estimated at a maximum of 3,068,578,525 bp, repeat length estimated at a maximum of 757,852,942 bp and unique length estimated at a maximum of 2,310,725,582 bp. **b**, **c**, Genomescope profiles of the maternal (**b**) and paternal (**c**) 21-mers collected from the raw Illumina data. The observed paternal data do not fit GenomeScope's robust model (black line) for a diploid organism and exhibit higher overall heterozygosity than the maternal data (0.216% compared to 0.173%). This supports a premise that the father's sequencing reads contain a level of chimerism, whereas the mother's reads contain negligible representation of alternative alleles, at most. Further analysis of the parental Illumina data shows that the k -mer multiplicity distribution varies greatly between the maternal and paternal sets. **d–g**, The maternal k -mers (**d**, **e** (**e** shows a magnified version of **d**)) show clear distributions with a distinct haploid peak at half coverage (around 35 \times), whereas the paternal k -mers (**f**, **g** (**g** shows a magnified version of **f**)) show an irregular distribution with no clearly defined haploid peak. This provides further evidence that the paternal data exhibit a level of chimerism.

Extended Data Fig. 2 Trio-based diploid genome assembly.

a, Hapmer (haplotype-specific k -mer) blob plot of the curated marmoset assemblies. Red, maternal haplotype; blue, paternal haplotype. The size of each blob indicates the total number of k -mers counted in an individual scaffold and the position of each blob is plotted according to the number of contained maternal and paternal hapmers. We see that maternal and paternal hapmers are highly phased, with some slight representation of paternal hapmers in several maternal scaffolds (those that do not lie directly on the x axis). We can also see a higher representation of paternal hapmers identified within scaffolds of the paternal assembly than maternal hapmers identified in scaffolds of the maternal assembly. **b**, Correlation between the assembled chromosome sizes and the chromosome lengths estimated by karyotype image data. A total of 23 chromosomes are plotted and the coefficient of determination is calculated for each assembly. **c**, Schematic plot mapping the assembled maternal and paternal assigned contigs onto marmoset assembled chromosomes. Top, maternal alleles; bottom, paternal alleles. Contig sizes, centromeres and telomeres are indicated.

Extended Data Fig. 3 Confirmation of the MSSDR translocation in the marmoset Y chromosome.

a, Marmoset Y-chromosome-specific BAC reads were obtained from the NCBI trace archive and constructed into a pseudo-Y chromosome according to their position from a previous study²⁰. The linear alignment between mCalJac1's Y chromosome and marmoset bacterial artificial chromosome mapped to the Y chromosome confirms the MSSDR translocation. The MSSDR translocation on the Y chromosome is highlighted in yellow and the two regions that span the break points and its flanking 50 kb are highlighted in dashed boxes. **b**, The region spanning *ASMTLY* and *P2RY8Y* is supported by PacBio reads and 10X linked-reads (only a proportion of them were shown). In the 10X linked-reads panel, each rectangle represents a read and each line represents a 10X DNA molecule. A total of 81 10X linked-read DNA molecules support the linkage of *ASMTLY* and *P2RY8Y*. **c**, The region spanning *CD99Y* and *DDX3Y* is supported by PacBio reads and 10X linked-reads (only a proportion of them shown). A total of 110 10X linked-read DNA molecules support the linkage of *CD99Y* and *DDX3Y*.

Supplementary information

Supplementary Information

This file contains details on the sample collection and methods used in this study. It also includes Supplementary Notes with the detailed analyses results, Supplementary Figures 1-36 and descriptions for Supplementary Tables 1-39 (Supplementary Tables supplied separately).

Reporting Summary

Supplementary Tables

This file contains Supplementary Tables 1-39 – see Supplementary Information document for full descriptions.

Rights and permissions

Open Access This article is licensed under a Creative Commons Attribution 4.0 International License, which permits use, sharing, adaptation, distribution and reproduction in any medium or format, as long as you give appropriate credit to the original author(s) and the source, provide a link to the Creative Commons license, and indicate if changes were made. The images or other third party material in this article are included in the article's Creative Commons license, unless indicated otherwise in a credit line to the material. If material is not included in the article's Creative Commons license and your intended use is not permitted by statutory regulation or exceeds the permitted use, you will need to obtain permission directly from the copyright holder. To view a copy of this license, visit <http://creativecommons.org/licenses/by/4.0/>.

[Reprints and Permissions](#)

About this article



Check for
updates

Cite this article

Yang, C., Zhou, Y., Marcus, S. *et al.* Evolutionary and biomedical insights from a marmoset diploid genome assembly. *Nature* **594**, 227–233 (2021).
<https://doi.org/10.1038/s41586-021-03535-x>

[Download citation](#)

- Received: 20 September 2020
- Accepted: 12 April 2021
- Published: 28 April 2021

- Issue Date: 10 June 2021
- DOI: <https://doi.org/10.1038/s41586-021-03535-x>

Comments

By submitting a comment you agree to abide by our [Terms](#) and [Community Guidelines](#). If you find something abusive or that does not comply with our terms or guidelines please flag it as inappropriate.

[Download PDF](#)

Associated Content

Special

[Vertebrate Genomes Project](#)

Advertisement

This article was downloaded by **calibre** from <https://www.nature.com/articles/s41586-021-03535-x>

Reconstruction of ancient microbial genomes from the human gut

[Download PDF](#)

- Article
- Open Access
- [Published: 12 May 2021](#)

Reconstruction of ancient microbial genomes from the human gut

- [Marsha C. Wibowo](#) [ORCID: orcid.org/0000-0001-7678-5447](#)^{1,2},
- [Zhen Yang](#)^{1,2,3},
- [Maxime Borry](#) [ORCID: orcid.org/0000-0001-9140-7559](#)⁴,
- [Alexander Hübner](#)⁴,
- [Kun D. Huang](#)^{5,6},
- [Braden T. Tierney](#) [ORCID: orcid.org/0000-0002-7533-8802](#)^{1,2,7},
- [Samuel Zimmerman](#)^{1,2},
- [Francisco Barajas-Olmos](#)⁸,
- [Cecilia Contreras-Cubas](#)⁸,
- [Humberto García-Ortiz](#) [ORCID: orcid.org/0000-0002-0453-980X](#)⁸,
- [Angélica Martínez-Hernández](#)⁸,
- [Jacob M. Luber](#)^{1,2,9},
- [Philipp Kirstahler](#)¹⁰,
- [Tre Blohm](#) [ORCID: orcid.org/0000-0003-2845-6475](#)¹¹,
- [Francis E. Smiley](#)¹²,
- [Richard Arnold](#)¹³,
- [Sonia A. Ballal](#)¹⁴,
- [Sünje Johanna Pamp](#) [ORCID: orcid.org/0000-0002-6236-1763](#)¹⁰,
- [Julia Russ](#)¹⁵,
- [Frank Maixner](#)¹⁶,
- [Omar Rota-Stabelli](#) [ORCID: orcid.org/0000-0002-0030-7788](#)^{6,17},
- [Nicola Segata](#) [ORCID: orcid.org/0000-0002-1583-5794](#)⁵,
- [Karl Reinhard](#)¹⁸,
- [Lorena Orozco](#) [ORCID: orcid.org/0000-0002-5801-9180](#)⁸,
- [Christina Warinner](#)^{4,19,20},
- [Meradeth Snow](#)¹¹,

- [Steven LeBlanc²¹](#) &
- [Aleksandar D. Kostic](#) [ORCID: orcid.org/0000-0002-0837-4360^{1,2}](#)

[Nature](#) volume **594**, pages 234–239 (2021) [Cite this article](#)

- 40k Accesses
- 1 Citations
- 1226 Altmetric
- [Metrics details](#)

Subjects

- [Archaeology](#)
- [Metagenomics](#)
- [Microbiome](#)

Abstract

Loss of gut microbial diversity^{1,2,3,4,5,6} in industrial populations is associated with chronic diseases⁷, underscoring the importance of studying our ancestral gut microbiome. However, relatively little is known about the composition of pre-industrial gut microbiomes. Here we performed a large-scale de novo assembly of microbial genomes from palaeofaeces. From eight authenticated human palaeofaeces samples (1,000–2,000 years old) with well-preserved DNA from southwestern USA and Mexico, we reconstructed 498 medium- and high-quality microbial genomes. Among the 181 genomes with the strongest evidence of being ancient and of human gut origin, 39% represent previously undescribed species-level genome bins. Tip dating suggests an approximate diversification timeline for the key human symbiont *Methanobrevibacter smithii*. In comparison to 789 present-day human gut microbiome samples from eight countries, the palaeofaeces samples are more similar to non-industrialized than industrialized human gut microbiomes. Functional profiling of the palaeofaeces samples reveals a markedly lower abundance of antibiotic-resistance and mucin-degrading genes, as well as enrichment of mobile genetic elements relative to industrial gut microbiomes. This study facilitates the discovery and characterization of previously undescribed gut microorganisms from ancient microbiomes and the investigation of the evolutionary history of the human gut microbiota through genome reconstruction from palaeofaeces.

[Download PDF](#)

Main

Previous studies have shown that industrial lifestyles are correlated with both a lower diversity in the gut microbiome^{1,2,3,4,5,6} and increased incidence of chronic diseases, such as obesity and autoimmune diseases⁷. Examining our ancestral gut microbiome may provide insights into aspects of human–microbiome symbioses that have become altered in the present-day industrialized world⁸.

Reconstruction of metagenome-assembled genomes (MAGs) is an emerging approach to recover high-quality genomes and previously undescribed species-level genome bins (SGBs) from shotgun metagenomics data. Sequencing reads are de novo assembled into contiguous sequences (contigs), and contigs are binned to form draft genomes⁹. The first large-scale initiative to de novo assemble genomes from metagenomic samples in 2017 recovered almost 8,000 MAGs¹⁰. In 2019, three studies separately reconstructed around 60,000 (ref. ¹¹), 90,000 (ref. ¹²) and 150,000 (ref. ¹³) MAGs—including many previously undescribed SGBs (that is, SGBs not assigned to any previously discovered species)—from human microbiome samples.

Despite the potential of de novo assembly to discover previously undescribed SGBs, this method has not been applied to palaeofaeces because of the challenges posed by highly damaged DNA. Therefore, previous studies have focused on describing the taxonomic composition of ancient microbiomes using reference-based approaches^{14,15,16} or the enrichment of sequences that match specific species and the reconstruction of genomes within that species^{6,17,18,19}. These approaches enable the recovery of microorganisms that belong to, or are closely related to, species that are present in the reference database, but not the discovery of new species. In this study, we performed a large-scale de novo assembly of microbial genomes from palaeofaeces.

Ethics

Although palaeofaeces are not subject to the Native American Graves Protection and Repatriation Act (NAGPRA) or other regulations, we engaged in consultation with living communities who maintain strong cultural ties to the palaeofaeces. This included involvement of the Robert S. Peabody Institute of Archaeology, which distributed correspondence to Southwest Tribal Historic Preservation Officers (THPOs) and tribal government offices to promote transparency and provide an opportunity to discuss the study. Consultation consisted of interactive short presentations to provide an overview of the research with time to respond to questions, as well as follow-up materials and opportunities for expanded dialogue to ensure topics of interest and concerns were addressed. We anticipate this process will

continue, despite the constraints of the COVID-19 pandemic. Additional information is provided in the Supplementary Information.

Overview of samples

We performed shotgun metagenomic sequencing on 15 palaeofaeces samples (Supplementary Table 1). The samples and authentication methods are described in Supplementary Information section 1. In brief, we excluded seven palaeofaeces samples because of poor de novo assembly results (Supplementary Table 1), evidence of archaeological soil contamination (Extended Data Fig. 1e) or a nonhuman host source (Supplementary Table 1). The remaining eight samples came from three sites (Boomerang Shelter, Arid West Cave and Zape) (Extended Data Fig. 1b). Their authenticity was extensively validated (Supplementary Information section 1), including their ancient origin (Extended Data Fig. 2) and human source (Extended Data Fig. 1c, Supplementary Tables 1, 2 and Supplementary Information section 2). Our results support that the palaeofaeces are faecal samples with minimal soil contamination (Fig. 1b, Extended Data Figs. 1d, e, 3 and Supplementary Tables 3, 4). The final eight samples are well-preserved and have long average DNA fragment sizes (average mode length = 174 base pairs (bp), s.d. = 30.15) (Extended Data Fig. 4). We confirmed that these long DNA fragments are not from contamination by modern DNA (Extended Data Fig. 5 and Supplementary Table 5).

Fig. 1: Phylum, family and species compositions of the palaeofaeces samples are similar to the gut microbiomes of present-day non-industrial individuals.

 **figure1**

a, Differentially abundant phyla (one-tailed Wilcoxon rank-sum test with FDR correction) as identified by MetaPhlAn2²⁰ (palaeofaeces, $n = 8$; non-industrial, $n = 370$; industrial, $n = 418$). Data are presented as box plots (middle line, median; lower hinge, first quartile; upper hinge, third quartile; lower whisker, the smallest value at most 1.5× the interquartile range from the hinge; upper whisker, the largest value no further than 1.5× the interquartile range from the hinge; data beyond the whiskers are outlying points). **b**, Principal component analysis of the species composition as identified by MetaPhlAn2²⁰. HMP, Human Microbiome Project. **c**, Presence–absence heat map (fuchsia, present; grey, absent) for differentially enriched species (two-tailed Fisher’s test, FDR correction). Species without fully specified species names are not shown (a complete list is included in Supplementary Table 3).

[Full size image](#)

As a comparison to the ancient gut microbiome, we analysed 789 present-day stool samples from both industrial and non-industrial populations across eight countries (Extended Data Fig. 1b and Supplementary Table 1). These include publicly available gut metagenomes and samples that we collected from 22 individuals living in a rural Mazahua farming community in central Mexico.

Reference-based taxonomic composition

We analysed the taxonomic composition with MetaPhlAn2²⁰ (Supplementary Table 3), which is a reference-based tool. Consistent with previous observations¹⁵, the taxonomic composition of the palaeofaeces is more similar to that of the non-industrial samples than the industrial samples (Fig. 1). None of the phyla is significantly different between the palaeofaeces and the non-industrial samples. By contrast, Bacteroidetes and Verrucomicrobia are enriched in the industrial samples compared to the palaeofaeces (one-tailed Wilcoxon rank-sum test with false-discovery rate (FDR) correction, $P = 0.0003$ and $P = 0.009$, respectively) and the non-industrial samples ($P = 4.6 \times 10^{-37}$ and $P = 1.1 \times 10^{-31}$, respectively) (Fig. 1a and Supplementary Table 3). Firmicutes, Proteobacteria and Spirochaetes are significantly less abundant in the industrial samples relative to the palaeofaeces ($P = 0.003$, $P = 0.002$ and $P = 2.8 \times 10^{-45}$, respectively) and the non-industrial samples ($P = 2.5 \times 10^{-16}$, $P = 1.7 \times 10^{-30}$ and $P = 3.6 \times 10^{-93}$, respectively).

At the family level, members of the VANISH (volatile and/or associated negatively with industrialized societies of humans) taxa²¹ are significantly enriched in the palaeofaeces samples relative to the industrial samples (Spirochaetaceae, $P = 1.8 \times 10^{-92}$; Prevotellaceae, $P = 0.003$) (Extended Data Fig. 1h and Supplementary Table 3). By contrast, members of the BloSSUM (bloom or selected in societies of urbanization/modernization) taxa²² are more abundant in the industrial samples compared to both the non-industrial samples and the palaeofaeces samples (Bacteroidaceae, $P = 1.6 \times 10^{-106}$ and $P = 0.0004$, respectively; Verrucomicrobiaceae, $P = 2.0 \times 10^{-31}$ and $P = 0.02$, respectively). In comparison to the non-industrial samples, only Spirochaetaceae is enriched in the palaeofaeces ($P = 0.004$).

The species composition of the palaeofaeces also reflects the present-day non-industrial gut microbiome (a complete description is provided in Supplementary Information section 3). Species-level principal component analysis shows that the palaeofaeces samples cluster with the non-industrial samples, and are distinct from the industrial samples (Fig. 1b). Species enriched in the industrial samples relative to both the palaeofaeces and the non-industrial samples include *Akkermansia muciniphila* (two-tailed Fisher's test with FDR correction, $P = 2.2 \times 10^{-2}$ and $P = 9.8 \times 10^{-30}$, respectively) and members of the *Alistipes* and *Bacteroides* genera (Fig. 1c and Supplementary Table 3). On the other hand, *Ruminococcus chamanellensis* ($P = 0.0003$ and $P = 9.6 \times 10^{-9}$, respectively) and members of the *Enterococcus* genus are enriched in the palaeofaeces compared to both the non-industrial and industrial samples. The spirochaete *Treponema succinifaciens* is enriched in both the palaeofaeces and the non-industrial samples relative to the industrial samples ($P = 2.4 \times 10^{-14}$ and $P = 1.1 \times 10^{-117}$, respectively). *Treponema succinifaciens* and, more generally, the phylum Spirochaetes (Fig. 1a) have been proposed to be lost in

industrial populations⁴. These results support that the industrial human gut microbiome has diverged from its ancestral state^{7,8}.

De novo genome reconstruction

The above reference-based analysis identified only taxa present in the database of MetaPhlAn2, which are mostly from industrialized samples. As expected, the palaeofaeces samples have a low percentage of reads mapped to the database (Extended Data Fig. 1f and Supplementary Information section 4). To discover microbial species that were not identifiable using a reference-based approach, we performed de novo genome reconstruction ([Methods](#)) from the palaeofaeces and the contemporary Mexican samples (Fig. 2, Extended Data Figs. 6–8 and Supplementary Table 6). Using simulated short-read sequencing data, we show that ancient DNA (aDNA) damage does not significantly affect the simulated assembled genomes (Extended Data Fig. 9 and Supplementary Information section 6).

Fig. 2: De novo genome reconstruction from palaeofaeces recovers 181 authenticated ancient gut microbial genomes, 39% of which are novel SGBs.

 **figure2**

a, GTDB-Tk²³ genus estimation for both novel and known species. **b**, Maximum likelihood tree of 178 highly damaged filtered ancient gut bacteria and 4,930 representative human gut microbiome genomes¹³. The tree was constructed using multiple sequence alignment of 120 bacterial marker genes identified by GTDB-Tk²³.

Novel and known ancient bin branches are highlighted in pink and blue, respectively. Tree scale, 1 nucleotide substitution per site.

[Full size image](#)

Following previously used quality-control criteria¹³, we selected medium-quality ($90\% \geq$ completeness $> 50\%$; contamination $< 5\%$) and high-quality (completeness $> 90\%$; contamination $< 5\%$) genomes for a total of 498 genomes from the palaeofaeces samples (Extended Data Figs. 6, 7 and Supplementary Table 6). To exclude contamination with modern DNA, we removed contigs with average read damage of less than 1% on either or both ends of the reads. After this filtering step, 209 medium-quality and high-quality filtered genomes were retained (Extended Data Fig. 6 and Supplementary Table 6).

To determine whether the genomes are gut microorganisms, we measured pairwise genetic distances between the filtered ancient genomes and 388,221 reference microbial genomes (Extended Data Fig. 6a). We labelled each ancient genome as ‘gut’, ‘environmental’ or ‘unsure’ on the basis of the source of isolation of its closest reference genome, and found that 203 out of the 209 filtered genomes are ‘gut’ (Supplementary Table 6), which suggests that there is limited contamination from soil. Out of the 203 filtered gut genomes, 181 are classified as highly damaged (Methods), confirming that they are ancient.

We calculated the pairwise average nucleotide identity (ANI) for the 181 high-damage filtered gut genomes and clustered genomes with more than 95% ANI into SGBs, which resulted in 158 SGBs with one representative genome per SGB (Extended Data Fig. 6a and Supplementary Table 6). SGBs with more than 95% ANI to at least one reference genome were classified as ‘known’ SGBs, and the rest were classified as ‘novel’ SGBs¹³. The results reveal that 61 (39%) of the ancient gut SGBs are novel SGBs (Extended Data Fig. 6a and Supplementary Table 6), 7 of which are shared across multiple palaeofaeces samples. With more than 15% genetic distance from the reference genomes¹³, 18 (11%) of the ancient SGBs belong to novel genera. By contrast, for the Mexican samples, only 1 of the 195 SGBs is novel (Extended Data Fig. 8 and Supplementary Table 6).

We annotated the taxa of the ancient SGBs using GTDB-Tk²³ and found that the most annotated genera include [*Eubacterium*], *Prevotella*, *Ruminococcus* and *Blautia* (Fig. 2a), which are typical human gut microbiome genera. However, this is an underestimate of the diversity of the SGBs because many could not be confidently assigned to a genus or species. Only 22 genomes were assigned species names (Extended Data Fig. 6f). Results for the 498 pre-filtered bins are shown in Extended Data Fig. 7 and Supplementary Table 6.

To visualize the distribution of the ancient genomes across phylogenies, we built a phylogenetic tree for the high-damage filtered gut bacterial genomes and 4,930 reference genomes that are representative of the human microbiome¹³ (Fig. 2b). The results indicate that the ancient genomes span many human gut microbiome-associated phyla, including Firmicutes, Bacteroidetes, Proteobacteria and Actinobacteria. Phylogenetic trees for *Prevotella* and *Ruminococcus* show that the previously undescribed ancient genomes do not cluster closely with the reference genomes (Supplementary Information section 7). In summary, the 181 reconstructed high-damage ancient microbial genomes belong to various human gut microbiome taxa and include 61 novel SGBs.

***Methanobrevibacter smithii* tip dating**

Next, we estimated the divergence times of *M. smithii* using two filtered (contigs < 1% damage were removed) ancient *M. smithii* genomes from samples UT30.3 and UT43.2 for tip calibrations (Methods and Supplementary Fig. 3a). Bayesian inference under a strict clock and the most fitting demographic model (Supplementary Table 7) shows that the ancient *M. smithii* genomes fall within the known diversity of contemporary *M. smithii* genomes (Fig. 3 and Supplementary Fig. 3a) and that *M. smithii* began to diversify around 85,000 years ago with a 95% highest posterior density (HPD) interval of 51,000–128,000 years (Fig. 3). This timeline is moderately later than the timeline of its sister species *Methanobrevibacter oralis* (HPD = 112,000–143,000 years)²⁴. The two estimates are compatible in terms of HPD overlap, and both occurred within or slightly after the estimated first human migration waves out of Africa around 90,000–194,000 years ago^{25,26}. In addition, the origin of the lineage leading to the two ancient *M. smithii* genomes is between 40,000 and 16,000 years ago (mean = 27,000 years ago). These estimates predate (although there is overlap towards the earlier 95% posterior estimates) the accepted age of human entry into North America through the Beringia bridge (20,000–16,000 years ago). The results did not significantly change when potential aDNA damage sites were removed (Supplementary Fig. 3b and Supplementary Information section 8), suggesting that damage did not notably affect our MAGs. We also validated these divergence date estimates using raw sequence divergence calculations (Extended Data Fig. 10 and Supplementary Information section 8). Overall, we show that using ancient genomes for calibrating *M. smithii* phylogenies, we could evolutionarily match previous studies of *M. oralis*²⁴. This supports the potential of using ancient MAGs to study the evolutionary history of gut symbionts. However, whether species within the genus actually follow the indicated diversification timeline needs to be investigated with additional ancient *Methanobrevibacter* genomes that span different time periods.

Fig. 3: Evolutionary context of a key human gut symbiont.

 **figure3**

A time-measured phylogenetic tree of *M. smithii* reconstructed on the basis of the core genome using a Bayesian approach under a strict clock model. Purple and orange violin plots illustrate the 95% HPD values (in parentheses) of estimated mean ages for the diversification of *M. smithii* and the split of the lineage leading to ancient *M. smithii* (highlighted in red), respectively.

[Full size image](#)

Functional genomic analysis

Our functional genomic analysis ([Methods](#)) reveals that the palaeofaeces are enriched in transposases (Fig. 4a, Supplementary Tables 8, 11 and Supplementary Information section 9) relative to industrial (two-tailed Fisher's test, $P = 3.2 \times 10^{-9}$) and non-industrial samples ($P = 3.2 \times 10^{-13}$). Transposases are also enriched in the non-industrial samples relative to the industrial samples ($P = 3.0 \times 10^{-9}$).

Fig. 4: Palaeofaeces exhibit a distinct functional genomic repertoire compared to present-day industrial stool samples.

 **figure4**

- a**, Heat map of the top-15 genes enriched in the palaeofaeces, industrial and non-industrial samples (complete results in Supplementary Table 8). Functions were annotated using PROKKA³⁸ (one-tailed Wilcoxon rank-sum tests with Bonferroni correction). The reads per kilobase per million reads (RPKM) values shown are on a log scale and scaled by row. An unscaled heat map is shown in Extended Data Fig. 12.
- b**, Volcano plots showing enriched CAZymes signatures (two-tailed Wilcoxon rank-sum test with FDR correction) comparing palaeofaeces and non-industrial samples (left), palaeofaeces and industrial samples (middle), and non-industrial and industrial samples (right). Each data point represents a CAZy family. CAZymes are colour-coded according to manually annotated broad substrate categories. The horizontal dashed red line indicates adjusted $P = 0.05$. The vertical dashed red line indicates \log_2 -transformed fold change = 0. For the left and middle plots, both the entire dataset and a magnified version are shown. For the right plot, the x -axis limits were set to -5 and 5 (as a result, eight statistically non-significant CAZymes were removed).

[Full size image](#)

On the other hand, both the industrial and the non-industrial samples are enriched in antibiotic-resistance genes (many of which are tetracycline-resistance genes) relative to the palaeofaeces (Fig. 4a, Extended Data Fig. 11 and Supplementary Table 8), consistent with the palaeofaeces being dated to the pre-antibiotic era²⁷. In the present-day samples, multiple tetracycline-resistance genes are present in *Streptococcus mitis* and *Collinsella* SGBs (Supplementary Information section 10). Our analysis suggests that these tetracycline-resistance genes are encoded chromosomally rather than on plasmids (Supplementary Information section 11). Moreover, several glycan degradation genes (endo-4-O-sulfatase and three SusD-like proteins) are enriched in the industrial samples compared to the palaeofaeces (Extended Data Fig. 12 and Supplementary Table 8). These genes are mostly found in Bacteroidetes SGBs, including *Bacteroides* and *Prevotella* species (Supplementary Information section 10).

Analysis of CAZymes (carbohydrate-active enzymes)²⁸ reveals similar enrichment patterns in the palaeofaeces and the non-industrial samples compared to the industrial samples (Fig. 4b). For instance, starch- and glycogen-degrading CAZymes are enriched in the palaeofaeces and the non-industrial samples, whereas mucin- and alginic-related CAZymes are enriched in the industrial samples. Chitin-degrading CAZymes are enriched in the palaeofaeces relative to both the non-industrial and industrial samples. This is in accordance with our microscopic dietary analysis that identified chitin sources (*Ustilago maydis*, mushrooms and insects) in the palaeofaeces (Supplementary Information section 2). These foods were commonly part of ancient Pueblo and Great Basin diets²⁹. These chitin CAZymes are prevalent in MAGs within Oscillospiraceae, Lachnospiraceae and Clostridiaceae families (Supplementary Information section 10). Taken together, the palaeofaeces share more features with non-industrial samples than with industrial samples.

Discussion

To date, it is not known to what extent the human microbiome has evolved over long time spans. Our analysis supports that present-day non-industrial human gut microbiomes more closely resemble the palaeofaeces, whereas the industrial gut microbiome has diverged from the ancient gut microbiome. Some species, such as *Ruminococcus callidus*, *Butyrivibrio crossotus* and *T. succinifaciens*, are more prevalent in the palaeofaeces and non-industrial samples than industrial samples (Fig. 1c and Supplementary Table 3). Furthermore, the industrial samples are enriched in mucin-degrading genes (Fig. 4) that are mostly found in our *Bacteroides* and *Prevotella* SGBs (Supplementary Information section 10). This is in line with the higher abundance of Bacteroidetes in the industrial samples (Fig. 1a), previous findings that members of the Bacteroidetes phylum possess many glycan-degrading genes³⁰ and the enrichment of mucin-using enzymes in the industrialized gut

microbiome¹. By contrast, the palaeofaeces and the non-industrial samples are enriched in starch- and/or glycogen-degrading CAZymes (Fig. 4b; probably because of a higher consumption of complex carbohydrates relative to simple sugars) and mobile genetic elements (Fig. 4a). This is in agreement with a previous observation of a higher abundance of mobile genetic elements in agrarian Fiji islanders compared to North American individuals³¹. Our finding supports the hypothesis that mobile genes are important for the colonization of the gut of non-industrial populations, perhaps for adaptation to an environment with greater variation, such as seasonal variation¹.

Moreover, we report the reconstruction of 181 authenticated ancient gut microbial genomes, 39% of which are novel SGBs (Fig. 2 and Extended Data Fig. 6). The highly degraded nature of aDNA is an obstacle to recovering MAGs from ancient samples. However, a recent study indicates that MAG recovery from mammalian dental calculus is possible with deeper sequencing³². Here, we show that large-scale de novo assembly and recovery of previously undescribed microorganisms from palaeofaeces are attainable. The reconstructed ancient microorganisms are of high quality and could be used for phylogenetic analysis and tip-based dating (Figs. 2b, 3), shedding light on the evolutionary relationships between the ancient genomes and their modern relatives. These analyses were possible due to the extraordinary preservation of the palaeofaeces, use of aDNA extraction methods suited for palaeofaeces³³, high sequencing depth (100,000,000–400,000,000 read pairs per sample) and advances in de novo genome reconstruction methodology¹³.

Although long DNA fragments are usually excluded from aDNA analysis, our findings suggest that some well-preserved palaeofaeces contain longer DNA fragments. Preservation of aDNA in palaeofaeces is relatively understudied, and known kinetics of DNA damage is largely based on mineralized tissues^{34,35,36}. Post-mortem decomposition of DNA is driven by the presence of water and because palaeofaeces are preserved only under extreme cases of desiccation or freezing with the absence or immobilization of water³³, they are expected to exhibit lower levels of hydrolytic damage. Furthermore, there is variation in the preservation of DNA across archaeological sites³⁷. Palaeofaeces from Zape are known to have well-preserved aDNA^{6,14,15}. Two of our palaeofaeces samples were from Boomerang Shelter, which is further north compared to Zape. The extreme aridity and lower temperature of the site probably contributed to the preservation of the samples. In addition, seasonality is relevant to the decomposition of palaeofaeces³⁷. Microbotanical analysis reveals that most of the palaeofaeces from Boomerang Shelter were deposited in the spring, summer or autumn, except for UT30.3, which was deposited in late autumn or early winter (Supplementary Table 2). This is the ideal environment for preservation owing to lack of decomposers³⁷ and might explain the low damage levels of UT30.3.

In this study, we establish that palaeofaeces with well-preserved DNA are abundant sources of microbial genomes, including previously undescribed microbial species, that may elucidate the evolutionary histories of human microbiomes. Similar future studies tapping into the richness of palaeofaeces will not only expand our knowledge of the human microbiome, but may also lead to the development of approaches to restore present-day gut microbiomes to their ancestral state.

Methods

Data reporting

No statistical methods were used to predetermine sample size and the experiments were not randomized. Metagenomic library construction, dietary analysis and seasonality interpretation were performed blindly. Blinding is not applicable to the metagenomic analysis; all samples were analysed computationally in a uniform manner.

Archaeological samples and sites

The eight palaeofaeces analysed in detail were collected from Boomerang Shelter, Arid West Cave and Zape as described below. Three soil samples were collected from Boomerang Shelter. Palaeofaeces from Boomerang Shelter are curated at the Edge of the Cedars State Park Museum, Blanding, Utah, USA. Samples from Arid West Cave are curated at The Robert S. Peabody Institute of Archaeology, Andover, Massachusetts, USA. The collection from Zape is curated at the Anthropology Department of the University of Nevada, Las Vegas, USA.

All samples are from dry rock shelters, sometimes called caves or alcoves. These are neither dark nor deep but have naturally eroded openings in the sides of cliffs that are only tens of metres wide at most. However, the palaeofaeces remain dry with exceptional preservation. Such rock shelters often even preserve feathers and other such material after a thousand or more years. Palaeofaeces, once deposited, would have been covered by windblown soil or human activity. As these shelters were used repeatedly over many years, some palaeofaeces could have been re-exposed and moved beyond the dry portion and become wet then once again moved and dried; or in a dry location exposed to dumped cooking water and so on. Those palaeofaeces samples seemed to have considerable evidence of fungi based on macroscopic evidence. Thus, we included only samples that do not appear to have been negatively affected by such events. Furthermore, such post-depositional movement can change the initial stratigraphic location of the specimens. We carbon-dated using ^{14}C dating all of the palaeofaeces samples and they were dated to anticipated dates (Extended Data Fig. 1b and Supplementary Table 1).

Boomerang Shelter

This shelter lies in southeastern Utah³⁹. The primary occupation was during Basketmaker II times, but a few pre-farmer artefacts dating to as early as 8310 years before present (bp) (around 7400 bc) have been recovered. However, most remains dated to between 2500 and 1500 bp and two of our samples dated to the first century ad in the middle of this range. By this time, the inhabitants were committed maize farmers with high proportions of maize in their diet as demonstrated by a previous study of palaeofaeces from the shelter⁴⁰. Furthermore, the site is only about 40 km from the contemporary Turkey Pen Ruin, palaeofaeces from which yielded similar dietary results and had good preservation of human, plant and animal aDNA, but bacterial DNA was not considered for this site⁴¹.

Arid West Cave

The precise location of this set of samples cannot be determined (samples labelled AW107, AW108, AW110A, and so on) as they are without location labels. The samples were found at a time before palaeofaeces were regularly collected and saved, and if saved they were never studied. We know these samples were collected in 1931 or a year or two before, which narrows the possibilities of where they are from. The radiocarbon dates and macro-remains (diet) of these palaeofaeces make clear that they are from the northern part of the American Southwest, but they could come from several different expeditions almost a century or more ago. There is a remote possibility that they come from an expedition mounted by the Peabody Museum of Archaeology and Ethnology at Harvard University. They could be from the Samuel Guernsey projects between 1920 and 1923⁴². However, none of the project records make any mention of palaeofaeces, nor do they fit the time frame and site types that he studied. Conversely, the Harvard Peabody Museum also undertook a series of expeditions to eastern parts of Utah between 1928 and 1931 (often referred to as the Claflin–Emerson or Morss projects) and they did recover palaeofaeces and did work in deposits of the appropriate time, in particular at the Rasmussen Ranch Cave site in east-central Utah^{43,44,45}. This is the most likely source, but it cannot be confirmed absolutely. Fortunately, for our purposes, the exact location is not critical. Knowing the time frame and general region is adequate for our purposes. The palaeofaeces are some 500 years or more closer to the present than those from Boomerang Shelter. The major difference is that these individuals would have had maize as a staple of their diets for an additional 500 years.

La Cueva de los Muertos Chiquitos (Zape)

The La Cueva de los Muertos Chiquitos site (ad 660–1430) is located near Zape, just north of Durango, Mexico (hereafter Zape). Excavated in the 1950s by Sheilagh and Richard Brooks, the cave primarily dates to the Gabriel San Loma cultural phase. The site is known for what appears to be a deliberate burial of a series of infants who died at or about the same time^{[46](#)}. However, the palaeofaeces in our sample came from a different layer in the cave and are not associated with that event. Our samples date from the 700s ad to the early 900s ad. No full report exists, but various aspects of the material have been published^{[46,47,48,49](#)}.

14C dating

The palaeofaeces samples were submitted to DirectAMS for accelerator mass spectrometry radiocarbon dating measurements. As shown in Extended Data Fig. [1b](#) and Supplementary Table [1](#), all dates fit with the known dates of the sites that the samples are from and are dated to the first ten centuries ad.

Dietary analysis

Our knowledge of the diets comes from the macro-remains analysis of the palaeofaeces plus archaeologically recovered information from these and similar shelters in the region. The diet of the individuals has been summarized as maize and other available remains (Supplementary Information section [2](#) and Supplementary Table [2](#)). Beans were not present for the inhabitants of the Boomerang Shelter and were a recent introduction for inhabitants of Arid West Cave, but had been present longer and with more varieties for the inhabitants of Zape cave. Wild plants would have included grasses and pinyon pine nuts, cactus, and agave and relatives, including the fruits, flowers and fleshy parts. Animals would have included deer and various rabbits, other mammals including a variety of rodents, as well as insects such as locusts and cicadas, both adult and larval stages, reptiles such as snakes, and birds. For most periods, the absence of beans would have required substantial animal protein.

Extraction, library preparation and sequencing of aDNA

Samples were sent to the Molecular Anthropology Laboratory at the University of Montana, which is a controlled access facility, wherein researchers are required to wear Tyvek clean suits, foot coverings, hair nets, face masks, arm coverings and gloves to enter. All work surfaces in the room, including specialized clothing, are bleached daily using a 50% household bleach solution and between each sample processing. Additionally, UV light overhead is run for an hour each evening, as well as a smaller targeted light on work surfaces, to aid in decontamination. The room

maintains a positively pressurized environment. Movement from a laboratory working with post-PCR products to the aDNA laboratory was not allowed at any time.

Samples were transferred to the University of Montana in conical tubes, and after the outside had been wiped down with a bleach solution, a small portion was scraped from the centre of the sample into a UV-irradiated (for a minimum of 15 min) 15-ml sterile tube. Soil samples were weighed out in sterilized weigh boats. Approximately a gram was taken from soil and faecal samples and 5 ml of EDTA (0.5 M, pH 8) was added to each. Samples were incubated at room temperature for approximately 48 h, after which 20 µl of 1 mg ml⁻¹ proteinase K was added to each, followed by sealing with Parafilm and further incubation at 52 °C with slow rotation (4 rpm) for 4 h. Once the samples were removed from incubation, they were extracted following a previously published protocol⁵⁰. This entailed spinning the sample to the bottom of the tube by centrifugation at 1,500g and 1.5 ml of the EDTA solution being pipetted into a sterile, UV-treated 15-ml polypropylene tube. Next, 13 ml of PB buffer (Qiagen) was added to each sample and mixed by inversion. The liquid was spun through Qiagen MinElute filters using 50-ml polypropylene tubes and nested conical reservoirs (Zymo) with attached filters. These filters were then removed, placed into a collection tube, washed twice with PE buffer (Qiagen) and eluted with two 50 µl DNase-free H₂O rinses into sterile, low-bind 2-ml tubes. A blank negative control was run through all of the previous and following steps, and in no instance was contamination in subsequent DNA quantifications or analyses detected.

Library preparation was completed using previously published protocols^{51,52}. This entailed using half of the extracted DNA to perform uracil DNA glycosylase (UDG) repair with the USER enzyme (Supplementary Information section [12](#) and Supplementary Table [10](#)). The other half of the extract was taken straight to blunt-end repair, followed by adaptor ligation and fill-in. Both the UDG-treated and untreated samples were separately indexed using a dual-index process with indexes from previously published studies^{53,54}. The sample concentration was then calculated using a Qubit 4 with the High Sensitivity DS DNA assay (ThermoFisher). Samples with more than 1 ng µl⁻¹ were pooled and sent for sequencing via overnight FedEx. Libraries were sequenced on the Illumina HiSeq 4000 platform in 2 × 150-bp paired-end format.

Overview of the present-day samples

The present-day samples were classified into two categories: present-day industrial samples and present-day non-industrial samples. An industrial lifestyle is defined here as one with consumption of a Western diet, common antibiotic use and sedentary lifestyle. Non-industrial lifestyle is characterized by consumption of unprocessed and self-produced foods, limited antibiotic use and a more active lifestyle.

In total, 789 present-day human gut metagenomes were analysed. Present-day industrial samples encompass metagenomes from 418 stool samples, including 169 individuals from the USA (147 from the HMP⁵⁵ and 22 from a previously published study⁴), 109 from Denmark⁵⁶ and 140 from Spain⁵⁶. Present-day non-industrial samples include publicly available gut metagenomes of 174 individuals from Fiji³¹, 36 from Peru⁴, 112 from Madagascar¹³ and 27 from Tanzania⁵⁷. In addition, stool samples from 22 individuals were collected from a Mazahua community in the centre of Mexico. They preserve a non-industrial lifestyle and have remained semi-isolated from urban areas. The affinity to a non-industrial Mexican diet was assessed by the application of a questionnaire about the frequency of consumption of fresh or industrial food, which was adapted from a previous study⁵⁸. The definition of a non-industrial Mexican diet is one that provides protein, carbohydrates, vitamins and minerals from the consumption of foods such as maize, legumes (mainly beans), fruits, vegetables such as pumpkins and nopales, as well as different types of herbs such as quelites and verdolagas⁵⁸. These individuals had not received antibiotic treatment in at least six months before sample collection. All study participants were recruited in accordance with a human participant research protocol (IRB number: CEI 2018/01) approved by the Institutional Review Board of INMEGEN. Each participant provided a statement of informed consent, and we have complied with all of the relevant ethical regulations.

Extraction, library preparation and sequencing of modern DNA

Stool samples from the individuals of Mexican ancestry were immediately put in dry ice after collection and sent to the Joslin Diabetes Center for processing. DNA extraction was performed using ZymoBIOMICS DNA Miniprep Kit (D4300). Sample concentrations were calculated using a Qubit 3.0 with the High Sensitivity DS DNA assay (ThermoFisher) and purity was assessed using a NanoDrop Spectrophotometer.

Library preparation was performed following a previously published protocol⁵⁹. Sample concentrations were again calculated using a Qubit 3.0 with the High Sensitivity DS DNA assay (ThermoFisher). Samples were pooled for a total of 11 samples per lane and sent for shotgun metagenomic sequencing via overnight FedEx. Libraries were sequenced on the Illumina HiSeq 4000 platform in 2×150 -bp paired-end format.

Read processing and quality control

Adapters were removed from paired Illumina reads using AdapterRemoval v.2⁶⁰. Human DNA sequences were filtered out using KneadData v.0.6.1 (<https://github.com/biobakery/kneaddata>) by mapping reads to the *Homo sapiens* reference database (build hg19)⁶¹. For the archaeological samples, short reads of fewer than 30 bp were removed using Cutadapt (v.2.8)⁶². All downstream analyses were done on these pre-processed reads unless otherwise specified.

Human DNA analysis

In this study, we performed shotgun metagenomic sequencing, which also gave us access to the human host DNA. Although we did not perform targeted enrichment of human DNA molecules, the small amount of randomly sequenced molecules that could be aligned to the human reference genome was large enough to authenticate the host of the faecal samples as human and not another organism, such as a dog (as the two can

be confused morphologically). These data further enabled us to investigate whether their mitochondrial haplogroups overlapped with the ones expected in the geographical region during the lifetime of the individuals. The human genetic data were not the target of the sampling process nor the research being undertaken and were used only to verify the microbial results. All of the human DNA analysis was performed before removal of human DNA by KneadData.

Owing to the high copy number of human mtDNA, almost complete inheritance on the maternal lineage and lack of recombination⁶³, we used human mtDNA from the low-coverage human data to infer the proportion of modern human contamination and for haplogroup identification. For the contamination estimate based on the observed minor allele frequencies at rarely polymorphic sites, we used contamMix (v.1.0-10)⁶⁴ as part of the ancient mtDNA pipeline of mitoBench v.1.6-beta (<https://github.com/mitobench/mitoBench> and <https://github.com/alexhbnr/mitoBench-ancientMT>). For haplogroup identification, reads were mapped to the human mtDNA reference genome (rCRS)⁶⁵ and duplicates were removed using Picard MarkDuplicates v.2.18.2 (<https://broadinstitute.github.io/picard>), followed by a left alignment to normalize indels. A Bayesian approach to variant analysis was performed using FreeBayes (v.1.1.0)⁶⁶ and haplogroups were identified by inputting the variant calling file into HaploGrep (v.2.1.21)⁶⁷. All steps for haplogroup identification were run through a custom-made workflow in Galaxy (2019 build version)⁶⁸ alongside command line executions for validation and replication.

Reference-based taxonomic classification

Reference-based taxonomic classification for the ancient, Mexican and Fijian samples was performed by running MetaPhlAn2 (v.2.7.5) on the pre-processed reads using default settings²⁰. For the other present-day industrial and non-industrial samples, MetaPhlAn2 output files were collected from the R package curatedMetagenomicData (v.1.16.0)⁶⁹. One sample from Fiji (SRS476326)³¹ was 100% unclassified and was excluded from the reference-based taxonomic analysis.

Prediction of the source of microbial communities

To predict the source of each sample, the species composition (from MetaPhlAn2) of the palaeofaeces was compared to 40 industrial gut microbiome samples, 40 non-industrial gut microbiome samples and a diverse set of environmental samples (Supplementary Table 9). These environmental samples include the 3 soil samples collected in this study, 40 Pleistocene sediment samples⁷⁰ and 7 Holocene human-associated sediments (which overlap in age with our palaeofaeces) from CoproID⁷¹. MetaPhlAn2 results for 40 industrialized and 40 non-industrialized human participants were obtained from the R package curatedMetagenomicData⁶⁹ (Supplementary Table 9). The rest of the samples were run through MetaPhlAn2²⁰ using default settings, then converted to biom format. The resulting species abundance matrix biom file was used as input for SourceTracker2⁷².

Host source prediction

To predict whether the source species of each palaeofaeces was *H. sapiens* or *Canis familiaris*, pre-processed reads were run through CoproID (v.1.0)⁷¹ using the following settings: --genome1 GRCh37 --genome2 CanFam3.1 --name1 ‘Homo_sapiens’ --name2 ‘Canis_familiaris’.

Parasite analysis

Paired reads were fused into single reads using bbmerge from BBSSuite (v.38.24)⁷³ using standard parameters. Classification of the fused reads against a custom nucleotide database was performed using Kraken 2 (v.2.0.8-beta)⁷⁴ using a threshold of 0.15. The custom Kraken 2 database was created from 160,946 publicly available genomes from RefSeq for bacteria, fungi, plants, mammalian vertebrates, other vertebrates and viruses (May 2019). In addition, 530 genomes were selected from 926 available protozoa, flatworm and roundworm genomes downloaded from GenBank (May 2019). The 530 genomes were selected based on assembly criteria, including N50, number of contigs and number of ambiguous sequences as described previously⁷⁵. Contigs with length less than 1,000 bp were

removed. For protozoa, flatworm and roundworm genomes, artificial nodes in the taxonomic tree were introduced. This means that below species or strain level, we have included further nodes for assembly and contig levels to increase the resolution of classification. To minimize the number of false-positive classifications, we used three different cut-offs in the Kraken-2-based analysis. Parasite species with hits below 1,000 reads were removed. To ensure that the hits were dispersed over the genome, we also required that the number of contigs with at least one hit was more than 10% of all of the contigs in the assembly and that the combined length of the contigs with hits represented at least 50% of the whole genome. Coverage of the genome and dispersion of reads were visually inspected for each candidate (Supplementary Table 4).

De novo assembly pipeline

Each sample was de novo assembled into contigs using MEGAHIT (v.1.2.9)⁷⁶ with default settings. Assembly statistics (number of contigs, number of bp in contigs, contig N50, contig L50 and the longest contig) were calculated using the statswrapper.sh function from BBMap (v.38.86) (<https://sourceforge.net/projects/bbmap/>) with default parameters (Supplementary Table 1).

Genome reconstruction

Ancient and Mexican genomes were reconstructed as previously described¹³. Pre-processed reads were de novo assembled into contigs using MEGAHIT (v.1.2.9)⁷⁶. For each sample, reads were mapped to contigs using Bowtie 2 (v.2.3.5.1)⁷⁷ with default settings (no minimum contig length). The resulting alignment file was sorted and indexed with SAMtools (v.1.9)⁷⁸. The sorted BAM file was used for contig binning using MetaBAT 2 (v.2.12.1)⁹ with default parameters (minimum contig size = 2.5 kb), resulting in putative genomes. Quality controls (completeness, contamination, genome size (bp), number of contigs, contig N50 values, mean contig length and the longest contig) were assessed using the lineage-specific workflow in CheckM with default settings (v.1.0.18)⁷⁹. Following recent guidelines⁸⁰, genomes with completeness between 50% and 90% and

contamination < 5% were classified as medium-quality genomes. Higher-quality genomes with completeness > 90% and contamination < 5% were classified as high-quality genomes. Coverage for each contig was calculated using the ‘coverage’ command in CheckM⁷⁹, and coverage per genome was calculated by averaging the coverage profiles across all contigs within the genome.

The relative abundance of each reconstructed genome (Supplementary Table 6) was calculated by dividing the number of reads aligned to the genome by the total number of raw reads from that sample. On average, the medium-quality and high-quality filtered genomes account for 11.5% (s.d. = 9.4) of the total raw reads per sample (Supplementary Table 6), and the novel medium-quality and high-quality filtered genomes constitute 3.3% (s.d. = 1.7) of the total raw reads per sample (Supplementary Table 6). To calculate the percentage of contigs binned in each genome, the number of contigs per genome was divided by the number of contigs binned from the sample. To calculate the percentage of bp from contigs binned in each genome, the genome size (in bp) was divided by the number of bp in the contigs binned from the same sample. The percentages across genomes from the same sample were summed to calculate the percentage per sample.

To cluster assembled genomes of the same species, pairwise ANIs for the assembled genomes were calculated using the ‘derePLICATE’ command in dRep (v.2.4.2)⁸¹ with the following settings: -comp 50 -pa 0.9 -sa 0.95 -nc 0.30 -cm larger. This dRep command uses MUMmer (v.3.23)⁸² to cluster genomes with more than 95% ANI together into a SGB and select one representative genome per SGB. This 5% distance metric follows the definition of a bacterial species⁸³.

To determine whether each of the SGBs belongs to a known microbial species, pairwise genetic distances were calculated between each of the representative genomes and each of the 388,221 reference microbial genomes. The reference genomes included previously reconstructed human gut MAGs^{11,12} (as previously catalogued⁸⁴), previously reconstructed MAGs¹³, 80,990 genomes from the NCBI GenBank database previously used as reference¹³, and MAGs from nonhuman primate gut metagenomes⁸⁵. Mash distances were calculated using Mash (v.2.1)⁸⁶ for

all of the genomes using default settings (sketch size = 1000). Subsequently, ANIs were calculated using FastANI (v.1.3)⁸³ for each ancient genome and its 100 closest reference genomes within 10% Mash distance. The ‘cluster’ command in dRep⁸¹ was used to run FastANI⁸³ using the default alignment fraction (0.1) and with the following settings: -sa 0.95 --S_algorithm fastANI. Bins with more than 95% ANI with at least one reference genome were classified as ‘known’ SGBs and the rest were classified as ‘novel’ SGBs. Each bin was labelled as ‘gut’, ‘environmental’ or ‘unsure’ on the basis of the source of its closest reference genome (that is, if the closest reference genome was a MAG or an isolate from a gut microbiome sample, then the bin was labelled as ‘gut’). The ‘classify’ workflow in GTDB-Tk (v.0.3.0; default settings) was used to assign taxa to the bins²³.

Damage pattern assessment

Assessment of host DNA damage was performed by mapping reads (before removal of human DNA by KneadData) to the human mtDNA reference genome (rCRS)⁶⁵ and inputting the alignment files into mapDamage2.0 (v.2.0.9)⁸⁷. Damage patterns for microbial DNA were assessed with DamageProfiler (v.0.4.7)⁸⁸ using each of the medium-quality and high-quality reconstructed genomes as reference for its respective sample. For each genome, reads were mapped to each contig, the resulting alignment file was sorted and indexed with SAMtools (v.1.9)⁷⁸, DamageProfiler⁸⁸ was run per contig, and the average damage levels and damage variation across reads per contig were calculated. The 498 medium-quality and high-quality assembled genomes from the palaeofaeces were further curated by removing contigs with average read damage < 1% at either or both ends of the reads. This is a conservative cut-off because the process removed some known gut bacterial species (for example, *T. succinifaciens*) from the medium-quality and high-quality bins (Extended Data Fig. 7g). Genomes were classified as having high damage if the average damage level at the ends of the reads was within the top 50th percentile damage level among the 498 medium-quality and high-quality bins. Genomes were classified as having high damage variance if the s.d. of the damage at the ends of the reads was within the top 50th percentile s.d. among the 498 medium-quality and high-quality bins. Genomes with high damage levels and low damage

variance are our most confident ancient genomes because most of the contigs in these genomes are highly damaged, hence they must contain minimal to no contamination with modern DNA.

Phylogenetic analysis

To build phylogenetic trees, the ‘classify’ workflow in GTDB-Tk (v.0.3.0; default settings) was used to identify 120 bacterial marker genes and build a multiple sequence alignment based on these marker genes²³. The resulting FASTA files containing multiple sequence alignments of the submitted genomes (align/<prefix>.[bac120/ar122].user_msa.fasta) were used for maximum likelihood phylogenetic tree inference using IQ-TREE (v.1.6.11)⁸⁹ with the following parameters: -nt AUTO -m LG. Newick tree output files were visualized with iTOL v.5 (<https://itol.embl.de/>).

For Fig. 2b, 4,930 representative human microbiome genomes that were previously reconstructed¹³ were used as reference genomes. For Supplementary Fig. 1, all genomes from the NCBI RefSeq database belonging to each genus were used as reference genomes. Ancient genomes included in the trees were bacterial genomes from the 181 high-damage bins that were assigned to each genus. Multiple sequence alignment files used to create the phylogenetic trees were visually inspected (Supplementary Fig. 2).

Divergence estimates of *M. smithii*

To calibrate the *M. smithii* phylogeny, we used as tip dating two *M. smithii* genomes reconstructed from ancient metagenome samples UT30.3 (1947 ± 30 bp) and UT43.2 (1994 ± 26 bp). We selected *M. smithii* because of its presence in two distinct palaeofaeces samples, a large number of available modern genomes, and a previous divergence estimate in the genus *Methanobrevibacter* that could be used as a comparison²⁴. We first studied the phylogenetic placement of these two ancient genomes by leveraging 488 contemporary *M. smithii* genomes, and inferring a high-resolution phylogeny composed of ancient and contemporary genomes using PhyloPhlAn (v.3.0)^{13,90}. Twenty-eight contemporary *M. smithii* genomes that were representative of the *M. smithii* phylogenetic expansion were

selected for further analysis, along with the two ancient genomes, compiling a dataset of 30 genomes (Supplementary Fig. 3). To build this dataset, orthologues were searched within the ancient genomes ($n = 2$) and their contemporary counterparts ($n = 28$) and were merged into one concatenated alignment with a length of 346,567 bp using Roary (v.3.13.0)⁹¹ with parameters -i 0.95 and -cd 90. To assess the certainty of core genome phylogeny of the 30 *M. smithii* genomes, we used RAxML (v.8.1.15)⁹² under a GTR model of substitution with 4 gamma categories and 100 bootstrap pseudo replicates. BEAST2 (v.2.5.1)⁹³ was used to infer the divergence times between genomes using a GTR model of substitution with 4 gamma categories. Convergence of posteriors was assessed by visualizing the log-transformed files with Tracer (v.1.7)⁹⁴. Following a previous divergence estimate of *Methanobrevibacter*²⁴, we used a strict clock model in BEAST2, and further performed model selection (Supplementary Table 7) to choose the most fitting demographic (tree) prior. We estimated the marginal likelihood via path sampling and stepping stone for five demographic models. We ran the chains up to 297 million generations to obtain convergence in accordance with the effective sample size of all parameters being over 200. We identified a coalescent Bayesian skyline⁹⁵ as the most fitting demographic model for our dataset (Supplementary Table 7), indicating that the genomes are evolving under Wright–Fisher dynamics⁹⁶. We further tested relaxed clocks, but the effective sample size of most parameters (including the prior and the root age, the latter of which varied by 2–3 orders of magnitude) were extremely low even after 500 million generations (more than 2-week running time). Moreover, the posterior mean, although not at convergence, was in the range of 10^{-5} – 10^{-6} mutations per site per year, a rate that is incompatible with the mutation rates of bacteria over a time range higher than 100 years⁹⁷. As various posteriors could not go to convergence after sufficient sampling and/or were not compatible with known patterns of bacterial evolution in realistic scenarios (Supplementary Table 7), we focused on the strict clock model.

We optimized our molecular clock analysis by ruling out possible artefacts that could be derived from aDNA degradation. Post-mortem DNA damage results in an elevated C-to-T substitution rate at the 5' end of reads (and an

elevated G-to-A substitution rate at the 3' end of reads)⁹⁸. To mitigate such bias, we repeated our BEAST2 analyses using genomes reconstructed from reads that aligned to the two ancient *M. smithii* genomes but had been trimmed at the first and last 5 bp using Cutadapt (v.2.8)⁶². To further inspect substitutions that could possibly be derived from aDNA damage, we searched the alignment for polymorphic positions at which all contemporary genomes had C/G as base and all ancient genomes had T/A as base. We visually assessed the pileup of reads on the ancient MAGs using Tablet (v.1.19.09.03)⁹⁹ and observed that 24 suspicious substitutions were located at the end of reads, suggesting that these sites could be prone to aDNA degradation. To minimize the effect of strain heterogeneity on the clocking analysis, we removed arbitrary sites of genomes that polymorphism dominance of mapped reads was lower than 0.8. Having identified and removed 11,938 sites, we obtained a carefully curated genome alignment with a length of 339,321 bp. This dataset was analysed using the most fitting demographic model under a GTR + G replacement model and a strict clock model (Supplementary Table 7).

Molecular function analysis

From contigs, genes were annotated with PROKKA (v.1.14.6)³⁸ with default parameters per sample. A non-redundant gene catalogue combining all of the predicted genes across all samples was generated with CD-HIT-EST (v.4.8.1)¹⁰⁰ with a 95% identity threshold using the following settings: -n 10 -c 0.95 -s 0.9 -aS 0.9. Genes labelled as ‘hypothetical protein’ were removed from the gene catalogue. Raw reads from each sample were aligned to the gene catalogue using Bowtie 2 (v.2.3.5.1)⁷⁷ with the following parameters: -D 20 -R 3 -N 1 -L 20 -i S,1.0,50 --local --mm. The output BAM file was sorted and indexed with SAMtools (v.1.9)⁷⁸. For each gene per sample, the relative abundance was calculated by dividing the number of reads aligned to the gene by the length of the gene and the total number of reads aligned to the gene catalogue per sample. RPKM values were calculated by multiplying the relative abundance values by 1,000 (for the per kb conversion) and 1,000,000 (for the per million conversion). Five samples from Madagascar (SRR7658580, SRR7658586, SRR7658642, SRR7658670 and SRR7658672)¹³ and one from Tanzania (SRR1930179)⁵⁷

were excluded because none of the reads aligned to the gene catalogue. A Wilcoxon rank-sum test with Bonferroni correction was performed for each of the genes. To ensure that genes enriched in the palaeofaeces were not merely soil contamination, we excluded genes enriched in the soil samples compared to the present-day samples from the list of genes enriched in the palaeofaeces (Supplementary Table 8).

CAZy analysis

To predict CAZymes²⁸ from PROKKA protein output files (.faa files), hmmsearch (v.3.1b2)¹⁰¹ was run against dbCAN HMMs v8¹⁰² and an *e*-value cut-off of less than 1×10^{-5} was used¹⁰². Five Fijian samples (SRS475540, SRS475681, SRS476013, SRS476143 and SRS476277)³¹, one HMP sample (SRS018313)¹⁰³ and one Spanish sample (V1.UC59.4)⁵⁶ were excluded because they had no predicted CAZyme. CAZyme relative abundances were calculated by dividing the number of times each CAZy family was predicted in each sample by the total number of CAZymes predicted in the sample. A two-tailed Wilcoxon rank-sum test with FDR correction was performed for each CAZy family. To identify CAZy families that were enriched in the soil samples relative to present-day samples, a one-tailed Wilcoxon rank-sum test with FDR correction was performed for each CAZy family. These soil-enriched CAZy families were removed from the list of CAZy families. Statistically significant CAZy families were manually annotated with broad substrate categories.

Jaccard distance matrix

To calculate pairwise Jaccard distances, binary matrices were used as inputs. For Extended Data Fig. 5a, a species binary matrix was created from MetaPhlAn2 output. To do this, MetaPhlAn2 output files were collapsed into a relative abundance matrix with the columns as samples and the rows as species. A binary matrix was created by recording non-zero cells as 1. For Extended Data Fig. 5b, a binary matrix was created with the columns as samples and the rows as genes. The presence of a gene in a sample was recorded as 1. Pairwise Jaccard distance was calculated using the Python package scikit-bio (<http://scikit-bio.org/>), specifically using the

`pw_distances` function from `skbio.diversity.beta` package. The result was visualized as a heat map.

Analysis of short versus long DNA fragments

To check whether the long DNA fragments found in the palaeofaeces were from contamination with modern DNA, we divided each sample into two subgroups: a subset containing only the long reads (>145 bp) and a subset of only the short reads (≤ 145 bp), and compared the species and gene composition among those subsamples. For Extended Data Fig. 5a, species were identified by MetaPhlAn2²⁰, and the resulting binary species matrix was used to calculate pairwise Jaccard distances. For Extended Data Fig. 5b, genes were identified by PROKKA (v.1.14.6)³⁸. The outputs were used to build a binary matrix to calculate the pairwise Jaccard distances.

Cloud computing

Analyses were conducted on Amazon Web Services spot instances using Aether¹⁰⁴ and on the O2 High Performance Compute Cluster, supported by the Research Computing Group, at Harvard Medical School (<http://rc.hms.harvard.edu>).

Statistics and reproducibility

Statistical significance was verified through Welch's *t*-test, Fisher's test or Wilcoxon rank-sum test as described. Multiple-hypothesis testing corrections were performed using either the FDR or the Bonferroni approach. Most of the statistical analysis and data visualization were performed in R using the packages tidyverse, ggplot2, purrr, tibble, dplyr, tidyr, stringr, readr,forcats, scales, grid, reshape2, Rtsne, ggfortify, factoextra, ggpibr, ggforce, ggrepel, RColorBrewer and pheatmap. Data analysis and visualization for *M. smithii* tip dating were performed using the Python libraries pandas, NumPy and Matplotlib. Simulation of the effects of aDNA damage on assembly was performed using the Python package SciPy. Throughout the Article, data presented as box plots are defined as follows: middle line, median; lower hinge, first quartile; upper

hinge, third quartile; the upper whisker extends from the hinge to the largest value no further than $1.5 \times$ the interquartile range from the hinge; the lower whisker extends from the hinge to the smallest value at most $1.5 \times$ the interquartile range from the hinge; data beyond the end of the whiskers are individually plotted outlying points.

For Extended Data Fig. 1c, the analyses for Zape1, Zape2 and Zape3 were part of a large review of samples from this site. Ten other samples were presented independently¹⁰⁵. An additional 50 samples were reviewed¹⁰⁶. Thus, these images were part of an extensive study of 63 samples from the site. Thirty hours of scanning electron microscopy beam time were involved in making the images. The UT30.3 images were taken as part of an ongoing analysis of 98 samples from the Colorado Plateau. A total of 110 h of scanning electron microscopy beam time have been applied to characterizing the dietary components.

Reporting summary

Further information on research design is available in the [Nature Research Reporting Summary](#) linked to this paper.

Data availability

Raw sequencing data has been uploaded to NCBI Sequence Read Archive (SRA) under BioProject accession number [PRJNA561510](#).

Code availability

Scripts used for data analysis are publicly accessible at <https://github.com/kosticlab/ancient-microbiome-denovo>. The code used to quantify the effect of ancient DNA damage on the assembled sequences is publicly accessible at https://github.com/alexhbnr/effect_aDNAdamage_denovoassembly.

References

1. 1.

Smits, S. A. et al. Seasonal cycling in the gut microbiome of the Hadza hunter-gatherers of Tanzania. *Science* **357**, 802–806 (2017).

[CAS](#) [PubMed](#) [PubMed Central](#) [Google Scholar](#)

2. 2.

De Filippo, C. et al. Impact of diet in shaping gut microbiota revealed by a comparative study in children from Europe and rural Africa. *Proc. Natl Acad. Sci. USA* **107**, 14691–14696 (2010).

[ADS](#) [Google Scholar](#)

3. 3.

Yatsunenko, T. et al. Human gut microbiome viewed across age and geography. *Nature* **486**, 222–227 (2012).

[ADS](#) [CAS](#) [Article](#) [Google Scholar](#)

4. 4.

Obregon-Tito, A. J. et al. Subsistence strategies in traditional societies distinguish gut microbiomes. *Nat. Commun.* **6**, 6505 (2015).

[ADS](#) [CAS](#) [PubMed](#) [PubMed Central](#) [Google Scholar](#)

5. 5.

Angelakis, E. et al. Gut microbiome and dietary patterns in different Saudi populations and monkeys. *Sci. Rep.* **6**, 32191 (2016).

[ADS](#) [CAS](#) [PubMed](#) [PubMed Central](#) [Google Scholar](#)

6. 6.

Tett, A. et al. The *Prevotella copri* complex comprises four distinct clades underrepresented in Westernized populations. *Cell Host Microbe* **26**, 666–679.e7 (2019).

[CAS](#) [PubMed](#) [PubMed Central](#) [Google Scholar](#)

7. 7.

Blaser, M. J. The theory of disappearing microbiota and the epidemics of chronic diseases. *Nat. Rev. Immunol.* **17**, 461–463 (2017).

[CAS](#) [Google Scholar](#)

8. 8.

Sonnenburg, E. D. & Sonnenburg, J. L. The ancestral and industrialized gut microbiota and implications for human health. *Nat. Rev. Microbiol.* **17**, 383–390 (2019).

[CAS](#) [Google Scholar](#)

9. 9.

Kang, D. D. et al. MetaBAT 2: an adaptive binning algorithm for robust and efficient genome reconstruction from metagenome assemblies. *PeerJ* **7**, e7359 (2019).

[PubMed](#) [PubMed Central](#) [Google Scholar](#)

10. 10.

Parks, D. H. et al. Recovery of nearly 8,000 metagenome-assembled genomes substantially expands the tree of life. *Nat. Microbiol.* **2**, 1533–1542 (2017).

[CAS](#) [Google Scholar](#)

11. 11.

Nayfach, S., Shi, Z. J., Seshadri, R., Pollard, K. S. & Kyrpides, N. C. New insights from uncultivated genomes of the global human gut microbiome. *Nature* **568**, 505–510 (2019).

[ADS](#) [CAS](#) [PubMed](#) [PubMed Central](#) [Google Scholar](#)

12. 12.

Almeida, A. et al. A new genomic blueprint of the human gut microbiota. *Nature* **568**, 499–504 (2019).

[ADS](#) [CAS](#) [PubMed](#) [PubMed Central](#) [Google Scholar](#)

13. 13.

Pasolli, E. et al. Extensive unexplored human microbiome diversity revealed by over 150,000 genomes from metagenomes spanning age, geography, and lifestyle. *Cell* **176**, 649–662 (2019).

[CAS](#) [PubMed](#) [PubMed Central](#) [Google Scholar](#)

14. 14.

Tito, R. Y. et al. Phylotyping and functional analysis of two ancient human microbiomes. *PLoS ONE* **3**, e3703 (2008).

[ADS](#) [PubMed](#) [PubMed Central](#) [Google Scholar](#)

15. 15.

Tito, R. Y. et al. Insights from characterizing extinct human gut microbiomes. *PLoS ONE* **7**, e51146 (2012).

[ADS](#) [CAS](#) [PubMed](#) [PubMed Central](#) [Google Scholar](#)

16. 16.

Santiago-Rodriguez, T. M. et al. Gut microbiome of an 11th century A.D. pre-Columbian Andean mummy. *PLoS ONE* **10**, e0138135

(2015).

[PubMed](#) [PubMed Central](#) [Google Scholar](#)

17. 17.

Bos, K. I. et al. A draft genome of *Yersinia pestis* from victims of the Black Death. *Nature* **478**, 506–510 (2011).

[ADS](#) [CAS](#) [PubMed](#) [PubMed Central](#) [Google Scholar](#)

18. 18.

Schuenemann, V. J. et al. Genome-wide comparison of medieval and modern *Mycobacterium leprae*. *Science* **341**, 179–183 (2013).

[ADS](#) [CAS](#) [Google Scholar](#)

19. 19.

Vågene, Å. J. et al. *Salmonella enterica* genomes from victims of a major sixteenth-century epidemic in Mexico. *Nat. Ecol. Evol.* **2**, 520–528 (2018).

[Google Scholar](#)

20. 20.

Truong, D. T. et al. MetaPhlAn2 for enhanced metagenomic taxonomic profiling. *Nat. Methods* **12**, 902–903 (2015).

[CAS](#) [PubMed](#) [PubMed Central](#) [Google Scholar](#)

21. 21.

Fragiadakis, G. K. et al. Links between environment, diet, and the hunter-gatherer microbiome. *Gut Microbes* **10**, 216–227 (2019).

[CAS](#) [PubMed](#) [PubMed Central](#) [Google Scholar](#)

22. 22.

Sonnenburg, J. L. & Sonnenburg, E. D. Vulnerability of the industrialized microbiota. *Science* **366**, eaaw9255 (2019).

[CAS](#) [PubMed](#) [PubMed Central](#) [Google Scholar](#)

23. 23.

Chaumeil, P.-A., Mussig, A. J., Hugenholtz, P. & Parks, D. H. GTDB-Tk: a toolkit to classify genomes with the Genome Taxonomy Database. *Bioinformatics* **36**, 1925–1927 (2019).

[Google Scholar](#)

24. 24.

Weyrich, L. S. et al. Neanderthal behaviour, diet, and disease inferred from ancient DNA in dental calculus. *Nature* **544**, 357–361 (2017).

[ADS](#) [CAS](#) [PubMed](#) [PubMed Central](#) [Google Scholar](#)

25. 25.

Grün, R. et al. U-series and ESR analyses of bones and teeth relating to the human burials from Skhul. *J. Hum. Evol.* **49**, 316–334 (2005).

[PubMed](#) [PubMed Central](#) [Google Scholar](#)

26. 26.

Hershkovitz, I. et al. The earliest modern humans outside Africa. *Science* **359**, 456–459 (2018).

[ADS](#) [CAS](#) [PubMed](#) [PubMed Central](#) [Google Scholar](#)

27. 27.

Gaynes, R. The discovery of penicillin—new insights after more than 75 years of clinical use. *Emerg. Infect. Dis.* **23**, 849–853 (2017).

[Google Scholar](#)

28. 28.

Lombard, V., Golaconda Ramulu, H., Drula, E., Coutinho, P. M. & Henrissat, B. The carbohydrate-active enzymes database (CAZy) in 2013. *Nucleic Acids Res.* **42**, D490–D495 (2014).

[CAS](#) [PubMed](#) [PubMed Central](#) [Google Scholar](#)

29. 29.

Reinhard, K. J. A coprological view of ancestral Pueblo cannibalism. *Am. Sci.* **94**, 254–261 (2006).

[Google Scholar](#)

30. 30.

Martens, E. C., Koropatkin, N. M., Smith, T. J. & Gordon, J. I. Complex glycan catabolism by the human gut microbiota: the Bacteroidetes Sus-like paradigm. *J. Biol. Chem.* **284**, 24673–24677 (2009).

[CAS](#) [PubMed](#) [PubMed Central](#) [Google Scholar](#)

31. 31.

Brito, I. L. et al. Mobile genes in the human microbiome are structured from global to individual scales. *Nature* **535**, 435–439 (2016).

[ADS](#) [CAS](#) [PubMed](#) [PubMed Central](#) [Google Scholar](#)

32. 32.

Brealey, J. C. et al. Dental calculus as a tool to study the evolution of the mammalian oral microbiome. *Mol. Biol. Evol.* **37**, 3003–3022 (2020).

[PubMed](#) [PubMed Central](#) [Google Scholar](#)

33. 33.

Hagan, R. W. et al. Comparison of extraction methods for recovering ancient microbial DNA from paleofeces. *Am. J. Phys. Anthropol.* **171**, 275–284 (2020).

[PubMed](#) [PubMed Central](#) [Google Scholar](#)

34. 34.

Allentoft, M. E. et al. The half-life of DNA in bone: measuring decay kinetics in 158 dated fossils. *Proc. R. Soc. B* **279**, 4724–4733 (2012).

[CAS](#) [PubMed](#) [PubMed Central](#) [Google Scholar](#)

35. 35.

Sawyer, S., Krause, J., Guschanski, K., Savolainen, V. & Pääbo, S. Temporal patterns of nucleotide misincorporations and DNA fragmentation in ancient DNA. *PLoS ONE* **7**, e34131 (2012).

[ADS](#) [CAS](#) [PubMed](#) [PubMed Central](#) [Google Scholar](#)

36. 36.

Mann, A. E. et al. Differential preservation of endogenous human and microbial DNA in dental calculus and dentin. *Sci. Rep.* **8**, 9822 (2018).

[ADS](#) [PubMed](#) [PubMed Central](#) [Google Scholar](#)

37. 37.

Reinhard, K. et al. Imaging coprolite taphonomy and preservation. *Archaeol. Anthropol. Sci.* **11**, 6017–6035 (2019).

[Google Scholar](#)

38. 38.

Seemann, T. Prokka: rapid prokaryotic genome annotation. *Bioinformatics* **30**, 2068–2069 (2014).

[CAS](#) [PubMed](#) [Google Scholar](#)

39. 39.

Smiley, F. E. & Robins, M. R. *Early Farmers in the Northern Southwest: Papers on Chronometry, Social Dynamics, and Ecology*. Animas-La Plata Archaeological Research Paper No. 7, 43–58 (Northern Arizona Univ. Anthropology Laboratories, 1997).

40. 40.

Androy, J. *Agriculture and Mobility During the Basketmaker II Period: The Coprolite Evidence* (Northern Arizona Univ., 2003).

41. 41.

Battillo, J. M. *Supplementing Maize Agriculture in Basketmaker II Subsistence: Dietary Analysis of Human Paleofeces from Turkey Pen Ruin (42SA3714)*. PhD thesis, Southern Methodist University (2017).

42. 42.

Guernsey, S. J. *Explorations in Northeastern Arizona: Report on the Archaeological Fieldwork of 1920–1923* (The Museum, 1931).

43. 43.

Morss, N. Notes on the archaeology of the Kaibito and Rainbow Plateaus in Arizona, report on the explorations, 1927. *Peabody*

Museum Papers Vol. XII, No. 2 (Peabody Museum of American Archaeology and Ethnology, 1931).

44. 44.

Morss, N. The ancient culture of the Fremont river in Utah: report on the explorations under the Claflin-Emerson Fund, 1928–29. *Peabody Museum Papers Vol. XII, No. 3* (Peabody Museum of American Archaeology and Ethnology, 1931).

45. 45.

Spangler, J. D. & Aton, J. M. *The Crimson Cowboys: The Remarkable Odyssey of the 1931 Claflin-Emerson Expedition* (Univ. Utah Press, 2018).

46. 46.

Crandall, J. J., Martin, D. L. & Thompson, J. L. Evidence of child sacrifice at La Cueva de los Muertos Chiquitos (660–1430 AD). *Landsc. Violence* **2**, 12 (2012).

[Google Scholar](#)

47. 47.

Brooks, R. H., Kaplan, L., Cutler, H. C. & Whitaker, T. W. Plant material from a cave on the Rio Zape, Durango, Mexico. *Am. Antiq.* **27**, 356–369 (1962).

[Google Scholar](#)

48. 48.

Jiménez, F. A. et al. Zoonotic and human parasites of inhabitants of Cueva de los Muertos Chiquitos, Rio Zape Valley, Durango, Mexico. *J. Parasitol.* **98**, 304–309 (2012).

[PubMed](#) [PubMed Central](#) [Google Scholar](#)

49. 49.

Morrow, J. J. & Reinhard, K. J. *Cryptosporidium parvum* among coprolites from La Cueva de los Muertos Chiquitos (600–800 CE), Rio Zape Valley, Durango, Mexico. *J. Parasitol.* **102**, 429–435 (2016).

[PubMed](#) [PubMed Central](#) [Google Scholar](#)

50. 50.

Dabney, J. et al. Complete mitochondrial genome sequence of a Middle Pleistocene cave bear reconstructed from ultrashort DNA fragments. *Proc. Natl Acad. Sci. USA* **110**, 15758–15763 (2013).

[ADS](#) [CAS](#) [PubMed](#) [PubMed Central](#) [Google Scholar](#)

51. 51.

Briggs, A. W. et al. Removal of deaminated cytosines and detection of in vivo methylation in ancient DNA. *Nucleic Acids Res.* **38**, e87 (2010).

[PubMed](#) [PubMed Central](#) [Google Scholar](#)

52. 52.

Shapiro, B. & Hofreiter, M. *Ancient DNA: Methods and Protocols* (Humana, 2012).

53. 53.

Kircher, M., Sawyer, S. & Meyer, M. Double indexing overcomes inaccuracies in multiplex sequencing on the Illumina platform. *Nucleic Acids Res.* **40**, e3 (2012).

[CAS](#) [PubMed](#) [PubMed Central](#) [Google Scholar](#)

54. 54.

Meyer, M. & Kircher, M. Illumina sequencing library preparation for highly multiplexed target capture and sequencing. *Cold Spring Harb. Protoc.* **2010**, db.prot5448 (2010).

[Google Scholar](#)

55. 55.

Human Microbiome Project Consortium. A framework for human microbiome research. *Nature* **486**, 215–221 (2012).

[ADS](#) [Google Scholar](#)

56. 56.

Li, J. et al. An integrated catalog of reference genes in the human gut microbiome. *Nat. Biotechnol.* **32**, 834–841 (2014).

[CAS](#) [Google Scholar](#)

57. 57.

Rampelli, S. et al. Metagenome sequencing of the Hadza hunter-gatherer gut microbiota. *Curr. Biol.* **25**, 1682–1693 (2015).

[CAS](#) [PubMed](#) [PubMed Central](#) [Google Scholar](#)

58. 58.

Santiago-Torres, M. et al. Genetic ancestry in relation to the metabolic response to a US versus traditional Mexican diet: a randomized crossover feeding trial among women of Mexican descent. *Eur. J. Clin. Nutr.* **71**, 395–401 (2017).

[CAS](#) [PubMed](#) [PubMed Central](#) [Google Scholar](#)

59. 59.

Baym, M. et al. Inexpensive multiplexed library preparation for megabase-sized genomes. *PLoS ONE* **10**, e0128036 (2015).

[PubMed](#) [PubMed Central](#) [Google Scholar](#)

60. 60.

Schubert, M., Lindgreen, S. & Orlando, L. AdapterRemoval v2: rapid adapter trimming, identification, and read merging. *BMC Res. Notes* **9**, 88 (2016).

[PubMed](#) [PubMed Central](#) [Google Scholar](#)

61. 61.

Rosenbloom, K. R. et al. The UCSC Genome Browser database: 2015 update. *Nucleic Acids Res.* **43**, D670–D681 (2015).

[CAS](#) [Google Scholar](#)

62. 62.

Martin, M. Cutadapt removes adapter sequences from high-throughput sequencing reads. *EMBnet. J.* **17**, 10–12 (2011).

[Google Scholar](#)

63. 63.

Pakendorf, B. & Stoneking, M. Mitochondrial DNA and human evolution. *Annu. Rev. Genomics Hum. Genet.* **6**, 165–183 (2005).

[CAS](#) [Google Scholar](#)

64. 64.

Fu, Q. et al. A revised timescale for human evolution based on ancient mitochondrial genomes. *Curr. Biol.* **23**, 553–559 (2013).

[CAS](#) [PubMed](#) [PubMed Central](#) [Google Scholar](#)

65. 65.

Andrews, R. M. et al. Reanalysis and revision of the Cambridge reference sequence for human mitochondrial DNA. *Nat. Genet.* **23**, 147 (1999).

[CAS](#) [Google Scholar](#)

66. 66.

Garrison, E. & Marth, G. Haplotype-based variant detection from short-read sequencing. Preprint at <https://arxiv.org/abs/1207.3907> (2012).

67. 67.

Kloss-Brandstätter, A. et al. HaploGrep: a fast and reliable algorithm for automatic classification of mitochondrial DNA haplogroups. *Hum. Mutat.* **32**, 25–32 (2011).

[PubMed](#) [PubMed Central](#) [Google Scholar](#)

68. 68.

Afgan, E. et al. The Galaxy platform for accessible, reproducible and collaborative biomedical analyses: 2018 update. *Nucleic Acids Res.* **46** (W1), W537–W544 (2018).

[CAS](#) [PubMed](#) [PubMed Central](#) [Google Scholar](#)

69. 69.

Pasolli, E. et al. Accessible, curated metagenomic data through ExperimentHub. *Nat. Methods* **14**, 1023–1024 (2017).

[CAS](#) [PubMed](#) [PubMed Central](#) [Google Scholar](#)

70. 70.

Slon, V. et al. Neandertal and Denisovan DNA from Pleistocene sediments. *Science* **356**, 605–608 (2017).

[ADS](#) [CAS](#) [Google Scholar](#)

71. 71.

Borry, M. et al. CoproID predicts the source of coprolites and paleofeces using microbiome composition and host DNA content. *PeerJ* **8**, e9001 (2020).

[PubMed](#) [PubMed Central](#) [Google Scholar](#)

72. 72.

Knights, D. et al. Bayesian community-wide culture-independent microbial source tracking. *Nat. Methods* **8**, 761–763 (2011).

[CAS](#) [PubMed](#) [PubMed Central](#) [Google Scholar](#)

73. 73.

Bushnell, B., Rood, J. & Singer, E. BBMerge — accurate paired shotgun read merging via overlap. *PLoS ONE* **12**, e0185056 (2017).

[PubMed](#) [PubMed Central](#) [Google Scholar](#)

74. 74.

Wood, D. E., Lu, J. & Langmead, B. Improved metagenomic analysis with Kraken 2. *Genome Biol.* **20**, 257 (2019).

[CAS](#) [PubMed](#) [PubMed Central](#) [Google Scholar](#)

75. 75.

Kirstahler, P. et al. Genomics-based identification of microorganisms in human ocular body fluid. *Sci. Rep.* **8**, 4126 (2018).

[ADS](#) [PubMed](#) [PubMed Central](#) [Google Scholar](#)

76. 76.

Li, D., Liu, C.-M., Luo, R., Sadakane, K. & Lam, T.-W. MEGAHIT: an ultra-fast single-node solution for large and complex metagenomics assembly via succinct de Bruijn graph. *Bioinformatics* **31**, 1674–1676 (2015).

[CAS](#) [Google Scholar](#)

77. 77.

Langmead, B. & Salzberg, S. L. Fast gapped-read alignment with Bowtie 2. *Nat. Methods* **9**, 357–359 (2012).

[CAS](#) [PubMed](#) [PubMed Central](#) [Google Scholar](#)

78. 78.

Li, H. et al. The sequence alignment/map format and SAMtools. *Bioinformatics* **25**, 2078–2079 (2009).

[PubMed](#) [PubMed Central](#) [Google Scholar](#)

79. 79.

Parks, D. H., Imelfort, M., Skennerton, C. T., Hugenholtz, P. & Tyson, G. W. CheckM: assessing the quality of microbial genomes recovered from isolates, single cells, and metagenomes. *Genome Res.* **25**, 1043–1055 (2015).

[CAS](#) [PubMed](#) [PubMed Central](#) [Google Scholar](#)

80. 80.

Bowers, R. M. et al. Minimum information about a single amplified genome (MISAG) and a metagenome-assembled genome (MIMAG) of bacteria and archaea. *Nat. Biotechnol.* **35**, 725–731 (2017).

[CAS](#) [PubMed](#) [PubMed Central](#) [Google Scholar](#)

81. 81.

Olm, M. R., Brown, C. T., Brooks, B. & Banfield, J. F. dRep: a tool for fast and accurate genomic comparisons that enables improved genome recovery from metagenomes through de-replication. *ISME J.* **11**, 2864–2868 (2017).

[CAS](#) [PubMed](#) [PubMed Central](#) [Google Scholar](#)

82. 82.

Kurtz, S. et al. Versatile and open software for comparing large genomes. *Genome Biol.* **5**, R12 (2004).

[PubMed](#) [PubMed Central](#) [Google Scholar](#)

83. 83.

Jain, C., Rodriguez-R, L. M., Phillippy, A. M., Konstantinidis, K. T. & Aluru, S. High throughput ANI analysis of 90K prokaryotic genomes reveals clear species boundaries. *Nat. Commun.* **9**, 5114 (2018).

[ADS](#) [PubMed](#) [PubMed Central](#) [Google Scholar](#)

84. 84.

Almeida, A. et al. A unified catalog of 204,938 reference genomes from the human gut microbiome. *Nat. Biotechnol.* **39**, 105–114 (2021).

[CAS](#) [Google Scholar](#)

85. 85.

Manara, S. et al. Microbial genomes from non-human primate gut metagenomes expand the primate-associated bacterial tree of life with over 1000 novel species. *Genome Biol.* **20**, 299 (2019).

[CAS](#) [PubMed](#) [PubMed Central](#) [Google Scholar](#)

86. 86.

Ondov, B. D. et al. Mash: fast genome and metagenome distance estimation using MinHash. *Genome Biol.* **17**, 132 (2016).

[PubMed](#) [PubMed Central](#) [Google Scholar](#)

87. 87.

Jónsson, H., Ginolhac, A., Schubert, M., Johnson, P. L. F. & Orlando, L. mapDamage2.0: fast approximate Bayesian estimates of ancient DNA damage parameters. *Bioinformatics* **29**, 1682–1684 (2013).

[PubMed](#) [PubMed Central](#) [Google Scholar](#)

88. 88.

Neukamm, J., Peltzer, A. & Nieselt, K. DamageProfiler: fast damage pattern calculation for ancient DNA. Preprint at <https://doi.org/10.1101/2020.10.01.322206> (2020).

89. 89.

Nguyen, L.-T., Schmidt, H. A., von Haeseler, A. & Minh, B. Q. IQ-TREE: a fast and effective stochastic algorithm for estimating maximum-likelihood phylogenies. *Mol. Biol. Evol.* **32**, 268–274 (2015).

[CAS](#) [Google Scholar](#)

90. 90.

Asnicar, F. et al. Precise phylogenetic analysis of microbial isolates and genomes from metagenomes using PhyloPhlAn 3.0. *Nat. Commun.* **11**, 2500 (2020).

[ADS](#) [CAS](#) [PubMed](#) [PubMed Central](#) [Google Scholar](#)

91. 91.

Page, A. J. et al. Roary: rapid large-scale prokaryote pan genome analysis. *Bioinformatics* **31**, 3691–3693 (2015).

[CAS](#) [PubMed](#) [PubMed Central](#) [Google Scholar](#)

92. 92.

Stamatakis, A. RAxML version 8: a tool for phylogenetic analysis and post-analysis of large phylogenies. *Bioinformatics* **30**, 1312–1313 (2014).

[CAS](#) [PubMed](#) [PubMed Central](#) [Google Scholar](#)

93. 93.

Bouckaert, R. et al. BEAST 2: a software platform for Bayesian evolutionary analysis. *PLoS Comput. Biol.* **10**, e1003537 (2014).

[PubMed](#) [PubMed Central](#) [Google Scholar](#)

94. 94.

Rambaut, A., Drummond, A. J., Xie, D., Baele, G. & Suchard, M. A. Posterior Summarization in Bayesian phylogenetics using Tracer 1.7. *Syst. Biol.* **67**, 901–904 (2018).

[CAS](#) [PubMed](#) [PubMed Central](#) [Google Scholar](#)

95. 95.

Baele, G., Lemey, P. & Vansteelandt, S. Make the most of your samples: Bayes factor estimators for high-dimensional models of sequence evolution. *BMC Bioinformatics* **14**, 85 (2013).

[PubMed](#) [PubMed Central](#) [Google Scholar](#)

96. 96.

Drummond, A. J., Rambaut, A., Shapiro, B. & Pybus, O. G. Bayesian coalescent inference of past population dynamics from molecular sequences. *Mol. Biol. Evol.* **22**, 1185–1192 (2005).

[CAS](#) [Google Scholar](#)

97. 97.

Duchêne, S. et al. Genome-scale rates of evolutionary change in bacteria. *Microb. Genom.* **2**, e000094 (2016).

[PubMed](#) [PubMed Central](#) [Google Scholar](#)

98. 98.

Briggs, A. W. et al. Patterns of damage in genomic DNA sequences from a Neandertal. *Proc. Natl Acad. Sci. USA* **104**, 14616–14621 (2007).

[ADS](#) [CAS](#) [Google Scholar](#)

99. 99.

Milne, I. et al. Using Tablet for visual exploration of second-generation sequencing data. *Brief. Bioinform.* **14**, 193–202 (2013).

[CAS](#) [Google Scholar](#)

100. 100.

Fu, L., Niu, B., Zhu, Z., Wu, S. & Li, W. CD-HIT: accelerated for clustering the next-generation sequencing data. *Bioinformatics* **28**, 3150–3152 (2012).

[CAS](#) [PubMed](#) [PubMed Central](#) [Google Scholar](#)

101. 101.

Eddy, S. R. Accelerated profile HMM searches. *PLoS Comput. Biol.* **7**, e1002195 (2011).

[ADS](#) [MathSciNet](#) [CAS](#) [PubMed](#) [PubMed Central](#) [Google Scholar](#)

102. 102.

Yin, Y. et al. dbCAN: a web resource for automated carbohydrate-active enzyme annotation. *Nucleic Acids Res.* **40**, W445–W451 (2012).

[CAS](#) [PubMed](#) [PubMed Central](#) [Google Scholar](#)

103. 103.

Human Microbiome Project Consortium. Structure, function and diversity of the healthy human microbiome. *Nature* **486**, 207–214 (2012).

[ADS](#) [Google Scholar](#)

104. 104.

Luber, J. M., Tierney, B. T., Cofer, E. M., Patel, C. J. & Kostic, A. D. Aether: leveraging linear programming for optimal cloud computing in genomics. *Bioinformatics* **34**, 1565–1567 (2018).

[CAS](#) [PubMed](#) [PubMed Central](#) [Google Scholar](#)

105. 105.

Pucu, E., Russ, J. & Reinhard, K. Diet analysis reveals pre-historic meals among the Loma San Gabriel at La Cueva de Los Muertos Chiquitos, Rio Zape, Mexico (600–800 CE). *Archaeol. Anthropol. Sci.* **12**, 25 (2020).

[Google Scholar](#)

106. 106.

Hammerl, E. E., Baier, M. A. & Reinhard, K. J. *Agave* chewing and dental wear: evidence from quids. *PLoS ONE* **10**, e0133710 (2015).

[PubMed](#) [PubMed Central](#) [Google Scholar](#)

107. 107.

Renaud, G., Hanghøj, K., Willerslev, E. & Orlando, L. *gargammel*: a sequence simulator for ancient DNA. *Bioinformatics* **33**, 577–579 (2017).

[CAS](#) [PubMed](#) [PubMed Central](#) [Google Scholar](#)

108. 108.

UniProt Consortium. UniProt: a worldwide hub of protein knowledge. *Nucleic Acids Res.* **47** (D1), D506–D515 (2019).

[Google Scholar](#)

[Download references](#)

Acknowledgements

We acknowledge and appreciate those individuals whose genetics and microorganisms were analysed for this research, as well as present-day individuals with associated genetic or cultural heritage. We thank members of the A.D.K. laboratory, especially T. A. Chavkin and M. Tran for discussion and reading of the manuscript, and L.-D. Pham for assistance with construction of sequencing libraries; J. A. Fellows Yates and A. B. Rohrlach for discussion, advice on metagenomic analysis and reading of the manuscript; Y.-H. Tseng for guidance and members of the Y.-H. Tseng laboratory for discussions; M. L. Taylor and R. J. Wheeler from the Robert S. Peabody Institute of Archaeology for their roles in initiating and assisting with consultation with Native American communities. Parasite-related sequence analysis was performed using the DeiC National Life Science Supercomputer at the Technical University of Denmark. This research was supported by the American Diabetes Association (ADA) Pathway to Stop Diabetes Initiator Award 1-17-INI-13 (A.D.K.), a Smith Family Foundation Award for Excellence in Biomedical Research (A.D.K.), the American Heart Association (AHA) Predoctoral Fellowship 19PRE34430165 (M.C.W.), a European Research Council grant ERC-STG Project MetaPG (N.S.), Werner Siemens Stiftung (M.B. and C.W.) and by the Deutsche Forschungsgemeinschaft (DFG, German Research Foundation) under Germany's Excellence Strategy EXC 2051, Project-ID 390713860 (A.H. and C.W.). Support was also provided by NIH grant no. P30DK036836-30 (principal investigator, G. L. King).

Author information

Affiliations

1. Section on Pathophysiology and Molecular Pharmacology, Joslin Diabetes Center, Boston, MA, USA

Marsha C. Wibowo, Zhen Yang, Braden T. Tierney, Samuel Zimmerman, Jacob M. Luber & Aleksandar D. Kostic

2. Department of Microbiology, Harvard Medical School, Boston, MA, USA

Marsha C. Wibowo, Zhen Yang, Braden T. Tierney, Samuel Zimmerman, Jacob M. Luber & Aleksandar D. Kostic

3. Department of Combinatorics and Optimization, University of Waterloo, Waterloo, Ontario, Canada

Zhen Yang

4. Department of Archaeogenetics, Max Planck Institute for the Science of Human History, Jena, Germany

Maxime Borry, Alexander Hübner & Christina Warinner

5. CIBIO Department, University of Trento, Trento, Italy

Kun D. Huang & Nicola Segata

6. Research and Innovation Centre, Fondazione Edmund Mach, San Michele all'Adige, Italy

Kun D. Huang & Omar Rota-Stabelli

7. Department of Biomedical Informatics, Harvard Medical School, Boston, MA, USA

Braden T. Tierney

8. Immunogenomics and Metabolic Diseases Laboratory, Secretaría de Salud, Instituto Nacional de Medicina Genómica, Mexico City, Mexico

Francisco Barajas-Olmos, Cecilia Contreras-Cubas, Humberto García-Ortiz, Angélica Martínez-Hernández & Lorena Orozco

9. Center for Cancer Research, National Cancer Institute, National Institutes of Health, Bethesda, MD, USA

Jacob M. Luber

10. Research Group for Genomic Epidemiology, National Food Institute,
Technical University of Denmark, Kongens Lyngby, Denmark

Philipp Kirstahler & Sünje Johanna Pamp

11. Department of Anthropology, University of Montana, Missoula, MT,
USA

Tre Blohm & Meradeth Snow

12. Department of Anthropology, Northern Arizona University, Flagstaff,
AZ, USA

Francis E. Smiley

13. Pahrump Paiute Tribe and Consolidated Group of Tribes and
Organizations, Pahrump, NV, USA

Richard Arnold

14. Department of Gastroenterology, Hepatology and Nutrition, Boston
Children's Hospital, Boston, MA, USA

Sonia A. Ballal

15. Morrison Microscopy Core Research Facility, Center for
Biotechnology, University of Nebraska-Lincoln, Lincoln, NE, USA

Julia Russ

16. Institute for Mummy Studies, EURAC Research, Bolzano, Italy

Frank Maixner

17. Center Agriculture Food Environment (C3A), University of Trento,
Trento, Italy

Omar Rota-Stabelli

18. School of Natural Resources, University of Nebraska-Lincoln, Lincoln, NE, USA

Karl Reinhard

19. Department of Anthropology, Harvard University, Cambridge, MA, USA

Christina Warinner

20. Faculty of Biological Sciences, Friedrich-Schiller University, Jena, Germany

Christina Warinner

21. Peabody Museum of Archaeology and Ethnology, Harvard University, Cambridge, MA, USA

Steven LeBlanc

Authors

1. Marsha C. Wibowo

[View author publications](#)

You can also search for this author in [PubMed](#) [Google Scholar](#)

2. Zhen Yang

[View author publications](#)

You can also search for this author in [PubMed](#) [Google Scholar](#)

3. Maxime Borry

[View author publications](#)

You can also search for this author in [PubMed](#) [Google Scholar](#)

4. Alexander Hübner

[View author publications](#)

You can also search for this author in [PubMed](#) [Google Scholar](#)

5. Kun D. Huang

[View author publications](#)

You can also search for this author in [PubMed](#) [Google Scholar](#)

6. Braden T. Tierney

[View author publications](#)

You can also search for this author in [PubMed](#) [Google Scholar](#)

7. Samuel Zimmerman

[View author publications](#)

You can also search for this author in [PubMed](#) [Google Scholar](#)

8. Francisco Barajas-Olmos

[View author publications](#)

You can also search for this author in [PubMed](#) [Google Scholar](#)

9. Cecilia Contreras-Cubas

[View author publications](#)

You can also search for this author in [PubMed](#) [Google Scholar](#)

10. Humberto García-Ortiz

[View author publications](#)

You can also search for this author in [PubMed](#) [Google Scholar](#)

11. Angélica Martínez-Hernández

[View author publications](#)

You can also search for this author in [PubMed](#) [Google Scholar](#)

12. Jacob M. Luber

[View author publications](#)

You can also search for this author in [PubMed](#) [Google Scholar](#)

13. Philipp Kirstahler

[View author publications](#)

You can also search for this author in [PubMed](#) [Google Scholar](#)

14. Tre Blohm

[View author publications](#)

You can also search for this author in [PubMed](#) [Google Scholar](#)

15. Francis E. Smiley

[View author publications](#)

You can also search for this author in [PubMed](#) [Google Scholar](#)

16. Richard Arnold

[View author publications](#)

You can also search for this author in [PubMed](#) [Google Scholar](#)

17. Sonia A. Ballal

[View author publications](#)

You can also search for this author in [PubMed](#) [Google Scholar](#)

18. Sünje Johanna Pamp

[View author publications](#)

You can also search for this author in [PubMed](#) [Google Scholar](#)

19. Julia Russ

[View author publications](#)

You can also search for this author in [PubMed](#) [Google Scholar](#)

20. Frank Maixner

[View author publications](#)

You can also search for this author in [PubMed](#) [Google Scholar](#)

21. Omar Rota-Stabelli

[View author publications](#)

You can also search for this author in [PubMed](#) [Google Scholar](#)

22. Nicola Segata

[View author publications](#)

You can also search for this author in [PubMed](#) [Google Scholar](#)

23. Karl Reinhard

[View author publications](#)

You can also search for this author in [PubMed](#) [Google Scholar](#)

24. Lorena Orozco

[View author publications](#)

You can also search for this author in [PubMed](#) [Google Scholar](#)

25. Christina Warinner

[View author publications](#)

You can also search for this author in [PubMed](#) [Google Scholar](#)

26. Meradeth Snow

[View author publications](#)

You can also search for this author in [PubMed](#) [Google Scholar](#)

27. Steven LeBlanc

[View author publications](#)

You can also search for this author in [PubMed](#) [Google Scholar](#)

28. Aleksandar D. Kostic

[View author publications](#)

You can also search for this author in [PubMed](#) [Google Scholar](#)

Contributions

M.C.W., S.L., A.D.K., C.W. and S.A.B. conceived the study. M.C.W. with the assistance of Z.Y., C.W., M.B., A.H., K.D.H., N.S., O.R.-S., F.M., B.T.T., S.Z., T.B., P.K., S.J.P. and J.M.L. performed genomic and metagenomic analyses. S.L. with the assistance of F.E.S. collected archaeological samples. M.S. processed ancient DNA and constructed sequencing libraries with help for post-library processing from M.C.W. K.R. and J.R. conducted electron microscopy and dietary analyses on ancient samples. L.O., F.B.-O., C.C.-C., H.G.-O. and A.M.-H. coordinated visits to the non-industrial Mazahua community and collected samples. M.C.W. processed DNA and constructed sequencing libraries for the Mazahua samples. M.C.W. wrote the manuscript with the assistance of A.D.K., S.L., M.S., K.R., M.B., A.H., C.W., Z.Y., K.D.H., F.M., O.R.-S., N.S., F.B.-O., H.G.-O., P.K., S.J.P. and R.A. and with input from the other co-authors.

Corresponding author

Correspondence to [Aleksandar D. Kostic](#).

Ethics declarations

Competing interests

A.D.K. is a co-founder and scientific advisor to FitBiomics. The other authors declare no competing interests.

Additional information

Peer review information *Nature* thanks Marcus de Goffau, Ben Good, Philip Hugenholtz, Eske Willerslev and the other, anonymous, reviewer(s) for their contribution to the peer review of this work. Peer reviewer reports are available.

Publisher's note Springer Nature remains neutral with regard to jurisdictional claims in published maps and institutional affiliations.

Extended data figures and tables

[Extended Data Fig. 1 Overview of samples, study design and quality measures to validate the authenticity of the palaeofaeces.](#)

a, Schematic of gene-catalogue and genome-reconstruction pipelines. **b**, Samples used in this study, archaeological sites and ^{14}C dating. Data were obtained from this study (Mexico) and previous studies: Fiji³¹, Peru⁴, Madagascar¹³, Tanzania⁵⁷, USA^{4,55}, Denmark⁵⁶ and Spain⁵⁶. Map data are from Google Maps (2021 Google, INEGI). **c**, Scanning electron microscopy images of dietary remains in the palaeofaeces. Zape1, maize pollen grains (more than 191,000 grains per gram) (top) and agave phytoliths (middle and bottom). Zape2, *U. maydis* spores (hundreds of millions per gram). Zape3, Chenopod or amaranth foliage and/or buds (smaller pollen) and squash (larger pollen with spines). UT30.3, druse phytoliths, annular xylem vessel secondary wall thickenings and epidermis of Cactaceae. A complete description is provided in Supplementary Information section 2. Reproducibility and independently repeated experiments are described in the Methods. **d**, Principal component analysis of the species composition of palaeofaeces, soil samples and publicly available archaeological sediment samples^{70,71}. Species were identified by MetaPhlAn2²⁰. **e**, Prediction of source of microbial communities by SourceTracker2⁷² using the species abundance matrix from MetaPhlAn2 as input. Archaeological sediment samples included three soil samples collected in this study, seven Holocene human-associated sediments from CoproID⁷¹ and 40 Pleistocene sediment samples⁷⁰. **f**, The percentage of reads aligned to the MetaPhlAn2 database per sample (HMP, $n = 146$; Mexican, $n = 22$; Fijian, $n = 174$; palaeofaeces,

$n = 8$; soil, $n = 3$) (Supplementary Information section 4). **g**, aDNA damage levels of Firmicutes and Bacteroidetes genomes for medium-quality and high-quality pre-filtered and filtered bins (two-tailed Wilcoxon rank-sum test; pre-filtered bins Bacteroidetes, $n = 69$ MAGs; pre-filtered bins Firmicutes, $n = 359$ MAGs; filtered bins Bacteroidetes, $n = 24$ MAGs; filtered bins Firmicutes, $n = 161$ MAGs) (Supplementary Information section 5). 5p, 5' end; 3p, 3' end. **h**, Abundances of VANISH²¹ and BloSSUM²² families as identified by MetaPhlAn2²⁰ (palaeofaeces $n = 8$; non-industrial $n = 370$; industrial $n = 418$). In **f–h**, data are presented as box plots (middle line, median; lower hinge, first quartile; upper hinge, third quartile; upper whisker extends from the hinge to the largest value no further than $1.5 \times$ the interquartile range from the hinge; lower whisker extends from the hinge to the smallest value at most $1.5 \times$ the interquartile range from the hinge; data beyond the end of the whiskers are individually plotted outlying points).

Extended Data Fig. 2 Microbial DNA and mtDNA damage patterns.

a, Microbial damage patterns of the palaeofaeces and the Boomerang soil samples as identified by DamageProfiler⁸⁸. A medium-quality or high-quality reconstructed genome was used as reference for its respective sample. All MAGs used as reference genomes for the palaeofaeces are of known gut microbial species. The red line indicates the average frequency of C-to-T substitutions across all contigs per bin and the blue line indicates the average frequency of G-to-A substitutions across all contigs per bin. The shaded areas show the s.d. (1026.1.4 Lib4_10_bin.21, $n = 488$ contigs; 1043.4.1 Lib4_11_bin.16, $n = 133$ contigs; 3567.1.1 Lib4_12_bin.1, $n = 278$ contigs; AW107 Lib4_1_bin.1, $n = 208$ contigs; AW108 Lib4_2_bin.20, $n = 337$ contigs; AW110A Lib4_3_bin.88, $n = 210$ contigs; UT30.3 s02_bin.338, $n = 74$ contigs; UT43.2 Lib3_9_bin.57, $n = 174$ contigs; Zape1 Lib4_6_bin.125, $n = 212$ contigs; Zape2 Lib4_7_bin.21, $n = 241$ contigs; Zape3 Lib4_8_bin.68, $n = 324$ contigs). Contigs with fewer than 1,000 reads aligned were removed from the analysis. **b**, mtDNA damage patterns of the palaeofaeces as identified by mapDamage2.0⁸⁷. Human mtDNA (rCRS) was used as reference. The red line indicates the

average frequency of C-to-T substitutions and the blue line indicates the average frequency of G-to-A substitutions. Samples AW110A and Zape2 did not have enough mtDNA reads for mtDNA damage assessment.

Extended Data Fig. 3 Parasites in the palaeofaeces and the soil samples classified using Kraken 2.

The bars represent the reads assigned with a Kraken⁷⁴ confidence threshold between 0.15 and 0.9. The value specifies the fraction of k -mers needed for the specific classification level. The grey dotted line indicates the 1,000 reads cut-off. The displayed parasites were detected above the cut-off in at least one sample. **a**, Parasites in the palaeofaeces. In six out of eight palaeofaeces samples, *Blastocystis* is above the cut-off. Subtype 1 is the dominant subtype in samples AW107, UT30.3, UT43.2 and Zape3, whereas subtype 3 is the dominant subtype in AW108 and AW110A. Other parasites do not meet the cut-off requirements described in the Methods. **b**, Parasites in the soil samples include *Acanthamoeba* (a parasite frequently found in soil) in sample 1026.1.4 and *Enterobius vermicularis* (human pinworm) in sample 3567.1.1.

Extended Data Fig. 4 BioAnalyzer results showing the length distribution of DNA fragments per library.

The libraries contain 120-bp adapters.

Extended Data Fig. 5 Species and gene content of long versus short DNA fragments and UDG-treated versus non-UDG-treated samples.

a, b, Pairwise comparison between whole samples, only subsets containing short reads and only subsets with long reads. **a**, Heat map of species-level pairwise Jaccard distances for whole samples, short-read subsets (reads \leq 145 bp) and long-read subsets (reads $>$ 145 bp). Species were identified by MetaPhlAn2²⁰. The groups cluster together by sample. **b**, Heat map of gene-level pairwise Jaccard distances for whole samples, short-read subsets and long-read subsets. Genes were identified by PROKKA³⁸ and a

count matrix was built from PROKKA output files. Groups from the same sample cluster together. **c–e**, Species and gene content comparison between UDG-treated libraries and non-UDG-treated libraries (Supplementary Information section [12](#) and Supplementary Table [10](#)). **c**, Heat map of species-level pairwise Jaccard distances between each pair of all UDG-treated and non-UDG-treated samples. Species were identified by MetaPhlAn2^{[20](#)}. Each UDG-treated library clusters with non-UDG-treated library from the same sample. **d**, Heat map of gene-level pairwise Jaccard distances between each pair of all UDG-treated and non-UDG-treated samples. Genes were identified by PROKKA^{[38](#)} and non-redundant gene catalogues were generated by collapsing genes within 10% amino acid identity distance. Each UDG-treated library clusters with non-UDG-treated library from the same sample. **e**, *t*-Distributed stochastic neighbour embedding (*t*-SNE) analysis at the species level shows clustering of each UDG-treated library with the non-UDG-treated library from the same sample.

Extended Data Fig. 6 De novo genome reconstruction from palaeofaeces recovers 181 authenticated ancient gut microbial genomes, 39% of which are novel SGBs.

Related to Fig. [2](#). **a–d**, CheckM^{[79](#)} quality estimation for de novo reconstructed microbial genomes for the 209 filtered bins (low-quality bins, $n = 285$; medium-quality bins, $n = 175$; high-quality bins, $n = 34$). Genomes were classified as low quality (LQ; completeness $\leq 50\%$ or contamination $> 5\%$), medium quality (MQ; $90\% \geq$ completeness $> 50\%$, contamination $< 5\%$) or high quality (HQ; completeness $> 90\%$ and contamination $< 5\%$). **a**, Filtering steps, number of bins that belong to each of the quality categories and classification of novel SGBs. **b**, Contamination and completeness distribution for the filtered bins. **c**, Distribution of the number of contigs for each of the quality categories. **d**, Distribution of contig N50 values for each of the quality categories. **e**, Damage levels, specifically C-to-T substitutions at the 5' end and G-to-A substitutions at the 3' end of the reads, for each ancient bin as estimated by DamageProfiler^{[88](#)} (medium-quality bins, $n = 175$; high-quality bins, $n = 34$). **f**, GTDB-Tk^{[23](#)} species assignment for the known species. In **c–e**,

data are presented as box plots (middle line, median; lower hinge, first quartile; upper hinge, third quartile; upper whisker extends from the hinge to the largest value no further than $1.5 \times$ the interquartile range from the hinge; lower whisker extends from the hinge to the smallest value at most $1.5 \times$ the interquartile range from the hinge; data beyond the end of the whiskers are individually plotted outlying points).

Extended Data Fig. 7 De novo genome reconstruction from palaeofaeces recovers 498 medium- and high-quality microbial genomes, 44% of which are novel SGBs.

Related to Fig. 2. **a–d**, CheckM⁷⁹ quality estimation of all 498 de novo reconstructed microbial genomes (low-quality bins, $n = 617$; medium-quality bins, $n = 339$; high-quality bins, $n = 159$). Genomes were classified as low quality (completeness $\leq 50\%$ or contamination $> 5\%$), medium quality ($90\% \geq$ completeness $> 50\%$ and contamination $< 5\%$) or high quality (completeness $> 90\%$ and contamination $< 5\%$). **a**, Number of bins that belong to each of the quality categories and classification of novel SGBs. **b**, Contamination and completeness distribution for the reconstructed genomes. **c**, Distribution of the number of contigs for each of the quality categories. **d**, Distribution of contig N50 values for each of the quality categories. **e**, Damage levels, specifically C-to-T substitutions at the 5' end and G-to-A substitutions at the 3' end of the reads, for each bin as estimated by DamageProfiler⁸⁸ (medium-quality bins, $n = 339$; high-quality bins, $n = 159$). **f**, GTDB-Tk²³ genus estimation for members of both the novel and known SGBs. **g**, GTDB-Tk²³ species assignment for members of the known SGBs. In **c–e**, data are presented as box plots (middle line, median; lower hinge, first quartile; upper hinge, third quartile; upper whisker extends from the hinge to the largest value no further than $1.5 \times$ the interquartile range from the hinge; lower whisker extends from the hinge to the smallest value at most $1.5 \times$ the interquartile range from the hinge; data beyond the end of the whiskers are individually plotted outlying points).

Extended Data Fig. 8 De novo genome reconstruction from present-day individuals of Mexican ancestry recovers 402

medium- and high-quality genomes, only 1 of which is a novel SGB.

Related to Fig. 2. **a–d**, CheckM⁷⁹ quality estimation of all de novo reconstructed microbial genomes (low-quality bins, $n = 611$; medium-quality bins, $n = 256$; high-quality bins, $n = 146$). Genomes were classified as low quality (completeness $\leq 50\%$ or contamination $> 5\%$), medium quality ($90\% \geq$ completeness $> 50\%$ and contamination $< 5\%$) or high quality (completeness $> 90\%$ and contamination $< 5\%$). **a**, The number of bins that belong to each of the quality categories and classification of novel SGBs. **b**, Contamination and completeness distribution for the reconstructed genomes. **c**, Distribution of the number of contigs for each of the quality categories. **d**, Distribution of contig N50 values for each of the quality categories. **e**, GTDB-Tk²³ genus estimation for members of both the novel and the known Mexican SGBs. **f**, GTDB-Tk²³ species assignment for members of the known Mexican SGBs. In **c**, **d**, data are presented as box plots (middle line, median; lower hinge, first quartile; upper hinge, third quartile; upper whisker extends from the hinge to the largest value no further than $1.5 \times$ the interquartile range from the hinge; lower whisker extends from the hinge to the smallest value at most $1.5 \times$ the interquartile range from the hinge; data beyond the end of the whiskers are individually plotted outlying points).

Extended Data Fig. 9 Effect of aDNA damage on the assembly of short-read data.

Related to Fig. 2, see Supplementary Information section 6. **a**, Distribution of the values of four sequencing data variables that may have an effect on the assembly of short-read data and were observed in the 498 medium-quality and high-quality MAGs assembled in this study. **b**, Overview of the parameter space of the variables GC content, sequencing depth, observed aDNA damage and read length that was used for simulating short-read sequencing using *gargammel*¹⁰⁷. **c**, Number of mismatches per 1 kb of alignable contig sequence with respect to the reference genome as observed at the 95% quantile for all combinations of reference genome, read length distribution, simulated aDNA damage and coverage averaged across the

five replicates. **d**, The log₂-transformed ratio of C-to-T substitutions to the average number of all other substitutions per 1 kb of alignable contig sequence for all combinations of reference genome, read length distribution, simulated aDNA damage and coverage averaged across the five replicates. Positive values indicate an excess of C-to-T substitutions.

Extended Data Fig. 10 Comparison of *M. smithii* divergence dates from BEAST2 analysis compared with raw genetic distance calculations.

Related to Fig. 3, see Supplementary Information section 8. **a**, The different *M. smithii* groups and genetic distances calculated are shown. **b**, Pairwise sequence divergences between M1 and M2 strains ($n = 96$), A and M1 strains ($n = 48$) and A and M2 strains ($n = 8$). Data are presented as box plots (middle line, median; lower hinge, first quartile; upper hinge, third quartile; upper whisker extends from the hinge to the largest value no further than $1.5 \times$ the interquartile range from the hinge; lower whisker extends from the hinge to the smallest value at most $1.5 \times$ the interquartile range from the hinge; data beyond the end of the whiskers are individually plotted outlying points). **c**, **d**, Comparison of the distribution of systematic differences between M1 and M2 and A and M2 divergences (**c**) and BEAST2 estimates (**d**). **c**, Systematic differences based on pairwise sequence divergences (measured by the single-nucleotide variant rate) between M1 and M2 and A and M2 strains. **d**, Products of the clock rates (substitutions per site per year) inferred using BEAST2⁹³ (Supplementary Table 7) and the inferred age of the common ancestor of the ancient strains. **e**, **f**, Comparison of distribution of pairwise time-resolved systematic differences based on raw sequences divergence (**e**) and the distribution of existing inferred clock rates (**f**). **e**, Time-resolved systematic differences calculated by dividing systematic differences (**c**) with the average ¹⁴C date of the palaeofaeces used in molecular clocking analysis. **f**, Clock rates inferred by BEAST2 analysis (Supplementary Table 7). **g**, Raw-sequence-based divergence dates between A and M1 strains, recalibrated using time-resolved systematic differences. **h**, Distribution of raw-sequence-based divergence dates when low-frequency outliers are excluded. **i**, Distribution

of estimated divergence dates between A and M1 strains based on BEAST2 analysis.

[Extended Data Fig. 11 Heat map of 120 antibiotic-resistance genes found in the palaeofaeces, industrial and non-industrial samples.](#)

Related to Fig. 4. Functions were annotated using PROKKA³⁸ with the UniProtKB database¹⁰⁸. Enriched genes were identified using one-tailed Wilcoxon rank-sum tests with Bonferroni correction. Non-enriched genes were sorted by fold change. RPKM values are shown on a log scale and scaled by row.

[Extended Data Fig. 12 Heat map of the top-40 genes enriched in the palaeofaeces, the industrial and the non-industrial samples.](#)

Related to Fig. 4, complete results are provided in Supplementary Table 8. Functions were annotated using PROKKA³⁸ with the UniProtKB database¹⁰⁸. Enriched genes were identified using one-tailed Wilcoxon rank-sum tests with Bonferroni correction. RPKM values are shown on a log scale without scaling.

Supplementary information

[Supplementary Information](#)

This file includes an Ethics Statement, Supplementary Information sections 1-12, Supplementary Figures 1-3, Supplementary Table 11, and Supplementary References.

[Reporting Summary](#)

[Supplementary Table 1](#)

Details of samples. Related to Extended Data Fig. 1. This includes description of archaeological samples, including C14 dating, assembly statistics, proportion of contaminant DNA, mtDNA haplogroups, and CoproID output. The file also describes details of the present-day Mexican samples and publicly available datasets used in this study.

Supplementary Table 2

Dietary analysis and seasonality interpretation of the paleofeces. Related to Extended Data Fig. 1c.

Supplementary Table 3

MetaPhlAn2 output. Related to Fig. 1 and Extended Data Fig. 1h. This includes complete taxonomic abundance matrix, a species binary matrix, and statistical analysis results for species, families, and phyla found in the samples.

Supplementary Table 4

Details of parasites found in the archaeological samples. Related to Extended Data Fig. 3.

Supplementary Table 5

Long vs. short reads analysis. Related to Extended Data Fig. 5a-b. This includes a complete taxonomic abundance matrix and a species binary matrix as identified by MetaPhlAn2, as well as a PROKKA-annotated gene abundance matrix.

Supplementary Table 6

Details of the MAGs. Related to Fig. 2 and Extended Data Figs. 6, 7, and 8.

Supplementary Table 7

Model selection for tip dating. Related to Fig. 3.

Supplementary Table 8

Molecular function analysis. Related to Fig. 4. This includes lists of enriched PROKKA-annotated genes, CAZyme analysis results, and lists of genes surrounding transposases. This file also includes lists of taxa that contain glycan-degrading enzymes, antibiotic resistance genes, and chitin CAZymes.

Supplementary Table 9

Details of all samples used in SourceTracker2 analysis. Related to Extended Data Fig. 1e.

Supplementary Table 10

Comparison of assembly results and species composition between UDG-treated and non-UDG treated libraries. Related to Extended Data Fig. 5c-e.

Peer Review File

Rights and permissions

Open Access This article is licensed under a Creative Commons Attribution 4.0 International License, which permits use, sharing, adaptation, distribution and reproduction in any medium or format, as long as you give appropriate credit to the original author(s) and the source, provide a link to the Creative Commons license, and indicate if changes were made. The images or other third party material in this article are included in the article's Creative Commons license, unless indicated otherwise in a credit line to the material. If material is not included in the article's Creative Commons license and your intended use is not permitted by statutory regulation or exceeds the permitted use, you will need to obtain permission directly from the copyright holder. To view a copy of this license, visit <http://creativecommons.org/licenses/by/4.0/>.

[Reprints and Permissions](#)

About this article



Check for
updates

Cite this article

Wibowo, M.C., Yang, Z., Borry, M. *et al.* Reconstruction of ancient microbial genomes from the human gut. *Nature* **594**, 234–239 (2021). <https://doi.org/10.1038/s41586-021-03532-0>

[Download citation](#)

- Received: 06 February 2020
- Accepted: 12 April 2021
- Published: 12 May 2021
- Issue Date: 10 June 2021
- DOI: <https://doi.org/10.1038/s41586-021-03532-0>

Further reading

- [Ancient human faeces reveal gut microbes of the past](#)
 - Matthew R. Olm
 - & Justin L. Sonnenburg

Nature (2021)

Comments

By submitting a comment you agree to abide by our [Terms](#) and [Community Guidelines](#). If you find something abusive or that does not comply with our terms or guidelines please flag it as inappropriate.

[Download PDF](#)

Associated Content

[Ancient human faeces reveal gut microbes of the past](#)

- Matthew R. Olm
- Justin L. Sonnenburg

Nature News & Views 17 May 2021

Advertisement

This article was downloaded by **calibre** from <https://www.nature.com/articles/s41586-021-03532-0>

| [Section menu](#) | [Main menu](#) |

SARS-CoV-2 uses a multipronged strategy to impede host protein synthesis
[Download PDF](#)

- Article
- [Published: 12 May 2021](#)

SARS-CoV-2 uses a multipronged strategy to impede host protein synthesis

- [Yaara Finkel](#) [ORCID: orcid.org/0000-0002-3843-2357](#)^{1 na1},
- [Avi Gluck](#)^{1 na1},
- [Aharon Nachshon](#)^{1 na1},
- [Roni Winkler](#)¹,
- [Tal Fisher](#)¹,
- [Batsheva Rozman](#)¹,
- [Orel Mizrahi](#)¹,
- [Yoav Lubelsky](#) [ORCID: orcid.org/0000-0001-6127-1152](#)²,
- [Binyamin Zuckerman](#) [ORCID: orcid.org/0000-0002-6216-011X](#)²,
- [Boris Slobodin](#)³,
- [Yfat Yahalom-Ronen](#)⁴,
- [Hadas Tamir](#)⁴,
- [Igor Ulitsky](#) [ORCID: orcid.org/0000-0003-0555-6561](#)²,
- [Tomer Israely](#) [ORCID: orcid.org/0000-0003-0246-4477](#)⁴,
- [Nir Paran](#) [ORCID: orcid.org/0000-0001-5143-9660](#)⁴,
- [Michal Schwartz](#) [ORCID: orcid.org/0000-0001-5442-0201](#)¹ &
- [Noam Stern-Ginossar](#) [ORCID: orcid.org/0000-0003-3583-5932](#)¹

[Nature](#) volume 594, pages 240–245 (2021) [Cite this article](#)

- 19k Accesses
- 282 Altmetric
- [Metrics details](#)

Subjects

- [SARS-CoV-2](#)
- [Virus–host interactions](#)

Abstract

The coronavirus SARS-CoV-2 is the cause of the ongoing pandemic of COVID-19¹. Coronaviruses have developed a variety of mechanisms to repress host mRNA translation to allow the translation of viral mRNA, and concomitantly block the cellular innate immune response^{2,3}. Although several different proteins of SARS-CoV-2 have previously been implicated in shutting off host expression^{4,5,6,7}, a comprehensive picture of the effects of SARS-CoV-2 infection on cellular gene expression is lacking. Here we combine RNA sequencing, ribosome profiling and metabolic labelling of newly synthesized RNA to comprehensively define the mechanisms that are used by SARS-CoV-2 to shut off cellular protein synthesis. We show that infection leads to a global reduction in translation, but that viral transcripts are not preferentially translated. Instead, we find that infection leads to the accelerated degradation of cytosolic cellular mRNAs, which facilitates viral takeover of the mRNA pool in infected cells. We reveal that the translation of transcripts that are induced in response to infection (including innate immune genes) is impaired. We demonstrate this impairment is probably mediated by inhibition of nuclear mRNA export, which prevents newly transcribed cellular mRNA from accessing ribosomes. Overall, our results uncover a multipronged strategy that is used by SARS-CoV-2 to take over the translation machinery and to suppress host defences.

[Download PDF](#)

Main

Upon SARS-CoV-2 infection, two overlapping open reading frames (ORFs) are translated from the positive-sense genomic RNA to generate continuous polypeptides that are cleaved into 16 nonstructural proteins (NSP1 to NSP16), which then facilitate the transcription of genomic and subgenomic RNA⁸. Subgenomic RNAs are translated into structural and accessory proteins^{8,9}. The translation of viral proteins relies on the cellular translation machinery, and coronaviruses have evolved diverse mechanisms—including the degradation of host mRNA and inhibition of host translation^{2,3}—to hijack the translation machinery and to inhibit antiviral defence mechanisms (including the interferon (IFN) response). The extent to which SARS-CoV-2 suppresses the IFN response is a key characteristic that distinguishes it from other respiratory viruses¹⁰, and the IFN response seems to have a critical role in the pathogenesis of SARS-CoV-2^{11,12}. Although several proteins of SARS-CoV-2 have previously been implicated in shutting off host expression^{4,5,6,7}, a comprehensive

depiction of the effect of SARS-CoV-2 infection on cellular gene expression and the underlying molecular mechanism is lacking.

To gain a detailed view of the changes that occur in translation over the course of SARS-CoV-2 infection, we infected a human lung epithelial cell line (Calu3 cells) with SARS-CoV-2 at multiplicity of infection of 3, which resulted in infection of the majority of the cells (Extended Data Fig. 1a) and thus a synchronous cell population. At 3, 5 and 8 h after infection, we collected infected cells as well as uninfected cells for RNA sequencing (RNA-seq) and ribosome profiling (Fig. 1a). To assess the reproducibility of our experiments, we prepared two independent biological replicates for the uninfected cells and cells collected at 8 h after infection: both the mRNA and footprint measurements were reproducible (Extended Data Fig. 1b,c). Footprint read-length distribution peaked at around 29 nt, consistent with previous analyses^{9,13} (Extended Data Fig. 1d). Metagene analysis revealed the expected profiles of footprints and mRNAs (Extended Data Fig. 1e-h). Using this data, we quantitatively assessed the expression pattern of 8,627 cellular transcripts and 12 viral ORFs that are expressed from the genomic and subgenomic RNAs along the course of SARS-CoV-2 infection. Our analysis of the mRNAs and footprints that originate from cellular and viral transcripts illustrates the dominance of SARS-CoV-2 over the mRNA pool. At 8 h after infection, viral mRNAs comprise almost 80% of the mRNAs in infected cells (Fig. 1b). At the same time point, viral mRNAs account for only about 34% of the RNA fragments engaged with ribosomes in the cells (Fig. 1c). To quantitatively evaluate the ability of SARS-CoV-2 to co-opt host ribosomes, we calculated the translation efficiency (the ratio of footprints to mRNAs for a given gene) of viral and cellular RNA over the course of infection. We then compared the translation efficiency of human genes to that of viral genes at each of the time points along infection. At 3 h after infection, the translation efficiencies of viral genes fall within the general range of cellular gene translation (Fig. 1d). This indicates that, when infection initiates, viral transcripts are translated with efficiencies similar to those of host transcripts. As infection progresses, the translation efficiency of viral genes is substantially reduced relative to that of cellular genes. Because double-membrane replication compartments are formed to accommodate viral genome replication and transcription¹⁴, one possibility is that, as infection proceeds, these compartments encompass a sizable fraction of the viral RNA molecules and thus prevent them from being translated.

Fig. 1: Global reduction of translation and of cellular mRNA levels during SARS-CoV-2 infection.

 **figure1**

a, Cells were left uninfected or infected with SARS-CoV-2 for 3, 5 or 8 h, and then collected for RNA-seq and ribosome profiling. **b, c**, Percentage of reads that aligned to human or viral coding regions for mRNAs (**b**) and footprints (**c**) in uninfected cells (un) and at 3, 5 and 8 h after infection (hpi, hours post-infection). Uninfected and 8 h after infection, $n = 2$; 3 and 5 h after infection, $n = 1$. Duplicate values for 8 h after infection are presented. **d**, Cumulative frequency of human (black) and viral (colours) genes, according to their relative translation efficiency (TE) at 3 h (left), 5 h (middle) and 8 h (right) after infection. **e**, Protein synthesis measurement by flow cytometry of uninfected cells or cells infected with SARS-CoV-2 (multiplicity of infection (MOI) = 3) for 3, 5 and 8 h after infection, following incorporation of *O*-propargyl puromycin. OPP fl., *O*-propargyl puromycin fluorescence. **f**, Percentage of reads that aligned to the human or viral transcripts as in **b**, but from total aligned RNA reads. **g**, Heat map of relative mRNA and footprint levels during SARS-CoV-2 infection of human transcripts that showed the strongest changes in their mRNA levels. Expression levels scaled by gene after partitioning clustering are shown.

[Full size image](#)

Deep sequencing measurements inherently provide relative values, but not absolute quantification of RNA and translation levels. Because the SARS-CoV-2-encoded protein NSP1 has recently been shown to interfere with translation by blocking the

mRNA entry channel of ribosomes^{6,7}, and because the extent to which SARS-CoV-2 interferes with the overall levels of cellular mRNA has not been assessed, we next examined whether SARS-CoV-2 infection affects global translation and RNA levels. To quantify absolute translation levels, we measured nascent protein synthesis levels by quantifying the incorporation of *O*-propargyl puromycin into elongating polypeptides¹⁵ (Extended Data Fig. 2a, b). We infected Calu3 cells with SARS-CoV-2 and measured protein synthesis in uninfected cells, and at 3, 5 and 8 h after infection. We observed a major reduction in global translation levels at 3 h after infection, which was augmented over time: at 8 h after infection, translation activity was reduced by 70% (Fig. 1e). In parallel, we measured the levels of rRNA and of total RNA extracted from uninfected cells and along the course of infection, which showed there are no major changes in total RNA or in rRNA levels during SARS-CoV-2 infection (Extended Data Fig. 3a, b). Because mRNA comprises only a small fraction of the cellular RNA, we assessed the relative abundance of cellular and viral mRNAs in uninfected and infected cells by sequencing total RNA (without rRNA depletion). Our analysis reveals an increase in the pool of mRNAs during infection, owing to the massive production of viral transcripts; however, the relative fraction of cellular mRNA is reduced by approximately twofold (Fig. 1f). This suggests that during infection there is a massive production of viral transcripts and a concomitant substantial reduction in the levels of cellular transcripts. We next assessed the expression pattern of cellular genes along the course of SARS-CoV-2 infection. We clustered the mRNA levels of genes that showed the strongest changes over the course of infection, which enabled us to group cellular transcripts into four main classes on the basis of temporal expression profiles from RNA-seq. Expression of the majority of transcripts was reduced during infection (with different kinetics), accompanied by a concurrent reduction in footprints, but there were also numerous transcripts that showed increased expression (Fig. 1g). The clustering of genes that showed elevated expression along the course of infection revealed mRNAs that were upregulated early or late, or which showed transient induction (Extended Data Fig. 4a). The cluster of genes that was induced in late kinetics was significantly enriched with genes related to the immune response, including Toll receptor signalling, and chemokine and cytokine signalling (Extended Data Fig. 4b, Supplementary Table 1). These genes include *IL6* and *IL8* (also known as *CXCL8*), which have an important role in the pathogenesis of SARS-CoV-2¹⁶, as well as several IFN-stimulated genes (such as *IFIT1*, *IFIT2*, *IFIT3* and *ISG15*) and genes encoding TNF-induced proteins.

Our results indicate that levels of the majority of cellular RNAs are reduced during SARS-CoV-2 infection and that this reduction probably contributes to the shutting off of cellular protein synthesis. The reduction in cellular RNA levels could be due to interference with RNA production and/or accelerated RNA degradation. To explore the molecular mechanism, we examined whether the reduction of cellular transcript levels is associated with the subcellular localization of these transcripts. We found that

the levels of transcripts that mostly localize to the cytoplasm are reduced more in infected cells, as compared to transcripts that are mostly nuclear (Fig. 2a, Extended Data Fig. 4c), and there was a clear correlation between subcellular localization and the extent of reduction in transcript levels (Extended Data Fig. 4d). Furthermore, mitochondrially encoded transcripts are much less affected by infection as compared to nuclear-encoded transcripts (Fig. 2b). The specific sensitivity of cytosolic transcripts indicates these transcripts may be targeted for degradation during SARS-CoV-2 infection. To directly evaluate mRNA decay, we used thiol (SH)-linked alkylation for the metabolic sequencing of RNA (SLAM-seq)¹⁷ on uninfected and SARS-CoV-2-infected cells (Extended Data Fig. 5a). This approach allowed us to measure the half-lives of endogenous mRNAs on the basis of the incorporation of 4-thiouridine (4sU) into newly synthesized RNA, the conversion of 4sU into a cytosine analogue and the quantification of these U-to-C conversions by RNA-seq^{17,18}. We obtained all of the characteristics of a high-quality SLAM-seq library: over 3,000 quantified genes, rising U-to-C mutation rates and an increase in the portion of labelled RNA over time, which was stronger in infected cells (indicating a faster turnover of RNA in infected cells) (Extended Data Fig. 5b–e). There was a strong correlation between the half-lives estimated from our measurements and estimates that were previously conducted¹⁹ in a different cell type (Extended Data Fig. 5f). Importantly, we observed a substantial reduction in the half-lives of cellular mRNAs upon SARS-CoV-2 infection (Fig. 2c), which indicates increased degradation of cellular mRNA in infected cells. Furthermore, the reduction in half-lives correlated with the reduction that we measured in RNA expression, which indicates that mRNA decay dominates changes in mRNA during infection (Extended Data Fig. 5g). Consistent with the changes in mRNA expression, the half-lives of cytoplasmic transcripts were more reduced than those of nuclear transcripts (Fig. 2d, Extended Data Fig. 5h). In coronaviruses, the most prominent and well-characterized protein linked to cellular shutoff is NSP1²⁰. Previous studies on NSP1 of SARS-CoV-2 have demonstrated that it restricts translation by directly binding to the ribosome 40S subunit^{6,7}, thereby globally inhibiting the initiation of translation. For SARS-CoV, in addition to this translation effect, the interaction of NSP1 with 40S has been shown to induce cleavage of translated cellular mRNAs, thereby accelerating their turnover^{21,22,23}. We therefore examined whether the degradation of cellular transcripts in SARS-CoV-2-infected cells is related to their translation. We observed a weak, but significant, correlation between the translation efficiency of cellular genes and the reduction in their mRNA half-life after infection (Extended Data Fig. 5i), which indicates that accelerated turnover of cellular transcripts in infected cells may be related to their translation. To assess the role of NSP1 in RNA degradation, we analysed RNA-seq data from cells transfected with NSP1²⁴, which revealed that ectopic NSP1 expression leads to weaker but similar signatures to those that we identified in infected cells: a stronger reduction of cytosolic transcripts compared to

nuclear transcripts, and a stronger sensitivity of nuclear-encoded transcripts (Extended Data Fig. [6a, b](#)).

Fig. 2: Cytosolic cellular RNAs are degraded during SARS-CoV-2 infection.

 [figure2](#)

a, \log_2 -transformed fold change in RNA level of cellular RNAs at 5 h after infection, relative to uninfected cells. RNAs were grouped into ten bins on the basis of their cytosol-to-nucleus localization ratio. P values calculated using two-sided t -test comparing the first and last bins. $n = 5,650$ genes. **b**, \log_2 -transformed fold change in RNA levels of nuclear-encoded ($n = 6,757$) or mitochondrially encoded transcripts ($n = 7$) over the course of infection, relative to uninfected cells. p -values calculated using two-sided Wilcoxon tests. **c**, Scatter plot of mRNA half-life in infected cells relative to uninfected cells, as calculated from SLAM-seq. **d**, Scatter plot depicting \log_2 -transformed fold changes in transcript half-life between infected and uninfected cells, relative to the \log_2 -transformed cytosol/nuclear ratio of cellular transcripts in uninfected cells. Pearson's R and two-sided P value are shown. **e**, Aligned RNA reads at the end of *IL32* from uninfected cells and at 8 h after infection. Rep., replicate. **f**, Box plots of ratio of intronic to exonic reads for genes ($n = 9,123$) over the course of infection, relative to uninfected cells. P values calculated using two-sided t -test. **g**, Percentage of reads that align to exonic or intronic regions relative to rRNA abundance, over the course of infection. **h**, Scatter plot of \log_2 -transformed fold change in the ratio of intronic to exonic reads of cellular genes between 7 h after infection and uninfected cells, relative to \log_2 -transformed fold changes in transcript half-life in infected cells relative to uninfected cells. Pearson's R and two-sided P value are shown. Box plots show median, first to third quartile, $1.5\times$ interquartile range and outliers.

[Full size image](#)

We noticed that SARS-CoV-2 infection also leads to increased levels of intronic reads in many cellular transcripts (Figs. 2e,f), which indicates that SARS-CoV-2 may interfere with cellular mRNA splicing (as has recently been suggested⁵). However, considerable degradation of mature cytosolic mRNAs may also generate a relative increase in intronic reads. We therefore analysed the ratio of intronic and exonic reads to rRNA, which we found to be unperturbed in infection (Extended Data Fig. 3b). Whereas exonic reads showed a marked reduction along the course of SARS-CoV-2 infection (relative to rRNA levels), the intronic read levels showed only a subtle change (Fig. 2g). Additionally, in our SLAM-seq measurements, we did not detect major changes in the turnover of intronic RNA in infected cells (Extended Data Fig. 7a). Furthermore, we observed a correlation between the reduction in transcript half-lives and the relative increase in intronic reads (Fig. 2h). Likewise, the increase in the ratio of intronic to exonic reads was greater in genes with expression that was reduced along infection, as compared to genes with expression that was induced (Extended Data Fig. 7b). These results imply that the increase in intronic reads compared to exonic reads during SARS-CoV-2 infection is driven mostly by the accelerated degradation of mature cellular transcripts, which leads to a relative reduction in exonic

reads. Overall, these findings demonstrate that SARS-CoV-2 infection leads to accelerated degradation of mature cytosolic cellular mRNAs.

An important aspect of host shutoff is the ability of the virus to hamper the translation of cellular transcripts, while recruiting the ribosome to its own transcripts. It has previously been suggested that SARS-CoV-2 mRNAs are refractory to the translation inhibition induced by NSP1^{5,25}. However, our measurements indicate that RNA degradation—which is probably mediated by NSP1—has a prominent role in remodelling the mRNA pool in infected cells, and that SARS-CoV-2 dominates the mRNA pool. All of the subgenomic RNAs that are encoded by SARS-CoV-2 contain a common 5' leader that is added during negative-strand synthesis. We therefore explored whether the genomic 5' untranslated region (UTR) or the common 5' leader protect viral mRNAs from NSP1-induced degradation. We fused the viral 5' leader, the genomic 5' UTR or a control host 5' UTR to a GFP reporter (Extended Data Fig. 8a) and transfected these constructs together with vectors encoding NSP1 or one of two controls (NSP2 or mCherry) into 293T cells (Extended Data Fig. 8b). We found that NSP1 expression suppresses the production of the control GFP but not of the GFP containing the viral 5' UTR or 5' leader (Fig. 3a,b, Extended Data Fig. 8c–e). We extracted RNA from these cells and observed that the NSP1-induced reduction in the level of control GFP was associated with an approximately 12-fold reduction in the GFP mRNA levels, whereas the levels of GFP mRNA fused to the viral 5' UTR or to the 5' leader were only mildly reduced by NSP1 expression (Fig. 3c, Extended Data Fig. 8f). The GFP reporter plasmid we used also contains an mCherry reporter that is expressed from an independent promoter. NSP1 also induces a reduction in mCherry protein and RNA levels when compared to NSP2 (Extended Data Fig. 8g–i). These results indicate that the 5' leader of viral RNAs provides protection from NSP1-induced degradation and that this protection contributes to the ability of the virus to dominate the mRNA pool in infected cells.

Fig. 3: The SARS-CoV-2 5' leader protects mRNA from degradation mediated by NSP1.

 **figure3**

a, b, Microscopy images (**a**) and flow cytometry analysis (**b**) of 293T cells co-transfected with mCherry or NSP1 together with a GFP reporter that includes control 5' UTR, SARS-CoV-2 5' UTR or SARS-CoV-2 5' leader. Representative of four independent replicates are shown. Scale bars, 100 μ m. **c**, Relative GFP RNA levels for the various GFP reporters in cells expressing NSP1 or mCherry, as measured by quantitative real-time PCR. Points show measurement of biological replicates.

[Full size image](#)

The results discussed so far exemplify how SARS-CoV-2 remodels the transcript pool in infected cells. To quantitatively evaluate the role of translational control during SARS-CoV-2 infection, we calculated the translation efficiency of cellular genes along the course of infection. We then clustered the genes that showed the strongest reduction or increase in their relative translation efficiency over the course of infection, which generated four clusters that largely reflect either increased or decreased relative translation efficiency during infection. The mRNA and footprint temporal profiles of these genes revealed a clear signature; the genes with a relative translation efficiency that decreased over the course of infection were genes with mRNA levels that increased during infection without a corresponding increase in footprints (Fig. 4a, Extended Data Fig. 9a). These clusters were enriched in immune-response genes (false-discovery rate $< 10^{-4}$) such as *IRF1*, *IL6* and *CXCL3*. Comparing changes in mRNA and translation efficiency levels of cellular genes along

the course of infection demonstrates that, generally, transcripts that are transcriptionally induced after infection show a reduction in their relative translation efficiency, and vice versa (Fig. 4a, b). These data indicate that newly generated transcripts are less likely to engage with ribosomes. One molecular mechanism that could explain these measurements is inhibition of nuclear mRNA export. To test whether SARS-CoV-2 interferes with nuclear mRNA export, we left Calu3 cells uninfected or infected them with SARS-CoV-2 and assessed the subcellular localization of polyadenylated transcripts by cytoplasmic/nuclear fractionation followed by RNA-seq. We obtained a strong correlation between our cytoplasmic/nuclear fractionation measurements and measurements that were previously conducted¹⁹ (Extended Data Fig. 9b). Infection led to a relative nuclear enrichment of most cellular transcripts (Fig. 4c). Furthermore, genes with relative translation efficiency that was reduced in infection showed a stronger nuclear enrichment, which suggests that the inability of induced transcripts to reach the ribosome may be explained by nuclear retention. Because there is considerable degradation of cytosolic mRNA in infected cells, the relative nuclear enrichment may be expected even with no interference in the export of nuclear mRNA. To more accurately assess whether this nuclear enrichment is also related to the inhibition of nuclear export, we used whole-cell extract samples to normalize the cytoplasmic/nuclear ratios, which enabled us to obtain absolute RNA localization values for each compartment²⁶. We observed that transcripts that are transcriptionally induced show a significant increase specifically in the nuclear fraction in infected cells (Fig. 4d), which indicates that SARS-CoV-2 infection disrupts their nucleocytoplasmic export. Because cytokine and IFN-induced genes are induced upon infection, this inability of nascent transcripts to exit the nucleus and reach the ribosomes may explain why infected cells do not launch a robust antiviral response¹¹.

Fig. 4: The translation of induced transcripts is impaired during infection.

 **figure4**

a, Heat map of relative translation efficiency, mRNA and footprints of the human genes that showed the strongest changes in their relative translation efficiency over the course of infection. Relative expression ratios, after partitioning clustering on the basis of changes in relative translation efficiency, are shown. Several immune-related genes are labelled. *CXCL1/3*, *CXCL1* and *CXCL3*; *NFKBIA/E*, *NFKBIA* and *NFKBIE*; *TNFAIP2/3*, *TNFAIP2* and *TNFAIP3*. **b**, Scatter plot of cellular transcript levels in uninfected cells and at 8 h after infection. Genes are coloured on the basis of the relative change in their translation efficiency between cells 8 h after infection and uninfected cells. Central cytokines and IFN-stimulated genes are labelled. RPKM, reads per kilobase of transcript per million mapped reads. **c**, Scatter plot of the cytosolic/nuclear ratio in infected (7 h after infection, MOI = 3) and uninfected cells. Genes that showed a reduced translation efficiency in **a** are labelled in purple. **d**, Effects of infection on the normalized abundance of cytosolic and nuclear RNA. Transcripts are divided according to their induction kinetics (Extended Data Fig. [4a](#)): induced late ($n = 91$), induced early ($n = 28$), induced mix ($n = 56$) and all the rest ($n = 7,283$). Coloured triangles represent the direction of the change between infected and uninfected samples. P values were calculated using a linear regression model. Box plots show median, first to third quartile, $1.5 \times$ interquartile range and outliers. **e**, Scheme of SARS-CoV-2 RNAs and ORFs. **f**, Relative translation efficiency of viral ORFs along infection. Genes are divided into three groups ('beginning', 'middle' and 'end') on the basis of their physical location along the genome. Mean at 8 h after

infection ($n = 2$), and values at 3 and 5 h after infection ($n = 1$), are shown. **g**, Model of SARS-CoV-2 suppression of host gene expression: (1) global translation reduction; (2) degradation of cytosolic cellular mRNAs; and (3) translation inhibition of induced cellular mRNAs (probably through inhibition of the export of nuclear mRNA).

[Full size image](#)

Finally, we used our measurements to examine viral translation dynamics along the course of infection. Viral ORFs are translated from the genomic RNA or from a nested series of subgenomic RNAs that contain a common 5' leader (Fig. 4e). We examined how the translation of viral genes is distributed between viral transcripts at different times after infection. This analysis revealed that the relative translation efficiency of ORFs that are located at the 5' end of the genome increases along infection. By contrast, the relative translation efficiency of ORFs that are encoded towards the 3' end of the genome decreases, and ORFs located in the middle of the genome show no major changes in their relative translation efficiency ($P = 0.002$ for differences in the slope of the translation efficiency changes using a linear mixed model) (Fig. 4f). We used published RNA-seq and ribosome profiling data¹³ to perform an analysis of the expression and translation of ORFs of mouse hepatitis virus strain A59 along the course of infection, which revealed a trend that was weaker than—but paralleled—that of our SARS-CoV-2 results (Extended Data Fig. 10a, b). Because subgenomic RNAs share the same 5' UTR, one possible explanation for these potential differences in translation is an unappreciated role for the 3' UTR or for viral transcript length, which varies greatly between viral transcripts (Fig. 4e).

Most SARS-CoV-2 ORFs are 3' proximal and translated from dedicated subgenomic mRNAs (Fig. 4e). However, several subgenomic RNAs encode additional out-of-frame ORFs (including ORF2b, ORF3c, ORF7b and ORF9b²⁷), probably via a leaky scanning mechanism. The translation of these out-of-frame ORFs correlated with the expression of the 3'-proximal main ORF, which indicates that there are no major changes in the efficiency of ribosome scanning of viral transcripts over the course of infection (Extended Data Fig. 10c).

Using unbiased measurements of translation and RNA expression along the course of SARS-CoV-2 infection, we identified three major routes by which SARS-CoV-2 interferes with cellular gene expression in infected cells: (1) global inhibition of protein translation, (2) degradation of cytosolic cellular transcripts and (3) specific translation inhibition of newly transcribed mRNAs, which is probably explained by inhibition of nuclear mRNA export. The disruption of cellular protein production using these three components represents a multipronged mechanism that synergistically acts to suppress the host antiviral response (Fig. 4g). These mechanisms may explain the molecular basis of the potent suppression of IFN

response that has been observed in animal models and in patients with severe COVID-19^{[10,12](#)}.

We reveal that, similar to what has previously been described for NSP1 of SARS-CoV, NSP1 of SARS-CoV-2 shuts down host protein translation by two mechanisms: first, it stalls mRNA translation (as has previously been reported^{[5,6,7](#)}), which leads to a general reduction in the translation capacity of infected cells. Second, NSP1 leads to accelerated degradation of cellular mRNA. NSP1 of SARS-CoV induces endonucleolytic cleavage and the subsequent degradation of host mRNAs, and this activity depends on the binding of NSP1 to the 40S ribosome subunit^{[2](#)}. Our results are consistent with a similar mechanism operating in SARS-CoV-2-infected cells, as we show that cytosolic RNAs are more susceptible to SARS-CoV-2-mediated degradation. Several previous studies have shown that mRNAs with the viral 5' leader are translated more efficiently in the presence of NSP1^{[5,25](#)}, but a further study has previously demonstrated that NSP1 inhibits the translation of reporter mRNA containing both cellular and viral 5' UTRs^{[6](#)}, which implies that viral mRNAs may not simply evade translation inhibition in the context of the 5' UTR sequence. Our results support a model in which NSP1 acts as a strong inhibitor of translation and at the same time leads to the accelerated degradation of cellular, but not of viral, mRNAs—thus providing the means for viral mRNA to quickly dominate the mRNA pool. This accumulation of SARS-CoV-2 mRNAs may explain how infected cells divert their translation towards viral mRNAs. Overall, our study provides an in-depth depiction of how SARS-CoV-2 efficiently interferes with cellular gene expression, leading to the shutdown of host protein production through a multipronged strategy.

Methods

No statistical methods were used to predetermine sample size. The experiments were not randomized, and investigators were not blinded to allocation during experiments and outcome assessment.

Cells and viruses

Calu3 cells (ATCC HTB-55) were cultured in 6-well or 10-cm plates with RPMI supplemented with 10% fetal bovine serum (FBS), MEM non-essential amino acids, 2 mM l-glutamine, 100 units per ml penicillin and 1% Na-pyruvate. Monolayers were washed once with RPMI without FBS and infected with SARS-CoV-2 virus, at an MOI of 3, in the presence of 20 µg per ml TPCK trypsin (Thermo scientific). Plates were incubated for 1 h at 37 °C to allow viral adsorption. Then, RPMI medium supplemented with 2% FBS, was added to each well. SARS-CoV-2 BavPat1/2020 Ref-SKU: 026V-03883 was provided by C. Drosten. It was propagated (5 passages)

and titred on Vero E6 cells and then sequenced⁹ before it was used. Handling and working with SARS-CoV-2 virus was conducted in a BSL3 facility in accordance with the biosafety guidelines of the Israel Institute for Biological, Chemical and Environmental sciences. The Institutional Biosafety Committee of Weizmann Institute approved the protocol used in these studies. Calu3 and 293T cells were authenticated by ATCC using STR profiling. All cell lines tested negative for mycoplasma.

Preparation of ribosome profiling and RNA-seq samples

SARS-CoV-2-infected cells were collected at 3, 5 and 8 h post infection (hpi): two independent biological replicates were done for the 8-hpi time point and for uninfected cells that were collected in parallel at 3 and 5 hpi. For RNA-seq, cells were washed with PBS and then collected with Tri-Reagent (Sigma-Aldrich), total RNA was extracted and poly-A selection was performed using Dynabeads mRNA DIRECT Purification Kit (Invitrogen). The mRNA sample was subjected to DNaseI treatment and 3' dephosphorylation using FastAP Thermosensitive Alkaline Phosphatase (Thermo Scientific) and T4 PNK (NEB) followed by 3' adaptor ligation using T4 ligase (NEB). The ligated products were used for reverse transcription with SSIII (Invitrogen) for first-strand cDNA synthesis. The cDNA products were 3'-ligated with a second adaptor using T4 ligase and amplified for 8 cycles in a PCR for final library products of 200–300 bp. For ribosome profiling libraries, cells were treated with 100 µg ml⁻¹ cycloheximide for 1 min. Cells were then placed on ice, washed twice with PBS containing 100 µg ml⁻¹ cycloheximide, scraped from 10-cm plates, pelleted and lysed with lysis buffer (1% triton in 20 mM Tris 7.5, 150 mM NaCl, 5 mM MgCl₂, 1 mM dithiothreitol supplemented with 10 U ml⁻¹ Turbo DNase and 100 µg ml⁻¹ cycloheximide). After lysis, samples stood on ice for 2 h and subsequent ribosome profiling library generation was performed, as previously described²⁸. In brief, cell lysate was treated with RNaseI for 45 min at room temperature followed by SUPERase-In quenching. Sample was loaded on sucrose solution (34% sucrose, 20 mM Tris 7.5, 150 mM NaCl, 5 mM MgCl₂, 1 mM dithiothreitol and 100 µg ml⁻¹ cycloheximide) and spun for 1 h at 100,000 rpm using TLA-110 rotor (Beckman) at 4 °C. The pellet was collected using TRI reagent and the RNA was collected using chloroform phase separation. For size selection, 15 µg of total RNA was loaded into 15% TBE-UREA gel for 65 min, and 28–34-nt footprints were excised using 28-nt and 34-nt flanking RNA oligonucleotides, followed by RNA extraction and ribosome profiling library construction as previously described²⁸.

Sequence alignment and metagene analysis

Sequencing reads were aligned as previously described⁹. In brief, linker (CTGTAGGCACCATCAAT) and poly-A sequences were removed and the remaining

reads were aligned to the hg19 and to the SARS-CoV-2 genome (Genebank NC_045512.2) with 3 changes to match the used strain (BetaCoV/Germany/BavPat1/2020 EPI_ISL_406862), (241:C>T, 3037:C>T and 23403:A>G). Alignment was performed using Bowtie v.1.1.2²⁹ with maximum two mismatches per read. Reads that were not aligned to the genome were aligned to the transcriptome (using the known canonical isoform UCSC gene annotations) and to SARS-CoV-2 junctions that were recently annotated³⁰. The aligned position on the genome was determined as the 5' position of RNA-seq reads, and for ribosome profiling reads the p-site of the ribosome was calculated according to read length using the offset from the 5' end of the reads that was calculated from canonical cellular ORFs. The offsets used were +12 for reads that were 28 or 29 bp and +13 for reads that were 30–33 bp. Footprint reads that were of other lengths were discarded. In all figures presenting ribosome density data, only footprint lengths of 28–33 nt are presented.

For the metagene analysis, only genes with CDS length of at least 300 nucleotides, UTRs of at least 50 nucleotides and more than 50 reads in the analysed window around the start or the stop codon were used. For each gene, reads were normalized to the sum of reads in the analysed window and then averaged.

Gene filtering, quantification and RPKM normalization

For cellular gene quantification, genes were filtered according to the number of reads as follows. The number of reads aligned to the CDS of each gene in each replicate, from at least one of the extreme conditions (uninfected or 8 hpi) had to be greater than 50 reads for the mRNA libraries and greater than 25 for the footprint libraries. In addition, genes with zero reads in any of the samples (mRNA or footprint of any of the time points) were excluded. Histone genes (which are not polyadenylated) were excluded from the analysis. RNA-seq read coverage on CDS was normalized to units of RPKM to normalize for CDS length and for sequencing depth. For analysis in which host and viral gene expression were compared (Fig. 1b–d, f), RPKM was calculated on the basis of the total number of uniquely aligned reads to the coding regions of both the host and the virus. For analysis that was focused on cellular gene expression, for RNA expression, the RPKM values were calculated on the basis of the total number of uniquely aligned reads to the cellular coding regions. RPKM values were further scaled according to the ratio of the aligned host mRNA reads to the total aligned reads, including viral, rRNA and tRNA reads in the total RNA sequencing (without polyA selection), to keep the total reads equal across samples. For footprint libraries, read coverage of cellular and viral genes was normalized to units of RPKM normalizing to the total CDS aligned ribosome profiling reads, including both viral and host reads.

Because the viral RNAs are widely overlapping, RNA-seq RPKM levels of viral genes were computed with deconvolution as was previously described for mouse hepatitis virus (MHV)¹³. First, values for each gene were calculated by subtracting the RPKM of an ORF from the RPKM of the ORF located just upstream of it in the genome. Then, for subgenomic RNAs, leader–body junctions were quantified on the basis of the number of uniquely mapped reads that span each canonical junction using STAR 2.5.3a aligner³¹. Finally, on the basis of the correlation between the deconvoluted RPKM and junction abundance of the subgenomic RNAs, the RPKM levels of all viral RNAs (including the genomic RNA) were estimated. Viral and host gene translation efficiency was calculated as the ratio between footprint RPKM and RNA RPKM. To compare viral translation efficiency along infection, the translation efficiency of viral genes was further normalized by dividing the translation efficiency of each viral gene by the sum of the viral gene translation efficiency in each sample and multiplying by 100. For comparing the relative translation levels of canonical ORFs and overlapping viral ORFs decoded from the same subgenomic RNA, we used ORF-RATER³². To estimate the error in our expression measurements of out-of-frame ORFs, for each of these ORFs, we defined 500 random partial ORF regions, which range in length between 50% and 100% of the original ORF, and used ORF-RATER to quantify the expression from these regions while keeping all other ORFs unmodified. On the basis of these values, we have added a standard deviation for the ORF expression measurement. Previous data¹³ were analysed for calculating changes in relative viral gene translation efficiency. Owing to differences in the per cent of aligned viral reads between the replicates, we analysed only replicate 1, which showed the expected gradual increase in viral mRNA and footprint reads along infection.

Clustering and heat maps

We performed clustering on 2,000 cellular genes that showed the strongest change on the basis of the fold change in RNA-seq expression levels between 8 hpi and uninfected samples (both averaged across duplicates). For clustering of upregulated genes, cellular genes that showed at least 1.5-fold increase in expression levels between 8 hpi and uninfected samples were used. RNA-seq and footprint measurements for each of these genes were scaled so that the minimum level across samples is 0 and the maximum is 100. Hierarchical clustering of these normalized values was performed using ward.D2 method on Pearson correlations between scaled RNA-seq measurements using the means of the uninfected and 8-hpi samples.

For presenting changes in relative translation efficiency, we performed clustering on the 35 most-increased and 35 most-decreased genes on the basis of the fold change in relative translation efficiency between 8 hpi and uninfected samples (averaged across duplicates, fold change > 1.7 or fold change < -2.4). Translation efficiency, RNA-seq and footprint measurements for these genes were scaled so that the average level for

each gene across samples is one, using mean expression from uninfected and 8-hpi duplicates. Hierarchical clustering of genes was performed using ward.D2 method on Pearson correlations between scaled relative translation efficiency measurements. With this clustering, we obtained four homogenous groups of genes, each one of which showed a clear different pattern of behaviour with time.

Quantification of intronic reads

Read density for introns was calculated as described for exons, with intron annotations based on the known canonical isoform UCSC gene annotations. To avoid biases from intron read count, genes without introns or genes for which one of the introns overlaps with an exon of another gene were excluded. In addition, genes with low number of reads (<20 on the exons and <2 on the introns) were omitted. The number of reads on exons and introns was normalized by the total length of the exons and introns, respectively, to get a quantification proportional to the number of molecules. Finally, the normalized number of reads on introns was calculated as percentage of the normalized number of reads on exons. Statistical significance (Fig. 2f) was tested using a paired *t*-test on the log values of the percentage (with offset of 0.1 to overcome zero values).

Protein synthesis measurement using OPP

The OPP assay (OPP, Thermo Fisher Scientific) was carried out following the manufacturer's instructions. In brief, cells were collected following treatment with 10 μM OPP for 30 min at 37 °C. The cells were then fixed for 15 min in 3.7% formaldehyde, and permeabilized in 0.1% Triton X-100 for 15 min. OPP was then fluorescently labelled by a 30-min incubation in Click-iT Plus OPP reaction cocktail with Alexa Fluor594 picolyl azide (Thermo Fisher Scientific). Cells were analysed using BD LSRII flow cytometer. The decrease in translation levels was calculated according to the median Alexa 594 fluorescence intensity between the 8 hpi and uninfected samples.

Pathway enrichment analysis

Enrichment analysis of cellular pathways in specific gene clusters (Fig. 4a, Extended Data Fig. 4a) was done with PANTHER version 15.0, with default settings and the PANTHER pathways dataset^{33,34}.

Fractionation assay

Uninfected or SARS-CoV-2-infected (MOI = 3) Calu3 cells at 7 hpi were washed in PBS, trypsinized and resuspended in cold PBS. A fraction of 10% of the cells was then

transferred to a new tube and RNA was extracted in Tri-reagent to obtain whole cellular extract. Remaining cells were pelleted for 5 min at 300g. Cells were resuspended in 150 µl fractionation buffer A (15 mM Tris-Cl pH 8, 15 mM NaCl, 60 mM KCl, 1 mM EDTA pH 8, 0.5 mM EGTA pH 8, 0.5 mM spermidine, and 10 U ml⁻¹ RNase inhibitor), and 150 µl 2× lysis buffer (15 mM Tris-Cl pH 8, 15 mM NaCl, 60 mM KCl, 1 mM EDTA pH 8, 0.5 mM EGTA pH 8, 0.5 mM spermidine, 10 U ml⁻¹ RNase inhibitor and 0.5% NP-40) was added followed by 10 min incubation on ice. The extract was pelleted for 5 min at 400g and the supernatant containing the cytoplasmic fraction was removed to a new tube. This was centrifuged again at 500g for 1 min, the supernatant was transferred to a new tube and RNA was extracted with Tri-reagent. The nuclear pellet was resuspended in 1 ml RLN buffer (50 mM Tris-Cl pH 8, 140 mM NaCl, 1.5 mM MgCl₂, 0.5% NP-40, 10 mM EDTA and 10 U ml⁻¹ RNase inhibitor) and incubated on ice for 5 min. The nuclear fraction was then pelleted for 5 min at 500g, the supernatant was removed and RNA was extracted from the pellet with Tri-reagent. RNA-seq libraries were then prepared from all three fractions as described in ‘Preparation of ribosome profiling and RNA-seq samples’.

Fractionation assay analysis

RNA-seq reads from total, nuclear and cytosolic fractions were aligned to the human and viral reference as described in ‘Sequence alignment and metagene analysis’. Human gene read counts were adjusted to RPKM as described in ‘Gene filtering, quantification and RPKM normalization’, and then converted to transcripts per million (TPM) by normalizing to the sum of RPKM in each sample, so that the expression levels in each sample sum up to the same value.

A list of 3,884 average-expressed genes was defined. These genes were genes with 25 or more reads across all samples and with a sum of TPM values in the total RNA samples across replicates within quantiles 0.4 and 0.9. On the basis of this list, for each replicate, a linear regression model was calculated of the total fraction as a linear combination of the cytosolic and the nuclear fractions. The regression coefficients were used to normalize the cytosolic and nuclear TPM values to obtain absolute localization values²⁶. To correct for changes in total mRNA levels, the absolute values were further scaled by a factor calculated from total RNA-seq as described in ‘Gene filtering, quantification and RPKM normalization’. To statistically compare the effect of infection on nuclear–cytosolic distribution of mRNAs from different clusters, *P* values were calculated from the interaction term in a linear model.

RNA labelling for SLAM-seq

For metabolic RNA labelling, growth medium of infected Calu3 cells (MOI = 3) at 3 hpi or uninfected cells was replaced with medium containing 4sU (T4509, Sigma) at a

final concentration of 200 μ M (a concentration that did not induce substantial cell cytotoxicity at 4 h labelling). Cells were collected with Tri-reagent at 1, 2, 3 and 4 h after medium replacement (corresponding to 4, 5, 6 and 7 hpi for infected cells). RNA was extracted under reducing conditions and treated with iodoacetamide (A3221, Sigma) as previously described¹⁷. RNA-seq libraries were prepared and sequenced as described in ‘Preparation of ribosome profiling and RNA-seq samples’ and paired-end reads were sequenced with 51 cycles for each end.

SLAM-seq data analysis and half-life calculation

Alignment of SLAM-seq reads was performed using STAR³¹, with parameters that were previously described⁹. First, reads were aligned to a reference containing human rRNA and tRNA, and all reads that were successfully aligned were filtered out. The remaining reads were aligned to a reference of the human and the virus as described in ‘Sequence alignment and metagene analysis’. Reads mapped to the virus were discarded and reads mapped to the human were used in the next steps. Output .bam files from STAR were used as input for the GRAND-SLAM analysis¹⁸ with default parameters and with trimming of 5 nucleotides in the 5' and 3' ends of each read. Infected and uninfected samples were analysed in separate runs. Each one of the runs also included an unlabelled sample (no 4sU) that was used for estimating the linear model of the background mutations. The output of GRAND-SLAM is the estimated ratio of newly synthesized out of total molecules for each gene (new to total ratio (NTR)). The old transcript fraction for each gene in each sample is 1 – NTR; this number reflects the pre-existing mRNA molecules (not labelled) and these values were used for half-life estimation of cellular genes. In the case of uninfected samples, we compared two approaches for calculating mRNA half-life: in the first, we assumed steady state and in the second, we analysed gene composition in each sample and the old fraction was normalized to the gene composition. These two approaches yielded highly similar values and the half-life values in uninfected cells that are presented in the figures are based on the calculation that assume steady state. In the case of the infected samples, the gene composition from the total RNA levels were used to normalize the expression of the old mRNA fraction as follows. The total number of reads in each sample was scaled according to the ratio of cellular mRNA to rRNA and tRNA, as calculated on the basis of sequencing of total RNA-seq without poly-A selection. These normalized ratios were used to normalize the old transcript fractions in each sample.

The half-life of each gene in uninfected and infected cells was calculated by linear regression of the log values of the calculated old transcript fraction. Estimated variance of the values as calculated by GRAND-SLAM were used as weights in the linear regression. The regression coefficient lambda was converted to half-life as

$-\log(2)/\lambda$. For further analysis, only genes for which the P value in the regression was < 0.01 and the adjusted $r^2 > 0.8$ were used.

For analysis of intronic RNA turnover, reads that were aligned to any transcript annotation in Ensembl hg19 annotations were filtered out (may represent exonic reads). The rest of the reads were aligned to hg19 genome and were used as input for GRAND-SLAM using intron annotations on the basis of the known canonical UCSC genes.

Immunofluorescence

Cells were plated on ibidi slides, infected as described in ‘Cells and viruses’ or left uninfected and at the indicated time point washed once with PBS, fixed in 3% paraformaldehyde for 20 min, washed in PBS, permeabilized with 0.5% Triton X-100 in PBS for 2 min, and then blocked with 2% FBS in PBS for 30 min. Immunostaining was performed with rabbit anti-SARS-CoV-2 serum³⁵ at a 1:200 dilution. Cells were washed and labelled with anti-rabbit FITC conjugated antibody at a 1:200 dilution and with DAPI (4',6-diamidino-2-phenylindole) at a 1:200 dilution. Imaging was performed on a Zeiss AxioObserver Z1 wide-field microscope using a $\times 40$ objective and Axiocam 506 mono camera.

Plasmids and cloning

pLVX-EF1alpha-SARS-CoV-2-nsp1-2XStrep-IRES-Puro and pLVX-EF1alpha-SARS-CoV-2-nsp2-2XStrep-IRES-Puro were provided by N. Krogan. mCherry–Flag was cloned in to the lentiCRISPR v.2 plasmid (Addgene no. 52961) instead of the Cas9 cassette. The viral genomic 5' UTR was constructed on the basis of nucleotides 4–265 of the reported sequence of SARS-CoV-2 isolate Wuhan-Hu-1 (NC_045512.2) by sequential annealing of DNA oligonucleotides (IDT, 5'UTR oligo_1-5 listed in Supplementary Table 2). The coding sequence for the first 12 amino acids of ORF1a as well as the GFP homology region were added to the 5' UTR by two PCR amplifications. The viral 5' UTR with the 12 amino acid region was cloned into pAcGFP1-C1 (Takara Biotech) using restriction-free cloning. The entire expression cassette from the promoter to the poly-A site was amplified and cloned into pDeck-mCherry (Addgene plasmid no. 78534) using restriction-free cloning. Primers for PCR amplification of fragments were ordered from Sigma-Aldrich. The viral subgenomic 5' leader was amplified from the viral 5' UTR plasmid using primers containing homologous regions to clone the 5' leader back into the plasmid. This was subsequently done using restriction-free cloning. For the human beta-globin (HBB) 5' UTR control plasmid, the HBB 5' UTR with GFP homology was ordered from Sigma-Aldrich as two oligonucleotides. These were used in a self-priming PCR reaction and

inserted upstream of GFP in place of the viral 5' UTR using restriction-free cloning. All primers and oligonucleotides used for cloning are listed in Supplementary Table 2.

Reporter assay

293T cells were transfected using JetPEI (Polyplus-transfection) following the manufacturer's instructions. Twenty-four h after transfection cells were imaged on a Zeiss AxioObserver Z1 wide-field microscope using a $\times 20$ objective and Axiocam 506 mono camera and assayed for reporter expression by flow cytometry on a BD Accuri C6 flow cytometer. In parallel, cells were assayed for expression of NSP1, NSP2 and mCherry–Flag and reporter mRNA levels as detailed in 'Flow cytometry analysis of Strep and Flag tags' and 'Quantitative real-time PCR analysis'.

Flow cytometry analysis of Strep and Flag tags

The expression of NSP1, NSP2 and mCherry was verified by staining of the fused tags, Strep tag for NSP1 and NSP2 and Flag tag for mCherry, followed by flow cytometry. Cells were fixed in 4% paraformaldehyde, permeabilized in 0.1% Triton X100, and stained using either Strep-TactinXT DY-649 (IBA-lifesciences) or Alexa Fluor647 anti-DYKDDDDK Tag Antibody (BioLegend). Flow cytometry analysis was performed on BD Accuri C6 and analysed on FlowJo. Normalization to the mode is presented in the histograms.

Quantitative real-time PCR analysis

Total RNA was extracted using Direct-zol RNA Miniprep Kit (Zymo Research) following the manufacturer's instructions. cDNA was prepared using qScript FLEX cDNA Synthesis Kit with random primers (Quanta Biosciences) following the manufacturer's instructions. Real-time PCR was performed using the SYBR Green PCR master-mix (ABI) on the QuantStudio 12K Flex (ABI) with the following primers (forward, reverse): *GFP* (TGACCCTGAAGTTCATCTGC, GAAGTCGTGCTGCTTCATGT); *mCherry* (ACCGCCAAGCTGAAGGTGAC, GACCTCAGCGTCGTAGTGGC); and *18S* (CTAACACACGGAAACCTCAC, CGCTCCACCAACTAAGAACG)

GFP and *mCherry* mRNA levels were calculated relative to 18S rRNA.

Graphics

Figure 4g was created with BioRender. Fluorescence-activated cell sorting figures were created with FlowJo and the rest of the figures were drawn with ggplot2 in R.

Reporting summary

Further information on research design is available in the [Nature Research Reporting Summary](#) linked to this paper.

Data availability

All next-generation sequencing data files have been deposited in Gene Expression Omnibus under accession number [GSE162323](#). NSP1 expression data analysed in this study are available from Gene Expression Omnibus with the accession number [GSE158374](#). MHV infection data are available from ArrayExpress database under the accession number E-MTAB-4111.

References

1. 1.

Zhou, P. et al. A pneumonia outbreak associated with a new coronavirus of probable bat origin. *Nature* **579**, 270–273 (2020).

[ADS](#) [CAS](#) [Article](#) [Google Scholar](#)

2. 2.

Kamitani, W., Huang, C., Narayanan, K., Lokugamage, K. G. & Makino, S. A two-pronged strategy to suppress host protein synthesis by SARS coronavirus Nsp1 protein. *Nat. Struct. Mol. Biol.* **16**, 1134–1140 (2009).

[CAS](#) [Article](#) [Google Scholar](#)

3. 3.

Lokugamage, K. G. et al. Middle East respiratory syndrome coronavirus Nsp1 inhibits host gene expression by selectively targeting mRNAs transcribed in the nucleus while sparing mRNAs of cytoplasmic origin. *J. Virol.* **89**, 10970–10981 (2015).

[CAS](#) [Article](#) [Google Scholar](#)

4. 4.

Addetia, A. et al. SARS-CoV-2 ORF6 disrupts bidirectional nucleocytoplasmic transport through interactions with Rae1 and Nup98. *mBio* **12**, e00065-21 (2021).

5. 5.

Banerjee, A. K. et al. SARS-CoV-2 disrupts splicing, translation, and protein trafficking to suppress host defenses. *Cell* **183**, 1325–1339.e21 (2020).

[CAS](#) [Article](#) [Google Scholar](#)

6. 6.

Schubert, K. et al. SARS-CoV-2 Nsp1 binds the ribosomal mRNA channel to inhibit translation. *Nat. Struct. Mol. Biol.* **27**, 959–966 (2020).

[CAS](#) [Article](#) [Google Scholar](#)

7. 7.

Thoms, M. et al. Structural basis for translational shutdown and immune evasion by the Nsp1 protein of SARS-CoV-2. *Science* **369**, 1249–1255 (2020).

[ADS](#) [CAS](#) [Article](#) [Google Scholar](#)

8. 8.

V'kovski, P., Kratzel, A., Steiner, S., Stalder, H. & Thiel, V. Coronavirus biology and replication: implications for SARS-CoV-2. *Nat. Rev. Microbiol.* **19**, 155–170 (2021).

[Article](#) [Google Scholar](#)

9. 9.

Finkel, Y. et al. The coding capacity of SARS-CoV-2. *Nature* **589**, 125–130 (2021).

[ADS](#) [CAS](#) [Article](#) [Google Scholar](#)

10. 10.

Blanco-Melo, D. et al. Imbalanced host response to SARS-CoV-2 drives development of COVID-19. *Cell* **181**, 1036–1045.e9 (2020).

[CAS](#) [Article](#) [Google Scholar](#)

11. 11.

Sa Ribero, M., Jouvenet, N., Dreux, M. & Nisole, S. Interplay between SARS-CoV-2 and the type I interferon response. *PLoS Pathog.* **16**, e1008737 (2020).

[CAS](#) [Article](#) [Google Scholar](#)

12. 12.

Hadjadj, J. et al. Impaired type I interferon activity and inflammatory responses in severe COVID-19 patients. *Science* **369**, 718–724 (2020).

[ADS](#) [CAS](#) [Article](#) [Google Scholar](#)

13. 13.

Irigoyen, N. et al. High-resolution analysis of coronavirus gene expression by RNA sequencing and ribosome profiling. *PLoS Pathog.* **12**, e1005473 (2016).

[Article](#) [Google Scholar](#)

14. 14.

Wolff, G. et al. A molecular pore spans the double membrane of the coronavirus replication organelle. *Science* **369**, 1395–1398 (2020).

[ADS](#) [CAS](#) [Article](#) [Google Scholar](#)

15. 15.

Liu, J., Xu, Y., Stoleru, D. & Salic, A. Imaging protein synthesis in cells and tissues with an alkyne analog of puromycin. *Proc. Natl Acad. Sci. USA* **109**, 413–418 (2012).

[ADS](#) [CAS](#) [Article](#) [Google Scholar](#)

16. 16.

Del Valle, D. M. et al. An inflammatory cytokine signature predicts COVID-19 severity and survival. *Nat. Med.* **26**, 1636–1643 (2020).

[Article](#) [Google Scholar](#)

17. 17.

Herzog, V. A. et al. Thiol-linked alkylation of RNA to assess expression dynamics. *Nat. Methods* **14**, 1198–1204 (2017).

[CAS](#) [Article](#) [Google Scholar](#)

18. 18.

Jürges, C., Dölken, L. & Erhard, F. Dissecting newly transcribed and old RNA using GRAND-SLAM. *Bioinformatics* **34**, i218–i226 (2018).

[Article](#) [Google Scholar](#)

19. 19.

Zuckerman, B., Ron, M., Mikl, M., Segal, E. & Ulitsky, I. Gene architecture and sequence composition underpin selective dependency of nuclear export of long RNAs on NXF1 and the TREX complex. *Mol. Cell* **79**, 251–267.e6 (2020).

[CAS](#) [Article](#) [Google Scholar](#)

20. 20.

Nakagawa, K., Lokugamage, K. G. & Makino, S. in *Advances in Virus Research*, vol. 96 (ed. Ziebuhr, J.) 165–192 (Academic, 2016).

21. 21.

Kamitani, W. et al. Severe acute respiratory syndrome coronavirus nsp1 protein suppresses host gene expression by promoting host mRNA degradation. *Proc. Natl Acad. Sci. USA* **103**, 12885–12890 (2006).

[ADS](#) [CAS](#) [Article](#) [Google Scholar](#)

22. 22.

Narayanan, K. et al. Severe acute respiratory syndrome coronavirus nsp1 suppresses host gene expression, including that of type I interferon, in infected cells. *J. Virol.* **82**, 4471–4479 (2008).

[CAS](#) [Article](#) [Google Scholar](#)

23. 23.

Huang, C. et al. SARS coronavirus nsp1 protein induces template-dependent endonucleolytic cleavage of mRNAs: viral mRNAs are resistant to nsp1-induced RNA cleavage. *PLoS Pathog.* **7**, e1002433 (2011).

[CAS](#) [Article](#) [Google Scholar](#)

24. 24.

Rao, S. et al. Genes with 5' terminal oligopyrimidine tracts preferentially escape global suppression of translation by the SARS-CoV-2 NSP1 protein. Preprint at <https://doi.org/10.1101/2020.09.13.295493> (2020).

25. 25.

Tidu, A. et al. The viral protein NSP1 acts as a ribosome gatekeeper for shutting down host translation and fostering SARS-CoV-2 translation. *RNA*, <https://doi.org/10.1261/rna.078121.120> (2020).

26. 26.

Carlevaro-Fita, J. & Johnson, R. Global positioning system: understanding long noncoding RNAs through subcellular localization. *Mol. Cell* **73**, 869–883 (2019).

[CAS](#) [Article](#) [Google Scholar](#)

27. 27.

Jungreis, I. et al. Conflicting and ambiguous names of overlapping ORFs in the SARS-CoV-2 genome: a homology-based resolution. *Virology* **558**, 145–151 (2021).

[CAS](#) [Article](#) [Google Scholar](#)

28. 28.

Finkel, Y. et al. Comprehensive annotations of human herpesvirus 6A and 6B genomes reveal novel and conserved genomic features. *eLife* **9**, e50960 (2020).

[CAS](#) [Article](#) [Google Scholar](#)

29. 29.

Langmead, B., Trapnell, C., Pop, M. & Salzberg, S. L. Ultrafast and memory-efficient alignment of short DNA sequences to the human genome. *Genome Biol.*

10, R25 (2009).

[Article](#) [Google Scholar](#)

30. 30.

Kim, D. et al. The architecture of SARS-CoV-2 transcriptome. *Cell* **181**, 914–921 (2020).

[CAS](#) [Article](#) [Google Scholar](#)

31. 31.

Dobin, A. et al. STAR: ultrafast universal RNA-seq aligner. *Bioinformatics* **29**, 15–21 (2013).

[CAS](#) [Article](#) [Google Scholar](#)

32. 32.

Fields, A. P. et al. A regression-based analysis of ribosome-profiling data reveals a conserved complexity to mammalian translation. *Mol. Cell* **60**, 816–827 (2015).

[CAS](#) [Article](#) [Google Scholar](#)

33. 33.

Mi, H. & Thomas, P. PANTHER pathway: an ontology-based pathway database coupled with data analysis tools. *Methods Mol. Biol.* **563**, 123–140 (2009).

[CAS](#) [Article](#) [Google Scholar](#)

34. 34.

Mi, H., Muruganujan, A., Ebert, D., Huang, X. & Thomas, P. D. PANTHER version 14: more genomes, a new PANTHER GO-slim and improvements in enrichment analysis tools. *Nucleic Acids Res.* **47**, D419–D426 (2019).

[CAS](#) [Article](#) [Google Scholar](#)

35. 35.

Yahalom-Ronen, Y. et al. A single dose of recombinant VSV-ΔG-spike vaccine provides protection against SARS-CoV-2 challenge. *Nat. Commun.* **11**, 6402 (2020).

[ADS](#) [CAS](#) [Article](#) [Google Scholar](#)

[Download references](#)

Acknowledgements

We thank members of the laboratory of N.S.-G. for providing valuable feedback; N. Krogan for the SARS-CoV-2 ORF expression plasmids; G. Jona and Weizmann Bacteriology and Genomic Repository Units for technical assistance; members of the virology research group at the IIBR for their contribution and support; and S. Weiss for biosafety guidance. This study was supported by a research grant from Weizmann Corona Response Fund. Work in the laboratory of N.S.-G. is supported by a European Research Council consolidator grant (CoG-2019-864012). N.S.-G. is an incumbent of the Skirball Career Development Chair in New Scientists and is a member of the European Molecular Biology Organization (EMBO) Young Investigator Program.

Author information

Author notes

1. These authors contributed equally: Yaara Finkel, Avi Gluck, Aharon Nachshon

Affiliations

1. Department of Molecular Genetics, Weizmann Institute of Science, Rehovot, Israel

Yaara Finkel, Avi Gluck, Aharon Nachshon, Roni Winkler, Tal Fisher, Batsheva Rozman, Orel Mizrahi, Michal Schwartz & Noam Stern-Ginossar

2. Department of Biological Regulation, Weizmann Institute of Science, Rehovot, Israel

Yoav Lubelsky, Binyamin Zuckerman & Igor Ulitsky

3. Department of Biomolecular Sciences, Weizmann Institute of Science, Rehovot, Israel

Boris Slobodin

4. Department of Infectious Diseases, Israel Institute for Biological, Chemical and Environmental Sciences, Ness Ziona, Israel

Yfat Yahalom-Ronen, Hadas Tamir, Tomer Israely & Nir Paran

Authors

1. Yaara Finkel

[View author publications](#)

You can also search for this author in [PubMed](#) [Google Scholar](#)

2. Avi Gluck

[View author publications](#)

You can also search for this author in [PubMed](#) [Google Scholar](#)

3. Aharon Nachshon

[View author publications](#)

You can also search for this author in [PubMed](#) [Google Scholar](#)

4. Roni Winkler

[View author publications](#)

You can also search for this author in [PubMed](#) [Google Scholar](#)

5. Tal Fisher

[View author publications](#)

You can also search for this author in [PubMed](#) [Google Scholar](#)

6. Batsheva Rozman

[View author publications](#)

You can also search for this author in [PubMed](#) [Google Scholar](#)

7. Orel Mizrahi

[View author publications](#)

You can also search for this author in [PubMed](#) [Google Scholar](#)

8. Yoav Lubelsky

[View author publications](#)

You can also search for this author in [PubMed](#) [Google Scholar](#)

9. Binyamin Zuckerman

[View author publications](#)

You can also search for this author in [PubMed](#) [Google Scholar](#)

10. Boris Slobodin

[View author publications](#)

You can also search for this author in [PubMed](#) [Google Scholar](#)

11. Yfat Yahalom-Ronen

[View author publications](#)

You can also search for this author in [PubMed](#) [Google Scholar](#)

12. Hadas Tamir

[View author publications](#)

You can also search for this author in [PubMed](#) [Google Scholar](#)

13. Igor Ulitsky

[View author publications](#)

You can also search for this author in [PubMed](#) [Google Scholar](#)

14. Tomer Israely

[View author publications](#)

You can also search for this author in [PubMed](#) [Google Scholar](#)

15. Nir Paran

[View author publications](#)

You can also search for this author in [PubMed](#) [Google Scholar](#)

16. Michal Schwartz

[View author publications](#)

You can also search for this author in [PubMed](#) [Google Scholar](#)

17. Noam Stern-Ginossar

[View author publications](#)

You can also search for this author in [PubMed](#) [Google Scholar](#)

Contributions

Y.F., R.W., A.N., A.G., N.P., M.S. and N.S.-G. conceptualized the study; A.G., R.W., T.F., B.R., O.M. and B.Z. performed experiments; Y.L. and B.S. provided reagents. Y.F., A.N. and R.W. undertook data analysis; Y.Y-R., H.T., T.I. and N.P. performed experiments with SARS-CoV-2; Y.F., A.G., T.F., A.N., I.U., N.P., M.S. and N.S.-G. interpreted data; and Y.F., M.S. and N.S.-G. wrote the manuscript with contributions from all other authors.

Corresponding authors

Correspondence to [Michal Schwartz](#) or [Noam Stern-Ginossar](#).

Ethics declarations

Competing interests

The authors declare no competing interests.

Additional information

Peer review information *Nature* thanks Lars Dölken and the other, anonymous, reviewer(s) for their contribution to the peer review of this work. Peer reviewer reports are available.

Publisher's note Springer Nature remains neutral with regard to jurisdictional claims in published maps and institutional affiliations.

Extended data figures and tables

[Extended Data Fig. 1 Ribosome profiling and RNA-seq along SARS-CoV-2 infection.](#)

a, Calu3 cells were infected with SARS-CoV-2 at an MOI = 3 and at 8 hpi the cells were fixed and stained with antisera against SARS-CoV-2 (green) and DAPI (blue). Representative images of two independent replicates are shown. Scale bars, 100 μ m.

b, c, Scatter plots depicting gene read counts derived from our two independent biological replicates for mRNA (**b**) and footprints (FP) (**c**), demonstrating reproducibility between our replicates. Pearson's *R* and two-sided *P* values from log values are presented. Coloured dots represent the different viral ORFs. **d**, Length

distribution of ribosome footprint fragments from SARS-CoV-2 genes (blue) or cellular genes (pink). **e–h**, Metagene analysis of read densities around the start and stop codon of cellular protein-coding genes (**e, f**) and viral genes (**g, h**) in ribosome profiling (**e, g**) or mRNA (**f, h**) libraries at different time points after infection. The *x* axis shows the nucleotide position relative to the start codon or the stop codon. The average normalized read densities of well-expressed genes (with more than 50 reads mapped to the CDS) are shown, with different colours indicating the three relative phases. The phase aligned with the translated frame is labelled in red (red, phase 0; black, phase +1; grey, phase +2).

Extended Data Fig. 2 Measurement of protein synthesis using the OPP assay.

a, Scheme of labelling and detection of nascent protein synthesis by OPP incorporation followed by fluorescent labelling. OPP is efficiently incorporated into newly translating proteins, releases the polypeptides and terminates translation. Following fixation, OPP is fluorescently labelled using Click reaction and can then be measured by flow cytometry. **b**, Protein synthesis measurement by flow cytometry of untreated 293T cells and 293T cells treated with cycloheximide leading to efficient translation inhibition. Unlabelled cells are shown as control.

Extended Data Fig. 3 Total RNA and ribosomal RNA levels in infected and uninfected Calu3 cells.

a, Total RNA was measured in uninfected Calu3 cells and in cells at 4, 5, 6 and 7 hpi by Qubit Fluorometer. **b**, rRNA concentration was measured in uninfected and infected Calu3 cells at 5 and 7 hpi by measuring the concentration in the 18S and 28S ribosomal RNA peaks using a TapeStation system.

Extended Data Fig. 4 Upregulated genes in SARS-CoV-2 infected cells.

a, Heat map presenting mRNA and footprints levels of transcripts with mRNA levels at 8 hpi relative to uninfected that were increased by at least 1.5-fold. Expression levels scaled by gene after partitioning clustering are presented. **b**, Summary of pathway enrichment analysis of genes in cluster A, induced late. Dot size reflects the number of genes from each pathway, and dot colour reflects the false-discovery rate (FDR) of the pathway enrichment. **c**, RNA-level fold change (FC) of cellular RNAs at 3 and 8 hpi relative to uninfected cells. RNAs were grouped to ten bins on the basis of their cytosol-to-nucleus localization ratio in uninfected Calu3 cells. *P* values calculated using two-sided *t*-test comparing the first and last bins in each time point, *n* = 5,650 genes. **d**, Scatter plots depicting log₂-transformed cytosol-to-nuclear ratios

of cellular transcripts relative to \log_2 -transformed fold changes in transcript levels between infected cells at the different time points during SARS-CoV-2 infection and uninfected cells. Pearson's R and two-sided P value on log values are presented.

Extended Data Fig. 5 SLAM-seq measurements in uninfected and SARS-CoV-2-infected cells.

a, Experimental design of the SLAM-seq measurements and the half-life calculation. **b, c**, Rates of nucleotide substitutions demonstrate efficient conversion rates in 4sU-treated samples compared to non-treated cells (no 4sU) for reads originating from both uninfected (**b**) and infected (**c**) cells. **d, e**, Proportion of new-to-total RNA (NTR) in uninfected (**d**) and infected (**e**) samples as calculated by GRAND-SLAM, a Bayesian method that computes the ratio in a quantitative manner¹⁸. **f**, Scatter plot of mRNA half-life in hours calculated from our SLAM-seq measurements in uninfected Calu3 cells relative to SLAM-seq based measurements of mRNA half-life in MCF7 cells¹⁹. Pearson's R and two-sided P value on log values are presented. **g**, Scatter plot of the changes due to infection in mRNA half-lives relative to changes in mRNA expression. Pearson's R and two-sided P value on log values are presented. **h**, Change in cellular transcripts half-lives in infected cells relative to uninfected cells. RNAs were grouped to ten bins on the basis of their cytosol-to-nucleus localization ratio. P value was calculated using t -test between the most-nuclear and the most-cytosolic bins, $n = 2,750$ with 275 genes in each bin. Box plots show median, first to third quartile, $1.5 \times$ interquartile range and outliers. **i**, Scatter plot depicting the changes in transcript half-life between uninfected and infected cells relative to translation efficiency of cellular transcripts in uninfected cells. Pearson's R and two-sided P value on log values are presented.

Extended Data Fig. 6 Analysis of RNA expression in NSP1-expressing cells.

a, mRNAs were binned on the basis of their cytosol-to-nucleus localization ratio. Fold change of each bin in RNA expression in cells transfected with NSP1 relative to cells transfected with NSP2 is presented. P value was calculated using two-sided t -test between the most-nuclear and the most-cytosolic bins, $n = 470$ with 47 genes in each bin. **b**, The change in mRNA expression of nuclear-encoded or mitochondrial encoded mRNAs in cells transfected with NSP1 relative to cells transfected with NSP2. P value was calculated using Wilcoxon's test, $n = 10$ mitochondrial genes, $n = 503$ nuclear genes. RNA-seq data of NSP1 and NSP2 transfected cells is a previous publication²⁴. Box plots show median, first to third quartile, $1.5 \times$ interquartile range and outliers.

Extended Data Fig. 7 Analysis of intronic reads.

a, Proportion of newly synthesized intronic RNA (NTR) in uninfected and infected samples as calculated by GRAND-SLAM. Values shown are for one replicate of each time point and mean value for the 5-hpi sample. The 6-hpi time point was omitted from the analysis as it did not contain enough intronic reads. **b**, Heat map presenting relative mRNA levels of well-expressed human transcripts (more than 50 reads) that showed the strongest changes in their mRNA levels at 8 hpi relative to uninfected, across time points during SARS-CoV-2 infection (as presented in Fig. 1g). Left, fold change in the ratio of intron to exon reads for each transcript in 8 hpi compared to uninfected.

Extended Data Fig. 8 SARS-CoV-2 5' leader protects mRNA from NSP1-mediated degradation.

a, 293T cells were co-transfected with an expression vector containing either NSP1–2×Strep, NSP2–2×Strep or mCherry–Flag (the two latter as controls) and with a GFP reporter that includes either the *HBB* 5' UTR as control (control-5'UTR), the viral genomic 5' UTR (CoV2-5'UTR) or the viral 5' leader (CoV2-leader). The reporter plasmids also contained an independent mCherry reporter. **b**, Flow cytometry analysis of the Flag tag in cells co-transfected with mCherry–Flag and for the Strep tag in cells co-transfected with NSP1 or NSP2. **c**, Microscopy images of GFP in cells co-transfected with NSP2 (top) or NSP1 (bottom), together with control 5' UTR reporter, SARS-CoV-2 5' UTR reporter or SARS-CoV-2 5' leader reporter. Representative images of four independent replicates are shown. Scale bars, 100 µm. **d**, Gating strategy used to determine the single-cell population for all flow cytometry analyses. **e**, Flow cytometry analysis of GFP in cells co-transfected with NSP1 or NSP2 together with control 5' UTR reporter, SARS-CoV-2 5' UTR reporter or SARS-CoV-2 5' leader reporter. **f**, Relative GFP RNA levels in cells expressing NSP1 or NSP2 together with control 5' UTR reporter, SARS-CoV-2 5' UTR reporter or SARS-CoV-2 5' leader reporter, as measured by quantitative real-time PCR. Data points show the measurement of biological replicates. One representative experiment out of two performed is shown. **g**, Microscopy images of mCherry in cells co-transfected with NSP2 (top) or NSP1 (bottom) together with the SARS-CoV-2 5' UTR reporter or SARS-CoV-2 5' leader reporter. Representative images of four independent replicates are shown. Scale bars, 100 µm. **h**, Flow cytometry analysis of mCherry in cells co-transfected with NSP1 or NSP2 together with SARS-CoV-2 5' UTR reporter or SARS-CoV-2 5' leader reporter. **i**, Relative mCherry RNA levels in cells expressing NSP1 or NSP2 together with SARS-CoV-2 5' UTR reporter or SARS-CoV-2 5' leader reporter, as measured by quantitative real-time PCR. Data points show the measurement of biological replicates. One representative experiment out of two performed is shown.

Extended Data Fig. 9 The translation of induced transcripts is impaired during infection.

a, mRNA and footprint levels of the indicated genes in uninfected cells and at 3, 5 and 8 hpi. Thirty-five genes that showed the strongest reduction in their relative translation efficiency are presented. **b**, Scatter plot of cytosolic-to-nuclear RNA ratio calculated from our fractionation experiment in uninfected Calu3 cells relative to fractionation-based measurements of cytosolic to nuclear RNA ratio in MCF7 cells¹⁹. Pearson's *R* and two-sided *P* value on log values are shown.

Extended Data Fig. 10 Translation of viral genes along the course of infection.

a, Schematic of the MHV genomic and subgenomic mRNAs, and the main ORFs. ORFs that are not expressed in the strain that was used for ribosome profiling (MHV-A59) are marked by empty rectangles. **b**, Relative translation efficiency of each canonical MHV ORF along infection. Genes are divided to two groups on the basis of their location on the genome. Expression was calculated from a previous publication¹³. **c**, Relative translation levels of the main ORFs (ORF7a, S and ORF3a, labelled by circle) and the out-of-frame ORFs (ORF7b, ORF2b and ORF3c, labelled by diamond) of the ORF7a, S, and ORF3a subgenomic transcripts, respectively, along the course of SARS-CoV-2 infection. ORF9b expression was low in our measurements and it was therefore excluded from this analysis. Translation levels were calculated from ribosome densities using ORF-RATER³². Duplicate values of 8 hpi are shown as lines. Standard deviation for our ORF expression measurement shown as rectangles calculated using 500 random partial ORF regions.

Supplementary information

Reporting Summary

Peer Review File

Supplementary Table 1

Expression values (RPKM) of genes induced more than 1.5-fold during infection, and their division into clusters. This table lists genes induced by more than 1.5-fold at 8 hours post infection compared to uninfected cells, with their respective expression values at the different times points normalized to reads per kilobase per million

(RPKM) and to total mRNA levels (see methods for normalization methods). Genes are divided into clusters (A-C) as shown in extended data figure 4a.

Supplementary Table 2

Primers used for cloning. This table lists primers used for cloning of constructs described in the manuscript and their sequence.

Rights and permissions

Reprints and Permissions

About this article



Check for
updates

Cite this article

Finkel, Y., Gluck, A., Nachshon, A. *et al.* SARS-CoV-2 uses a multipronged strategy to impede host protein synthesis. *Nature* **594**, 240–245 (2021).
<https://doi.org/10.1038/s41586-021-03610-3>

Download citation

- Received: 24 November 2020
- Accepted: 04 May 2021
- Published: 12 May 2021
- Issue Date: 10 June 2021
- DOI: <https://doi.org/10.1038/s41586-021-03610-3>

Comments

By submitting a comment you agree to abide by our [Terms](#) and [Community Guidelines](#). If you find something abusive or that does not comply with our terms or guidelines please flag it as inappropriate.

[Download PDF](#)

Associated Content

Collection

[Coronavirus](#)

Advertisement

This article was downloaded by **calibre** from <https://www.nature.com/articles/s41586-021-03610-3>

| [Section menu](#) | [Main menu](#) |

Multilevel proteomics reveals host perturbations by SARS-CoV-2 and SARS-CoV
[Download PDF](#)

- Article
- [Published: 12 April 2021](#)

Multilevel proteomics reveals host perturbations by SARS-CoV-2 and SARS-CoV

- [Alexey Stukalov](#)¹ na1,
- [Virginie Girault](#) [ORCID: orcid.org/0000-0002-3240-4400](#)¹ na1,
- [Vincent Grass](#) [ORCID: orcid.org/0000-0001-7710-4789](#)¹ na1,
- [Ozge Karayel](#) [ORCID: orcid.org/0000-0003-2541-1159](#)² na1,
- [Valter Bergant](#) [ORCID: orcid.org/0000-0003-3458-9506](#)¹ na1,
- [Christian Urban](#) [ORCID: orcid.org/0000-0002-4080-2468](#)¹ na1,
- [Darya A. Haas](#) [ORCID: orcid.org/0000-0001-5543-4875](#)¹ na1,
- [Yiqi Huang](#) [ORCID: orcid.org/0000-0001-7256-8699](#)¹ na1,
- [Lila Oubraham](#) [ORCID: orcid.org/0000-0002-9991-5336](#)¹,
- [Anqi Wang](#)¹,
- [M. Sabri Hamad](#)¹,
- [Antonio Piras](#)¹,
- [Fynn M. Hansen](#)²,
- [Maria C. Tanzer](#)²,
- [Igor Paron](#)²,
- [Luca Zinzula](#) [ORCID: orcid.org/0000-0001-6489-7070](#)³,
- [Thomas Engleitner](#)⁴,
- [Maria Reinecke](#)^{5,6,7},
- [Teresa M. Lavacca](#) [ORCID: orcid.org/0000-0002-0851-524X](#)¹,
- [Rosina Ehmann](#)^{8,9},
- [Roman Wölfel](#)^{8,9},
- [Jörg Jores](#) [ORCID: orcid.org/0000-0003-3790-5746](#)¹⁰,
- [Bernhard Kuster](#) [ORCID: orcid.org/0000-0002-9094-1677](#)^{5,6,7},
- [Ulrike Protzer](#) [ORCID: orcid.org/0000-0002-9421-1911](#)^{1,9},
- [Roland Rad](#) [ORCID: orcid.org/0000-0002-6849-9659](#)⁴,

- [John Ziebuhr](#) ORCID: [orcid.org/0000-0002-5741-8825¹¹](https://orcid.org/0000-0002-5741-8825),
- [Volker Thiel](#) ORCID: [orcid.org/0000-0002-5783-0887^{12,13}](https://orcid.org/0000-0002-5783-0887),
- [Pietro Scaturro](#) ORCID: [orcid.org/0000-0001-9098-3087^{1,14}](https://orcid.org/0000-0001-9098-3087),
- [Matthias Mann](#) ORCID: [orcid.org/0000-0003-1292-4799²](https://orcid.org/0000-0003-1292-4799) &
- [Andreas Pichlmair](#) ORCID: [orcid.org/0000-0002-0166-1367^{1,9}](https://orcid.org/0000-0002-0166-1367)

Nature volume **594**, pages 246–252 (2021)[Cite this article](#)

- 56k Accesses
- 1 Citations
- 574 Altmetric
- [Metrics details](#)

Subjects

- [Protein–protein interaction networks](#)
- [SARS-CoV-2](#)
- [Systems analysis](#)
- [Virology](#)

Abstract

The emergence and global spread of SARS-CoV-2 has resulted in the urgent need for an in-depth understanding of molecular functions of viral proteins and their interactions with the host proteome. Several individual omics studies have extended our knowledge of COVID-19 pathophysiology^{1,2,3,4,5,6,7,8,9,10}. Integration of such datasets to obtain a holistic view of virus–host interactions and to define the pathogenic properties of SARS-CoV-2 is limited by the heterogeneity of the experimental systems. Here we report a concurrent multi-omics study of SARS-CoV-2 and SARS-CoV. Using state-of-the-art proteomics, we profiled the interactomes of both viruses, as well as their influence on the transcriptome, proteome, ubiquitinome and phosphoproteome of a lung-derived human cell line. Projecting these data onto the global network of cellular interactions revealed crosstalk between the perturbations taking place upon infection with SARS-CoV-2 and SARS-CoV at different levels and enabled identification of distinct and common molecular mechanisms of these closely related coronaviruses. The TGF-β pathway, known for its involvement in tissue fibrosis, was specifically dysregulated by SARS-CoV-2 ORF8 and autophagy was specifically dysregulated by SARS-CoV-2 ORF3. The extensive dataset (available at <https://covinet.innatelab.org>) highlights many hotspots that could be targeted by

existing drugs and may be used to guide rational design of virus- and host-directed therapies, which we exemplify by identifying inhibitors of kinases and matrix metalloproteases with potent antiviral effects against SARS-CoV-2.

[Download PDF](#)

Main

To identify protein–protein interactions of SARS-CoV-2 and SARS-CoV and cellular proteins, we transduced A549 lung carcinoma cells with lentiviruses expressing individual haemagglutinin-tagged viral proteins (Fig. 1a, Extended Data Fig. 1a, Supplementary Table 1). Statistical modelling of quantitative data from affinity purification followed by mass spectrometry (AP–MS) analysis identified 1,801 interactions between 1,086 cellular proteins and 24 SARS-CoV-2 and 27 SARS-CoV bait proteins (Fig. 1b, Extended Data Fig. 1b, Supplementary Table 2), substantially increasing the number of reported interactions of SARS-CoV-2 and SARS-CoV^{1,2,5,6,10,11} (Supplementary Table 10). The resulting virus–host interaction network revealed a wide range of cellular activities intercepted by SARS-CoV-2 and SARS-CoV (Fig. 1b, Extended Data Table 1, Supplementary Table 2). In particular, we observed that SARS-CoV-2 targets a number of key innate immunity regulators (ORF7b–MAVS and ORF7b–UNC93B1), stress response components (N–HSPA1A) and DNA damage response mediators (ORF7a–ATM and ORF7a–ATR) (Fig. 1b, Extended Data Fig. 1c–e). Additionally, SARS-CoV-2 proteins interact with molecular complexes involved in intracellular trafficking (for example, endoplasmic reticulum–Golgi trafficking) and transport (for example, solute carriers and ion transport by ATPases) as well as cellular metabolism (for example, mitochondrial respiratory chain and glycolysis) (Fig. 1b, Extended Data Table 1, Supplementary Table 2). Comparing the AP–MS data of homologous SARS-CoV-2 and SARS-CoV proteins identified differences in the enrichment of individual host targets, highlighting potential virus-specific interactions (Fig. 1b (edge colour), c, Extended Data Figs. 1f, 2a, b, Supplementary Table 2). For instance, we recapitulated the known interactions between SARS-CoV NSP2 and prohibitins¹² (PHB and PHB2), but this interaction was not conserved with SARS-CoV-2 NSP2, suggesting that the two viruses differ in their ability to modulate mitochondrial function and homeostasis through NSP2 (Extended Data Fig. 2a). The exclusive interaction of SARS-CoV-2 ORF8 with the TGF-β1–LTBP1 complex is another interaction that potentially explains the differences in pathogenicity of the two viruses (Extended Data Figs. 1f, 2b). Notably, disbalanced TGF-β signalling has been linked to lung fibrosis and oedema, a common complication of severe pulmonary diseases including COVID-19^{13,14,15,16}.

Fig. 1: Joint analysis of SARS-CoV-2 and SARS-CoV virus–host protein–protein interactomes.

 **figure1**

a, Systematic comparison of interactomes and host proteome changes (effectomes) of the 24 SARS-CoV-2 and 27 SARS-CoV viral proteins, using 3 homologues from human coronaviruses (HCoV-NL63 and HCoV-229E) as reference for pan-coronavirus specificity. **b**, Combined virus–host protein-interaction network of SARS-CoV-2 and SARS-CoV measured by AP–MS. Homologous viral proteins are displayed as a single node. Shared and virus-specific interactions are denoted by the edge colour. The edge intensity reflects the *P*-value for the interaction (with the smallest *P*-value represented by solid edges and the highest *P*-value (<0.001) represented by faded edges). ECM, extracellular matrix; ER, endoplasmic reticulum; GPCR, G-protein-coupled receptor; HOPS, homotypic fusion and protein-sorting; MHC, major histocompatibility complex; SNARE, soluble *N*-ethylmaleimide-sensitive factor attachment protein receptor; COG, conserved oligomeric Golgi. **c**, The numbers of unique and shared host interactions between the homologous proteins of SARS-CoV-2 and SARS-CoV.

[Full size image](#)

To map the virus–host interactions to the functions of viral proteins, we conducted a study of total proteomes of A549 cells expressing 54 individual viral proteins comprising the ‘effectome’ (Fig. 1a, Supplementary Table 3). This dataset provides clear links between changes in protein expression and virus–host interactions, as

exemplified by ORF9b, which leads to a dysregulation of mitochondrial functions and binds to TOMM70, a known regulator of mitophagy^{2,17} (Fig. 1b, Supplementary Tables 2, 3). Global pathway-enrichment analysis of the effectome dataset confirmed that ORF9b of both viruses led to mitochondrial dysregulation^{2,18} (Extended Data Fig. 2c, Supplementary Table 3) and further highlighted virus-specific effects, as exemplified by the upregulation of proteins involved in cholesterol metabolism (CYP51A1, DHCR7, IDI1 and SQLE) by SARS-CoV-2 NSP6 but not by SARS-CoV NSP6. Of note, cholesterol metabolism was recently shown to be implicated in SARS-CoV-2 replication and has been suggested as a promising target for drug development^{19,20,21}. Besides perturbations at the pathway level, viral proteins also specifically modulated single host proteins, possibly explaining more specific molecular mechanisms involved in viral protein function. Focusing on the 180 most affected host proteins, we identified RCOR3, a putative transcriptional corepressor, as strongly upregulated by NSP4 of both viruses (Extended Data Figs. 2d, 3a). Notably, apolipoprotein B (APOB) was substantially regulated by ORF3 and NSP1 of SARS-CoV-2, suggesting that it has an important role in SARS-CoV-2 biology (Extended Data Fig. 3b).

Multi-omics profiling of virus infection

Although the interactome and the effectome provide in-depth information on the activity of individual viral proteins, we aimed to directly study their combined activities in the context of viral infection. To this end, we infected A549 cells expressing angiotensin-converting enzyme 2 (ACE2) (A549-ACE2 cells) (Extended Data Fig. 4a,b) with SARS-CoV-2 or SARS-CoV, and profiled the effects of viral infection on mRNA expression, protein abundance, ubiquitination and phosphorylation in a time-resolved manner (Fig. 2 a-b).

Fig. 2: Multi-level profiling of SARS-CoV-2 and SARS-CoV infection.

 **figure2**

a, Time-resolved profiling of parallel SARS-CoV-2 and SARS-CoV infection by multiple omics methods. The plot shows the mass spectroscopy (MS) intensity estimates for spike proteins of SARS-CoV-2 and SARS-CoV over time ($n = 4$ independent experiments). MOI, multiplicity of infection. **b**, The numbers of distinct transcripts, proteins, ubiquitination and phosphorylation sites that are significantly up- or downregulated at given time points after infection (relative to mock infection at the same time point). Transcripts, proteins or sites that are regulated similarly by SARS-CoV-2 and SARS-CoV infection are shown in grey, those regulated specifically by SARS-CoV-2 are in orange and those regulated by SARS-CoV are in brown. **c, d**, Comparison of host transcriptome 12 h (**c**) and ubiquitinome 24 h (**d**) after infection (hpi) with SARS-CoV-2 (x-axis) or SARS-CoV (y-axis) (\log_2 fold change in comparison to the mock infection samples at the same time point). Significantly regulated transcripts by moderated *t*-test with false discovery rate-corrected two-sided *P*-value ≤ 0.05 (**c**) and significantly regulated sites by Bayesian linear model-based unadjusted two-sided *P*-value $\leq 10^{-3}$, $|\log_2$ fold change| ≥ 0.5 (**d**) are coloured according to specificity as indicated. Diamonds indicate that the actual \log_2 fold change was truncated to fit into the plot. $n = 3$ independent experiments. **e**, Phosphorylation (purple squares) and ubiquitination (red circles) sites on EGFR that are regulated upon SARS-CoV-2 infection. The plot shows median \log_2 fold change of abundance compared with mock infection at 24 and 36 hpi. All identified phosphorylation sites have known regulatory function. **f**, Profile plots of time-resolved EGFR K754 ubiquitination, EGFR T693 and S991 phosphorylation, and total EGFR

protein levels in A549-ACE2 cells infected with SARS-CoV-2 or SARS-CoV with indicated median (line), 50% (shaded region) and 95% (dotted line) confidence intervals. $n = 3$ (ubiquitination) or 4 (phosphorylation and total protein) independent experiments.

[Full size image](#)

In line with previous reports^{9,22}, we found that both SARS-CoV-2 and SARS-CoV can downregulate the type I interferon response and activate a pro-inflammatory signature at transcriptome and proteome levels (Fig. 2a–c, Extended Data Fig. 4c–f, i, Supplementary Tables 4, 8, Supplementary Discussion 1). However, SARS-CoV elicited a more pronounced activation of the NF- κ B pathway, correlating with its higher replication rate and potentially explaining the lower severity of pulmonary disease in cases of SARS-CoV-2 infection²³ (Supplementary Tables 4, 5). By contrast, SARS-CoV-2 infection led to higher expression of FN1 and SERPINE1, which may be linked to the specific recruitment of TGF- β factors (Fig. 1b), supporting regulation of TGF- β signalling by SARS-CoV-2.

To better understand the mechanisms underlying perturbation of cellular signalling, we performed comparative ubiquitination and phosphorylation profiling following infection with SARS-CoV-2 or SARS-CoV. This analysis showed that 1,108 of 16,541 detected ubiquitination sites were differentially regulated by infection with SARS-CoV-2 or SARS-CoV (Fig. 2a, b, d, Extended Data Fig. 5a, Supplementary Table 6). More than half of the significant sites were regulated in a similar manner by both viruses. These included sites on SLC35 and SUMO family proteins, indicating possible regulation of sialic acid transport and the SUMO activity. SARS-CoV-2 specifically increased ubiquitination on autophagy-related factors (MAP1LC3A, GABARAP, VPS33A and VAMP8) as well as specific sites on EGFR (for example, K739, K754 and K970). In some cases, the two viruses targeted distinct sites on the same cellular protein, as exemplified by HSP90 family members (for example, K84, K191 and K539 on HSP90AA1) (Fig. 2d). Notably, a number of proteins (for example, ALCAM, ALDH3B1, CTNNA1, EDF1 and SLC12A2) exhibited concomitant ubiquitination and a decrease at the protein level after infection, pointing to ubiquitination-mediated protein degradation (Fig. 2d, Extended Data Figs. 4f, 5a, Supplementary Tables 5, 6). Among these downregulated proteins, EDF1 has a pivotal role in the maintenance of endothelial integrity and may be a link to endothelial dysfunctions described for COVID-19^{24,25}. Profound regulation of cellular signalling pathways was also observed at the phosphoproteomic level: among 16,399 total quantified phosphorylation sites, 4,643 showed significant changes after infection with SARS-CoV-2 or SARS-CoV (Extended Data Fig. 5b, c, Supplementary Table 7). Highly regulated sites were identified for the proteins of the MAPK pathways (for example, MAPKAPK2, MAP2K1, JUN and SRC), and proteins involved in autophagy

signalling (for example, DEPTOR, RICTOR, OPTN, SQSTM1 and LAMTOR1) and viral entry (for example, ACE2 and RAB7A) (Extended Data Fig. 5b, d). Notably, RAB7A was recently shown to be an important host factor for SARS-CoV-2 infection that assists endosomal trafficking of ACE2 to the plasma membrane²⁶. We observed higher phosphorylation at S72 of RAB7A in SARS-CoV-2 infection compared with SARS-CoV or mock infection; this site is implicated in RAB7A intracellular localization and molecular association²⁷. The regulation of known phosphorylation sites suggests an involvement of central kinases (cyclin dependent kinases, AKT, MAPKs, ATM, and CHEK1) linked to cell survival, cell cycle progression, cell growth and motility, stress responses and the DNA damage response; this was also supported by the analysis of enriched motifs (Extended Data Fig. 5e, f, Supplementary Tables 7, 8). Notably, SARS-CoV-2 infection, but not SARS-CoV infection, led to phosphorylation of the antiviral kinase EIF2AK2 (also known as PKR) at the critical regulatory residue S33²⁸. This differential activation of EIF2AK2 could contribute to the difference in the growth kinetics of the two viruses (Supplementary Table 4, 5).

Our data clearly point to an interplay of phosphorylation and ubiquitination patterns on individual host proteins. For instance, EGFR showed increased ubiquitination on 6 lysine residues at 24 h post-infection (hpi) accompanied by increased phosphorylation of T693, S695 and S991 at 24 and 36 hpi (Fig. 2e, f). Ubiquitination of all six lysine residues on EGFR was more pronounced following infection with SARS-CoV-2 than with SARS-CoV. Moreover, vimentin, a central co-factor for coronavirus entry²⁹ and pathogenicity^{30,31}, displayed distinct phosphorylation and ubiquitination patterns on several sites early (for example, S420) or late (for example, S56, S72 and K334) in infection (Extended Data Fig. 6a, b). These findings underscore the value of testing different post-translational modifications simultaneously and suggest a concerted engagement of regulatory machineries to modify target protein functions and abundance.

Post-translational modification of viral proteins

The majority of viral proteins were also post-translationally modified. Of the 27 detected SARS coronavirus proteins, 21 were ubiquitinated. Nucleocapsid (N), spike (S), NSP2 and NSP3 were the most heavily modified proteins in both viruses (Extended Data Fig. 6c, Supplementary Table 6). Many ubiquitination sites were common to both viruses. Around half of the sites that were exclusively ubiquitinated in either virus were conserved between SARS-CoV and SARS-CoV-2. The remaining specifically regulated ubiquitination sites were unique to each virus, indicating that these acquired adaptations can be post-translationally modified and may recruit cellular proteins with distinct functions (Fig. 3a). Our interactome data identified several host E3 ligases (for example, we identified interactions between SARS-CoV-2

ORF3 and TRIM47, WWP1, WWP2 and STUB1; and between SARS-CoV-2 M and TRIM7) and deubiquitinating enzymes (for example, interactions between SARS-CoV-2 ORF3 and USP8; SARS-CoV-2 ORF7a and USP34; and SARS-CoV N and USP9X), suggesting crosstalk between ubiquitination and viral protein functions (Fig. 1b, Extended Data Fig. 6d, Supplementary Table 2). Of particular interest are extensive ubiquitination events on the S protein of both viruses (K97, K528, K825, K835, K921 and K947), which are distributed on functional domains (N-terminal domain, C-terminal domain (CTD), fusion peptide and heptad repeat 1 domain), potentially indicating critical regulatory functions that are conserved between the two viruses (Extended Data Fig. 6e). We observed phosphorylation of 5 SARS-CoV-2 proteins (M, N, S, NSP3 and ORF9b) and 8 SARS-CoV proteins (M, N, S, NSP1, NSP2, NSP3, ORF3 and ORF9b) (Extended Data Fig. 6f, Supplementary Table 7), on sites corresponding to known recognition motifs. In particular, CAMK4 and MAPKAPK2 potentially phosphorylate sites on S and N, respectively.

Phosphorylation of cellular proteins suggested that the activities of these kinases were enriched in cells infected with SARS-CoV-2 or SARS-CoV (Extended Data Figs. 5e, f, 6e,g). Moreover, N proteins of both SARS-CoV-2 and SARS-CoV recruit GSK3, which could potentially be linked to phosphorylation events on these viral proteins (Fig. 1b, Extended Data Fig. 6g, Supplementary Table 7). Notably, we identified novel post-translationally modified sites located at functional domains of viral proteins; we detected ubiquitination at SARS-CoV-2 N K338 and phosphorylation on SARS-CoV-2 and SARS-CoV N S310 and S311 (Extended Data Fig. 6g). Mapping these sites to the atomic structure of the CTD^{32,33} highlights critical positions for the function of the protein (Fig. 3c, Extended Data Fig. 6h, Supplementary Discussion 2). Collectively, while the identification of differentially regulated sites may indicate pathogen-specific functions, insights from conserved post-translational modifications may also provide useful knowledge for the development of targeted pan-antiviral therapies.

Fig. 3: Phosphorylation and ubiquitination of SARS-CoV-2 and SARS-CoV viral proteins.

 **figure3**

a, Distribution of identified shared, differentially regulated and selectively encoded (sequence-specific) ubiquitination and phosphorylation sites on SARS-CoV-2 and SARS-CoV homologous proteins after infection of A549-ACE2 cells. PTM, post-translational modification. **b**, Mapping of the ubiquitination (red circles) and phosphorylation (purple squares) sites on an alignment of SARS-CoV-2 ORF3 and SARS-CoV ORF3a proteins, showing median \log_2 intensities in virus-infected A549-ACE2 cells at 24 hpi. Functional (blue) and topological (yellow) domains are mapped on each sequence. Ubiquitin-modifying enzymes binding to ORF3 and ORF3a as identified in our AP-MS experiments (Extended Data Fig. [1b](#)) are indicated (green). TM, transmembrane domain. **c**, Surface and ribbon representation of superimposed SARS-CoV (Protein Data Bank (PDB) ID: 2CJR, brown) and SARS-CoV-2 (PDB ID: 6YUN, orange) N protein CTD dimers (r.m.s.d. values of 0.492 Å for 108 matching

$\text{C}\alpha$ atoms). Secondary structures are numbered in grey (prefixed with α for α -helix, β for β -strand and η for non-structured regions). Side chains are colour coded depending on whether they are in ubiquitinated (red), phosphorylated (purple) or unmodified (grey) sites. The K338 ubiquitination site unique to SARS-CoV-2 is shown as a close-up for both monomers (bottom right). Close-ups of inter-chain residue interactions established by non-phosphorylated (top right) and phosphorylated (middle right) SARS-CoV-2 S310 or SARS-CoV S311.

[Full size image](#)

Viral perturbation of key cellular pathways

Our unified experimental design in a syngeneic system enabled direct time-resolved comparison of SARS-CoV-2 and SARS-CoV infection across different levels.

Integrative pathway-enrichment analysis demonstrated that both viruses largely perturb the same cellular processes at multiple levels, albeit with distinct temporal patterns (Extended Data Fig. 7a). For instance, transcriptional downregulation of proteins involved in tau protein kinase activity and Fe ion sequestration at 6 hpi was followed by a decrease in protein abundance after 12 hpi (Supplementary Table 8). RHO GTPase activation, mRNA processing and the role of ABL in ROBO–SLIT signalling appeared to be regulated mostly through phosphorylation (Extended Data Fig. 7a). By contrast, processes connected to cellular integrity such as the formation of senescence-associated heterochromatin foci, apoptosis-induced DNA fragmentation and amino acid transport across the plasma membrane were modulated through concomitant phosphorylation and ubiquitination events, suggesting molecular links between these post-translational modifications. Ion transporters, especially the SLC12 family of cation-coupled chloride cotransporters—previously identified as cellular factors in pulmonary inflammation³⁴—were also regulated at multiple levels, evidenced by reduced protein abundance as well as differential post-translational modifications (Extended Data Fig. 7a).

The pathway-enrichment analysis provided a global and comprehensive picture of how SARS-CoV-2 and SARS-CoV affect the host. We next applied an automated approach to systematically explore the underlying molecular mechanisms contained in the viral interactome and effectome data. We mapped the measured interactions and effects of each viral protein onto the global network of cellular interactions³⁵ and applied a network diffusion approach³⁶ (Fig. 4a). This type of analysis uses known cellular protein–protein interactions, signalling and regulation events to identify connection points between cellular proteins that interact with viral proteins and the proteins affected by the expression of these viral proteins (Extended Data Figs. 1b, 2d, Supplementary Tables 2, 3). The connections inferred from the real data were significantly shorter than for randomized data, validating the relevance of the approach

and the quality of the data (Extended Data Fig. 8a, b). The findings from this approach include the potential mechanisms by which ORF3 and NSP6 may regulate autophagy, the modulation of innate immunity by M, ORF3 and ORF7b, and the perturbation of integrin–TGF- β –EGFR–receptor tyrosine kinase signalling by ORF8 of SARS-CoV-2 (Fig. 4b, Extended Data Fig. 8c, d). Enriching these subnetworks with data on SARS-CoV-2 infection-dependent mRNA abundance, protein abundance, phosphorylation and ubiquitination (Fig. 4a) provided insights into the regulatory mechanisms activated by SARS-CoV-2. For instance, the analysis confirmed a role of NSP6 in both SARS-CoV-2- and SARS-CoV-induced autophagy³⁷ and revealed the SARS-CoV-2 specific inhibition of autophagic flux by ORF3 protein, leading to the accumulation of autophagy receptors (SQSTM1, GABARAPL2, NBR1, CALCOCO2, MAP1LC3A, MAP1LC3B and TAX1BP1), consistent with the accumulation of MAP1LC3B protein observed in cells infected with SARS-CoV-2 (Fig. 4c, Extended Data Fig. 8e, f). This inhibition may be a result of the interaction of the ORF3 protein with the HOPS complex (VPS11, VPS16, VPS18, VPS39 and VPS41), which is essential for autophagosome–lysosome fusion, as well as the differential phosphorylation of regulatory sites (for example, on TSC2, mTORC1 complex, ULK1, RPS6 and SQSTM1) and ubiquitination of key components (MAP1LC3A, GABARAPL2, VPS33A and VAMP8) (Fig. 4c, Extended Data Fig. 8g). This inhibition of autophagosome function may have direct consequences for protein degradation. The abundance of APOB, a protein that is degraded via autophagy³⁸, was selectively increased after SARS-CoV-2 infection or expression of SARS-CoV-2 ORF3 (Extended Data Fig. 3b, 8h). Accumulating APOB levels could increase the risk of arterial thrombosis³⁹, one of the main complications contributing to lung, heart and kidney failure in patients with COVID-19⁴⁰. The inhibition of the interferon (IFN)- α and IFN- β response observed at transcriptional and proteome levels was similarly explained by the network diffusion analysis (Extended Data Fig. 8i), which implicated multiple proteins of SARS-CoV-2 in the disruption of antiviral immunity. Further experiments functionally corroborated the inhibition of IFN- α and IFN- β induction or signalling by ORF3, ORF6, ORF7a, ORF7b and ORF9b (Extended Data Fig. 8j). Upon virus infection, we observed the regulation of TGF- β and EGFR pathways modulating cell survival, motility and innate immune responses (Extended Data Fig. 9a–d). Specifically, our network diffusion analysis revealed a connection between the binding of the ORF8 and ORF3 proteins to TGF- β -associated factors (TGF- β 1, TGF- β 2, LTBP1, TGFB2, FURIN and BAMBI), the differential expression of extracellular matrix regulators (FERMT2 and CDH1) and the virus-induced upregulation of fibrinogens (FGA, FGB), fibronectin (FN1) and SERPINE1⁴¹ (Extended Data Fig. 9a, b). The increased phosphorylation of proteins involved in MAPK signalling (for example, SHC1 (on S139), SOS1 (S1134/S1229), JUN (S63/S73), MAPKAPK2 (T334) and p38 (T180/Y182)) and receptor tyrosine kinase signalling (for example, phosphorylation of PI3K complex members PDK1 (S241) and RPS6KA1 (S380)) as well as a higher expression of JUN, FOS and EGR1 are

further indications of regulation of TGF- β and EGFR pathways (Extended Data Fig. 9a,c,d). In turn, TGF- β and EGFR signalling are known to be potentiated by integrin signalling and activation of YAP-dependent transcription⁴², which we observed to be regulated in a time-dependent manner upon SARS-CoV-2 infection (Extended Data Fig. 9a). As well as promoting virus replication, activation of these pathways has been implicated in fibrosis^{13,14,15}, one of the hallmarks of COVID-19¹⁶.

Fig. 4: A network diffusion approach enables identification of molecular pathways linking protein–protein interactions with downstream changes in the host proteome.

 **figure4**

a, The network diffusion approach to identify functional connections between the host targets of a viral protein and downstream proteome changes. The results of network diffusion are integrated with omics datasets of SARS coronavirus infection to streamline the identification of affected host pathways. **b**, Subnetworks of the network

diffusion linking host targets of SARS-CoV-2 ORF3 to factors involved in autophagy. The thickness of directed edges is proportional to the random-walk transition probability. Black edges denote connections present in ReactomeFI. **c**, Overview of perturbations to host-cell autophagy induced by SARS-CoV-2. The pathway regulation is derived from the network diffusion model for SARS-CoV-2 ORF3 and NSP6 and is overlaid with the changes in protein levels, ubiquitination (Ubi) and phosphorylation (Pho) induced by SARS-CoV-2 infection. FC, fold change; PM, plasma membrane.

[Full size image](#)

Data-guided drug identification and testing

Together, the viral protein–host protein interactions and regulation of pathways observed at multiple levels identify potential points for targeting SARS-CoV and SARS-CoV-2 using well-characterized selective antiviral drugs. To test antiviral efficacy, we used time-lapse fluorescent microscopy of infection with a GFP reporter SARS-CoV-2⁴³. Inhibition of virus replication by treatment with IFN- α corroborated previous conclusions that efficient SARS-CoV-2 replication involves the inactivation of this pathway at an early step^{9,44} and confirmed the reliability of this screening approach (Extended Data Fig. 10a). We tested a panel of 48 drugs that modulate the pathways perturbed by the virus for their effects on SARS-CoV-2 replication (Fig. 5a, Supplementary Table 9). Of note, inhibitors of B-RAF (sorafenib, regorafenib and dabrafenib), JAK1/2 (baricitinib) and MAPK (SB239063), which are commonly used to treat cancer and autoimmune diseases^{45,46,47}, significantly increased virus growth in an in vitro model of infection (Fig. 5a, Extended Data Fig. 10b, Supplementary Table 9). By contrast, inducers of DNA damage (tirapazamine and rabusertib) or an mTOR inhibitor (rapamycin) suppressed virus growth. The highest antiviral activity was observed for gilteritinib (a designated inhibitor of FLT3 and AXL), ipatasertib (an AKT inhibitor), prinomastat and marimastat (matrix metalloprotease (MMP) inhibitors) (Fig. 5a, b, Extended Data Fig. 10c, Supplementary Table 9). These compounds profoundly inhibited replication of SARS-CoV-2 while having no effects or minor effects on cell growth (Extended Data Fig. 10b, Supplementary Table 9). Quantitative PCR analysis indicated antiviral activities for gilteritinib and tirapazamine against SARS-CoV-2 and SARS-CoV (Fig. 5c, Extended Data Fig. 10d, e). Notably, prinomastat and marimastat, specific inhibitors of MMP2 and MMP9, showed selective activity against SARS-CoV-2 but not against SARS-CoV (Fig. 5c, Extended Data Fig. 10f,g). Activities of MMPs have been linked to TGF- β activation and pleural effusions, alveolar damage and neuroinflammation (for example, Kawasaki disease), all of which are characteristic of COVID-19^{23,48,49,50,51}.

Fig. 5: Identification of pathways targeted by SARS-CoV-2 using a multi-omics profiling approach enables systematic testing of candidate antiviral therapies.

 **figure5**

a, b, A549-ACE2 cells were treated with the indicated drugs 6 h before infection with SARS-CoV-2-GFP (MOI of 3). Changes in cell viability and virus growth (**a**) in drug-treated cells compared with untreated A549-ACE2 cells at 48 hpi. A confluence cut-off of $-0.2 \log_2$ fold change was applied to remove cytotoxic compounds. **b**, Time courses of virus replication after pre-treatment of cells with prinomastat or gilteritinib. $n = 4$ independent experiments; * $P \leq 0.01$ compared with control treatment, unadjusted two-sided Wilcoxon test. Norm., normalized. **c**, Drugs potentially targeting pathways identified in our study. Colour indicates antiviral activity against SARS-CoV-2 or SARS-CoV (brown–orange gradient) or SARS-CoV-2 specifically (orange), as inferred from in vitro experiments.

[Full size image](#)

This drug screen demonstrates the value of our combined dataset, which profiles SARS-CoV-2 infection at multiple levels. We expect that further exploration of these rich data by the scientific community and additional studies of the interplay between different omics levels will substantially advance our molecular understanding of coronavirus biology, including the pathogenicity associated with specific human coronaviruses, such as SARS-CoV-2 and SARS-CoV. Moreover, this resource, together with complementary approaches^{26,52,53,54}, will streamline the search for antiviral compounds and serve as a base for rational design of combination therapies that target the virus from multiple synergistic angles, thus potentiating the effect of individual drugs while minimizing potential side effects on healthy tissues.

Methods

No statistical methods were used to predetermine sample size. The experiments were not randomized. The investigators were not blinded to allocation during experiments and outcome assessment.

Cell lines and reagents

HEK293T, A549, Vero E6 and HEK293-R1 cells were authenticated by PCR-single-locus-technology and their respective culturing conditions were described previously⁵⁵. All cell lines were tested to be mycoplasma free. Expression constructs for C-terminal HA-tagged viral open reading frames were synthesized (Twist Bioscience and BioCat) and cloned into pWPI vector as described previously⁵⁶ with the following modifications: a starting ATG codon was added, internal canonical splicing sites were replaced with synonymous mutations and a C-terminal HA-tag, followed by an amber stop codon, was added to individual viral open reading frames. A C-terminally HA-tagged ACE2 sequence was amplified from an ACE2 expression vector (provided by S. Pöhlmann)⁵⁷ into the lentiviral vector pWPI-puro. A549 cells were transduced twice, and A549-ACE2 cells were selected with puromycin. Lentivirus production, transduction of cells and antibiotic selection were performed as described previously⁵². RNA isolation (Macherey–Nagel NucleoSpin RNA plus), reverse transcription (TaKaRa Bio PrimeScript RT with gDNA eraser) and quantitative PCR with reverse transcription (RT–qPCR) (Thermo-Fisher Scientific PowerUp SYBR green) were performed as described previously⁵⁴. RNA isolation for next generation sequencing applications was performed according to the manufacturer's protocol (Qiagen RNeasy mini kit, RNase free DNase set). For detection of protein abundance by western blotting, HA–horseradish peroxidase (HRP) (Sigma-Aldrich; H6533; 1:2,500 dilution), ACTB–HRP (Santa Cruz; sc-47778; 1:5,000 dilution), MAP1LC3B (Cell Signaling; 3868; 1:1,000 dilution), MAVS (Cell Signaling; 3993; 1:1,000 dilution), HSPA1A (Cell Signaling; 4873; 1:1,000 dilution), TGF-β (Cell

Signaling; 3711; 1:1,000 dilution), phospho-p38 (T180/Y182) (Cell Signaling; 4511; 1:1,000 dilution), p38 (Cell Signaling; 8690; 1:1,000 dilution) and SARS-CoV-2 or SARS-CoV N protein (Sino Biological; 40143-MM05; 1:1,000 dilution) antibodies were used. Secondary antibodies detecting mouse (Cell Signaling; 7076; 1:5,000 dilution; Jackson ImmunoResearch; 115-035-003; 1:5,000 dilution), rat (Invitrogen; 31470; 1:5,000 dilution), and rabbit IgG (Cell Signaling; 7074; 1:5,000 dilution) were coupled to HRP. For AP–MS and affinity purification–western blotting applications, HA beads (Sigma-Aldrich and Thermo Fisher Scientific) and Streptactin II beads (IBA Lifesciences) were used. Imaging of western blots was performed as described⁵⁸. Recombinant human IFN- α used for stimulation of cells in the reporter assay was a gift from P. Stäheli (Institute of Virology, University of Freiburg), recombinant human IFN- γ was purchased from PeproTech, and IVT4 was produced as described before⁵⁹. All compounds tested in the viral inhibitor assay are listed in Supplementary Table 9.

Virus strains, stock preparation, plaque assay and in vitro infection

SARS-CoV-Frankfurt-1, SARS-CoV-2-MUC-IMB-1 and SARS-CoV-2-GFP strains⁴³ were produced by infecting Vero E6 cells cultured in DMEM medium (10% FCS, 100 μ g ml⁻¹ Streptomycin, 100 IU ml⁻¹ penicillin) for 2 days (MOI of 0.01). Viral stock was collected and spun twice (1,000g for 10 min) before storage at -80 °C. Titre of viral stock was determined by plaque assay. Confluent monolayers of Vero E6 cells were infected with serial fivefold dilutions of virus supernatants for 1 h at 37 °C. The inoculum was removed and replaced with serum-free MEM (Gibco, Life Technologies) containing 0.5% carboxymethylcellulose (Sigma-Aldrich). Two days after infection, cells were fixed for 20 min at room temperature with formaldehyde added directly to the medium to a final concentration of 5%. Fixed cells were washed extensively with PBS before staining with water containing 1% crystal violet and 10% ethanol for 20 min. After rinsing with PBS, the number of plaques was counted and the virus titre was calculated.

A549-ACE2 cells were infected with either SARS-CoV-Frankfurt-1 or SARS-CoV-2-MUC-IMB-1 strains (MOI of 2) for the subsequent experiments. At each time point, the samples were washed once with 1× TBS buffer and collected in sodium deoxycholate (SDC) lysis buffer (100 mM Tris HCl pH 8.5; 4% SDC) for proteome-phosphoproteome-ubiquitinome analysis, sodium dodecyl sulfate (SDS) lysis buffer (62.5 mM Tris HCl pH 6.8; 2% SDS; 10% glycerol; 50 mM DTT; 0.01% bromophenol blue) for western blot, or buffer RLT (Qiagen) for transcriptome analysis. The samples were heat-inactivated and frozen at -80 °C until further processing.

Affinity purification and mass spectrometric analyses of SARS-CoV-2, SARS-CoV, HCoV-229E and HCoV-NL63 proteins expressed in A549

cells

To determine the interactomes of SARS-CoV-2 and SARS-CoV and the interactomes of an accessory protein (encoded by ORF4 or ORF4a of HCoV-229E or ORF3 of HCoV-NL63) that presumably represents a homologue of the ORF3 and ORF3a proteins of SARS-CoV-2 and SARS-CoV, respectively, four replicate affinity purifications were performed for each HA-tagged viral protein. A549 cells (6×10^6 cells per 15-cm dish) were transduced with lentiviral vectors encoding HA-tagged SARS-CoV-2, SARS-CoV or HCoV-229E/NL63 proteins and protein lysates were prepared from cells collected 3 days after transduction. Cell pellets from two 15-cm dishes were lysed in lysis buffer (50 mM Tris-HCl pH 7.5, 100 mM NaCl, 1.5 mM MgCl₂, 0.2% (v/v) NP-40, 5% (v/v) glycerol, cOmplete protease inhibitor cocktail (Roche), 0.5% (v/v) 750 U/μl Sm DNase) and sonicated (5 min, 4 °C, 30 s on, 30 s off, low settings; Bioruptor, Diagenode). Following normalization of protein concentrations of cleared lysates, virus protein-bound host proteins were enriched by adding 50 μl anti-HA-agarose slurry (Sigma-Aldrich, A2095) with constant agitation for 3 h at 4 °C. Non-specifically bound proteins were removed by four subsequent washes with lysis buffer followed by three detergent-removal steps with washing buffer (50 mM Tris-HCl pH 7.5, 100 mM NaCl, 1.5 mM MgCl₂, 5% (v/v) glycerol). Enriched proteins were denatured, reduced, alkylated and digested by addition of 200 μl digestion buffer (0.6 M guanidinium chloride, 1 mM tris(2-carboxyethyl)phosphine (TCEP), 4 mM chloroacetamide (CAA), 100 mM Tris-HCl pH 8, 0.5 μg LysC (WAKO Chemicals) and 0.5 μg trypsin (Promega) at 30 °C overnight. Peptide purification on StageTips with three layers of C18 Empore filter discs (3M) and subsequent mass spectrometry analysis was performed as described previously^{55,56}. In brief, purified peptides were loaded onto a 20-cm reverse-phase analytical column (75 μm diameter; ReproSil-Pur C18-AQ 1.9 μm resin; Dr Maisch) and separated using an EASY-nLC 1200 system (Thermo Fisher Scientific). A binary buffer system consisting of buffer A (0.1% formic acid (FA) in H₂O) and buffer B (80% acetonitrile (ACN), 0.1% FA in H₂O) with a 90-min gradient (5–30% buffer B (65 min), 30–95% buffer B (10 min), wash out at 95% buffer B (5 min), decreased to 5% buffer B (5 min), and 5% buffer B (5 min)) was used at a flow rate of 300 nl per min. Eluting peptides were directly analysed on a Q-Exactive HF mass spectrometer (Thermo Fisher Scientific). Data-dependent acquisition included repeating cycles of one MS1 full scan (300–1650 *m/z*, *R* = 60,000 at 200 *m/z*) at an ion target of 3×10^6 , followed by 15 MS2 scans of the highest abundant isolated and higher-energy collisional dissociation (HCD) fragmented peptide precursors (*R* = 15,000 at 200 *m/z*). For MS2 scans, collection of isolated peptide precursors was limited by an ion target of 1×10^5 and a maximum injection time of 25 ms. Isolation and fragmentation of the same peptide precursor was eliminated by dynamic exclusion for 20 s. The isolation window

of the quadrupole was set to 1.4 m/z and HCD was set to a normalized collision energy of 27%.

Proteome analyses of cells expressing SARS-CoV-2, SARS-CoV, HCoV-229E or HCoV-NL63 proteins

For the determination of proteome changes in A549 cells expressing SARS-CoV-2, SARS-CoV, HCoV-229E or HCoV-NL63 proteins, a fraction of 1×10^6 lentivirus-transduced cells from the affinity purification samples were lysed in guanidinium chloride buffer (6 M guanidinium chloride, 10 mM TCEP, 40 mM CAA, 100 mM Tris-HCl pH 8), boiled at 95 °C for 8 min and sonicated (10 min, 4 °C, 30 s on, 30 s off, high settings). Protein concentrations of cleared lysates were normalized to 50 µg, and proteins were pre-digested with 1 µg LysC at 37 °C for 1 h followed by a 1:10 dilution (100 mM Tris-HCl pH 8) and overnight digestion with 1 µg trypsin at 30 °C. Peptide purification on StageTips with three layers of C18 Empore filter discs (3M) and subsequent mass spectrometry analysis was performed as described previously^{55,56}. In brief, 300 ng of purified peptides were loaded onto a 50-cm reversed-phase column (75 µm inner diameter, packed in house with ReproSil-Pur C18-AQ 1.9 µm resin (Dr Maisch)). The column temperature was maintained at 60 °C using a homemade column oven. A binary buffer system, consisting of buffer A (0.1% FA) and buffer B (80% ACN, 0.1% FA), was used for peptide separation, at a flow rate of 300 nl min⁻¹. An EASY-nLC 1200 system (Thermo Fisher Scientific), directly coupled online with the mass spectrometer (Q Exactive HF-X, Thermo Fisher Scientific) via a nano-electrospray source, was employed for nano-flow liquid chromatography. Peptides were eluted by a linear 80 min gradient from 5% to 30% buffer B (0.1% v/v FA, 80% v/v ACN), followed by a 4 min increase to 60% B, a further 4 min increase to 95% B, a 4 min plateau phase at 95% B, a 4 min decrease to 5% B and a 4 min wash phase of 5% B. To acquire MS data, the data-independent acquisition (DIA) scan mode operated by the XCalibur software (Thermo Fisher) was used. DIA was performed with one full MS event followed by 33 MS/MS windows in one cycle resulting in a cycle time of 2.7 s. The full MS settings included an ion target value of 3×10^6 charges in the 300–1,650 m/z range with a maximum injection time of 60 ms and a resolution of 120,000 at m/z 200. DIA precursor windows ranged from 300.5 m/z (lower boundary of first window) to 1,649.5 m/z (upper boundary of 33rd window). MS/MS settings included an ion target value of 3×10^6 charges for the precursor window with an Xcalibur-automated maximum injection time and a resolution of 30,000 at m/z 200.

To generate the proteome library for DIA measurements purified peptides from the first and the fourth replicates of all samples were pooled separately and 25 µg of peptides from each pool were fractionated into 24 fractions by high pH reversed-phase chromatography as described earlier⁶⁰. During each separation, fractions were

concatenated automatically by shifting the collection tube every 120 s. In total 48 fractions were dried in a vacuum centrifuge, resuspended in buffer A* (0.2% trifluoroacetic acid (TFA), 2% ACN) and subsequently analysed by a top-12 data-dependent acquisition (DDA) scan mode using the same LC gradient and settings. The mass spectrometer was operated by the XCalibur software (Thermo Fisher). DDA scan settings on full MS level included an ion target value of 3×10^6 charges in the 300–1,650 m/z range with a maximum injection time of 20 ms and a resolution of 60,000 at m/z 200. At the MS/MS level the target value was 10^5 charges with a maximum injection time of 60 ms and a resolution of 15,000 at m/z 200. For MS/MS events only, precursor ions with 2–5 charges that were not on the 20-s dynamic exclusion list were isolated in a 1.4 m/z window. Fragmentation was performed by higher-energy C-trap dissociation with a normalized collision energy of 27 eV.

Infected time-course proteome–phosphoproteome–diGly proteome sample preparation

Frozen lysates of infected A549-ACE2 cells collected at 6, 12 and 24 hpi (and 36 hpi for the phosphoproteomics study) were thawed on ice, boiled for 5 min at 95 °C and sonicated for 15 min (Branson Sonifierer). Protein concentrations were estimated by tryptophan assay⁶¹. To reduce and alkylate proteins, samples were incubated for 5 min at 45 °C with TCEP (10 mM) and CAA (40 mM). Samples were digested overnight at 37 °C using trypsin (1:100 w/w, enzyme/protein, Sigma-Aldrich) and LysC (1:100 w/w, enzyme/protein, Wako).

For proteome analysis, 10 µg of peptide material were desalted using SDB-RPS StageTips (Empore)⁶¹. In brief, samples were diluted with 1% TFA in isopropanol to a final volume of 200 µl and loaded onto StageTips, subsequently washed with 200 µl of 1% TFA in isopropanol and 200 µl 0.2% TFA/ 2% ACN. Peptides were eluted with 75 µl of 1.25% ammonium hydroxide (NH₄OH) in 80% ACN and dried using a SpeedVac centrifuge (Eppendorf, Concentrator Plus). They were resuspended in buffer A* (0.2% TFA, 2% ACN) before LC–MS/MS analysis. Peptide concentrations were measured optically at 280 nm (Nanodrop 2000, Thermo Scientific) and subsequently equalized using buffer A*. One microgram of peptide was analysed by LC–MS/MS.

The rest of the samples were diluted fourfold with 1% TFA in isopropanol and loaded onto SDB-RPS cartridges (Strata-X-C, 30 mg per 3 ml, Phenomenex), pre-equilibrated with 4 ml 30% MeOH/1% TFA and washed with 4 ml 0.2% TFA. Samples were washed twice with 4 ml 1% TFA in isopropanol, once with 0.2% TFA/2% ACN and eluted twice with 2 ml 1.25% NH₄OH/80% ACN. Eluted peptides were diluted with ddH₂O to a final ACN concentration of 35%, snap frozen and lyophilized.

For phosphopeptide enrichment, lyophilized peptides were resuspended in 105 µl of equilibration buffer (1% TFA/80% ACN) and the peptide concentration was measured optically at 280 nm (Nanodrop 2000, Thermo Scientific) and subsequently equalized using equilibration buffer. The AssayMAP Bravo robot (Agilent) performed the enrichment for phosphopeptides (150 µg) by priming AssayMAP cartridges (packed with 5 µl Fe³⁺-NTA) with 0.1% TFA in 99% ACN followed by equilibration in equilibration buffer and loading of peptides. Enriched phosphopeptides were eluted with 1% ammonium hydroxide, which was evaporated using a Speedvac for 20 min. Dried peptides were resuspended in 6 µl buffer A* and 5 µl was analysed by LC–MS/MS.

For diGly peptide enrichment, lyophilized peptides were reconstituted in IAP buffer (50 mM MOPS, pH 7.2, 10 mM Na₂HPO₄, 50 mM NaCl) and the peptide concentration was estimated by tryptophan assay. K-ε-GG remnant containing peptides were enriched using the PTMScan Ubiquitin Remnant Motif (K-ε-GG) Kit (Cell Signaling Technology). Cross-linking of antibodies to beads and subsequent immunopurification was performed with slight modifications as previously described⁶². In brief, two vials of cross-linked beads were combined and equally split into 16 tubes (~31 µg of antibody per tube). Equal peptide amounts (600 µg) were added to cross-linked beads, and the volume was adjusted with IAP buffer to 1 ml. After 1 h of incubation at 4 °C and gentle agitation, beads were washed twice with cold IAP and 5 times with cold ddH₂O. Thereafter, peptides were eluted twice with 50 µl 0.15% TFA. Eluted peptides were desalted and dried as described for proteome analysis with the difference that 0.2% TFA instead of 1%TFA in isopropanol was used for the first wash. Eluted peptides were resuspended in 9 µl buffer A* and 4 µl was subjected to LC–MS/MS analysis.

DIA measurements

Samples were loaded onto a 50-cm reversed-phase column (75 µm inner diameter, packed in house with ReproSil-Pur C18-AQ 1.9 µm resin (Dr Maisch)). The column temperature was maintained at 60 °C using a homemade column oven. A binary buffer system, consisting of buffer A (0.1% FA) and buffer B (80% ACN plus 0.1% FA) was used for peptide separation, at a flow rate of 300 n l min⁻¹. An EASY-nLC 1200 system (Thermo Fisher Scientific), directly coupled online with the mass spectrometer (Orbitrap Exploris 480, Thermo Fisher Scientific) via a nano-electrospray source, was employed for nano-flow liquid chromatography. The FAIMS device was placed between the nanoelectrospray source and the mass spectrometer and was used for measurements of the proteome and the PTM-library samples. Spray voltage was set to 2,650 V, RF level to 40 and heated capillary temperature to 275 °C.

For proteome measurements we used a 100 min gradient starting at 5% buffer B followed by a stepwise increase to 30% in 80 min, 60% in 4 min and 95% in 4 min. The buffer B concentration stayed at 95% for 4 min, decreased to 5% in 4 min and stayed there for 4 min. The mass spectrometer was operated in data-independent mode (DIA) with a full scan range of 350–1,650 m/z at 120,000 resolution at 200 m/z , normalized automatic gain control (AGC) target of 300% and a maximum fill time of 28 ms. One full scan was followed by 22 windows with a resolution of 15,000, normalized AGC target of 1,000% and a maximum fill time of 25 ms in profile mode using positive polarity. Precursor ions were fragmented by HCD (NCE 30%). Each of the selected compensation voltage (CV) (-40 , -55 and -70 V) was applied to sequential survey scans and MS/MS scans; the MS/MS CV was always paired with the appropriate CV from the corresponding survey scan.

For phosphopeptide samples, 5 μ l were loaded and eluted with a 70-min gradient starting at 3% buffer B followed by a stepwise increase to 19% in 40 min, 41% in 20 min, 90% in 5 min and 95% in 5 min. The mass spectrometer was operated in DIA mode with a full scan range of 300–1,400 m/z at 120,000 resolution at 200 m/z and a maximum fill time of 60 ms. One full scan was followed by 32 windows with a resolution of 30,000. Normalized AGC target and maximum fill time were set to 1,000% and 54 ms, respectively, in profile mode using positive polarity. Precursor ions were fragmented by HCD (NCE stepped 25–27.5–30%). For the library generation, we enriched A549 cell lysates for phosphopeptides and measured them with 7 different CV settings (-30 , -40 , -50 , -60 , -70 , -80 or -90 V) using the same DIA method. The noted CVs were applied to the FAIMS electrodes throughout the analysis.

For the analysis of K- ϵ -GG peptide samples, half of the samples were loaded. We used a 120-min gradient starting at 3% buffer B followed by a stepwise increase to 7% in 6 min, 20% in 49 min, 36% in 39 min, 45% in 10 min and 95% in 4 min. The buffer B concentration stayed at 95% for 4 min, decreased to 5% in 4 min and stayed there for 4 min. The mass spectrometer was operated in DIA mode with a full scan range of 300–1,350 m/z at 120,000 resolution at m/z 200, normalized AGC target of 300% and a maximum fill time of 20 ms. One full scan was followed by 46 windows with a resolution of 30,000. Normalized AGC target and maximum fill time were set to 1,000% and 54 ms, respectively, in profile mode using positive polarity. Precursor ions were fragmented by HCD (NCE 28%). For K- ϵ -GG peptide library, we mixed the first replicate of each sample and measured them with eight different CV setting (-35 , -40 , -45 , -50 , -55 , -60 , -70 or -80 V) using the same DIA method.

Processing of raw MS data

AP-MS data

Raw MS data files of AP–MS experiments conducted in DDA mode were processed with MaxQuant (version 1.6.14) using the standard settings and label-free quantification (LFQ) enabled (LFQ min ratio count 1, normalization type none, stabilize large LFQ ratios disabled). Spectra were searched against forward and reverse sequences of the reviewed human proteome including isoforms (UniprotKB, release 2019.10) and C-terminally HA-tagged SARS-CoV-2, SARS-CoV and HCoV proteins by the built-in Andromeda search engine⁶³.

In-house Julia scripts (<https://doi.org/10.5281/zenodo.4541090>) were used to define alternative protein groups: only the peptides identified in AP–MS samples were considered for being protein group-specific, protein groups that differed by the single specific peptide or had less than 25% different specific peptides were merged to extend the set of peptides used for protein group quantitation and reduce the number of protein isoform-specific interactions.

Viral protein overexpression and DIA MS data

Spectronaut version 13 (Biognosys) with the default settings was used to generate the proteome libraries from DDA runs by combining files of respective fractionations using the human fasta file (Uniprot, 2019.10, 42 431 entries) and viral bait sequences. Proteome DIA files were analysed using the proteome library with the default settings and disabled cross run normalization.

SARS-CoV-2/SARS-CoV-infected proteome/PTM DIA MS data

Spectronaut version 14 (Biognosys)⁶⁴ was used to generate the libraries and analyse all DIA files using the human fasta file (UniprotKB, release 2019.10) and sequences of SARS-CoV-2/SARS-CoV proteins (UniProt, release 2020.08). Orf1a polyprotein sequences were split into separate protein chains according to the cleavage positions specified in the UniProt. For the generation of the PTM-specific libraries, the DIA single CV runs were combined with the actual DIA runs and either phosphorylation at serine, threonine or tyrosine, or GlyGly at lysine, was added as variable modification to default settings. The maximum number of fragment ions per peptide was increased to 25. The proteome DIA files were analysed using direct DIA approach with default settings and disabled cross run normalization. All post-translational modification DIA files were analysed using their respective hybrid library and either phosphorylation at Serine/Threonine/Tyrosine or GlyGly at Lysine was added as an additional variable modification to default settings with LOESS normalization and disabled PTM localization filter.

A collection of in-house Julia scripts(<https://doi.org/10.5281/zenodo.4541090>) were used to process the elution group (EG) -level Spectronaut reports, identify PTMs and

assign EG-level measurements to PTMs. The PTM was considered if at least once it was detected with ≥ 0.75 localization probability in EG with q -value $\leq 10^{-3}$. For further analysis of given PTM, only the measurements with ≥ 0.5 localization probability and EG q -value $\leq 10^{-2}$ were used.

Bioinformatic analysis

Unless otherwise specified, the bioinformatic analysis was done in R (version 3.6), Julia (version 1.5) and Python (version 3.8) using a collection of in-house scripts (<https://doi.org/10.5281/zenodo.4541090> and <https://doi.org/10.5281/zenodo.4541082>).

Datasets

The following public datasets were used in the study: Gene Ontology and Reactome annotations

(http://download.baderlab.org/EM_Genesets/April_01_2019/Human/UniProt/Human_GO_AllPathways_with_GO_iea_April_01_2019_UniProt.gmt); IntAct Protein Interactions (<https://www.ebi.ac.uk/intact/>, v2019.12); IntAct Protein Complexes (<https://www.ebi.ac.uk/complexportal/home>, v2019.12); CORUM Protein Complexes (<http://mips.helmholtz-muenchen.de/corum/download/allComplexes.xml.zip>, v2018.3); Reactome Functional Interactions (https://reactome.org/download/tools/ReactomeFIs/FIsInGene_020720_with_annotations.txt.zip); Human (v2019.10), Human-CoV, SARS-CoV-2 and SARS-CoV (v2020.08) protein sequences: <https://uniprot.org>.

Statistical analysis of MS data

MaxQuant and Spectronaut output files were imported into R using in-house maxquantUtils R package (<https://doi.org/10.5281/zenodo.4536603>). For all MS datasets, the Bayesian linear random effects models were used to define how the abundances of proteins change between the conditions. To specify and fit the models we used the msglm R package (<https://doi.org/10.5281/zenodo.4536605>), which uses the rstan package (version 2.19)⁶⁵ for inferring the posterior distribution of the model parameters. In all the models, the effects corresponding to the experimental conditions have regularized horseshoe+ priors⁶⁶, whereas the batch effects have normally distributed priors. Laplacian distribution was used to model the instrumental error of MS intensities. For each MS instrument used, the heteroscedastic intensities noise model was calibrated with the technical replicate MS data of the instrument. These data were also used to calibrate the logit-based model of missing MS data (the probability that the MS instrument will fail to identify the protein given its expected abundance in the sample). The model was fit using unnormalized MS intensities data. Instead of transforming the data by normalization, the inferred protein abundances were scaled by the normalization multiplier of each individual

MS sample to match the expected MS intensity of that sample. This allows taking the signal-to-noise variation between the samples into account when fitting the model. Due to high computational intensity, the model was applied to each protein group separately. For all the models, 4,000 iterations (2,000 warmup + 2,000 sampling) of the no-U-turn Markov Chain Monte Carlo were performed in 7 or 8 independent chains, every 4th sample was collected for posterior distribution of the model parameters. For estimating the statistical significance of protein abundance changes between the two experimental conditions, the *P*-value was defined as the probability that a random sample from the posterior distribution of the first condition would be smaller (or larger) than a random sample drawn from the second condition. No-multiple hypothesis testing corrections were applied, since this is handled by the choice of the model priors.

Statistical analysis of AP–MS data and filtering for specific interactions

The statistical model was applied directly to the MS1 intensities of protein group-specific LC peaks (evidence.txt table of MaxQuant output). In R GLM formula language, the model could be specified as

```
$$\log(\{\rm{I}\} \{\rm{n}\} \{\rm{t}\} \{\rm{e}\} \{\rm{n}\} \{\rm{s}\} \{\rm{i}\} \\ \{\rm{t}\} \{\rm{y}\}) \approx 1 + \{\rm{A}\} \{\rm{P}\} \{\rm{M}\} \{\rm{S}\} + \\ \{\rm{B}\} \{\rm{a}\} \{\rm{i}\} \{\rm{t}\} + \{\rm{B}\} \{\rm{a}\} \{\rm{i}\} \\ \{\rm{t}\} : \{\rm{V}\} \{\rm{i}\} \{\rm{r}\} \{\rm{u}\} \{\rm{s}\} + \{\rm{M}\} \\ \{\rm{S}\} \{\rm{1}\} \{\rm{p}\} \{\rm{e}\} \{\rm{a}\} \{\rm{k}\} + \{\rm{M}\} \{\rm{S}\} \\ \{\rm{b}\} \{\rm{a}\} \{\rm{t}\} \{\rm{c}\} \{\rm{h}\} , $$
```

where the APMS effect models the average shift of intensities in AP–MS data in comparison to full proteome samples, Bait is the average enrichment of a protein in AP–MS experiments of homologous proteins of both SARS-CoV and SARS-CoV-2, and Bait:Virus corresponds to the virus-specific changes in protein enrichment. MS1peak is the log ratio between the intensity of a given peak and the total protein abundance (the peak is defined by its peptide sequence, PTMs and the charge; it is assumed that the peak ratios do not depend on experimental conditions⁶⁷), and MSbatch accounts for batch-specific variations of protein intensity. APMS, Bait and

Bait: Virus effects were used to reconstruct the batch effect-free abundance of the protein in AP–MS samples.

The modelling provided the enrichment estimates for each protein in each AP experiment. Specific AP–MS interactions had to pass the two tests. In the first test, the enrichment of the candidate protein in a given bait AP was compared against the background, which was dynamically defined for each interaction to contain the data from all other baits, where the abundance of the candidate was within 50–90% percentile range (excluding top 10% baits from the background allowed the protein to be shared by a few baits in the resulting AP–MS network). The non-targeting control and Gaussian luciferase baits were always preserved in the background. Similarly, to filter out any potential side-effects of very high bait protein expression, the ORF3 homologues were always present in the background of M interactors and vice versa. To rule out the influence of the batch effects, the second test was applied. It was defined similarly to the first one, but the background was constrained to the baits of the same batch, and 40–80% percentile range was used. In both tests, the protein has to be fourfold enriched over the background (16 fold for highly expressed baits: ORF3, M, NSP13, NSP5, NSP6, ORF3a, ORF7b, ORF8b and HCoV-229E ORF4a) with *P*-value $\leq 10^{-3}$.

Additionally, we excluded the proteins that, in the viral protein expression data, have shown upregulation, and their enrichment in AP–MS data was less than 16 times stronger than observed upregulation effects. Finally, to exclude the carryover of material between the samples sequentially analysed by MS, we removed the putative interactors, which were also enriched at higher levels in the samples of the preceding bait, or the one before it.

For the analysis of interaction specificity between the homologous viral proteins, we estimated the significance of interaction enrichment difference (corrected by the average difference between the enrichment of the shared interactors to adjust for the bait expression variation). Specific interactions have to be fourfold enriched in comparison to the homologue with *P*-value $\leq 10^{-3}$.

Statistical analysis of DIA proteome effects upon viral protein overexpression

The statistical model of the viral protein overexpression dataset was similar to AP–MS data, except that protein-level intensities provided by Spectronaut were used. The PCA analysis of the protein intensities has identified that the second principal component is associated with the batch-dependent variations between the samples. To exclude their influence, this principal component was added to the experimental design matrix as an additional batch effect.

As with AP–MS data, the two statistical tests were used to identify the significantly regulated proteins (column ‘is_change’ in Supplementary Table 3). First, the absolute value of median \log_2 -fold change of the protein abundance upon overexpression of a given viral protein in comparison to the background had to be above 1.0 with P -value $\leq 10^{-3}$. The background was individually defined for each analysed protein. It was composed of experiments, where the abundance of given protein was within the 20–80% percentile range of all measured samples. Second, the protein had to be significantly regulated (same median \log_2 -fold change and P -value thresholds applied) against the batch-specific background (defined similarly to the global background, but using only the samples of the same batch).

An additional stringent criterion was applied to select the most significant changes (column ‘is_top_change’ in Supplementary Table 3; Extended Data Fig. 1i).

For each protein we classified bait-induced changes as: ‘high’ when $|\text{median } \log_2 \text{ fold-change}| \geq 1$ and $P\text{-value} \leq 10^{-10}$ both in background and batch comparisons; ‘medium’ if $10^{-10} < P\text{-value} \leq 10^{-4}$ with same fold-change requirement; and ‘low’ if $10^{-4} < P\text{-value} \leq 10^{-2}$ with the same fold-change requirement. All other changes were considered non-significant.

We then required that ‘shared’ top-regulated proteins should have exactly one pair of SARS-CoV-2 and SARS-CoV high- or medium-significant homologous baits among the baits with either up- or downregulated changes and no other baits with significant changes of the same type.

We further defined ‘SARS-CoV-2-specific’ or ‘SARS-CoV-specific’ top-regulated proteins to be the ones with exactly one high-significant change, and no other significant changes of the same sign. For ‘specific’ hits we additionally required that in the comparison of high-significant bait to its homologue $|\text{median } \log_2 \text{ fold-change}| \geq 1$ and $P\text{-value} \leq 10^{-3}$. When the homologous bait was missing (SARS-CoV-2 NSP1, SARS-CoV ORF8a and SARS-CoV ORF8b), we instead required that in the comparison of the high-significant change to the background $|\text{median } \log_2 \text{ fold-change}| \geq 1.5$.

The resulting network of most affected proteins was imported and prepared for publication in Cytoscape v.3.8.1⁶⁸.

Statistical analysis of DIA proteomic data of SARS-CoV-2 and SARS-CoV-infected A549-ACE2 cells

Similarly to the AP–MS DDA data, the linear Bayesian model was applied to the EG-level intensities. To model the protein intensity, the following linear model (in R notation) was used:

$$\$ \$ \log (\{\rm Intensity\}(t)) \sim 1 + \sum_{t_i} \{ t_i \leq t \} (\{\rm after\}) \\ (\{t_i\}) + (\{\rm infection\} \pm \{\rm CoV2\}) : (\{\rm after\})(\{t_i\}) + \{\rm EG\}, \$ \$$$

where the $\text{after}(t_i)$ effect corresponds to the protein abundance changes in mock-infected samples that happened between t_{i-1} and t_i after infection and it is applied to the modelled intensity at all time points starting from t_i ; $\text{infection:after}(t_i)$ ($t_i = 6, 12, 24$) is the common effect of SARS-CoV-2 and SARS-CoV infections occurring between t_{i-1} and t_i ; $\text{CoV2:after}(t_i)$ is the virus-specific effect within t_{i-1} and t_i hpi that is added to the log intensity for SARS-CoV-2-infected samples and subtracted from the intensity for SARS-CoV ones; EG is the elution group-specific shift in the measured log-intensities.

The absolute value of median \log_2 fold change between the conditions above 0.25 and the corresponding unadjusted $P\text{-value} \leq 10^{-3}$ were used to

define the significant changes at a given time point in comparison to mock infection. We also required that the protein group is quantified in at least two replicates of at least one of the compared conditions. Additionally, if for one of the viruses (for example, SARS-CoV-2) only the less stringent condition ($|\text{median } \log_2 \text{ fold-change}| \geq 0.125$, $P\text{-value} \leq 10^{-2}$) was fulfilled, but the change was significant in the infection of the other virus (SARS-CoV), and the difference between the viruses was not significant, the observed changes were considered significant for both viruses.

Statistical analysis of DIA phosphoproteome and ubiquitinome data of SARS-CoV-2 and SARS-CoV infections

The data from single- double- and triple-modified peptides were analysed separately and, for a given PTM, the most significant result was reported.

The data were analysed with the same Bayesian linear model as proteome SARS-CoV and SARS-CoV-2 infection data. In addition to the intensities normalization, for each replicate sample the scale of the effects in the experimental design matrix was adjusted, so that on average the correlation between log fold changes of the replicates was 1:1. The same logic as for the proteome analysis, was applied to identify significant changes, but the median \log_2 fold change had to be larger than 0.5, or 0.25 for the less stringent test. We additionally required that the PTM peptides are quantified in at least two replicates of at least one of the compared conditions. To ignore the changes in PTM site intensities that are due to proteome-level regulation, we excluded PTM sites on significantly regulated proteins if the directions of protein and PTM site changes were the same and the difference between their median \log_2 fold changes was less than two.

Phosphoproteomics data were further analysed with Ingenuity Pathway Analysis software (Qiagen;
<https://www.qiagenbioinformatics.com/products/ingenuity-pathway-analysis>)

Transcriptomic analysis of SARS-CoV-2 and SARS-CoV infected A549-ACE2 cells

For the analysis of the transcriptome data, Gencode gene annotations v28 and the human reference genome GRCh38 were derived from the Gencode homepage (EMBL-EBI). Viral genomes were derived from GenBank (SARS-CoV-2 - LR824570.1, and SARS-CoV - AY291315.1). Dropseq tool v1.12 was used for mapping raw sequencing data to the reference genome. The resulting UMI filtered count matrix was imported into R v3.4.4. CPM (counts per million) values were calculated for the raw data and genes having a mean cpm value less than 1 were removed from the dataset. A dummy variable combining the covariates infection status (mock, SARS-CoV, SARS-CoV-2) and time point was used for modelling the data within Limma (v3.46.0)⁶⁹.

Data were transformed with the Voom method⁶⁹ followed by quantile normalization. Differential testing was performed between infection states at individual time points by calculating moderated *t*-statistics and *P*-values for each host gene. A gene was considered to be significantly regulated if the false discovery rate-adjusted *P*-value was below 0.05.

Gene set enrichment analysis

We used Gene Ontology, Reactome and other EnrichmentMap gene sets of human proteins (version 2020.10)⁷⁰ as well as protein complexes annotations from IntAct Complex Portal (version 2019.11)⁷¹ and CORUM (version 2019)⁷². PhosphoSitePlus (version 2020.08) was used for known kinase-substrate and regulatory sites annotations, Perseus (version 1.6.14.0)⁷³ was used for annotation of known kinase motifs. For transcription factor enrichment analysis (Extended Data Fig. 2e) the significantly regulated transcripts were submitted to ChEA3 web-based application⁷⁴ and ENCODE data on transcription factor–target gene associations were used⁷⁵.

To find the non-redundant collection of annotations describing the unique and shared features of multiple experiments in a dataset (Fig. 1d, Extended Data Fig. 2l, m), we used in-house Julia package OptEnrichedSetCover.jl (<https://doi.org/10.5281/zenodo.4536596>), which employs evolutionary multi-objective optimization technique to find a collection of annotation

terms that have both significant enrichments in the individual experiments and minimal pairwise overlaps.

The resulting set of terms was further filtered by requiring that the annotation term has to be significant with the specified unadjusted Fisher's exact test *P*-value cut-off in at least one of the experiments or comparisons (the specific cut-off value is indicated in the figure legend of the corresponding enrichment analysis).

The generation of diagonally-split heat maps was done with the VegaLite.jl package (<https://github.com/queryverse/VegaLite.jl>).

Viral PTMs alignment

For matching the PTMs of SARS-CoV-2 and SARS-CoV the protein sequences were aligned using the BioAlignments.jl Julia package (v.2.0; <https://github.com/BioJulia/BioAlignments.jl>) with the Needleman–Wunsch algorithm using BLOSUM80 substitution matrix, and applying -5 and -3 penalties for the gap and extension, respectively.

For the cellular proteins, we required that the viral phosphorylation or ubiquitination site is observed with q -value $\leq 10^{-3}$ and localization probability ≥ 0.75 . For the PTMs with lower confidence (q -value $\leq 10^{-2}$ and localization probability ≥ 0.5) we required that the same site is observed with high confidence at the matching position of the orthologous protein of the other virus.

Network diffusion analysis

To systematically detect functional interactions, which may connect the cellular targets of each viral protein (interactome dataset) with the downstream changes it induces on proteome level (effectome dataset), we have used the network diffusion-based HierarchicalHotNet method³⁶ as implemented in Julia package HierarchicalHotNet.jl (<https://doi.org/10.5281/zenodo.4536590>). Specifically, for network diffusion with restart, we used the ReactomeFI network (version 2019)³⁵ of

cellular functional interactions, reversing the direction of functional interaction (for example, replacing kinase→substrate interaction with substrate→kinase). The proteins with significant abundance changes upon bait overexpression ($|\text{median}(\log_2 \text{fold change})| \geq 0.25$, $P \leq 10^{-2}$ both in the comparison against the controls and against the baits of the same batch) were used as the sources of signal diffusion with weights set to $\langle w \rangle_i = \sqrt{\langle m \rangle_e \langle m \rangle_d \langle m \rangle_i \langle m \rangle_a \langle m \rangle_n \langle \log_2 \rangle_2 (\langle m \rangle_f \langle m \rangle_o \langle m \rangle_l \langle m \rangle_d \langle m \rangle_c \langle m \rangle_h \langle m \rangle_a \langle m \rangle_n \langle m \rangle_g \langle m \rangle_e) \cdot \langle \log_2 \rangle_{10} P \text{text{-}} \langle m \rangle_v \langle m \rangle_a \langle m \rangle_l \langle m \rangle_u \langle m \rangle_e)} \rangle$, otherwise the node weight was set to zero. The weight of the edge $g_i \rightarrow g_j$ was set to

$w_{ij} = 1 + w_j$. The restart probability was set to 0.4, as suggested in the original publication, so that the probability of the random walk to stay in the direct neighbourhood of the node is the same as the probability to visit more distant nodes. To find the optimal cutting threshold of the resulting hierarchical tree of strongly connected components (SCCs) of the weighted graph corresponding to the stationary distribution of signal diffusion and to confirm the relevance of predicted functional connections, the same procedure was applied to 1,000 random permutations of vertex weights as described in Reyna et al.³⁶ (vertex weights are randomly shuffled between the vertices with similar in and out degrees). Since cutting the tree of SCCs at any threshold t (keeping only the edges with weights above t) and collapsing each resulting SCC into a single node produces the directed acyclic graph of connections between SCCs, it allowed efficient enumeration of the paths from the ‘source’ nodes (proteins strongly perturbed by viral protein expression with vertex weight w , $w \geq 1.5$) to the ‘sink’ nodes (interactors of the viral protein). At each threshold t , the average inverse of the path length from source to sink nodes was calculated as:

$$\langle L \rangle_{\text{avg}}(t) = \frac{1}{N_{\text{source}}} \sum_{p=1}^{N_{\text{sink}}} L_{\text{SCC}}(p)$$

where N_{source} is the number of sources, N_{sink} is the number of sinks, $L_{\text{SCC}}(p)$ is the number of SCCs that the given path p from source to sink goes through, and the sum is for all paths from sources to sinks. The metric

changes from 1 (all sources and sinks in the same SCC) to 0 (no or infinitely long paths between sources and sinks). For the generation of the diffusion networks we were using the t_{opt} threshold that maximized the difference between $\langle L \rangle_{\{\text{rm}\{\text{avg}\}\}}^{-1}(t)$ for the real data and the third quartile of $\langle L \rangle_{\{\text{rm}\{\text{avg}\}\}}^{-1}(t)$ for randomly shuffled data.

In the generated SCC networks, the direction of the edges was reverted back, and the results were exported as GraphML files using in-house Julia scripts (<https://doi.org/10.5281/zenodo.4541090>). The catalogue of the networks for each viral bait is available as Supplementary Data 1.

To assess the significance of edges in the resulting network, we calculated the P -value of the edge $g_i \rightarrow g_j$ as the probability that the transition probability between the given pair of genes based on permuted data is higher than the transition probability based on the real data:

```
$$P(\{w\}_{\{\text{rm}\{\text{real}\}\}}(\{g\}_{\{i\}},\{g\}_{\{j\}}) \leq \{w\}_{\{\text{rm}\{\text{perm}\}\}}(\{g\}_{\{i\}},\{g\}_{\{j\}})).$$
```

This P -value was stored as the ‘prob_perm_walkweight_greater’ edge attribute of GraphML output. The specific subnetworks predicted by the network diffusion (Fig. 4b–d) were filtered for edges with $P \leq 0.05$.

When the $g_i \rightarrow g_j$ connection was not present in the ReactomeFI network, to recover the potential short pathways connecting g_i and g_j , ReactomeFI was searched for intermediate g_k nodes, such that the edges $g_i \rightarrow g_k$ and $g_k \rightarrow g_j$ are present in ReactomeFI. The list of these short pathways is provided as the ‘flowpaths’ edge attribute in GraphML output.

The GraphML output of network diffusion was prepared for publication using yEd (v.3.20; <https://www.yworks.com>).

Intersection with other SARS coronavirus datasets

The intersection between the data generated by this study and other publicly available datasets was done using the information from respective supplementary tables. When multiple viruses were used in a study, only the

comparisons with SARS-CoV and SARS-CoV-2 were included. For time-resolved data, all time points up to 24 hpi were considered. The dataset coverage was defined as the number of reported distinct protein groups for proteomic studies and genes for transcriptomic studies. Confident interactions or significant regulations were filtered according to the criteria specified in the original study. A hit was considered as ‘confirmed’ when it was significant both in the present study and the external data and showed the same trend.

qRT–PCR analysis

RNA isolation from SARS-CoV and SARS-CoV-2 infected A549-ACE2 cells was performed as described above (Qiagen). Five hundred nanograms total RNA was used for reverse transcription with PrimeScript RT with gDNA eraser (Takara). For relative transcript quantification PowerUp SYBR Green (Applied Biosystems) was used. Primer sequences can be provided upon request.

Co-immunoprecipitation and western blot analysis

HEK293T cells were transfected with pWPI plasmid encoding single HA-tagged viral proteins, alone or together with pTO-SII-HA expressing host factor of interest. 48 h after transfection, cells were washed in PBS, flash frozen in liquid nitrogen and kept at –80 °C until further processing. Co-immunoprecipitation experiments were performed as described previously^{55,56}. In brief, cells were lysed in lysis buffer (50 mM Tris-HCl pH 7.5, 100 mM NaCl, 1.5 mM MgCl₂, 0.2% (v/v) NP-40, 5% (v/v) glycerol, cOmplete protease inhibitor cocktail (Roche), 0.5% (v/v) 750 U µl^{−1} Sm DNase) and sonicated (5 min, 4 °C, 30 s on, 30 s off, low settings; Bioruptor, Diagenode SA). HA or Streptactin beads were added to cleared lysates and samples were incubated for 3 h at 4 °C under constant rotation. Beads were washed six times in the lysis buffer and resuspended in 1× SDS sample buffer (62.5 mM Tris-HCl pH 6.8, 2% SDS, 10% glycerol, 50 mM DTT, 0.01% bromophenol blue). After boiling for 5 min at 95 °C, a fraction of the input lysate and elution were loaded on NuPAGE Novex 4–12% Bis-Tris (Invitrogen), and further submitted to western blotting using

Amersham Protran nitrocellulose membranes. Imaging was performed by HRP luminescence (ECL, Perkin Elmer).

SARS-CoV-2 infected A549-ACE2 cell lysates were sonicated (10 min, 4 °C, 30 s on, 30 s off, low settings; Bioruptor, Diagenode). Protein concentration was adjusted based on Pierce660 assay supplemented with ionic detergent compatibility reagent. After boiling for 5 min at 95 °C and brief centrifugation at maximum speed, the samples were loaded on NuPAGE Novex 4–12% Bis-Tris (Invitrogen), and blotted onto 0.22 µm Amersham Protran nitrocellulose membranes (Merck). Primary and secondary antibody stainings were performed according to the manufacturer's recommendations. Imaging was performed by HRP luminescence using Femto kit (ThermoFischer Scientific) or Western Lightning PlusECL kit (Perkin Elmer).

Mapping of post-translational modification sites on the N CTD structure

N CTD dimers of SARS-CoV-2 (PDB: 6YUN) and SARS-CoV (PDB: 2CJR) were superimposed by aligning the α -carbons backbone over 111 residues (from position 253/254 to position 364/365 following SARS-CoV-2/SARS-CoV numbering) by using the tool MatchMaker⁷⁶ as implemented in the Chimera software⁷⁷. Ubiquitination sites were visually inspected and mapped by using the PyMOL software (<https://pymol.org>). Phosphorylation on Ser310/311 was simulated in silico by using the PyTMs plugin as implemented in PyMOL⁷⁸. Inter-chain residue contacts, dimer interface area, free energy and complex stability were comparatively analysed between non-phosphorylated and phosphorylated SARS-CoV-2 and SARS-CoV N CTD by using the PDBePISA server⁷⁹. Poisson–Boltzmann electrostatic surface potential of native and post-translationally modified N CTD was calculated by using the PBEQ Solver tool on the CHARMM-GUI server by preserving existing hydrogen bonds⁸⁰. Molecular graphics depictions were produced with the PyMOL software.

Reporter assay and IFN bioassay

The following reporter constructs were used in this study: pISRE-luc was purchased from Stratagene, EF1- α -ren was obtained from E. Gürlevik (Department of Gastroenterology, Hepatology and Endocrinology, Hannover Medical School, Germany), pCAGGS-Flag-RIG-I was obtained from C. Basler (Department of Microbiology, Mount Sinai School of Medicine, USA), pIRF1-GAS-ff-luc, pWPI-SMN1-flag and pWPI-NS5 (ZIKV)-HA was described previously^{[56,81](#)}.

For the reporter assay, HEK293-R1 cells were plated in 24-well plates 24 h before transfection. Firefly reporter and *Renilla* transfection control were transfected together with plasmids expressing viral proteins using polyethylenimine (PEI, Polysciences) for untreated and treated conditions. In 18 h cells were stimulated for 8 h with a corresponding inducer and collected in the passive lysis buffer (Promega). Luminescence of Firefly and *Renilla* luciferases was measured using dual-luciferase-reporter assay (Promega) according to the manufacturer's instructions in a microplate reader (Tecan).

Total amounts of IFN- α and IFN- β in cell supernatants were measured by using 293T cells stably expressing the firefly luciferase gene under the control of the mouse Mx1 promoter (Mx1-luc reporter cells)^{[82](#)}. In brief, HEK293-R1 cells were seeded, transfected with pCAGGS-flag-RIG-I plus viral protein constructs and stimulated as described above. Cell supernatants were collected in 8 h. Mx1-luc reporter cells were seeded into 96-well plates in triplicates and were treated 24 h later with supernatants. At 16 h after incubation, cells were lysed in the passive lysis buffer (Promega), and luminescence was measured with a microplate reader (Tecan). The assay sensitivity was determined by a standard curve.

Viral inhibitor assay

A549-ACE2 cells were seeded into 96-well plates in DMEM medium (10% FCS, 100 μ g ml⁻¹ streptomycin, 100 IU ml⁻¹ penicillin) one day before infection. Six hours before infection, or at the time of infection, the medium was replaced with 100 μ l of DMEM medium containing either the compounds of interest or DMSO as a control. Infection was performed by adding 10 μ l of SARS-CoV-2-GFP (MOI of 3) per well and plates were

placed in the IncuCyte S3 Live-Cell Analysis System (Essen Bioscience), where whole well real-time images of mock (phase channel) and infected (GFP and phase channel) cells were captured every 4 h for 48 h. Cell viability (mock) and virus growth (mock and infected) were assessed as the cell confluence per well (phase area) and GFP area normalized by cell confluence per well (GFP area/phase area) respectively using IncuCyte S3 Software (Essen Bioscience; version 2019B rev2).

For comparative analysis of antiviral treatment activity against SARS-CoV and SARS-CoV-2, A549-ACE2 cells were seeded in 24-well plates, as previously described. Treatment was performed for 6 h with 0.5 ml of DMEM medium containing either the compounds of interest or DMSO as a control, and infected with SARS-CoV-Frankfurt-1 or SARS-CoV-2-MUC-IMB-1 (MOI of 1) for 24 h. Total cellular RNA was collected and analysed by RT-qPCR, as previously described.

Reporting summary

Further information on research design is available in the [Nature Research Reporting Summary](#) linked to this paper.

Data availability

The raw sequencing data for this study have been deposited with the ENA at EMBL-EBI under accession number [PRJEB38744](#). The mass spectrometry proteomics data have been deposited to the ProteomeXchange Consortium via the PRIDE⁸³ partner repository with the dataset identifiers [PXD022282](#), [PXD020461](#) and [PXD020222](#). Protein interactions identified in this study have been submitted to the IMEx (<https://www.imexconsortium.org>) consortium through IntAct⁸⁴ with the identifier IM-28109. The data and analysis results are accessible online via the interactive web interface at <https://covinet.innatelab.org>.

Code availability

In-house R and Julia packages and scripts used for the bioinformatics analysis of the data have been deposited to public GitHub repositories:
<https://doi.org/10.5281/zenodo.4536605>,
<https://doi.org/10.5281/zenodo.4536603>,
<https://doi.org/10.5281/zenodo.4536590>,
<https://doi.org/10.5281/zenodo.4536596>,
<https://doi.org/10.5281/zenodo.4541090> and
<https://doi.org/10.5281/zenodo.4541082>.

References

1. 1.

Gordon, D. E. et al. A SARS-CoV-2 protein interaction map reveals targets for drug repurposing. *Nature* **583**, 459–468 (2020).

[ADS](#) [CAS](#) [PubMed](#) [PubMed Central](#) [Google Scholar](#)

2. 2.

Gordon, D. E. et al. Comparative host–coronavirus protein interaction networks reveal pan-viral disease mechanisms. *Science* **370**, eabe9403 (2020).

[CAS](#) [PubMed](#) [PubMed Central](#) [Google Scholar](#)

3. 3.

Bojkova, D. et al. Proteomics of SARS-CoV-2-infected host cells reveals therapy targets. *Nature* **583**, 469–472 (2020).

[ADS](#) [CAS](#) [PubMed](#) [Google Scholar](#)

4. 4.

Messner, C. B. et al. Ultra-high-throughput clinical proteomics reveals classifiers of COVID-19 infection. *Cell Syst.* **11**, 11–24.e4 (2020).

[CAS](#) [PubMed](#) [PubMed Central](#) [Google Scholar](#)

5. 5.

Samavarchi-Tehrani, P. et al. A SARS-CoV-2–host proximity interactome. Preprint at <https://doi.org/10.1101/2020.09.03.282103> (2020).

6. 6.

Laurent, E. M. N. et al. Global BioID-based SARS-CoV-2 proteins proximal interactome unveils novel ties between viral polypeptides and host factors involved in multiple COVID19-associated mechanisms. Preprint at <https://doi.org/10.1101/2020.08.28.272955> (2020).

7. 7.

Klann, K. et al. Growth factor receptor signaling inhibition prevents SARS-CoV-2 replication. *Mol. Cell* **80**, 164–174.e4 (2020).

[CAS](#) [PubMed](#) [PubMed Central](#) [Google Scholar](#)

8. 8.

Huang, J. et al. SARS-CoV-2 infection of pluripotent stem cell-derived human lung alveolar type 2 cells elicits a rapid epithelial-intrinsic inflammatory response. *Cell Stem Cell* **27**, 962–973.e7 (2020).

[CAS](#) [PubMed](#) [PubMed Central](#) [Google Scholar](#)

9. 9.

Blanco-Melo, D. et al. Imbalanced host response to SARS-CoV-2 drives development of COVID-19. *Cell* **181**, 1036–1045.e9 (2020).

[CAS](#) [PubMed](#) [PubMed Central](#) [Google Scholar](#)

10. 10.

Li, J. et al. Virus–host interactome and proteomic survey reveal potential virulence factors influencing SARS-CoV-2 pathogenesis. *Med* **2**, 99–112.e7 (2021).

[PubMed](#) [Google Scholar](#)

11. 11.

von Brunn, A. et al. Analysis of intraviral protein–protein interactions of the SARS coronavirus ORFeome. *PLoS ONE* **2**, e459 (2007).

[ADS](#) [Google Scholar](#)

12. 12.

Cornillez-Ty, C. T., Liao, L., Yates, J. R., III, Kuhn, P. & Buchmeier, M. J. Severe acute respiratory syndrome coronavirus nonstructural protein 2 interacts with a host protein complex involved in mitochondrial biogenesis and intracellular signaling. *J. Virol.* **83**, 10314–10318 (2009).

[CAS](#) [PubMed](#) [PubMed Central](#) [Google Scholar](#)

13. 13.

Andrianifahanana, M. et al. ERBB receptor activation is required for profibrotic responses to transforming growth factor β . *Cancer Res.* **70**, 7421–7430 (2010).

[CAS](#) [PubMed](#) [PubMed Central](#) [Google Scholar](#)

14. 14.

Pittet, J.-F. et al. TGF- β is a critical mediator of acute lung injury. *J. Clin. Invest.* **107**, 1537–1544 (2001).

[CAS](#) [PubMed](#) [PubMed Central](#) [Google Scholar](#)

15. 15.

George, P. M., Wells, A. U. & Jenkins, R. G. Pulmonary fibrosis and COVID-19: the potential role for antifibrotic therapy. *Lancet Respir. Med.* **8**, 807–815 (2020).

[CAS](#) [PubMed](#) [PubMed Central](#) [Google Scholar](#)

16. 16.

Mo, X. et al. Abnormal pulmonary function in COVID-19 patients at time of hospital discharge. *Eur. Respir. J.* **55**, 2001217 (2020).

[CAS](#) [PubMed](#) [PubMed Central](#) [Google Scholar](#)

17. 17.

Heo, J.-M. et al. Integrated proteogenetic analysis reveals the landscape of a mitochondrial-autophagosome synapse during PARK2-dependent mitophagy. *Sci. Adv.* **5**, eaay4624 (2019).

[ADS](#) [CAS](#) [PubMed](#) [PubMed Central](#) [Google Scholar](#)

18. 18.

Shi, C.-S. et al. SARS-coronavirus open reading frame-9b suppresses innate immunity by targeting mitochondria and the MAVS/TRAF3/TRAF6 signalosome. *J. Immunol.* **193**, 3080–3089 (2014).

[CAS](#) [PubMed](#) [PubMed Central](#) [Google Scholar](#)

19. 19.

Hoagland, D. A. et al. Modulating the transcriptional landscape of SARS-CoV-2 as an effective method for developing antiviral compounds. Preprint at <https://doi.org/10.1101/2020.07.12.199687> (2020).

20. 20.

Castiglione, V., Chiriacò, M., Emdin, M., Taddei, S. & Vergaro, G. Statin therapy in COVID-19 infection. *Eur. Heart J. Cardiovasc. Pharmacother.* **6**, 258–259 (2020).

[PubMed](#) [Google Scholar](#)

21. 21.

Radenkovic, D., Chawla, S., Pirro, M., Sahebkar, A. & Banach, M. Cholesterol in relation to COVID-19: should we care about it? *J. Clin. Med.* **9**, 1909 (2020).

[CAS](#) [PubMed Central](#) [Google Scholar](#)

22. 22.

Chu, H. et al. Comparative replication and immune activation profiles of SARS-CoV-2 and SARS-CoV in human lungs: an ex vivo study with implications for the pathogenesis of COVID-19. *Clin. Infect. Dis.* **71**, 1400–1409 (2020).

[CAS](#) [PubMed](#) [Google Scholar](#)

23. 23.

Zhu, Z. et al. From SARS and MERS to COVID-19: a brief summary and comparison of severe acute respiratory infections caused by three highly pathogenic human coronaviruses. *Respir. Res.* **21**, 224 (2020).

[CAS](#) [PubMed](#) [PubMed Central](#) [Google Scholar](#)

24. 24.

Cazzaniga, A., Locatelli, L., Castiglioni, S. & Maier, J. The contribution of EDF1 to PPAR γ transcriptional activation in VEGF-treated human endothelial cells. *Int. J. Mol. Sci.* **19**, 1830 (2018).

[PubMed Central](#) [Google Scholar](#)

25. 25.

Gavriilaki, E. et al. Endothelial dysfunction in COVID-19: lessons learned from coronaviruses. *Curr. Hypertens. Rep.* **22**, 63 (2020).

[CAS](#) [PubMed](#) [PubMed Central](#) [Google Scholar](#)

26. 26.

Daniloski, Z. et al. Identification of required host factors for SARS-CoV-2 infection in human cells. *Cell* **184**, 92–105 (2021).

[CAS](#) [PubMed](#) [Google Scholar](#)

27. 27.

Shinde, S. R. & Maddika, S. PTEN modulates EGFR late endocytic trafficking and degradation by dephosphorylating Rab7. *Nat. Commun.* **7**, 10689 (2016).

[ADS](#) [CAS](#) [PubMed](#) [PubMed Central](#) [Google Scholar](#)

28. 28.

Wang, D. et al. Auto-phosphorylation represses protein kinase R activity. *Sci. Rep.* **7**, 44340 (2017).

[ADS](#) [PubMed](#) [PubMed Central](#) [Google Scholar](#)

29. 29.

Yu, Y. T.-C. et al. Surface vimentin is critical for the cell entry of SARS-CoV. *J. Biomed. Sci.* **23**, 14 (2016).

[PubMed](#) [PubMed Central](#) [Google Scholar](#)

30. 30.

dos Santos, G. et al. Vimentin regulates activation of the NLRP3 inflammasome. *Nat. Commun.* **6**, 6574 (2015).

[ADS](#) [PubMed](#) [PubMed Central](#) [Google Scholar](#)

31. 31.

Ramos, I., Stamatakis, K., Oeste, C. L. & Pérez-Sala, D. Vimentin as a multifaceted player and potential therapeutic target in viral infections. *Int. J. Mol. Sci.* **21**, 4675 (2020).

[CAS](#) [PubMed](#) [PubMed Central](#) [Google Scholar](#)

32. 32.

Zinzula, L. et al. High-resolution structure and biophysical characterization of the nucleocapsid phosphoprotein dimerization domain from the Covid-19 severe acute respiratory syndrome coronavirus 2. *Biochem. Biophys. Res. Commun.* **538**, 54–62 (2021).

[CAS](#) [PubMed](#) [Google Scholar](#)

33. 33.

Chen, C.-Y. et al. Structure of the SARS coronavirus nucleocapsid protein RNA-binding dimerization domain suggests a mechanism for helical packaging of viral RNA. *J. Mol. Biol.* **368**, 1075–1086 (2007).

[CAS](#) [PubMed](#) [PubMed Central](#) [Google Scholar](#)

34. 34.

Perry, J. S. A. et al. Interpreting an apoptotic corpse as anti-inflammatory involves a chloride sensing pathway. *Nat. Cell Biol.* **21**, 1532–1543 (2019).

[CAS](#) [PubMed](#) [PubMed Central](#) [Google Scholar](#)

35. 35.

Wu, G., Dawson, E., Duong, A., Haw, R. & Stein, L. ReactomeFIViz: a Cytoscape app for pathway and network-based data analysis. *F1000Res.* **3**, 146 (2014).

[PubMed](#) [PubMed Central](#) [Google Scholar](#)

36. 36.

Reyna, M. A., Leiserson, M. D. M. & Raphael, B. J. Hierarchical HotNet: identifying hierarchies of altered subnetworks. *Bioinformatics* **34**, i972–i980 (2018).

[CAS](#) [PubMed](#) [PubMed Central](#) [Google Scholar](#)

37. 37.

Cottam, E. M., Whelband, M. C. & Wileman, T. Coronavirus NSP6 restricts autophagosome expansion. *Autophagy* **10**, 1426–1441 (2014).

[CAS](#) [PubMed](#) [PubMed Central](#) [Google Scholar](#)

38. 38.

Ohsaki, Y., Cheng, J., Fujita, A., Tokumoto, T. & Fujimoto, T. Cytoplasmic lipid droplets are sites of convergence of proteasomal and autophagic degradation of apolipoprotein B. *Mol. Biol. Cell* **17**, 2674–2683 (2006).

[CAS](#) [PubMed](#) [PubMed Central](#) [Google Scholar](#)

39. 39.

Khalil, M. F., Wagner, W. D. & Goldberg, I. J. Molecular interactions leading to lipoprotein retention and the initiation of atherosclerosis. *Arterioscler. Thromb. Vasc. Biol.* **24**, 2211–2218 (2004).

[CAS](#) [PubMed](#) [Google Scholar](#)

40. 40.

Nicolai, L. et al. Immunothrombotic dysregulation in COVID-19 pneumonia is associated with respiratory failure and coagulopathy. *Circulation* **142**, 1176–1189 (2020).

[CAS](#) [PubMed](#) [PubMed Central](#) [Google Scholar](#)

41. 41.

Zavadil, J. et al. Genetic programs of epithelial cell plasticity directed by transforming growth factor- β . *Proc. Natl Acad. Sci. USA* **98**, 6686–6691 (2001).

[ADS](#) [CAS](#) [PubMed](#) [Google Scholar](#)

42. 42.

Qin, Z., Xia, W., Fisher, G. J., Voorhees, J. J. & Quan, T. YAP/TAZ regulates TGF- β /Smad3 signaling by induction of Smad7 via AP-1 in human skin dermal fibroblasts. *Cell Commun. Signal.* **16**, 18 (2018).

[PubMed](#) [PubMed Central](#) [Google Scholar](#)

43. 43.

Thi Nhu Thao, T. et al. Rapid reconstruction of SARS-CoV-2 using a synthetic genomics platform. *Nature* **582**, 561–565 (2020).

[ADS](#) [Google Scholar](#)

44. 44.

Mantlo, E., Bukreyeva, N., Maruyama, J., Paessler, S. & Huang, C. Antiviral activities of type I interferons to SARS-CoV-2 infection. *Antiviral Res.* **179**, 104811 (2020).

[CAS](#) [PubMed](#) [PubMed Central](#) [Google Scholar](#)

45. 45.

Seebacher, N. A., Stacy, A. E., Porter, G. M. & Merlot, A. M. Clinical development of targeted and immune based anti-cancer therapies. *J. Exp. Clin. Cancer Res.* **38**, 156 (2019).

[CAS](#) [PubMed](#) [PubMed Central](#) [Google Scholar](#)

46. 46.

O’Shea, J. J., Kontzias, A., Yamaoka, K., Tanaka, Y. & Laurence, A. Janus kinase inhibitors in autoimmune diseases. *Ann. Rheum. Dis.* **72** (Suppl 2), ii111–ii115 (2013).

[PubMed](#) [PubMed Central](#) [Google Scholar](#)

47. 47.

Yong, H.-Y., Koh, M.-S. & Moon, A. The p38 MAPK inhibitors for the treatment of inflammatory diseases and cancer. *Expert Opin. Investig. Drugs* **18**, 1893–1905 (2009).

[CAS](#) [PubMed](#) [Google Scholar](#)

48. 48.

Hsieh, W.-Y. et al. ACE/ACE2 ratio and MMP-9 activity as potential biomarkers in tuberculous pleural effusions. *Int. J. Biol. Sci.* **8**, 1197–1205 (2012).

[CAS](#) [PubMed](#) [PubMed Central](#) [Google Scholar](#)

49. 49.

Ueland, T. et al. Distinct and early increase in circulating MMP-9 in COVID-19 patients with respiratory failure. *J. Infect.* **81**, e41–e43 (2020).

[CAS](#) [PubMed](#) [PubMed Central](#) [Google Scholar](#)

50. 50.

Villalta, P. C., Rocic, P. & Townsley, M. I. Role of MMP2 and MMP9 in TRPV4-induced lung injury. *Am. J. Physiol. Lung Cell. Mol. Physiol.* **307**, L652–L659 (2014).

[CAS](#) [PubMed](#) [PubMed Central](#) [Google Scholar](#)

51. 51.

Marten, N. W. & Zhou, J. in *Experimental Models of Multiple Sclerosis* (eds Lavi, E. & Constantinescu, C. S.) 839–848 (Springer, 2005).

52. 52.

Zhang, J.-Y. et al. Single-cell landscape of immunological responses in patients with COVID-19. *Nat. Immunol.* **21**, 1107–1118 (2020).

[CAS](#) [PubMed](#) [Google Scholar](#)

53. 53.

Ellinghaus, D. et al. Genomewide association study of severe Covid-19 with respiratory failure. *N. Engl. J. Med.* **383**, 1522–1534 (2020).

[CAS](#) [PubMed](#) [Google Scholar](#)

54. 54.

Ali, A. & Vijayan, R. Dynamics of the ACE2–SARS-CoV-2/SARS-CoV spike protein interface reveal unique mechanisms. *Sci. Rep.* **10**, 14214 (2020).

[ADS](#) [CAS](#) [PubMed](#) [PubMed Central](#) [Google Scholar](#)

55. 55.

Hubel, P. et al. A protein-interaction network of interferon-stimulated genes extends the innate immune system landscape. *Nat. Immunol.* **20**, 493–502 (2019).

[CAS](#) [PubMed](#) [Google Scholar](#)

56. 56.

Scaturro, P. et al. An orthogonal proteomic survey uncovers novel Zika virus host factors. *Nature* **561**, 253–257 (2018).

[ADS](#) [CAS](#) [PubMed](#) [Google Scholar](#)

57. 57.

Hoffmann, M. et al. SARS-CoV-2 cell entry depends on ACE2 and TMPRSS2 and is blocked by a clinically proven protease inhibitor. *Cell* **181**, 271–280.e8 (2020).

[CAS](#) [PubMed](#) [PubMed Central](#) [Google Scholar](#)

58. 58.

Gebhardt, A. et al. The alternative cap-binding complex is required for antiviral defense in vivo. *PLoS Pathog.* **15**, e1008155 (2019).

[PubMed](#) [PubMed Central](#) [Google Scholar](#)

59. 59.

Goldeck, M., Schlee, M., Hartmann, G. & Hornung, V. Enzymatic synthesis and purification of a defined RIG-I ligand. *Methods Mol. Biol.* **1169**, 15–25 (2014).

[CAS](#) [PubMed](#) [Google Scholar](#)

60. 60.

Kulak, N. A., Geyer, P. E. & Mann, M. Loss-less nano-fractionator for high sensitivity, high coverage proteomics. *Mol. Cell. Proteomics* **16**, 694–705 (2017).

[CAS](#) [PubMed](#) [PubMed Central](#) [Google Scholar](#)

61. 61.

Kulak, N. A., Pichler, G., Paron, I., Nagaraj, N. & Mann, M. Minimal, encapsulated proteomic-sample processing applied to copy-number estimation in eukaryotic cells. *Nat. Methods* **11**, 319–324 (2014).

[CAS](#) [PubMed](#) [Google Scholar](#)

62. 62.

Udeshi, N. D., Mertins, P., Svinkina, T. & Carr, S. A. Large-scale identification of ubiquitination sites by mass spectrometry. *Nat. Protoc.* **8**, 1950–1960 (2013).

[CAS](#) [PubMed](#) [PubMed Central](#) [Google Scholar](#)

63. 63.

Tyanova, S., Temu, T. & Cox, J. The MaxQuant computational platform for mass spectrometry-based shotgun proteomics. *Nat. Protoc.* **11**, 2301–2319 (2016).

[CAS](#) [PubMed](#) [Google Scholar](#)

64. 64.

Bober, M. & Miladinovic, S. General guidelines for validation of decoy models for HRM/DIA/SWATH as exemplified using Spectronaut. *F1000posters* <https://f1000research.com/posters/1097512> (2015).

65. 65.

Carpenter, B. et al. Stan: a probabilistic programming language. *J. Stat. Softw.* **76**, 1–32 (2017).

[Google Scholar](#)

66. 66.

Bhadra, A., Datta, J., Polson, N. G. & Willard, B. The Horseshoe+ estimator of ultra-sparse signals. *Bayesian Anal.* **12**, 1105–1131 (2017).

[MathSciNet](#) [MATH](#) [Google Scholar](#)

67. 67.

Goeminne, L. J. E., Gevaert, K. & Clement, L. Peptide-level robust ridge regression improves estimation, sensitivity, and specificity in data-dependent quantitative label-free shotgun proteomics. *Mol. Cell. Proteomics* **15**, 657–668 (2016).

[CAS](#) [PubMed](#) [Google Scholar](#)

68. 68.

Shannon, P. et al. Cytoscape: a software environment for integrated models of biomolecular interaction networks. *Genome Res.* **13**, 2498–2504 (2003).

[CAS](#) [PubMed](#) [PubMed Central](#) [Google Scholar](#)

69. 69.

Ritchie, M. E. et al. limma powers differential expression analyses for RNA-sequencing and microarray studies. *Nucleic Acids Res.* **43**, e47 (2015).

[PubMed](#) [PubMed Central](#) [Google Scholar](#)

70. 70.

Merico, D., Isserlin, R., Stueker, O., Emili, A. & Bader, G. D. Enrichment map: a network-based method for gene-set enrichment visualization and interpretation. *PLoS ONE* **5**, e13984 (2010).

[ADS](#) [PubMed](#) [PubMed Central](#) [Google Scholar](#)

71. 71.

Meldal, B. H. M. et al. Complex Portal 2018: extended content and enhanced visualization tools for macromolecular complexes. *Nucleic Acids Res.* **47** (D1), D550–D558 (2019).

[CAS](#) [PubMed](#) [Google Scholar](#)

72. 72.

Giurgiu, M. et al. CORUM: the comprehensive resource of mammalian protein complexes-2019. *Nucleic Acids Res.* **47** (D1), D559–D563 (2019).

[CAS](#) [PubMed](#) [Google Scholar](#)

73. 73.

Tyanova, S. et al. The Perseus computational platform for comprehensive analysis of (prote)omics data. *Nat. Methods* **13**, 731–740 (2016).

[CAS](#) [Google Scholar](#)

74. 74.

Keenan, A. B. et al. ChEA3: transcription factor enrichment analysis by orthogonal omics integration. *Nucleic Acids Res.* **47** (W1), W212–W224 (2019).

[MathSciNet](#) [CAS](#) [PubMed](#) [PubMed Central](#) [Google Scholar](#)

75. 75.

Landt, S. G. et al. ChIP-seq guidelines and practices of the ENCODE and modENCODE consortia. *Genome Res.* **22**, 1813–1831 (2012).

[CAS](#) [PubMed](#) [PubMed Central](#) [Google Scholar](#)

76. 76.

Meng, E. C., Pettersen, E. F., Couch, G. S., Huang, C. C. & Ferrin, T. E. Tools for integrated sequence-structure analysis with UCSF Chimera. *BMC Bioinformatics* **7**, 339 (2006).

[PubMed](#) [PubMed Central](#) [Google Scholar](#)

77. 77.

Pettersen, E. F. et al. UCSF Chimera—a visualization system for exploratory research and analysis. *J. Comput. Chem.* **25**, 1605–1612 (2004).

[CAS](#) [Google Scholar](#)

78. 78.

Warnecke, A., Sandalova, T., Achour, A. & Harris, R. A. PyTMs: a useful PyMOL plugin for modeling common post-translational modifications. *BMC Bioinformatics* **15**, 370 (2014).

[PubMed](#) [PubMed Central](#) [Google Scholar](#)

79. 79.

Paxman, J. J. & Heras, B. Bioinformatics tools and resources for analyzing protein structures. *Methods Mol. Biol.* **1549**, 209–220 (2017).

[CAS](#) [PubMed](#) [Google Scholar](#)

80. 80.

Jo, S., Vargyas, M., Vasko-Szedlar, J., Roux, B. & Im, W. PBEQ-Solver for online visualization of electrostatic potential of biomolecules. *Nucleic Acids Res.* **36**, W270–W275 (2008).

[CAS](#) [PubMed](#) [PubMed Central](#) [Google Scholar](#)

81. 81.

Vogt, C. et al. The interferon antagonist ML protein of thogoto virus targets general transcription factor IIB. *J. Virol.* **82**, 11446–11453 (2008).

[CAS](#) [PubMed](#) [PubMed Central](#) [Google Scholar](#)

82. 82.

Jorns, C. et al. Rapid and simple detection of IFN-neutralizing antibodies in chronic hepatitis C non-responsive to IFN-alpha. *J. Med. Virol.* **78**, 74–82 (2006).

[CAS](#) [PubMed](#) [Google Scholar](#)

83. 83.

Perez-Riverol, Y. et al. The PRIDE database and related tools and resources in 2019: improving support for quantification data. *Nucleic Acids Res.* **47** (D1), D442–D450 (2019).

[CAS](#) [PubMed](#) [PubMed Central](#) [Google Scholar](#)

84. 84.

Orchard, S. et al. The MIntAct project–IntAct as a common curation platform for 11 molecular interaction databases. *Nucleic Acids Res.* **42**, D358–D363 (2014).

[CAS](#) [PubMed](#) [Google Scholar](#)

[Download references](#)

Acknowledgements

We thank S. Pöhlmann for sharing ACE2 plasmids and R. Baier for technical assistance, M. Trojan for advice on drugs, J. Pancorbo and J. Albert-von der Gönna from the Leibniz Supercomputing Centre (<https://www.lrz.de>) for technical assistance. We further thank the Karl Max von Bauernfeind–Verein for support for the screening microscope. Work in the authors' laboratories was supported by an ERC consolidator grant (ERC-CoG ProDAP, 817798), the German Research Foundation (PI 1084/3, PI 1084/4, PI 1084/5, TRR179/TP11, TRR237/A07), the Bavarian State Ministry of Science and Arts (Bavarian Research Network FOR-COVID) and the German Federal Ministry of Education and Research (COVINET) to A. Pichlmair. This work was also supported by the German Federal Ministry of Education and Research (CLINSPECT-M) to B.K. A.W. was supported by the China Scholarship Council (CSC). The work of J.Z. was supported by the German Research Foundation (SFB1021, A01 and B01; KFO309, P3), the State of Hessen through the LOEWE Program (DRUID, B02) and the German Ministry for Education and Research (COVINET, RAPID). The work of P.S. is supported by the Free and Hanseatic City of Hamburg and the German Research Foundation (SC 314/1-1). We thank R. Polakiewicz, F. Gnad and Cell Signaling Technology for the gift of the PTMScan Ubiquitin Remnant Motif (K-ε-GG) Kits.

Author information

Author notes

1. These authors contributed equally: Alexey Stukalov, Virginie Girault, Vincent Grass, Ozge Karayel, Valter Bergant, Christian Urban, Darya A. Haas, Yiqi Huang

Affiliations

1. Technical University of Munich, School of Medicine, Institute of Virology, Munich, Germany

Alexey Stukalov, Virginie Girault, Vincent Grass, Valter Bergant, Christian Urban, Darya A. Haas, Yiqi Huang, Lila Oubrahim, Anqi Wang, M. Sabri Hamad, Antonio Piras, Teresa M. Lavacca, Ulrike Protzer, Pietro Scaturro & Andreas Pichlmair

2. Department of Proteomics and Signal Transduction, Max-Planck Institute of Biochemistry, Martinsried, Germany

Ozge Karayel, Fynn M. Hansen, Maria C. Tanzer, Igor Paron & Matthias Mann

3. Department of Molecular Structural Biology, Max-Planck Institute of Biochemistry, Martinsried, Germany

Luca Zinzula

4. Institute of Molecular Oncology and Functional Genomics and Department of Medicine II, School of Medicine, Technical University of Munich, Munich, Germany

Thomas Engleitner & Roland Rad

5. Chair of Proteomics and Bioanalytics, Technical University of Munich, Freising, Germany

Maria Reinecke & Bernhard Kuster

6. German Cancer Consortium (DKTK), Munich Partner Site, Munich, Germany

Maria Reinecke & Bernhard Kuster

7. German Cancer Research Center (DKFZ), Heidelberg, Germany

Maria Reinecke & Bernhard Kuster

8. Bundeswehr Institute of Microbiology, Munich, Germany

Rosina Ehmann & Roman Wölfel

9. German Center for Infection Research (DZIF), Munich Partner Site,
Munich, Germany

Rosina Ehmann, Roman Wölfel, Ulrike Protzer & Andreas Pichlmair

10. Institute of Veterinary Bacteriology, Department of Infectious Diseases
and Pathobiology, University of Bern, Bern, Switzerland

Jörg Jores

11. Justus Liebig University Giessen, Institute of Medical Virology,
Giessen, Germany

John Ziebuhr

12. Institute of Virology and Immunology (IVI), Bern, Switzerland

Volker Thiel

13. Department of Infectious Diseases and Pathobiology, University of
Bern, Bern, Switzerland

Volker Thiel

14. Leibniz Institute for Experimental Virology, Hamburg, Germany

Pietro Scaturro

Authors

1. Alexey Stukalov

[View author publications](#)

You can also search for this author in [PubMed](#) [Google Scholar](#)

2. Virginie Girault

[View author publications](#)

You can also search for this author in [PubMed](#) [Google Scholar](#)

3. Vincent Grass

[View author publications](#)

You can also search for this author in [PubMed](#) [Google Scholar](#)

4. Ozge Karayel

[View author publications](#)

You can also search for this author in [PubMed](#) [Google Scholar](#)

5. Valter Bergant

[View author publications](#)

You can also search for this author in [PubMed](#) [Google Scholar](#)

6. Christian Urban

[View author publications](#)

You can also search for this author in [PubMed](#) [Google Scholar](#)

7. Darya A. Haas

[View author publications](#)

You can also search for this author in [PubMed](#) [Google Scholar](#)

8. Yiqi Huang

[View author publications](#)

You can also search for this author in [PubMed](#) [Google Scholar](#)

9. Lila Oubrahim

[View author publications](#)

You can also search for this author in [PubMed](#) [Google Scholar](#)

10. Anqi Wang

[View author publications](#)

You can also search for this author in [PubMed](#) [Google Scholar](#)

11. M. Sabri Hamad

[View author publications](#)

You can also search for this author in [PubMed](#) [Google Scholar](#)

12. Antonio Piras

[View author publications](#)

You can also search for this author in [PubMed](#) [Google Scholar](#)

13. Fynn M. Hansen

[View author publications](#)

You can also search for this author in [PubMed](#) [Google Scholar](#)

14. Maria C. Tanzer

[View author publications](#)

You can also search for this author in [PubMed](#) [Google Scholar](#)

15. Igor Paron

[View author publications](#)

You can also search for this author in [PubMed](#) [Google Scholar](#)

16. Luca Zinzula

[View author publications](#)

You can also search for this author in [PubMed](#) [Google Scholar](#)

17. Thomas Engleitner

[View author publications](#)

You can also search for this author in [PubMed](#) [Google Scholar](#)

18. Maria Reinecke

[View author publications](#)

You can also search for this author in [PubMed](#) [Google Scholar](#)

19. Teresa M. Lavacca

[View author publications](#)

You can also search for this author in [PubMed](#) [Google Scholar](#)

20. Rosina Ehmann

[View author publications](#)

You can also search for this author in [PubMed](#) [Google Scholar](#)

21. Roman Wölfel

[View author publications](#)

You can also search for this author in [PubMed](#) [Google Scholar](#)

22. Jörg Jores

[View author publications](#)

You can also search for this author in [PubMed](#) [Google Scholar](#)

23. Bernhard Kuster

[View author publications](#)

You can also search for this author in [PubMed](#) [Google Scholar](#)

24. Ulrike Protzer

[View author publications](#)

You can also search for this author in [PubMed](#) [Google Scholar](#)

25. Roland Rad

[View author publications](#)

You can also search for this author in [PubMed](#) [Google Scholar](#)

26. John Ziebuhr

[View author publications](#)

You can also search for this author in [PubMed](#) [Google Scholar](#)

27. Volker Thiel

[View author publications](#)

You can also search for this author in [PubMed](#) [Google Scholar](#)

28. Pietro Scaturro

[View author publications](#)

You can also search for this author in [PubMed](#) [Google Scholar](#)

29. Matthias Mann

[View author publications](#)

You can also search for this author in [PubMed](#) [Google Scholar](#)

30. Andreas Pichlmair

[View author publications](#)

You can also search for this author in [PubMed](#) [Google Scholar](#)

Contributions

Conceptualization: A.S., V. Girault, V. Grass, O.K., V.B., C.U., D.A.H., Y.H., J.Z., P.S., M.M. and A. Pichlmair. Investigation: V. Girault, V. Grass, O.K., V.B., C.U., D.A.H., Y.H., L.O., A.W., A. Piras, F.M.H., M.C.T., I.P., T.M.L., R.E., J.J. and P.S. Data analysis: A.S., V. Girault, V. Grass, V.B., O.K., C.U., D.A.H., Y.H., M.S.H., F.M.H., M.C.T., L.Z., T.E. and M.R. Funding acquisition: R.W., B.K., U.P., R.R., J.Z., V.T., M.M. and A. Pichlmair. Supervision: M.M., R.R. and A. Pichlmair. Writing: A.S., V. Girault, V. Grass, O.K., V.B., C.U., D.A.H., Y.H., L.Z., M.M. and A. Pichlmair.

Corresponding author

Correspondence to [Andreas Pichlmair](#).

Ethics declarations

Competing interests

The authors declare no competing interests.

Additional information

Peer review information *Nature* thanks Ivan Dikic, Trey Ideker, Michael Weekes, and the other, anonymous, reviewer(s) for their contribution to the peer review of this work. Peer reviewer reports are available.

Publisher's note Springer Nature remains neutral with regard to jurisdictional claims in published maps and institutional affiliations.

Extended data figures and tables

[Extended Data Fig. 1 SARS-CoV-2 and SARS-CoV proteins expressed in A549 cells target host proteins.](#)

a, Expression of HA-tagged viral proteins in stably transduced A549 cells, used in AP–MS and proteome expression measurements. When several bands are present in a single lane, * or ► mark the band with the expected molecular weight ($n = 4$ independent experiments). For gel source data, see Supplementary Fig. 1. **b**, Extended version of the virus-host protein–protein interaction network with 24 SARS-CoV-2 and 27 SARS-CoV proteins, as well as ORF3 of HCoV-NL63 and ORF4 and ORF4a of HCoV-229E, used as baits. Host targets regulated upon viral protein overexpression are highlighted (see the in-plot legend). **c–f**, Co-precipitation experiments in HEK293T cells showing a specific enrichment of endogenous MAVS co-precipitated with C-terminal HA-tagged ORF7b of SARS-CoV-2 and SARS-CoV (negative controls: SARS-CoV-2 ORF6-HA, ORF7a-HA) (**c**), ORF7b-HA of SARS-CoV-2 and SARS-CoV co-precipitated with SII-HA-UNC93B1 (control precipitation: SII-HA-RSAD2) (**d**), endogenous HSPA1A co-precipitated with N-HA of SARS-CoV-2 and SARS-CoV (control: SARS-CoV-2 ORF6-HA) (**e**) and endogenous TGF- β with ORF8-HA of SARS-CoV-2 vs ORF8-HA, ORF8a-HA, ORF8b-HA of SARS-CoV or ORF9b-HA of SARS-CoV-2 (**f**), ($n = 2$ independent experiments). For

gel source data, see Supplementary Fig. 1. AP–MS: affinity-purification coupled to mass spectrometry; MD: Macro domain; NSP: Non-structural protein.

Extended Data Fig. 2 SARS-CoV-2 and SARS-CoV proteins trigger shared and specific interactions with host factors, and induce changes to the host proteome.

a, b, Differential enrichment of proteins in NSP2 (**a**) and ORF8 (**b**) of SARS-CoV-2 (x-axis) vs SARS-CoV (y-axis) AP–MS experiments ($n = 4$ independent experiments). **c**, Gene Ontology Biological Processes enriched among the cellular proteins that are up- (red arrow) or down- (blue arrow) regulated upon overexpression of individual viral proteins. **d**, The most affected proteins from the effectome data of protein changes upon viral bait overexpression in A549 cells (see materials and methods for the exact protein selection criteria). Homologous viral proteins are displayed as a single node. Shared and virus-specific effects are denoted by the edge colour. NSP: Non-structural protein.

Extended Data Fig. 3 RCOR3 and APOB regulation upon SARS-CoV-2 and SARS-CoV protein overexpression.

a, b, Normalized intensities of selected candidates specifically perturbed by individual viral proteins: RCOR3 was upregulated both by SARS-CoV-2 and SARS-CoV NSP4 proteins (**a**), APOB was upregulated by ORF3 and downregulated by NSP1 specifically to SARS-CoV-2 (**b**). The box and the whiskers represent 50% and 95% confidence intervals, and the white line corresponds to the median of the \log_2 fold change upon viral protein overexpression ($n = 4$ independent experiments).

Extended Data Fig. 4 Tracking of virus-specific changes in infected A549-ACE2 cells by transcriptomics and proteomics.

a, Western blot showing ACE2-HA expression levels in A549 cells untransduced (wild-type) or transduced with ACE2-HA-encoding lentivirus ($n = 2$ independent experiments). For gel source data, see Supplementary

Fig. 1. **b**, mRNA expression levels of SARS-CoV-2 *N* relative to *RPLP0* as measured by qRT–PCR upon infection of wild-type A549 and A549-ACE2 cells at the indicated MOIs. Error bars represent mean and standard deviation ($n = 3$ independent experiments). **c**, Volcano plot of mRNA expression changes of A549-ACE2 cells, infected with SARS-CoV-2 at an MOI of 2 in comparison to mock infection at 12 hpi. Significant hits are highlighted in grey (moderated *t*-test false discovery rate-corrected two-sided *P*-value, $n = 3$ independent experiments). Diamonds indicate that the actual \log_2 fold change or *P*-value were truncated to fit into the plot. **d**, Expression levels, as measured by qRT–PCR, of SARS-CoV-2/SARS-CoV *N* and host transcripts relative to *RPLP0* in infected (MOI of 2) A549-ACE2 cells with SARS-CoV-2 (orange) and SARS-CoV (brown) at indicated time points. Error bars correspond to mean and standard deviation (Two-sided student *t*-test, unadjusted *P*-value, $n = 3$ independent experiments). **P*-value ≤ 0.05 ; ***P*-value ≤ 0.01 ; ****P*-value $\leq 10^{-3}$. **e**, Analysis of transcription factors, whose targets are significantly enriched among up- (red arrow) and down- (blue arrow) regulated genes of A549-ACE2 cells infected with SARS-CoV-2 (upper triangle) and SARS-CoV (lower triangle) for indicated time points (Fisher’s exact test unadjusted one-sided *P*-value $\leq 10^{-4}$). **f**, Volcano plot of SARS-CoV-2-induced protein abundance changes at 24 hpi in comparison to mock. Viral proteins are highlighted in orange, selected significant hits are marked in black (Bayesian linear model-based unadjusted two-sided *P*-value $\leq 10^{-3}$, $|\text{median } \log_2 \text{ fold change}| \geq 0.25$, $n = 4$ independent experiments). Diamonds indicate that the actual \log_2 fold change was truncated to fit into the plot. **g**, Western blot showing the total levels of ACE2-HA protein at 6, 12, 24 and 36 hpi (mock, SARS-CoV-2 and SARS-CoV infections); N viral protein as infection and ACTB as loading controls ($n = 3$ independent experiments). For gel source data, see Supplementary Fig. 1. **h**, Stable expression of *ACE2* mRNA transcript relative to *RPLP0*, as measured by qRT–PCR, after SARS-CoV-2 and SARS-CoV infections (MOI of 2) of A549-ACE2 cells at indicated hpi (error bars show mean and standard deviation, $n = 3$ independent experiments). **i**, Scatter plots comparing the host proteome of SARS-CoV-2 (x-axis) and SARS-CoV (y-axis) infection at 24 hpi (\log_2 fold change in comparison to the mock infection samples at the same time point). Significantly regulated proteins (Bayesian linear model-based

unadjusted two-sided P -value $\leq 10^{-3}$, $|\log_2 \text{fold change}| \geq 0.25$, $n = 4$ independent experiments), are colored according to their specificity in both infections. Diamonds indicate that the actual \log_2 fold change was truncated to fit into the plot.

Extended Data Fig. 5 Post-translational modifications modulated during SARS-CoV-2 or SARS-CoV infection.

a, Volcano plots of SARS-CoV-2-induced ubiquitination changes at 24 hpi in comparison to mock. The viral PTM sites are highlighted in orange and selected significant hits in black. **b**, Scatter plots comparing the host phosphoproteome of SARS-CoV-2 (x -axis) and SARS-CoV (y -axis) infection at 24 hpi (\log_2 fold change in comparison to the mock infection samples at the same time point). Significantly regulated sites are colored according to their specificity in both infections. **c**, Volcano plots of SARS-CoV-2-induced phosphorylation changes at 24 hpi in comparison to mock. The viral PTM sites are highlighted in orange and selected significant hits in black. For **a–c**, a change is defined significant if its Bayesian linear model-based unadjusted two-sided P -value $\leq 10^{-3}$ and $|\log_2 \text{fold change}| \geq 0.5$, $n = 3$ independent experiments for ubiquitination and $n = 4$ independent experiments for phosphorylation data. Diamonds in **a–c** indicate that the actual median \log_2 fold change was truncated to fit into the plot. **d**, Profile plots showing the time-resolved phosphorylation of ACE2 (S787) and RAB7A (S72) with indicated median, 50% and 95% confidence intervals, $n = 4$ independent experiments. **e**, The enrichment of host kinase motifs among the significantly regulated phosphorylation sites of SARS-CoV-2 (upper triangle) and SARS-CoV-infected (lower triangle) A549-ACE2 cells (MOI of 2) at the indicated time points (Fisher's exact test, unadjusted one-sided P -value $\leq 10^{-3}$). **f**, The enrichment of specific kinases among the ones known to phosphorylate significantly regulated sites at the indicated time points and annotated in PhosphoSitePlus database (Fisher's exact test, unadjusted one-sided P -value $\leq 10^{-2}$).

Extended Data Fig. 6 Integration of multi-omics data from SARS-CoV-2 and SARS-CoV infection identified co-regulation

of host and viral factors.

a, Phosphorylation (purple square) and ubiquitination (red circles) sites on vimentin (VIM) regulated upon SARS-CoV-2 infection. The plot shows the medians of \log_2 fold changes compared to mock at 6, 12, 24 and 36 hpi, regulatory sites are indicated with a thick black border. **b**, Profile plots of VIM K334 ubiquitination, S56 and S72 phosphorylation, and total protein levels in SARS-CoV-2 or SARS-CoV infected A549-ACE2 cells at indicated times after infection, with indicated median, 50% and 95% confidence intervals, $n = 3$ (ubiquitination) or $n = 4$ (total protein levels, phosphorylation) independent experiments. **c**, Number of ubiquitination sites identified on each SARS-CoV-2 or SARS-CoV proteins in infected A549-ACE2 cells. **d, e**, Mapping the ubiquitination and phosphorylation sites of SARS-CoV-2/SARS-CoV M and S proteins on their aligned sequence showing median \log_2 intensities in infected A549-ACE2 cells at 24 hpi ($n = 4$ independent experiments for phosphorylation and $n = 3$ independent experiments for ubiquitination data) with functional (blue) and topological (yellow) domains highlighted. Ubiquitin modifying enzymes binding to both M proteins and the host kinases that potentially recognize motifs associated with the reported sites and overrepresented among cellular motifs enriched upon infection (Extended Data Fig. 5e,f) or interacting with given viral protein (Extended Data Fig. 1b) are indicated (green). **f**, Number of phosphorylation sites identified on each SARS-CoV-2 or SARS-CoV proteins in infected A549-ACE2 cells. **g**, Mapping the ubiquitination (red circle) and phosphorylation (purple square) sites of SARS-CoV-2/SARS-CoV N protein on their aligned sequence showing median \log_2 intensities in A549-ACE2 cells infected with the respective virus at 24 hpi ($n = 4$ independent experiments) with functional domains highlighted in blue. The host kinases that potentially recognize motifs associated with the reported sites and overrepresented among cellular motifs enriched upon infection (Extended Data Fig. 5e,f) or interacting with given viral protein (Extended Data Fig. 1b) (green). **h**, Electrostatic surface potential analysis of non-phosphorylated and phosphorylated SARS-CoV and SARS-CoV-2 N CTD dimers; red, white and blue regions represent areas with negative, neutral and positive electrostatic potential, respectively (scale from -50 to $+50$ $kT e^{-1}$). NTD, N-terminal domain;

hACE2, binding site of human ACE2; FP, fusion peptide; HR1/2, Heptad region 1/2; CP, cytoplasmic region. CoV2 Cleav., SARS-CoV-2 cleavage sites.

Extended Data Fig. 7 Reactome pathways enrichment in multi-omics data of SARS-CoV-2 and SARS-CoV infection.

a, Reactome pathways enriched in up- (red arrow) or downregulated (blue arrow) transcripts, proteins, ubiquitination and phosphorylation sites (Fisher's exact test unadjusted P -value $\leq 10^{-4}$) in SARS-CoV-2 or SARS-CoV-infected A549-ACE2 cells at indicated times after infection.

Extended Data Fig. 8 SARS-CoV-2 uses a multi-pronged approach to perturb host-pathways at several levels.

a, The host subnetwork perturbed by SARS-CoV-2 M predicted by the network diffusion approach. Edge thickness reflects the transition probability in random walk with restart, directed edges represent the walk direction, and ReactomeFI connections are highlighted in black. **b**, Selection of the optimal threshold for the network diffusion model of SARS-CoV-2 M-induced proteome changes. The plot shows the relationship between the minimal allowed edge weight of the random walk graph (x -axis) and the mean inverse length of the path from the regulated proteins to the host targets of the viral protein along the edges of the resulting filtered subnetwork (y -axis). The red curve represents the metric for the network diffusion analysis of the actual data. The grey band shows 50% confidence interval, and dashed lines correspond to 95% confidence interval for the average inverse path length distribution for 1,000 randomized datasets. Optimal edge weight threshold that maximizes the difference between the metric based on the real data and its 3rd quartile based on randomized data are highlighted by the red vertical line. **c, d**, Subnetworks of the network diffusion predictions linking host targets of SARS-CoV-2 ORF7b (**c**) to the factors involved in innate immunity and ORF8 (**d**) to the factors involved in TGF- β signalling. **e, f**, Western blot showing the accumulation of the autophagy-associated factor MAP1LC3B upon SARS-CoV-2 ORF3 expression in HEK293-R1 cells ($n = 3$

independent experiments) (**e**) and SARS-CoV-2/SARS-CoV infection of A549-ACE2 cells ($n = 3$ independent experiments) (**f**). For gel source data, see Supplementary Fig. 1. **g, h**, Profile plots showing the time-resolved ubiquitination of the autophagy regulators MAP1LC3A, GABARAP, VPS33A and VAMP8 ($n = 3$ independent experiments) (**g**), as well as an increase in total protein abundance of APOB with indicated median, 50% and 95% confidence intervals ($n = 4$ independent experiments) (**h**). **i**, Overview of perturbations to host-cell innate immunity-related pathways, induced by distinct proteins of SARS-CoV-2, derived from the network diffusion model and overlaid with transcriptional, ubiquitination and phosphorylation changes upon SARS-CoV-2 infection. **j**, Heat map showing the effects of the indicated SARS-CoV-2 proteins on type-I IFN expression levels, ISRE and GAS promoter activation in HEK293-R1. Accumulation of type-I IFN in the supernatant was evaluated by testing supernatants of PPP-RNA (IVT4) stimulated cells on MX1-luciferase reporter cells, ISRE promoter activation—by luciferase assay after IFN- α stimulation, and GAS promoter activation—by luciferase assay after IFN- γ stimulation in cells expressing SARS-CoV-2 proteins as compared to the controls (ZIKV NS5 and SMN1) ($n = 3$ independent experiments).

Extended Data Fig. 9 Perturbation of host integrin-TGF- β -EGFR-receptor tyrosine kinase signalling by SARS-CoV-2.

a, Overview of perturbations to host-cell Integrin-TGF- β -EGFR-receptor tyrosine kinase signalling, induced by distinct proteins of SARS-CoV-2, derived from the network diffusion model and overlaid with transcriptional, ubiquitination and phosphorylation changes upon SARS-CoV-2 infection. **b**, Profile plots of total protein levels of SERPINE1 and FN1 in SARS-CoV-2 or SARS-CoV-infected A549-ACE2 cells at 6, 12, and 24 hpi, with indicated median, 50% and 95% confidence intervals ($n = 4$ independent experiments). **c**, Profile plots showing intensities of indicated phosphosites on NCK2, JUN, SOS1 and MAPKAPK2 in SARS-CoV-2 or SARS-CoV-infected A549-ACE2 cells at 6, 12, 24 and 36 hpi, with indicated median, 50% and 95% confidence intervals ($n = 4$ independent experiments). **d**, Western blot showing phosphorylated (T180/Y182) and total protein levels of p38 in SARS-CoV-2 or SARS-CoV infected A549-ACE2 cells ($n = 3$ independent experiments). For gel source data, see Supplementary Fig. 1.

Extended Data Fig. 10 Drug repurposing screen, focusing on pathways perturbed by SARS-CoV-2, reveals potential candidates for use in antiviral therapy.

a, A549-ACE2 cells exposed for 6 h to the specified concentrations of IFN- α and infected with SARS-CoV-2-GFP reporter virus (MOI of 3). GFP signal and cell confluence were analysed by live-cell imaging for 48 hpi. Time-courses show virus growth over time as the mean of GFP-positive area normalized to the total cell area ($n = 4$ independent experiments). **b**, A549-ACE2 cells were pre-treated for 6 h or treated at the time of infection with SARS-CoV-2-GFP reporter virus (MOI of 3). GFP signal and cell growth were tracked for 48 hpi by live-cell imaging using an Incucyte S3 platform. Left heat map: the cell growth rate (defined as the change of cell confluence between t_i and t_{i-1} timepoints divided by cell confluence at t_{i-1}) over time in drug-treated uninfected conditions. Middle (6 h of pre-treatment) and right (treatment at the time of infection) heat maps: treatment-induced changes in virus growth over time (GFP signal normalized to total cell confluence log₂ fold change between the treated and control (water, DMSO) conditions). Only non-cytotoxic treatments with significant effects on SARS-CoV-2-GFP are shown. Asterisks indicate significance of the difference to the control treatment (Wilcoxon test; unadjusted two-sided P -value ≤ 0.05 , $n = 4$ independent experiments). **c**, A549-ACE2 cells exposed for 6 h to the specified concentrations of ipatasertib and infected with SARS-CoV-2-GFP reporter virus (MOI of 3). GFP signal and cell confluence were analysed by live-cell imaging for 48 hpi. Time-courses show virus growth over time as the mean of GFP-positive area normalized to the total cell area ($n = 4$ independent experiments). **d–g**, mRNA expression levels at 24 hpi of SARS-CoV-2 (orange) and SARS-CoV (brown) N relative to *RPLP0*, compared to DMSO-treated cells, as measured by qRT-PCR in infected A549-ACE2 cells (MOI of 1) pre-treated for 6 h with gilteritinib (**d**), tirapazamine (**e**), prinomastat (**f**) or marimastat (**g**). Error bars represent mean and standard deviation (Student t -test, two-sided, unadjusted P -value, $n = 3$ independent experiments). * P -value ≤ 0.05 ; ** P -value ≤ 0.01 ; *** P -value $\leq 10^{-3}$.

Extended Data Table 1 Functional annotations of the protein–protein interaction network of SARS-CoV-2 and SARS-CoV (AP–MS)

[Full size table](#)

Supplementary information

Supplementary Information

This file contains Supplementary Discussions 1-2 and Supplementary Figure 1 (full membrane images of western-blot raw gels).

Reporting Summary

Supplementary Data 1

Diffusion networks of SARS-CoV-2 and SARS-CoV proteins – see readme.txt inside the zip for detailed description and display instructions.

Supplementary Table 1

Sequences of coronavirus proteins used as baits in AP-MS experiments.

Supplementary Table 2

Virus-host protein-protein interaction network of SARS-CoV-2 and SARS-CoV in A549 cells.

Supplementary Table 3

Total proteome of A549 cells expressing individual coronavirus proteins, the “effectome”.

Supplementary Table 4

Transcriptome of A549-ACE2 cells infected with SARS-CoV-2 and SARS-CoV.

Supplementary Table 5

Total proteome of A549-ACE2 cells infected with SARS-CoV-2 and SARS-CoV.

Supplementary Table 6

Ubiquitinome of A549-ACE2 cells infected with SARS-CoV-2 and SARS-CoV.

Supplementary Table 7

Phosphoproteome of A549-ACE2 cells infected with SARS-CoV-2 and SARS-CoV.

Supplementary Table 8

Biological functions and pathways enriched in A549-ACE2 cells infected with SARS-CoV-2 and SARS-CoV.

Supplementary Table 9

Viral inhibitor assay.

Supplementary Table 10

Intersection with other SARS-CoV-2 studies to date.

Peer Review File

Rights and permissions

Reprints and Permissions

About this article



Check for
updates

Cite this article

Stukalov, A., Girault, V., Grass, V. *et al.* Multilevel proteomics reveals host perturbations by SARS-CoV-2 and SARS-CoV. *Nature* **594**, 246–252 (2021). <https://doi.org/10.1038/s41586-021-03493-4>

[Download citation](#)

- Received: 12 June 2020
- Accepted: 25 March 2021
- Published: 12 April 2021
- Issue Date: 10 June 2021
- DOI: <https://doi.org/10.1038/s41586-021-03493-4>

Further reading

- [Comparative transcriptome analysis reveals key epigenetic targets in SARS-CoV-2 infection](#)
 - Marisol Salgado-Albarrán
 - , Erick I. Navarro-Delgado
 - , Aylin Del Moral-Morales
 - , Nicolas Alcaraz
 - , Jan Baumbach
 - , Rodrigo González-Barrios
 - & Ernesto Soto-Reyes

npj Systems Biology and Applications (2021)

Comments

By submitting a comment you agree to abide by our [Terms](#) and [Community Guidelines](#). If you find something abusive or that does not comply with our terms or guidelines please flag it as inappropriate.

[Download PDF](#)

Advertisement

This article was downloaded by **calibre** from <https://www.nature.com/articles/s41586-021-03493-4>

| [Section menu](#) | [Main menu](#) |

Adjuvanting a subunit COVID-19 vaccine to induce protective immunity

[Download PDF](#)

- Article
- [Published: 19 April 2021](#)

Adjuvanting a subunit COVID-19 vaccine to induce protective immunity

- [Prabhu S. Arunachalam¹](#),
- [Alexandra C. Walls](#) [ORCID: orcid.org/0000-0002-9636-8330²](#),
- [Nadia Golden³](#),
- [Caroline Atyeo⁴](#),
- [Stephanie Fischinger](#) [ORCID: orcid.org/0000-0003-2307-3379⁴](#),
- [Chunfeng Li¹](#),
- [Pyone Aye³](#),
- [Mary Jane Navarro²](#),
- [Lilin Lai⁵](#),
- [Venkata Viswanadh Edara](#) [ORCID: orcid.org/0000-0001-9321-7839⁵](#),
- [Katharina Röltgen](#) [ORCID: orcid.org/0000-0002-1582-1720⁶](#),
- [Kenneth Rogers⁷](#),
- [Lisa Shirreff⁷](#),
- [Douglas E. Ferrell⁷](#),
- [Samuel Wrenn^{2,8}](#),
- [Deleah Pettie](#) [ORCID: orcid.org/0000-0002-5477-7195^{2,8}](#),
- [John C. Kraft](#) [ORCID: orcid.org/0000-0002-7931-7478^{2,8}](#),
- [Marcos C. Miranda^{2,8}](#),
- [Elizabeth Kepl](#) [ORCID: orcid.org/0000-0003-2835-003X^{2,8}](#),
- [Claire Sydeman^{2,8}](#),
- [Natalie Brunette^{2,8}](#),
- [Michael Murphy](#) [ORCID: orcid.org/0000-0002-8438-2653^{2,8}](#),
- [Brooke Fiala^{2,8}](#),
- [Lauren Carter^{2,8}](#),
- [Alexander G. White^{9,10}](#),
- [Meera Trisal¹](#),
- [Ching-Lin Hsieh¹¹](#),

- [Kasi Russell-Lodrigue](#) ORCID: [orcid.org/0000-0003-3719-0779³](https://orcid.org/0000-0003-3719-0779),
- [Christopher Monjure³](#),
- [Jason Dufour³](#),
- [Skye Spencer](#) ORCID: [orcid.org/0000-0001-9570-9634²](https://orcid.org/0000-0001-9570-9634),
- [Lara Doyle-Meyers³](#),
- [Rudolph P. Bohm³](#),
- [Nicholas J. Maness](#) ORCID: [orcid.org/0000-0002-9332-7891³](https://orcid.org/0000-0002-9332-7891),
- [Chad Roy](#) ORCID: [orcid.org/0000-0002-1710-6974³](https://orcid.org/0000-0002-1710-6974),
- [Jessica A. Plante¹²](#),
- [Kenneth S. Plante¹²](#),
- [Alex Zhu](#) ORCID: [orcid.org/0000-0003-1712-8310⁴](https://orcid.org/0000-0003-1712-8310),
- [Matthew J. Gorman⁴](#),
- [Sally Shin](#) ORCID: [orcid.org/0000-0002-9306-2264⁴](https://orcid.org/0000-0002-9306-2264),
- [Xiaoying Shen¹³](#),
- [Jane Fontenot⁷](#),
- [Shakti Gupta¹⁴](#),
- [Derek T. O'Hagan¹⁵](#),
- [Robbert Van Der Most¹⁶](#),
- [Rino Rappuoli](#) ORCID: [orcid.org/0000-0002-8827-254X¹⁷](https://orcid.org/0000-0002-8827-254X),
- [Robert L. Coffman¹⁸](#),
- [David Novack¹⁸](#),
- [Jason S. McLellan](#) ORCID: [orcid.org/0000-0003-3991-542X¹¹](https://orcid.org/0000-0003-3991-542X),
- [Shankar Subramaniam¹⁴](#),
- [David Montefiori¹³](#),
- [Scott D. Boyd](#) ORCID: [orcid.org/0000-0003-0963-044X⁶](https://orcid.org/0000-0003-0963-044X),
- [JoAnne L. Flynn](#) ORCID: [orcid.org/0000-0001-7874-8981⁹](https://orcid.org/0000-0001-7874-8981),
- [Galit Alter](#) ORCID: [orcid.org/0000-0002-7680-9215⁴](https://orcid.org/0000-0002-7680-9215),
- [Francois Villinger⁷](#),
- [Harry Kleanthous¹⁹](#),
- [Jay Rappaport^{3,20}](#),
- [Mehul S. Suthar⁵](#),
- [Neil P. King](#) ORCID: [orcid.org/0000-0002-2978-4692^{2,7}](https://orcid.org/0000-0002-2978-4692),
- [David Veesler](#) ORCID: [orcid.org/0000-0002-6019-8675²](https://orcid.org/0000-0002-6019-8675) &
- [Bali Pulendran](#) ORCID: [orcid.org/0000-0001-6517-4333^{1,6,21}](https://orcid.org/0000-0001-6517-4333)

[Nature](#) volume **594**, pages 253–258 (2021) [Cite this article](#)

- 18k Accesses
- 1 Citations

- 160 Altmetric
- [Metrics details](#)

Subjects

- [Adjuvants](#)
- [SARS-CoV-2](#)
- [Vaccines](#)

Abstract

The development of a portfolio of COVID-19 vaccines to vaccinate the global population remains an urgent public health imperative¹. Here we demonstrate the capacity of a subunit vaccine, comprising the SARS-CoV-2 spike protein receptor-binding domain displayed on an I53-50 protein nanoparticle scaffold (hereafter designated RBD–NP), to stimulate robust and durable neutralizing-antibody responses and protection against SARS-CoV-2 in rhesus macaques. We evaluated five adjuvants including Essai O/W 1849101, a squalene-in-water emulsion; AS03, an α -tocopherol-containing oil-in-water emulsion; AS37, a Toll-like receptor 7 (TLR7) agonist adsorbed to alum; CpG1018-alum, a TLR9 agonist formulated in alum; and alum. RBD–NP immunization with AS03, CpG1018-alum, AS37 or alum induced substantial neutralizing-antibody and CD4 T cell responses, and conferred protection against SARS-CoV-2 infection in the pharynges, nares and bronchoalveolar lavage. The neutralizing-antibody response to live virus was maintained up to 180 days after vaccination with RBD–NP in AS03 (RBD–NP-AS03), and correlated with protection from infection. RBD–NP immunization cross-neutralized the B.1.1.7 SARS-CoV-2 variant efficiently but showed a reduced response against the B.1.351 variant. RBD–NP-AS03 produced a 4.5-fold reduction in neutralization of B.1.351 whereas the group immunized with RBD–NP-AS37 produced a 16-fold reduction in neutralization of B.1.351, suggesting differences in the breadth of the neutralizing-antibody response induced by these adjuvants. Furthermore, RBD–NP-AS03 was as immunogenic as a prefusion-stabilized spike immunogen (HexaPro) with AS03 adjuvant. These data highlight the efficacy of the adjuvanted RBD–NP vaccine in promoting protective immunity against SARS-CoV-2 and have led to phase I/II clinical trials of this vaccine (NCT04742738 and NCT04750343).

[Download PDF](#)

Main

Subunit vaccines are among the safest and most widely used vaccines, and have been highly effective against a variety of infectious diseases, such as hepatitis B, diphtheria, pertussis, tetanus and shingles in diverse age groups². Therefore, the development of a safe and effective subunit vaccine against SARS-CoV-2 would represent an important step in controlling the COVID-19 pandemic. An essential component of subunit vaccines is the adjuvant, an immune-stimulatory agent that enhances the magnitude, quality and durability of the immune responses induced by vaccination, even with lower doses of antigen³. Alum, the most widely used adjuvant, has been used in billions of vaccine doses over the last century. During the past two decades, novel adjuvants have been developed including the α -tocopherol-containing squalene-based oil-in-water adjuvant AS03 and the TLR9 ligand CpG1018, which are included in licensed vaccines against pandemic influenza and hepatitis B, respectively. In particular, AS03 and CpG1018 are currently being developed as adjuvants for use in candidate subunit SARS-CoV-2 vaccines^{3,4}; however, their capacity to stimulate protective immunity against SARS-CoV-2 remains unknown. In this Article, we evaluate the use of AS03, CpG1018 formulated in alum (CpG-alum), squalene-in-water emulsion (O/W), AS37 and alum as adjuvants for a subunit vaccine in which 60 copies of the SARS-CoV-2 RBD are displayed in a highly immunogenic array using a computationally designed self-assembling protein nanoparticle (RBD–NP)⁵, and demonstrate protective immunity against SARS-CoV-2 in non-human primates.

Robust and durable neutralizing-antibody responses

To assess the immunogenicity and protective efficacy of RBD–NP vaccination with different adjuvants, we immunized 29 rhesus macaques with 25 μ g RBD antigen (71 μ g total RBD–NP immunogen) (Extended Data Fig. 1a–d) formulated with one of the five adjuvants: O/W, AS03, AS37, CpG-alum or alum (Extended Data Fig. 1e). Four additional monkeys were administered saline as a control (Extended Data Table 1). All immunizations were administered via the intramuscular route in forelimbs on days 0 and 21. Four weeks after the booster immunization, the monkeys were challenged with SARS-CoV-2 via the intratracheal–intranasal routes. Five of the ten monkeys immunized with RBD–NP–AS03 were not challenged, to enable longitudinal analysis of the durability of the immune responses.

Evaluation of binding-antibody responses showed that spike-specific IgG was detected 21 days after primary immunization in all vaccination groups and the response increased in magnitude after boosting (Fig. 1a). RBD–NP–AS03 induced the highest magnitude (geometric mean titre (GMT) half-maximal effective concentration (EC_{50}) 1:8,551) and RBD–NP–O/W induced the lowest (GMT EC_{50} 1:1,308) on day 42. The I53-50 nanoparticle scaffold also elicited an antibody response in all groups, which correlated with spike-specific antibody responses (Extended Data Fig. 1f,g).

Immunization with RBD–NP induced detectable neutralizing-antibody responses against a SARS-CoV-2 spike pseudotyped virus⁶ in most of the monkeys (except in the RBD–NP-O/W group after primary immunization), which significantly increased in all groups after the booster immunization (Extended Data Fig. [2a](#)). The neutralizing antibody titres in all groups except the RBD–NP-O/W group were higher than that of 4 samples from convalescent human individuals who had suffered mild-to-moderate COVID-19 (GMT 1:76) and NIBSC control human convalescent plasma (NIBSC code 20/130, neutralizing-antibody titre 1:241) (Extended Data Fig. [2b](#)) assayed simultaneously. Next, we measured neutralizing-antibody responses against authentic SARS-CoV-2 virus using focus reduction neutralization titre (FRNT) assay⁷, which was used to analyse the recent clinical trials of the Moderna mRNA SARS-CoV-2 vaccine^{8,9}. Consistent with the pseudovirus neutralizing-antibody titres, vaccinations with all adjuvants induced robust neutralizing-antibody titres against live virus after the secondary immunization, with the RBD–NP-AS03 group showing the highest titres (GMT 1:4,145, Fig. [1b](#)). There was a strong correlation between pseudovirus and live-virus neutralizing-antibody titres, as observed in previous studies^{10,11} (Extended Data Fig. [2c](#)). In addition, there was a robust induction of RBD–NP-specific plasmablast responses four days after secondary immunization (Extended Data Fig. [2d](#)), the magnitude of which correlated with the observed antibody responses (Extended Data Fig. [2e](#)).

Fig. 1: RBD–NP immunization induces robust antibody responses.

 [figure1](#)

a, SARS-CoV-2 spike-specific IgG titres in sera following immunization with RBD–NP and the indicated adjuvant measured by ELISA. Boxes represent median, and 25th and 75th percentiles and whiskers show the range. **b, c**, Serum neutralizing-antibody titres determined by authentic SARS-CoV-2 assay at indicated time points. The black

line represents the geometric mean of all data points and numbers show GMT on day 42 (**b**) and subsequent time points (**c**). IC₅₀, half-maximal inhibitory concentration. **d**, Neutralizing-antibody titres against live wild-type (circles) or B.1.1.7 or B.1.351 variant (squares) SARS-CoV-2 virus measured in serum on day 42. Numbers indicate GMT. **e**, The fold change in neutralizing-antibody titres for the B.1.351 variant versus wild-type SARS-CoV-2. **f**, Serum neutralizing-antibody titres against the live wild-type (circles) or B.1.351 variant (squares) viruses measured on day 42 or day 154. **a**, **b**, **e**, Two-sided Mann–Whitney rank-sum test. **c**, **f**, Two-sided Wilcoxon matched-pairs signed-rank test. Each symbol represents one monkey. $n = 4$ (O/W), 10 (AS03) and 5 (all other groups).

[Source data](#)

[Full size image](#)

To determine the durability of the neutralizing-antibody responses, we monitored 5 monkeys immunized with RBD–NP-AS03 without challenge for 6 months. The pseudovirus neutralizing-antibody titres declined moderately until day 126, but did not differ significantly between days 42 and 126 (Extended Data Fig. 2f). Neutralizing-antibody response measured against the authentic SARS-CoV-2 virus was durably maintained up to day 180 (Fig. 1c). The GMT titres decreased by 7.2-fold between days 42 and 180. Furthermore, we observed little to no reduction in the efficiency of blocking of ACE2 binding to the RBD—a correlate of neutralizing-antibody response¹²—by sera collected at these time points (Extended Data Fig. 2g). These results demonstrate that the RBD–NP-AS03 immunization induces potent and durable neutralizing-antibody responses.

Neutralization of variants of concern

SARS-CoV-2 variants of concern, B.1.1.7 and B.1.351, first identified in the United Kingdom and South Africa, respectively, have since been found to be circulating globally. We used live virus and pseudovirus neutralization assays to evaluate sera from the immunized monkeys against these variants. Neutralizing-antibody titres against the B.1.1.7 variant were similar to those against the wild-type virus (Fig. 1d, left, Extended Data Fig. 2h); by contrast, titres against the B.1.351 variant were considerably lower (Fig. 1d, right, Extended Data Table 2), as seen in vaccinated humans^{13,14}. Of note, there was a greater reduction of titre in the RBD–NP-AS37 group (median of 16-fold) compared with RBD–NP-AS03 (4.5-fold) and other adjuvant groups (Fig. 1e). These data suggest that the adjuvants not only enhance immunogenicity, but also that different adjuvants vary in their potential to elicit neutralizing antibodies that provide a greater breadth of neutralization. Furthermore, the neutralizing-antibody response against the B.1.351 variant was as durable as that

of the responses to the wild-type virus in the RBD–NP-AS03 durability group (Fig. 1e).

Induction of CD4 T cell responses

RBD–NP immunization resulted in an antigen-specific CD4 T cell response but limited CD8 T cell response following ex vivo stimulation of peripheral blood mononuclear cells (PBMCs) with an overlapping peptide pool. RBD-specific CD4 responses were significantly enhanced only after the secondary immunization and were highest in the RBD–NP-AS03 and RBD–NP-CpG-alum groups (Fig. 2a,b). The responses were dominated by IL-2- and TNF-secreting cells (Extended Data Fig. 3a), which remained detectable at day 42 (3 weeks after secondary immunization). There was a low but detectable IL-4 response in both the RBD–NP-AS03 and RBD–NP-CpG-alum groups that peaked on day 28 but declined to near-baseline levels by day 42 (Fig. 2b). Whereas 75% of monkeys in the RBD–NP-alum group and 50% of those in the RBD–NP-O/W group showed induction of RBD-specific CD4 T cells, RBD–NP-AS37 induced a weak T cell response, less than that of the alum group, despite inducing potent antibody responses in all of the monkeys. This is in contrast to findings in mice with the same antigen (L. Grigoryan et al., manuscript in preparation) and in non-human primates with an HIV antigen¹⁵. However, a direct comparison with the alum group is confounded by the larger amount of aluminium hydroxide in the alum group compared with the RBD–NP-AS37 group (Extended Data Fig. 1e). We assessed the polyfunctional profile of antigen-specific CD4 T cells expressing IL-2, IFN γ , IL-4 and TNF (Extended Data Fig. 3b). Although IL-2 $^+$, TNF $^+$ and IL-2 $^+$ TNF $^+$ cells formed the majority (around 70%) in all adjuvant groups, differences between the groups were apparent. RBD–NP-AS03 elicited similar proportions of T helper 1 (T_H1) and T_H2 CD4 T cells, a balanced T_H1 – T_H2 profile. RBD–NP-CpG-alum showed a slightly higher T_H1 -type response, whereas RBD–NP-alum showed a higher T_H2 -type response. We further extended our analyses to measure IL-21 and CD154, markers of circulating T follicular helper (T_{FH})-like cells for their critical role in germinal centre formation and generation of durable B cell responses. We observed detectable IL-21 responses in the RBD–NP-AS03 and RBD–NP-CpG-alum groups (Fig. 2c). All cells secreting IL-21 were CD154 $^+$, and the IL-21 $^+$ CD154 $^+$ double-positive cells were significantly higher in the RBD–NP-AS03 and RBD–NP-CpG-alum groups compared with the RBD–NP-AS37 group (Fig. 2d).

Fig. 2: Cell-mediated immune responses to RBD–NP immunization.

 **figure2**

a, b, RBD-specific CD4 T cell responses measured in blood at indicated time points. CD4 T cells secreting IL-2, IFN γ , or TNF are plotted as T_H1-type responses (**a**) and IL-4-producing CD4 T cells are shown as T_H2-type responses (**b**). **c**, Flow cytometry plots showing expression of IL-21 and CD154 after ex vivo stimulation with DMSO (no peptide, top) or an overlapping peptide pool spanning the SARS-CoV-2 RBD (bottom). **d**, RBD-specific CD154 $^{+}$ and CD154 $^{+}$ IL-21 $^{+}$ CD4 T cell responses measured in blood at day 28 after inoculation. Boxes show median, 25th and 75th percentiles and whiskers show the range. **a, b**, Two-sided Wilcoxon matched-pairs signed-rank test. **d**, Two-sided Mann–Whitney rank-sum test. * $P < 0.05$, ** $P < 0.01$. Each symbol represents one monkey. $n = 4$ (O/W), 10 (AS03) and 5 (all other groups).

[Source data](#)

[Full size image](#)

We also stimulated PBMCs with a peptide pool spanning the nanoparticle component sequences I53-50A and I53-50B to determine whether RBD–NP immunization induces T cells targeting the nanoparticle scaffold. We observed a significant proportion of CD4 T cells targeting the I53-50 subunits with a response pattern similar to that of the RBD-specific T cells (Extended Data Fig. 3c). The frequencies of nanoparticle-specific CD4 T cells were about threefold higher than those of RBD-specific CD4 T cells (Extended Data Fig. 3d), an observation consistent with the RBD making up approximately one-third of the total peptidic mass of the immunogen.

Protection against SARS-CoV-2 challenge

To assess the protective efficacy, we challenged the monkeys four weeks after secondary immunization with SARS-CoV-2 via the intratracheal and intranasal routes. Two days after challenge, 4 out of 4 control monkeys had a subgenomic viral load (3.1×10^5 to 3.5×10^8 copies of the virus) in the pharyngeal and the nasal compartments. By day 7, the viral load had decreased to baseline levels, consistent with previous studies^{16,17}. All adjuvanted groups, except RBD–NP-O/W, afforded protection from infection (Fig. 3a, Extended Data Fig. 4a). None of the five monkeys in the RBD–NP-AS03 group had detectable viral RNA in pharyngeal swabs at any time and one monkey had a viral load in nasal swabs, at a level approximately 1,000-fold lower than the median in control monkeys (2.2×10^4 versus 2.5×10^7 viral copies). By contrast, viral RNA was detectable in pharyngeal and nasal swabs of all monkeys in the RBD–NP-O/W group, albeit at lower levels than the control group. Only one out of five monkeys in the RBD–NP-CpG-alum group had detectable viral RNA in pharyngeal or nasal swabs. The RBD–NP-AS37 group and the RBD–NP-alum group also showed undetectable viral RNA in both compartments in 3 of the 5 monkeys. We measured the subgenomic viral RNA in bronchoalveolar lavage (BAL) fluid to assess protection in the lung. We used a more sensitive PCR assay to measure the product of the *N* gene¹⁸, as we found only two control monkeys with a positive viral load in the BAL fluid using E subgenomic RNA (sgRNA). Two days after the challenge, all 4 of the 4 control monkeys showed a viral load in the range of 10^4 – 10^6 viral copies. By contrast, none of the monkeys in the vaccinated groups (except one in the RBD–NP-O/W group) showed any detectable virus, suggesting effective protection in the lower respiratory tracts of all vaccinated groups, including the RBD–NP-O/W group. There were no signs of clinical disease in any monkeys, whether or not they had been vaccinated (Extended Data Fig. 4b); however, the control monkeys—but not the vaccinated monkeys—responded with an increase in neutralizing-antibody titres (Extended Data Fig. 4c), consistent with reports that SARS-CoV-2 infection of rhesus macaques results in mild disease^{19,20}.

Fig. 3: Protection against SARS-CoV-2 challenge.

 **figure3**

a, b, SARS-CoV-2 viral load in nares (**a**) and BAL fluid (**b**) measured using subgenomic PCR. The numbers shown on the plots denote number of infected monkeys/total number of monkeys within each group. Statistically significant differences compared with the no-vaccine control group by two-sided Mann–Whitney rank-sum test. * $P = 0.01$, ** $P = 0.008$. Each symbol represents a monkey. $n = 4$ for control and O/W, 5 for all other groups.

[Source data](#)

[Full size image](#)

Vaccine-associated enhanced respiratory disease (VAERD) has previously been described for respiratory infections with respiratory syncytial virus and SARS-CoV^{21,22}. We evaluated inflammation in the lung tissues of a subset of the tested monkeys using positron emission tomography with computed tomography (PET–CT) on the day of the challenge and four to five days after challenge. Of the 6 monkeys we evaluated (2 unvaccinated, 2 from the AS03 group and 2 from the CpG-alum group, selected randomly), we found inflammation in both control monkeys on day 4 compared with baseline, as measured by enhanced 2-deoxy-2-[¹⁸F]fluoroglucose (FDG) uptake. By contrast, only one of the four vaccinated monkeys showed FDG uptake, to a much lower extent than the control monkeys (Extended Data Fig. [4d, e](#)).

Additionally, we performed a comprehensive analysis of cytokine responses in all the monkeys one week after challenge, and observed no increase in inflammation in the lungs of the vaccinated monkeys (Extended Data Fig. [5a, b](#)), whereas there were increases of cytokines such as IL-6, IL-8, IFN γ and MCP4 in the lungs of control monkeys (Extended Data Fig. [5c](#)). These data are consistent with an absence of VAERD in these monkeys. However, these results should be interpreted with caution, as VAERD is expected to occur as immunity decreases after immunization.

Immune correlates of protection

Next, we correlated humoral and cellular immune responses measured at peak time points (day 42 for antibody responses and day 28 for T cell responses) with the viral load (nasal or pharyngeal) to determine the putative correlates of protection in an unbiased approach. Neutralizing titres for both live virus and pseudovirus emerged as the top statistically significant correlates of protection (Fig. [4](#), Extended Data Fig. [6a, b](#)) in both nasal and pharyngeal compartments. Of note, the nanoparticle-specific IL-2 $^{+}$ TNF $^{+}$ CD4 T cell response also emerged as a significant correlate of protection in both compartments (Extended Data Fig. [6a–c](#)), the frequencies of which positively correlated with neutralizing-antibody titres (Extended Data Fig. [6d](#)). This is consistent with the possibility that nanoparticle-specific CD4 T cells could offer T cell help to RBD-specific B cells.

Fig. 4: Immune correlates of protection.



Spearman's correlation between peak nasal viral load and neutralizing and binding antibody responses, the top three parameters from the correlates analysis shown in Extended Data Fig. [6a](#). Shaded areas represent 95% confidence intervals. Each symbol represents a monkey. $n = 4$ (control and O/W) and 5 (all other groups).

[Source data](#)

[Full size image](#)

In addition to characterizing neutralizing-antibody and T cell responses to vaccination, we sought to understand the humoral functional profile elicited by each adjuvant. Vaccines rapidly induced an increase in different anti-spike antibody isotypes (Extended Data Fig. 7a–c), Fc-receptor-binding (Extended Data Fig. 7d) and antibody-dependent neutrophil phagocytosis (ADNP) (Extended Data Fig. 7e) at day 21 and day 42. To understand how differences in the humoral response could lead to viral breakthrough, we performed a partial least-squares discriminant analysis (PLSDA) on the antibody features measured at day 42, using least absolute shrinkage and selection operator (LASSO) to select features to prevent overfitting (Extended Data Fig. 7f). The PLSDA analysis showed separation between protected and infected monkeys (Extended Data Fig. 7f), marked by an enrichment in IgA, FcR3A and ADNP in the protected monkeys (Extended Data Fig. 7g). Next, we determined the correlation of each measured antibody feature and the peak nasal and pharyngeal viral load to further dissect the antibody features that provide protection against viral break-through. Although the neutralizing-antibody response still represented the strongest correlate of protection, we observed additional functional features, including FcR binding and ADNP, that were negatively correlated with nasal or pharyngeal viral loads (Extended Data Fig. 7h). These data demonstrated an additive role for functional antibody responses in protection. Furthermore, each adjuvant group mounted a distinct profile of antibody response that correlated with protection against the virus (Extended Data Fig. 7i).

RBD–NP versus prefusion spike HexaPro

The data described thus far demonstrate that RBD–NP immunogen when adjuvanted with AS03, AS37, CpG-alum or alum induces robust protective immunity. Next, we compared the immunogenicity of the RBD–NP immunogen to that of HexaPro, a highly stable variant of the prefusion spike trimer²³, in either soluble form or attached to a nanoparticle (HexaPro–NP, with 20 HexaPro trimers displayed on the I53-50 nanoparticle). We immunized three cohorts of rhesus macaques with RBD–NP, soluble HexaPro or HexaPro–NP, each with AS03 as adjuvant (Extended Data Fig. 8a, Extended Data Table 1). The RBD–NP-AS03 immunization induced neutralizing-antibody titres consistent with those described in Fig. 1, with a detectable titre on day 21 and a robust increase on day 42. Compared with RBD–NP immunization, immunization with soluble HexaPro or HexaPro–NP induced notably higher neutralizing-antibody titres after a single immunization. However, the neutralizing-antibody titres on day 42 were similar in all three groups (Fig. 5a, Extended Data Fig. 8b). Furthermore, HexaPro-AS03 immunization also elicited cross-reactive

neutralizing responses against the SARS-CoV-2 B.1.1.7 and B.1.351 variants (Fig. 5b), similar to the response to RBD–NP immunization (Fig. 1d). Together, these data indicate that the RBD–NP is as potent an immunogen as the highly stable HexaPro, consistent with previous observations that the vast majority of the neutralizing response targets the RBD¹². Moreover, these data also suggest that AS03 may be a suitable adjuvant for clinical use with various forms of the spike protein.

Fig. 5: RBD–NP or HexaPro immunization with AS03 elicit similar neutralizing-antibody responses.

 figure5

a, Neutralizing-antibody responses in serum on day 21 and day 42 against SARS-CoV-2 virus. The box plot shows median, 25th and 75th percentiles and the whiskers show the range. Numbers indicate GMT. Statistically significant differences between two groups by two-sided Mann–Whitney rank-sum test. * $P = 0.02$, ** $P = 0.006$. Open circles denote monkeys from the earlier study shown in Fig. 1. **b**, Neutralizing-antibody titres measured against live wild-type (circles) or B.1.1.7 or B.1.351 variants (squares) in sera collected on day 42 from monkeys that received soluble HexaPro. Each symbol represents one monkey. $n = 13$ for RBD–NP and 6 for soluble HexaPro and HexaPro–NP groups.

[Source data](#)

[Full size image](#)

Discussion

Despite the deployment of several million doses of vaccines worldwide^{8,24,25,26}, only a small fraction of the global population has been vaccinated to date. There remains a

stark gap between the vaccination rates in different countries, with many developing countries yet to report a single dose. Furthermore, specific subpopulations such as infants and the elderly could benefit from the use of adjuvanted subunit vaccine platforms with a demonstrable history of safety and efficacy in such populations^{27,28}. Here, we have evaluated five adjuvants, and all five induced substantial neutralizing-antibody titres. O/W induced relatively lower neutralizing titres than the other adjuvants; although O/W is an oil-in-water emulsion similar to AS03, it does not contain α -tocopherol, which is thought to be required for the potent antibody responses observed with AS03²⁹. Notably, there were also potent CD4 T cell responses specific to the nanoparticle scaffold.

The different adjuvants produced varying levels of protection against SARS-CoV-2. The neutralizing response was the primary correlate of protection, as previously seen^{10,16}. However, the frequency of nanoparticle-specific IL-2⁺TNF⁺ cells were also correlated with protection and neutralizing-antibody titres (Extended Data Fig. 6c,d). Thus, these nanoparticle-scaffold-specific CD4 T cells may provide T cell help to RBD-specific B cells, thereby promoting B cell responses³⁰. In addition, the T cells could provide a complementary mechanism of protection that synergizes with the neutralizing-antibody response³¹. The adjuvants also induced different T_H1–T_H2 profiles, with RBD–NP–AS03 stimulating a mixed T_H1–T_H2 response, whereas RBD–NP–CpG-alum and RBD–NP–AS37 stimulated a T_H1-biased response and RBD–NP–alum and RBD–NP–O/W induced T_H2-biased responses. We saw no evidence of VAERD in the challenged monkeys.

In addition to evaluating clinically relevant adjuvants, we also compared the immunogenicity of RBD and HexaPro. Our results demonstrate that the RBD–NP immunogen was as potent as HexaPro in inducing neutralizing-antibody titres. Whether differences in immunogenicity become apparent at lower doses of antigen warrants further investigation. Nevertheless, these results demonstrate that AS03 is a potent adjuvant when used with either RBD–NP or HexaPro. It will be of particular interest to the field to evaluate whether the neutralizing responses elicited by RBD–NP or HexaPro-based immunogens induce a broad response not only against the emerging SARS-CoV-2 variants, but also against other coronaviruses.

In summary, this study represents a comprehensive immunological benchmarking of clinically relevant adjuvants for their capacity to enhance the protective immunity of a SARS-CoV-2 vaccine. On the basis of these results, two phase I/II clinical trials (NCT04742738 and NCT04750343) have been initiated by SK Bioscience in collaboration with Coalition for Epidemic Preparedness Innovations (CEPI) for the development of COVID-19 vaccines.

Methods

No statistical methods were used to predetermine sample size. The experiments were not randomized. The investigators were not blinded to allocation during experiments and outcome assessment.

Animal subjects and experimentation

Thirty-three male rhesus macaques (*Macaca mulatta*) of Indian origin, aged 3–9 years, were assigned to the study (Extended Data Table 1). The animals were distributed between the groups such that the age and weight distribution were comparable across the groups. Animals were housed and maintained as per National Institutes of Health (NIH) guidelines at the New Iberia Research Center (NIRC) of the University of Louisiana at Lafayette in accordance with the rules and regulations of the Committee on the Care and Use of Laboratory Animal Resources. The entire study (protocol 2020-8808-15) was reviewed and approved by the University of Louisiana at Lafayette Institutional Animal Care and Use Committee (IACUC). All animals were negative for simian immunodeficiency virus, simian T cell leukaemia virus and simian retrovirus. For the challenge, the animals were transferred to the Regional Biosafety Level 3 facility at the Tulane National Primate Research Center, where the study was reviewed and approved by the Tulane University IACUC (protocol 3918).

RBD-16GS-I53-50 nanoparticle immunogen production

Nanoparticle immunogen components and nanoparticles were produced as previously described in detail⁵, with the exception that the nanoparticle was in a buffer containing 50 mM Tris pH 8, 150 mM NaCl, 100 mM l-arginine and 5% sucrose.

Nanoparticle biochemical characterization

Dynamic light scattering, negative stain electron microscopy, and maACE2-Fc and CR3022 IgG biolayer interferometry were performed as described previously⁵.

Adjuvant formulations and immunization

Essai O/W 1849101, a squalene-in-water emulsion (O/W) was provided by Seppic. For each dose, RBD–NP was diluted to 50 µg ml⁻¹ (RBD component) in 250 µl of phosphate buffered saline (PBS) with 150 mM NaCl and mixed with an equal volume of O/W. The dose of O/W was 50% (v/v) AS03 and AS37 were provided by GSK Vaccines. AS03 is an oil-in-water emulsion that contains 11.86 mg α-tocopherol, 10.69 mg squalene, and 4.86 mg polysorbate 80 (Tween-80) in PBS, whereas AS37 is a

TLR-7 agonist ($200 \mu\text{g ml}^{-1}$) adsorbed to aluminium hydroxide (2 mg ml^{-1}). For each dose, RBD–NP was diluted to $50 \mu\text{g ml}^{-1}$ (RBD component) in $250 \mu\text{l}$ of Tris-buffered saline (TBS) and mixed with an equal volume of AS03 or AS37. The dose of AS03 was 50% (v/v) (equivalent of one human dose), AS37 included $50 \mu\text{g}$ TLR-7 agonist and 0.5 mg aluminium hydroxide. CpG 1018 was provided by Dynavax Technologies at a concentration of 12 mg ml^{-1} . Alum (Alhydrogel 2%) was purchased from Croda Healthcare (batch 0001610348). Of note, we used CpG-alum rather than CpG 1018 (no alum), which is used in Heplisav-B. For each dose of CpG-alum, $25 \mu\text{g}$ antigen (RBD component) in TBS was mixed with 0.75 mg alum and incubated on ice for 30 min. After 30 min of incubation, 1.5 mg of CpG 1018 was added and mixed rapidly. Each dose contained 1.5 mg CpG 1018 and 0.75 mg alum. For each dose of alum, $25 \mu\text{g}$ antigen (RBD component) in TBS was mixed with 0.75 mg alum, matching the concentration of alum in the CpG-alum formulation, and incubated on ice for 30 min. Soluble HexaPro or HexaPro–NP used in the experiment to compare RBD–NP versus HexapPro (described in Fig. 5) was diluted to $50 \mu\text{g ml}^{-1}$ in $250 \mu\text{l}$ TBS and mixed with an equal volume of AS03. All immunizations were administered via the intramuscular route in right forelimbs. The volume of each dose was 0.5 ml .

Anti-spike binding ELISA

SARS-CoV-2 spike protein was produced in HEK 293T cells (Atum). Ninety-six-well Corning Costar high-binding plates (Thermo Fisher Scientific) were coated with SARS-CoV-2 spike protein in PBS at a concentration of $0.2 \mu\text{g}$ per well overnight at 4°C . On the next day, wells were washed 3 times with PBS, 0.1% Tween 20 (PBS-T) and blocked with PBS-T containing 3% non-fat milk powder for 1 h at room temperature. Wells were then incubated with plasma samples from non-human primates at different dilutions starting at 1:100 in PBS-T containing 1% non-fat milk for 1 h at 37°C . After washing 3 times with PBS-T, horseradish peroxidase (HRP)-conjugated goat anti-monkey IgG (γ -chain specific, Alpha Diagnostics, 1:4,000 dilution), in PBS-T containing 1% non-fat milk was added and incubated for 1 h at room temperature. Wells were washed 3 times with PBS-T before addition of 3,3',5,5'-tetramethylbenzidine (TMB) substrate solution. The reaction was stopped after 12 min by addition of 0.16 M sulfuric acid. The optical density (OD) at 450 nanometers was measured with a Tecan Infinite M Nano Plus microplate reader.

Anti-I53-50 ELISA

The protocol was adapted from Tiller et al.³². In brief, recombinant I53-50 protein nanoparticles, SARS-CoV-2 S2P trimers, or goat anti-human IgG (Jackson ImmunoResearch, 109-005-044) were immobilized on 96-well Nunc MaxiSorp (Thermo Fisher Scientific) plates ($2 \mu\text{g ml}^{-1}$, $50 \mu\text{l}$ per well). After 1 h incubation at

room temperature, plates were blocked with 200 µl TBS, 2% (w/v) BSA and 0.05% (v/v) Tween 20 for 1 h. Plates were washed 3 times in TBST with a plate washer (BioTek), and 50 µl of 1:5 serial dilutions starting at 1:100 of non-human primate sera in TBST incubated for 1 h in wells with I53-50 or spike protein. In wells with anti-human IgG capture antibody, human IgG control (SinoBiological, HG1K) was serially diluted from 0.5–500 ng ml⁻¹ in TBST in triplicate and 50 µl of each dilution incubated for 1 h. Plates were washed 3 times in TBST, then HRP-conjugated goat anti-monkey IgG (Alpha Diagnostics, 70021) was diluted 1:5,000 in 2% BSA in TBST and 50 µl was incubated in each well for 30 min. Plates were washed 3 times in TBST and 100 µl TMB (SeraCare) was added to each well for 2 min. The reaction was quenched by adding 100 µl of 1 N HCl. Plates were immediately read at 450 nm on a SpectraMax M5 plate reader (Molecular Devices). The data were plotted with GraphPad Prism. A sigmoidal 4PL curve was fit with x being log (concentration) to determine the EC₅₀ values. A logarithmic equation fit to the linear portion of the sigmoidal curve of the human IgG control was used to calculate concentration (in mg ml⁻¹) of IgG in sera for anti-I53-50 and anti-spike titres. All steps were performed at ambient temperature.

Pseudovirus production and neutralization assay

Pseudovirus production has been described in Walls et al.⁶. In brief, MLV-based SARS-CoV-2 spike pseudotyped viruses were prepared as previously^{6,33,34} except that the SARS-CoV-2 spike construct contained the D614G mutation and a truncation of the C-terminal 21 residues^{11,35}.

For neutralization assays, HEK-hACE2 cells were cultured in DMEM with 10% FBS (Hyclone) and 1% penicillin-streptomycin with 8% CO₂ in a 37 °C incubator on 96 well plates coated with poly-l-lysine (Sigma). To coat plates, 40 µl poly-l-lysine (Sigma) was incubated with rotation for 5 min. Poly-l-lysine was removed, plates were dried for 5 min then washed once with water before plating cells. The following day, cells were checked to be at 80% confluence. In a half-area 96-well plate a 1:3 serial dilution of sera was made in DMEM in 22 µl final volume. Twenty-two microlitres of pseudovirus was then added to the serial dilution and incubated at room temperature for 30–60 min at room temperature. The medium on the HEK-hACE2 plate was removed and 40 µl of the sera–virus mixture was added to the cells and incubated for 2 h at 37 °C with 8% CO₂. Following incubation, 40 µl 20% FBS and 2% PenStrep containing DMEM was added to the cells. Following 48–72 h infection, One-Glo-EX (Promega) was added to the cells in half culturing volume (40 µl added) and incubated in the dark for 5 min before reading on a Varioskan LUX plate reader (Thermo Fisher Scientific). Measurements were performed on all sera samples from each group in at least duplicates. Relative luciferase units were plotted and normalized in Prism

(GraphPad) using a zero value of cells alone and a 100% value of 1:2 virus alone. Nonlinear regression of log(inhibitor) versus normalized response was used to determine IC₅₀ values from curve fits. The human convalescent samples assayed in parallel were obtained from individuals aged 37–67 years, all of whom had mild-to-moderate disease with fever, cough, chills, shivering, runny nose, muscle aches, trouble breathing and fatigue as symptoms. The use of samples was approved by the University of Washington Human Subjects Division Institutional Review Board (IRB00009810).

FRNT assay

Neutralization assays with authentic SARS-CoV-2 virus were performed as previously described^{[36](#)}. Plasma or serum were serially diluted (threefold) in serum-free Dulbecco's modified Eagle's medium (DMEM) in duplicate wells and incubated with 100–200 focus forming units (FFU) infectious clone-derived SARS-CoV-2-mNG virus^{[37](#)} at 37 °C for 1 h. The antibody–virus mixture was added to VeroE6 cell (C1008, ATCC, CRL-1586) monolayers seeded in 96-well blackout plates and incubated at 37 °C for 1 h. After incubation, the inoculum was removed and replaced with pre-warmed complete DMEM containing 0.85% methylcellulose. Plates were incubated at 37 °C for 24 h. After 24 h, methylcellulose overlay was removed, cells were washed twice with PBS and fixed with 2% paraformaldehyde in PBS for 30 min at room temperature. Following fixation, plates were washed twice with PBS and foci were visualized on a fluorescence ELISPOT reader (CTL ImmunoSpot S6 Universal Analyzer) and counted using Viridot^{[38](#)}. The neutralization titres were calculated as follows: 1 – (mean number of foci in the presence of sera/number of foci at the highest dilution of the respective serum sample). Each specimen was tested in two independent assays performed at different times. The FRNT-mNG₅₀ titres were interpolated using a 4-parameter nonlinear regression in GraphPad Prism 8.4.3. Samples with an FRNT-mNG₅₀ value that was below the limit of detection were plotted at 10. For these samples, this value was used in fold-reduction calculations.

ACE2 blocking assay

Antibodies blocking the binding of SARS-CoV-2 spike RBD to ACE2 were detected with a V-PLEX SARS-CoV-2 Panel 2 (ACE2) Kit (Meso Scale Diagnostics) according to the manufacturer's instructions. Serum samples from non-human primates were analysed in duplicate at a dilution of 1:100 and per cent inhibition was calculated as $(1 - \text{average sample ECL signal}/\text{average ECL signal of calibrator } 7) \times 100$.

Pseudovirus neutralization assay against UK B.1.1.7 variant

A neutralization assay comparing the ability of sera from vaccinated animals to neutralize wild-type (with D614G in spike) SARS-CoV-2 versus the B.1.1.7 variant were performed using a pseudotyped virus-neutralization assay as previously reported³⁹, with minor modifications. In brief, mutations were introduced into a plasmid expressing codon-optimized spike of the Wuhan-1 strain that contains the D614G mutation using site-directed mutagenesis. Pseudovirions were produced in HEK 293T/17 cells by co-transfection of a lentivirus backbone plasmid, a spike-expressing plasmid, and a firefly luciferase reporter gene plasmid. Pseudotyped viruses were titrated in 293T/ACE2.MF cells for median tissue culture infectious dose (TCID₅₀) and used for neutralization assay. Viruses were incubated with serial diluted serum samples at 37 °C for 1 h, and subsequently added to cells and incubated for 66–72 h. Luminescence was measured using a GloMax Navigator luminometer (Promega). Neutralization titres are the inhibitory dilution (ID) of serum samples at which relative luminescence unit (RLU) readings were reduced by either 50% (ID₅₀) or 80% (ID₈₀) compared to virus control wells after subtraction of background RLUs.

FRNT assay against the variants of concern

The wild-type infectious clone SARS-CoV-2 (icSARS-CoV-2), derived from the 2019-nCoV/USA_WA1/2020 strain, was propagated in VeroE6 cells (ATCC) and sequenced³⁷. The B.1.1.7 variant (SARS-CoV-2/human/USA/CA_CDC_5574/2020) was isolated from a residual nasopharyngeal swab collected from a patient in San Diego, CA, propagated in Vero cells and sequenced. The RSA B.1.351 variant was isolated as previously described⁴⁰. Our laboratory plaque-isolated the virus on VeroE6 cells followed by a single round of propagation on VeroE6 cells (multiplicity of infection 0.05), aliquoted to generate a working stock and sequenced. Viral titres were determined by focus-forming assay on VeroE6 cells. Viral stocks were stored at –80 °C until use.

FRNT assays were performed as previously described for the wild-type FRNT assay. The assay with each variant was performed simultaneously with wild-type controls. The samples were diluted 3-fold in 8 serial dilutions using DMEM in duplicates with an initial dilution of 1:10 in a total volume of 60 µl. Serially diluted samples were incubated with an equal volume of wild-type or variant SARS-CoV-2 (100–200 foci per well) at 37 °C for 1 h in a round-bottomed 96-well culture plate. The antibody–virus mixture was then added to Vero cells and incubated at 37 °C for 1 h. After incubation, the antibody–virus mixture was removed and 100 µl of prewarmed 0.85% overlay was added to each well. Plates were incubated at 37 °C for 24 h. After 24 h, methylcellulose overlay was removed, and cells were washed 3 times with PBS. Cells were then fixed with 2% paraformaldehyde in PBS (Electron Microscopy Sciences) for 30 min. Following fixation, plates were washed twice with PBS and 100 µl of permeabilization buffer (0.1% BSA, saponin in PBS), was added to the fixed Vero

cells for 20 min. Cells were incubated with an anti-SARS-CoV spike primary antibody directly conjugated to biotin (CR3022-biotin) for 1 h at room temperature. Next, the cells were washed three times in PBS and avidin–HRP was added for 1 h at room temperature followed by three washes in PBS. Foci were visualized using TrueBlue HRP substrate (KPL, 5510-0050) and imaged on an ELISPOT reader (CTL).

Intracellular cytokine staining assay

Antigen-specific T cell responses were measured using the intracellular cytokine staining assay. Live frozen PBMCs were revived, counted and resuspended at a density of 10^6 live cells per ml in complete RPMI (RPMI supplemented with 10% FBS and antibiotics). The cells were rested overnight at 37 °C in a CO₂ incubator.

Next morning, the cells were counted again, resuspended at a density of 15×10^6 per ml in complete RPMI and 100 µl of cell suspension containing 1.5×10^6 cells was added to each well of a 96-well round-bottomed tissue culture plate. Each sample was treated with three conditions, no stimulation, a peptide pool spanning the RBD region of spike at a concentration of 1.2 µg ml⁻¹ of each peptide and a peptide pool spanning the I53-50A, and I53-50B components of the nanoparticle scaffold (1.2 µg ml⁻¹ of each peptide) in the presence of 1 µg ml⁻¹ of anti-CD28 (clone CD28.2, BD Biosciences) and anti-CD49d (clone 9F10, BD Biosciences) as well as anti-CXCR3 and anti-CXCR5. The peptides were custom synthesized to 90% purity using GenScript, a commercial vendor. All samples contained 0.5% (v/v) DMSO in total volume of 200 µl per well. The samples were incubated at 37 °C in CO₂ incubators for 2 h before addition of 10 µg ml⁻¹ brefeldin A. The cells were incubated for an additional 4 h. The cells were washed with PBS and stained with Zombie UV fixable viability dye (Biolegend). The cells were washed with PBS containing 5% FCS, before the addition of surface antibody cocktail. The cells were stained for 20 min at 4 °C in 100 µl volume. Subsequently, the cells were washed, fixed and permeabilized with cytofix/cytoperm buffer (BD Biosciences) for 20 min. The permeabilized cells were stained with intracellular cytokine staining antibodies for 20 min at room temperature in 1× perm/wash buffer (BD Biosciences). Cells were then washed twice with perm/wash buffer and once with staining buffer before acquisition using the BD Symphony Flow Cytometer and the associated BD FACS Diva software. All flow cytometry data were analysed using Flowjo software v10 (TreeStar Inc.).

Viral challenge

Animals were inoculated via the intratracheal and intranasal routes with a total of 3.2×10^6 plaque-forming units of SARS-CoV-2, isolate USA WA1/2020 (accession: MN985325). The virus stock was generated by expansion of a seed stock on Vero E6 cells and titred by plaque assay on Vero E6 cells. It was deep sequenced and found to

contain no polymorphisms at greater than 5% of reads relative to the original patient isolate. The furin cleavage site, a site with frequent culture adaptation in Vero E6 cells, harboured no polymorphisms at greater than 1% of sequence reads in this stock.

Sampling of nares and pharynges

The monkeys were anaesthetized and placed in dorsal recumbency or a chair designed to maintain an upright posture. The pharynx was visualized using a laryngoscope. A sterile swab was gently rubbed and rolled across the lateral surfaces of the pharynx for approximately 5 s, including the tonsillar fossa and posterior pharynx. Care was taken to avoid touching the soft palate, uvula, buccal mucosa, tongue or lips. After all pertinent surfaces had been sampled, the swab was removed and placed into either culture medium or an appropriate container for transport. The pharyngeal swabs were done before the nasal swabs to reduce blood contamination from the nasal cavity into the pharyngeal area.

Sterile swabs were gently inserted into the nares. Once inserted, the sponge or swab was rotated several times within the cavity or region and immediately withdrawn.

BAL collection and processing

The animals were anaesthetized using Telazol and placed in a chair designed specifically for the proper positioning for BAL procedures. A local anaesthetic (2% lidocaine) may be applied to the larynx at the discretion of the veterinarian. A laryngoscope was used to visualize the epiglottis and larynx. A feeding tube was carefully introduced into the trachea after which the stylet was removed. The tube was advanced further into the trachea until slight resistance was encountered. The tube was slightly retracted and the syringe attached. Aliquots of warmed normal saline were instilled into the bronchus. The saline was aspirated between each lavage before a new aliquot was instilled. When the procedure was complete, the monkey was placed in right lateral recumbency. The monkey was carefully monitored, with observation of the heart rate, respiratory rate and effort, and mucous membrane colour. An oxygen facemask may be used following the procedure at the discretion of the veterinarian. The monkey was returned to its cage, positioned on the cage floor in right lateral recumbency and was monitored closely until recovery is complete.

The BAL samples were filtered twice via 100- μ l strainers and collected in 50-ml centrifuge tubes. The samples were centrifuged at 300g for 10 min at 4 °C. The supernatant was transferred into new tubes, aliquoted and stored at –80 °C until RNA isolation. The cells were washed, lysed for red-blood cells using ammonium-chloride-potassium (ACK) lysis buffer and live-frozen in 90% FBS with 10% DMSO.

Viral load

Quantitative PCR with reverse transcription (RT–qPCR) was performed as described previously⁴¹. RT–qPCR for the subgenomic (sg) RNA encoding the envelope (E) protein was performed as described⁴² and RT–qPCR for the sgRNA encoding the nucleocapsid (N) protein was performed using the same cycling conditions as used for the E sgRNA using an unpublished assay provided by D. Hartigan-O'Connor and J. Dutra (U. California-Davis). Primers and probes for the N sqRNA qRT–PCR were as follows: forward 5'-CGATCTCTGTAGATCTGTTCTC-3', reverse 5'-GGTGAACCAAGACGCAGTAT-3', probe 5'-FAM-TAACCCAGAATGGAGAACGCAGTGGG-BHQ1-3'. Both PCRs were run in a 20 µl volume containing 5 µl sample, 900 nM primers, 250 nM probe with TaqPath 1-step RT-qPCR master mix, CG (Thermo Fisher Scientific). The PCR conditions were 2 min at 25 °C for uracil N-glycosylase incubation, 15 min at 50 °C for reverse transcription, 2 min at 95 °C (Taq activation), followed by 40 cycles of 95 °C for 3 s (denaturation) and 60 °C for 30 s (annealing and elongation).

PET–CT administration, acquisition and data collection

The animals were anaesthetized and brought to the PET–CT suite where they were monitored and prepared for imaging. An intravenous catheter is placed and the animals were intubated and placed on a gas anaesthetic (isoflurane). FDG was administered as an intravenous bolus at a dose of 0.5 mCi kg⁻¹ in the animal preparatory room. The catheter was flushed, and the animals were transferred to the PET–CT imaging room. Images were acquired on a Mediso LFER 150 PET–CT (Mediso Medical Imaging Systems). The animals were then placed on the table in a ‘head-in-supine’ position with heat support. Scout CT images of side and top views were obtained for positioning purposes and preferred scanning ranges. The number of fields of view (FOV) was determined depending on the size of the animal (each FOV covers 15 cm and takes 10 min to obtain with PET). A CT scan was captured at 80 kVp and 1 mA with a time range of 1–5 min depending on the FOV. Breath holds were performed during the CT scan on animals that can be imaged in one FOV. A breath hold lasts for the majority of the CT scan which is approximately 45–60 s. PET images were obtained following FDG uptake time (45–60 min) and the CT scan. Once the images were captured, the animal’s fluids were discontinued and the animal was removed from isoflurane. When swallowing reflexes returned, the animal was extubated and returned to its home cage. Images were reconstructed using Nucline software with the following parameters: Mediso Tera-Tomo 3D algorithm, 8 iterations, 9 subsets, voxel size 0.7 mm.

PET–CT data analysis

PET–CT images were analysed using OsiriX MD or 64-bit (v.11, Pixmeo). Before analysis, the PET images were Gaussian smoothed in OsiriX and smoothing was applied to raw data with a 3×3 matrix size and a matrix normalization value of 24. Whole lung FDG uptake was measured by first creating a whole lung region-of-interest (ROI) on the lung in the CT scan by creating a 3D growing region highlighting every voxel in the lungs between –1024 and –500 Hounsfield units. This whole lung ROI is copied and pasted to the PET scan and gaps within the ROI are filled in using a closing ROI brush tool with a structuring element radius of 4. All voxels within the lung ROI with a standard uptake value (SUV) below 1.5 are set to zero and the SUVs of the remaining voxels are summed for a total lung FDG uptake (total inflammation) value. Total FDG uptake values were normalized to back muscle FDG uptake that was measured by drawing cylinder ROIs on the back muscles adjacent to the spine at the same axial level as the carina (SUVCMR; cylinder-muscle-ratio)⁴³. PET quantification values were organized in Microsoft Excel. 3D images were created using the 3D volume rendering tool on OsiriX MD.

Luminex isotype and FcR binding assay

To determine relative concentrations of antigen-specific antibody isotypes and Fc receptor binding activity, a Luminex isotype assay was performed as previously described⁴⁴. Antigens (SARS-CoV-2 spike, RBD, S1, S2, HKU1 RBD and OC43 RBD) were covalently coupled to Luminex microplex carboxylated bead regions (Luminex Corporation) using NHS-ester linkages with Sulfo-NHS and EDC (Thermo Fisher Scientific) according to manufacturer recommendations. Immune complexes were formed by incubating antigen-coupled beads with diluted samples. Mouse-anti-rhesus antibody detectors were then added for each antibody isotype (IgG1, IgG2, IgG3, IgG4 and IgA (NIH Nonhuman Primate Reagent Resource supported by AI126683 and OD010976)). Tertiary anti-mouse-IgG detector antibodies conjugated to phycoerythrin (PE) were then added. FcR binding was quantified similarly by using recombinant non-human primate FcRs (FcγR2A-1, FcγR2A-2 and FcγR3A (Duke Protein Production Facility)) conjugated to PE as secondary detectors. Flow cytometry was performed using an iQue (Intellicyt) and an S-LAB robot (PAA), and analysis was performed on IntelliCyt ForeCyt (v 8.1).

Systems serology

To quantify antibody functionality of plasma samples, bead-based assays were used to measure antibody-dependent cellular phagocytosis (ADCP), ADNP and antibody-dependent complement deposition (ADCD), as previously described^{45,46,47,48}. SARS-CoV-2 spike protein (HexaPro antigen (from E. Ollmann Saphire, La Jolla Institute for Immunology)) was coupled to fluorescent streptavidin beads (Thermo Fisher) and incubated with serum samples to allow antibody binding to occur. For ADCP, cultured

human monocytes (THP-1 cell line) were incubated with immune complexes, during which phagocytosis occurred. For ADNP, primary PMBCs were isolated from whole blood using an ACK lysis buffer. After phagocytosis of immune complexes, neutrophils were stained with an anti-CD66b Pacific Blue detection antibody (Biolegend) before flow cytometry. For ADCD, lyophilized guinea pig complement (Cedarlane) was reconstituted according to manufacturer's instructions and diluted in a gelatin veronal buffer with calcium and magnesium (Boston BioProducts). After antibody-dependent complement deposition occurred, C3 bound to immune complexes was detected with FITC-Conjugated Goat IgG Fraction to Guinea Pig Complement C3 (MP Biomedicals). For quantification of antibody-dependent natural killer (NK) cell activation, diluted plasma samples were incubated in Nunc MaxiSorp plates (Thermo Fisher Scientific) coated with antigen. Human NK cells were isolated the evening before using RosetteSep Human NK cell Enrichment cocktail (Stemcell Technologies) from healthy buffy coat donors and incubated overnight with human recombinant IL-15 (STEMCELL Technologies). NK cells were incubated with immune complexes, CD107a PE-Cy5 (BD), Golgi stop (BD) and brefeldin A (Sigma-Aldrich). After incubation, cells were stained using anti-CD16 APC-Cy7 (BD), anti-CD56 PE-Cy7 (BD) and anti-CD3 Pacific Blue (BD), and then fixed (Perm A, Life Tech). Intracellular staining using anti-IFN γ FITC (BD) and anti-MIP-1 β PE (BD) was performed after permeabilizing the NK cells with Perm B (Thermo Fisher). Flow cytometry acquisition of all assays was performed using an iQue (IntelliCyt) and a S-LAB robot (PAA). For ADCP, phagocytosis events were gated on bead-positive cells. For ADNP, neutrophils were identified by gating on CD66b $^+$ cells, phagocytosis was identified by gating on bead-positive cells. A phagocytosis score for ADCP and ADNP was calculated as (percentage of bead-positive cells) \times (MFI of bead-positive cells) divided by 10,000. ADCD quantification was reported as MFI of FITC-anti-C3. For antibody-dependent NK activation, NK cells were identified by gating on CD3 $^-$, CD16 $^+$ and CD56 $^+$ cells. Data were reported as the percentage of cells positive for CD107a, IFN γ and MIP-1 β .

Statistics and data visualization

The difference between any two groups at a time point was measured using a two-tailed nonparametric Mann–Whitney unpaired rank-sum test. The difference between time points within a group was measured using a Wilcoxon matched-pairs signed-rank test. All correlations were Spearman's correlations based on ranks. All the statistical analyses were performed using GraphPad Prism v.9.0.0 or R version 3.6.1. All the figures were made in GraphPad Prism or R and organized in Adobe Illustrator.

Reporting summary

Further information on research design is available in the [Nature Research Reporting Summary](#) linked to this paper.

Data availability

All data from the study are included in the manuscript and associated files. [Source data](#) are provided with this paper.

References

1. 1.

Krammer, F. SARS-CoV-2 vaccines in development. *Nature* **586**, 516–527 (2020).

[ADS](#) [CAS](#) [PubMed](#) [PubMed Central](#) [Article](#) [Google Scholar](#)

2. 2.

Pollard, A. J. & Bijker, E. M. A guide to vaccinology: from basic principles to new developments. *Nat. Rev. Immunol.* **21**, 83–100 (2021).

[CAS](#) [PubMed](#) [Article](#) [Google Scholar](#)

3. 3.

Pulendran, B., S Arunachalam, P. & O'Hagan, D. T. Emerging concepts in the science of vaccine adjuvants. *Nat. Rev. Drug Discov.* <https://doi.org/10.1038/s41573-021-00163-y> (2021).

4. 4.

Thanh Le, T. et al. The COVID-19 vaccine development landscape. *Nat. Rev. Drug Discov.* **19**, 305–306 (2020).

[CAS](#) [PubMed](#) [Article](#) [Google Scholar](#)

5. 5.

Walls, A. C. et al. Elicitation of potent neutralizing antibody responses by designed protein nanoparticle vaccines for SARS-CoV-2. *Cell* **183**, 1367–1382 (2020).

[CAS](#) [PubMed](#) [PubMed Central](#) [Article](#) [Google Scholar](#)

6. 6.

Walls, A. C. et al. Structure, function, and antigenicity of the SARS-CoV-2 spike glycoprotein. *Cell* **181**, 281–292 (2020).

[CAS](#) [PubMed](#) [PubMed Central](#) [Article](#) [Google Scholar](#)

7. 7.

Suthar, M. S. et al. Rapid generation of neutralizing antibody responses in COVID-19 patients. *Cell Rep. Med.* **1**, 100040 (2020).

[PubMed](#) [PubMed Central](#) [Article](#) [Google Scholar](#)

8. 8.

Anderson, E. J. et al. Safety and immunogenicity of SARS-CoV-2 mRNA-1273 vaccine in older adults. *N. Engl. J. Med.* **383**, 2427–2438 (2020).

[CAS](#) [PubMed](#) [Article](#) [Google Scholar](#)

9. 9.

Widge, A. T. et al. Durability of responses after SARS-CoV-2 mRNA-1273 vaccination. *N. Engl. J. Med.* **384**, 80–82 (2021).

[CAS](#) [PubMed](#) [Article](#) [Google Scholar](#)

10. 10.

Mercado, N. B. et al. Single-shot Ad26 vaccine protects against SARS-CoV-2 in rhesus macaques. *Nature* **586**, 583–588 (2020).

[ADS](#) [CAS](#) [PubMed](#) [PubMed Central](#) [Article](#) [Google Scholar](#)

11. 11.

Case, J. B. et al. Neutralizing antibody and soluble ACE2 inhibition of a replication-competent VSV-SARS-CoV-2 and a clinical isolate of SARS-CoV-2. *Cell Host Microbe* **28**, 475–485 (2020).

[CAS](#) [PubMed](#) [PubMed Central](#) [Article](#) [Google Scholar](#)

12. 12.

Piccoli, L. et al. Mapping neutralizing and immunodominant sites on the SARS-CoV-2 spike receptor-binding domain by structure-guided high-resolution serology. *Cell* **183**, 1024–1042 (2020).

[CAS](#) [PubMed](#) [PubMed Central](#) [Article](#) [Google Scholar](#)

13. 13.

Wu, K. et al. Serum neutralizing activity elicited by mRNA-1273 vaccine—preliminary report. *N. Engl. J. Med.* **384**, 1468–1470 (2021).

[PubMed](#) [Article](#) [PubMed Central](#) [Google Scholar](#)

14. 14.

Liu, Y. et al. Neutralizing activity of BNT162b2-elicited serum. *N. Engl. J. Med.* **384**, 1466–1468 (2021).

[PubMed](#) [Article](#) [PubMed Central](#) [Google Scholar](#)

15. 15.

Francica, J. R. et al. Innate transcriptional effects by adjuvants on the magnitude, quality, and durability of HIV envelope responses in NHPs. *Blood Adv.* **1**, 2329–2342 (2017).

[CAS](#) [PubMed](#) [PubMed Central](#) [Article](#) [Google Scholar](#)

16. 16.

Corbett, K. S. et al. Evaluation of the mRNA-1273 vaccine against SARS-CoV-2 in nonhuman primates. *N. Engl. J. Med.* **383**, 1544–1555 (2020).

[CAS](#) [PubMed](#) [Article](#) [PubMed Central](#) [Google Scholar](#)

17. 17.

van Doremalen, N. et al. ChAdOx1 nCoV-19 vaccine prevents SARS-CoV-2 pneumonia in rhesus macaques. *Nature* **586**, 578–582 (2020).

[ADS](#) [PubMed](#) [Article](#) [CAS](#) [PubMed Central](#) [Google Scholar](#)

18. 18.

Kim, D. et al. The architecture of SARS-CoV-2 transcriptome. *Cell* **181**, 914–921 (2020).

[CAS](#) [PubMed](#) [PubMed Central](#) [Article](#) [Google Scholar](#)

19. 19.

Hewitt, J. A. et al. ACTIVating resources for the COVID-19 pandemic: in vivo models for vaccines and therapeutics. *Cell Host Microbe* **28**, 646–659 (2020).

[CAS](#) [PubMed](#) [PubMed Central](#) [Article](#) [Google Scholar](#)

20. 20.

Vogel, A. B. et al. BNT162b vaccines protect rhesus macaques from SARS-CoV-2. *Nature* **592**, 283–289 (2021).

[ADS](#) [CAS](#) [PubMed](#) [Article](#) [Google Scholar](#)

21. 21.

Acosta, P. L., Caballero, M. T. & Polack, F. P. Brief history and characterization of enhanced respiratory syncytial virus disease. *Clin. Vaccine Immunol.* **23**, 189–195 (2015).

[PubMed](#) [Article](#) [CAS](#) [Google Scholar](#)

22. 22.

Bolles, M. et al. A double-inactivated severe acute respiratory syndrome coronavirus vaccine provides incomplete protection in mice and induces increased eosinophilic proinflammatory pulmonary response upon challenge. *J. Virol.* **85**, 12201–12215 (2011).

[CAS](#) [PubMed](#) [PubMed Central](#) [Article](#) [Google Scholar](#)

23. 23.

Hsieh, C. L. et al. Structure-based design of prefusion-stabilized SARS-CoV-2 spikes. *Science* **369**, 1501–1505 (2020).

[ADS](#) [CAS](#) [PubMed](#) [Article](#) [Google Scholar](#)

24. 24.

Sadoff, J. et al. Interim results of a phase 1–2a trial of Ad26.COV2.S Covid-19 vaccine. *N. Engl. J. Med.*
<https://doi.org/10.1056/NEJMoa2034201> (2021).

25. 25.

Voysey, M. et al. Safety and efficacy of the ChAdOx1 nCoV-19 vaccine (AZD1222) against SARS-CoV-2: an interim analysis of four randomised controlled trials in Brazil, South Africa, and the UK. *Lancet* **397**, 99–111 (2021).

[CAS](#) [PubMed](#) [PubMed Central](#) [Article](#) [Google Scholar](#)

26. 26.

Walsh, E. E. et al. Safety and immunogenicity of two RNA-based Covid-19 vaccine candidates. *N. Engl. J. Med.* **383**, 2439–2450 (2020).

[CAS](#) [PubMed](#) [Article](#) [Google Scholar](#)

27. 27.

Doherty, M. et al. Vaccination of special populations: Protecting the vulnerable. *Vaccine* **34**, 6681–6690 (2016).

[PubMed](#) [Article](#) [Google Scholar](#)

28. 28.

Cohet, C. et al. Safety of AS03-adjuvanted influenza vaccines: A review of the evidence. *Vaccine* **37**, 3006–3021 (2019).

[CAS](#) [PubMed](#) [Article](#) [Google Scholar](#)

29. 29.

Morel, S. et al. Adjuvant system AS03 containing α -tocopherol modulates innate immune response and leads to improved adaptive immunity. *Vaccine* **29**, 2461–2473 (2011).

[CAS](#) [PubMed](#) [Article](#) [Google Scholar](#)

30. 30.

Brouwer, P. J. M. et al. Two-component spike nanoparticle vaccine protects macaques from SARS-CoV-2 infection. *Cell* **184**, 1188–1200 (2021).

[CAS](#) [PubMed](#) [PubMed Central](#) [Article](#) [Google Scholar](#)

31. 31.

Arunachalam, P. S. et al. T cell-inducing vaccine durably prevents mucosal SHIV infection even with lower neutralizing antibody titers.

Nat. Med. **26**, 932–940 (2020).

[CAS](#) [PubMed](#) [PubMed Central](#) [Article](#) [Google Scholar](#)

32. 32.

Tiller, T. et al. Efficient generation of monoclonal antibodies from single human B cells by single cell RT-PCR and expression vector cloning. *J. Immunol. Methods* **329**, 112–124 (2008).

[CAS](#) [PubMed](#) [Article](#) [PubMed Central](#) [Google Scholar](#)

33. 33.

Millet, J. K. & Whittaker, G. R. Murine leukemia virus (MLV)-based coronavirus spike-pseudotyped particle production and infection. *Bio Protoc.* **6**, e2035 (2016).

[PubMed](#) [PubMed Central](#) [Article](#) [Google Scholar](#)

34. 34.

Pinto, D. et al. Cross-neutralization of SARS-CoV-2 by a human monoclonal SARS-CoV antibody. *Nature* **583**, 290–295 (2020).

[ADS](#) [CAS](#) [PubMed](#) [Article](#) [PubMed Central](#) [Google Scholar](#)

35. 35.

Crawford, K. H. D. et al. Protocol and reagents for pseudotyping lentiviral particles with SARS-CoV-2 spike protein for neutralization assays. *Viruses* **12**, E513 (2020).

[PubMed](#) [Article](#) [CAS](#) [PubMed Central](#) [Google Scholar](#)

36. 36.

Vanderheiden, A. et al. Development of a rapid focus reduction neutralization test assay for measuring SARS-CoV-2 neutralizing

antibodies. *Curr. Protoc. Immunol.* **131**, e116 (2020).

[CAS](#) [PubMed](#) [PubMed Central](#) [Google Scholar](#)

37. 37.

Xie, X. et al. An infectious cDNA clone of SARS-CoV-2. *Cell Host Microbe* **27**, 841–848 (2020).

[CAS](#) [PubMed](#) [PubMed Central](#) [Article](#) [Google Scholar](#)

38. 38.

Katzelnick, L. C. et al. Viridot: an automated virus plaque (immunofocus) counter for the measurement of serological neutralizing responses with application to dengue virus. *PLoS Negl. Trop. Dis.* **12**, e0006862 (2018).

[PubMed](#) [PubMed Central](#) [Article](#) [Google Scholar](#)

39. 39.

Weissman, D. et al. D614G spike mutation increases SARS CoV-2 susceptibility to neutralization. *Cell Host Microbe* **29**, 23–31 (2021).

[CAS](#) [Article](#) [Google Scholar](#)

40. 40.

Tegally, H. et al. Emergence and rapid spread of a new severe acute respiratory syndrome-related coronavirus 2 (SARS-CoV-2) lineage with multiple spike mutations in South Africa. Preprint at <https://doi.org/10.1101/2020.12.21.20248640> (2020).

41. 41.

Blair, R. V. et al. Acute respiratory distress in aged, SARS-CoV-2-infected African green monkeys but not rhesus macaques. *Am. J. Pathol.* **191**, 274–282 (2021).

[CAS](#) [PubMed](#) [PubMed Central](#) [Article](#) [Google Scholar](#)

42. 42.

Wölfel, R. et al. Virological assessment of hospitalized patients with COVID-2019. *Nature* **581**, 465–469 (2020).

[ADS](#) [PubMed](#) [PubMed Central](#) [Article](#) [CAS](#) [Google Scholar](#)

43. 43.

White, A. G. et al. Analysis of 18FDG PET/CT imaging as a tool for studying *Mycobacterium tuberculosis* infection and treatment in non-human primates. *J. Vis. Exp.* **127**, 56375

44. 44.

Brown, E. P. et al. High-throughput, multiplexed IgG subclassing of antigen-specific antibodies from clinical samples. *J. Immunol. Methods* **386**, 117–123 (2012).

[CAS](#) [PubMed](#) [PubMed Central](#) [Article](#) [Google Scholar](#)

45. 45.

Ackerman, M. E. et al. A robust, high-throughput assay to determine the phagocytic activity of clinical antibody samples. *J. Immunol. Methods* **366**, 8–19 (2011).

[CAS](#) [PubMed](#) [Article](#) [Google Scholar](#)

46. 46.

Fischinger, S. et al. A high-throughput, bead-based, antigen-specific assay to assess the ability of antibodies to induce complement activation. *J. Immunol. Methods* **473**, 112630 (2019).

[CAS](#) [PubMed](#) [PubMed Central](#) [Article](#) [Google Scholar](#)

47. 47.

Karsten, C. B. et al. A versatile high-throughput assay to characterize antibody-mediated neutrophil phagocytosis. *J. Immunol. Methods* **471**, 46–56 (2019).

[CAS](#) [PubMed](#) [PubMed Central](#) [Article](#) [Google Scholar](#)

48. 48.

Lu, L. L. et al. A functional role for antibodies in tuberculosis. *Cell* **167**, 433–443 (2016).

[CAS](#) [PubMed](#) [PubMed Central](#) [Article](#) [Google Scholar](#)

[Download references](#)

Acknowledgements

This study was supported by the Bill and Melinda Gates Foundation INV–018675 to B.P. and INV–017592 to J.S.M.; OPP1156262 to D.V. and N.P.K., a generous gift from the Audacious Project, a generous gift from J. Green and M. Halperin, a generous gift from the Hanauer family, the Defense Threat Reduction Agency (HDTRA1-18-1-0001 to N.P.K.), the National Institute of General Medical Sciences (R01GM120553 to D.V.), the National Institute of Allergy and Infectious Diseases (DP1AI158186 and HHSN272201700059C to D.V.; and R01-AI127521 to J.S.M.), a Pew Biomedical Scholars Award (D.V.), Investigators in the Pathogenesis of Infectious Disease Awards from the Burroughs Wellcome Fund (D.V.), Fast Grants (D.V.); Bill and Melinda Gates Foundation INV – 018417 (J.L.F.); and NIAID-NIH Contract: HHSN272201800004C to D.M. We thank the staff at the New Iberia Research Center, UL Lafayette and the Tulane National Primate Research Center for conducting the animal studies; M. Pepper for coordination of human convalescent samples; and L. Stuart at the Bill and Melinda Gates Foundation for inputs and insights throughout the study; all the members of GSK, Dynavax and Seppic for critical reading of the manuscript. We acknowledge the generous help of Rashmi

Ravichandran for protein production. The schematics were made using BioRender.

Author information

Affiliations

1. Institute for Immunity, Transplantation and Infection, Stanford University School of Medicine, Stanford University, Stanford, CA, USA

Prabhu S. Arunachalam, Chunfeng Li, Meera Trisal & Bali Pulendran

2. Department of Biochemistry, University of Washington, Seattle, WA, USA

Alexandra C. Walls, Mary Jane Navarro, Samuel Wrenn, Deleah Pettie, John C. Kraft, Marcos C. Miranda, Elizabeth Kepl, Claire Sydeman, Natalie Brunette, Michael Murphy, Brooke Fiala, Lauren Carter, Neil P. King & David Veesler

3. Tulane National Primate Research Center, Covington, LA, USA

Nadia Golden, Pyone Aye, Kasi Russell-Lodrigue, Christopher Monjure, Jason Dufour, Skye Spencer, Lara Doyle-Meyers, Rudolph P. Bohm, Nicholas J. Maness, Chad Roy & Jay Rappaport

4. Ragon Institute of MIT, MGH and Harvard, Cambridge, MA, USA

Caroline Atyeo, Stephanie Fischinger, Alex Zhu, Matthew J. Gorman, Sally Shin & Galit Alter

5. Yerkes National Primate Research Center, Atlanta, Georgia, USA

Lilin Lai, Venkata Viswanadh Edara & Mehul S. Suthar

6. Department of Pathology, Stanford University School of Medicine, Stanford University, Stanford, CA, USA

Katharina Röltgen, Scott D. Boyd & Bali Pulendran

7. New Iberia Research Center, University of Louisiana at Lafayette,
New Iberia, LA, USA

Kenneth Rogers, Lisa Shirreff, Douglas E. Ferrell, Jane
Fontenot, Francois Villinger & Neil P. King

8. Institute for Protein Design, University of Washington, Seattle, WA,
USA

Samuel Wrenn, Deleah Pettie, John C. Kraft, Marcos C.
Miranda, Elizabeth Kepl, Claire Sydeman, Natalie Brunette, Michael
Murphy, Brooke Fiala & Lauren Carter

9. Department of Microbiology and Molecular Genetics, University of
Pittsburgh School of Medicine, Pittsburgh, PA, USA

Alexander G. White & JoAnne L. Flynn

10. Center for Vaccine Research, University of Pittsburgh School of
Medicine, Pittsburgh, PA, USA

Alexander G. White

11. Department of Molecular Biosciences, University of Texas, Austin,
TX, USA

Ching-Lin Hsieh & Jason S. McLellan

12. World Reference Center for Emerging Viruses and Arboviruses,
University of Texas Medical Branch, Galveston, TX, USA

Jessica A. Plante & Kenneth S. Plante

13. Department of Surgery, Duke University School of Medicine, Durham,
NC, USA

Xiaoying Shen & David Montefiori

14. Department of Bioengineering, University of California, San Diego,
La Jolla, CA, USA

Shakti Gupta & Shankar Subramaniam

15. GSK, Rockville, MD, USA

Derek T. O'Hagan

16. GSK, Rixensart, Belgium

Robbert Van Der Most

17. GSK, Siena, Italy

Rino Rappuoli

18. Dynavax Technologies Corporation, Emeryville, CA, USA

Robert L. Coffman & David Novack

19. Bill and Melinda Gates Foundation, Seattle, WA, USA

Harry Kleanthous

20. Department of Microbiology and Immunology, Tulane University
School of Medicine, New Orleans, LA, USA

Jay Rappaport

21. Department of Microbiology and Immunology, Stanford University
School of Medicine, Stanford University, Stanford, CA, USA

Bali Pulendran

Authors

1. Prabhu S. Arunachalam

[View author publications](#)

You can also search for this author in [PubMed](#) [Google Scholar](#)

2. Alexandra C. Walls

[View author publications](#)

You can also search for this author in [PubMed](#) [Google Scholar](#)

3. Nadia Golden

[View author publications](#)

You can also search for this author in [PubMed](#) [Google Scholar](#)

4. Caroline Atyeo

[View author publications](#)

You can also search for this author in [PubMed](#) [Google Scholar](#)

5. Stephanie Fischinger

[View author publications](#)

You can also search for this author in [PubMed](#) [Google Scholar](#)

6. Chunfeng Li

[View author publications](#)

You can also search for this author in [PubMed](#) [Google Scholar](#)

7. Pyone Aye

[View author publications](#)

You can also search for this author in [PubMed](#) [Google Scholar](#)

8. Mary Jane Navarro

[View author publications](#)

You can also search for this author in [PubMed](#) [Google Scholar](#)

9. Lilin Lai

[View author publications](#)

You can also search for this author in [PubMed](#) [Google Scholar](#)

10. Venkata Viswanadh Edara
[View author publications](#)

You can also search for this author in [PubMed](#) [Google Scholar](#)

11. Katharina Röltgen
[View author publications](#)

You can also search for this author in [PubMed](#) [Google Scholar](#)

12. Kenneth Rogers
[View author publications](#)

You can also search for this author in [PubMed](#) [Google Scholar](#)

13. Lisa Shirreff
[View author publications](#)

You can also search for this author in [PubMed](#) [Google Scholar](#)

14. Douglas E. Ferrell
[View author publications](#)

You can also search for this author in [PubMed](#) [Google Scholar](#)

15. Samuel Wrenn
[View author publications](#)

You can also search for this author in [PubMed](#) [Google Scholar](#)

16. Deleah Pettie
[View author publications](#)

You can also search for this author in [PubMed](#) [Google Scholar](#)

17. John C. Kraft
[View author publications](#)

You can also search for this author in [PubMed](#) [Google Scholar](#)

18. Marcos C. Miranda

[View author publications](#)

You can also search for this author in [PubMed](#) [Google Scholar](#)

19. Elizabeth Kepl

[View author publications](#)

You can also search for this author in [PubMed](#) [Google Scholar](#)

20. Claire Sydeman

[View author publications](#)

You can also search for this author in [PubMed](#) [Google Scholar](#)

21. Natalie Brunette

[View author publications](#)

You can also search for this author in [PubMed](#) [Google Scholar](#)

22. Michael Murphy

[View author publications](#)

You can also search for this author in [PubMed](#) [Google Scholar](#)

23. Brooke Fiala

[View author publications](#)

You can also search for this author in [PubMed](#) [Google Scholar](#)

24. Lauren Carter

[View author publications](#)

You can also search for this author in [PubMed](#) [Google Scholar](#)

25. Alexander G. White

[View author publications](#)

You can also search for this author in [PubMed](#) [Google Scholar](#)

26. Meera Trisal

[View author publications](#)

You can also search for this author in [PubMed](#) [Google Scholar](#)

27. Ching-Lin Hsieh

[View author publications](#)

You can also search for this author in [PubMed](#) [Google Scholar](#)

28. Kasi Russell-Lodrigue

[View author publications](#)

You can also search for this author in [PubMed](#) [Google Scholar](#)

29. Christopher Monjure

[View author publications](#)

You can also search for this author in [PubMed](#) [Google Scholar](#)

30. Jason Dufour

[View author publications](#)

You can also search for this author in [PubMed](#) [Google Scholar](#)

31. Skye Spencer

[View author publications](#)

You can also search for this author in [PubMed](#) [Google Scholar](#)

32. Lara Doyle-Meyers

[View author publications](#)

You can also search for this author in [PubMed](#) [Google Scholar](#)

33. Rudolph P. Bohm

[View author publications](#)

You can also search for this author in [PubMed](#) [Google Scholar](#)

34. Nicholas J. Maness

[View author publications](#)

You can also search for this author in [PubMed](#) [Google Scholar](#)

35. Chad Roy

[View author publications](#)

You can also search for this author in [PubMed](#) [Google Scholar](#)

36. Jessica A. Plante

[View author publications](#)

You can also search for this author in [PubMed](#) [Google Scholar](#)

37. Kenneth S. Plante

[View author publications](#)

You can also search for this author in [PubMed](#) [Google Scholar](#)

38. Alex Zhu

[View author publications](#)

You can also search for this author in [PubMed](#) [Google Scholar](#)

39. Matthew J. Gorman

[View author publications](#)

You can also search for this author in [PubMed](#) [Google Scholar](#)

40. Sally Shin

[View author publications](#)

You can also search for this author in [PubMed](#) [Google Scholar](#)

41. Xiaoying Shen

[View author publications](#)

You can also search for this author in [PubMed](#) [Google Scholar](#)

42. Jane Fontenot

[View author publications](#)

You can also search for this author in [PubMed](#) [Google Scholar](#)

43. Shakti Gupta

[View author publications](#)

You can also search for this author in [PubMed](#) [Google Scholar](#)

44. Derek T. O'Hagan

[View author publications](#)

You can also search for this author in [PubMed](#) [Google Scholar](#)

45. Robbert Van Der Most

[View author publications](#)

You can also search for this author in [PubMed](#) [Google Scholar](#)

46. Rino Rappuoli

[View author publications](#)

You can also search for this author in [PubMed](#) [Google Scholar](#)

47. Robert L. Coffman

[View author publications](#)

You can also search for this author in [PubMed](#) [Google Scholar](#)

48. David Novack

[View author publications](#)

You can also search for this author in [PubMed](#) [Google Scholar](#)

49. Jason S. McLellan

[View author publications](#)

You can also search for this author in [PubMed](#) [Google Scholar](#)

50. Shankar Subramaniam
[View author publications](#)

You can also search for this author in [PubMed](#) [Google Scholar](#)

51. David Montefiori
[View author publications](#)

You can also search for this author in [PubMed](#) [Google Scholar](#)

52. Scott D. Boyd
[View author publications](#)

You can also search for this author in [PubMed](#) [Google Scholar](#)

53. JoAnne L. Flynn
[View author publications](#)

You can also search for this author in [PubMed](#) [Google Scholar](#)

54. Galit Alter
[View author publications](#)

You can also search for this author in [PubMed](#) [Google Scholar](#)

55. Francois Villinger
[View author publications](#)

You can also search for this author in [PubMed](#) [Google Scholar](#)

56. Harry Kleanthous
[View author publications](#)

You can also search for this author in [PubMed](#) [Google Scholar](#)

57. Jay Rappaport
[View author publications](#)

You can also search for this author in [PubMed](#) [Google Scholar](#)

58. Mehul S. Suthar

[View author publications](#)

You can also search for this author in [PubMed](#) [Google Scholar](#)

59. Neil P. King

[View author publications](#)

You can also search for this author in [PubMed](#) [Google Scholar](#)

60. David Veesler

[View author publications](#)

You can also search for this author in [PubMed](#) [Google Scholar](#)

61. Bali Pulendran

[View author publications](#)

You can also search for this author in [PubMed](#) [Google Scholar](#)

Contributions

B.P., N.P.K. and H.K. conceptualized the study; B.P., P.S.A., A.C.W., F.V., N.P.K., D.V. and J.R. designed the study and were responsible for overall conduct of the study; S.W., D.P., M.C.M., E.K., C.S., N.B., M.M., B.F. and L.C. produced and purified RBD–NP and HexaPro–NP immunogens under the supervision of N.P.K.; J.F. and K. Rogers organized and performed all macaque immunizations under the supervision of F.V.; L.S., D.E.F. and K. Rogers processed all samples collected during the immunization phase; P.S.A. and K. Röltgen performed binding ELISA in Fig. 1 under the supervision of S.D.B.; A.C.W. and M.J.N, performed pseudovirus neutralizing-antibody response assays against the wild-type virus under the supervision of D.V.; V.V.E. and L.L. performed all authentic virus neutralizing-antibody assays under the supervision of M.S.S.; J.C.K. performed anti-spike and anti-NP binding-antibody assays; P.S.A., C.L. and M.T. performed T cell assays; N.G. and P.A., organized all challenge

experiments. N.G., P.A., K.R.-L., J.D., L.D.-M., C.M., R.P.B. and N.J.M. performed all post-challenge experiments; J.A.P., K.S.P. and C.R. provided challenge virus; A.G.W. and J.L.F. analysed PET–CT data; P.S.A. and S.G. performed immune correlates analysis under the supervision of S. Subramaniam; C.A., S.F., A.Z., M.J.G. and S. Shin performed, analysed and prepared figures of systems serology under the supervision of G.A.; C.-L.H. and J.S.M. provided HexaPro; X.S. and D.M. measured pseudovirus neutralizing-antibody response against the B.1.1.7 variant; D.T.O., R.V.D.M. and R.R. provided AS03 and AS37 and guided formulation with the two adjuvants; R.L.C. and D.N. provided and guided CpG 1018 and its formulation with alum; H.K. provided guidance throughout the project. P.S.A. and B.P. were responsible for the formal analysis of all datasets and preparation of figures; P.S.A. and B.P. wrote the manuscript with suggestions and assistance from all co-authors. All the authors read and accepted the final contents of the manuscript.

Corresponding author

Correspondence to [Bali Pulendran](#).

Ethics declarations

Competing interests

B.P. serves on the External Immunology Board of GlaxoSmithKline, and on the Scientific Advisory Board of Medicago. D.T.O., R.V.D.M. and R.R. are employees of the GSK group of companies. R.L.C. and D.N. are employees of Dynavax Technologies Corporation. H.K. is an employee of Bill and Melinda Gates Foundation. C.-L.H. and J.S.M. are inventors on US patent application no. 63/032,502 ‘Engineered Coronavirus Spike (S) Protein and Methods of Use Thereof’. N.P.K. is a co-founder, shareholder, paid consultant, and chair of the scientific advisory board of Icosavax, Inc. and has received an unrelated sponsored research agreement from Pfizer. D.V. is a consultant for Vir Biotechnology Inc. The Veesler laboratory has received an unrelated sponsored research agreement from Vir Biotechnology Inc.

Additional information

Peer review information *Nature* thanks Alan Barrett, Wolfgang Baumgärtner and the other, anonymous, reviewer(s) for their contribution to the peer review of this work. Peer reviewer reports are available.

Publisher's note Springer Nature remains neutral with regard to jurisdictional claims in published maps and institutional affiliations.

Extended data figures and tables

Extended Data Fig. 1 Study design and binding ELISA titres.

a, Structural model of the RBD-16GS-I53-50 (RBD–NP) immunogen. The genetic linker connecting the RBD antigen to the I53-50A trimer is expected to be flexible and thus the RBD may adopt alternate orientations to that shown. **b**, Negative-stain electron microscopy of RBD–NP. Scale bar, 100 nm. **c**, Dynamic light scattering (DLS) of RBD–NP and unmodified I53-50 lacking displayed antigen. The data indicate the presence of monodisperse nanoparticles with size distributions centred around 36 nm for RBD–NP and 30 nm for I53-50. In **b** and **c**, the samples were analysed following a single freeze/thaw cycle. **d**, Antigenic characterization by biolayer interferometry (BLI). RBD–NP was bound to immobilized CR3022 monoclonal antibody and maACE2-Fc receptor, both before and after one freeze/thaw cycle. Monomeric SARS-CoV-2 RBD was used as a reference antigen. **e**, Schematic representation of the study design. **f**, Serum concentrations of anti-spike IgG and anti-I53-50 NP IgG (anti-I53-50) in individual non-human primates detected by ELISA at day 42. Boxes show median, 25th and 75th percentiles and the whiskers show the range. The statistical difference between anti-spike and anti-I53-50 IgG response was determined using two-sided Wilcoxon matched-pairs signed-rank test. **g**, Spearman's correlation between anti-spike IgG (described in Fig. 1) and anti-NP IgG responses at day 42. The error bands represent 95% confidence limits. Each symbol represents an animal. $N = 4$ for O/W, 10 for AS03 and 5 for all other groups.

Extended Data Fig. 2 Antibody responses to adjuvanted RBD–NP immunization.

a, Serum neutralizing antibodies (nAb) titres determined using a SARS-CoV-2 S pseudovirus entry assay at day -7, 21 and 42. **b**, Pseudovirus nAb response against human convalescent sera from 4 COVID-19 patients. **c**, Spearman's correlation between pseudovirus and authentic virus nAb titres measured at day 42. **d**, RBD–NP-specific IgG secreting plasmablast response measured at day 4 post-secondary vaccination using ELISPOT. Boxes show median, 25th and 75th percentiles and the whiskers show the range. **e**, Spearman's correlation between plasmablast response on day 25 and pseudovirus nAb titre measured at day 42. **f**, Pseudovirus nAb response measured in the AS03 durability group at time points indicated on the *x* axis. **g**, ACE2 blocking measured in sera collected at time points indicated on the *x* axis. **h**, SARS-CoV-2 nAb titres against pseudovirus wild-type containing D614G mutation on the Wuhan-1 spike (circles) or the B.1.1.7 variant (squares) strain measured in day 42 sera. The difference between groups in **a** and **d** was analysed using two-sided Mann–Whitney rank-sum test. The error bands in **c** and **e** represent 95% confidence limits. $N = 4$ for O/W, 10 for AS03 and 5 for all other groups.

Extended Data Fig. 3 Cell-mediated immune responses to RBD–NP immunization.

a, RBD-specific CD4 T cell responses measured in blood at time points indicated on the *x* axis. The differences between time points within a group were analysed by two-sided Wilcoxon matched-pairs signed-rank test ($*P = 0.016$, $**P < 0.01$). **b**, Pie charts representing the proportions of RBD-specific CD4 T cells expressing one, two, or three cytokines as shown in the legend. **c**, NP-specific CD4 T cell responses in blood at time points indicated on the *x* axis. **d**, Ratio of frequencies of RBD-specific to NP-specific CD4 T cells expressing cytokines indicated within each plot. Boxes show median, 25th and 75th percentiles and the whiskers show the range. The dotted horizontal lines indicate a ratio of 1. $N = 4$ for O/W, 10 for AS03 and 5 for all other groups.

Extended Data Fig. 4 Analysis of immune responses post SARS-CoV-2 challenge.

a, SARS-CoV-2 viral load in pharynges measured using subgenomic PCR. The numbers within the plots denote number of infected animals per total number of animals within each group. Asterisks indicate statistically significant differences in comparison to the no vaccine control group determined using two-sided Mann–Whitney rank-sum (** $P = 0.008$). **b**, Clinical parameters measured on the day of challenge, 2 days, 1-, 2- and 3-weeks post SARS-CoV-2 challenge. Body weight (kg), body temperature (°F), Oxygen saturation (SpO_2) and respiratory rate (BPM) are shown in first, second, third and fourth rows, respectively. **c**, Serum nAb titres (plotted as reciprocal IC_{50}) determined using a SARS-CoV-2 S pseudovirus entry assay on the day of challenge, 1, 2 and 3 weeks post challenge. The black line represents the geometric mean of all data points. The circle and triangle shape of the points represent animals protected or infected (in any compartment, that is, nares, pharynges or BAL), respectively. $N = 4$ for no vaccine and O/W groups and 5 for all other groups. **d**, FDG activity in the lungs of two animals from each group indicated in the legend, pre-challenge (day 0) and post-challenge (day 4 or 5 after infection), measured using PET–CT scans. **e**, PET–CT images obtained from the lungs of SARS-CoV-2 infected animals from no vaccine, AS03, or CpG-Alum groups pre-challenge (day 0) and post-challenge (day 4 or 5). PET signal is scaled 0 to 15 SUV and shown in red. Each symbol represents an animal.

Extended Data Fig. 5 Cytokine analysis in BAL fluid post SARS-CoV-2 challenge.

a, Heat map showing expression of 24 cytokines measured in BAL fluid collected 1 week post SARS-CoV-2 challenge. **b**, Expression of Eotaxin-3 (CCL26), an eosinophil-recruiting chemokine known to be induced by the $T_{H}2$ cytokine IL-13, and IL-5, a $T_{H}2$ cytokine in the BAL fluid collected 1 week post challenge shows no significant increase in vaccinated animals compared to no vaccine controls. **c**, Abundance of cytokines known to be induced by SARS-CoV-2 infection in humans such as IL-8, MCP4, IL-6 and IFN γ in BAL collected 1 week post challenge. All the box plots show

median, 25th and 75th percentiles and the whiskers show the range. $N = 4$ for control and O/W, 5 for all other groups.

Extended Data Fig. 6 Immune correlates of protection.

a, b, Heat map showing two-sided Spearman's correlation between peak nasal (**a**) and pharyngeal (**b**) viral load (day 2) and various immune parameters. All measurements were from peak time points (day 42 for antibodies, day 25 for plasmablast, and day 28 for T cell responses). The P values were corrected for multiple-testing. Asterisks represent statistical significance (* $P < 0.05$, ** $P < 0.01$, *** $P < 0.001$ and **** $P < 0.0001$). **c**, Spearman's correlation plots between peak nasal (left) or pharyngeal (right) viral load and the frequency of NP-specific IL-2⁺TNF⁺ CD4 T cells measured at day 28, 1 week after secondary immunization. **d**, Spearman's correlation between the frequency of NP-specific IL-2⁺TNF⁺ CD4 T cells measured at day 28 and nAb response measured on day 42. The error bands in **b** and **c** represent 95% confidence limits. $N = 4$ for control and O/W, 5 for all other groups.

Extended Data Fig. 7 Functional antibody profiling by systems serology.

a–c, SARS-CoV-2 spike-specific binding IgM (**a**), IgG1 (**b**) and IgA (**c**) responses in sera collected at days -7, 21 and 42. **d, e**, FcR-binding antibody responses FcR3A (**d**) and antibody-dependent neutrophil phagocytosis (ADNP) (**e**) measured in serum collected at days -7, 21 and 42. **f**, PLSDA analysis of all antibody features measured using systems serology. **g**, The top 3 antibody features discriminating protected vs. infected animals on day 42 in the PLSDA analysis. **h**, Heat map showing Spearman's correlation between peak nasal viral load (left) or pharyngeal vial load (right) and antibody responses (day 42) indicated on the y axis. **i**, Heat map showing Spearman's correlation between peak nasal viral load and antibody responses within each group. In **a–e**, the boxes show median, 25th and 75th percentiles and the whiskers show the range. Asterisks represent statistically significant difference between two groups determined by two-sided Mann–Whitney rank-sum test. In **h, i**, the P values were

calculated for Spearman's correlation. * $P < 0.05$, ** $P < 0.01$, *** $P < 0.001$ and **** $P < 0.0001$.

[Extended Data Fig. 8 RBD–NP or HexaPro immunization with AS03 elicits comparable nAb responses.](#)

a, A schematic of the study design. **b**, Pseudovirus nAb responses in serum on day 21 and 42. The box plots show median, 25th and 75th percentiles and the whiskers show the range. The numbers indicate GMT. Asterisks represent statistically significant differences between two groups analysed by two-sided Mann–Whitney rank-sum test (* $P < 0.05$).

Extended Data Table 1 List of animals used in the study

[Full size table](#)

Extended Data Table 2 Cross-neutralization of SA B.1.351 in different adjuvant groups

[Full size table](#)

Supplementary information

[Supplementary Figure](#)

Gating strategy.

[Reporting Summary](#)

[Peer Review File](#)

Source data

[Source Data Fig. 1](#)

[Source Data Fig. 2](#)

[Source Data Fig. 3](#)

Source Data Fig. 4

Source Data Fig. 5

Rights and permissions

Reprints and Permissions

About this article



Check for
updates

Cite this article

Arunachalam, P.S., Walls, A.C., Golden, N. *et al.* Adjuvanting a subunit COVID-19 vaccine to induce protective immunity. *Nature* **594**, 253–258 (2021). <https://doi.org/10.1038/s41586-021-03530-2>

Download citation

- Received: 10 February 2021
- Accepted: 09 April 2021
- Published: 19 April 2021
- Issue Date: 10 June 2021
- DOI: <https://doi.org/10.1038/s41586-021-03530-2>

Further reading

- **Phase 1 randomized trial of a plant-derived virus-like particle vaccine for COVID-19**

- Brian J. Ward
- , Philipe Gobeil
- , Annie Séguin
- , Judith Atkins
- , Iohann Boulay
- , Pierre-Yves Charbonneau
- , Manon Couture
- , Marc-André D'Aoust
- , Jiwanjeet Dhaliwall
- , Carolyn Finkle
- , Karen Hager
- , Asif Mahmood
- , Alexander Makarkov
- , Matthew P. Cheng
- , Stéphane Pillet
- , Patricia Schimke
- , Sylvie St-Martin
- , Sonia Trépanier
- & Nathalie Landry

Nature Medicine (2021)

Comments

By submitting a comment you agree to abide by our [Terms](#) and [Community Guidelines](#). If you find something abusive or that does not comply with our terms or guidelines please flag it as inappropriate.

[Download PDF](#)

Advertisement

| [Section menu](#) | [Main menu](#) |

High-dimensional characterization of post-acute sequelae of COVID-19

[Download PDF](#)

- Article
- [Published: 22 April 2021](#)

High-dimensional characterization of post-acute sequelae of COVID-19

- [Ziyad Al-Aly](#) [ORCID: orcid.org/0000-0002-2600-0434](#)^{1,2,3,4,5},
- [Yan Xie](#) [ORCID: orcid.org/0000-0002-2457-9382](#)^{1,2,6} &
- [Benjamin Bowe](#)^{1,2,6}

Nature volume 594, pages 259–264 (2021) [Cite this article](#)

- 197k Accesses
- 3 Citations
- 5529 Altmetric
- [Metrics details](#)

Subjects

- [Outcomes research](#)
- [Policy](#)
- [SARS-CoV-2](#)
- [Signs and symptoms](#)
- [Viral infection](#)

Abstract

The acute clinical manifestations of COVID-19 have been well characterized^{1,2}, but the post-acute sequelae of this disease have not been comprehensively described. Here we use the national healthcare databases of the US Department of Veterans Affairs to systematically and comprehensively identify 6-month incident sequelae—including diagnoses, medication use and laboratory abnormalities—in patients with COVID-19

who survived for at least 30 days after diagnosis. We show that beyond the first 30 days of illness, people with COVID-19 exhibit a higher risk of death and use of health resources. Our high-dimensional approach identifies incident sequelae in the respiratory system, as well as several other sequelae that include nervous system and neurocognitive disorders, mental health disorders, metabolic disorders, cardiovascular disorders, gastrointestinal disorders, malaise, fatigue, musculoskeletal pain and anaemia. We show increased incident use of several therapeutic agents—including pain medications (opioids and non-opioids) as well as antidepressant, anxiolytic, antihypertensive and oral hypoglycaemic agents—as well as evidence of laboratory abnormalities in several organ systems. Our analysis of an array of prespecified outcomes reveals a risk gradient that increases according to the severity of the acute COVID-19 infection (that is, whether patients were not hospitalized, hospitalized or admitted to intensive care). Our findings show that a substantial burden of health loss that spans pulmonary and several extrapulmonary organ systems is experienced by patients who survive after the acute phase of COVID-19. These results will help to inform health system planning and the development of multidisciplinary care strategies to reduce chronic health loss among individuals with COVID-19.

[Download PDF](#)

Main

COVID-19 is a viral illness caused by the coronavirus SARS-CoV-2. The acute clinical manifestations of COVID-19 have been well characterized and involve both pulmonary and extrapulmonary systemic manifestations^{1,2}. Emerging reports suggest that—for some individuals—the symptoms of COVID-19 persist beyond the acute setting. However, the post-acute sequelae of COVID-19 are not yet clear.

Here we leveraged the breadth and depth of the US Department of Veterans Affairs electronic health databases to undertake a high-dimensional approach to comprehensively identify the 6-month outcomes of incident diagnoses (from 379 diagnostic categories), incident medication use (from 380 medication classes) and incident laboratory abnormalities (from 62 laboratory tests) in people who survived for at least the first 30 days after their COVID-19 diagnosis.

Non-hospitalized patients with COVID-19

The cohort included 73,435 users of the Veterans Health Administration (VHA) with COVID-19 who survived for at least the first 30 days after their COVID-19 diagnosis and who were not hospitalized, and 4,990,835 VHA users who did not have COVID-19 and were not hospitalized (Supplementary Fig. [1a, b](#)). The median follow-ups were

126 (81–203; for all reported median values, parenthetical ranges refer to the interquartile range) and 130 (82–205) days for patients with COVID-19 and VHA users, respectively (Extended Data Table [1a](#)). We examined a panel of negative-outcome controls, which yielded results that were consistent with our a priori expectations (for example, hazard ratios of 1.03 (0.94–1.12; for all hazard ratios and burdens, parenthetical ranges refer to 95% confidence intervals) and 1.03 (0.95–1.12) for neoplasms and accidental injuries, respectively); the results of all the negative-outcome controls are provided in Extended Data Table [2a](#). Our examination of the standardized differences of all high-dimensional variables across all outcome-specific cohorts (including those that were selected and those that were not selected in the models) showed that more than 99.99% of standardized differences were <0.1 after adjustment (Supplementary Fig. [2a,b](#)), which resulted in similar distributions of baseline characteristics in each group after adjustment (Supplementary Table [1](#)).

Beyond the first 30 days of illness, individuals with COVID-19 had an increased risk of death (hazard ratio of 1.59 (1.46–1.73)). We also estimated the adjusted excess burden of death due to COVID-19 per 1,000 persons at 6 months on the basis of the difference between the estimated incidence rate in individuals with COVID-19 and all VHA users. The excess death was estimated at 8.39 (7.09–9.58) per 1,000 patients with COVID-19 at 6 months. Individuals with COVID-19 had a higher risk of requiring outpatient care (hazard ratio of 1.20 (1.19–1.21)), at an excess burden of 33.22 (30.89–35.58; all excess burdens are given per 1,000 patients with COVID-19 at 6 months) and at a greater frequency of 0.47 (0.44–0.49) additional encounters every 30 days (Extended Data Table [2b,c](#)).

We evaluated the risk of incident occurrence of 379 diagnoses (that were categorized according to ICD-10 codes based on Clinical Classifications Software Refined), 380 classes of medication and 62 laboratory tests beyond the first 30 days. For each of the outcomes we examined, we built a cohort who were free of the related outcome at baseline to identify the risk of incident outcome during follow-up. We found that several conditions in almost every organ system exhibited an adjusted hazard ratio that was greater than 1 and a *P* value lower than 6.57×10^{-5} (significance level adjusted for multiple comparisons). The adjusted hazard ratio and burden for all outcomes are presented in Fig. [1a–c](#) and Supplementary Tables [2–4](#). The result for outcomes that were positively associated with COVID-19 are presented in Fig. [2a–c](#), Extended Data Fig. [1a–c](#), Supplementary Table [5](#) and are discussed here.

Fig. 1: High-dimensional identification of the incident post-acute sequelae of COVID-19.

 **figure1**

a–c, Incident diagnoses (**a**), incident medication use (**b**) and incident laboratory abnormalities (**c**). All VHA users served as the referent category. Post-acute sequelae were ascertained from 30 days after infection until end of follow-up. Beginning from the outside ring, the first ring represents hazard ratios for the post-acute sequelae of COVID-19. A higher bar indicates a larger hazard ratio. Hazard ratios with a point estimate larger than one and that was statistically significant are shown in yellow. The second ring represents the excess burden per 1,000 patients with COVID-19 at 6 months. The colour of the cell indicates the value of the excess burden (deeper shades of red indicate a higher excess burden and deeper shades of blue indicate a greater reduced burden). The third ring represents the baseline incident rate in the control group (deeper shades of red indicate a higher incident rate). The fourth ring represents negative log of the *P* value; a higher bar indicates a smaller *P* value and yellow indicates that the value is statistically significant. ACR, albumin/creatinine

ratio; AD, antidotes; AH, antihistamine drugs; Alb, albumin; ALP, alkaline phosphatase; ALT, alanine aminotransferase; AN, antineoplastic agents; AP, antiparasitic agents; AST, aspartate aminotransferase; AU, autonomic; BNP, brain natriuretic peptide; BUN, blood urea nitrogen; CD4, CD4 cell count; CD4/8, CD4/CD8 ratio; Cl, chloride; Cr, creatinine; CRP, C-reactive protein; dBIL, direct bilirubin; Derm, dermatological; DG, diagnostic; DT, dental; GFR, glomerular filtration rate; GT, genitourinary; HbA1c, haemoglobin A1c; HCT, haematocrit; HDL, high-density-lipoprotein cholesterol; Hgb, haemoglobin; hsCRP, high-sensitivity C-reactive protein; ID, irrigation or dialysis; IM, immunological; INR, international normalized ratio; IP, intrapleural; K, potassium; LDL, low-density-lipoprotein cholesterol; MS, musculoskeletal; pBNP, pro-B natriuretic peptide; Plt, platelet; Protein, total protein; PT, prothrombin time; PTT, partial thromboplastin time; RT, rectal; TBIL, total bilirubin; TC, total cholesterol; TG, triglycerides; TnI, troponin I; TnT, troponin T; WBC, white blood cell.

[Full size image](#)

Fig. 2: Burden of post-acute sequelae of COVID-19.

 figure2

a–c, Incident diagnoses (**a**), incident medication use (**b**) and incident laboratory abnormalities (**c**). All VHA users served as the referent category. Post-acute sequelae were ascertained from 30 days after infection until end of follow-up. Sequelae were selected on the basis of having a hazard ratio of more than 1 and a *P* value of less than 6.57×10^{-5} . Excess burdens per 1,000 patients with COVID-19 at 6 months are presented with 95% confidence intervals in parentheses. Outcomes are ranked within each domain on the basis of the excess burden, from high to low. Diagnoses are coloured on the basis of the diagnosis group, medications are coloured on the basis of

their class and laboratory abnormalities are coloured on the basis of their being higher or lower than the normal range. F, female; M, male; NSAIDs, non-steroidal anti-inflammatory drugs.

[Full size image](#)

Respiratory conditions

The most common excess burden at 6 months after a COVID-19 infection that did not result in a hospitalization in the first 30 days was that of respiratory conditions, which included respiratory signs and symptoms (excess burden of 28.51 (26.40–30.50)), respiratory failure, insufficiency and arrest (3.37 (2.71–3.92)), and lower respiratory disease (4.67 (3.96–5.28)). There was also evidence of a high burden of incident use of bronchodilators (22.23 (20.68–23.67)), antitussive and expectorant agents (12.83 (11.61–13.95)), anti-asthmatic agents (8.87 (7.65–9.97)) and glucocorticoids (7.65 (5.67–9.50)).

Diseases of the nervous system

An excess burden of nervous system conditions was also evident, and included nervous system signs and symptoms (14.32 (12.16–16.36)), neurocognitive disorders (3.17 (2.24–3.98)), nervous system disorders (4.85 (3.65–5.93)) and headache (4.10 (2.49–5.58)).

Mental health burden

Our results also showed an excess burden of sleep–wake disorders (14.53 (11.53–17.36), anxiety and fear-related disorders (5.42 (3.42–7.29)), and trauma- and stress-related disorders (8.93 (6.62–11.09)). These findings were coupled with evidence of excess burden of incident use of non-opioid (19.97 (17.41–22.40)) and opioid (9.39 (7.21–11.43)) analgesic drugs, antidepressant agents (7.83 (5.19–10.30)), and benzodiazepine, sedative and anxiolytic agents (22.23 (20.68–23.67)).

Metabolic disorders

An excess burden of several metabolic disorders was evident, including disorders of lipid metabolism (12.32 (8.18–16.24)), diabetes mellitus (8.23 (6.36, 9.95)) and obesity (9.53 (7.55–11.37)). These was also evidence of an excess burden of incident use of antilipaemic agents (11.56 (8.73–14.19)), oral hypoglycaemic drugs (5.39 (3.99–6.64)) and insulin (4.95 (3.87–5.90)), as well as an excess burden of elevated

low-density lipoprotein cholesterol (9.48 (7.02–11.81)), total cholesterol (9.94 (6.61, 13.11)), triglycerides (9.40 (6.63–12.03)) and haemoglobin A1c (10.66 (6.77–14.35)).

Poor general wellbeing

Individuals with COVID-19 exhibited an excess burden of poor general wellbeing, including malaise and fatigue (12.64 (11.24–13.93)), muscle disorders (5.73 (4.60–6.74)), musculoskeletal pain (13.89 (9.89–17.71)) and anaemia (4.79 (3.53–5.93)). These diagnoses were coupled with laboratory evidence of an excess burden of anaemia, comprising decreased haemoglobin (31.03 (28.16–33.76)), decreased haematocrit levels (30.73 (27.64, 33.67)) and low serum albumin (6.44 (4.84, 7.92)).

Cardiovascular conditions

There was an excess burden of cardiovascular conditions, including hypertension (15.18 (11.53–18.62)), cardiac dysrhythmias (8.41 (7.18–9.53)), circulatory signs and symptoms (6.65 (5.18–8.01)), chest pain (10.08 (8.63–11.42)), coronary atherosclerosis (4.38 (2.96–5.67)) and heart failure (3.94 (2.97–4.80)). There was also evidence of excess burden of incident use of beta blockers (9.74 (8.06–11.27)), calcium channel blockers (7.18 (5.61–8.61)), loop diuretic agents (4.72 (3.59–5.72)), thiazide diuretic agents (2.52 (1.37–3.54)), and anti-arrhythmic drugs (1.28 (0.79–1.67)).

Gastrointestinal system

There was evidence of an excess burden of the following conditions: oesophageal disorders (6.90 (4.58–9.07)), gastrointestinal disorders (3.58 (2.15–4.88)), dysphagia (2.83 (1.79–3.76)) and abdominal pain (5.73 (3.7–7.62)). These conditions were coupled with evidence for an increased use of laxatives (9.22 (6.99–11.31)), anti-emetic agents (9.22 (6.99–11.31)), histamine antagonists (4.83 (3.63–5.91)), other antacids (1.07 (0.62–1.42)) and antidiarrhoeal agents (2.87 (1.70–3.91)). Laboratory abnormalities included an increased risk of incident high levels of alanine aminotransferase (7.62 (5.20–9.90)).

Other sequelae

There was also evidence of an excess burden in incident acute pulmonary embolism (2.63 (2.25–2.92)) and use of anticoagulant drugs (16.43 (14.85–17.89)). Other conditions included excess burden of skin disorders (7.52 (5.17–9.73)), arthralgia and

arthritis (5.16 (3.18–7.01)) and infections, including urinary tract infections (2.99 (1.94–3.93)) (Fig. [2a–c](#), Supplementary Tables [2–5](#)).

COVID-19 requiring hospitalization versus influenza

To gain a better understanding of the spectrum of clinical manifestations in patients with COVID-19 who were hospitalized, we undertook a comparative evaluation of a cohort of hospitalized individuals with COVID-19 versus individuals who were hospitalized with seasonal influenza (a well-known and well-characterized respiratory viral illness).

This cohort included 13,654 people with COVID-19 and 13,997 people with influenza who survived for at least 30 days after hospital admission (Supplementary Fig. [3a, b](#)). The median follow-ups were 150 (84–217) and 157 (87–220) days for patients with COVID-19 and influenza, respectively (Extended Data Table [1a](#)). We tested a panel of negative-outcome controls, which yielded results that were consistent with our a priori expectations (for example, hazard ratio of 0.98 (0.83–1.16) and 1.02 (0.90–1.15) for neoplasms and accidental injuries, respectively); the results of all the negative-outcome controls are provided in Extended Data Table [2a](#). Our examination of standardized differences of all high-dimensional variables (including those that were selected and those that were not selected in the models) in all outcome-specific cohorts showed that more than 99.75% of standardized differences were <0.1 after adjustment (Supplementary Fig. [4a, b](#)), which resulted in similar distributions of baseline characteristics in each group after adjustment (Supplementary Table [6](#)).

Beyond the first 30 days of illness, individuals with COVID-19 who had been hospitalized for this disease had an increased risk of death (hazard ratio of 1.51 (1.30–1.76)); we estimated excess death at 28.79 (19.52–36.85) per 1,000 persons at 6 months. Individuals with COVID-19 exhibited a higher risk of requiring outpatient care (hazard ratio of 1.12 (1.08–1.17)), at an excess burden of 6.37 (4.01–9.03) and with greater frequency of 1.45 (1.28–1.63) additional encounters every 30 days (Extended Data Table [2b, c](#)).

Compared to individuals who were hospitalized with seasonal influenza (and beyond the first 30 days of illness), patients who had been hospitalized for COVID-19 had a higher burden of a broad array of pulmonary and extrapulmonary systemic manifestations, including neurological disorders (burdens of 19.78 (12.58–26.19) and 16.16 (10.40–21.19) for nervous system disorders and neurocognitive disorders, respectively), mental health disorders (for example, a burden of 7.75 (4.72–10.10) for mental and substance-use conditions), metabolic disorders (for example, a burden of 43.53 (28.71–57.08) for disorders of lipid metabolism), cardiovascular disorders (for example, a burden of 17.92 (10.73–24.35) for circulatory signs and symptoms),

gastrointestinal disorders (for example, a burden of 19.28 (12.75–25.13) for dysphagia), coagulation disorders (14.31 (10.08–17.89)), pulmonary embolism (18.31 (15.83–20.25)) and other disorders including malaise and fatigue (36.49 (28.13–44.15)) and anaemia (19.08 (10.58–26.81)) (Extended Data Figs. [2a–f](#), [3a–c](#), Supplementary Tables [7–10](#)). Analyses of risk and the burden of clinical manifestations that additionally adjusted for the severity of the acute infection yielded consistent results in both the direction and magnitude of estimates (Extended Data Figs. [4a–f](#), [5a–c](#), Supplementary Tables [11–14](#)). Our high-dimensional comparative evaluation of six-month outcomes in a cohort of hospitalized individuals with COVID-19 ($n = 13,654$) versus individuals who were hospitalized for other causes ($n = 901,516$) yielded consistent results (Extended Data Figs. [6a–f](#), [7a–c](#), Supplementary Tables [15–18](#)).

Analysing risk of prespecified COVID-19 outcomes

To complement our high-dimensional approach and to gain a deeper understanding of the clinical manifestations of post-acute COVID-19 across the severity of the initial acute disease, we evaluated the risks of a panel of prespecified outcomes across the care setting of the acute phase of the disease (using whether individuals were non-hospitalized, hospitalized or admitted to intensive care, as a proxy indicator of disease severity) and benchmarked risk in these populations to a common reference group (the broader population of the Veterans Affairs Health Care System ($n = 4,990,835$)) (Extended Data Table [1b](#)). Our assessment of standardized differences across the four groups showed that none of these differences was less than 0.1 after adjustment (Supplementary Fig. [5](#)). Our results reveal (1) an increased risk of a broad array of specific clinical manifestations that include acute coronary disease, arrhythmias, acute kidney injury, chronic kidney disease, memory problems and thromboembolic disease (Fig. [3](#), Supplementary Tables [19, 20](#)); (2) that this risk was evident even in individuals who were not hospitalized with COVID-19; and (3) a risk gradient that increased across the care setting of the acute COVID-19 infection from non-hospitalized individuals to those who were hospitalized, and risk was highest in patients who were admitted to intensive care (Fig. [3](#), Supplementary Tables [19, 20](#)).

Fig. 3: Risks and burdens of incident prespecified high-resolution post-acute COVID-19 outcomes.



Risks and burdens were assessed at 6 months in mutually exclusive cohorts comprising non-hospitalized individuals with COVID-19, people who were hospitalized for COVID-19 and people who were admitted to intensive care for COVID-19 during the acute phase (first 30 days) of the infection. All VHA users

served as the referent category. Outcomes were ascertained from day 30 after COVID-19 diagnosis until the end of follow-up. Adjusted hazard ratios and excess burdens are presented; error bars represent the 95% confidence interval. GERD, gastrointestinal reflux disease; ICU, intensive care unit.

[Full size image](#)

To gain a better understanding of whether these post-acute, prespecified outcomes are unique to COVID-19 or whether they represent a general post-viral syndrome, we further conducted comparative analyses (which were adjusted as specified in Methods, including adjusting for the severity of the acute infection) of the prespecified outcomes among people who were hospitalized with COVID-19 or seasonal influenza (Extended Data Table [1a](#), Supplementary Table [6](#)). Our results show an increased risk and excess burden of a broad array of symptoms as well as multiple organ involvement among people with COVID-19 (Extended Data Fig. [8](#), Supplementary Table [21](#)).

Negative-exposure controls

In addition to testing negative-outcome controls (Extended data Table [2a](#)) and to further test the robustness of our approach, we developed and tested a pair of negative-exposure controls. We posited that exposure to influenza vaccination in odd- and even-numbered months between 1 October 2017 and 30 September 2019 should be associated with similar risks of clinical outcomes. We therefore tested associations between exposure to influenza vaccine in even- ($n = 762,039$) versus odd- ($n = 599,981$) numbered months and the full complement of 821 high-dimensional clinical outcomes considered in this study (including all diagnoses, medications and laboratory test results). We used the same data sources, cohort-building algorithm, variable definitions, analytical approach (including weighting method) and outcome specification, as well as a similar length of follow-up and interpretation method. Our results showed that none of the associations met the threshold of significance ($P < 6.57 \times 10^{-5}$) considered in this study (Supplementary Fig. [6](#), Supplementary Tables [22–24](#)).

Discussion

Here we use a high-dimensional approach to identify the spectrum of clinical abnormalities (incident diagnoses, incident medication use and incident laboratory abnormalities) experienced by individuals with COVID-19 who survive beyond the first 30 days of illness. The results suggest that, beyond the first 30 days of illness, people with COVID-19 are at higher risk of death and are more likely to use healthcare resources, and exhibit a broad array of incident pulmonary and

extrapulmonary clinical manifestations (including nervous system and neurocognitive disorders, mental health disorders, metabolic disorders, cardiovascular disorders and gastrointestinal disorders) as well as signs and symptoms related to poor general wellbeing (including malaise, fatigue, musculoskeletal pain and anaemia). We observed an increased risk of the incident use of several classes of medication, including pain medications (opioid and non-opioid), antidepressant, anxiolytic, antihypertensive, antihyperlipidaemic and oral hypoglycaemic drugs and insulin. Our analyses of prespecified outcomes complement the high-dimensional approach to identify specific post-acute sequelae with greater diagnostic resolution and reveal two key findings: (1) that the risk and associated burden of post-acute sequelae is evident even among individuals whose acute disease was not severe enough to require hospitalization (representing the majority of people with COVID-19) and (2) that the risk and associated burden increases across the severity spectrum of the acute COVID-19 infection (from non-hospitalized to hospitalized individuals, to those admitted to intensive care). Our comparative approach to examining post-acute sequelae in individuals who are hospitalized with COVID-19 versus individuals with seasonal influenza (using a high-dimensional approach and through examination of prespecified outcomes) suggests that there is a substantially higher burden of a broad array of post-acute sequelae in the individuals who are hospitalized with COVID-19, which provides features that differentiate post-acute COVID-19 (both in the magnitude of risk and the breadth of organ involvement) from a post-influenza viral syndrome. Our results show that individuals who survive for 30 days or more after their COVID-19 diagnosis exhibit an increased risk of death and are more likely to use health resources, as well as a substantial burden of health loss that spans the pulmonary and several extrapulmonary organ systems; this highlights the need for holistic and integrated multidisciplinary long-term care of patients with COVID-19.

The mechanism or mechanisms that underlie the post-acute manifestations of COVID-19 are not entirely clear. Some of the manifestations may be driven by a direct effect of the viral infection, and may be explained by virus persisting in immune-privileged sites, an aberrant immune response, hyperactivation of the immune system or autoimmunity³. Indirect effects—including changes in social (for example, reduced social contact and loneliness), economic (for example, loss of employment) and behavioural conditions (for example, changes in diet and exercise)—that may be differentially experienced by people with COVID-19 may also shape health outcomes, and may be drivers of some of the post-acute clinical manifestations^{4,5,6,7,8}. A better delineation of the direct and indirect effects, and a deeper understanding of the underlying biological mechanisms and epidemiological drivers, of the multifaceted long-term consequences of COVID-19 is needed⁹.

To our knowledge, this is the largest study of the post-acute sequelae of COVID-19; it involves 73,435 non-hospitalized patients with COVID-19, and 4,990,835 control

individuals (corresponding to 2,070,615.52 person years of follow-up), as well as 13,654 hospitalized patients with COVID-19 and 13,997 patients hospitalized with seasonal influenza (corresponding to 12,179.05 person years of follow-up). We leveraged the breadth and depth of the national healthcare databases of the US Department of Veterans Affairs (the largest nationally integrated healthcare delivery system in the US) to undertake a comprehensive high-dimensional comparative approach (relative to control groups) to identify the 6-month health outcomes and clinical manifestations in patients who survived the first 30 days of COVID-19. We further examined risk in a prespecified set of outcomes with higher diagnostic resolution across care settings to enable a deeper understanding of the clinical symptomatology and diagnoses of post-acute COVID-19 across the spectrum of severity of the acute phase of the infection.

This study has several limitations. Although our approach identifies the incident post-acute sequelae in patients with COVID-19, it does not delineate which sequelae may be direct or indirect consequences of COVID-19 infection. Because of the predominantly male composition of the Veterans Affairs population, our findings may not identify clinical features of post-acute COVID-19 that may be much more pronounced in women, or non-expressed or very rare in men. Our approach demonstrated balance for more than 1,150 variables across several data domains (diagnoses, medications and laboratory data) and yielded successful testing of negative-exposure and -outcome controls, but we cannot completely rule out residual confounding effects. Finally, as the global pandemic of COVID-19 continues to evolve, as treatment strategies improve, as new variants of the virus emerge and as vaccine availability increases, it is likely that the epidemiology and short- and long-term outcomes of COVID-19 will also change over time.

Our findings show that, beyond the first 30 days of illness, a substantial burden of health loss that spans pulmonary and several extrapulmonary organ systems is experienced by individuals who survived the acute phase of COVID-19. Our results will inform global discussions on the post-acute manifestations of COVID-19, as well as health system planning and the development of care strategies that are aimed at reducing chronic and permanent health loss and optimizing wellness among patients with COVID-19.

Methods

All eligible participants were enrolled in the study, no statistical methods were used to predetermine sample size. The experiments were not randomized, and investigators were not blinded to allocation during experiments and outcome assessment.

Setting

Cohort participants were selected from US Department of Veterans Affairs (VA) electronic healthcare databases. The VHA provides healthcare to discharged veterans of the US armed forces and operates the largest nationally integrated healthcare system in the USA, with 1,255 healthcare facilities (including 170 VA Medical Centers and 1,074 outpatient sites) located across the USA. Veterans who are enrolled with the VHA have access to the comprehensive medical benefits package of the VA (which includes inpatient hospital care, outpatient services, preventive, primary and specialty care, prescriptions, mental healthcare, home healthcare, geriatric and extended care, medical equipment, and prosthetics). The VA electronic healthcare databases are updated daily.

Cohort

The cohort was constructed from 5,808,018 participants who had encountered the VHA between 1 January 2019 and 31 December 2019. Of those who were alive on 1 March 2020 ($n = 5,606,309$), a COVID-19 group was selected as individuals who had a positive test for COVID-19 between 1 March 2020 and 30 November 2020 ($n = 98,661$). Participants without hospitalization within the first 30 days of their first positive test were further selected ($n = 76,877$). To examine post-acute outcomes, we then selected from the COVID-19 group those alive on the 30th day after their positive test (participants with COVID-19, $n = 73,435$). To generate a comparison group that had a similar distribution of length of follow-up, we then matched each participant with COVID-19 with 70 VHA users who did not have a positive test for COVID-19 without replacement. In matching, the dates of cohort enrolment for the corresponding 70 VHA users were matched with time of cohort enrolment of the participant with COVID-19—that is, the date of testing positive (control group $n = 5,140,450$). In the VHA user group, we similarly selected individuals who were without hospitalization and alive during the first 30 days after the date of enrolment (control group $n = 4,990,835$) (Supplementary Fig. [1a, b](#)). Participants were followed until 31 January 2021.

To compare post-acute outcomes of hospitalized participants with COVID-19 and hospitalized participants with seasonal influenza, we selected 15,846 participants with COVID-19 who were admitted to a hospital within 30 days after or 5 days before their first positive test (from the 98,661 patients with a positive COVID-19 test between 1 March 2020 and 30 November 2020). Similarly, we selected 62,909 patients who had their first positive seasonal influenza test between 1 October 2016 and 29 February 2020 and who had encountered the VHA at least once in the calendar year before the test was collected. Of these patients, 14,948 were admitted to a hospital within 30 days after or 5 days before their first positive influenza test. The hospitalized cohort was further restricted to those alive at the 30th day after hospital admission (COVID-19 $n = 13,654$; seasonal influenza $n = 14,212$), where for 215 patients who were in both

the hospitalized COVID-19 and seasonal influenza group, only their COVID-19 hospitalizations were used in the analyses (Supplementary Fig. [3a](#),[b](#)). In this cohort, participants were considered to be enrolled at the time of hospitalization. To balance the duration of follow-up in the hospitalized COVID-19 and seasonal influenza groups, each participant in the seasonal influenza group was independently randomly assigned a duration of follow-up on the basis of the distribution of length of follow-up of the participants in the hospitalized COVID-19 group who were followed from date of hospitalization to 31 January 2021.

To examine high-resolution, prespecified post-acute COVID-19 outcomes across the severity spectrum of the initial acute disease, we built four mutually exclusive cohorts: VHA users without COVID-19 ($n = 4,990,835$), VHA users with COVID-19 ($n = 73,435$), VHA users who were hospitalized with COVID-19 within the first 30 days of follow-up ($n = 10,068$) and VHA users with COVID-19 who were admitted to the intensive care within the first 30 days of follow-up ($n = 3,586$). Participants in these cohorts were followed up until 31 January 2021.

Data sources

Electronic health records from VA Corporate Data Warehouse (CDW) were used in this study [10](#),[11](#),[12](#),[13](#). The CDW ‘outpatient encounters’ domains provided information related to outpatient encounters and ‘inpatient encounters’ domains provided information between hospital admission and discharge [14](#). The CDW ‘outpatient pharmacy’ domain and CDW ‘bar code medication administration’ domain were used to collect medication data, and CDW ‘patient’ domain was used to collect demographic information. The CDW ‘laboratory results’ domain was used to collect laboratory test information, and the ‘COVID-19 shared data resource’ was used to collect COVID-19 test and demographic information for patients with COVID-19. In addition, the area deprivation index—which is a composite measure of income, education, employment and housing—was obtained from the University of Wisconsin [15](#).

Post-acute use of health resources and death

Outcomes that occurred after 30 days of cohort enrolment—including death, incident outpatient encounter and frequency of outpatient encounter—were examined in both cohorts. The frequency of outpatient encounters was computed on the basis of the number of days with outpatient encounter divided by days of follow-up after 30 days, and is reported as the number of outpatient encounters per 30 days.

High dimensional post-acute clinical characteristics

Negative outcome and exposure controls

The application of negative controls in clinical epidemiology may help to detect both suspected and unsuspected sources of spurious bias, and may lessen concerns about unmeasured confounding and other latent biases¹⁶. Here we followed a previously published approach¹⁶ to examine a panel of eight negative-outcome controls (including neoplasms, accidental injuries, scars, fitting or adjustment of orthodontic or dental prosthetic device, fitting or adjustment of hearing device, fitting or adjustment or orthotics, fitting or adjustment of casts, and bandages), for which (based on current knowledge) there should be no causal relation between the exposures and risks of the negative-outcome controls. We also developed and tested a pair of negative-exposure controls (defined as exposure to influenza vaccine in odd- or even-numbered months during the period between 1 October 2017 and 30 September 2019). We posited that there should be no differences in risk of clinical outcomes associated with receipt in influenza vaccine in odd- versus even-numbered months. The negative-exposure controls were tested in all 821 high-dimensional outcomes considered in our analyses, including diagnoses, medications and laboratory test results; we used the same data sources, cohort-building algorithm, variable definitions, analytical approaches and outcome specification, as well as a similar length of follow-up and interpretation method. In the assessment of negative-outcome and negative-exposure controls, the relation of the exposure–outcome pairs may share the same potential biases with COVID-19 and the outcomes examined in this study (including biases in the underlying data, algorithms for the construction of cohorts, unmeasured confounders, misspecification of modelling algorithms, outcome ascertainment, analytical considerations, result interpretation and other latent biases)^{16,17}. The successful testing of negative controls reduces concerns about both suspected and unsuspected sources of spurious associations, including associations owing to unmeasured confounding, flaws in the analytical approach, differences in outcome ascertainment and other sources of bias¹⁶. In particular, the successful testing of the outcome controls may reduce concerns about biases in outcome ascertainment and unmeasured confounding between the comparison groups (for example, if there was bias in ascertainment of clinical outcomes in one arm versus another, this bias may also extend to ascertainment of neoplasms, accidental injuries or other negative-outcome controls tested in this study); the successful testing of the exposure control may reduce concerns about biases in the analytical approach and underlying data (for example, if there was bias related to the analytic approach, it may also bias the negative-exposure control).

Diagnoses

All ICD-10 diagnosis codes from cohort participants from day 30 after COVID-19 diagnosis until the end of follow-up were used to define the post-acute diagnosis outcomes. More than 70,000 ICD-10 diagnosis codes were classified into 540 diagnostic categories based on the Clinical Classifications Software Refined (CCSR) version 2021.1, which is developed as part of the Healthcare Cost and Utilization Project sponsored by the Agency for Healthcare Research and Quality^{[18,19,20](#)}. We examined only diagnostic categories that may plausibly be considered post-acute sequelae of COVID-19 in the adult population. Some diagnostic categories—including external causes of morbidity, injury, poisoning and some other consequences of external causes, congenital malformations, deformations and chromosomal abnormalities, some conditions originating in the perinatal period or outcome from pregnancy, childbirth and the puerperium—were not examined, yielding 379 diagnostic categories.

Medication use

The prescription records of cohort participants from day 30 after COVID-19 diagnosis until the end of follow-up were used to define the post-acute medication use. We classified 3,425 medications on the basis of the VA drug classification system, into 543 medication classes^{[21,22](#)}. After removing items in the medication group of investigational agents or prosthetics, supplies and devices, we examined 380 different medication outcomes in total.

Laboratory abnormalities

In total, 62 laboratory test abnormalities from 38 laboratory measurements from day 30 after COVID-19 diagnosis until the end of follow-up were examined including absolute T cell count, alanine aminotransferase, aspartate aminotransferase, blood urea nitrogen, brain natriuretic peptide, C-reactive protein, carbon dioxide, CD4/CD8 ratio, direct bilirubin, estimated glomerular filtration rate, ferritin, haematocrit, haemoglobin, haemoglobin A1c, high-density-lipoprotein cholesterol, high-sensitivity C-reactive protein, international normalized ratio, low-density-lipoprotein cholesterol, microalbumin/creatinine ratio, partial thromboplastin time, platelet count, pro B natriuretic peptide, prothrombin time, serum albumin, serum alkaline phosphatase, serum calcium, serum chloride, serum creatinine, serum phosphate, serum potassium, serum sodium, serum total protein, total bilirubin, total cholesterol, total white blood cell count, triglycerides, troponin I and troponin T were identified on the basis of ‘Logical Observation Identifiers Names and Codes’. Each laboratory test result was classified into abnormally high or abnormally low on the basis of whether results were above the upper normal range or below the lower normal range (in instances in which a high or low result might be clinically possible for a given laboratory test). The

definition of the abnormality for each laboratory test is presented in Supplementary Tables [4](#), [9](#).

High-resolution, prespecified post-acute COVID-19 outcomes

To identify clinical manifestations of post-acute COVID-19 with greater diagnostic resolution, we specified a list of outcomes on the basis of data from the Center of Disease Control and the National Institute of Health workshop on post-acute COVID-19. Outcomes were defined on the basis of previous definitions that have been validated for use with electronic health records, and integrated information from diagnoses, medications and laboratory measurements when appropriate^{[23,24,25,26,27,28,29](#)}. To gain a deeper understanding of the risks of these outcomes across the severity scale of the acute infection, we examined the risk across the care setting of the acute disease—a proxy indicator of clinical severity—in four mutually exclusive cohorts (VHA users (who served as the referent category); people with COVID-19; people hospitalized for COVID-19; and people admitted to intensive care for COVID-19). In addition, we estimated the risks of these prespecified outcomes in individuals hospitalized with COVID-19 and seasonal influenza. The prespecified, high-resolution outcomes included acute coronary disease, acute kidney injury, anxiety, arrhythmias, bradycardia, chest pain, chronic kidney disease, constipation, cough, depression, diarrhoea, type 2 diabetes mellitus, fatigue, gastric oesophageal reflux disease, hair loss, headache, heart failure, hyperlipidaemia, hypoxaemia, joint pain, memory problems, muscle weakness, obesity, shortness of breath, skin rash, sleep disorder, smell disorder, stroke, tachycardia and thromboembolism. We restricted capture of incident acute coronary disease, stroke and thromboembolism to inpatient diagnoses that were not present on admission. All other prespecified outcomes that may plausibly be encountered in either the outpatient or inpatient setting were accordingly ascertained in the setting in which they first occurred. Among individuals with COVID-19, and for each prespecified outcome, the percentages of outcomes that were ascertained from outpatient and inpatient data are presented in Supplementary Tables [19](#), [20](#).

Covariates

The predefined covariates for analyses included demographics (such as age, race (white, black and other), sex and receipt of long-term care) and proxies of healthcare use (such as number of outpatient encounters, number of hospital admissions, number of outpatient prescriptions and number of outpatient eGFR measurements in the year before enrolment). In addition, we included the area deprivation index at the residency address of patients as a summary measurement of socio-economic deprivation. We used the Sequential Organ Failure Assessment (SOFA) score to adjust for the severity of the acute infection in additional high-dimensional analyses of the hospitalized

COVID-19 versus hospitalized seasonal influenza cohorts^{30,31}. To address potential nonlinear associations, all continuous variables were adjusted as restricted cubic spline functions.

To further adjust the models in the most optimal manner, we leveraged the multidimensionality of the electronic healthcare databases of the VA to algorithmically identify covariates (potential confounders) that span multiple domains (diagnoses, pharmacy records and laboratory tests) and that showed evidence of difference in prevalence between the comparison groups²⁴. In the COVID-19 versus VHA users cohort (and separately in the hospitalized COVID-19 versus influenza cohort), high-dimensional covariates were ascertained within one year before the date of enrolment. Within all diagnoses, medication classes and laboratory tests, we first selected variables that occurs in at least 10 patients in both groups. We then estimated the unadjusted relative risk of each variable with being in the COVID-19 or comparator group. The top 100 high-dimensional variables with the strongest association with group membership were used, along with predefined covariates, in the analyses.

To most optimally estimate the risk of the set of prespecified outcomes across the intensity of care needed during the acute infection, we ascertained four sets of high-dimensional covariates (corresponding to the four mutually exclusive groups (all VHA users, people with COVID-19, people who were hospitalized with COVID-19 and people who were admitted to intensive care with COVID-19)) in total, on the basis of the unadjusted relative risk of being in each group compared to being in the remaining three groups. High-dimensional covariates were used along with predefined covariates in the analyses³².

Statistical analyses

The characteristics of the VHA users who were not hospitalized for COVID-19, VHA users who were without COVID-19, hospitalized participants with COVID-19 and hospitalized participants with seasonal influenza are described in Extended Data Table 1a. The flow charts of the overall analytical approach are presented in Supplementary Figs. 7, 8.

We estimated the risk of health resource use and death, and the risk of each diagnosis, medication use and laboratory abnormality between individuals with COVID-19 and all VHA users, and—separately—between individuals who had been hospitalized for COVID-19 or seasonal influenza. To estimate the risk of each incident outcome, we built a cohort of participants without a history of the outcome being examined (for example, risk of insulin use was estimated within a cohort of participants without history of insulin use in the year before cohort enrolment). For each outcome-specific cohort, propensity scores based on predefined variables and high-dimensional

algorithmically selected variables were estimated. The propensity scores were then used to compute the overlap weight, which is the probability of membership in the non-observed exposure group (one minus the propensity of in the observed group)^{33,34}. We then—for all outcome models—assessed covariate balance, calculating the standardized difference after application of the overlap weight for all predefined variables, 100 algorithmically selected high-dimensional variables, and all high-dimensional variables that were not selected for inclusion in the propensity score models. We present the distribution of these standardized differences for 20 randomly selected outcome-specific cohorts, and across all outcomes, and the covariate distributions in overall cohort after adjustment.

The risks of health resource use—including outpatient encounter and death between individuals with COVID-19 and all VHA users, and between COVID-19 hospitalization and influenza hospitalization—were estimated from a Cox survival model weighted by overlap weights, in which death was considered as a competing risk in the evaluation of health resource use. The frequency of outpatient encounter was modelled on the basis of a weighted linear regression. Hazard ratios for each of the outcomes—including incident diagnoses, incident medication use and incident laboratory abnormalities—were estimated from cause-specific hazard models weighted by overlap weights, in which occurrence of death was considered as a competing risk. Event rates per 1,000 participants at 6 months (180 days) of follow-up in each group, and the adjusted excess burden based on the differences between two groups, were estimated. Models were built only for outcomes that occurred in at least 10 participants from each group. A Bonferroni correction was applied in consideration of multiple hypotheses testing for high-dimensional outcomes. A *P* values of less than 6.57×10^{-5} was considered statistically significant. Results are additionally presented with a focus on identified post-acute sequelae of COVID-19, in which we selected those sequelae with a hazard ratio greater than 1 and *P* values of less than 6.57×10^{-5} . High-dimensional analyses of individuals who were hospitalized for COVID-19 versus seasonal influenza, which were adjusted for the severity of the acute infection (through inclusion of SOFA scores), were additionally undertaken. In addition, high-dimensional analyses were also conducted to evaluate the risk of six-month clinical outcomes in people who were hospitalized for COVID-19 versus those who were hospitalized for other causes. Participants who were hospitalized for other causes who survived the first 30 days after hospital admission were enrolled between 1 October 2016 and 29 February 2020 ($n = 901,516$).

We examined the risk of high-resolution, prespecified outcomes across care settings of the acute phase of the disease, analysing differences in risk of clinical manifestations of post-acute COVID-19 between mutually exclusive groups of people who were positive for COVID-19 (non-hospitalized, hospitalized and admitted to intensive care), and VHA users who were not positive for COVID-19. Propensity scores for group

membership were estimated in outcome-specific cohorts free of the related disease at baseline³². Standardized differences in the predefined and algorithmically selected high-dimensional covariates are presented after application of overlap weighting³⁵. The percentage of outcomes ascertained in the COVID-19 group in an inpatient and outpatient setting are presented. We then constructed Cox survival models to analyse the risk of outcomes using overlap weighting for multiple treatments. We report hazard ratios and event rate differences between each group. We also estimated the risks of prespecified outcomes among individuals who were hospitalized with COVID-19 or seasonal influenza, which were additionally adjusted using SOFA scores.

All analyses were done using SAS Enterprise Guide version 7.1. Data visualizations were performed in R 4.0.3. The study was approved by the Institutional Review Board of the Department of Veterans Affairs St. Louis Health Care System.

Reporting summary

Further information on research design is available in the [Nature Research Reporting Summary](#) linked to this paper.

Data availability

The data that support the findings of this study are available from the VA. VA data are made freely available to researchers behind the VA firewall with an approved VA study protocol. More information is available at <https://www.virec.research.va.gov> or by contacting the VA Information Resource Center (VIReC) at VIReC@va.gov.

Code availability

SAS and R programming codes are available at <https://github.com/yxie618/HDlongCOVID>.

References

1. 1.

Wang, D. et al. Clinical characteristics of 138 hospitalized patients with 2019 novel coronavirus-infected pneumonia in Wuhan, China. *J. Am. Med. Assoc.* **323**, 1061–1069 (2020).

[CAS Article](#) [Google Scholar](#)

2. 2.

Xie, Y., Bowe, B., Maddukuri, G. & Al-Aly, Z. Comparative evaluation of clinical manifestations and risk of death in patients admitted to hospital with Covid-19 and seasonal influenza: cohort study. *Br. Med. J.* **371**, m4677 (2020).

[Article](#) [Google Scholar](#)

3. 3.

Advisory Group of the British Society for Immunology. *Long-term Immunological Health Consequences of COVID-19 (British Society for Immunology, 2020)*.

4. 4.

Figueroa, J. D. et al. Distinguishing between direct and indirect consequences of Covid-19. *Br. Med. J.* **369**, m2377 (2020).

[Article](#) [Google Scholar](#)

5. 5.

Townsend, E. COVID-19 policies in the UK and consequences for mental health. *Lancet Psychiatry* **7**, 1014–1015 (2020).

[Article](#) [Google Scholar](#)

6. 6.

Knipe, D., Evans, H., Marchant, A., Gunnell, D. & John, A. Mapping population mental health concerns related to COVID-19 and the consequences of physical distancing: a Google trends analysis. *Wellcome Open Res.* **5**, 82 (2020).

[Article](#) [Google Scholar](#)

7. 7.

Raker, E. J., Zacher, M. & Lowe, S. R. Lessons from Hurricane Katrina for predicting the indirect health consequences of the COVID-19 pandemic. *Proc. Natl Acad. Sci. USA* **117**, 12595–12597 (2020).

[CAS](#) [Article](#) [Google Scholar](#)

8. 8.

Mahase, E. Covid-19: mental health consequences of pandemic need urgent research, paper advises. *Br. Med. J.* **369**, m1515 (2020).

[Article](#) [Google Scholar](#)

9. 9.

Del Rio, C., Collins, L. F. & Malani, P. Long-term health consequences of COVID-19. *J. Am. Med. Assoc.* (2020).

10. 10.

Xie, Y. et al. Proton pump inhibitors and risk of incident CKD and progression to ESRD. *J. Am. Soc. Nephrol.* **27**, 3153–3163 (2016).

[CAS](#) [Article](#) [Google Scholar](#)

11. 11.

Xie, Y. et al. Risk of death among users of proton pump inhibitors: a longitudinal observational cohort study of United States veterans. *BMJ Open* **7**, e015735 (2017).

[Article](#) [Google Scholar](#)

12. 12.

Xie, Y. et al. Long-term kidney outcomes among users of proton pump inhibitors without intervening acute kidney injury. *Kidney Int.* **91**, 1482–1494 (2017).

[CAS](#) [Article](#) [Google Scholar](#)

13. 13.

Xie, Y. et al. Higher blood urea nitrogen is associated with increased risk of incident diabetes mellitus. *Kidney Int.* **93**, 741–752 (2018).

[CAS](#) [Article](#) [Google Scholar](#)

14. 14.

Vincent, B. M., Wiitala, W. L., Burns, J. A., Iwashyna, T. J. & Prescott, H. C. Using Veterans Affairs corporate data warehouse to identify 30-day hospital

readmissions. *Health Serv. Outcomes Res. Methodol.* **18**, 143–154 (2018).

[Article](#) [Google Scholar](#)

15. 15.

Kind, A. J. H. & Buckingham, W. R. Making neighborhood-disadvantage metrics accessible – the neighborhood atlas. *N. Engl. J. Med.* **378**, 2456–2458 (2018).

[Article](#) [Google Scholar](#)

16. 16.

Lipsitch, M., Tchetgen Tchetgen, E. & Cohen, T. Negative controls: a tool for detecting confounding and bias in observational studies. *Epidemiology* **21**, 383–388 (2010).

[Article](#) [Google Scholar](#)

17. 17.

Shi, X., Miao, W. & Tchetgen, E. T. A selective review of negative control methods in epidemiology. *Curr. Epidemiol. Rep.* **7**, 190–202 (2020).

[Article](#) [Google Scholar](#)

18. 18.

Wei, Y. et al. Short term exposure to fine particulate matter and hospital admission risks and costs in the Medicare population: time stratified, case crossover study. *Br. Med. J.* **367**, l6258 (2019).

[Article](#) [Google Scholar](#)

19. 19.

Aubert, C. E. et al. Best definitions of multimorbidity to identify patients with high health care resource utilization. *Mayo Clin. Proc. Innov. Qual. Outcomes* **4**, 40–49 (2020).

[Article](#) [Google Scholar](#)

20. 20.

HCUP CCSR. *Healthcare Cost and Utilization Project (HCUP)* (Agency for Healthcare Research and Quality, 2020).

21. 21.

Olvey, E. L., Claushee, S. & Malone, D. C. Comparison of critical drug–drug interaction listings: the Department of Veterans Affairs medical system and standard reference compendia. *Clin. Pharmacol. Ther.* **87**, 48–51 (2010).

[CAS Article](#) [Google Scholar](#)

22. 22.

Greene, M., Steinman, M. A., McNicholl, I. R. & Valcour, V. Polypharmacy, drug–drug interactions, and potentially inappropriate medications in older adults with human immunodeficiency virus infection. *J. Am. Geriatr. Soc.* **62**, 447–453 (2014).

[Article](#) [Google Scholar](#)

23. 23.

Xie, Y. et al. Estimates of all cause mortality and cause specific mortality associated with proton pump inhibitors among US veterans: cohort study. *Br. Med. J.* **365**, l1580 (2019).

[Article](#) [Google Scholar](#)

24. 24.

Xie, Y. et al. Comparative effectiveness of SGLT2 inhibitors, GLP-1 receptor agonists, DPP-4 inhibitors, and sulfonylureas on risk of kidney outcomes: emulation of a target trial using health care databases. *Diabetes Care* **43**, 2859–2869 (2020).

[Article](#) [Google Scholar](#)

25. 25.

Xie, Y. et al. Comparative effectiveness of the sodium-glucose cotransporter 2 inhibitor empagliflozin versus other antihyperglycemics on risk of major adverse kidney events. *Diabetes Care* **43**, 2785–2795 (2020).

[CAS Article](#) [Google Scholar](#)

26. 26.

Bowe, B. et al. Acute kidney injury in a national cohort of hospitalized US veterans with COVID-19. *Clin. J. Am. Soc. Nephrol.* **16**, 14–25 (2021).

[CAS](#) [Article](#) [Google Scholar](#)

27. 27.

Bowe, B. et al. The 2016 global and national burden of diabetes mellitus attributable to PM_{2.5} air pollution. *Lancet Planet. Health* **2**, e301–e312 (2018).

[Article](#) [Google Scholar](#)

28. 28.

Bowe, B., Xie, Y., Xian, H., Balasubramanian, S. & Al-Aly, Z. Low levels of high-density lipoprotein cholesterol increase the risk of incident kidney disease and its progression. *Kidney Int.* **89**, 886–896 (2016).

[CAS](#) [Article](#) [Google Scholar](#)

29. 29.

Bowe, B. et al. High density lipoprotein cholesterol and the risk of all-cause mortality among U.S. veterans. *Clin. J. Am. Soc. Nephrol.* **11**, 1784–1793 (2016).

[CAS](#) [Article](#) [Google Scholar](#)

30. 30.

Vincent, J. L. et al. The SOFA (sepsis-related organ failure assessment) score to describe organ dysfunction/failure. on behalf of the Working Group on Sepsis-Related Problems of the European Society of Intensive Care Medicine. *Intensive Care Med.* **22**, 707–710 (1996).

[CAS](#) [Article](#) [Google Scholar](#)

31. 31.

Vincent, J. L. et al. Use of the SOFA score to assess the incidence of organ dysfunction/failure in intensive care units: results of a multicenter, prospective study. *Crit. Care Med.* **26**, 1793–1800 (1998).

[CAS](#) [Article](#) [Google Scholar](#)

32. 32.

McCaffrey, D. F. et al. A tutorial on propensity score estimation for multiple treatments using generalized boosted models. *Stat. Med.* **32**, 3388–3414 (2013).

[MathSciNet](#) [Article](#) [Google Scholar](#)

33. 33.

Thomas, L. E., Li, F. & Pencina, M. J. Overlap weighting: a propensity score method that mimics attributes of a randomized clinical trial. *J. Am. Med. Assoc.* **323**, 2417–2418 (2020).

[Article](#) [Google Scholar](#)

34. 34.

Li, F., Morgan, K. L. & Zaslavsky, A. M. Balancing covariates via propensity score weighting. *J. Am. Stat. Assoc.* **113**, 390–400 (2018).

[MathSciNet](#) [CAS](#) [Article](#) [Google Scholar](#)

35. 35.

Li, F. & Li, F. Propensity score weighting for causal inference with multiple treatments. *Ann. Appl. Stat.* **13**, 2389–2415 (2019).

[MathSciNet](#) [MATH](#) [Google Scholar](#)

[Download references](#)

Acknowledgements

This study used data from the VA COVID-19 Shared Data Resource. M. Cai developed the data visualization and A. K. Gibson provided technical and editorial assistance. This research was funded by the United States Department of Veterans Affairs and the Institute for Public Health at Washington University in Saint Louis (for Z.A.-A.), and two American Society of Nephrology and KidneyCure fellowship awards (for Y.X. and B.B.). The funders of this study had no role in study design; collection, analysis and interpretation of data; writing the report; and the decision to submit the report for publication. This research project was reviewed and approved by

the Institutional Review Board of the Department of Veterans Affairs Saint Louis Health Care System.

Author information

Affiliations

1. Clinical Epidemiology Center, Research and Development Service, VA Saint Louis Health Care System, Saint Louis, MO, USA

Ziyad Al-Aly, Yan Xie & Benjamin Bowe

2. Veterans Research and Education Foundation of Saint Louis, Saint Louis, MO, USA

Ziyad Al-Aly, Yan Xie & Benjamin Bowe

3. Nephrology Section, Medicine Service, VA Saint Louis Health Care System, Saint Louis, MO, USA

Ziyad Al-Aly

4. Department of Medicine, Washington University School of Medicine, Saint Louis, MO, USA

Ziyad Al-Aly

5. Institute for Public Health, Washington University in Saint Louis, Saint Louis, MO, USA

Ziyad Al-Aly

6. Department of Epidemiology and Biostatistics, College for Public Health and Social Justice, Saint Louis University, Saint Louis, MO, USA

Yan Xie & Benjamin Bowe

Authors

1. Ziyad Al-Aly

[View author publications](#)

You can also search for this author in [PubMed](#) [Google Scholar](#)

2. Yan Xie

[View author publications](#)

You can also search for this author in [PubMed](#) [Google Scholar](#)

3. Benjamin Bowe

[View author publications](#)

You can also search for this author in [PubMed](#) [Google Scholar](#)

Contributions

Z.A.-A., Y.X. and B.B. contributed to the development of the study concept and design. Y.X. and B.B. contributed to data acquisition. Z.A.-A., Y.X. and B.B. contributed to data analysis and interpretation. Y.X. and B.B. contributed to statistical analysis. Z.A.-A. and Y.X. drafted the manuscript. Z.A.-A., Y.X. and B.B. contributed to critical revision of the manuscript. Z.A.-A. provided administrative, technical and material support. Z.A.-A. provided supervision and mentorship. Each author contributed important intellectual content during manuscript drafting or revision, and accepts accountability for the overall work by ensuring that questions pertaining to the accuracy or integrity of any portion of the work are appropriately investigated and resolved. All authors approved the final version of the report. The corresponding author attests that all the listed authors meet the authorship criteria and that no others meeting the criteria have been omitted.

Corresponding author

Correspondence to [Ziyad Al-Aly](#).

Ethics declarations

Competing interests

The authors declare no competing interests.

Additional information

Peer review information *Nature* thanks Paul Garner, Sachin Yende and the other, anonymous, reviewer(s) for their contribution to the peer review of this work.

Publisher's note Springer Nature remains neutral with regard to jurisdictional claims in published maps and institutional affiliations.

Extended data figures and tables

Extended Data Fig. 1 Risk of incident post-acute sequelae in COVID-19.

a–c, Incident diagnoses (**a**), incident medication use (**b**) and incident laboratory abnormalities (**c**). All VHA users served as the referent category. Outcomes were ascertained from day 30 after COVID-19 diagnosis until the end of follow-up. Adjusted hazard ratios for incident sequelae that are larger than 1 and P value less than 6.57×10^{-5} are presented. Hazard ratios (dots) and 95% confidence intervals (bars) are presented on \log_{10} scale.

Extended Data Fig. 2 High-dimensional identification of the incident post-acute sequelae in people who were hospitalized for COVID-19.

a–f, incident diagnoses (**a, d**), incident medication use (**b, e**) and incident laboratory abnormalities (**c, f**). Individuals who were hospitalized with seasonal influenza served as the referent category. Post-acute sequelae were ascertained from 30 days after infection until the end of follow-up. **a–c**, Beginning from the outside ring, the first ring represents hazard ratios for the post-acute sequelae of COVID-19. A higher bar indicates a larger hazard ratio. Hazard ratios with a point estimate larger than one and that are statistically significant are coloured in yellow. The second ring represents excess burden per 1,000 patients with COVID-19 at 6 months. Colour of the cell indicates value of the excess burden; deeper shades of red indicate higher excess burden and deeper shades of blue indicate greater reduced burden. The third ring represents the baseline incident rate in the control group; deeper shades of red indicate higher incident rate. The fourth ring represents negative log of the P value; a higher bar indicates a smaller P value and yellow indicates statistically significant. **d–f**, Sequelae were selected based on having a hazard ratio larger than one and P value less than 6.57×10^{-5} . Excess burdens per 1,000 patients with COVID-19 at 6 months are presented. Within each domain, outcomes are ranked based on excess burden from high to low. Diagnoses are coloured based on diagnosis group, medications are coloured based on medication class, and laboratory abnormalities are coloured based on higher or lower than normal range.

Extended Data Fig. 3 Risk of incident post-acute sequelae in people who were hospitalized for COVID-19.

a–c, Incident diagnoses (**a**), incident medication use (**b**) and incident laboratory abnormalities (**c**). People who were hospitalized with seasonal influenza served as the referent category. Outcomes were ascertained from day 30 after hospital admission until the end of follow-up. Adjusted hazard ratios for incident sequelae that are larger than 1 and P value less than 6.57×10^{-5} are presented. Hazard ratios (dots) and 95% confidence intervals (bars) are presented on a \log_{10} scale.

Extended Data Fig. 4 High-dimensional identification of the incident post-acute sequelae in people who were hospitalized for COVID-19 after additionally adjusting for severity of the acute infection.

a–f, Incident diagnoses (**a, d**), incident medication use (**b, e**) and incident laboratory abnormalities (**c, f**). Individuals who were hospitalized with seasonal influenza served as the referent category. Post-acute sequelae were ascertained from 30 days after infection until the end of follow-up. **a–c**, Beginning from the outside ring, the first ring represents hazard ratios for the post-acute sequelae of COVID-19. A higher bar indicates a larger hazard ratio. Hazard ratios with a point estimate larger than 1 and that are statistically significant are coloured in yellow. The second ring represents excess burden per 1,000 patients with COVID-19 at 6 months. The colour of the cell indicates the value of the excess burden; deeper shades of red indicate higher excess burden and deeper shades of blue indicate greater reduced burden. The third ring represents the baseline incident rate in the control group; deeper shades of red indicate higher incident rate. The fourth ring represents negative log of the P value; a higher bar indicates smaller P value and yellow bar indicates statistically significant. **d–f**, Sequelae were selected based on hazard ratio larger than 1 and P value less than 6.57×10^{-5} . Excess burdens per 1,000 patients with COVID-19 at 6 months are presented. Within each domain, outcomes are ranked based on excess burden from high to low. Diagnoses are coloured based on diagnosis group, medications are coloured based on medication class, and laboratory abnormalities are coloured based on higher or lower than normal range.

Extended Data Fig. 5 Risk of incident post-acute sequelae in people who were hospitalized for COVID-19 after additionally adjusting for severity of the acute infection.

a–c, Incident diagnoses (**a**), incident medication use (**b**) and incident laboratory abnormalities (**c**). People who had been hospitalized with seasonal influenza served as the referent category. Outcomes were ascertained from day 30 after hospital admission until the end of follow-up. Adjusted hazard ratios for incident sequelae that are larger than 1 and P value less than 6.57×10^{-5} are presented. Hazard ratios (dots) and 95% confidence intervals (bars) are presented on \log_{10} scale.

Extended Data Fig. 6 High-dimensional identification of the incident post-acute sequelae of people who were hospitalized for COVID-19.

a–f, Incident diagnoses (**a, d**), incident medication use (**b, e**) and incident laboratory abnormalities (**c, f**). Individuals who were hospitalized for other causes served as the referent category. Post-acute sequelae were ascertained from 30 days after infection until the end of follow-up. **a–c**, Beginning from the outside ring, the first ring represents hazard ratios for the post-acute sequelae of COVID-19. A higher bar indicates a larger hazard ratio. Hazard ratios with a point estimate larger than one and that are statistically significant are coloured in yellow. The second ring represents excess burden per 1,000 patients with COVID-19 at 6 months. Colour of the cell indicates value of the excess burden; deeper shades of red indicate higher excess burden and deeper shades of blue indicate greater reduced burden. The third ring represents the baseline incident rate in the control group; deeper shades of red indicate higher incident rate. The fourth ring represents negative log of the *P* value; a higher bar indicates smaller *P* value and yellow bar indicates statistically significant. **d–f**, Sequelae were selected on the basis of a hazard ratio larger than one and *P* value less than 6.57×10^{-5} . Excess burdens per 1,000 patients with COVID-19 at 6 months are presented. Within each domain, outcomes are ranked based on excess burden from high to low. Diagnoses are coloured based on diagnosis group, medications are coloured based on medication class, and laboratory abnormalities are coloured based on higher or lower than normal range.

Extended Data Fig. 7 Risk of incident post-acute sequelae in people with COVID-19 who were hospitalized for COVID-19.

a–c, Incident diagnoses (**a**), incident medication use (**b**) and incident laboratory abnormalities (**c**). People who had been hospitalized for other causes served as the referent category. Outcomes were ascertained from day 30 after hospital admission until the end of follow-up. Adjusted hazard ratios for incident sequelae that are larger than 1 and *P* value less than 6.57×10^{-5} are presented. Hazard ratios (dots) and 95% confidence intervals (bars) are presented on \log_{10} scale.

Extended Data Fig. 8 Risks and burdens of incident prespecified high-resolution post-acute COVID-19 outcomes at 6 months in hospitalized people with COVID-19 versus seasonal influenza.

Hospitalized people with seasonal influenza served as the referent category. Outcomes were ascertained from day 30 after hospital admission until the end of follow-up. Hazard ratios and 95% confidence intervals and excess burdens per 1,000 patients and 95% confidence intervals at 6 months are presented.

Extended Data Table 1 Characteristics of study cohorts

[Full size table](#)

Extended Data Table 2 Results of negative controls, and evidence of high risk of death and health resource use

[Full size table](#)

Supplementary information

Supplementary Figures

This file contains Supplementary Figures 1-8.

Reporting Summary

Supplementary Table 1

Balance of baseline variables after overlap weighting in COVID-19 vs VHA users.

Supplementary Table 2

Identification of the post-acute incident diagnoses in COVID-19 vs. all VHA users.

Supplementary Table 3

Identification of the post-acute incident medication use in COVID-19 vs. all VHA users.

Supplementary Table 4

Identification of the post-acute incident laboratory abnormalities in COVID-19 vs. all VHA users.

Supplementary Table 5

Burden of post-acute sequelae of COVID-19. Excess burdens were estimated vs. a comparator group of all users of the Veteran Health Administration.

Supplementary Table 6

Balance of baseline variables after overlap weighting in hospitalized COVID-19 vs seasonal influenza.

Supplementary Table 7

Identification of the post-acute incident diagnoses in people who had been hospitalized with COVID-19 vs. those who had been hospitalized with seasonal influenza.

Supplementary Table 8

Identification of the post-acute incident medication use in people who had been hospitalized with COVID-19 vs. those who had been hospitalized with seasonal influenza.

Supplementary Table 9

Identification of the post-acute incident laboratory abnormalities in people who had been hospitalized with COVID-19 vs. those who had been hospitalized with seasonal influenza.

Supplementary Table 10

Burden of post-acute sequelae of COVID-19 which required hospitalization during the acute infection. Excess burdens were estimated vs. a comparator group of people with seasonal influenza which required hospitalization during the acute infection.

Supplementary Table 11

Identification of the post-acute incident diagnoses in people who had been hospitalized with COVID-19 vs. those who had been hospitalized with seasonal influenza after additionally adjusting for severity of the acute infection.

Supplementary Table 12

Identification of the post-acute incident medication use in people who had been hospitalized with COVID-19 vs. those who had been hospitalized with seasonal influenza after additionally adjusting for severity of the acute infection.

Supplementary Table 13

Identification of the post-acute incident laboratory abnormalities in people who had been hospitalized with COVID-19 vs. those who had been hospitalized with seasonal influenza after additionally adjusting for severity of the acute infection.

Supplementary Table 14

Burden of post-acute sequelae of COVID-19 which required hospitalization during the acute infection after additionally adjusting for severity of the acute infection. Excess burdens were estimated vs. a comparator group of people with seasonal influenza which required hospitalization during the acute infection.

Supplementary Table 15

Identification of the post-acute incident diagnoses in people who had been hospitalized with COVID-19 vs. those who had been hospitalized for other causes.

Supplementary Table 16

Identification of the post-acute incident medication use in people who had been hospitalized with COVID-19 vs. those who had been hospitalized for other causes.

Supplementary Table 17

Identification of the post-acute incident laboratory abnormalities in people who had been hospitalized with COVID-19 vs. those who had been hospitalized for other causes.

Supplementary Table 18

Burden of post-acute sequelae of COVID-19 which required hospitalization during the acute infection. Excess burdens were estimated vs. a comparator group of people who required hospitalization for other causes. Estimates are provided per 1000 persons at 6-month.

Supplementary Table 19

Risks of incident pre-specified high resolution post-acute COVID-19 outcomes at 6 months in all users of the Veteran Health Administration healthcare system (referent category), people with COVID-19, people hospitalized for COVID-19, and people admitted to intensive care for COVID-19.

Supplementary Table 20

Pairwise comparison of risks of incident pre-specified high resolution post-acute COVID-19 outcomes at 6 months in all users of the Veteran Health Administration

healthcare system, people with COVID-19, people hospitalized for COVID-19, and people admitted to intensive care for COVID-19.

Supplementary Table 21

Risks of incident pre-specified high resolution post-acute COVID-19 outcomes at 6 months in hospitalized people with COVID-19 vs. seasonal influenza (the referent category). Outcomes were ascertained from day 30 after COVID-19 diagnosis until end of follow-up.

Supplementary table 22

Measures of the association between negative exposure control (exposure to influenza vaccine in even vs. odd months) and the risks of incident diagnoses.

Supplementary Table 23

Measures of the association between negative exposure control (exposure to influenza vaccine in even vs. odd months) and the risks of incident medication use.

Supplementary Table 24

Measures of the association between negative exposure control (exposure to influenza vaccine in even vs. odd months) and the risks of incident laboratory abnormalities.

Rights and permissions

Reprints and Permissions

About this article



Check for
updates

Cite this article

Al-Aly, Z., Xie, Y. & Bowe, B. High-dimensional characterization of post-acute sequelae of COVID-19. *Nature* **594**, 259–264 (2021). <https://doi.org/10.1038/s41586-021-03553-9>

[Download citation](#)

- Received: 18 January 2021
- Accepted: 14 April 2021
- Published: 22 April 2021
- Issue Date: 10 June 2021
- DOI: <https://doi.org/10.1038/s41586-021-03553-9>

Further reading

- [Cellular Tropism of SARS-CoV-2 across Human Tissues and Age-related Expression of ACE2 and TMPRSS2 in Immune-inflammatory Stromal Cells](#)
 - Ming Zheng

Aging and disease (2021)
- [Unpacking post-covid symptoms](#)
 - Elaine Maxwell

BMJ (2021)
- [Long-COVID Syndrome? A Study on the Persistence of Neurological, Psychological and Physiological Symptoms](#)
 - Graziella Orrù
 - , Davide Bertelloni
 - , Francesca Diolaiuti
 - , Federico Mucci
 - , Mariagrazia Di Giuseppe
 - , Marco Biella
 - , Angelo Gemignani
 - , Rebecca Ciacchini
 - & Ciro Conversano

Healthcare (2021)

Comments

By submitting a comment you agree to abide by our [Terms](#) and [Community Guidelines](#). If you find something abusive or that does not comply with our terms or guidelines please flag it as inappropriate.

[Download PDF](#)

Advertisement

This article was downloaded by **calibre** from <https://www.nature.com/articles/s41586-021-03553-9>

| [Section menu](#) | [Main menu](#) |

Swarm Learning for decentralized and confidential clinical machine learning
[Download PDF](#)

- Article
- Open Access
- [Published: 26 May 2021](#)

Swarm Learning for decentralized and confidential clinical machine learning

- [Stefanie Warnat-Herresthal](#) ORCID: [orcid.org/0000-0002-0890-5774](#)^{1,2 na1},
- [Hartmut Schultze](#) ORCID: [orcid.org/0000-0001-5008-7851](#)^{3 na1},
- [Krishnaprasad Lingadahalli Shastry](#)^{3 na1},
- [Sathyaranarayanan Manamohan](#) ORCID: [orcid.org/0000-0002-3612-6276](#)^{3 na1},
- [Saikat Mukherjee](#)^{3 na1},
- [Vishesh Garg](#) ORCID: [orcid.org/0000-0001-5133-5896](#)^{3,4 na1},
- [Ravi Sarveswara](#)^{3 na1},
- [Kristian Händler](#)^{1,5 na1},
- [Peter Pickkers](#)^{6 na1},
- [N. Ahmad Aziz](#) ORCID: [orcid.org/0000-0001-6184-458X](#)^{7,8 na1},
- [Sofia Ktena](#)^{9 na1},
- [Florian Tran](#) ORCID: [orcid.org/0000-0002-3735-9872](#)^{10,11},
- [Michael Bitzer](#)¹²,
- [Stephan Ossowski](#)^{13,14},
- [Nicolas Casadei](#) ORCID: [orcid.org/0000-0003-2209-0580](#)^{13,14},
- [Christian Herr](#) ORCID: [orcid.org/0000-0001-9422-6569](#)¹⁵,
- [Daniel Petersheim](#)¹⁶,
- [Uta Behrends](#)¹⁷,
- [Fabian Kern](#) ORCID: [orcid.org/0000-0002-8223-3750](#)¹⁸,
- [Tobias Fehlmann](#) ORCID: [orcid.org/0000-0003-1967-2918](#)¹⁸,
- [Philipp Schommers](#)¹⁹,
- [Clara Lehmann](#)^{19,20,21},
- [Max Augustin](#) ORCID: [orcid.org/0000-0002-2300-9337](#)^{19,20,21},
- [Jan Rybníkář](#)^{19,20,21},
- [Janine Altmüller](#)²²,
- [Neha Mishra](#)¹¹,

- [Joana P. Bernardes](#)¹¹,
- [Benjamin Krämer](#)²³,
- [Lorenzo Bonaguro](#) [ORCID: orcid.org/0000-0001-9675-7208](#)^{1,2},
- [Jonas Schulte-Schrepping](#)^{1,2},
- [Elena De Domenico](#) [ORCID: orcid.org/0000-0003-0336-8284](#)^{1,5},
- [Christian Siever](#) [ORCID: orcid.org/0000-0002-2991-9307](#)³,
- [Michael Kraut](#)^{1,5},
- [Milind Desai](#)³,
- [Bruno Monnet](#)³,
- [Maria Saridaki](#)⁹,
- [Charles Martin Siegel](#)³,
- [Anna Drews](#)^{1,5},
- [Melanie Nuesch-Germano](#)^{1,2},
- [Heidi Theis](#) [ORCID: orcid.org/0000-0001-6339-2521](#)^{1,5},
- [Jan Heyckendorf](#)²³,
- [Stefan Schreiber](#)¹⁰,
- [Sarah Kim-Hellmuth](#)¹⁶,
- [COVID-19 Aachen Study \(COVAS\)](#),
- [Jacob Nattermann](#)^{24,25},
- [Dirk Skowasch](#)²⁶,
- [Ingo Kurth](#) [ORCID: orcid.org/0000-0002-5642-8378](#)²⁷,
- [Andreas Keller](#) [ORCID: orcid.org/0000-0002-5361-0895](#)^{18,28},
- [Robert Bals](#)¹⁵,
- [Peter Nürnberg](#)²²,
- [Olaf Rieß](#)^{13,14},
- [Philip Rosenstiel](#)¹¹,
- [Mihai G. Netea](#) [ORCID: orcid.org/0000-0003-2421-6052](#)^{29,30},
- [Fabian Theis](#) [ORCID: orcid.org/0000-0002-2419-1943](#)³¹,
- [Sach Mukherjee](#)³²,
- [Michael Backes](#)³³,
- [Anna C. Aschenbrenner](#) [ORCID: orcid.org/0000-0002-9429-5457](#)^{1,2,5,29},
- [Thomas Ulas](#) [ORCID: orcid.org/0000-0002-9785-4197](#)^{1,2},
- [Deutsche COVID-19 Omics Initiative \(DeCOI\)](#),
- [Monique M. B. Breteler](#) [ORCID: orcid.org/0000-0002-0626-9305](#)^{7,34 na2},
- [Evangelos J. Giamarellos-Bourboulis](#) [ORCID: orcid.org/0000-0003-4713-3911](#)^{9 na2},
- [Matthijs Kox](#) [ORCID: orcid.org/0000-0001-6537-6971](#)^{6 na2},
- [Matthias Becker](#) [ORCID: orcid.org/0000-0002-7120-4508](#)^{1,5 na2},
- [Sorin Cheran](#)^{3 na2},

- [Michael S. Woodacre^{3 na2}](#),
- [Eng Lim Goh ORCID: orcid.org/0000-0002-3449-9634^{3 na2}](#) &
- [Joachim L. Schultze ORCID: orcid.org/0000-0003-2812-9853^{1,2,5 na2}](#)

Nature volume **594**, pages 265–270 (2021)[Cite this article](#)

- 27k Accesses
- 377 Altmetric
- [Metrics details](#)

Subjects

- [Computational models](#)
- [Diagnostic markers](#)
- [Machine learning](#)
- [Predictive medicine](#)
- [Viral infection](#)

Abstract

Fast and reliable detection of patients with severe and heterogeneous illnesses is a major goal of precision medicine^{1,2}. Patients with leukaemia can be identified using machine learning on the basis of their blood transcriptomes³. However, there is an increasing divide between what is technically possible and what is allowed, because of privacy legislation^{4,5}. Here, to facilitate the integration of any medical data from any data owner worldwide without violating privacy laws, we introduce Swarm Learning—a decentralized machine-learning approach that unites edge computing, blockchain-based peer-to-peer networking and coordination while maintaining confidentiality without the need for a central coordinator, thereby going beyond federated learning. To illustrate the feasibility of using Swarm Learning to develop disease classifiers using distributed data, we chose four use cases of heterogeneous diseases (COVID-19, tuberculosis, leukaemia and lung pathologies). With more than 16,400 blood transcriptomes derived from 127 clinical studies with non-uniform distributions of cases and controls and substantial study biases, as well as more than 95,000 chest X-ray images, we show that Swarm Learning classifiers outperform those developed at individual sites. In addition, Swarm Learning completely fulfils local confidentiality regulations by design. We believe that this approach will notably accelerate the introduction of precision medicine.

[Download PDF](#)

Main

Identification of patients with life-threatening diseases, such as leukaemias, tuberculosis or COVID-19^{6,7}, is an important goal of precision medicine². The measurement of molecular phenotypes using ‘omics’ technologies¹ and the application of artificial intelligence (AI) approaches^{4,8} will lead to the use of large-scale data for diagnostic purposes. Yet, there is an increasing divide between what is technically possible and what is allowed because of privacy legislation^{5,9,10}. Particularly in a global crisis^{6,7}, reliable, fast, secure, confidentiality- and privacy-preserving AI solutions can facilitate answering important questions in the fight against such threats^{11,12,13}. AI-based concepts range from drug target prediction¹⁴ to diagnostic software^{15,16}. At the same time, we need to consider important standards relating to data privacy and protection, such as Convention 108+ of the Council of Europe¹⁷.

AI-based solutions rely intrinsically on appropriate algorithms¹⁸, but even more so on large training datasets¹⁹. As medicine is inherently decentral, the volume of local data is often insufficient to train reliable classifiers^{20,21}. As a consequence, centralization of data is one model that has been used to address the local limitations²². While beneficial from an AI perspective, centralized solutions have inherent disadvantages, including increased data traffic and concerns about data ownership, confidentiality, privacy, security and the creation of data monopolies that favour data aggregators¹⁹. Consequently, solutions to the challenges of central AI models must be effective, accurate and efficient; must preserve confidentiality, privacy and ethics; and must be secure and fault-tolerant by design^{23,24}. Federated AI addresses some of these aspects^{19,25}. Data are kept locally and local confidentiality issues are addressed²⁶, but model parameters are still handled by central custodians, which concentrates power. Furthermore, such star-shaped architectures decrease fault tolerance.

We hypothesized that completely decentralized AI solutions would overcome current shortcomings, and accommodate inherently decentral data structures and data privacy and security regulations in medicine. The solution (1) keeps large medical data locally with the data owner; (2) requires no exchange of raw data, thereby also reducing data traffic; (3) provides high-level data security; (4) guarantees secure, transparent and fair onboarding of decentral members of the network without the need for a central custodian; (5) allows parameter merging with equal rights for all members; and (6) protects machine learning models from attacks. Here, we introduce Swarm Learning (SL), which combines decentralized hardware infrastructures, distributed machine learning based on standardized AI engines with a permissioned blockchain to securely onboard members, to dynamically elect the leader among members, and to merge model parameters. Computation is orchestrated by an SL library (SLL) and an iterative AI learning procedure that uses decentral data ([Supplementary Information](#)).

Concept of Swarm Learning

Conceptually, if sufficient data and computer infrastructure are available locally, machine learning can be performed locally (Fig. 1a). In cloud computing, data are moved centrally so that machine learning can be carried out by centralized computing (Fig. 1b), which can substantially increase the amount of data available for training and thereby improve machine learning results¹⁹, but poses disadvantages such as data duplication and increased data traffic as well as challenges for data privacy and security²⁷. Federated computing approaches²⁵ have been developed, wherein dedicated parameter servers are responsible for aggregating and distributing local learning (Fig. 1c); however, a remainder of a central structure is kept.

Fig. 1: Concept of Swarm Learning.



a, Illustration of the concept of local learning with data and computation at different, disconnected locations. **b**, Principle of cloud-based machine learning. **c**, Federated learning, with data being kept with the data contributor and computing performed at the site of local data storage and availability, but parameter settings orchestrated by a central parameter server. **d**, Principle of SL without the need for a central custodian. **e**, Schematic of the Swarm network, consisting of Swarm edge nodes that exchange parameters for learning, which is implemented using blockchain technology. Private data are used at each node together with the model provided by the Swarm network. **f–l**, Descriptions of the transcriptome datasets used. **f**, **g**, Datasets A1 (**f**; $n = 2,500$) and A2 (**g**; $n = 8,348$): two microarray-based transcriptome datasets of PBMCs. **h**, Dataset A3: 1,181 RNA-seq-based transcriptomes of PBMCs. **i**, Dataset B: 1,999 RNA-seq-based whole blood transcriptomes. **j**, Dataset E: 2,400 RNA-seq-based whole blood and granulocyte transcriptomes. **k**, Dataset D: 2,143 RNA-seq-based whole blood transcriptomes. **l**, Dataset C: 95,831 X-ray images. CML, chronic myeloid leukaemia; CLL, chronic lymphocytic leukaemia; Inf., infections; Diab., type II diabetes; MDS, myelodysplastic syndrome; MS, multiple sclerosis; JIA, juvenile idiopathic arthritis; TB, tuberculosis; HIV, human immunodeficiency virus; AID, autoimmune disease.

[Full size image](#)

As an alternative, we introduce SL, which dispenses with a dedicated server (Fig. 1d), shares the parameters via the Swarm network and builds the models independently on private data at the individual sites (short ‘nodes’ called Swarm edge nodes) (Fig. 1e). SL provides security measures to support data sovereignty, security, and confidentiality (Extended Data Fig. 1a) realized by private permissioned blockchain technology (Extended Data Fig. 1b). Each participant is well defined and only pre-authorized participants can execute transactions. Onboarding of new nodes is dynamic, with appropriate authorization measures to recognize network participants. A new node enrolls via a blockchain smart contract, obtains the model, and performs local model training until defined conditions for synchronization are met (Extended Data Fig. 1c). Next, model parameters are exchanged via a Swarm application programming interface (API) and merged to create an updated model with updated parameter settings before starting a new training round ([Supplementary Information](#)).

At each node, SL is divided into middleware and an application layer. The application environment contains the machine learning platform, the blockchain, and the SLL (including a containerized Swarm API to execute SL in heterogeneous hardware infrastructures), whereas the application layer contains the models (Extended Data Fig. 1d, [Supplementary Information](#)); for example, analysis of blood transcriptome data from patients with leukaemia, tuberculosis and COVID-19 (Fig. 1f–k) or radiograms (Fig. 1l). We selected both heterogeneous and life-threatening diseases to exemplify the immediate medical value of SL.

Swarm Learning predicts leukaemias

First, we used peripheral blood mononuclear cell (PBMC) transcriptomes from more than 12,000 individuals (Fig. 1f-h) in three datasets (A1–A3, comprising two types of microarray and RNA sequencing (RNA-seq))³. If not otherwise stated, we used sequential deep neural networks with default settings²⁸. For each real-world scenario, samples were split into non-overlapping training datasets and a global test dataset²⁹ that was used for testing the models built at individual nodes and by SL (Fig. 2a). Within training data, samples were ‘silenced’ at each of the Swarm nodes in different distributions, thereby mimicking clinically relevant scenarios (Supplementary Table 1). As cases, we used samples from individuals with acute myeloid leukaemia (AML); all other samples were termed ‘controls’. Each node within this simulation could stand for a medical centre, a network of hospitals, a country or any other independent organization that generates such medical data with local privacy requirements.

Fig. 2: Swarm Learning to predict leukaemias from PBMC data.

 **figure2**

a, Overview of the experimental setup. Data consisting of biological replicates are split into non-overlapping training and test sets. Training data are siloed in Swarm edge nodes 1–3 and testing node T is used as independent test set. SL is achieved by integrating nodes 1–3 for training following the procedures described in the

Supplementary Information. Red and blue bars illustrate the scenario-specific distribution of cases and controls among the nodes; percentages depict the percentage of samples from the full dataset. **b**, Scenario using dataset A2 with uneven distributions of cases and controls and of samples sizes among nodes. **c**, Scenario with uneven numbers of cases and controls at the different training nodes but similar numbers of samples at each node. **d**, Scenario with samples from independent studies from A2 sampled to different nodes, resulting in varying numbers of cases and controls per node. **e**, Scenario in which each node obtained samples from different transcriptomic technologies (nodes 1–3: datasets A1–A3). The test node obtained samples from each dataset A1–A3. **b–e**, Box plots show accuracy of 100 permutations performed for the 3 training nodes individually and for SL. All samples are biological replicates. Centre dot, mean; box limits, 1st and 3rd quartiles; whiskers, minimum and maximum values. Accuracy is defined for the independent fourth node used for testing only. Statistical differences between results derived by SL and all individual nodes including all permutations performed were calculated using one-sided Wilcoxon signed-rank test with continuity correction; * $P < 0.05$, exact P values listed in Supplementary Table 5.

[Full size image](#)

First, we distributed cases and controls unevenly at and between nodes (dataset A2) (Fig. 2b, Extended Data Fig. 2a, [Supplementary Information](#)), and found that SL outperformed each of the nodes (Fig. 2b). The central model performed only slightly better than SL in this scenario (Extended Data Fig. 2b). We obtained very similar results using datasets A1 and A3, which strongly supports the idea that the improvement in performance of SL is independent of data collection (clinical studies) or the technologies (microarray or RNA-seq) used for data generation (Extended Data Fig. 2c–e).

We tested five additional scenarios on datasets A1–A3: (1) using evenly distributed samples at the test nodes with case/control ratios similar to those in the first scenario (Fig. 2c, Extended Data Fig. 2f–j, [Supplementary Information](#)); (2) using evenly distributed samples, but siloing samples from particular clinical studies to dedicated training nodes and varying case/control ratios between nodes (Fig. 2d, Extended Data Fig. 3a–h, [Supplementary Information](#)); (3) increasing sample size for each training node (Extended Data Fig. 4a–f, [Supplementary Information](#)); (4) siloing samples generated with different technologies at dedicated training nodes (Fig. 2e, Extended Data Fig. 4g–i, [Supplementary Information](#)); and (5) using different RNA-seq protocols (Extended Data Fig. 4j–k, Supplementary Table 7, [Supplementary Information](#)). In all these scenarios, SL outperformed individual nodes and was either close to or equivalent to the central models.

We repeated several of the scenarios with samples from patients with acute lymphoblastic leukaemia (ALL) as cases, extended the prediction to a multi-class problem across four major types of leukaemia, extended the number of nodes to 32, tested onboarding of nodes at a later time point (Extended Data Fig. 5a–j) and replaced the deep neural network with LASSO (Extended Data Fig. 6a–c), and the results echoed the above findings ([Supplementary Information](#)).

Swarm Learning to identify tuberculosis

We built a second use case to identify patients with tuberculosis (TB) from blood transcriptomes^{30,31} (Fig. 1i, [Supplementary Information](#)). First, we used all TB samples (latent and active) as cases and distributed TB cases and controls evenly among the nodes (Extended Data Fig. 7a). SL outperformed individual nodes and performed slightly better than a central model under these conditions (Extended Data Fig. 7b, [Supplementary Information](#)). Next, we predicted active TB only. Latently infected TB cases were treated as controls (Extended Data Fig. 7a) and cases and controls were kept even, but the number of training samples was reduced (Fig. 3a). Under these more challenging conditions, overall performance dropped, but SL still performed better than any of the individual nodes. When we further reduced training sample numbers by 50%, SL still outperformed the nodes, but all statistical readouts at nodes and SL showed lower performance; however, SL was still equivalent to a central model (Extended Data Fig. 7c, [Supplementary Information](#)), consistent with general observations that AI performs better when training data are increased¹⁹. Dividing up the training data at three nodes into six smaller nodes reduced the performance of each individual node, whereas the SL results did not deteriorate (Fig. 3b, [Supplementary Information](#)).

Fig. 3: Swarm Learning to identify patients with TB or lung pathologies.



a–c, Scenarios for the prediction of TB with experimental setup as in Fig. 2a. **a**, Scenario with even number of cases at each node; 10 permutations. **b**, Scenario similar to **a** but with six training nodes; 10 permutations. **c**, Scenario in which the training nodes have evenly distributed numbers of cases and controls at each training node, but node 2 has fewer samples; 50 permutations. **d**, Scenario for multilabel prediction of dataset C with uneven distribution of diseases at nodes; 10 permutations. **a–d**, Box plots show accuracy of all permutations for the training nodes individually and for SL. All samples are biological replicates. Centre dot, mean; box limits, 1st and 3rd quartiles; whiskers, minimum and maximum values. Accuracy is defined for the independent fourth node used for testing only. Statistical differences between results derived by SL and all individual nodes including all permutations performed were calculated with one-sided Wilcoxon signed rank test with continuity correction; * $P < 0.05$, exact P values listed in Supplementary Table 5.

[Full size image](#)

As TB has endemic characteristics, we used TB to simulate potential outbreak scenarios to identify the benefits and potential limitations of SL and determine how to address them (Fig. 3c, Extended Data Fig. 7d–f, [Supplementary Information](#)). The first scenario reflects a situation in which three independent regions (simulated by the nodes) would already have sufficient but different numbers of disease cases (Fig. 3c, [Supplementary Information](#)). In this scenario, the results for SL were almost comparable to those in Fig. 3a, whereas the results for node 2 (which had the smallest numbers of cases and controls) dropped noticeably. Reducing prevalence at the test node caused the node results to deteriorate, but the performance of SL was almost unaffected (Extended Data Fig. 7d, [Supplementary Information](#)).

We decreased case numbers at node 1 further, which reduced test performance for this node (Extended Data Fig. 7e), without substantially impairing SL performance. When we lowered prevalence at the test node, all performance parameters, including the F1 score (a measure of accuracy), were more resistant for SL than for individual nodes (Extended Data Fig. 7f–j).

We built a third use case for SL that addressed a multi-class prediction problem using a large publicly available dataset of chest X-rays³² (Figs. 11, 3d, [Supplementary Information](#), [Methods](#)). SL outperformed each node in predicting all radiological findings included (atelectasis, effusion, infiltration and no finding), which suggests that SL is also applicable to non-transcriptomic data spaces.

Identification of COVID-19

In the fourth use case, we addressed whether SL could be used to detect individuals with COVID-19 (Fig. 1k, Supplementary Table 6). Although COVID-19 is usually detected by using PCR-based assays to detect viral RNA³³, assessing the specific host response in addition to disease prediction might be beneficial in situations for which the pathogen is unknown, specific pathogen tests are not yet possible, existing tests might produce false negative results, and blood transcriptomics can contribute to the understanding of the host's immune response^{34,35,36}.

In a first proof-of-principle study, we simulated an outbreak situation node with evenly distributed cases and controls at training nodes and test nodes (Extended Data Fig. 8a, b); this showed very high statistical performance parameters for SL and all nodes. Lowering the prevalence at test nodes reduced performance (Extended Data Fig. 8c), but F1 scores deteriorated only when we reduced prevalence further (1:44 ratio) (Extended Data Fig. 8d); even under these conditions, SL performed best. When we reduced cases at training nodes, all performance measures remained very high at the test node for SL and individual nodes (Extended Data Fig. 8e–j). When we tested outbreak scenarios with very few cases at test nodes and varying prevalence at the independent test node (Fig. 4a), nodes 2 and 3 showed decreased performance; SL outperformed these nodes (Fig. 4b, Extended Data Fig. 8k, l) and was equivalent to the central model (Extended Data Fig. 8m). The model showed no sign of overfitting (Extended Data Fig. 8n) and comparable results were obtained when we increased the number of training nodes (Extended Data Fig. 9a–d).

Fig. 4: Identification of patients with COVID-19 in an outbreak scenario.

 **figure4**

a, An outbreak scenario for COVID-19 using dataset D with experimental setup as in Fig. 2a. **b**, Evaluation of **a** with even prevalence showing accuracy, sensitivity, specificity and F1 score of 50 permutations for each training node and SL, on the test node. **c**, An outbreak scenario with dataset E, particularly E1–6 with an 80:20 training:test split. Training data are distributed to six training nodes, independent test data are placed at the test node. **d**, Evaluation of **c** showing AUC, accuracy, sensitivity, specificity and F1 score of 20 permutations. All samples are biological replicates.

Centre dot, mean; box limits, 1st and 3rd quartiles; whiskers, minimum and maximum values. Statistical differences between results derived by SL and all individual nodes including all permutations performed were calculated with one-sided Wilcoxon signed-rank test with continuity correction; * $P < 0.05$, all P values listed in Supplementary Table 5.

[Full size image](#)

We recruited further medical centres in Europe that differed in controls and distributions of age, sex, and disease severity ([Supplementary Information](#)), which yielded eight individual centre-specific sub-datasets (E1–8; Extended Data Fig. 9e).

In the first setting, centres E1–E6 teamed up and joined the Swarm network with 80% of their local data; 20% of each centre's dataset was distributed to a test node²⁹ (Fig. 4c) and the model was also tested on two external datasets, one with convalescent COVID-19 cases (E7) and one of granulocyte-enriched COVID-19 samples (E8). SL outperformed all nodes in terms of area under the curve (AUC) for the prediction of the global test datasets (Fig. 4d, Extended Data Fig. 9f, [Supplementary Information](#)). When looking at performance on testing samples split by centre of origin, it became clear that individual centre nodes could not have predicted samples from other centres (Extended Data Fig. 9g). By contrast, SL predicted samples from these nodes successfully. This was similarly true when we reduced the scenario, using E1, E2, and E3 as training nodes and E4 as an independent test node (Extended Data Fig. 9h).

In addition, SL can cope with biases such as sex distribution, age or co-infection bias (Extended Data Fig. 10a–c, [Supplementary Information](#)) and SL outperformed individual nodes when distinguishing mild from severe COVID-19 (Extended Data Fig. 10d,e). Collectively, we provide evidence that blood transcriptomes from COVID-19 patients represent a promising feature space for applying SL.

Discussion

With increasing efforts to enforce data privacy and security^{5,9,10} and to reduce data traffic and duplication, a decentralized data model will become the preferred choice for handling, storing, managing, and analysing any kind of large medical dataset¹⁹. Particularly in oncology, success has been reported in machine-learning-based tumour detection^{3,37}, subtyping³⁸, and outcome prediction³⁹, but progress is hindered by the limited size of datasets¹⁹, with current privacy regulations^{5,9,10} making it less appealing to develop centralized AI systems. SL, as a decentralized learning system, replaces the current paradigm of centralized data sharing in cross-institutional medical research. SL's blockchain technology gives robust measures against dishonest participants or adversaries attempting to undermine a Swarm network. SL provides

confidentiality-preserving machine learning by design and can inherit new developments in differential privacy algorithms⁴⁰, functional encryption⁴¹, or encrypted transfer learning approaches⁴² ([Supplementary Information](#)).

Global collaboration and data sharing are important quests¹³ and both are inherent characteristics of SL, with the further advantage that data sharing is not even required and can be transformed into knowledge sharing, thereby enabling global collaboration with complete data confidentiality, particularly if using medical data. Indeed, statements by lawmakers have emphasized that privacy rules apply fully during a pandemic⁴³. Particularly in such crises, AI systems need to comply with ethical principles and respect human rights¹². Systems such as SL—allowing fair, transparent, and highly regulated shared data analytics while preserving data privacy—are to be favoured. SL should be explored for image-based diagnosis of COVID-19 from patterns in X-ray images or CT scans^{15,16}, structured health records¹², or data from wearables for disease tracking¹². Collectively, SL and transcriptomics (or other medical data) are a very promising approach to democratize the use of AI among the many stakeholders in the domain of medicine, while at the same time resulting in improved data confidentiality, privacy, and data protection, and a decrease in data traffic.

Methods

Pre-processing

PBMC transcriptome dataset (dataset A)

We used a previously published dataset compiled for predicting AML in blood transcriptomes derived from PBMCs ([Supplementary Information](#))³. In brief, all raw data files were downloaded from GEO (<https://www.ncbi.nlm.nih.gov/geo/>) and the RNA-seq data were preprocessed using the kallisto v0.43.1 aligner against the human reference genome gencode v27 (GRCh38.p10). For normalization, we considered all platforms independently, meaning that normalization was performed separately for the samples in datasets A1, A2 and A3. Microarray data (datasets A1 and A2) were normalized using the robust multichip average (RMA) expression measures, as implemented in the R package affy v.1.60.0. The RNA-seq data (dataset A3) were normalized using the R package DESeq2 (v 1.22.2) with standard parameters. To keep the datasets comparable, data were filtered for genes annotated in all three datasets, which resulted in 12,708 genes. No filtering of low-expressed genes was performed. All scripts used in this study for pre-processing are provided as a docker container on Docker Hub (v 0.1, https://hub.docker.com/r/schultzelab/ml_classifier).

Whole-blood-derived transcriptome datasets (datasets B, D and E)

As alignment of whole blood transcriptome data can be performed in many ways, we re-aligned all downloaded and collected datasets ([Supplementary Information](#); these were 30.6 terabytes in size and comprised a total of 63.4 terabases) to the human reference genome gencode v33 (GRCh38.p13) and quantified transcript counts using STAR, an ultrafast universal RNA-seq aligner (v.2.7.3a). For all samples in datasets B, D, and E, raw counts were imported using DESeq (v.1.22.2, DESeqData SetFromMatrix function) and size factors for normalization were calculated using the DESeq function with standard parameters. This was done separately for datasets B, D, and E. As some of the samples were prepared with poly-A selection to enrich for protein-coding mRNAs, we filtered the complete dataset for protein-coding genes to ensure greater comparability across library preparation protocols. Furthermore, we excluded all ribosomal protein-coding genes, as well as mitochondrial genes and genes coding for haemoglobins, which resulted in 18,135 transcripts as the feature space in dataset B, 19,358 in dataset D and 19,399 in dataset E. Furthermore, transcripts with overall expression <100 were excluded from further analysis. Other than that, no filtering of transcripts was performed. Before using the data in machine learning, we performed a rank transformation to normality on datasets B, D and E. In brief, transcript expression values were transformed from RNA-seq counts to their ranks. This was done transcript-wise, meaning that all transcript expression values per sample were given a rank based on ordering them from lowest to highest value. The rankings were then turned into quantiles and transformed using the inverse cumulative distribution function of the normal distribution. This leads to all transcripts following the exact same distribution (that is, a standard normal with a mean of 0 and a standard deviation of 1 across all samples). All scripts used in this study for pre-processing are provided on Github (https://github.com/schultzelab/swarm_learning) and normalized and rank-transformed count matrices used for predictions are provided via FASTGenomics at <https://beta.fastgenomics.org/p/swarm-learning>.

X-ray dataset (dataset C)

The National Institutes of Health (NIH) chest X-Ray dataset ([Supplementary Information](#)) was downloaded from <https://www.kaggle.com/nih-chest-xrays/data>³². To preprocess the data, we used Keras (v.2.3.1) real-time data augmentation and generation APIs (keras.preprocessing.image.ImageDataGenerator and flow_from_dataframe). The following pre-processing arguments were used: height or width shift range (about 5%), random rotation range (about 5°), random zoom range (about 0.15), sample-wise centre and standard normalization. In addition, all images were resized to 128 × 128 pixels from their original size of 1,024 × 1,024 pixels and 32 images per batch were used for model training.

The Swarm Learning framework

SL builds on two proven technologies, distributed machine learning and blockchain ([Supplementary Information](#)). The SLL is a framework to enable decentralized training of machine learning models without sharing the data. It is designed to make it possible for a set of nodes—each node possessing some training data locally—to train a common machine learning model collaboratively without sharing the training data. This can be achieved by individual nodes sharing parameters (weights) derived from training the model on the local data. This allows local measures at the nodes to maintain the confidentiality and privacy of the raw data. Notably, in contrast to many existing federated learning models, a central parameter server is omitted in SL. Detailed descriptions of the SLL, the architecture principles, the SL process, implementation, and the environment can be found in the [Supplementary Information](#).

Hardware architecture used for simulations

For all simulations provided in this project we used two HPE Apollo 6500 Gen 10 servers, each with four Intel(R) Xeon(R) CPU E5-2698 v4 @ 2.20 GHz, a 3.2-terabyte hard disk drive, 256 GB RAM, eight Tesla P100 GPUs, a 1-GB network interface card for LAN access and an InfiniBand FDR for high speed interconnection and networked storage access. The Swarm network is created with a minimum of 3 up to a maximum of 32 training nodes, and each node is a docker container with access to GPU resources. Multiple experiments were run in parallel using this configuration.

Overall, we performed 16,694 analyses including 26 scenarios for AML, four scenarios for ALL, 13 scenarios for TB, one scenario for detection of atelectasis, effusion, and/or infiltration in chest X-rays, and 18 scenarios for COVID-19 ([Supplementary Information](#)). We performed 5–100 permutations per scenario and each permutation took approximately 30 min, which resulted in a total of 8,347 computer hours.

Computation and algorithms

Neural network algorithm

We leveraged a deep neural network with a sequential architecture as implemented in Keras (v 2.3.1)²⁸. Keras is an open source software library that provides a Python interface to neural networks. The Keras API was developed with a focus on fast experimentation and is standard for deep learning researchers. The model, which was already available in Keras for R from the previous study³, has been translated from R to Python to make it compatible with the SLL ([Supplementary Information](#)). In brief, the neural network consists of one input layer, eight hidden layers and one output layer. The input layer is densely connected and consists of 256 nodes, a rectified linear unit activation function and a dropout rate of 40%. From the first to the eighth hidden layer, nodes are reduced from 1,024 to 64 nodes, and all layers contain a rectified linear unit activation function, a kernel regularization with an L2 regularization factor of 0.005 and a dropout rate of 30%. The output layer is densely connected and consists of one node and a sigmoid activation function. The model is configured for training with Adam optimization and to compute the binary cross-entropy loss between true labels and predicted labels.

The model is used for training both the individual nodes and SL. The model is trained over 100 epochs, with varying batch sizes. Batch sizes of 8, 16, 32, 64 and 128 are used, depending on the number of training samples. The full code for the model is provided on Github (https://github.com/schultzelab/swarm_learning/)

Least absolute shrinkage and selection operator (LASSO)

SL is not restricted to any particular classification algorithm. We therefore adapted the l1-penalized logistic regression³ to be used with the SLL in the form of a Keras single dense layer with linear activation. The regularization parameter lambda was set to 0.01. The full code for the model is provided on Github (https://github.com/schultzelab/swarm_learning/)

Parameter tuning

For most scenarios, default settings were used without parameter tuning. For some of the scenarios we tuned model hyperparameters. For some scenarios we also tuned SL parameters to get better performance (for example, higher sensitivity) (Supplementary Table 8). For example, for AML (Fig. 2e,f, Extended Data Fig. 2), the dropout rate was reduced to 10% to get better performance. For AML (Fig. 2b), the dropout rate was reduced to 10% and the epochs increased to 300 to get better performance. We also used the adaptive_rv parameter in the SL API to adjust the merge frequency dynamically on the basis of model convergence, to improve the training time. For TB and COVID-19, the test dropout rate was reduced to 10% for all scenarios. For the TB scenarios (Extended Data Fig. 7f,g), the node_weightage parameter of the SL callback API was used to give more weight to nodes that had more case samples. Supplementary Table 8 provides a complete overview of all tuning parameters used.

Parameter merging

Different functions are available for parameter merging as a configuration of the Swarm API, which are then applied by the leader at every synchronization interval. The parameters can be merged as average, weighted average, minimum, maximum, or median functions.

In this Article, we used the weighted average, which is defined as

$$\$ \$ \{P\}_M = \frac{\sum_{k=1}^n (W_k \times P_k)}{n \times \sum_{k=1}^n W_k} \$ \$$$

in which P_M is merged parameters, P_k is parameters from the k th node, W_k is the weight of the k th node, and n is the number of nodes participating in the merge process.

Unless stated otherwise, we used a simple average without weights to merge the parameter for neural networks and for the LASSO algorithm.

Quantification and statistical analysis

We evaluated binary classification model performance with sensitivity, specificity, accuracy, F1 score, and AUC metrics, which were determined for every test run. The 95% confidence intervals of all performance metrics were estimated using bootstrapping. For AML and ALL, 100 permutations per scenario were run for each scenario. For TB, the performance metrics were collected by running 10 to 50 permutations. For the X-ray images, 10 permutations were performed. For COVID-19 the performance metrics were collected by running 10 to 20 permutations for each scenario. All metrics are listed in Supplementary Tables [3](#), [4](#).

Differences in performance metrics were tested using the one-sided Wilcoxon signed rank test with continuity correction. All test results are provided in Supplementary Table [5](#).

To run the experiments, we used Python version 3.6.9 with Keras version 2.3.1 and TensorFlow version 2.2.0-rc2. We used scikit-learn library version 0.23.1 to calculate values for the metrics. Summary statistics and hypothesis tests were calculated using R version 3.5.2. Calculation of each metric was done as follows:

$$\begin{aligned} \text{Sensitivity} &= \frac{\text{TP}}{\text{TP} + \text{FN}} \\ \text{Specificity} &= \frac{\text{TN}}{\text{TN} + \text{FP}} \\ \text{Accuracy} &= \frac{\text{TP} + \text{TN}}{\text{TP} + \text{FP} + \text{TN} + \text{FN}} \\ \text{F1score} &= \frac{2\{\text{TP}\}}{\{\text{TP}\} + \{\text{FN}\} + 2\{\text{TP}\}} \end{aligned}$$

where TP is true positive, FP is false positive, TN is true negative and FN is false negative. The area under the ROC curve was calculated using the R package ROCR version 1.0-11.

No statistical methods were used to predetermine sample size. The experiments were not randomized, but permutations were performed. Investigators were not blinded to allocation during experiments and outcome assessment.

Reporting summary

Further information on research design is available in the [Nature Research Reporting Summary](#) linked to this paper.

Data availability

Processed data from datasets A1–A3 can be accessed from GEO via the superseries [GSE122517](#) or the individual subseries [GSE122505](#) (dataset A1), [GSE122511](#) (dataset A2) and [GSE122515](#) (dataset A3). Dataset B consists of the following series, which can be accessed at GEO: [GSE101705](#), [GSE107104](#), [GSE112087](#), [GSE128078](#), [GSE66573](#), [GSE79362](#), [GSE84076](#), and [GSE89403](#). Furthermore, it contains the data from the Rhineland Study. The Rhineland Study dataset falls under current General Data Protection Regulations (GDPR). Access to these data can be provided to scientists in accordance with the Rhineland Study's Data Use and Access Policy. Requests to access the Rhineland Study's dataset should be directed to RS-DUAC@dzne.de. New samples generated for datasets D and E have been deposited at the European Genome-Phenome Archive (EGA), which is hosted by the EBI and the CRG, under accession number [EGAS00001004502](#). The healthy RNA-seq data included from Saarbrücken are available on application from PPMI through the LONI data archive at <https://www.ppmi-info.org/data>. Samples received from other public repositories are listed in Supplementary Table 2. Dataset C (NIH chest X-ray dataset) is available on Kaggle (<https://www.kaggle.com/nih-chest-xrays/data>). Normalized log-transformed and rank transformed expressions as used for the predictions are available via FASTGenomics at <https://beta.fastgenomics.org/p/swarm-learning>.

Code availability

The code for preprocessing and for predictions can be found at GitHub (https://github.com/schultzelab/swarm_learning). The Swarm Learning software can be downloaded from <https://myenterprisicense.hpe.com/>.

References

1. 1.

Aronson, S. J. & Rehm, H. L. Building the foundation for genomics in precision medicine. *Nature* **526**, 336–342 (2015).

[ADS](#) [CAS](#) [Article](#) [Google Scholar](#)

2. 2.

Haendel, M. A., Chute, C. G. & Robinson, P. N. Classification, ontology, and precision medicine. *N. Engl. J. Med.* **379**, 1452–1462 (2018).

[CAS](#) [Article](#) [Google Scholar](#)

3. 3.

Warnat-Herresthal, S. et al. Scalable prediction of acute myeloid leukemia using high-dimensional machine learning and blood transcriptomics. *iScience* **23**, 100780 (2020).

[ADS](#) [CAS](#) [Article](#) [Google Scholar](#)

4. 4.

Wiens, J. et al. Do no harm: a roadmap for responsible machine learning for health care. *Nat. Med.* **25**, 1337–1340 (2019).

[CAS](#) [Article](#) [Google Scholar](#)

5. 5.

Price, W. N., II & Cohen, I. G. Privacy in the age of medical big data. *Nat. Med.* **25**, 37–43 (2019).

[CAS](#) [Article](#) [Google Scholar](#)

6. 6.

Berlin, D. A., Gulick, R. M. & Martinez, F. J. Severe Covid-19. *N. Engl. J. Med.* **383**, 2451–2460 (2020).

[CAS](#) [Article](#) [Google Scholar](#)

7. 7.

Gandhi, R. T., Lynch, J. B. & Del Rio, C. Mild or moderate Covid-19. *N. Engl. J. Med.* **383**, 1757–1766 (2020).

[CAS](#) [Article](#) [Google Scholar](#)

8. 8.

He, J. et al. The practical implementation of artificial intelligence technologies in medicine. *Nat. Med.* **25**, 30–36 (2019).

[CAS](#) [Article](#) [Google Scholar](#)

9. 9.

Kels, C. G. HIPAA in the era of data sharing. *J. Am. Med. Assoc.* **323**, 476–477 (2020).

[Article](#) [Google Scholar](#)

10. 10.

McCall, B. What does the GDPR mean for the medical community? *Lancet* **391**, 1249–1250 (2018).

[Article](#) [Google Scholar](#)

11. 11.

Cho, A. AI systems aim to sniff out coronavirus outbreaks. *Science* **368**, 810–811 (2020).

[ADS](#) [CAS](#) [Article](#) [Google Scholar](#)

12. 12.

Luengo-Oroz, M. et al. Artificial intelligence cooperation to support the global response to COVID-19. *Nat. Mach. Intell.* **2**, 295–297 (2020).

[Article](#) [Google Scholar](#)

13. 13.

Peiffer-Smadja, N. et al. Machine learning for COVID-19 needs global collaboration and data-sharing. *Nat. Mach. Intell.* **2**, 293–294 (2020).

[Article](#) [Google Scholar](#)

14. 14.

Ge, Y. et al. An integrative drug repositioning framework discovered a potential therapeutic agent targeting COVID-19. *Signal Transduct. Target Ther.* **6**, 165 (2021).

[CAS](#) [Article](#) [Google Scholar](#)

15. 15.

Mei, X. et al. Artificial intelligence-enabled rapid diagnosis of patients with COVID-19. *Nat. Med.* **26**, 1224–1228 (2020).

[CAS](#) [Article](#) [Google Scholar](#)

16. 16.

Zhang, K. et al. Clinically applicable AI system for accurate diagnosis, quantitative measurements, and prognosis of COVID-19 pneumonia using computed tomography. *Cell* **182**, 1360 (2020).

[CAS](#) [Article](#) [Google Scholar](#)

17. 17.

Council of Europe: Convention for the Protection of Individuals with Regard to Automatic Processing of Personal Data. *Intl Legal Materials* **20**, 317–325 (1981).

[Article](#) [Google Scholar](#)

18. 18.

LeCun, Y., Bengio, Y. & Hinton, G. Deep learning. *Nature* **521**, 436–444 (2015).

[ADS](#) [CAS](#) [Article](#) [Google Scholar](#)

19. 19.

Kaissis, G. A., Makowski, M. R., Rückert, D. & Braren, R. F. Secure, privacy-preserving and federated machine learning in medical imaging. *Nat. Mach. Intell.* **2**, 305–311 (2020).

[Article](#) [Google Scholar](#)

20. 20.

Rajkomar, A., Dean, J. & Kohane, I. Machine learning in medicine. *N. Engl. J. Med.* **380**, 1347–1358 (2019).

[Article](#) [Google Scholar](#)

21. 21.

Savage, N. Calculating disease. *Nature* **550**, S115–S117 (2017).

[ADS](#) [CAS](#) [Article](#) [Google Scholar](#)

22. 22.

Ping, P., Hermjakob, H., Polson, J. S., Benos, P. V. & Wang, W. Biomedical informatics on the cloud: A treasure hunt for advancing cardiovascular medicine. *Circ. Res.* **122**, 1290–1301 (2018).

[CAS](#) [Article](#) [Google Scholar](#)

23. 23.

Char, D. S., Shah, N. H. & Magnus, D. Implementing machine learning in health care—addressing ethical challenges. *N. Engl. J. Med.* **378**, 981–983 (2018).

[Article](#) [Google Scholar](#)

24. 24.

Finlayson, S. G. et al. Adversarial attacks on medical machine learning. *Science* **363**, 1287–1289 (2019).

[ADS](#) [CAS](#) [Article](#) [Google Scholar](#)

25. 25.

Konečný, J. et al. Federated learning: strategies for improving communication efficiency. Preprint at <https://arxiv.org/abs/1610.05492> (2016).

26. 26.

Shokri, R. & Shmatikov, V. Privacy-preserving deep learning. *2015 53rd Annual Allerton Conf. Communication, Control, and Computing* 909–910 (IEEE, 2015).

27. 27.

Dove, E. S., Joly, Y., Tassé, A. M. & Knoppers, B. M. Genomic cloud computing: legal and ethical points to consider. *Eur. J. Hum. Genet.* **23**, 1271–1278 (2015).

[Article](#) [Google Scholar](#)

28. 28.

Chollet, F. *Keras* <https://github.com/keras-team/keras> (2015).

29. 29.

Zhao, Y. et al. Federated learning with non-IID data. Preprint at <https://arxiv.org/abs/1806.00582> (2018).

30. 30.

Leong, S. et al. Existing blood transcriptional classifiers accurately discriminate active tuberculosis from latent infection in individuals from south India. *Tuberculosis* **109**, 41–51 (2018).

[Article](#) [Google Scholar](#)

31. 31.

Zak, D. E. et al. A blood RNA signature for tuberculosis disease risk: a prospective cohort study. *Lancet* **387**, 2312–2322 (2016).

[CAS](#) [Article](#) [Google Scholar](#)

32. 32.

Wang, X. et al. ChestX-Ray8: Hospital-scale chest X-ray database and benchmarks on weakly-supervised classification and localization of common thorax diseases. *2017 IEEE Conf. Computer Vision and Pattern Recognition (CVPR)* 3462–3471 (IEEE, 2017).

33. 33.

Corman, V. M. et al. Detection of 2019 novel coronavirus (2019-nCoV) by real-time RT-PCR. *Euro Surveill.* **25**, 2000045 (2020).

[PubMed Central](#) [Google Scholar](#)

34. 34.

Aschenbrenner, A. C. et al. Disease severity-specific neutrophil signatures in blood transcriptomes stratify COVID-19 patients. *Genome Med.* **13**, 7 (2021).

[CAS](#) [Article](#) [Google Scholar](#)

35. 35.

Chaussabel, D. Assessment of immune status using blood transcriptomics and potential implications for global health. *Semin. Immunol.* **27**, 58–66 (2015).

[CAS](#) [Article](#) [Google Scholar](#)

36. 36.

Schulte-Schrepping, J. et al. Severe COVID-19 is marked by a dysregulated myeloid cell compartment. *Cell* **182**, 1419–1440.e23 (2020).

[CAS](#) [Article](#) [Google Scholar](#)

37. 37.

Esteva, A. et al. Dermatologist-level classification of skin cancer with deep neural networks. *Nature* **542**, 115–118 (2017).

[ADS](#) [CAS](#) [Article](#) [Google Scholar](#)

38. 38.

Kaassis, G. et al. A machine learning algorithm predicts molecular subtypes in pancreatic ductal adenocarcinoma with differential response to gemcitabine-based versus FOLFIRINOX chemotherapy. *PLoS One* **14**, e0218642 (2019).

[CAS](#) [Article](#) [Google Scholar](#)

39. 39.

Elshafeey, N. et al. Multicenter study demonstrates radiomic features derived from magnetic resonance perfusion images identify pseudoprogression in glioblastoma. *Nat. Commun.* **10**, 3170 (2019).

[ADS](#) [Article](#) [Google Scholar](#)

40. 40.

Abadi, M. et al. Deep learning with differential privacy. *Proc. 2016 ACM SIGSAC Conf. Computer and Communications Security—CCS'16* 308–318 (ACM Press, 2016).

41. 41.

Ryffel, T., Dufour-Sans, E., Gay, R., Bach, F. & Pointcheval, D. Partially encrypted machine learning using functional encryption. Preprint at <https://arxiv.org/abs/1905.10214> (2019).

42. 42.

Salem, M., Taheri, S. & Yuan, J.-S. Utilizing transfer learning and homomorphic encryption in a privacy preserving and secure biometric recognition system. *Computers* **8**, 3 (2018).

[Article](#) [Google Scholar](#)

43. 43.

Kędzior, M. The right to data protection and the COVID-19 pandemic: the European approach. *ERA Forum* **21**, 533–543 (2021).

[Article](#) [Google Scholar](#)

[Download references](#)

Acknowledgements

We thank the Michael J. Fox Foundation and the Parkinson's Progression Markers Initiative (PPMI) for contributing RNA-seq data; the CORSAAR study group for additional blood transcriptome samples; the collaborators who contributed to the collection of COVID-19 samples (B. Schlegelberger, I. Bernemann, J. C. Hellmuth, L. Jocham, F. Hanes, U. Hehr, Y. Khodamoradi, L. Kaldjob, R. Fendel, L. T. K. Linh, P. Rosenberger, H. Häberle and J. Böhne); and the NGS Competence Center Tübingen (NCCT), who contributed to the generation of data and the data sharing (in particular, J. Frick, M. Sonnabend, J. Geissert, A. Angelov, M. Pogoda, Y. Singh, S. Poths, S. Nahnsen and M. Gauder). This work was supported in part by the German Research Foundation (DFG) to J.L.S., O.R., P.R., P.N. (INST 37/1049-1, INST 216/981-1, INST 257/605-1, INST 269/768-1, INST 217/988-1, INST 217/577-1, INST 217/1011-1, INST 217/1017-1 and INST 217/1029-1); under Germany's Excellence Strategy (DFG – EXC2151 – 390873048); by the HGF Incubator grant sparse2big (ZT-I-0007); by EU projects SYSCID (grant 733100, P.R.) and ImmunoSep (grant 84722, J.L.S.); and by HPE to the DZNE for generating whole blood transcriptome data from patients with COVID-19. J.L.S. was further supported by the BMBF-funded excellence project Diet–Body–Brain (DietBB) (grant 01EA1809A), and J.L.S. and J.R. by NaFoUniMedCovid19 (FKZ: 01KX2021, project acronym COVIM). S.K. is supported by the Hellenic Institute for the Study of Sepsis. The clinical study in Greece was supported by the Hellenic Institute for the Study of Sepsis. E.J.G.-B. received funding from the FrameWork 7 programme HemoSpec (granted to the National and Kapodistrian University of Athens), the Horizon2020 Marie-Curie Project European Sepsis Academy (676129, granted to the National and Kapodistrian University of Athens), and the Horizon 2020 European Grant ImmunoSep (granted to the Hellenic Institute for the Study of Sepsis). P.R. was supported by DFG ExC2167, a stimulus fund from Schleswig-Holstein and the DFG NGS Centre CCGA. The clinical study in Munich was supported by the Care-for-Rare Foundation. S.K.-H. is a scholar of the Reinhard-Frank Stiftung. D.P. is funded by the Hector Fellow Academy. The work was additionally supported by the Michael J. Fox Foundation for Parkinson' Research under grant 14446. M.G.N. was supported by an ERC Advanced Grant (833247) and a Spinoza Grant of the Netherlands Organization for Scientific Research. R.B. and A.K. were supported by Dr. Rolf M. Schwiete Stiftung, Staatskanzlei des Saarlandes

and Saarland University. J.N. is supported by the DFG (SFB TR47, SPP1937) and the Hector Foundation (M88). M.A. is supported by COVIM: NaFoUniMedCovid19 (FKZ: 01KX2021). M. Becker is supported by the HGF Helmholtz AI grant Pro-Gene-Gen (ZT-I-PF-5-23).

Funding

Open access funding provided by Deutsches Zentrum für Neurodegenerative Erkrankungen e.V. (DZNE) in der Helmholtz-Gemeinschaft.

Author information

Author notes

1. These authors contributed equally: Stefanie Warnat-Herresthal, Hartmut Schultze, Krishnaprasad Lingadahalli Shastry, Sathyanarayanan Manamohan, Saikat Mukherjee, Vishesh Garg, Ravi Sarveswara, Kristian Händler, Peter Pickkers, N. Ahmad Aziz, Sofia Ktena
2. These authors jointly supervised this work: Monique M. B. Breteler, Evangelos J. Gihamarellos-Bourboulis, Matthijs Kox, Matthias Becker, Sorin Cheran, Michael S. Woodacre, Eng Lim Goh, Joachim L. Schultze

Affiliations

1. Systems Medicine, Deutsches Zentrum für Neurodegenerative Erkrankungen (DZNE), Bonn, Germany
Stefanie Warnat-Herresthal, Kristian Händler, Lorenzo Bonaguro, Jonas Schulte-Schrepping, Elena De Domenico, Michael Kraut, Anna Drews, Melanie Nuesch-Germano, Heidi Theis, Anna C. Aschenbrenner, Thomas Ulas, Matthias Becker & Joachim L. Schultze

2. Genomics and Immunoregulation, Life & Medical Sciences (LIMES)
Institute, University of Bonn, Bonn, Germany

Stefanie Warnat-Herresthal, Lorenzo Bonaguro, Jonas Schulte-Schrepping, Melanie Nuesch-Germano, Anna C. Aschenbrenner, Thomas Ulas, Mariam L. Sharaf & Joachim L. Schultze

3. Hewlett Packard Enterprise, Houston, TX, USA

Hartmut Schultze, Krishnaprasad Lingadahalli Shastry, Sathyanarayanan Manamohan, Saikat Mukherjee, Vishesh Garg, Ravi Sarveswara, Christian Siever, Milind Desai, Bruno Monnet, Charles Martin Siegel, Sorin Cheran, Michael S. Woodacre & Eng Lim Goh

4. Mesh Dynamics, Bangalore, India

Vishesh Garg

5. PRECISE Platform for Single Cell Genomics and Epigenomics,
Deutsches Zentrum für Neurodegenerative Erkrankungen (DZNE) and
the University of Bonn, Bonn, Germany

Kristian Händler, Elena De Domenico, Michael Kraut, Anna Drews, Heidi Theis, Anna C. Aschenbrenner, Matthias Becker & Joachim L. Schultze

6. Department of Intensive Care Medicine and Radboud Center for
Infectious Diseases (RCI), Radboud University Medical Center,
Nijmegen, The Netherlands

Peter Pickkers & Matthijs Kox

7. Population Health Sciences, Deutsches Zentrum für
Neurodegenerative Erkrankungen (DZNE), Bonn, Germany

N. Ahmad Aziz & Monique M. B. Breteler

8. Department of Neurology, Faculty of Medicine, University of Bonn,
Bonn, Germany

N. Ahmad Aziz

9. 4th Department of Internal Medicine, National and Kapodistrian
University of Athens, Medical School, Athens, Greece

Sofia Ktena, Maria Saridaki & Evangelos J. Giamarellos-Bourboulis

10. Department of Internal Medicine I, Christian-Albrechts-University and
University Hospital Schleswig-Holstein, Kiel, Germany

Florian Tran & Stefan Schreiber

11. Institute of Clinical Molecular Biology, Christian-Albrechts-University
and University Hospital Schleswig-Holstein, Kiel, Germany

Florian Tran, Neha Mishra, Joana P. Bernardes, Philip
Rosenstiel & Sören Franzenburg

12. Department of Internal Medicine I, University Hospital, University of
Tübingen, Tübingen, Germany

Michael Bitzer & Siri Göpel

13. Institute of Medical Genetics and Applied Genomics, University of
Tübingen, Tübingen, Germany

Stephan Ossowski, Nicolas Casadei, Olaf Rieß, Daniela
Bezdan & Yogesh Singh

14. NGS Competence Center Tübingen, Tübingen, Germany

Stephan Ossowski, Nicolas Casadei, Olaf Rieß, Angel
Angelov, Daniela Bezdan, Julia-Stefanie Frick, Gisela Gabernet, Marie
Gauder, Janina Geißert, Sven Nahnsen, Silke Peter, Yogesh
Singh & Michael Sonnabend

15. Department of Internal Medicine V, Saarland University Hospital,
Homburg, Germany

Christian Herr & Robert Bals

16. Department of Pediatrics, Dr. von Hauner Children's Hospital,
University Hospital LMU Munich, Munich, Germany

Daniel Petersheim, Sarah Kim-Hellmuth & Christoph Klein

17. Children's Hospital, Medical Faculty, Technical University Munich,
Munich, Germany

Uta Behrends

18. Clinical Bioinformatics, Saarland University, Saarbrücken, Germany

Fabian Kern, Tobias Fehlmann & Andreas Keller

19. Department I of Internal Medicine, Faculty of Medicine and
University Hospital of Cologne, University of Cologne, Cologne,
Germany

Philipp Schommers, Clara Lehmann, Max Augustin & Jan Rybniker

20. Center for Molecular Medicine Cologne (CMMC), University of
Cologne, Cologne, Germany

Clara Lehmann, Max Augustin & Jan Rybniker

21. German Center for Infection Research (DZIF), Partner Site Bonn-
Cologne, Cologne, Germany

Clara Lehmann, Max Augustin, Jan Rybniker & Janne Vehreschild

22. Cologne Center for Genomics, West German Genome Center,
University of Cologne, Cologne, Germany

Janine Altmüller & Peter Nürnberg

23. Clinical Infectious Diseases, Research Center Borstel and German Center for Infection Research (DZIF), Partner Site Hamburg-Lübeck-Borstel-Riems, Borstel, Germany

Benjamin Krämer, Jan Heyckendorf & Adam Grundhoff

24. Department of Internal Medicine I, University Hospital Bonn, Bonn, Germany

Jacob Nattermann

25. German Center for Infection Research (DZIF), Braunschweig, Germany

Jacob Nattermann

26. Department of Internal Medicine II - Cardiology/Pneumology, University of Bonn, Bonn, Germany

Dirk Skowasch

27. Institute of Human Genetics, Medical Faculty, RWTH Aachen University, Aachen, Germany

Thomas Eggermann & Ingo Kurth

28. Department of Neurology and Neurological Sciences, Stanford University School of Medicine, Stanford, CA, USA

Andreas Keller

29. Department of Internal Medicine and Radboud Center for Infectious Diseases (RCI), Radboud University Medical Center, Nijmegen, The Netherlands

Mihai G. Netea & Anna C. Aschenbrenner

30. Immunology & Metabolism, Life and Medical Sciences (LIMES) Institute, University of Bonn, Bonn, Germany

Mihai G. Netea

31. Institute of Computational Biology, Helmholtz Center Munich (HMGU), Neuherberg, Germany

Fabian Theis & Maria Colome-Tatche

32. Statistics and Machine Learning, Deutsches Zentrum für Neurodegenerative Erkrankungen (DZNE), Bonn, Germany

Sach Mukherjee

33. CISPA Helmholtz Center for Information Security, Saarbrücken, Germany

Michael Backes

34. Institute for Medical Biometry, Informatics and Epidemiology (IMBIE), Faculty of Medicine, University of Bonn, Bonn, Germany

Monique M. B. Breteler

35. Department of Cardiology, Angiology and Intensive Care Medicine, University Hospital RWTH Aachen, Aachen, Germany

Paul Balfanz

36. Institute of Pathology & Department of Nephrology, University Hospital RWTH Aachen, Aachen, Germany

Peter Boor

37. Institute of Clinical Pharmacology, University Hospital RWTH Aachen, Aachen, Germany

Ralf Hausmann

38. Institute for Biology I, RWTH Aachen University, Aachen, Germany

Hannah Kuhn

39. Department of Hematology, Oncology, Hemostaseology and Stem Cell Transplantation, Medical School, RWTH Aachen University, Aachen, Germany

Susanne Isfort

40. Institute of Clinical Pharmacology, University Hospital RWTH Aachen, Aachen, Germany

Julia Carolin Stingl & Günther Schmalzing

41. Department of Diagnostic and Interventional Radiology, University Hospital RWTH Aachen, Aachen, Germany

Christiane K. Kuhl

42. Institute of Medical Informatics, University Hospital RWTH Aachen, Aachen, Germany

Rainer Röhrig

43. Department of Intensive Care, University Hospital RWTH Aachen, Aachen, Germany

Gernot Marx

44. Institute of Pharmacology and Toxicology, Medical Faculty Aachen, RWTH Aachen University, Aachen, Germany

Stefan Uhlig

45. Molecular Oncology Group, Institute of Pathology, Medical Faculty, RWTH Aachen University, Aachen, Germany

Edgar Dahl

46. RWTH centralized Biomaterial Bank (RWTH cBMB) of the Medical Faculty, RWTH Aachen University, Aachen, Germany

Edgar Dahl

47. Department of Internal Medicine I, University Hospital RWTH Aachen, Aachen, Germany

Dirk Müller-Wieland & Nikolaus Marx

48. Department of Pneumology and Intensive Care Medicine, University Hospital RWTH Aachen, Aachen, Germany

Michael Dreher

49. Institute of Medical Microbiology and Hygiene, University of Tübingen, Tübingen, Germany

Angel Angelov, Julia-Stefanie Frick, Janina Geißert, Silke Peter & Michael Sonnabend

50. Geomicrobiology, German Research Centre for Geosciences (GFZ), Potsdam, Germany

Alexander Bartholomäus

51. LOEWE Center for Synthetic Microbiology (SYNMIKRO), Philipps-Universität Marburg, Marburg, Germany

Anke Becker

52. Institute for Medical Virology and Epidemiology of Viral Diseases, University of Tübingen, Tübingen, Germany

Daniela Bezdan, Tina Ganzenmueller, Thomas Iftner & Angelika Iftner

53. Fraunhofer Institute for Cell Therapy and Immunology (IZI), Leipzig, Germany

Conny Blumert, Friedemann Horn & Kristin Reiche

54. Center for Regenerative Therapies Dresden (CRTD), Dresden, Germany

Ezio Bonifacio

55. European Molecular Biology Laboratory (EMBL), Heidelberg, Germany

Peer Bork, Jan Korbel & Oliver Stegle

56. DSMZ - German Collection of Microorganisms and Cell Cultures, Leibniz Institute, Braunschweig, Germany

Bunk Boyke & Jörg Overmann

57. Gene Center - Functional Genomics Analysis, Ludwig-Maximilians-Universität München, München, Germany

Helmut Blum

58. Institute for Medical Microbiology, University Hospital Aachen, RWTH Aachen, Germany

Thomas Clavel

59. European Research Institute for the Biology of Ageing, University of Groningen, Groningen, The Netherlands

Maria Colome-Tatche

60. TUM School of Life Sciences Weihenstephan, Technical University of Munich, Freising, Germany

Maria Colome-Tatche

61. Klinik für Gastroenterologie, Hepatologie und Endokrinologie, Medizinische Hochschule Hannover (MHH), Hannover, Germany

Markus Cornberg & Isabell Pink

62. Centre for Individualised Infection Medicine (CiiM), Hannover, Germany

Markus Cornberg

63. German Center for Infection Research (DZIF), Hannover, Germany

Markus Cornberg

64. Genome Analysis Center, Helmholtz Zentrum München Deutsches Forschungszentrum für Gesundheit und Umwelt, Neuherberg, Germany

Inti Alberto De La Rosa Velázquez

65. Institut für Mikrobiologie und Infektionsimmunologie, Charité – Universitätsmedizin Berlin, Berlin, Germany

Andreas Diefenbach

66. Institut für Medizinische Mikrobiologie und Krankenhaushygiene, Universitätsklinikum Düsseldorf, Heinrich-Heine-Universität Düsseldorf, Düsseldorf, Germany

Alexander Dilthey & Klaus Pfeffer

67. Institut für Medizinische Mikrobiologie, Virologie und Hygiene, Universitätsklinikum Hamburg- Eppendorf (UKE), Hamburg, Germany

Nicole Fischer

68. German Information Centre for Life Sciences (ZB MED), Cologne, Germany

Konrad Förstner

69. Quantitative Biology Center, University of Tübingen, Tübingen, Germany

Gisela Gabernet, Marie Gauder & Sven Nahnsen

70. Informatik 29 - Computational Molecular Medicine, Technische Universität München, München, Germany

Julien Gagneur & Christian Mertes

71. Bioinformatics and Systems Biology, Justus Liebig University Giessen, Giessen, Germany

Alexander Goesmann

72. Leibniz Institut für Experimentelle Virologie, Hamburg, Germany

Adam Grundhoff

73. Institute for Infection Prevention and Hospital Hygiene, Universitätsklinikum Freiburg, Freiburg, Germany

Hajo Grundmann

74. Institute of Medical Microbiology, Justus Liebig University Giessen, Giessen, Germany

Torsten Hain

75. Krankenhaushygiene und Infektiologie, Universitätsklinikum Regensburg, Regensburg, Germany

Frank Hanses & Wulf Schneider

76. Zentrum für Humangenetik Regensburg, Regensburg, Germany

Ute Hehr

77. Institute of Human Genetics, University of Bonn, School of Medicine & University Hospital Bonn, Bonn, Germany

André Heimbach, Kerstin U. Ludwig & Markus Nöthen

78. Klinik für Pneumonologie, Medizinische Hochschule Hannover (MHH), Hannover, Germany

Marius Hooper

79. Computational Oncology, Molecular Diagnostics Program, National Center for Tumor Diseases (NCT) Heidelberg and German Cancer Research Center (DKFZ), Heidelberg, Germany

Daniel Hübschmann

80. Heidelberg Institute for Stem Cell Technology and Experimental Medicine (HI-STEM), Heidelberg, Germany

Daniel Hübschmann

81. German Cancer Consortium (DKTK), Heidelberg, Germany

Daniel Hübschmann

82. Institute for Pathology, Molecular Pathology, Charité – Universitätsmedizin Berlin, Berlin, Germany

Michael Hummel

83. German Biobank Node (bbmri.de), Berlin, Germany

Michael Hummel

84. Medizinische Hochschule Hannover (MHH), Hannover Unified Biobank and Institute of Human Genetics, Hannover, Germany

Thomas Illig & Sonja Volland

85. Algorithmic Bioinformatics, Justus Liebig University Giessen,
Giessen, Germany

Stefan Janssen

86. Center for Biotechnology (CeBiTec), Bielefeld University, Bielefeld,
Germany

Jörn Kalinowski, Alfred Pühler & Alexander Sczyrba

87. Department of Environmental Microbiology, Helmholtz-Zentrum für
Umweltforschung (UFZ), Leipzig, Germany

René Kallies & Ulisses Nunes da Rocha

88. Algorithmische Bioinformatik, RCI Regensburger Centrum für
Interventionelle Immunologie, Universitätsklinikum Regensburg,
Regensburg, Germany

Birte Kehr

89. Max von Pettenkofer Institute & Gene Center, Virology, National
Reference Center for Retroviruses, LMU München, Munich, Germany

Oliver T. Keppler & Maximilian Münchhoff

90. German Center for Infection Research (DZIF), partner site Munich,
München, Germany

Oliver T. Keppler & Maximilian Münchhoff

91. Center for Molecular Biology (ZMBH), Heidelberg University,
Heidelberg, Germany

Michael Knop

92. Cell Morphogenesis and Signal Transduction, German Cancer
Research Center (DKFZ), Heidelberg, Germany

Michael Knop

93. Applied Bioinformatics, University of Tübingen, Tübingen, Germany

Oliver Kohlbacher

94. Translational Bioinformatics, University Hospital, University of Tübingen, Tübingen, Germany

Oliver Kohlbacher

95. Genomics & Transcriptomics Labor (GTL), Universitätsklinikum Düsseldorf, Heinrich-Heine-Universität Düsseldorf, Düsseldorf, Germany

Karl Köhrer

96. Medical Clinic Internal Medicine VII, University Hospital, University of Tübingen, Tübingen, Germany

Peter G. Kremsner

97. Transmission, Infection, Diversification and Evolution Group, Max Planck Institute for the Science of Human History, Jena, Germany

Denise Kühnert

98. Berlin Institute for Medical Systems Biology, Max Delbrück Center for Molecular Medicine in the Helmholtz Association (MDC), Berlin, Germany

Markus Landthaler & Nikolaus Rajewsky

99. Centre for Individualized Infection Medicine (CiIM) & TWINCORE, joint ventures between the Helmholtz-Centre for Infection Research (HZI) and the Hannover Medical School (MHH), Hannover, Germany

Yang Li

100. Institute for Infection Medicine and Hospital Hygiene (IIMK),
Uniklinikum Jena, Jena, Germany

Oliwia Makarewicz

101. Michael Stifel Center Jena, Jena, Germany

Manja Marz

102. Bioinformatics/High-Throughput Analysis, Faculty of Mathematics
and Computer Science, Friedrich-Schiller-Universität Jena, Jena,
Germany

Manja Marz

103. Computational Biology for Infection Research, Helmholtz Centre for
Infection Research (HZI), Brunswick, Germany

Alice C. McHardy

104. Institute for Tropical Medicine, University Hospital, University of
Tübingen, Tübingen, Germany

Francine Ntoumi & Thirumalaisamy P. Velavan

105. Biotechnology Center (BIOTEC) TU Dresden, National Center for
Tumor Diseases, Dresden, Germany

Anna R. Poetsch

106. Institute of Virology, Technical University of Munich, Munich,
Germany

Ulrike Protzer

107. Institute of Biochemistry, Charité – Universitätsmedizin Berlin, Berlin,
Germany

Markus Ralser

108. Department of Psychiatry and Neurosciences, Charité –
Universitätsmedizin Berlin, Berlin, Germany

Stephan Ripke

109. Helmholtz Institute for RNA-based Infection Research (HIRI),
Helmholtz-Center for Infection Research, Würzburg, Germany

Antoine-Emmanuel Saliba & Jörg Vogel

110. Department of Internal Medicine with emphasis on Infectiology,
Respiratory-, and Critical-Care-Medicine, Charité –
Universitätsmedizin Berlin, Berlin, Germany

Leif Erik Sander

111. Institute of Medical Immunology, Charité – Universitätsmedizin
Berlin, Berlin, Germany

Birgit Sawitzki

112. Institute of Infection Control and Infectious Diseases, University
Medical Center, Georg August University, Göttingen, Germany

Simone Scheithauer

113. Institute of Zoology, University of Cologne, Cologne, Germany

Philipp Schiffer

114. Institute of Clinical Chemistry and Clinical Pharmacology, University
Hospital, University of Bonn, Bonn, Germany

Jonathan Schmid-Burgk

115. Klinik für Psychiatrie und Psychotherapie and Institut für
Psychiatrische Phänomik und Genomik, LMU München, Munich,
Germany

Eva-Christina Schulte

116. Division of Computational Genomics and Systems Genetics, German Cancer Research Center (DKFZ), Heidelberg, Germany

Oliver Stegle

117. Genome Informatics, University of Bielefeld, Bielefeld, Germany

Jens Stoye

118. Department I of Internal Medicine, University Hospital of Cologne, University of Cologne, Cologne, Germany

Janne Vehreschild

119. University Hospital Frankfurt, Frankfurt am Main, Germany

Janne Vehreschild

120. Institute for Bioinformatics, Freie Universität Berlin, Berlin, Germany

Max von Kleist

121. Robert Koch Institute, Berlin, Germany

Max von Kleist

122. Institut für Virologie, Universitätsklinikum Düsseldorf, Heinrich-Heine-Universität Düsseldorf, Düsseldorf, Germany

Andreas Walker

123. Genetics and Epigenetics, Saarland University, Saarbrücken, Germany

Jörn Walter

124. Institut für Humangenetik, Universitätsklinikum Düsseldorf, Heinrich-Heine-Universität Düsseldorf, Düsseldorf, Germany

Dagmar Wieczorek

125. Max Planck Institute of Molecular Cell Biology and Genetics,
Dresden, Germany and DRESDEN concept Genome Center, TU
Dresden, Dresden, Germany

Sylke Winkler

126. Institute of Medical Virology, Justus Liebig University Giessen,
Giessen, Germany

John Ziebuhr

Authors

1. Stefanie Warnat-Herresthal
[View author publications](#)

You can also search for this author in [PubMed](#) [Google Scholar](#)

2. Hartmut Schultze
[View author publications](#)

You can also search for this author in [PubMed](#) [Google Scholar](#)

3. Krishnaprasad Lingadahalli Shastry
[View author publications](#)

You can also search for this author in [PubMed](#) [Google Scholar](#)

4. Sathyanarayanan Manamohan
[View author publications](#)

You can also search for this author in [PubMed](#) [Google Scholar](#)

5. Saikat Mukherjee
[View author publications](#)

You can also search for this author in [PubMed](#) [Google Scholar](#)

6. Vishesh Garg

[View author publications](#)

You can also search for this author in [PubMed](#) [Google Scholar](#)

7. Ravi Sarveswara

[View author publications](#)

You can also search for this author in [PubMed](#) [Google Scholar](#)

8. Kristian Händler

[View author publications](#)

You can also search for this author in [PubMed](#) [Google Scholar](#)

9. Peter Pickkers

[View author publications](#)

You can also search for this author in [PubMed](#) [Google Scholar](#)

10. N. Ahmad Aziz

[View author publications](#)

You can also search for this author in [PubMed](#) [Google Scholar](#)

11. Sofia Ktena

[View author publications](#)

You can also search for this author in [PubMed](#) [Google Scholar](#)

12. Florian Tran

[View author publications](#)

You can also search for this author in [PubMed](#) [Google Scholar](#)

13. Michael Bitzer

[View author publications](#)

You can also search for this author in [PubMed](#) [Google Scholar](#)

14. Stephan Ossowski

[View author publications](#)

You can also search for this author in [PubMed](#) [Google Scholar](#)

15. Nicolas Casadei

[View author publications](#)

You can also search for this author in [PubMed](#) [Google Scholar](#)

16. Christian Herr

[View author publications](#)

You can also search for this author in [PubMed](#) [Google Scholar](#)

17. Daniel Petersheim

[View author publications](#)

You can also search for this author in [PubMed](#) [Google Scholar](#)

18. Uta Behrends

[View author publications](#)

You can also search for this author in [PubMed](#) [Google Scholar](#)

19. Fabian Kern

[View author publications](#)

You can also search for this author in [PubMed](#) [Google Scholar](#)

20. Tobias Fehlmann

[View author publications](#)

You can also search for this author in [PubMed](#) [Google Scholar](#)

21. Philipp Schommers

[View author publications](#)

You can also search for this author in [PubMed](#) [Google Scholar](#)

22. Clara Lehmann

[View author publications](#)

You can also search for this author in [PubMed](#) [Google Scholar](#)

23. Max Augustin

[View author publications](#)

You can also search for this author in [PubMed](#) [Google Scholar](#)

24. Jan Rybníkér

[View author publications](#)

You can also search for this author in [PubMed](#) [Google Scholar](#)

25. Janine Altmüller

[View author publications](#)

You can also search for this author in [PubMed](#) [Google Scholar](#)

26. Neha Mishra

[View author publications](#)

You can also search for this author in [PubMed](#) [Google Scholar](#)

27. Joana P. Bernardes

[View author publications](#)

You can also search for this author in [PubMed](#) [Google Scholar](#)

28. Benjamin Krämer

[View author publications](#)

You can also search for this author in [PubMed](#) [Google Scholar](#)

29. Lorenzo Bonaguro

[View author publications](#)

You can also search for this author in [PubMed](#) [Google Scholar](#)

30. Jonas Schulte-Schrepping

[View author publications](#)

You can also search for this author in [PubMed](#) [Google Scholar](#)

31. Elena De Domenico

[View author publications](#)

You can also search for this author in [PubMed](#) [Google Scholar](#)

32. Christian Siever

[View author publications](#)

You can also search for this author in [PubMed](#) [Google Scholar](#)

33. Michael Kraut

[View author publications](#)

You can also search for this author in [PubMed](#) [Google Scholar](#)

34. Milind Desai

[View author publications](#)

You can also search for this author in [PubMed](#) [Google Scholar](#)

35. Bruno Monnet

[View author publications](#)

You can also search for this author in [PubMed](#) [Google Scholar](#)

36. Maria Saridaki

[View author publications](#)

You can also search for this author in [PubMed](#) [Google Scholar](#)

37. Charles Martin Siegel

[View author publications](#)

You can also search for this author in [PubMed](#) [Google Scholar](#)

38. Anna Drews

[View author publications](#)

You can also search for this author in [PubMed](#) [Google Scholar](#)

39. Melanie Nuesch-Germano

[View author publications](#)

You can also search for this author in [PubMed](#) [Google Scholar](#)

40. Heidi Theis

[View author publications](#)

You can also search for this author in [PubMed](#) [Google Scholar](#)

41. Jan Heyckendorf

[View author publications](#)

You can also search for this author in [PubMed](#) [Google Scholar](#)

42. Stefan Schreiber

[View author publications](#)

You can also search for this author in [PubMed](#) [Google Scholar](#)

43. Sarah Kim-Hellmuth

[View author publications](#)

You can also search for this author in [PubMed](#) [Google Scholar](#)

44. Jacob Nattermann

[View author publications](#)

You can also search for this author in [PubMed](#) [Google Scholar](#)

45. Dirk Skowasch

[View author publications](#)

You can also search for this author in [PubMed](#) [Google Scholar](#)

46. Ingo Kurth

[View author publications](#)

You can also search for this author in [PubMed](#) [Google Scholar](#)

47. Andreas Keller

[View author publications](#)

You can also search for this author in [PubMed](#) [Google Scholar](#)

48. Robert Bals

[View author publications](#)

You can also search for this author in [PubMed](#) [Google Scholar](#)

49. Peter Nürnberg

[View author publications](#)

You can also search for this author in [PubMed](#) [Google Scholar](#)

50. Olaf Rieß

[View author publications](#)

You can also search for this author in [PubMed](#) [Google Scholar](#)

51. Philip Rosenstiel

[View author publications](#)

You can also search for this author in [PubMed](#) [Google Scholar](#)

52. Mihai G. Netea

[View author publications](#)

You can also search for this author in [PubMed](#) [Google Scholar](#)

53. Fabian Theis

[View author publications](#)

You can also search for this author in [PubMed](#) [Google Scholar](#)

54. Sach Mukherjee

[View author publications](#)

You can also search for this author in [PubMed](#) [Google Scholar](#)

55. Michael Backes

[View author publications](#)

You can also search for this author in [PubMed](#) [Google Scholar](#)

56. Anna C. Aschenbrenner

[View author publications](#)

You can also search for this author in [PubMed](#) [Google Scholar](#)

57. Thomas Ulas

[View author publications](#)

You can also search for this author in [PubMed](#) [Google Scholar](#)

58. Monique M. B. Breteler

[View author publications](#)

You can also search for this author in [PubMed](#) [Google Scholar](#)

59. Evangelos J. Giamarellos-Bourboulis

[View author publications](#)

You can also search for this author in [PubMed](#) [Google Scholar](#)

60. Matthijs Kox

[View author publications](#)

You can also search for this author in [PubMed](#) [Google Scholar](#)

61. Matthias Becker

[View author publications](#)

You can also search for this author in [PubMed](#) [Google Scholar](#)

62. Sorin Cheran

[View author publications](#)

You can also search for this author in [PubMed](#) [Google Scholar](#)

63. Michael S. Woodacre

[View author publications](#)

You can also search for this author in [PubMed](#) [Google Scholar](#)

64. Eng Lim Goh

[View author publications](#)

You can also search for this author in [PubMed](#) [Google Scholar](#)

65. Joachim L. Schultze

[View author publications](#)

You can also search for this author in [PubMed](#) [Google Scholar](#)

Consortia

COVID-19 Aachen Study (COVAS)

- Paul Balfanz
- , Thomas Eggermann
- , Peter Boor
- , Ralf Hausmann
- , Hannah Kuhn
- , Susanne Isfort
- , Julia Carolin Stingl
- , Günther Schmalzing
- , Christiane K. Kuhl
- , Rainer Röhrig
- , Gernot Marx
- , Stefan Uhlig
- , Edgar Dahl
- , Dirk Müller-Wieland

- , Michael Dreher
- & Nikolaus Marx

Deutsche COVID-19 Omics Initiative (DeCOI)

- , Janine Altmüller
- , Angel Angelov
- , Anna C. Aschenbrenner
- , Robert Bals
- , Alexander Bartholomäus
- , Anke Becker
- , Matthias Becker
- , Daniela Bezdan
- , Michael Bitzer
- , Conny Blumert
- , Ezio Bonifacio
- , Peer Bork
- , Bunk Boyke
- , Helmut Blum
- , Nicolas Casadei
- , Thomas Clavel
- , Maria Colome-Tatche
- , Markus Cornberg
- , Inti Alberto De La Rosa Velázquez
- , Andreas Diefenbach
- , Alexander Dilthey
- , Nicole Fischer
- , Konrad Förstner
- , Sören Franzenburg
- , Julia-Stefanie Frick
- , Gisela Gabernet
- , Julien Gagneur
- , Tina Ganzenmueller
- , Marie Gauder
- , Janina Geißert
- , Alexander Goesmann
- , Siri Göpel
- , Adam Grundhoff
- , Hajo Grundmann

- , Torsten Hain
- , Frank Hanses
- , Ute Hehr
- , André Heimbach
- , Marius Hooper
- , Friedemann Horn
- , Daniel Hübschmann
- , Michael Hummel
- , Thomas Iftner
- , Angelika Iftner
- , Thomas Illig
- , Stefan Janssen
- , Jörn Kalinowski
- , René Kallies
- , Birte Kehr
- , Andreas Keller
- , Oliver T. Keppler
- , Sarah Kim-Hellmuth
- , Christoph Klein
- , Michael Knop
- , Oliver Kohlbacher
- , Karl Köhrer
- , Jan Korbel
- , Peter G. Kremsner
- , Denise Kühnert
- , Ingo Kurth
- , Markus Landthaler
- , Yang Li
- , Kerstin U. Ludwig
- , Oliwia Makarewicz
- , Manja Marz
- , Alice C. McHardy
- , Christian Mertes
- , Maximilian Münchhoff
- , Sven Nahnsen
- , Markus Nöthen
- , Francine Ntoumi

- , Peter Nürnberg
- , Stephan Ossowski
- , Jörg Overmann
- , Silke Peter
- , Klaus Pfeffer
- , Isabell Pink
- , Anna R. Poetsch
- , Ulrike Protzer
- , Alfred Pühler
- , Nikolaus Rajewsky
- , Markus Ralser
- , Kristin Reiche
- , Olaf Rieß
- , Stephan Ripke
- , Ulisses Nunes da Rocha
- , Philip Rosenstiel
- , Antoine-Emmanuel Saliba
- , Leif Erik Sander
- , Birgit Sawitzki
- , Simone Scheithauer
- , Philipp Schiffer
- , Jonathan Schmid-Burgk
- , Wulf Schneider
- , Eva-Christina Schulte
- , Joachim L. Schultze
- , Alexander Sczyrba
- , Mariam L. Sharaf
- , Yogesh Singh
- , Michael Sonnabend
- , Oliver Stegle
- , Jens Stoye
- , Fabian Theis
- , Thomas Ulas
- , Janne Vehreschild
- , Thirumalaisamy P. Velavan
- , Jörg Vogel
- , Sonja Volland

- , Max von Kleist
- , Andreas Walker
- , Jörn Walter
- , Dagmar Wieczorek
- , Sylke Winkler
- & John Ziebuhr

Contributions

The idea was conceived by H.S., K.L.S., E.L.G., and J.L.S. Subprojects and clinical studies were directed by H.S., K.L.S., K.H., M. Bitzer, J.R., S.K.-H., J.N., I.K., A.K., R.B., P.N., O.R., P.R., M.M.B.B., M. Becker, and J.L.S. The conceptualization was performed by S.W.-H., H.S., K.L.S., M. Becker, S.C., M.S.W., E.L.G., and J.L.S. Direction of the clinical programs, collection of clinical information and patient diagnostics were done by P.P., N.A.A., S.K., F.T., M. Bitzer, C.H., D.P., U.B., F.K., T.F., P.S., C.L., M.A., J.R., B.K., M.S., J.H., S.S., S.K.-H., J.N., D.S., I.K., A.K., R.B., M.G.N., M.M.B.B., E.J.G.-B, and M.K. Patient samples were provided by P.P., N.A.A., S.K., F.T., M. Bitzer, S.O., N.C., C.H., D.P., U.B., F.K., T.F., P.S., C.L., M.A., J.R., B.K., M.S., J.H., S.S., S.K.-H., J.N., D.S., I.K., A.K., R.B., M.G.N., M.M.B.B., E.J.G.-B, and M.K. Laboratory experiments were performed by K.H., S.O., N.C., J.A., L.B., J.S.-S., E.D.D., M.K., and H.T. Primary data analysis and data QC were provided by S.W.-H., K.H., S.O., N.C., J.A., N.M., J.P.B., L.B., J.S.-S., E.D.D., M.N.-G., A.K., P.N., O.R., P.R., T.U., M. Becker, and J.L.S. Programming and coding for the current project were done by S.W.-H., Saikat Mukherjee, V.G., R.S., C.S., M.D., C.M.S., and M. Becker. The Swarm Learning environment was developed by S. Manamohan, Saikat Mukherjee, V.G., R.S., M.D., B.M., S.C., M.S.W., and E.L.G. Statistics and machine learning were done by S.W.-H., Saikat Mukherjee, V.G., R.S., M.D., F.T., Sach Mukherjee, S.C., E.L.G., and J.L.S. Data privacy and confidentiality concepts were developed by H.S., K.L.S., M. Backes, E.L.G., and J.L.S. Data interpretation was done by S.W.-H., H.S., Saikat Mukherjee, A.C.A., M. Becker, and J.L.S. Data were visualized by S.W.-H., H.S., M. Becker, and J.L.S. The original draft was written by S.W.-H., H.S., K.L.S., A.C.A., M. Becker, and J.L.S. Writing, reviewing and editing of revisions was done by S.W.-H., H.S., K.L.S., A.C.A., M.M.B.B., M. Becker, E.L.G., and J.L.S. Project management and

administration were performed by H.S., K.L.S., A.D., A.C.A., M. Becker, and J.L.S. Funding was acquired by H.S., S.K., D.P., M.A., J.R., S.K.-H., J.N., A.K., R.B., P.N., O.R., P.R., M.G.N., F.T., E.J.G.-B, M.B., S.C., and J.L.S. All authors commented on the manuscript.

Corresponding author

Correspondence to [Joachim L. Schultze](#).

Ethics declarations

Competing interests

H.S., K.L.S., S. Manamohan, Saikat Mukherjee, V.G., R.S., C.S., M.D., B.M, C.M.S., S.C., M.S.W. and E.L.G. are employees of Hewlett Packard Enterprise. Hewlett Packard Enterprise developed the SLL in its entirety as described in this work and has submitted multiple associated patent applications. E.J.G.-B. received honoraria from AbbVie USA, Abbott CH, InflaRx GmbH, MSD Greece, XBiotech Inc. and Angelini Italy and independent educational grants from AbbVie, Abbott, Astellas Pharma Europe, AxisShield, bioMérieux Inc, InflaRx GmbH, and XBiotech Inc. All other authors declare no competing interests.

Additional information

Peer review information *Nature* thanks Dianbo Liu, Christopher Mason and the other, anonymous, reviewer(s) for their contribution to the peer review of this work. Peer reviewer reports are available.

Publisher's note Springer Nature remains neutral with regard to jurisdictional claims in published maps and institutional affiliations.

Extended data figures and tables

[Extended Data Fig. 1 Corresponding to Fig. 1.](#)

a, Overview of SL and the relationship to data privacy, confidentiality and trust. **b**, Concept and outline of the private permissioned blockchain network as a layer of the SL network. Each node consists of the blockchain, including the ledger and smart contract, as well as the SLL with the API to interact with other nodes within the network. **c**, The principles of the SL workflow once the nodes have been enrolled within the Swarm network via private permissioned blockchain contract and dynamic onboarding of new Swarm nodes. **d**, Application and middleware layer as part of the SL concept.

Extended Data Fig. 2 Scenario corresponding to Fig. 2b,c in datasets A1 and A3.

Main settings and representation of schema and data visualization as described in Fig. 2a. **a**, Evaluation of test accuracy for 100 permutations of the scenario shown in Fig. 2b. **b**, Evaluation of SL versus central model for the scenario shown in Fig. 2b for 100 permutations. **c**, Scenario with different prevalences of AML and numbers of samples at each training node. The test dataset has an even distribution. **d**, Evaluation of test accuracy for 100 permutations of dataset A1 per node and SL. **e**, Evaluation using dataset A3 for 100 permutations. **f**, Scenario with similar training set sizes per node but decreasing prevalence. The test dataset ratio is 1:1. **g**, Evaluation of test accuracy for 100 permutations of the scenario shown in Fig. 2c. **h**, Evaluation of SL versus central model of the scenario shown in Fig. 2c for 100 permutations. **i**, Evaluation of test accuracy over 100 permutations for dataset A1 with the scenario shown in f. **j**, Evaluation of test accuracy over 100 permutations for dataset A3 with the scenario shown in f. **b, d, e, h-j**, Box plots show representation of accuracy of 100 permutations performed for the 3 training nodes individually as well as the results obtained by SL. All samples are biological replicates. Centre dot, mean; box limits, 1st and 3rd quartiles; whiskers, minimum and maximum values. Accuracy is defined for the independent fourth node used for testing only. Statistical differences between results derived by SL and all individual nodes including all permutations performed were calculated with one-sided Wilcoxon signed rank test with continuity correction; * $P < 0.05$, exact P values listed in Supplementary Table 5.

Extended Data Fig. 3 Scenario to test for batch effects of siloed studies in datasets A1–A3 and scenario with multiple consortia.

Main settings and representation of schema and data visualization are as in Fig. 2a. **a**, Scenario with training nodes coming from independent clinical studies for local models (left), central model (middle) and the Swarm network (right) and testing on a non-overlapping global test with samples from the same studies. **b**, Evaluation of test accuracy over 100 permutations for dataset A2 with the scenario shown in **a** (right) and Fig. 2d. **c**, Comparison of test accuracy between central model (**a**, middle) and SL (**a**, right). **d**, Comparison of test accuracy on the local test datasets (**a**, left) for 100 permutations. **e**, Evaluation of test accuracy of individual nodes versus SL over 100 permutations for dataset A1 when training nodes have data from independent clinical studies. **f**, Evaluation of test accuracy of individual nodes versus SL over 100 permutations for dataset A3 when training nodes have data from independent clinical studies. **g**, Scenario with three consortia contributing training nodes and a fourth one providing the testing node. **h**, Evaluation of test accuracy for scenario shown in **g** over 100 permutations for dataset A2. **d–f, h**, Box plots show representation of accuracy of all permutations performed for the 3 training nodes individually as well as the results obtained by SL (**d** only for local models). All samples are biological replicates. Centre dot, mean; box limits, 1st and 3rd quartiles; whiskers, minimum and maximum values. Performance measures are defined for the independent fourth node used for testing only. Statistical differences between results derived by SL and all individual nodes including all permutations performed were calculated with one-sided Wilcoxon signed rank test with continuity correction; * $P < 0.05$, exact P values are listed in Supplementary Table 5.

Extended Data Fig. 4 Scenario corresponding to Fig. 2e in datasets A1 and A3 and scenario using different data generation methods in each training node.

Main settings and representation of schema and data visualization are as in Fig. 2a. **a**, Scenario with even distribution of cases and controls at each training node and the test node, but different numbers of samples at each

node and overall increase in numbers of samples. **b, c**, Test accuracy for evaluation of dataset A2 over 100 permutations. **d**, Comparison of central model with SL over 100 permutations. **e**, Test accuracy for evaluation of dataset A1 over 99 permutations. **f**, Test accuracy for evaluation of dataset A3 over 100 permutations. **g**, Scenario where datasets A1, A2, and A3 are assigned to a single training node each. **h**, Evaluation of test accuracy over 100 permutations. **i**, Comparison of the test accuracy of central model and SL over 98 permutations. **j**, Scenario similar to **g** but where the nodes use datasets from different RNA-seq protocols. **k**, Evaluation of results for accuracy, AUC, sensitivity, and specificity over five permutations. **d–f, i, k**, Box plots show predictive performance over all permutations performed for the three training nodes individually as well as the results obtained by SL. All samples are biological replicates. Centre dot, mean; box limits, 1st and 3rd quartiles; whiskers, minimum and maximum values. Performance measures are defined for the independent fourth node used for testing only. Statistical differences between results derived by SL and all individual nodes including all permutations performed were calculated with one-sided Wilcoxon signed rank test with continuity correction; * $P < 0.05$, exact P values listed in Supplementary Table [5](#).

Extended Data Fig. 5 Scenario for ALL in dataset 2 and multi-class prediction and expansion of SL.

Main settings are identical to what is described in Fig. [2a](#). Here cases are samples derived from patients with ALL, while all other samples are controls (including AML). **a**, Scenario for the detection of ALL in dataset A2. The training sets are evenly distributed among the nodes with varying prevalence at the testing node. Data from independent clinical studies are samples to each node, as described for AML in Fig. [2d](#). **b**, Evaluation of scenario in **a** for test accuracy over 100 permutations with a prevalence ratio of 1:1. **c**, Evaluation using a test dataset with prevalence ratio of 10:100 over 100 permutations. **d**, Evaluation using a test dataset with prevalence ratio of 5:100 over 100 permutations. **e**, Evaluation using a test dataset with prevalence ratio of 1:100. **f**, Scenario for multi-class prediction of different types of leukaemia in dataset A2. Each node has a different prevalence. **g**, Test accuracy for the different types of leukaemia over 20 permutations. **h**, Scenario that simulates 32 small Swarm nodes. **i**,

Evaluation of test accuracy for the 32 nodes and the Swarm over 10 permutations. **j**, Development of accuracy over training epochs with addition of new nodes. **b–e, g, i**, Box plots show performance of all permutations performed for the training nodes individually as well as the results obtained by SL. All samples are biological replicates. Centre dot, mean; box limits, 1st and 3rd quartiles; whiskers, minimum and maximum values. Performance measures are defined for the independent test node used for testing only. Statistical differences between results derived by SL and all individual nodes including all permutations performed were calculated with one-sided Wilcoxon signed rank test with continuity correction; * $P < 0.05$, exact P values listed in Supplementary Table 5.

Extended Data Fig. 6 Comparison of LASSO and neural networks.

a, Scenario for training different models in the Swarm. **b**, Evaluation of a LASSO model for accuracy, sensitivity, specificity and F1 score over 100 permutations. **c**, Evaluation of a Neural Network model for accuracy, sensitivity, specificity and F1 score over 100 permutations. **b, c**, Box plots show performance of all permutations performed for the training nodes individually as well as the results obtained by SL. All samples are biological replicates. Centre dot, mean; box limits, 1st and 3rd quartiles; whiskers, minimum and maximum values. Performance measures are defined for the independent fourth node used for testing only. Statistical differences between results derived by SL and all individual nodes including all permutations performed were calculated with one-sided Wilcoxon signed rank test with continuity correction; * $P < 0.05$, exact P values listed in Supplementary Table 5.

Extended Data Fig. 7 Scenarios for detecting all TB versus controls and for detecting active TB with low prevalence at training nodes.

Main settings are as in Fig. 2a. **a**, Different group settings used with assignment of latent TB to control or case. **b**, Left, evaluation of a scenario where active and latent TB are cases. The data are evenly distributed among

the training nodes. Right, test accuracy, sensitivity and specificity for nodes, Swarm and a central model over 10 permutations. **c**, Left, scenario similar to **b** but with latent TB as control. Right, test accuracy, sensitivity and specificity for nodes, Swarm and a central model over 10 permutations. **d**, Left, scenario with reduced prevalence at the test node. Right, test accuracy, sensitivity and specificity for nodes and Swarm over 10 permutations. **e**, Scenario with even distribution of cases and controls at each training node, where node 1 has a very small training set. The test dataset is evenly distributed. Right, test accuracy, sensitivity and specificity over 50 permutations. **f**, Left, scenario similar to **e** but with uneven distribution in the test node. Right, test accuracy, sensitivity and specificity over 50 permutations. **g**, Scenario with each training node having a different prevalence. Three prevalence scenarios were used in the test dataset. **h**, Accuracy, sensitivity, specificity and F1 score over five permutations for testing set T1 as shown in **g**. **i**, As in **h** but with prevalence changed to 1:3 cases:controls in the training set. **j**, As in **h** but with prevalence changed to 1:10 cases:controls in the training set. **b–f**, **h–j**, Box plots show performance of all permutations performed for the training nodes individually as well as the results obtained by SL. All samples are biological replicates. Centre dot, mean; box limits, 1st and 3rd quartiles; whiskers, minimum and maximum values. Performance measures are defined for the independent fourth node used for testing only. Statistical differences between results derived by SL and all individual nodes including all permutations performed were calculated with one-sided Wilcoxon signed rank test with continuity correction; * $P < 0.05$, exact P values listed in Supplementary Table 5.

Extended Data Fig. 8 Baseline scenario for detecting patients with COVID-19 and scenario with reduced prevalence at training nodes.

Main settings are as in Fig. 2a. **a**, Scenario for detecting COVID-19 with even training set distribution among nodes 1–3. Three testing sets with different prevalences were simulated. **b**, Accuracy, sensitivity, specificity and F1 score over 50 permutations for scenario in **a** with a 22:25 case:control ratio. **c**, As in **b** for an 11:25 ratio. **d**, As in **b** for a 1:44 ratio. **e**, Scenario with the same sample size at each training node, but prevalence

decreasing from node 1 to node 3. There are two test datasets (**f**, **g**). **f**, Evaluation of scenario in **e** with 22:25 ratio at the test node over 50 permutations. **g**, Evaluation of scenario in **e** with reduced prevalence over 50 permutations. **h**, Scenario similar to **e** but with a steeper decrease in prevalence between nodes 1 and 3. **i**, Evaluation of scenario in **h** with a ratio of 37:50 at the test node over 50 permutations. **j**, Evaluation of scenario in **h** with a reduced prevalence compared to **i** over 50 permutations. **k**, Scenario as in Fig. [4a](#) using a 1:5 ratio for cases and controls in the test dataset evaluated over 50 permutations. **l**, Scenario as in Fig. [4a](#) using a 1:10 ratio in the test dataset to simulate detection in regions with new infections, evaluated over 50 permutations. **m**, Performance of central models for **k**, **l** and Fig. [4b](#). **n**, Loss function of training and validation loss over 100 training epochs. **b–d**, **f**, **g**, **i–m**, Box plots show performance of all permutations performed for the training nodes individually as well as the results obtained by SL. All samples are biological replicates. Centre dot, mean; box limits, 1st and 3rd quartiles; whiskers, minimum and maximum values. Performance measures are defined for the independent fourth node used for testing only. Statistical differences between results derived by SL and all individual nodes including all permutations performed were calculated with one-sided Wilcoxon signed rank test with continuity correction; * $P < 0.05$, exact P values listed in Supplementary Table [5](#).

[Extended Data Fig. 9 Scenario with reduced prevalence in training and test datasets and multi-centre scenario at a four-node setting.](#)

Main settings as in Fig. [2a](#). **a**, Scenario with prevalences from 10% at node 1 to 3% at node 4. There are three test datasets (**b–d**) with decreasing prevalence and increasing total sample size. **b**, Evaluation of scenario in **a** with 111:100 ratio over 50 permutations. **c**, Evaluation of scenario in **a** with 1:4 ratio and increased sample number of the test dataset over 50 permutations. **d**, Evaluation of scenario in **a** with 1:10 prevalence and increased sample number of the test dataset over 50 permutations. **e**, Dataset properties for the participating cities E1–E8, indicating case:control ratio and demographic properties. **f**, AUC, accuracy, sensitivity, specificity and F1 score over 20 permutations for scenario that uses E1–E6 as training

nodes and E7 as external test node. **g**, Evaluation of a multi-city scenario where a medical centre (in each row) serves as a test node. The AUC for each training node and the SL is shown for 20 permutations. **h**, Multi-city scenario. Only three nodes (E1–E3) are used for training and the external test node E4 uses data from a different sequencing facility. AUC, accuracy, sensitivity and specificity as well as the confusion matrix for one prediction. **b–d, f, g**, Box plots show performance of all permutations performed for the training nodes individually as well as the results obtained by SL. All samples are biological replicates. Centre dot, mean; box limits, 1st and 3rd quartiles; whiskers, minimum and maximum values. Performance measures are defined for the independent fourth node used for testing only. Statistical differences between results derived by SL and all individual nodes including all permutations performed were calculated with one-sided Wilcoxon signed rank test with continuity correction; * $P < 0.05$, exact P values listed in Supplementary Table 5.

Extended Data Fig. 10 Scenarios for testing different factors and scenario for testing disease severity.

Main settings as in Fig. 2a. **a**, Top, scenario to test influence of sex with three training nodes. Training node 1 has only male cases, node 2 has only female cases. Training node 3 and the test node have a 50%/50% split. Bottom, accuracy, sensitivity, specificity and F1 score for each training node and the Swarm in 10 permutations. **b**, Top, scenario to test influence of age with three training nodes. Training node 1 only has cases younger than 65 years, node 2 only has cases older than 65 years. Training node 3 and the test node have a 50%/50% split of cases above and below 65 years. Bottom, accuracy, sensitivity, specificity and F1 score for each training node and the Swarm in 10 permutations. **c**, Top, scenario to test influence of co-infections with three training nodes. Training node 1 has only cases with co-infections, node 2 has no cases with co-infections. Training node 3 and the test node have a 50%/50% split. Bottom, accuracy, sensitivity, specificity and F1 score for each training node and the Swarm in 10 permutations. **d**, Prediction setting. Severe cases of COVID-19 are cases, mild cases of COVID-19 and healthy donors are controls. **e**, Left, scenario to test influence of disease severity with three training nodes. Training node 1 has 20% mild or healthy and 80% severe cases, node 3 has 40% mild or

healthy and 60% severe cases. Training node 2 and the test node have 30% mild or healthy and 70% severe cases. Right, accuracy, sensitivity, specificity and F1 score for each training node and the Swarm for 10 permutations. **a–c, e**, Box plots show performance all permutations performed for the training nodes individually as well as the results obtained by SL. All samples are biological replicates. Centre dot, mean; box limits, 1st and 3rd quartiles; whiskers, minimum and maximum values. Performance measures are defined for the independent fourth node used for testing only. Statistical differences between results derived by SL and all individual nodes including all permutations performed were calculated with one-sided Wilcoxon signed rank test with continuity correction; * $P < 0.05$, exact P values listed in Supplementary Table 5.

Supplementary information

Supplementary Information

This file contains a more detailed description of Swarm Learning and the scenarios that were used for evaluation, as well as a Supplementary Discussion.

Reporting Summary

Peer Review File

Supplementary Table 1

Overview over all sample numbers and scenarios.

Supplementary Table 2

Dataset annotations of datasets A-E.

Supplementary Table 3

Prediction results for all scenarios and permutations.

Supplementary Table 4

Summary statistics on all prediction scenarios.

Supplementary Table 5

Statistical tests comparing single node vs. Swarm predictions.

Supplementary Table 6

COVID-19 Patient characteristics.

Supplementary Table 7

Library preparation and sequencing details of studies included in Extended Data Figure 4i.

Supplementary Table 8

List of all tuning parameters used for all scenarios.

Rights and permissions

Open Access This article is licensed under a Creative Commons Attribution 4.0 International License, which permits use, sharing, adaptation, distribution and reproduction in any medium or format, as long as you give appropriate credit to the original author(s) and the source, provide a link to the Creative Commons license, and indicate if changes were made. The images or other third party material in this article are included in the article's Creative Commons license, unless indicated otherwise in a credit line to the material. If material is not included in the article's Creative Commons license and your intended use is not permitted by statutory regulation or exceeds the permitted use, you will need to obtain permission directly from the copyright holder. To view a copy of this license, visit <http://creativecommons.org/licenses/by/4.0/>.

Reprints and Permissions

About this article



Check for
updates

Cite this article

Warnat-Herresthal, S., Schultze, H., Shastry, K.L. *et al.* Swarm Learning for decentralized and confidential clinical machine learning. *Nature* **594**, 265–270 (2021). <https://doi.org/10.1038/s41586-021-03583-3>

Download citation

- Received: 03 July 2020
- Accepted: 26 April 2021
- Published: 26 May 2021
- Issue Date: 10 June 2021
- DOI: <https://doi.org/10.1038/s41586-021-03583-3>

Comments

By submitting a comment you agree to abide by our [Terms](#) and [Community Guidelines](#). If you find something abusive or that does not comply with our terms or guidelines please flag it as inappropriate.

Download PDF

Advertisement

This article was downloaded by **calibre** from <https://www.nature.com/articles/s41586-021-03583-3>

| [Section menu](#) | [Main menu](#) |

- Article
- [Published: 28 April 2021](#)

***PIK3CA* and CCM mutations fuel cavernomas through a cancer-like mechanism**

- [Aileen A. Ren](#) ORCID: [orcid.org/0000-0002-1116-900X^{1 na1}](https://orcid.org/0000-0002-1116-900X),
- [Daniel A. Snellings](#) ORCID: [orcid.org/0000-0003-0615-9111^{2 na1}](https://orcid.org/0000-0003-0615-9111),
- [Yourong S. Su³](#),
- [Courtney C. Hong](#) ORCID: [orcid.org/0000-0003-0515-6816¹](https://orcid.org/0000-0003-0515-6816),
- [Marco Castro](#) ORCID: [orcid.org/0000-0001-7851-7446⁴](https://orcid.org/0000-0001-7851-7446),
- [Alan T. Tang](#) ORCID: [orcid.org/0000-0003-1422-0349¹](https://orcid.org/0000-0003-1422-0349),
- [Matthew R. Detter](#) ORCID: [orcid.org/0000-0003-1207-2565²](https://orcid.org/0000-0003-1207-2565),
- [Nicholas Hobson⁵](#),
- [Romuald Girard](#) ORCID: [orcid.org/0000-0002-5893-9315⁵](https://orcid.org/0000-0002-5893-9315),
- [Sharbel Romanos⁵](#),
- [Rhonda Lightle⁵](#),
- [Thomas Moore⁵](#),
- [Robert Shenkar](#) ORCID: [orcid.org/0000-0002-1300-6845⁵](https://orcid.org/0000-0002-1300-6845),
- [Christian Benavides²](#),
- [M. Makenzie Beaman](#) ORCID: [orcid.org/0000-0003-4066-2060²](https://orcid.org/0000-0003-4066-2060),
- [Helge Müller-Fielitz](#) ORCID: [orcid.org/0000-0003-2815-4426⁸](https://orcid.org/0000-0003-2815-4426),
- [Mei Chen¹](#),
- [Patricia Mericko¹](#),
- [Jisheng Yang¹](#),
- [Derek C. Sung](#) ORCID: [orcid.org/0000-0001-6966-2596¹](https://orcid.org/0000-0001-6966-2596),
- [Michael T. Lawton⁶](#),
- [J. Michael Ruppert⁷](#),
- [Markus Schwaninger](#) ORCID: [orcid.org/0000-0002-4510-9718⁸](https://orcid.org/0000-0002-4510-9718),

- [Jakob Körbelin](#) [ORCID: orcid.org/0000-0002-5435-7182⁹](#),
- [Michael Potente](#) [ORCID: orcid.org/0000-0002-5689-0036^{4,10,11}](#),
- [Issam A. Awad⁵](#),
- [Douglas A. Marchuk](#) [ORCID: orcid.org/0000-0002-3110-6671²](#) &
- [Mark L. Kahn](#) [ORCID: orcid.org/0000-0002-6489-7086¹](#)

[Nature](#) volume **594**, pages 271–276 (2021) [Cite this article](#)

- 6633 Accesses
- 140 Altmetric
- [Metrics details](#)

Subjects

- [Stroke](#)
- [Translational research](#)

Abstract

Vascular malformations are thought to be monogenic disorders that result in dysregulated growth of blood vessels. In the brain, cerebral cavernous malformations (CCMs) arise owing to inactivation of the endothelial CCM protein complex, which is required to dampen the activity of the kinase MEKK3^{1,2,3,4}. Environmental factors can explain differences in the natural history of CCMs between individuals⁵, but why single CCMs often exhibit sudden, rapid growth, culminating in strokes or seizures, is unknown. Here we show that growth of CCMs requires increased signalling through the phosphatidylinositol-3-kinase (PI3K)–mTOR pathway as well as loss of function of the CCM complex. We identify somatic gain-of-function mutations in *PIK3CA* and loss-of-function mutations in the CCM complex in the same cells in a majority of human CCMs. Using mouse models, we show that growth of CCMs requires both PI3K gain of function and CCM loss of function in endothelial cells, and that both CCM loss of function and increased expression of the transcription factor KLF4 (a downstream

effector of MEKK3) augment mTOR signalling in endothelial cells. Consistent with these findings, the mTORC1 inhibitor rapamycin effectively blocks the formation of CCMs in mouse models. We establish a three-hit mechanism analogous to cancer, in which aggressive vascular malformations arise through the loss of vascular ‘suppressor genes’ that constrain vessel growth and gain of a vascular ‘oncogene’ that stimulates excess vessel growth. These findings suggest that aggressive CCMs could be treated using clinically approved mTORC1 inhibitors.

Access options

Subscribe to Journal

Get full journal access for 1 year

\$199.00

only \$3.90 per issue

[Subscribe](#)

All prices are NET prices.

VAT will be added later in the checkout.

Tax calculation will be finalised during checkout.

Rent or Buy article

Get time limited or full article access on ReadCube.

from \$8.99

[Rent or Buy](#)

All prices are NET prices.

Additional access options:

- [Log in](#)

- [Access through your institution](#)
- [Learn about institutional subscriptions](#)

Fig. 1: LOF of CCM genes and GOF of *PIK3CA* synergize during cavernous malformation in the neonatal brain, and are both required for malformations in the adult brain.

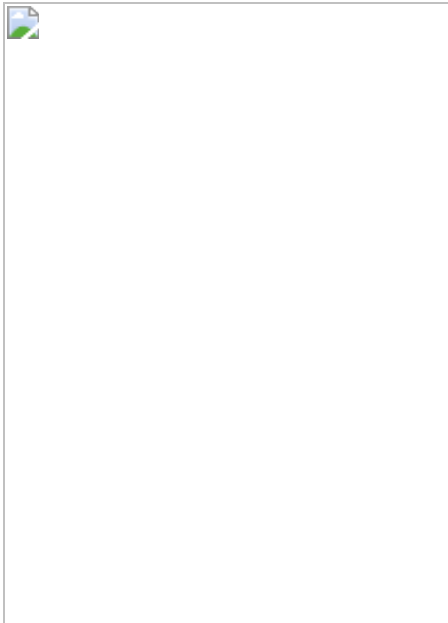


Fig. 2: GOF *PIK3CA* mutations and LOF CCM gene mutations co-exist in the same cell in human CCMs.

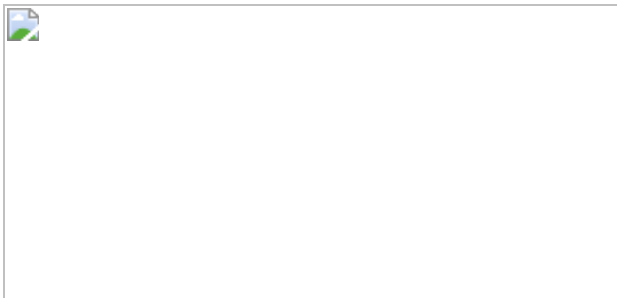


Fig. 3: Endothelial CCM LOF augments PI3K-mTORC1 signalling through KLF4.

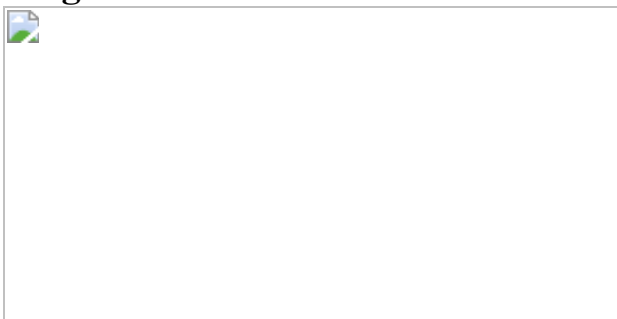
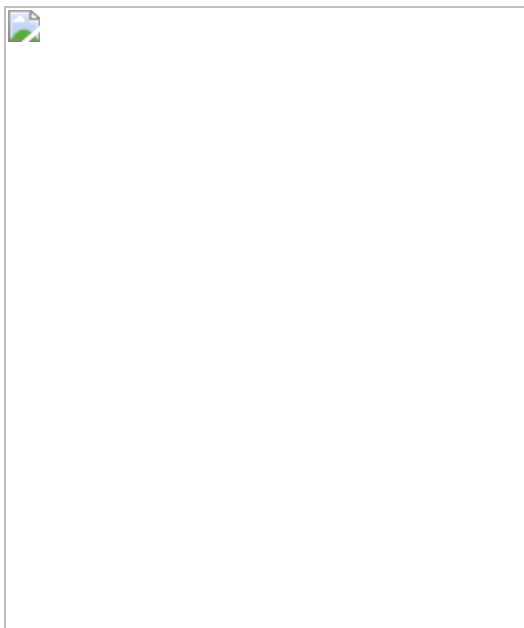


Fig. 4: Rapamycin prevents lesion formation due to CCM LOF and KLF4 GOF in neonatal and adult mice.



Data availability

The data that support the findings of this study are available from the corresponding authors upon reasonable request. DNA sequencing data are available on request from D.A.M. The data are not publicly available as they contain information that could compromise the privacy and consent of research participants. Public datasets used here are available at COSMIC (cancer.sanger.ac.uk/cosmic), dbSNP (ncbi.nlm.nih.gov/snp), 1000 Genomes Project (internationalgenome.org) and ExAC (gnomad.broadinstitute.org). [Source data](#) are provided with this paper.

Code availability

Variant-calling software was implemented as part of Gonomics, an ongoing effort to develop an open-source genomics platform in the Go programming language. Gonomics can be accessed at github.com/vertgenlab/gonomics.

References

1. 1.

Cuttano, R. et al. KLF4 is a key determinant in the development and progression of cerebral cavernous malformations. *EMBO Mol. Med.* **8**, 6–24 (2015).

[PubMed Central](#) [Article](#) [CAS](#) [Google Scholar](#)

2. 2.

Zhou, Z. et al. Cerebral cavernous malformations arise from endothelial gain of MEKK3-KLF2/4 signalling. *Nature* **532**, 122–126 (2016).

[ADS](#) [CAS](#) [PubMed](#) [PubMed Central](#) [Article](#) [Google Scholar](#)

3. 3.

Renz, M. et al. Regulation of β 1 integrin-Klf2-mediated angiogenesis by CCM proteins. *Dev. Cell* **32**, 181–190 (2015).

[CAS](#) [PubMed](#) [Article](#) [PubMed Central](#) [Google Scholar](#)

4. 4.

Otten, C. et al. Systematic pharmacological screens uncover novel pathways involved in cerebral cavernous malformations. *EMBO Mol. Med.* **10**, e9155 (2018).

[PubMed](#) [PubMed Central](#) [Article](#) [CAS](#) [Google Scholar](#)

5. 5.

Tang, A. T. et al. Endothelial TLR4 and the microbiome drive cerebral cavernous malformations. *Nature* **545**, 305–310 (2017).

[ADS](#) [CAS](#) [PubMed](#) [PubMed Central](#) [Article](#) [Google Scholar](#)

6. 6.

Fischer, A., Zalvide, J., Faurobert, E., Albiges-Rizo, C. & Tournier-Lasserve, E. Cerebral cavernous malformations: from CCM genes to endothelial cell homeostasis. *Trends Mol. Med.* **19**, 302–308 (2013).

[CAS](#) [PubMed](#) [Article](#) [PubMed Central](#) [Google Scholar](#)

7. 7.

Fisher, O. S. & Boggon, T. J. Signaling pathways and the cerebral cavernous malformations proteins: lessons from structural biology. *Cell. Mol. Life Sci.* **71**, 1881–1892 (2014).

[CAS](#) [PubMed](#) [Article](#) [PubMed Central](#) [Google Scholar](#)

8. 8.

Plummer, N. W., Zawistowski, J. S. & Marchuk, D. A. Genetics of cerebral cavernous malformations. *Curr. Neurol. Neurosci. Rep.* **5**, 391–396 (2005).

[CAS](#) [PubMed](#) [Article](#) [PubMed Central](#) [Google Scholar](#)

9. 9.

Al-Shahi Salman, R. et al. Untreated clinical course of cerebral cavernous malformations: a prospective, population-based cohort study. *Lancet Neurol.* **11**, 217–224 (2012).

[PubMed](#) [Article](#) [PubMed Central](#) [Google Scholar](#)

10. 10.

Awad, I. A. & Polster, S. P. Cavernous angiomas: deconstructing a neurosurgical disease. *J. Neurosurg.* **131**, 1–13 (2019).

[CAS](#) [PubMed](#) [PubMed Central](#) [Article](#) [Google Scholar](#)

11. 11.

Porter, P. J., Willinsky, R. A., Harper, W. & Wallace, M. C. Cerebral cavernous malformations: natural history and prognosis after clinical deterioration with or without hemorrhage. *J. Neurosurg.* **87**, 190–197 (1997).

[CAS](#) [PubMed](#) [Article](#) [PubMed Central](#) [Google Scholar](#)

12. 12.

Boulday, G. et al. Developmental timing of CCM2 loss influences cerebral cavernous malformations in mice. *J. Exp. Med.* **208**, 1835–1847 (2011).

[CAS](#) [PubMed](#) [PubMed Central](#) [Article](#) [Google Scholar](#)

13. 13.

Maddaluno, L. et al. EndMT contributes to the onset and progression of cerebral cavernous malformations. *Nature* **498**, 492–496 (2013).

[ADS](#) [CAS](#) [PubMed](#) [Article](#) [PubMed Central](#) [Google Scholar](#)

14. 14.

Detter, M. R., Snellings, D. A. & Marchuk, D. A. Cerebral cavernous malformations develop through clonal expansion of mutant endothelial cells. *Circ. Res.* **123**, 1143–1151 (2018).

[CAS](#) [PubMed](#) [PubMed Central](#) [Article](#) [Google Scholar](#)

15. 15.

Malinverno, M. et al. Endothelial cell clonal expansion in the development of cerebral cavernous malformations. *Nat. Commun.* **10**, 2761 (2019).

[ADS](#) [PubMed](#) [PubMed Central](#) [Article](#) [CAS](#) [Google Scholar](#)

16. 16.

Ramírez-Zamora, A. & Biller, J. Brainstem cavernous malformations: a review with two case reports. *Arq. Neuropsiquiatr.* **67** (3B), 917–921 (2009).

[PubMed](#) [Article](#) [PubMed Central](#) [Google Scholar](#)

17. 17.

Castro, M. et al. CDC42 deletion elicits cerebral vascular malformations via increased MEKK3-dependent KLF4 expression. *Circ. Res.* **124**, 1240–1252 (2019).

[CAS](#) [PubMed](#) [Article](#) [PubMed Central](#) [Google Scholar](#)

18. 18.

Hong, C. C. et al. Cerebral cavernous malformations are driven by ADAMTS5 proteolysis of versican. *J. Exp. Med.* **217**, e20200140 (2020).

[PubMed](#) [PubMed Central](#) [Article](#) [CAS](#) [Google Scholar](#)

19. 19.

Lissbrant, I. F., Lissbrant, E., Persson, A., Damberg, J. E. & Bergh, A. Endothelial cell proliferation in male reproductive organs of adult rat is high and regulated by testicular factors. *Biol. Reprod.* **68**, 1107–1111 (2003).

[CAS](#) [PubMed](#) [Article](#) [PubMed Central](#) [Google Scholar](#)

20. 20.

Samuels, Y. et al. Mutant PIK3CA promotes cell growth and invasion of human cancer cells. *Cancer Cell* **7**, 561–573 (2005).

[CAS](#) [PubMed](#) [Article](#) [PubMed Central](#) [Google Scholar](#)

21. 21.

Rodriguez-Laguna, L. et al. Somatic activating mutations in *PIK3CA* cause generalized lymphatic anomaly. *J. Exp. Med.* **216**, 407–418 (2019).

[CAS](#) [PubMed](#) [PubMed Central](#) [Article](#) [Google Scholar](#)

22. 22.

Castillo, S. D. et al. Somatic activating mutations in *Pik3ca* cause sporadic venous malformations in mice and humans. *Sci. Transl. Med.* **8**, 332ra43 (2016).

[PubMed](#) [PubMed Central](#) [Article](#) [CAS](#) [Google Scholar](#)

23. 23.

Castel, P. et al. Somatic PIK3CA mutations as a driver of sporadic venous malformations. *Sci. Transl. Med.* **8**, 332ra42 (2016).

[PubMed](#) [PubMed Central](#) [Article](#) [CAS](#) [Google Scholar](#)

24. 24.

Luks, V. L. et al. Lymphatic and other vascular malformative/overgrowth disorders are caused by somatic mutations in PIK3CA. *J. Pediatr.* **166**, 1048–1054 (2015).

[CAS](#) [PubMed](#) [PubMed Central](#) [Article](#) [Google Scholar](#)

25. 25.

Limaye, N. et al. Somatic activating PIK3CA mutations cause venous malformation. *Am. J. Hum. Genet.* **97**, 914–921 (2015).

[CAS](#) [PubMed](#) [PubMed Central](#) [Article](#) [Google Scholar](#)

26. 26.

Storck, S. E. et al. Endothelial LRP1 transports amyloid- β (1-42) across the blood-brain barrier. *J. Clin. Invest.* **126**, 123–136 (2016).

[PubMed](#) [Article](#) [PubMed Central](#) [Google Scholar](#)

27. 27.

Rigamonti, D. et al. Cerebral cavernous malformations. Incidence and familial occurrence. *N. Engl. J. Med.* **319**, 343–347 (1988).

[CAS](#) [PubMed](#) [Article](#) [PubMed Central](#) [Google Scholar](#)

28. 28.

Dogruluk, T. et al. Identification of variant-specific functions of PIK3CA by rapid phenotyping of rare mutations. *Cancer Res.* **75**, 5341–5354 (2015).

[CAS](#) [PubMed](#) [PubMed Central](#) [Article](#) [Google Scholar](#)

29. 29.

Gault, J., Shenkar, R., Recksiek, P. & Awad, I. A. Biallelic somatic and germ line CCM1 truncating mutations in a cerebral cavernous malformation lesion. *Stroke* **36**, 872–874 (2005).

[PubMed](#) [Article](#) [PubMed Central](#) [Google Scholar](#)

30. 30.

Akers, A. L., Johnson, E., Steinberg, G. K., Zabramski, J. M. & Marchuk, D. A. Biallelic somatic and germline mutations in cerebral cavernous malformations (CCMs): evidence for a two-hit mechanism of CCM pathogenesis. *Hum. Mol. Genet.* **18**, 919–930 (2009).

[CAS](#) [PubMed](#) [Article](#) [PubMed Central](#) [Google Scholar](#)

31. 31.

McDonald, D. A. et al. Lesions from patients with sporadic cerebral cavernous malformations harbor somatic mutations in the CCM genes: evidence for a common biochemical pathway for CCM pathogenesis. *Hum. Mol. Genet.* **23**, 4357–4370 (2014).

[CAS](#) [PubMed](#) [PubMed Central](#) [Article](#) [Google Scholar](#)

32. 32.

Xu, L. et al. Clonal evolution and changes in two AML patients detected with a novel single-cell DNA sequencing platform. *Sci. Rep.* **9**, 11119 (2019).

[ADS](#) [PubMed](#) [PubMed Central](#) [Article](#) [CAS](#) [Google Scholar](#)

33. 33.

Lopez-Ramirez, M. A. et al. Thrombospondin1 (TSP1) replacement prevents cerebral cavernous malformations. *J. Exp. Med.* **214**, 3331–3346 (2017).

[CAS](#) [PubMed](#) [PubMed Central](#) [Article](#) [Google Scholar](#)

34. 34.

Marchi, S. et al. Defective autophagy is a key feature of cerebral cavernous malformations. *EMBO Mol. Med.* **7**, 1403–1417 (2015).

[CAS](#) [PubMed](#) [PubMed Central](#) [Article](#) [Google Scholar](#)

35. 35.

Abdulrauf, S. I., Kaynar, M. Y. & Awad, I. A. A comparison of the clinical profile of cavernous malformations with and without associated venous malformations. *Neurosurgery* **44**, 41–46, discussion 46–47 (1999).

[CAS](#) [PubMed](#) [Article](#) [PubMed Central](#) [Google Scholar](#)

36. 36.

Tan, W. H. et al. The spectrum of vascular anomalies in patients with PTEN mutations: implications for diagnosis and management. *J. Med. Genet.* **44**, 594–602 (2007).

[CAS](#) [PubMed](#) [PubMed Central](#) [Article](#) [Google Scholar](#)

37. 37.

Adams, D. M. et al. Efficacy and safety of sirolimus in the treatment of complicated vascular anomalies. *Pediatrics* **137**, e20153257 (2016).

[PubMed](#) [PubMed Central](#) [Article](#) [Google Scholar](#)

38. 38.

Ozeki, M. et al. The impact of sirolimus therapy on lesion size, clinical symptoms, and quality of life of patients with lymphatic anomalies. *Orphanet J. Rare Dis.* **14**, 141 (2019).

[PubMed](#) [PubMed Central](#) [Article](#) [Google Scholar](#)

39. 39.

Triana, P. et al. Sirolimus in the treatment of vascular anomalies. *Eur. J. Pediatr. Surg.* **27**, 86–90 (2017).

[PubMed](#) [Article](#) [PubMed Central](#) [Google Scholar](#)

40. 40.

Venot, Q. et al. Targeted therapy in patients with PIK3CA-related overgrowth syndrome. *Nature* **558**, 540–546 (2018).

[ADS](#) [CAS](#) [PubMed](#) [PubMed Central](#) [Article](#) [Google Scholar](#)

41. 41.

Wang, Y. et al. Ephrin-B2 controls VEGF-induced angiogenesis and lymphangiogenesis. *Nature* **465**, 483–486 (2010).

[ADS](#) [CAS](#) [PubMed](#) [Article](#) [PubMed Central](#) [Google Scholar](#)

42. 42.

Ridder, D. A. et al. TAK1 in brain endothelial cells mediates fever and lethargy. *J. Exp. Med.* **208**, 2615–2623 (2011).

[CAS](#) [PubMed](#) [PubMed Central](#) [Article](#) [Google Scholar](#)

43. 43.

Claxton, S. et al. Efficient, inducible Cre-recombinase activation in vascular endothelium. *Genesis* **46**, 74–80 (2008).

[CAS](#) [PubMed](#) [Article](#) [PubMed Central](#) [Google Scholar](#)

44. 44.

Chan, A. C. et al. Mutations in 2 distinct genetic pathways result in cerebral cavernous malformations in mice. *J. Clin. Invest.* **121**, 1871–1881 (2011).

[ADS](#) [CAS](#) [PubMed](#) [PubMed Central](#) [Article](#) [Google Scholar](#)

45. 45.

Foster, K. W. et al. Induction of KLF4 in basal keratinocytes blocks the proliferation-differentiation switch and initiates squamous epithelial dysplasia. *Oncogene* **24**, 1491–1500 (2005).

[CAS](#) [PubMed](#) [PubMed Central](#) [Article](#) [Google Scholar](#)

46. 46.

Trotman, L. C. et al. Pten dose dictates cancer progression in the prostate. *PLoS Biol.* **1**, E59 (2003).

[PubMed](#) [PubMed Central](#) [Article](#) [Google Scholar](#)

47. 47.

Adams, J. R. et al. Cooperation between Pik3ca and p53 mutations in mouse mammary tumor formation. *Cancer Res.* **71**, 2706–2717 (2011).

[CAS](#) [PubMed](#) [Article](#) [PubMed Central](#) [Google Scholar](#)

48. 48.

Körbelin, J. et al. A brain microvasculature endothelial cell-specific viral vector with the potential to treat neurovascular and neurological diseases. *EMBO Mol. Med.* **8**, 609–625 (2016).

[PubMed](#) [PubMed Central](#) [Article](#) [CAS](#) [Google Scholar](#)

49. 49.

Hurst, C. D., Zuiverloon, T. C., Hafner, C., Zwarthoff, E. C. & Knowles, M. A. A SNaPshot assay for the rapid and simple detection of four common hotspot codon mutations in the PIK3CA gene. *BMC Res. Notes* **2**, 66 (2009).

[PubMed](#) [PubMed Central](#) [Article](#) [CAS](#) [Google Scholar](#)

50. 50.

Martelotto, L. G. ‘Frankenstein’ protocol for nuclei isolation from fresh and frozen tissue for snRNAseq. *protocols.io*
<https://doi.org/10.17504/protocols.io.3fkgjkw> (2020).

[Download references](#)

Acknowledgements

We thank the members of the Kahn laboratory for thoughtful comments and advice; A. Alliance for enrolling patients; the University of Chicago

PaleoCT core facility for its expertise in imaging and image quantification; the Penn CDB Microscopy Core for support with microscopy; Duke University School of Medicine for use of the Sequencing and Genomic Technologies Shared Resource for library preparation and sequencing; and K. Wood (Duke University) for providing the cell-line DNA used as a positive control in the ddPCR assay design. Flow cytometry was performed in the Duke Human Vaccine Institute Research Flow Cytometry Shared Resource Facility. These studies were supported by National Institute of Health grants R01HL094326 and R01NS100949 (to M.L.K.), P01NS092521 (M.L.K., D.A.M. and I.A.A.) the Leducq Foundation (M.L.K. and M.P.), the AHA-Allen foundation (M.L.K.), T32 HL007150 (A.A.R.), F31HL152738 (D.A.S.), F31NS115256 (C.C.H.) and F30NS100252 (A.T.T.); European Research Council (ERC) Synergy grant-2019-WATCH-810331 (to M.S.); and ERC Consolidator grant EMERGE-773047 (to M.P.).

Author information

Author notes

1. These authors contributed equally: Aileen A. Ren, Daniel A. Snellings

Affiliations

1. Department of Medicine and Cardiovascular Institute, University of Pennsylvania, Philadelphia, PA, USA

Aileen A. Ren, Courtney C. Hong, Alan T. Tang, Mei Chen, Patricia Mericko, Jisheng Yang, Derek C. Sung & Mark L. Kahn

2. Department of Molecular Genetics and Microbiology, Duke University School of Medicine, Durham, NC, USA

Daniel A. Snellings, Matthew R. Detter, Christian Benavides, M. Makenzie Beaman & Douglas A. Marchuk

3. Department of Neurosurgery, University of Pennsylvania,
Philadelphia, PA, USA

Yourong S. Su

4. Angiogenesis and Metabolism Laboratory, Max Planck institute for
Heart and Lung Research, Bad Nauheim, Germany

Marco Castro & Michael Potente

5. Neurovascular Surgery Program, Section of Neurosurgery, Department
of Surgery, The University of Chicago Medicine and Biological
Sciences, Chicago, IL, USA

Nicholas Hobson, Romuald Girard, Sharbel Romanos, Rhonda
Lightle, Thomas Moore, Robert Shenkar & Issam A. Awad

6. Department of Neurosurgery, The Barrow Neurological Institute,
Phoenix, AZ, USA

Michael T. Lawton

7. Cancer Institute, West Virginia University, Morgantown, WV, USA

J. Michael Ruppert

8. Institute for Experimental and Clinical Pharmacology and Toxicology,
Center of Brain, Behavior and Metabolism, University of Lübeck,
Lübeck, Germany

Helge Müller-Fielitz & Markus Schwaninger

9. University Medical Center Hamburg-Eppendorf, Department of
Oncology, Hematology and Bone Marrow Transplantation, Hamburg,
Germany

Jakob Körbelin

10. Berlin Institute of Health (BIH) and Charité–Universitätsmedizin Berlin, corporate member of Freie Universität Berlin, Humboldt-Universität zu Berlin, Berlin, Germany

Michael Potente

11. Max Delbrück Center for Molecular Medicine (MDC), Berlin, Germany

Michael Potente

Authors

1. Aileen A. Ren

[View author publications](#)

You can also search for this author in [PubMed](#) [Google Scholar](#)

2. Daniel A. Snellings

[View author publications](#)

You can also search for this author in [PubMed](#) [Google Scholar](#)

3. Yourong S. Su

[View author publications](#)

You can also search for this author in [PubMed](#) [Google Scholar](#)

4. Courtney C. Hong

[View author publications](#)

You can also search for this author in [PubMed](#) [Google Scholar](#)

5. Marco Castro

[View author publications](#)

You can also search for this author in [PubMed](#) [Google Scholar](#)

6. Alan T. Tang

[View author publications](#)

You can also search for this author in [PubMed](#) [Google Scholar](#)

7. Matthew R. Detter

[View author publications](#)

You can also search for this author in [PubMed](#) [Google Scholar](#)

8. Nicholas Hobson

[View author publications](#)

You can also search for this author in [PubMed](#) [Google Scholar](#)

9. Romuald Girard

[View author publications](#)

You can also search for this author in [PubMed](#) [Google Scholar](#)

10. Sharbel Romanos

[View author publications](#)

You can also search for this author in [PubMed](#) [Google Scholar](#)

11. Rhonda Lightle

[View author publications](#)

You can also search for this author in [PubMed](#) [Google Scholar](#)

12. Thomas Moore

[View author publications](#)

You can also search for this author in [PubMed](#) [Google Scholar](#)

13. Robert Shenkar

[View author publications](#)

You can also search for this author in [PubMed](#) [Google Scholar](#)

14. Christian Benavides

[View author publications](#)

You can also search for this author in [PubMed](#) [Google Scholar](#)

15. M. Makenzie Beaman

[View author publications](#)

You can also search for this author in [PubMed](#) [Google Scholar](#)

16. Helge Müller-Fielitz

[View author publications](#)

You can also search for this author in [PubMed](#) [Google Scholar](#)

17. Mei Chen

[View author publications](#)

You can also search for this author in [PubMed](#) [Google Scholar](#)

18. Patricia Mericko

[View author publications](#)

You can also search for this author in [PubMed](#) [Google Scholar](#)

19. Jisheng Yang

[View author publications](#)

You can also search for this author in [PubMed](#) [Google Scholar](#)

20. Derek C. Sung

[View author publications](#)

You can also search for this author in [PubMed](#) [Google Scholar](#)

21. Michael T. Lawton

[View author publications](#)

You can also search for this author in [PubMed](#) [Google Scholar](#)

22. J. Michael Ruppert

[View author publications](#)

You can also search for this author in [PubMed](#) [Google Scholar](#)

23. Markus Schwaninger

[View author publications](#)

You can also search for this author in [PubMed](#) [Google Scholar](#)

24. Jakob Körbelin

[View author publications](#)

You can also search for this author in [PubMed](#) [Google Scholar](#)

25. Michael Potente

[View author publications](#)

You can also search for this author in [PubMed](#) [Google Scholar](#)

26. Issam A. Awad

[View author publications](#)

You can also search for this author in [PubMed](#) [Google Scholar](#)

27. Douglas A. Marchuk

[View author publications](#)

You can also search for this author in [PubMed](#) [Google Scholar](#)

28. Mark L. Kahn

[View author publications](#)

You can also search for this author in [PubMed](#) [Google Scholar](#)

Contributions

A.A.R. designed and performed most of the mouse and tissue culture experiments and wrote the manuscript. D.A.S. carried out the genetic

studies of human CCM lesions and wrote the manuscript. Y.S.S. created and carried out the cranial window assays in adult mice. C.C.H., A.T.T., M.R.D. and H.M.-F. contributed to mouse genetic studies. M. Castro and M. Chen performed in vitro studies. N.H., R.G., S.R., R.L., T.M., R.S. and I.A.A. carried out microCT imaging and quantification of CCM lesions in a blinded manner. M. Chen, C.B. and P.M. assisted with mouse genetic studies. M.M.B. assisted with snDNA-seq studies. J.Y. and D.C.S. carried out histological studies. M.T.L. provided surgically excised human samples. M.R.D., M.S., J.M.R. and J.K. provided critical reagents. M.P., I.A.A., D.A.M. and M.L.K. designed experiments and wrote the manuscript.

Corresponding authors

Correspondence to [Douglas A. Marchuk](#) or [Mark L. Kahn](#).

Ethics declarations

Competing interests

The authors declare no competing interests. I.A.A. is Chairman of the Scientific Advisory Board for Angioma Alliance and provides expert opinions related to clinical care of cerebral cavernous malformations.

Additional information

Peer review information *Nature* thanks Marcus Goncalves, Mustafa Sahin, Salim Seyfried and the other, anonymous, reviewer(s) for their contribution to the peer review of this work. Peer reviewer reports are available.

Publisher's note Springer Nature remains neutral with regard to jurisdictional claims in published maps and institutional affiliations.

Extended data figures and tables

Extended Data Fig. 1 Loss of CCM gene function in endothelial cells in adult mice confers cavernous vascular malformations in the testis but not the brain.

a, Experimental design for investigating the effects of deleting CCM gene activity in neonatal endothelial cells. **b**, Cavernous malformations form by P10 in the hindbrain of *Krit1*^{iECKO} animals with a susceptible gut microbiome. Shown are images of hindbrains from the indicated animals (top panels), and haematoxylin-and-eosin (H&E)-stained histological sections (lower four panels). The arrow indicates a CCM lesion in the venous vessel of the white matter. **c**, Schematic showing deletion of CCM genes in endothelial cells (ECs) of adult mice on a susceptible microbiome background. **d**, Cavernous malformations are not detected in the brains of six-month-old *Krit1*^{iECKO} animals following administration of tamoxifen. Images of hindbrains from the indicated animals are shown above, and H&E-stained histological sections below. **e**, Cavernous malformations are detected in the testes of six-month-old *Krit1*^{iECKO} animals. Images of testis from the indicated animals are shown above, and H&E-stained histological sections below. Asterisks indicate blood-filled testes. Arrows indicate cavernous blood-filled vessels around the seminiferous tubules. In **b**, **d**, **e**, visual images are representative of $n = 4$ animals per genotype; H&E histology is representative of six tissue sections from $n = 4$ animals. Scale bars for visual images, 1 mm; scale bars for histology, 0.1 mm. **f**, Immunostaining for KLF4 and the endothelial-cell marker PECAM1 in brain (top) and testis (bottom) from the experiment in **c**. Note that endothelial CCM LOF in adult mice results in upregulation of KLF4 without CCM formation in the brain. Arrows indicate KLF4-positive nuclei in PECAM1-positive ECs. Yellow arrowheads indicate KLF4-positive peritubular myoid cells. Scale bars, 50 μ m. **g**, Quantification of KLF4-positive and KLF4-negative ECs identified using co-staining for KLF4 and PECAM1 in testis. Quantification from ten individual 800 μ m \times 800 μ m high-power fields from three individual animals. **h**, Immunostaining for DPEAAE, a versican neo-epitope exposed by ADAMTS-mediated proteolysis, in *Krit1*^{iECKO} testis. Arrows indicate peri-endothelial cell detection of DPEAAE around testicular cavernomas. Scale bars, 0.1 mm. The control animals in **b**, **d–g** had genotypes of either *Cdh5*–

$\text{CreERT2;Krit1}^{\text{fl}/+}$ or $\text{Krit1}^{\text{fl}/\text{fl}}$. Immunofluorescence images in **f**, **h** are representative of six tissue sections from $n = 4$ individual animals per genotype.

Extended Data Fig. 2 Vascular lesions due to CCM LOF and/or PIK3CA GOF arise in veins of the white matter.

a, Neonatal endothelial induction of *Krit1* deletion and/or PIK3CA^{H1047R} expression. **b**, **c**, H&E staining of saggital hindbrain sections from P6 control, *Pik3ca*^{iBECGOF}, *Krit1*^{iBECKO}; *Pik3ca*^{iBECGOF} (**b** and **b'**) and *Krit1*^{iBECKO} (**c** and **c'**) animals with a resistant (Res) or susceptible (Susc) microbiome. Samples in **b'**, **c'** were obtained from animals distinct from those in **b**, **c**. Note that lesions form in the white matter with both CCM LOF and PIK3CA GOF. Boxes in the upper images of each panel denote the area of the magnified image immediately below. Dotted lines outline the white matter of the cerebellum. Arrows indicate lesions in the veins and venules of the white matter. H&E images are representative of six tissue sections from $n = 4$ animals per genotype. *wm*, white matter. Scale bars, 0.1 mm.

Extended Data Fig. 3 Endothelial *Pten* LOF synergizes with *Krit1* LOF in a dose-dependent manner.

a, Tamoxifen (TMX)-induced deletion of *Krit1* and of either none or one allele of *Pten* in neonatal endothelial cells, using a *Pdgfb*-CreERT2 transgene. **b**, Representative visual (top) and paired microCT (bottom) images of *Krit1*^{iECKO} and *Krit1*^{iECKO}; *Pten*^{fl/+} littermate mice on a susceptible microbiome background at P12. Scale bars, 1 mm. These mice were produced from a *Pten*^{fl/+} by *Pten*^{fl/+} cross; however, no *Krit1*^{iECKO}; *Pten*^{fl/fl} littermates survived to P12. **c**, MicroCT-based quantification of lesion volumes at P12. *Krit1*^{iECKO}, $n = 6$; *Krit1*^{iECKO}; *Pten*^{fl/+}, $n = 13$. **d**, Induction of *Krit1* deletion and deletion of either one or both alleles of *Pten* in neonatal endothelial cells using a *Pdgfb*-CreERT2 transgene with brains harvested at P7. These mice were produced from a *Pten*^{fl/+} by *Pten*^{fl/fl} cross. **e**, Representative visual and paired microCT images in *Krit1*^{iECKO}; *Pten*^{fl/+} and *Krit1*^{iECKO}; *Pten*^{iECKO}

littermate mice at P7. Scale bars, 1 mm. **f**, MicroCT quantification of lesion volumes at P7. *Krit1*^{iECKO}; *Pten*^{fl/+}, $n = 13$; *Krit1*^{iECKO}; *Pten*^{iECKO}, $n = 8$. Data are means \pm s.e.m. Unpaired, two-tailed Welch's *t*-test. [Source data](#)

Extended Data Fig. 4 Uninduced *Slco1c1*–CreERT2; *Krit1*^{fl/fl}; i*Pik3ca*^{H1047R} animals develop focal lesions owing to endothelial leakage of the *Slco1c1*–CreERT2 transgene.

a, Generation of a survival curve in the absence of tamoxifen administration. **b**, Postnatal survival curves in the absence of tamoxifen administration for the indicated genotypes. *Slco1c1*–CreERT2; *Krit1*^{fl/fl}, $n = 15$, *Slco1c1*–CreERT2; *Krit1*^{fl/+}; i*Pik3ca*^{H1047R}, $n = 10$; *Slco1c1*–CreERT2; *Krit1*^{fl/fl}; i*Pik3ca*^{H1047R}, $n = 39$. Log-rank test. **c**, Representative visual and paired microCT images of brains harvested from untreated P28 littermates. Scale bars, 1 mm. **d**, MicroCT quantification of lesion volumes of untreated P28 animals. *Slco1c1*–CreERT2; *Krit1*^{fl/fl}, $n = 5$; *Slco1c1*–CreERT2; *Krit1*^{fl/+}; i*Pik3ca*^{H1047R}, $n = 9$; *Slco1c1*–CreERT2; *Krit1*^{fl/fl}; i*Pik3ca*^{H1047R}, $n = 10$. Data are shown as means \pm s.e.m. Unpaired, two-tailed Welch's *t*-test. **e**, Additional visual images of brains from a superior and inferior perspective from animals harvested at various time points (P19 to P36). Arrows point to focal vascular lesions. Scale bars, 1 mm. **f**, Leak assessed by immunostaining of brain sections with antibodies against GFP to identify Cre-expressing cells, and against cell-surface marker PECAM1 (top) and nuclear protein ERG (bottom) to identify endothelial cells. Scale bars, 50 μ m. Immunofluorescence images are representative of ten tissue sections from $n = 4$ individual animals per genotype. **g**, Quantitation of GFP- and ERG-positive nuclei ($n = 242$) and GFP-positive, ERG-negative nuclei ($n = 3$) from 20 individual 800 μ m \times 800 μ m high-power fields. [Source data](#)

Extended Data Fig. 5 Exogenous delivery of Cre recombinase via AAV vector to drive combined loss of CCM function and gain of PIK3CA function results in formation of CCMs in the adult brain.

a, Experimental approach in which a cranial window is created and AAV–Cre virus injected into the brains of 2-month-old mice, with serial imaging at post-operative days 1, 7, 10, 14, 18 and 21. **b**, Representative visual images of brains harvested 21 days after injection of AAV–Cre into adult animals. Dotted circles indicate the site of the cranial window and AAV–Cre injection. This panel includes the visual images displayed in Fig. 1. Scale bars, 1 mm. **c**, Serial images obtained through the cranial window of mice of the indicated genotypes following injection of AAV–Cre. The *iPik3ca*^{H1047R} designation includes *iPik3ca*^{H1047R} and/or *Krit1*^{fl/+}; *iPik3ca*^{H1047R} genotypes. White arrows indicate cavernous malformations in *Krit1*^{fl/fl}; *iPik3ca*^{H1047R} mice. Black arrows indicate hypervascularity in *iPik3ca*^{H1047R} mice. **d**, Staining for perilesional iron deposition in brains, indicative of chronic bleeding, from four independent *Krit1*^{fl/fl}; *iPik3ca*^{H1047R} mice at post-operative day 21. Scale bars, 200 µm.

[Extended Data Fig. 6 Lineage tracing of AAV–Cre activity after direct injection into the mouse brain.](#)

AAV–Cre was injected into the brain of Ai14 Cre reporter animals, and Cre activity was assessed by detection of the tdTomato (red fluorescent protein, RFP) reporter 14 days after injection. **a–c**, Confocal microscopic overviews of: **a**, the injection site; **b**, the border region of viral spread; and **c**, the contralateral cortex of AAV–Cre-injected Ai14 mice, two weeks after stereotactic injection. AAV–Cre-transduced cells expressed RFP (shown in white). RFP-positive vessels were identified by colocalization with PECAM1 (red). White arrows point to representative RFP-positive vessels. Yellow arrowheads point to RFP-expressing neuronal cells. Scale bars, 100 µm. The numbered boxed regions are shown at higher magnification on the right: 1 and 2 show anti-PECAM1 staining for endothelial cells, overlaid with RFP signal; 1' and 2' show PECAM staining alone; 1'' and 2'' show RFP staining alone. These data are representative of 12 separate images from 8 tissue sections from $n = 2$ individual animals. Scale bar, 20 µm.

[Extended Data Fig. 7 Characterization of snDNA-seq of human CCM samples.](#)

a, Relationship between somatic *PIK3CA* and CCM mutations detected in bulk sequencing. Points indicate individual mutations in either a CCM gene or *PIK3CA*. Lines connect the CCM gene and *PIK3CA* mutations present in a single sample. Box plots show the aggregate frequencies of *PIK3CA* and CCM mutations. Centre lines show medians; box limits indicate the 25th and 75th percentiles; whiskers extend 1.5 times the interquartile range from the 25th to 75th percentiles; outliers are represented by dots. $n = 21$ sample points for both plots. **b**, Representative FANS plots of unstained (top row) and DAPI-stained (bottom row) CCM homogenates. Doublets are discriminated by forward scatter profiles for DAPI-stained samples. FSC, forward scatter; SSC, side scatter. Plots consist of 100,000 events. The unstained sample contains one event (0%) in the DAPI-positive singlet gate. The DAPI-stained samples contain 2,414 events (2.4%) in the DAPI-positive singlet gate. **c**, Total reads and average coverage per nucleus from snDNA-seq for each mutation detected by bulk sequencing. The dotted line shows $20\times$ coverage, the minimum cutoff used for establishing genotype. **d**, Pseudobulk allele frequency from snDNA-seq for each mutation detected by bulk sequencing. The dotted line shows an allele frequency of 1%. VAF, variant allele frequency. Note that the data point with the arrow in **c**, **d** shows a mutation in sample 5079 detected in bulk sequencing, which, owing to poor amplification during snDNA-seq, received insufficient coverage per nucleus ($4.5\times$) to establish nuclear genotypes, but is clearly present in pseudobulk reads (1,849 of 9,814). **e**, Comparison of mutation allele frequency as detected by bulk sequencing and snDNA-seq. As nuclei are diploid for the relevant autosomes, the x -axis is equal to the fraction of mutant nuclei divided by two. The dotted line shows perfect correlation at $x = y$. R and P were calculated by Pearson's correlation coefficient. **f**, A summary of snDNA-seq results for three sporadic and two familial CCMs. The number of nuclei with each possible genotype are listed. Plus symbols indicate wild-type alleles; asterisks indicate mutant alleles. Note that only one somatic CCM mutation was identified in samples 5038 and 5079. P values were determined by two-tailed chi-squared tests between the observed and expected triple-mutant nuclei (or double-mutant for lesions 5038 and 5079) determined by Poisson distribution (see [Methods](#)).

[Extended Data Fig. 8 PI3K signalling does not augment MEKK3–KLF2/4 signalling.](#)

a, How gain of PI3K signalling might augment CCM formation by acting upstream of MEKK3–KLF2/4 signalling in endothelial cells. **b**, Immunostaining for KLF4 and PECAM1 in hindbrain sections from P6 control, *Krit1*^{BECKO}, *Pik3ca*^{iBECGOF} and *Krit1*^{iBECKO}; *Pik3ca*^{iBECGOF} neonates with either a susceptible (Susc) or resistant (Res) gut microbiome. White arrows indicate endothelial-cell nuclear KLF4 staining. Immunofluorescence images are representative of ten tissue sections from $n = 4$ individual animals per genotype. Control animals are either *Slco1c1*–Cre; *Krit1*^{f/+} or *Krit1*^{f/f}. Scale bars, 50 μ m. **c**, Measurement of *Klf2* and *Klf4* mRNA in endothelial cells isolated from the hindbrains of P6 control, *Krit1*^{BECKO} and *Pik3ca*^{iBECGOF} neonates. Control, $n = 8$; *Krit1*^{BECKO}, $n = 6$; *Pik3ca*^{iBECGOF}, $n = 8$. **d**, Measurement of *KLF2* and *KLF4* mRNA in HUVECs treated with the indicated siRNAs or lentiviral vectors. $n = 6$ individual wells per group over two independent experiments. Data are shown as means \pm s.e.m. Unpaired, two-tailed Welch's *t*-test. [Source data](#)

Extended Data Fig. 9 The CCM effector KLF4 augments endothelial cell PI3K-mTORC1 signalling.

a, Neonatal endothelial induction of KLF4 expression in KLF4^{iBECGOF} animals. **b**, Immunostaining for KLF4 and PECAM1 in hindbrain sections from P6 control and KLF4^{iBECGOF} animals. Boxes in the upper images denote the area of the magnified images immediately below. Immunofluorescence images are representative of six tissue sections from $n = 4$ individual animals per genotype. Scale bars, 50 μ m. hKLF4, hindbrain KLF4. **c**, H&E-stained sections of hindbrain from control and KLF4^{iBECGOF} littermates. Boxes in the upper images denote the area of the magnified images immediately below. Black arrows indicate lesions. Dotted lines outline the white matter (wm) of the cerebellum. Note that the dilated white-matter venules are similar to those observed with CCM LOF and PIK3CA GOF in Extended Data Fig. 2. The H&E histology is representative of six tissue sections from $n = 4$ animals per genotype. Scale bars, 0.1 mm. **d**, Immunostaining for phosphorylated S6 ribosomal protein (p-S6) and PECAM1 in hindbrain sections from P6 control and KLF4^{iBECGOF} animals. White and yellow arrows indicate p-S6-positive endothelial and nonendothelial cells, respectively. Immunofluorescence

images are representative of six tissue sections from $n = 4$ individual animals per genotype. Scale bars, 50 μm . **e**, Immunoblot detection of KLF4, KLF4–GFP and eNOS (whose gene is a KLF4 target) in HUVECs without and with inducible lentiviral expression of KLF4–GFP (iKLF4 cells) or control lentivirus. Tubulin is shown as a loading control.

Extended Data Fig. 10 Rapamycin-mediated rescue of CCM formation is independent of KLF4.

a, Experimental approach in which a cranial window is created and AAV–Cre is injected into the brains of two-month-old mice, followed by daily injection of vehicle, 100 μg of rapamycin (low) or 400 μg of rapamycin (high) from post-operative day 7 to day 21, with serial imaging at post-operative days 1, 7, 10, 14, 18 and 21. **b**, Representative visual images of brains harvested 21 days after injection of AAV–Cre and 2 weeks of daily vehicle or rapamycin treatment in *Krit1*^{fl/fl};i*Pik3ca*^{H1047R} mice. Dotted circles indicate the site of cranial window and AAV–Cre injection. Arrows indicate detached lesions. Scale bars, 1 mm. **c**, Serial images were obtained through the cranial window of *Krit1*^{fl/fl};i*Pik3ca*^{H1047R} mice following injection of AAV–Cre and subsequent treatment. Arrows indicate the formation and growth of individual cavernous malformations. **d**, MicroCT quantification of lesion volumes 21 days after creation of the cranial window and injection of AAV–Cre. The values shown include those from Fig. 4 (vehicle and low-dose treatments). Vehicle, $n = 6$; rapamycin low, $n = 7$; rapamycin high, $n = 7$. Data are shown as means \pm s.e.m. Unpaired, two-tailed Welch's *t*-test. **e**, Neonatal endothelial induction of *Krit1* deletion and treatment with rapamycin or vehicle control at P2. **f**, Immunostaining for PECAM1 and p-S6 of hindbrain sections from P6 *Krit1*^{iBECKO} animals treated with vehicle or rapamycin. White arrows indicate p-S6-positive endothelial cells, seen in the control but not rapamycin-treated animals. Yellow arrowheads indicate p-S6-positive neuronal cells. **g**, Immunostaining for PECAM1 and KLF4 of hindbrain sections from P6 *Krit1*^{iBECKO} animals treated with vehicle or rapamycin. White arrows indicate KLF4-positive endothelial cells, detected in control and rapamycin-treated animals. Scale bars, 50 μm . [Source data](#)

Supplementary information

Supplementary Figure 1

This file contains the uncropped gels.

Reporting Summary

Supplementary Table 1

Human CCM bulk tissue mutation data. Mutation data for each human CCM analyzed in this study using targeted sequencing, ddPCR, or SNaPshot. Each sample is notated as either familial (F), sporadic (S), or unknown (blank) as well as the affected gene for familial samples (CCM1/2/3). ddPCR and SNaPshot assay results for *PIK3CA* E542K, E545K, and H1047R for each sample are listed including the detected allele frequency as well as final mutation call. SNaPshot calls are color coded by variant and ddPCR results are colored according to the detected allele frequency for each variant. Sequencing data for *PIK3CA* are reported as the number of alt and ref reads supporting the listed variant, the allele frequency, and the final mutation call. *PIK3CA* variants shown in red text denote samples with insufficient coverage to make a definitive variant call per the thresholds detailed in the methods section; variant calls for these samples rely on a positive result by ddPCR and confirmation by a tertiary assay (SNaPshot). Germline and somatic mutations in the CCM genes are reported in respective columns listing the chromosomal coordinates in hg19, the predicted functional consequence of the variant, the number of reads supporting the alt and ref alleles, and the resulting allele frequency. The functional consequence of missense and in-frame indels are predicted by *in silico* tools SIFT (scale: 0-1, higher is more damaging) and PROVEAN (scale: continuous, <-2.5 predicted damaging) where available.

Supplementary Table 2

Human CCM snDNA-seq read counts. Number of total, mutant, and wild type supporting reads present in each nucleus for *PIK3CA* and CCM

mutations. Each nucleus is denoted by an 18bp oligo barcode which is incorporated into each read to define the nucleus of origin. These data were processed to generate Fig 2e. and Extended Data Figure 7c-f.

[Peer Review File](#)

Source data

[Source Data Fig. 1](#)

[Source Data Fig. 3](#)

[Source Data Fig. 4](#)

[Source Data Extended Data Fig. 3](#)

[Source Data Extended Data Fig. 4](#)

[Source Data Extended Data Fig. 8](#)

[Source Data Extended Data Fig. 10](#)

Rights and permissions

[Reprints and Permissions](#)

About this article



Check for
updates

Cite this article

Ren, A.A., Snellings, D.A., Su, Y.S. *et al.* PIK3CA and CCM mutations fuel cavernomas through a cancer-like mechanism. *Nature* **594**, 271–276 (2021). <https://doi.org/10.1038/s41586-021-03562-8>

[Download citation](#)

- Received: 25 August 2020
- Accepted: 16 April 2021
- Published: 28 April 2021
- Issue Date: 10 June 2021
- DOI: <https://doi.org/10.1038/s41586-021-03562-8>

Comments

By submitting a comment you agree to abide by our [Terms](#) and [Community Guidelines](#). If you find something abusive or that does not comply with our terms or guidelines please flag it as inappropriate.

[Access through your institution](#)

[Change institution](#)

[Buy or subscribe](#)

Advertisement

This article was downloaded by **calibre** from <https://www.nature.com/articles/s41586-021-03562-8>

- Article
- [Published: 26 May 2021](#)

NF1 mutation drives neuronal activity-dependent initiation of optic glioma

- [Yuan Pan](#) [ORCID: orcid.org/0000-0002-9465-8289](#)¹,
- [Jared D. Hysinger](#)¹,
- [Tara Barron](#)¹,
- [Nicki F. Schindler](#)¹,
- [Olivia Cobb](#)²,
- [Xiaofan Guo](#)²,
- [Belgin Yalçın](#) [ORCID: orcid.org/0000-0001-9689-9062](#)¹,
- [Corina Anastasaki](#)²,
- [Sara B. Mulinyawe](#)¹,
- [Anitha Ponnuswami](#)¹,
- [Suzanne Scheaffer](#)²,
- [Yu Ma](#)²,
- [Kun-Che Chang](#) [ORCID: orcid.org/0000-0002-0871-5612](#)³,
- [Xin Xia](#)³,
- [Joseph A. Toonen](#)²,
- [James J. Lennon](#)¹,
- [Erin M. Gibson](#)^{1,4},
- [John R. Huguenard](#)¹,
- [Linda M. Liau](#) [ORCID: orcid.org/0000-0002-4053-0052](#)⁵,
- [Jeffrey L. Goldberg](#)³,
- [Michelle Monje](#) [ORCID: orcid.org/0000-0002-3547-237X](#)^{1,4,6,7,8 na1}
&
- [David H. Gutmann](#) [ORCID: orcid.org/0000-0002-3127-5045](#)^{2 na1}

- 5923 Accesses
- 235 Altmetric
- [Metrics details](#)

Subjects

- [Cancer in the nervous system](#)
- [CNS cancer](#)

Abstract

Neurons have recently emerged as essential cellular constituents of the tumour microenvironment, and their activity has been shown to increase the growth of a diverse number of solid tumours¹. Although the role of neurons in tumour progression has previously been demonstrated², the importance of neuronal activity to tumour initiation is less clear—particularly in the setting of cancer predisposition syndromes. Fifteen per cent of individuals with the neurofibromatosis 1 (NF1) cancer predisposition syndrome (in which tumours arise in close association with nerves) develop low-grade neoplasms of the optic pathway (known as optic pathway gliomas (OPGs)) during early childhood^{3,4}, raising the possibility that postnatal light-induced activity of the optic nerve drives tumour initiation. Here we use an authenticated mouse model of OPG driven by mutations in the neurofibromatosis 1 tumour suppressor gene (*Nf1*)⁵ to demonstrate that stimulation of optic nerve activity increases optic glioma growth, and that decreasing visual experience via light deprivation prevents tumour formation and maintenance. We show that the initiation of *Nf1*-driven OPGs (*Nf1*-OPGs) depends on visual experience during a developmental period in which *Nf1*-mutant mice are susceptible to tumorigenesis. Germline *Nf1* mutation in retinal neurons results in aberrantly increased shedding of neuroligin 3 (NLGN3) within the optic nerve in response to retinal neuronal activity. Moreover, genetic *Nlgn3* loss or pharmacological inhibition of

NLGN3 shedding blocks the formation and progression of *Nf1*-OPGs. Collectively, our studies establish an obligate role for neuronal activity in the development of some types of brain tumours, elucidate a therapeutic strategy to reduce OPG incidence or mitigate tumour progression, and underscore the role of *Nf1* mutation-mediated dysregulation of neuronal signalling pathways in mouse models of the NF1 cancer predisposition syndrome.

Access options

Subscribe to Journal

Get full journal access for 1 year

\$199.00

only \$3.90 per issue

[Subscribe](#)

All prices are NET prices.

VAT will be added later in the checkout.

Tax calculation will be finalised during checkout.

Rent or Buy article

Get time limited or full article access on ReadCube.

from \$8.99

[Rent or Buy](#)

All prices are NET prices.

Additional access options:

- [Log in](#)
- [Access through your institution](#)

- [Learn about institutional subscriptions](#)

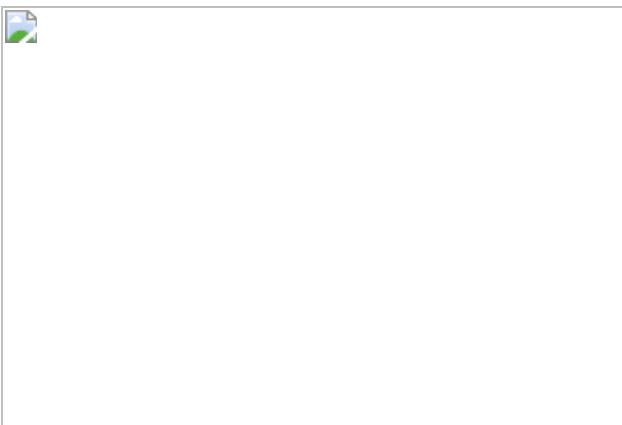
Fig. 1: The initiation and maintenance of *Nfl*-OPGs requires retinal activity.



Fig. 2: NLGN3 promotes *Nfl* optic gliomagenesis.



Fig. 3: *Nfl* mutation increases activity-regulated NLGN3 shedding and inhibition of NLGN3 shedding decreases optic glioma initiation and growth.



Data availability statement

Original western blots are included in the [Supplementary Information](#) ([supplementary Fig. 1](#)). Human pilocytic astrocytoma RNA-seq data are deposited with the Gene Expression Omnibus under accession number [GSE163071](#). The cell lines and other reagents described here are freely available and can be obtained by contacting the corresponding authors and with a standard materials transfer agreement. Any other relevant data are available from the corresponding authors upon reasonable request. [Source data](#) are provided with this paper.

References

1. 1.

Monje, M. et al. Roadmap for the emerging field of cancer neuroscience. *Cell* **181**, 219–222 (2020).

[CAS](#) [Article](#) [Google Scholar](#)

2. 2.

Zahalka, A. H. & Frenette, P. S. Nerves in cancer. *Nat. Rev. Cancer* **20**, 143–157 (2020).

[CAS](#) [Article](#) [Google Scholar](#)

3. 3.

Listernick, R., Louis, D. N., Packer, R. J. & Gutmann, D. H. Optic pathway gliomas in children with neurofibromatosis 1: consensus statement from the NF1 Optic Pathway Glioma Task Force. *Ann. Neurol.* **41**, 143–149 (1997).

[CAS](#) [Article](#) [Google Scholar](#)

4. 4.

Listernick, R., Charrow, J., Greenwald, M. & Mets, M. Natural history of optic pathway tumors in children with neurofibromatosis type 1: a

longitudinal study. *J. Pediatr.* **125**, 63–66 (1994).

[CAS](#) [Article](#) [Google Scholar](#)

5. 5.

Bajenaru, M. L. et al. Optic nerve glioma in mice requires astrocyte *Nf1* gene inactivation and *Nf1* brain heterozygosity. *Cancer Res.* **63**, 8573–8577 (2003).

[CAS](#) [Google Scholar](#)

6. 6.

Gutmann, D. H. et al. Somatic neurofibromatosis type 1 (NF1) inactivation characterizes NF1-associated pilocytic astrocytoma. *Genome Res.* **23**, 431–439 (2013).

[CAS](#) [Article](#) [Google Scholar](#)

7. 7.

Zhu, Y. et al. Inactivation of NF1 in CNS causes increased glial progenitor proliferation and optic glioma formation. *Development* **132**, 5577–5588 (2005).

[CAS](#) [Article](#) [Google Scholar](#)

8. 8.

Toonen, J. A., Ma, Y. & Gutmann, D. H. Defining the temporal course of murine neurofibromatosis-1 optic gliomagenesis reveals a therapeutic window to attenuate retinal dysfunction. *Neuro-Oncol.* **19**, 808–819 (2017).

[CAS](#) [Google Scholar](#)

9. 9.

Venkatesh, H. S. et al. Neuronal activity promotes glioma growth through neuroligin-3 secretion. *Cell* **161**, 803–816 (2015).

[CAS](#) [Article](#) [Google Scholar](#)

10. 10.

Arenkiel, B. R. et al. In vivo light-induced activation of neural circuitry in transgenic mice expressing channelrhodopsin-2. *Neuron* **54**, 205–218 (2007).

[CAS](#) [Article](#) [Google Scholar](#)

11. 11.

Johnson, J. et al. Melanopsin-dependent light avoidance in neonatal mice. *Proc. Natl Acad. Sci. USA* **107**, 17374–17378 (2010).

[ADS](#) [CAS](#) [Article](#) [Google Scholar](#)

12. 12.

Tian, N. & Copenhagen, D. R. Visual deprivation alters development of synaptic function in inner retina after eye opening. *Neuron* **32**, 439–449 (2001).

[CAS](#) [Article](#) [Google Scholar](#)

13. 13.

Toonen, J. A., Solga, A. C., Ma, Y. & Gutmann, D. H. Estrogen activation of microglia underlies the sexually dimorphic differences in *Nfl* optic glioma-induced retinal pathology. *J. Exp. Med.* **214**, 17–25 (2017).

[CAS](#) [Article](#) [Google Scholar](#)

14. 14.

Eckel-Mahan, K. & Sassone-Corsi, P. Phenotyping circadian rhythms in mice. *Curr. Protoc. Mouse Biol.* **5**, 271–281 (2015).

[Article](#) [Google Scholar](#)

15. 15.

Kennaway, D. J. Resetting the suprachiasmatic nucleus clock. *Front. Biosci.* **9**, 56–62 (2004).

[CAS](#) [Article](#) [Google Scholar](#)

16. 16.

Venkatesh, H. S. et al. Electrical and synaptic integration of glioma into neural circuits. *Nature* **573**, 539–545 (2019).

[ADS](#) [CAS](#) [Article](#) [Google Scholar](#)

17. 17.

Venkatesh, H. S. et al. Targeting neuronal activity-regulated neuroligin-3 dependency in high-grade glioma. *Nature* **549**, 533–537 (2017).

[ADS](#) [Article](#) [Google Scholar](#)

18. 18.

Chen, Y. H. et al. Mouse low-grade gliomas contain cancer stem cells with unique molecular and functional properties. *Cell Rep.* **10**, 1899–1912 (2015).

[CAS](#) [Article](#) [Google Scholar](#)

19. 19.

Iyer, R. et al. Entrectinib is a potent inhibitor of Trk-driven neuroblastomas in a xenograft mouse model. *Cancer Lett.* **372**, 179–

186 (2016).

[CAS](#) [Article](#) [Google Scholar](#)

20. 20.

Pan, Y. et al. Whole tumor RNA-sequencing and deconvolution reveal a clinically-prognostic PTEN/PI3K-regulated glioma transcriptional signature. *Oncotarget* **8**, 52474–52487 (2017).

[Article](#) [Google Scholar](#)

21. 21.

Lambert, S. R. et al. Differential expression and methylation of brain developmental genes define location-specific subsets of pilocytic astrocytoma. *Acta Neuropathol.* **126**, 291–301 (2013).

[CAS](#) [Article](#) [Google Scholar](#)

22. 22.

Venkataramani, V. et al. Glutamatergic synaptic input to glioma cells drives brain tumour progression. *Nature* **573**, 532–538 (2019).

[ADS](#) [CAS](#) [Article](#) [Google Scholar](#)

23. 23.

Narahashi, T., Moore, J. W. & Scott, W. R. Tetrodotoxin blockage of sodium conductance increase in lobster giant axons. *J. Gen. Physiol.* **47**, 965–974 (1964).

[CAS](#) [Article](#) [Google Scholar](#)

24. 24.

Lee, D. Y., Gianino, S. M. & Gutmann, D. H. Innate neural stem cell heterogeneity determines the patterning of glioma formation in

children. *Cancer Cell* **22**, 131–138 (2012).

[Article](#) [Google Scholar](#)

25. 25.

Daginakatte, G. C. & Gutmann, D. H. Neurofibromatosis-1 (*Nf1*) heterozygous brain microglia elaborate paracrine factors that promote *Nf1*-deficient astrocyte and glioma growth. *Hum. Mol. Genet.* **16**, 1098–1112 (2007).

[CAS](#) [Article](#) [Google Scholar](#)

26. 26.

Wang, Y., Nicol, G. D., Clapp, D. W. & Hingtgen, C. M. Sensory neurons from *Nf1* haploinsufficient mice exhibit increased excitability. *J. Neurophysiol.* **94**, 3670–3676 (2005).

[CAS](#) [Article](#) [Google Scholar](#)

27. 27.

Guo, X., Pan, Y. & Gutmann, D. H. Genetic and genomic alterations differentially dictate low-grade glioma growth through cancer stem cell-specific chemokine recruitment of T cells and microglia. *Neuro-oncol.* **21**, 1250–1262 (2019).

[CAS](#) [Article](#) [Google Scholar](#)

28. 28.

Sharif, S. et al. A molecular analysis of individuals with neurofibromatosis type 1 (NF1) and optic pathway gliomas (OPGs), and an assessment of genotype–phenotype correlations. *J. Med. Genet.* **48**, 256–260 (2011).

[CAS](#) [Article](#) [Google Scholar](#)

29. 29.

Brannan, C. I. et al. Targeted disruption of the neurofibromatosis type-1 gene leads to developmental abnormalities in heart and various neural crest-derived tissues. *Genes Dev.* **8**, 1019–1029 (1994).

[ADS](#) [CAS](#) [Article](#) [Google Scholar](#)

30. 30.

Zhu, Y. et al. Ablation of NF1 function in neurons induces abnormal development of cerebral cortex and reactive gliosis in the brain. *Genes Dev.* **15**, 859–876 (2001).

[CAS](#) [Article](#) [Google Scholar](#)

31. 31.

Bajenaru, M. L. et al. Astrocyte-specific inactivation of the neurofibromatosis 1 gene (*NF1*) is insufficient for astrocytoma formation. *Mol. Cell. Biol.* **22**, 5100–5113 (2002).

[CAS](#) [Article](#) [Google Scholar](#)

32. 32.

Pan, Y. et al. Athymic mice reveal a requirement for T-cell-microglia interactions in establishing a microenvironment supportive of *Nf1* low-grade glioma growth. *Genes Dev.* **32**, 491–496 (2018).

[CAS](#) [Article](#) [Google Scholar](#)

33. 33.

Hegedus, B. et al. Preclinical cancer therapy in a mouse model of neurofibromatosis-1 optic glioma. *Cancer Res.* **68**, 1520–1528 (2008).

[CAS](#) [Article](#) [Google Scholar](#)

34. 34.

Dobin, A. et al. STAR: ultrafast universal RNA-seq aligner. *Bioinformatics* **29**, 15–21 (2013).

[CAS](#) [Article](#) [Google Scholar](#)

35. 35.

Love, M. I., Huber, W. & Anders, S. Moderated estimation of fold change and dispersion for RNA-seq data with DESeq2. *Genome Biol.* **15**, 550 (2014).

[Article](#) [Google Scholar](#)

36. 36.

Subramanian, A. et al. Gene set enrichment analysis: a knowledge-based approach for interpreting genome-wide expression profiles. *Proc. Natl Acad. Sci. USA* **102**, 15545–15550 (2005).

[ADS](#) [CAS](#) [Article](#) [Google Scholar](#)

37. 37.

Mootha, V. K. et al. PGC-1 α -responsive genes involved in oxidative phosphorylation are coordinately downregulated in human diabetes. *Nat. Genet.* **34**, 267–273 (2003).

[CAS](#) [Article](#) [Google Scholar](#)

[Download references](#)

Acknowledgements

This work was supported by grants from the Department of Defense (W81XWH-15-1-0131 to M.M. and D.H.G., and W81XWH-19-1-0260 to Y.P.), National Institute of Neurological Disorders and Stroke

(R01NS092597 to M.M. and R35NS07211 to D.H.G.), NIH Director's Pioneer Award (DP1NS111132 to M.M.), National Cancer Institute (P50CA165962), National Eye Institute (P30EY026877 to J.L.G. and F32EY029137 to K.-C.C.), Brantley's Project supported by Ian's Friends Foundation (to Y.P. and M.M.), Gilbert Family Foundation (to D.H.G. and J.L.G.), Robert J. Kleberg, Jr. and Helen C. Kleberg Foundation (to M.M.), Cancer Research UK (to M.M.), Unravel Pediatric Cancer (to M.M.), McKenna Claire Foundation (to M.M.), Kyle O'Connell Foundation (to M.M.), Virginia and D. K. Ludwig Fund for Cancer Research (to M.M.), Waxman Family Research Fund (to M.M.), Stanford Maternal and Child Health Research Institute (to E.M.G.), Stanford Bio-X Institute (to J.D.H.), Will Irwin Research Fund (to M.M.), Research to Prevent Blindness, Inc. (to J.L.G.) and Alex's Lemonade Stand Foundation (to Y.P.) The authors thank G. Grant and A. Bet for low-grade glioma samples from the Stanford Center for Childhood Brain Tumors Tissue Bank; C. Gardner from The St. Louis Children's Hospital Pediatric Tumor Bank (supported by the St. Louis Children's Hospital Foundation and Children's Surgical Sciences Institute); and Stanford Animal Histology Services for optic nerve paraffin-block sectioning.

Author information

Author notes

1. These authors contributed equally: Michelle Monje & David H. Gutmann

Affiliations

1. Department of Neurology and Neurological Sciences, Stanford University, Stanford, CA, USA

Yuan Pan, Jared D. Hysinger, Tara Barron, Nicki F. Schindler, Belgin Yalçın, Sara B. Mulinyawe, Anitha Ponnuswami, James J. Lennon, Erin M. Gibson, John R. Huguenard & Michelle Monje

2. Department of Neurology, Washington University School of Medicine, St Louis, MO, USA

Olivia Cobb, Xiaofan Guo, Corina Anastasaki, Suzanne Scheaffer, Yu Ma, Joseph A. Toonen & David H. Gutmann

3. Spencer Center for Vision Research, Byers Eye Institute, Stanford University, Stanford, CA, USA

Kun-Che Chang, Xin Xia & Jeffrey L. Goldberg

4. Department of Psychiatry and Behavioral Sciences, Stanford University, Stanford, CA, USA

Erin M. Gibson & Michelle Monje

5. Department of Neurosurgery, University of California Los Angeles, Los Angeles, CA, USA

Linda M. Liau

6. Department of Pediatrics, Stanford University, Stanford, CA, USA

Michelle Monje

7. Department of Neurosurgery, Stanford University, Stanford, CA, USA

Michelle Monje

8. Department of Pathology, Stanford University, Stanford, CA, USA

Michelle Monje

Authors

1. Yuan Pan

[View author publications](#)

You can also search for this author in [PubMed](#) [Google Scholar](#)

2. Jared D. Hysinger

[View author publications](#)

You can also search for this author in [PubMed](#) [Google Scholar](#)

3. Tara Barron

[View author publications](#)

You can also search for this author in [PubMed](#) [Google Scholar](#)

4. Nicki F. Schindler

[View author publications](#)

You can also search for this author in [PubMed](#) [Google Scholar](#)

5. Olivia Cobb

[View author publications](#)

You can also search for this author in [PubMed](#) [Google Scholar](#)

6. Xiaofan Guo

[View author publications](#)

You can also search for this author in [PubMed](#) [Google Scholar](#)

7. Belgin Yalçın

[View author publications](#)

You can also search for this author in [PubMed](#) [Google Scholar](#)

8. Corina Anastasaki

[View author publications](#)

You can also search for this author in [PubMed](#) [Google Scholar](#)

9. Sara B. Mulinyawe

[View author publications](#)

You can also search for this author in [PubMed](#) [Google Scholar](#)

10. Anitha Ponnuswami

[View author publications](#)

You can also search for this author in [PubMed](#) [Google Scholar](#)

11. Suzanne Scheaffer

[View author publications](#)

You can also search for this author in [PubMed](#) [Google Scholar](#)

12. Yu Ma

[View author publications](#)

You can also search for this author in [PubMed](#) [Google Scholar](#)

13. Kun-Che Chang

[View author publications](#)

You can also search for this author in [PubMed](#) [Google Scholar](#)

14. Xin Xia

[View author publications](#)

You can also search for this author in [PubMed](#) [Google Scholar](#)

15. Joseph A. Toonen

[View author publications](#)

You can also search for this author in [PubMed](#) [Google Scholar](#)

16. James J. Lennon

[View author publications](#)

You can also search for this author in [PubMed](#) [Google Scholar](#)

17. Erin M. Gibson

[View author publications](#)

You can also search for this author in [PubMed](#) [Google Scholar](#)

18. John R. Huguenard

[View author publications](#)

You can also search for this author in [PubMed](#) [Google Scholar](#)

19. Linda M. Liau

[View author publications](#)

You can also search for this author in [PubMed](#) [Google Scholar](#)

20. Jeffrey L. Goldberg

[View author publications](#)

You can also search for this author in [PubMed](#) [Google Scholar](#)

21. Michelle Monje

[View author publications](#)

You can also search for this author in [PubMed](#) [Google Scholar](#)

22. David H. Gutmann

[View author publications](#)

You can also search for this author in [PubMed](#) [Google Scholar](#)

Contributions

M.M. and D.H.G. conceived the project. Y.P., J.D.H., T.B., N.F.S., X.G., B.Y., C.A., S.B.M., A.P., S.S., Y.M., K.C.-C., X.X., J.A.T., E.M.G., J.R.H. and J.J.L. conducted experiments. Y.P., M.M. and D.H.G. designed the experiments and wrote the manuscript. Y.P., J.D.H., N.F.S. and Y.M. performed data analyses. O.C. provided statistical expertise and RNA-seq analyses. K.C-C., X.X. and J.L.G. provided vision science expertise and performed PERGs. L.M.L. provided samples of human pilocytic astrocytoma. All authors contributed to manuscript editing. M.M. and D.H.G supervised all aspects of the work.

Corresponding authors

Correspondence to [Michelle Monje](#) or [David H. Gutmann](#).

Ethics declarations

Competing interests

M.M. is an SAB member for Cygnal Therapeutics. M.M. is listed as an inventor on a patent (US10377818B2) coordinated through Stanford University related to targeting neuron–glioma interactions for therapy.

Additional information

Peer review information *Nature* thanks Botond Roska, Rosalind Segal and Frank Winkler for their contribution to the peer review of this work. Peer reviewer reports are available.

Publisher's note Springer Nature remains neutral with regard to jurisdictional claims in published maps and institutional affiliations.

Extended data figures and tables

[Extended Data Fig. 1 Increased activity of the optic nerve drives growth of *Nfl*-OPG.](#)

a, Representative fluorescence microscopy images reveal YFP expression within the optic nerve and retina freshly isolated from *Thy1::ChR2-YFP*, but not wild-type, mice. $n = 3$ mice from each group were examined with similar results. Scale bar, 30 μm . **b**, Immunohistochemistry using green fluorescent protein (GFP)- and yellow fluorescent protein (YFP)-specific antibodies reveals YFP expression (green) specifically in the retinal ganglion cells (BRN3A $^+$) (red) of *Thy1::ChR2-YFP*, but not wild-type, mice. $n = 3$ mice from each group were examined with similar results. Scale bar, 15 μm . Arrow, cells shown in the inset. GCL, ganglion cell layer, IPL, inner plexiform layer, INL, inner nuclear layer, OPL, outer plexiform layer, ONL, outer nuclear layer. **c**, Representative Ki67 immunohistochemistry

images (arrows indicate Ki67⁺ cells) and quantification of unstimulated (unstim) ($n = 6$) and stimulated (stim) ($n = 6$) $Nf1^{OPG}; Thy1::ChR2-YFP$ mice. Scale bar, 20 μm . Unpaired *t*-test with Welch's correction. **d**, Plotting optic nerve volume against proliferation shows separation between unstimulated and stimulated groups. **e**, Immunofluorescence images of S100 β (red), IBA1 (green) and DAPI (blue) reveal increased per cent of S100 β^+ ($P = 0.005$), but not IBA1⁺ ($P = 0.6739$), cells in the stimulated group ($n = 6$ mice), relative to the unstimulated group ($n = 5$ mice). Unpaired *t*-test with Welch's correction. **f**, PERG performed on $Nf1^{OPG}$ mice raised in regular light cycles (12:12) ($n = 6$ eyes) or reared in dark ($n = 6$ eyes) from 6–12 weeks of age. Mann–Whitney test. **g**, Dark-rearing experimental paradigm. $n = 5$ (wild type 12:12), 7 ($Nf1^{OPG}$ 12:12), 6 ($Nf1^{OPG}$ dark 6–16 weeks old) and 12 ($Nf1^{OPG}$ dark 6–12 weeks old). Data are mean \pm s.e.m. NS, not significant ($P > 0.05$). Each data point is one mouse in **c–e**. All tests were two-sided. Illustrations created with BioRender.com (**f, g**).

Extended Data Fig. 2 Retinal activity during a susceptible period is required for initiation of *Nf1*-OPG.

a, Representative Ki67 immunohistochemistry (arrows, Ki67⁺ cells), S100 β immunofluorescence (green) and haematoxylin and eosin (H&E) (arrows indicate abnormal nuclei) images. Scale bar, 20 μm . **b**, Quantification of the per cent of S100 β^+ cells in $Nf1^{OPG}$ mice reared in regular light cycles (12:12) or dark-reared (24-h darkness) from 6 to 16 or 6 to 12 weeks of age. $n = 4$ (wild type 12:12), 5 ($Nf1^{OPG}$ 12:12), 5 ($Nf1^{OPG}$ dark 6–16 weeks old) and 5 ($Nf1^{OPG}$ dark 6–12 weeks old) mice. **c**, Representative immunohistochemistry images (white, BRN3A; blue, DAPI) in the ganglion cell layer, and quantification of per cent BRN3A⁺ cells in wild-type mice reared in regular light cycles (12:12, $n = 5$ mice), or dark (24-h darkness, $n = 6$ mice). $P = 0.9307$. Scale bar, 10 μm . **d**, Dark-rearing experimental paradigm with observation until 24 weeks after return to regular light cycles at 12 weeks. Half-yellow and half-grey lightbulbs and yellow bars indicate 12-h light/12-h dark cycles (12:12). Grey lightbulbs and black bars indicate dark-rearing periods (24-h darkness). Arrow, tumour initiation. **e**, Optic nerve volume (left) and proliferation (per cent Ki67⁺

cells) (right) of Nfl^{OPG} mice reared in regular light cycles (12:12) or dark-reared (24-h darkness) from 6 to 12 weeks of age and observed until 24 weeks. $n = 7$ (wild type 12:12), 6 (Nfl^{OPG} 12:12) and 6 (Nfl^{OPG} dark 6–12 weeks old) mice. **f**, Plotting optic nerve volume against proliferation shows no OPG (tumour) in the dark-reared Nfl^{OPG} mice. Tumour is gated against the maximum volumes and proliferation of 24-week-old wild-type mice. **g**, IBA1 (green) immunofluorescence images and quantification. Scale bars, 20 μm . $n = 4$ mice in each group. **h, i**, Quantification of CD8 $^+$ ($n = 6$ and 4 mice in 12:12 and dark groups, respectively) and PDGFR α^+ cell density ($n = 5$ and 6 mice in 12:12 and dark groups, respectively). Data are mean \pm s.e.m. Mann–Whitney test (**c**). Brown–Forsythe and Welch ANOVA tests with Dunnett’s T3 correction for multiple comparison (**b**, $F = 11.18$, $P = 0.0071$; **e**, volume, $F = 11.19$, $P = 0.0011$). Kruskal–Wallis test with Dunn’s correction for multiple comparisons (**e**, proliferation, $P = 0.0008$). Unpaired *t*-test with Welch’s correction (**g–i**). NS, not significant ($P > 0.05$). Each data point is one mouse in **b**, **e–i**. Each data point is one eye in **c**. All tests were two-sided. Illustrations created with BioRender.com (**d**).

Extended Data Fig. 3 The intrinsic circadian clock associated with constant darkness does not contribute to Nfl -OPG initiation.

a, Entrained dark-rearing paradigm. Half-yellow and half-grey lightbulbs and yellow bars indicate 12-h light/12-h dark cycles (12:12). Grey lightbulbs and dashed black bars indicate entrained dark-rearing periods (24-h darkness with 15 min of light at 07.00 and 19.00). Arrow, tumour initiation. **b**, Optic nerve volume (left) and proliferation (per cent Ki67 $^+$ cells) (right) of $Nfl^{+/-}$ mice (no tumour control, $n = 3$) and Nfl^{OPG} mice reared in regular light cycles (12:12, $n = 5$), or dark-reared (entrained) from 6 to 16 weeks of age ($n = 7$). Kruskal–Wallis test (volume, $P = 0.0014$; proliferation, $P = 0.0005$). **c**, Plotting optic nerve volume against proliferation shows few OPGs (tumours) in entrained dark-reared Nfl^{OPG} mice. Tumour is gated against volume and proliferation of 16-week-old wild-type mice (22 mice raised in regular light cycles; grey regions mark the range of values). **d**, Representative Ki67 immunohistochemistry images

of $Nfl^{+/+}$ mice (no tumour control, $n = 3$) and Nfl^{OPG} mice reared in regular light cycles (12:12, $n = 5$), or dark-reared (entrained) from 6 to 16 weeks of age ($n = 7$). Arrows, $Ki67^+$ cells. Scale bar, 20 μm . NS, not significant ($P > 0.05$). Each data point is one mouse in **b**, **c**. All tests were two-sided. Illustrations created with BioRender.com (**a**).

Extended Data Fig. 4 Targeting BDNF or TrkB signalling does not prevent formation of Nfl -OPGs.

a, Left, generation of retina + optic nerve explants for collecting secreted proteins in the conditioned medium. Right, retina + optic nerve explant preparations from $Nfl^{+/+}; Thy1::ChR2-YFP$ mice were stimulated by blue light (stim) or unstimulated (unstim) (complete darkness + 1 nM TTX), followed by conditioned medium collection and mass spectrometry measurement of BDNF and NLGN3. Fold changes of BDNF and NLGN3 in the conditioned medium between stimulated and unstimulated conditions are indicated. **b**, Representative EdU immunofluorescence images of Fig. 2a, showing increased Nfl optic glioma cell proliferation (EdU incorporation) to increasing concentrations of NLGN3. Scale bar, 25 μm . $n = 4$ (vehicle (veh)), 3 (10 nM), 3 (30 nM) and 3 (70 nM) wells. **c**, Increased Nfl optic glioma cell proliferation (EdU incorporation) to 70 nM NLGN1 ($n = 3$ wells), NLGN2 ($n = 4$ wells), NLGN3 ($n = 7$ wells) and BDNF ($n = 3$ wells), relative to vehicle ($n = 8$ wells for NLGN1, NLGN2 and NLGN3 and 3 wells for BDNF). **d**, Entrectinib (ent) treatment paradigm. Blue bar, time intervals when entrectinib was administered. Arrow, tumour initiation. **e**, Optic nerve volume (left) ($P = 0.8690$) and proliferation (per cent $Ki67^+$ cells) (right) ($P = 0.4536$) of Nfl^{OPG} + vehicle ($n = 3$), and Nfl^{OPG} + entrectinib ($n = 6$) groups. **f**, Plotting optic nerve volume against proliferation shows OPG (tumour) in all Nfl^{OPG} + entrectinib mice. Tumour is gated against volume and proliferation of 16-week-old wild-type mice (22 mice raised in regular light cycles; grey regions mark the range of values). Unpaired *t*-test with Welch's correction (**c**, BDNF; **e**, proliferation). Brown-Forsythe and Welch ANOVA tests with Dunnett's T3 correction for multiple comparison (**c**, NLGN1, NLGN2 and NLGN3, $F = 44.85$, $P < 0.0001$). Mann–Whitney test (**e**, volume). Data are mean \pm s.e.m. NS, not significant ($P > 0.05$). Each data point is one well in

c. Each data point is one mouse in **e**, **f**. All tests were two-sided. Illustrations created with BioRender.com (**a**).

Extended Data Fig. 5 *NLGN3* expression analyses in human pilocytic astrocytomas.

a, qRT–PCR using Washington University School of Medicine (WUSM) samples reveals increased *NLGN3* levels in NF1-associated pilocytic astrocytoma (NF1-PA) ($n = 9$); *NLGN3* levels were not significantly increased in sporadic pilocytic astrocytoma (S-PA) in this dataset ($n = 14$), relative to non-neoplastic brain controls (NB) ($n = 9$); the same non-neoplastic brain cases are shown in each comparison). These results should be considered in the context of the larger dataset presented in **b** and the cases presented in Fig. 2e. **b**, *NLGN3* expression of a previously published microarray dataset (GSE44971)²¹ reveals increased *NLGN3* levels in pilocytic astrocytoma ($n = 49$), relative to non-neoplastic brain controls ($n = 9$). Red dots, NF1-associated pilocytic astrocytomas. **c**, No association between *NLGN3* expression and sex, location or age was observed in the pilocytic astrocytoma RNA-seq dataset. From left to right, $n = 6, 3, 6, 4, 4, 5, 6, 4, 4, 5, 6$ and 4 samples. **d**, *NLGN3* expression of the previously published microarray dataset²¹ reveals increased *NLGN3* levels in all methylation groups, pilocytic astrocytomas located in cerebellum and diencephalon, relative to non-neoplastic brains. From left to right, $n = 9, 12, 28, 9, 9, 35, 5, 6$ and 3 samples. **e**, GO terms and differentially expressed genes in *NLGN3*-high and *NLGN3*-low groups from the pilocytic astrocytoma RNA-seq database. **f**, Gene set enrichment analysis reveals neuronal and immune signatures in *NLGN3*-high and *NLGN3*-low pilocytic astrocytomas, respectively. Mann–Whitney test (**a**, NB versus NF1-PA). Unpaired *t*-test with Welch’s correction (**a**, NB versus S-PA; **b**). Brown–Forsythe and Welch ANOVA tests with Dunnett’s T3 correction for multiple comparison (**c**, all comparisons are not statistically significant; **d**, methylation, $F = 11.71, P = 0.0001$; **d**, location, $F = 23.48, P < 0.0001$). Data are mean \pm s.e.m. Each data point is one human sample in **a–d**. All tests were two-sided.

Extended Data Fig. 6 Optogenetic stimulation of retina + optic nerve explants.

a, Immunoblotting of retina + optic nerve tissues reveals no change in cleaved caspase-3 (CC3) levels (normalized to the amount of total caspase-3 (Cas-3)) between the unstimulated (unstim) and stimulated (stim) groups. $n = 3$ mice. $P = 0.8938$. **b**, Immunoblotting reveals the same levels of shed NLGN3 (s-NLGN3) in the conditioned medium of unstimulated $NfI^{+/+}; Thy1::ChR2$ ($n = 6$ mice) and $NfI^{+-}; Thy1::ChR2$ ($n = 6$ mice) retina + optic nerve explants. **c**, Immunoblotting of optic nerve lysate reveals same levels of shed NLGN3 in dark-reared wild-type ($n = 3$) and NfI^{+-} ($n = 5$) mice. **d**, ADAM10-mediated NLGN3 shedding. **e**, Immunoblotting reveals reduced shed NLGN3 levels in optic nerves of NfI^{+-} mice after treatment with the ADAM10 inhibitor (ADAM10i) (GI254023X) ($n = 4$ mice), relative to vehicle ($n = 3$ mice) treatment. **f**, Immunoblotting of conditioned medium reveals increased ADAM10 in light-stimulated $NfI^{+-}; Thy1::ChR2$ (left) ($n = 7$ mice), but not $NfI^{+/+}; Thy1::ChR2$ (right) ($n = 3$ mice), retina + optic nerve explants relative to their unstimulated (dark + TTX) counterparts. ns, not significant. Data are mean \pm s.e.m. Wilcoxon test (**a, f**). Unpaired *t*-test with Welch's correction (**b, c, e**). Each data point is one mouse in **a–c, e, f**. All tests were two-sided. Illustrations created with BioRender.com (**d**).

Extended Data Fig. 7 Targeting NLGN3 shedding prevents NfI^{OPG} proliferation.

a, Representative Ki67 immunohistochemistry images of wild-type + vehicle ($n = 3$), NfI^{OPG} + vehicle 6–16 weeks old ($n = 7$) and NfI^{OPG} + ADAM10i 6–16 weeks old ($n = 9$) groups. **b**, Representative Ki67 immunohistochemistry images of NfI^{OPG} + vehicle ($n = 9$) and NfI^{OPG} + ADAM10i 12–16 weeks old ($n = 8$) groups. Arrows, Ki67⁺ cells. Scale bar, 20 μ m.

Extended Data Table 1 Human pilocytic astrocytoma samples used in the RNA-seq study

[Full size table](#)

Extended Data Table 2 Human pilocytic astrocytoma samples used in qRT–PCR study

[Full size table](#)

Supplementary information

Supplementary Figure 1

The uncropped western blots.

Reporting Summary

Peer Review File

Source data

Source Data Fig. 1

Source Data Fig. 2

Source Data Fig. 3

Rights and permissions

Reprints and Permissions

About this article



Check for
updates

Cite this article

Pan, Y., Hysinger, J.D., Barron, T. *et al.* *NF1* mutation drives neuronal activity-dependent initiation of optic glioma. *Nature* **594**, 277–282 (2021). <https://doi.org/10.1038/s41586-021-03580-6>

[Download citation](#)

- Received: 22 April 2020
- Accepted: 21 April 2021
- Published: 26 May 2021
- Issue Date: 10 June 2021
- DOI: <https://doi.org/10.1038/s41586-021-03580-6>

Comments

By submitting a comment you agree to abide by our [Terms](#) and [Community Guidelines](#). If you find something abusive or that does not comply with our terms or guidelines please flag it as inappropriate.

[Access through your institution](#)

[Change institution](#)

[Buy or subscribe](#)

Associated Content

[Activation of retinal neurons triggers tumour formation in cancer-prone mice](#)

- Varun Venkataramani
- Frank Winkler

Nature News & Views 26 May 2021

Advertisement

This article was downloaded by **calibre** from <https://www.nature.com/articles/s41586-021-03580-6>

| [Section menu](#) | [Main menu](#) |

- Article
- [Published: 12 May 2021](#)

RNA transcripts stimulate homologous recombination by forming DR-loops

- [Jian Ouyang](#)^{1,na1},
- [Tribhuwan Yadav](#)^{1,na1},
- [Jia-Min Zhang](#)¹,
- [Haibo Yang](#)^{1,2},
- [Esther Rheinbay](#)¹,
- [Hongshan Guo](#)^{1,3},
- [Daniel A. Haber](#) [ORCID: orcid.org/0000-0003-1378-6551](#)^{1,3},
- [Li Lan](#) [ORCID: orcid.org/0000-0003-0383-6172](#)^{1,2} &
- [Lee Zou](#) [ORCID: orcid.org/0000-0003-3094-1058](#)^{1,4}

[Nature](#) volume 594, pages 283–288 (2021) [Cite this article](#)

- 8771 Accesses
- 1 Citations
- 117 Altmetric
- [Metrics details](#)

Subjects

- [DNA](#)
- [DNA metabolism](#)

- [Homologous recombination](#)

Abstract

Homologous recombination (HR) repairs DNA double-strand breaks (DSBs) in the S and G2 phases of the cell cycle^{1,2,3}. Several HR proteins are preferentially recruited to DSBs at transcriptionally active loci^{4,5,6,7,8,9,10}, but how transcription promotes HR is poorly understood. Here we develop an assay to assess the effect of local transcription on HR. Using this assay, we find that transcription stimulates HR to a substantial extent. Tethering RNA transcripts to the vicinity of DSBs recapitulates the effects of local transcription, which suggests that transcription enhances HR through RNA transcripts. Tethered RNA transcripts stimulate HR in a sequence- and orientation-dependent manner, indicating that they function by forming DNA–RNA hybrids. In contrast to most HR proteins, RAD51-associated protein 1 (RAD51AP1) only promotes HR when local transcription is active. RAD51AP1 drives the formation of R-loops in vitro and is required for tethered RNAs to stimulate HR in cells. Notably, RAD51AP1 is necessary for the DSB-induced formation of DNA–RNA hybrids in donor DNA, linking R-loops to D-loops. In vitro, RAD51AP1-generated R-loops enhance the RAD51-mediated formation of D-loops locally and give rise to intermediates that we term ‘DR-loops’, which contain both DNA–DNA and DNA–RNA hybrids and favour RAD51 function. Thus, at DSBs in transcribed regions, RAD51AP1 promotes the invasion of RNA transcripts into donor DNA, and stimulates HR through the formation of DR-loops.

Access options

Subscribe to Journal

Get full journal access for 1 year

\$199.00

only \$3.90 per issue

Subscribe

All prices are NET prices.
VAT will be added later in the checkout.
Tax calculation will be finalised during checkout.

Rent or Buy article

Get time limited or full article access on ReadCube.

from \$8.99

Rent or Buy

All prices are NET prices.

Additional access options:

- [Log in](#)
- [Access through your institution](#)
- [Learn about institutional subscriptions](#)

Fig. 1: HR is stimulated by local transcription.

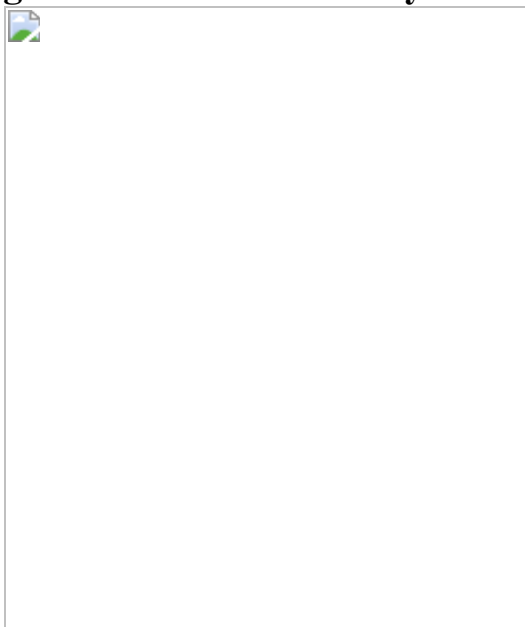


Fig. 2: Tethering of RNA transcripts to DSB recapitulates the effects of local transcription on HR.

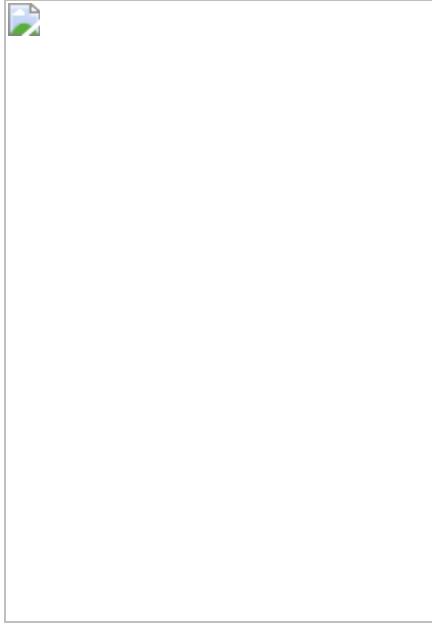


Fig. 3: RAD51AP1 promotes HR in a transcription- and RNA-dependent manner.

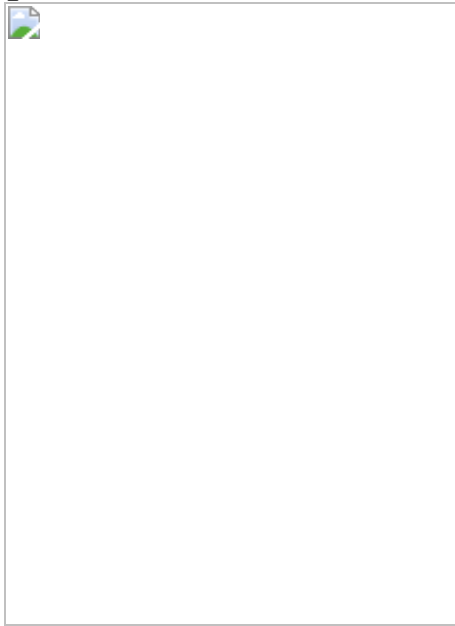
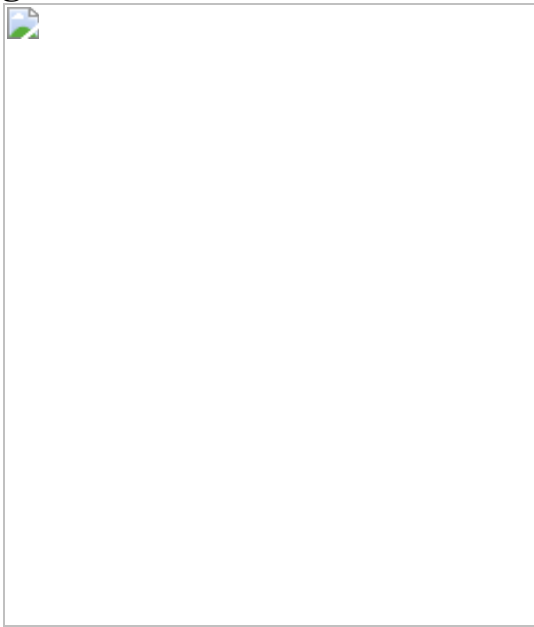


Fig. 4: RAD51AP1 drives R-loop formation in vitro and in cells.



Fig. 5: RAD51AP1 and RAD51 act together to form DR-loops.



Data availability

All relevant data are included in the Article and/or Supplementary Figs. [1](#), [2](#).

References

1. 1.

Prakash, R., Zhang, Y., Feng, W. & Jasin, M. Homologous recombination and human health: the roles of BRCA1, BRCA2, and associated proteins. *Cold Spring Harb. Perspect. Biol.* **7**, a016600 (2015).

[PubMed](#) [PubMed Central](#) [Article](#) [CAS](#) [Google Scholar](#)

2. 2.

Heyer, W. D., Ehmsen, K. T. & Liu, J. Regulation of homologous recombination in eukaryotes. *Annu. Rev. Genet.* **44**, 113–139 (2010).

[CAS](#) [PubMed](#) [PubMed Central](#) [Article](#) [Google Scholar](#)

3. 3.

Daley, J. M., Gaines, W. A., Kwon, Y. & Sung, P. Regulation of DNA pairing in homologous recombination. *Cold Spring Harb. Perspect. Biol.* **6**, a017954 (2014).

[PubMed](#) [PubMed Central](#) [Article](#) [Google Scholar](#)

4. 4.

Marnef, A., Cohen, S. & Legube, G. Transcription-coupled DNA double-strand break repair: active genes need special care. *J. Mol. Biol.* **429**, 1277–1288 (2017).

[CAS](#) [PubMed](#) [Article](#) [Google Scholar](#)

5. 5.

Ouyang, J., Lan, L. & Zou, L. Regulation of DNA break repair by transcription and RNA. *Sci. China Life Sci.* **60**, 1081–1086 (2017).

[CAS](#) [PubMed](#) [PubMed Central](#) [Article](#) [Google Scholar](#)

6. 6.

Tang, J. et al. Acetylation limits 53BP1 association with damaged chromatin to promote homologous recombination. *Nat. Struct. Mol. Biol.* **20**, 317–325 (2013).

[CAS](#) [PubMed](#) [PubMed Central](#) [Article](#) [Google Scholar](#)

7. 7.

Aymard, F. et al. Transcriptionally active chromatin recruits homologous recombination at DNA double-strand breaks. *Nat. Struct. Mol. Biol.* **21**, 366–374 (2014).

[CAS](#) [PubMed](#) [PubMed Central](#) [Article](#) [Google Scholar](#)

8. 8.

Wei, L. et al. DNA damage during the G0/G1 phase triggers RNA-templated, Cockayne syndrome B-dependent homologous recombination. *Proc. Natl Acad. Sci. USA* **112**, E3495–E3504 (2015).

[CAS](#) [PubMed](#) [Article](#) [Google Scholar](#)

9. 9.

Teng, Y. et al. ROS-induced R loops trigger a transcription-coupled but BRCA1/2-independent homologous recombination pathway through CSB. *Nat. Commun.* **9**, 4115 (2018).

[ADS](#) [PubMed](#) [PubMed Central](#) [Article](#) [CAS](#) [Google Scholar](#)

10. 10.

Chen, H. et al. m⁵C modification of mRNA serves a DNA damage code to promote homologous recombination. *Nat. Commun.* **11**, 2834 (2020).

[ADS](#) [CAS](#) [PubMed](#) [PubMed Central](#) [Article](#) [Google Scholar](#)

11. 11.

Pierce, A. J., Johnson, R. D., Thompson, L. H. & Jasin, M. XRCC3 promotes homology-directed repair of DNA damage in mammalian cells. *Genes Dev.* **13**, 2633–2638 (1999).

[CAS](#) [PubMed](#) [PubMed Central](#) [Article](#) [Google Scholar](#)

12. 12.

Zetsche, B. et al. Cpf1 is a single RNA-guided endonuclease of a class 2 CRISPR–Cas system. *Cell* **163**, 759–771 (2015).

[CAS](#) [PubMed](#) [PubMed Central](#) [Article](#) [Google Scholar](#)

13. 13.

Pinder, J., Salsman, J. & Dellaire, G. Nuclear domain ‘knock-in’ screen for the evaluation and identification of small molecule enhancers of CRISPR-based genome editing. *Nucleic Acids Res.* **43**, 9379–9392 (2015).

[CAS](#) [PubMed](#) [PubMed Central](#) [Article](#) [Google Scholar](#)

14. 14.

Chavez, A. et al. Highly efficient Cas9-mediated transcriptional programming. *Nat. Methods* **12**, 326–328 (2015).

[CAS](#) [PubMed](#) [PubMed Central](#) [Article](#) [Google Scholar](#)

15. 15.

Modesti, M. et al. RAD51AP1 is a structure-specific DNA binding protein that stimulates joint molecule formation during RAD51-mediated homologous recombination. *Mol. Cell* **28**, 468–481 (2007).

[CAS](#) [PubMed](#) [Article](#) [Google Scholar](#)

16. 16.

Wiese, C. et al. Promotion of homologous recombination and genomic stability by RAD51AP1 via RAD51 recombinase enhancement. *Mol. Cell* **28**, 482–490 (2007).

[CAS](#) [PubMed](#) [PubMed Central](#) [Article](#) [Google Scholar](#)

17. 17.

Liang, F. et al. Promotion of RAD51-mediated homologous DNA pairing by the RAD51AP1–UAF1 complex. *Cell Rep.* **15**, 2118–2126 (2016).

[CAS](#) [PubMed](#) [PubMed Central](#) [Article](#) [Google Scholar](#)

18. 18.

Kovalenko, O. V., Golub, E. I., Bray-Ward, P., Ward, D. C. & Radding, C. M. A novel nucleic acid-binding protein that interacts with human rad51 recombinase. *Nucleic Acids Res.* **25**, 4946–4953 (1997).

[CAS](#) [PubMed](#) [PubMed Central](#) [Article](#) [Google Scholar](#)

19. 19.

Dunlop, M. H. et al. Mechanistic insights into RAD51-associated protein 1 (RAD51AP1) action in homologous DNA repair. *J. Biol. Chem.* **287**, 12343–12347 (2012).

[CAS](#) [PubMed](#) [PubMed Central](#) [Article](#) [Google Scholar](#)

20. 20.

Taylor, S. C., Laperriere, G. & Germain, H. Droplet digital PCR versus qPCR for gene expression analysis with low abundant targets: from variable nonsense to publication quality data. *Sci. Rep.* **7**, 2409 (2017).

[ADS](#) [PubMed](#) [PubMed Central](#) [Article](#) [CAS](#) [Google Scholar](#)

21. 21.

Francia, S. et al. Site-specific DICER and DROSHA RNA products control the DNA-damage response. *Nature* **488**, 231–235 (2012).

[ADS](#) [CAS](#) [PubMed](#) [PubMed Central](#) [Article](#) [Google Scholar](#)

22. 22.

Wei, W. et al. A role for small RNAs in DNA double-strand break repair. *Cell* **149**, 101–112 (2012).

[CAS](#) [PubMed](#) [Article](#) [Google Scholar](#)

23. 23.

Michelini, F. et al. Damage-induced lncRNAs control the DNA damage response through interaction with dRNAs at individual double-strand breaks. *Nat. Cell Biol.* **19**, 1400–1411 (2017).

[CAS](#) [PubMed](#) [PubMed Central](#) [Article](#) [Google Scholar](#)

24. 24.

Sharma, S. et al. MRE11-RAD50-NBS1 complex is sufficient to promote transcription by RNA polymerase II at double-strand breaks by melting DNA ends. *Cell Rep.* **34**, 108565 (2021).

[CAS](#) [PubMed](#) [PubMed Central](#) [Article](#) [Google Scholar](#)

25. 25.

Petukhova, G., Sung, P. & Klein, H. Promotion of Rad51-dependent D-loop formation by yeast recombination factor Rdh54/Tid1. *Genes Dev.* **14**, 2206–2215 (2000).

[CAS](#) [PubMed](#) [PubMed Central](#) [Article](#) [Google Scholar](#)

26. 26.

Van Komen, S., Petukhova, G., Sigurdsson, S., Stratton, S. & Sung, P. Superhelicity-driven homologous DNA pairing by yeast recombination factors Rad51 and Rad54. *Mol. Cell* **6**, 563–572 (2000).

[PubMed](#) [Article](#) [Google Scholar](#)

27. 27.

Benson, F. E., Stasiak, A. & West, S. C. Purification and characterization of the human Rad51 protein, an analogue of *E. coli* RecA. *EMBO J.* **13**, 5764–5771 (1994).

[CAS](#) [PubMed](#) [PubMed Central](#) [Article](#) [Google Scholar](#)

28. 28.

Keskin, H. et al. Transcript-RNA-templated DNA recombination and repair. *Nature* **515**, 436–439 (2014).

[ADS](#) [CAS](#) [PubMed](#) [PubMed Central](#) [Article](#) [Google Scholar](#)

29. 29.

Mazina, O. M., Keskin, H., Hanamshet, K., Storici, F. & Mazin, A. V. Rad52 inverse strand exchange drives RNA-templated DNA double-strand break repair. *Mol. Cell* **67**, 19–29.e3 (2017).

[CAS](#) [PubMed](#) [PubMed Central](#) [Article](#) [Google Scholar](#)

30. 30.

Meers, C. et al. Genetic characterization of three distinct mechanisms supporting RNA-driven DNA repair and modification reveals major role of DNA polymerase ζ . *Mol. Cell* **79**, 1037–1050 (2020).

[PubMed](#) [Article](#) [CAS](#) [Google Scholar](#)

31. 31.

Yasuhara, T. et al. Human Rad52 promotes XPG-mediated R-loop processing to initiate transcription-associated homologous recombination repair. *Cell* **175**, 558–570 (2018).

[CAS](#) [PubMed](#) [Article](#) [Google Scholar](#)

32. 32.

McDevitt, S., Rusanov, T., Kent, T., Chandramouly, G. & Pomerantz, R. T. How RNA transcripts coordinate DNA recombination and repair. *Nat. Commun.* **9**, 1091 (2018).

[ADS](#) [PubMed](#) [PubMed Central](#) [Article](#) [CAS](#) [Google Scholar](#)

33. 33.

Hatchi, E. et al. BRCA1 and RNAi factors promote repair mediated by small RNAs and PALB2–RAD52. *Nature* **591**, 665–670 (2021).

[ADS](#) [CAS](#) [PubMed](#) [Article](#) [Google Scholar](#)

34. 34.

D'Alessandro, G. et al. BRCA2 controls DNA:RNA hybrid level at DSBs by mediating RNase H2 recruitment. *Nat. Commun.* **9**, 5376 (2018).

[ADS](#) [PubMed](#) [PubMed Central](#) [Article](#) [CAS](#) [Google Scholar](#)

35. 35.

Shanbhag, N. M., Rafalska-Metcalf, I. U., Balane-Bolivar, C., Janicki, S. M. & Greenberg, R. A. ATM-dependent chromatin changes silence transcription in *cis* to DNA double-strand breaks. *Cell* **141**, 970–981 (2010).

[CAS](#) [PubMed](#) [PubMed Central](#) [Article](#) [Google Scholar](#)

36. 36.

Greene, E. C. DNA sequence alignment during homologous recombination. *J. Biol. Chem.* **291**, 11572–11580 (2016).

[CAS](#) [PubMed](#) [PubMed Central](#) [Article](#) [Google Scholar](#)

37. 37.

Baumann, P., Benson, F. E. & West, S. C. Human Rad51 protein promotes ATP-dependent homologous pairing and strand transfer reactions in vitro. *Cell* **87**, 757–766 (1996).

[CAS](#) [PubMed](#) [Article](#) [Google Scholar](#)

38. 38.

Cohen, S. et al. Senataxin resolves RNA:DNA hybrids forming at DNA double-strand breaks to prevent translocations. *Nat. Commun.* **9**, 533 (2018).

[ADS](#) [PubMed](#) [PubMed Central](#) [Article](#) [CAS](#) [Google Scholar](#)

39. 39.

Ohle, C. et al. Transient RNA–DNA hybrids are required for efficient double-strand break repair. *Cell* **167**, 1001–1013 (2016).

[CAS](#) [PubMed](#) [Article](#) [Google Scholar](#)

40. 40.

O'Connor, M. J. Targeting the DNA damage response in cancer. *Mol. Cell* **60**, 547–560 (2015).

[PubMed](#) [Article](#) [CAS](#) [Google Scholar](#)

41. 41.

Ouyang, J. et al. Noncovalent interactions with SUMO and ubiquitin orchestrate distinct functions of the SLX4 complex in genome

maintenance. *Mol. Cell* **57**, 108–122 (2015).

[CAS](#) [PubMed](#) [Article](#) [Google Scholar](#)

42. 42.

Meerbrey, K. L. et al. The pINDUCER lentiviral toolkit for inducible RNA interference in vitro and in vivo. *Proc. Natl Acad. Sci. USA* **108**, 3665–3670 (2011).

[ADS](#) [CAS](#) [PubMed](#) [Article](#) [Google Scholar](#)

43. 43.

Chailleux, C. et al. Quantifying DNA double-strand breaks induced by site-specific endonucleases in living cells by ligation-mediated purification. *Nat. Protocols* **9**, 517–528 (2014).

[CAS](#) [PubMed](#) [Article](#) [Google Scholar](#)

44. 44.

Kleinstiver, B. P. et al. Engineered CRISPR–Cas12a variants with increased activities and improved targeting ranges for gene, epigenetic and base editing. *Nat. Biotechnol.* **37**, 276–282 (2019).

[CAS](#) [PubMed](#) [PubMed Central](#) [Article](#) [Google Scholar](#)

45. 45.

Tumini, E. & Aguilera, A. The sister-chromatid exchange assay in human cells. *Methods Mol. Biol.* **2153**, 383–393 (2021).

[CAS](#) [PubMed](#) [Article](#) [Google Scholar](#)

46. 46.

Moquin, D. M. et al. Localized protein biotinylation at DNA damage sites identifies ZPET, a repressor of homologous recombination. *Genes*

Dev. **33**, 75–89 (2019).

[CAS](#) [PubMed](#) [PubMed Central](#) [Article](#) [Google Scholar](#)

47. 47.

Nguyen, H. D. et al. Functions of replication protein A as a sensor of R loops and a regulator of RNaseH1. *Mol. Cell* **65**, 832–847.e4 (2017).

[CAS](#) [PubMed](#) [PubMed Central](#) [Article](#) [Google Scholar](#)

[Download references](#)

Acknowledgements

We thank P. Sung, G. Legube, J. K. Joung, J. Jin and G. Gill for reagents, and N. Dyson, A. Elia and members of the L.Z. and N. Dyson laboratories for discussions. L.Z. is the James & Patricia Poitras Endowed Chair in Cancer Research. This work is supported by grants from the NIH (CA197779 and CA218856) to L.Z.

Author information

Author notes

1. These authors contributed equally: Jian Ouyang, Tribhuwan Yadav

Affiliations

1. Massachusetts General Hospital Cancer Center, Harvard Medical School, Charlestown, MA, USA

Jian Ouyang, Tribhuwan Yadav, Jia-Min Zhang, Haibo Yang, Esther Rheinbay, Hongshan Guo, Daniel A. Haber, Li Lan & Lee Zou

2. Department of Radiation Oncology, Massachusetts General Hospital, Harvard Medical School, Charlestown, MA, USA

Haibo Yang & Li Lan

3. Howard Hughes Medical Institute, Massachusetts General Hospital, Charlestown, MA, USA

Hongshan Guo & Daniel A. Haber

4. Department of Pathology, Massachusetts General Hospital, Harvard Medical School, Boston, MA, USA

Lee Zou

Authors

1. Jian Ouyang

[View author publications](#)

You can also search for this author in [PubMed](#) [Google Scholar](#)

2. Tribhuwan Yadav

[View author publications](#)

You can also search for this author in [PubMed](#) [Google Scholar](#)

3. Jia-Min Zhang

[View author publications](#)

You can also search for this author in [PubMed](#) [Google Scholar](#)

4. Haibo Yang

[View author publications](#)

You can also search for this author in [PubMed](#) [Google Scholar](#)

5. Esther Rheinbay

[View author publications](#)

You can also search for this author in [PubMed](#) [Google Scholar](#)

6. Hongshan Guo

[View author publications](#)

You can also search for this author in [PubMed](#) [Google Scholar](#)

7. Daniel A. Haber

[View author publications](#)

You can also search for this author in [PubMed](#) [Google Scholar](#)

8. Li Lan

[View author publications](#)

You can also search for this author in [PubMed](#) [Google Scholar](#)

9. Lee Zou

[View author publications](#)

You can also search for this author in [PubMed](#) [Google Scholar](#)

Contributions

J.O., T.Y. and L.Z. designed the study. J.O. and T.Y. performed the experiments and data analyses. L.Z. supervised the experiments and data analyses. J.-M.Z., H.Y. and H.G. provided technical support. E.R. analysed gene expression data. D.A.H. and L.L. helped to supervise the study. J.O., T.Y. and L.Z. prepared the manuscript with contributions from all authors.

Corresponding authors

Correspondence to [Jian Ouyang](#) or [Lee Zou](#).

Ethics declarations

Competing interests

The authors declare no competing interests.

Additional information

Peer review information *Nature* thanks the anonymous reviewer(s) for their contribution to the peer review of this work.

Publisher's note Springer Nature remains neutral with regard to jurisdictional claims in published maps and institutional affiliations.

Extended data figures and tables

Extended Data Fig. 1 Characterizations of Tet-DR-GFP and ASCL1-mClover HR reporters.

a, Flow cytometry analysis of a U2OS-derivative cell line in which the Tet-DR-GFP reporter is stably integrated. Cells were mock transfected, transfected with a control plasmid expressing mCherry or transfected with a plasmid expressing I-SceI-T2A-mCherry. GFP⁺ cells were only detected when I-SceI-T2A-mCherry was expressed and transcription of *sceGFP* was induced by Dox. **b**, Detection of repaired *eGFP* by qPCR. Cells carrying the Tet-DR-GFP reporter were mock transfected or transfected with a plasmid expressing I-Sce-T2A-mCherry (-/+ DSBs) in the absence and presence of Dox (-/+Dox). Genomic DNA was analysed for the repaired *eGFP* sequence by qPCR. **c**, FACS- and qPCR-based HR assays detect changes of HR efficiency similarly. Cells were transfected with siRNAs to knock down the indicated HR proteins and analysed by FACS- and qPCR-based HR assays. **d, e**, The transcription status of *sceGFP* does not affect I-SceI induced DSB formation. The I-SceI-induced DNA ends in *sceGFP* were ligated to a sequence-specific adaptor and quantified by qPCR. **d**, Amplification plot of qPCR. **e**, Linear quantification of DSBs by qPCR. The indicated amounts of genomic DNA containing I-SceI-generated DSBs were mixed with uncut genomic DNA, so that a total of 1 µg genomic DNA was analysed in each qPCR sample. **f**, Two additional stable U2OS clones carrying the Tet-DR-GFP reporter were used to analyse the ratio of HR levels in transcriptionally off and on states (-Dox/+Dox). Data are mean ($n = 2$ independent experiments). **g**, Total RNA isolated from HEK293T cells was reversely transcribed using random primers. cDNA was subjected

to qPCR analysis to determine the relative expression levels of CRISPR-dCas9-VPR-activated *ASCL1* and a panel of endogenous genes using the *GAPDH* transcript as a reference. Data of *ASCL1* are mean ($n = 4$ independent experiments).

Extended Data Fig. 2 Effects of tethered RNA on HR.

a, The indicated fusion RNAs were tethered to a unique sequence 5' to the I-SceI site in *sceGFP*. HR efficiency in cells expressing various fusion RNAs was analysed by qPCR in the transcriptionally on and off states. For each RNA, the HR level in the transcriptionally on state is defined as 1. The ratios of HR levels between the transcriptionally off and on states (−Dox/+Dox) were determined. Data are mean ± s.e.m. ($n = 3$ independent experiments). **b**, Two fusion RNAs containing 120-nt or 81-nt *GFP* sequence were tethered to a unique sequence 5' to the I-SceI site in *sceGFP*. Relative HR efficiencies in cells expressing either of the two fusion RNAs or no fusion RNA were measured by qPCR in the transcriptionally off state (−Dox). The HR efficiency of cells expressing no fusion RNA in the transcriptionally on state (+Dox) serves as a reference. Data are mean ± s.e.m. ($n = 3$ independent experiments). **c**, Schematic to explain why only sense *GFP* RNA and not anti-sense *GFP* RNA can hybridize DNA when tethered 5' to the I-SceI site. It also explains why anti-sense *GFP* RNA can hybridize DNA when tethered 3' to the I-SceI site.

Extended Data Fig. 3 Effects of depletion of RAD51AP1, UAF1 and RAD52 on HR.

a, Cells were transfected with control or two independent *RAD51AP1* siRNAs. Levels of endogenous *RAD51AP1* and β-actin (loading control) were analysed by western blot. A representative western blot of three similar experiments is shown. **b**, HR efficiency was measured by FACS using U2OS-Tet-DR-GFP reporter cells after knockdown of *RAD51AP1*. Data are mean ± s.e.m ($n = 3$ independent experiments). **c**, Cells were transfected with control or *UAF1* siRNA. Levels of *UAF1* mRNA were analysed by RT–qPCR. Data are mean ($n = 2$ independent experiments). **d**, Cells were transfected with control, *RAD51AP1* or *UAF1* siRNA. Levels of endogenous *RAD51AP1* and β-actin (loading control) were analysed by

western blot. A representative western blot of three similar experiments is shown. **e**, HR efficiency was measured by FACS using U2OS-Tet-DR-GFP reporter cells after knockdown of RAD51AP1 or UAF1. Data are mean ($n = 2$ independent experiments). **f**, Cells were transfected with control or two independent *RAD52* siRNAs. Levels of endogenous RAD52 and KU80 (loading control) were analysed by western blot. A representative western blot of three similar experiments is shown. **g**, HR efficiency was measured by FACS using U2OS-Tet-DR-GFP reporter cells after knockdown of RAD52. Data are mean \pm s.e.m ($n = 3$ independent experiments). **h**, HR efficiency was measured by qPCR in transcriptionally on and off states (+/–Dox) after knockdown of RAD52. The HR efficiency of control siRNA transfected cells in the transcriptionally on state (+Dox) serves as a reference. Data are mean \pm s.e.m ($n = 3$ independent experiments).

Extended Data Fig. 4 Functions and localization of RAD51AP1 in the DSB response.

a, Representative mitotic spreads showing SCEs. Samples were prepared from U2OS cells transfected with control or *RAD51AP1* siRNA, and treated with 3 nM CPT or vehicle for 24 h. Scale bars, 10 μ m. **b**, **c**, Survival analyses of cells treated with etoposide (**b**) or CPT (**c**). Data are mean ($n = 2$ independent experiments). **d**, **e**, ChIP–qPCR analysis of RAD51AP1 (**d**) or RAD51 (**e**) at sites of AsiSI-induced DSBs in transcriptionally active and inactive regions. AsiSI-ER was activated by 4-OHT. **f**, RAD51AP1 ChIP signals at several transcriptionally active and inactive AsiSI sites were normalized to XRCC4 ChIP signals. XRCC4, which binds to DSBs independently of transcription, serves as a reference for RAD51AP1. RAD51AP1 knockdown substantially reduced RAD51AP1 ChIP signals, confirming the specificity of RAD51AP1 ChIP. Data in **a–c** are mean ($n = 2$ independent experiments).

Extended Data Fig. 5 Regulation of RAD51AP1 localization to DSBs.

a, U2OS cells carrying an array of tetracycline responsive elements (TREs) were transfected with a plasmid expressing the TetR-VP16-KillerRed (TA-

KR) fusion protein. The TA-KR fusion protein binds the TRE array and induces DSBs upon light activation. The formation of RAD51AP1 or RAD51 foci at the TA-KR-marked locus was analysed by immunostaining. Scale bars, 10 µm. **b**, Immunostaining of RAD51AP1 in cells that were not irradiated or were irradiated with 2 Gy IR. Cells were analysed 2 h after IR. Scale bars, 10 µm. **c**, Correlation between the numbers of RAD51AP1 and RPA32 foci in IR-treated cells as determined by linear regression. The numbers of RAD51AP1 and RPA32 foci were quantified in individual cells ($n = 260$ cells analysed in one experiment). Individual cells were plotted according to the numbers of RAD51AP1 and RPA32 foci in them. **d–g**, Asynchronously growing U2OS cells were treated with or without DRB for 4 h, exposed to 2 Gy IR or mock-treated, and analysed in 2 h. **d**, Immunostaining of RAD51AP1 and γH2AX. Scale bars, 10 µm. **e**, Numbers of RAD51AP1 foci in individual cells were plotted as mean ± s.d. ($n = 401$ cells for no IR, $n = 408$ cells for +IR, and $n = 408$ cells for +IR +DRB, analysed in one experiment). **f**, Numbers of γH2AX foci in individual cells were plotted as mean ± s.d. ($n = 313$ cells for –DRB and $n = 294$ cells for +DRB, analysed in one experiment). **g**, Numbers of RAD51AP1 foci in PCNA⁺ cells were plotted as mean ± s.d. ($n = 360$ cells for –DRB and $n = 303$ cells for +DRB, analysed in one experiment). **h, i**, U2OS cells transfected with control, *UAF1* (**h**) or *CtIP* (**i**) siRNA were irradiated with 2 Gy IR. Immunostaining of RAD51AP1 was done 2 h after IR. Numbers of RAD51AP1 foci in individual cells were plotted as mean ± s.d. *** $P < 0.001$ (two-sided Student's *t* test; $P < 0.0001$ in **h, i**. **h**, $n = 483$ cells for siCTRL, $n = 527$ cells for si*UAF1* analysed in one experiment. **i**, $n = 200$ cells for siCTRL, $n = 182$ cells for si*CtIP* analysed in one experiment.

Extended Data Fig. 6 Characterizations of the ssDNA-, ssRNA- and dsDNA-binding activities of RAD51AP1.

a, Purified GST, GST-RAD51AP1^{WT} and GST-RAD51AP1^{DBM} were analysed by SDS–PAGE stained with Coomassie blue. Representative gel images from 3 similar experiments are shown. **b**, Increasing concentrations of RAD51AP1^{WT} or RAD51AP1^{DBM} (0, 12.5, 25, 50 and 100 nM) were incubated with labelled 63-nt ssDNA. Formation of the RAD51AP1–ssDNA complex was analysed by EMSA. The efficiency of complex

formation was determined by quantifying the reduction in free ssDNA. Representative results from three similar experiments are shown. **c**, Increasing concentrations of RAD51AP1^{WT} or RAD51AP1^{DBM} (0, 50, 100, 200 and 400 nM) were incubated with labelled 55-bp dsDNA. Formation of the RAD51AP1–dsDNA complex was analysed by EMSA. The efficiency of complex formation was determined by quantifying the reduction in free dsDNA. Data are mean ($n = 2$ independent experiments). **d**, Increasing concentrations of RAD51AP1^{WT} (0, 6.25, 12.5, 25 and 50 nM) were incubated with labelled 63-nt ssRNA and 80-nt ssDNA. Formation of the complex was analysed by EMSA. The efficiency of complex formation was determined by quantifying the reduction in free ssDNA or ssRNA. Representative results from three similar experiments are shown. **e**, In Fig. [4a](#), the efficiency of RAD51AP1–ssRNA complex formation was determined by quantifying the reduction in free ssRNA. Data are mean \pm s.d. ($n = 3$ independent experiments).

Extended Data Fig. 7 Characterizations of the RNA-binding and R-loop-formation activities of RAD51AP1.

a, In Fig. [4b](#), the efficiency of RAD51AP1–hybrid complex formation was determined by quantifying the reduction in free DNA–RNA hybrid. Data are mean \pm s.d. ($n = 3$ independent experiments). **b**, Increasing concentrations of RAD51AP1^{WT} or RAD51AP1^{DBM} (0, 50, 100, 200 and 400 nM) were incubated with labelled 25-bp dsRNA. Formation of the RAD51AP1–dsRNA complex was analysed by EMSA. The efficiency of complex formation was determined by quantifying the reduction in free dsRNA. Data are presented as mean ($n = 2$ independent experiments). **c**, Increasing concentrations of RAD51AP1^{WT} (0, 50, 100, 200 and 400 nM) were incubated with labelled 25-nt ssRNA. Formation of the RAD51AP1–ssRNA complex was analysed by EMSA. The efficiency of complex formation was determined by quantifying the reduction in free ssRNA. Data are mean ($n = 2$ independent experiments). **d**, In Fig. [4c](#), the efficiency of R-loop formation was determined by quantifying the shifted and unshifted bands in light exposures of the gel. Data are mean ($n = 2$ independent experiments). **e**, In Fig. [4d](#), the efficiency of R-loop formation was determined as in **d**. Data are mean ($n = 2$ independent experiments). **f**, In

vitro R-loop formation with RAD51AP1 (0.4 μ M) and labelled scrambled ssRNA or ssRNA (50 nM) with homology to dsDNA. Formation of R-loops was analysed by native gel electrophoresis. Representative results from three similar experiments are shown. **g**, R-loop formation with increasing concentration of RAD51AP1 (0.1, 0.2 μ M), labelled ssRNA (50 nM) and a dsDNA plasmid containing a sequence homologous to the ssRNA in buffer D without ATP. Formation of R-loops was analysed by native gel electrophoresis. Representative results from three similar experiments are shown. **h**, In vitro strand exchange between ssRNA and dsDNA. Increasing concentrations of RAD51AP1 (0.25, 0.5, 1, 2 μ M) were first incubated with ssRNA (63 nt, 200 nM) and then with fluorescent labelled linear dsDNA (30 nM). Strand-exchanged products were separated by 10% native polyacrylamide-TBE gel and imaged. Data are mean ($n = 2$ independent experiments).

Extended Data Fig. 8 Comparing RAD51AP1, RAD51 and RAD52 in R-loop formation.

a, In vitro D-loop formation with RAD51AP1 and RAD51. RAD51 was incubated with labelled 90-nt ssDNA for 5 min and then with RAD51AP1 for another 5 min. A dsDNA plasmid containing a sequence homologous to the ssDNA was then added to the reactions. Formation of D-loops was analysed by native gel electrophoresis. The efficiency of D-loop formation was determined by quantifying the shifted and unshifted bands in a light exposure of the gel. Representative results from three similar experiments are shown. **b**, In vitro R-loop formation with RAD51AP1 and RAD51. RAD51 was incubated with labelled 63-nt ssRNA and then with RAD51AP1 for another 5 min. A dsDNA plasmid containing a sequence homologous to the ssRNA was then added to the reactions. The concentrations of RAD51 and RAD51AP1 are indicated. Formation of R-loops was analysed by native gel electrophoresis. Representative results from three similar experiments are shown. **c**, In vitro R-loop formation with RAD51AP1 and RAD51 was analysed as in **b**. The concentrations of RAD51 and RAD51AP1 are indicated. Representative results from three similar experiments are shown. **d**, RAD51AP1 was incubated with labelled 63-nt ssRNA for 5 min and then with increasing concentrations of RAD51 for another 5 min. A dsDNA plasmid containing a sequence homologous to

the ssRNA was then added to the reactions. Formation of R-loops were analysed by native gel electrophoresis. Representative results from two similar experiments are shown. **e**, In vitro R-loop formation activities of RAD51AP1 and RAD52. Increasing concentrations of RAD51AP1 (0.1, 0.2 and 0.4 μ M) or RAD52 (0.1, 0.2 and 0.4 μ M) were incubated with labelled 63-nt ssRNA and then with a dsDNA plasmid containing a sequence homologous to the ssRNA. Formation of R-loops were analysed by native gel electrophoresis. The efficiency of R-loop formation was determined by quantifying the shifted and unshifted bands in a light exposure of the gel. Data are mean ($n = 2$ independent experiments).

Extended Data Fig. 9 UAF1 stimulates RAD51AP1-mediated R-loop formation in vitro.

a, In vitro D-loop formation with RAD51 or the RAD51AP1–UAF1 complex. RAD51 was incubated with labelled 60-nt ssDNA and then with RAD51AP1 or the RAD51AP1–UAF1 complex. A dsDNA plasmid containing a sequence homologous to the ssDNA was then added to the reactions. Formation of D-loops was analysed by native gel electrophoresis. Representative results from 2 similar experiments are shown. **b**, In vitro R-loop formation with the RAD51AP1–UAF1 complex. Preformed RAD51AP1–UAF1 complexes were incubated with labelled 63-nt ssRNA and then with a dsDNA plasmid containing a sequence homologous to the ssRNA. Formation of R-loops was analysed by native gel electrophoresis. The efficiency of R-loop formation was determined by quantifying the shifted and unshifted bands in a light exposure of the gel. Data are mean \pm s.d. ($n = 3$ independent experiments).

Extended Data Fig. 10 Characterizations of RNA transcripts and DNA–RNA hybrids at *sceGFP* and *iGFP* loci.

a, Total RNA isolated from U2OS-Tet-DR-GFP cells treated or untreated with Dox were digested with dsDNase and reverse-transcribed using random primers. cDNA was subjected to qPCR analysis to determine the relative levels of *sceGFP* and *iGFP* transcripts using the *GAPDH* transcript as a reference. The *sceGFP* transcript was increased by more than 60-fold

by Dox. In the absence of Dox, the *sceGFP* transcript was more than 300-fold more abundant than the *iGFP* transcript. In the presence of Dox, the *sceGFP* transcript was more than 2,500-fold more abundant than the *iGFP* transcript. These results suggest that only *sceGFP*, and not *iGFP*, is transcribed in the presence of Dox. **b**, The accumulation of DNA–RNA hybrids in *sceGFP* and *iGFP* was analysed by DRIP–ddPCR as in Fig. 4f. In the +RNH (RNaseH) samples, extracted total nucleic acids were treated with RNaseH before being subjected to DRIP analysis. Data are mean ($n = 2$ independent experiments). **c**, The levels of DNA–RNA hybrids were tested by DRIP–ddPCR using primers that specifically detect an internal region between *sceGFP* and *iGFP* (orange arrowheads). These specific primers do not detect any *sceGFP* or *iGFP* containing DNA fragments after the restriction digestion during DRIP–ddPCR. The levels of DNA–RNA hybrids were measured in transcriptionally on and off states (+/− Dox) after DSB induction (+I-SceI). Data are mean ($n = 2$ independent experiments).

Extended Data Fig. 11 RAD51AP1 promotes the formation of DR-loops in donor DNA.

a, Experimental design for in vitro DR-loop formation using biotinylated ssRNA and fluorescently labelled ssDNA. **b**, In vitro DR-loop formation with biotinylated ssRNA (63 nt, 30 nM), RAD51AP1 (1 μ M), RAD51 (0.25 μ M), fluorescently labelled ssDNA (60 nt, 20 nM) and a dsDNA plasmid. The presence or absence of the indicated reaction components is shown above the dot blot. The levels of ssDNA captured by biotinylated ssRNA via DR-loops were measured by dot blot and quantified over blot background. Data are mean ($n = 2$ –3 independent experiments). **c**, In vitro DR-loop formation with biotinylated ssRNA (50 nt, 30 nM), RAD51AP1^{WT} (0.5 μ M) or RAD51AP1^{DBM} (0.5 μ M), RAD51 (0.25 μ M), fluorescently labelled ssDNA (50 nt, 20 nM) and a dsDNA plasmid. The presence or absence of the indicated reaction components is shown above the dot blot. The levels of ssDNA captured by biotinylated ssRNA via DR-loops were measured by dot blot and quantified over blot background. Representative results from two similar experiments are shown. **d**, In vitro DR-loop confirmation with RNaseH treatment. Data are mean ($n = 2$ –3 independent experiments). **e**, In vitro DR-loop formation with different ssRNA and ssDNA oligos and dsDNA plasmids. Top, schematic of the ssRNA and

ssDNA oligos tested. Red, biotinylated ssRNA; purple, fluorescently labelled ssDNA. The lengths and relative annealing positions of the oligos are indicated. pBSK+ and pMLM-mini are two different dsDNA plasmids that were used in the reactions. Both of them contain sequences homologous to the ssRNA and ssDNA oligos. **f**, Schematic of the three ssDNA oligos (red) and the ssRNA oligo (green) used in Fig. 5c, d. **g**, In vitro D-loop formation with RAD51 and ssDNA oligos A–C. RAD51 (0.25 μM) was incubated with labelled 60-nt ssDNA oligos A, B or C (30 nM) and then with a dsDNA plasmid containing sequences homologous to oligos A and B but not C. Formation of D-loops was analysed by native gel electrophoresis. The efficiency of D-loop formation was determined by quantifying the shifted and unshifted bands in a light exposure of the gel. Data are mean ± s.d. ($n = 3$ independent experiments).

Extended Data Fig. 12 Model of the role of DR-loops in HR.

The formation of DSBs in transcribed regions triggers the recruitment of both RAD51 and RAD51AP1. RAD51AP1 may associate with RNA transcripts through direct RNA binding. In S and G2 cells, RAD51AP1 promotes the invasion of RNA transcripts into donor DNA on sister chromatids. The presence of R-loops and RAD51AP1 in donor DNA may facilitate the invasion of RAD51 filaments, stabilize invaded ssDNA, help RAD51 find homologous sequences and promote the extension of ssDNA ends in DR-loops. It is also possible that RNA transcripts anneal with the displaced ssDNA in D-loops, helping to stabilize invaded ssDNA and extend ssDNA ends in DR-loops. The DNA–RNA hybrids in DR-loops are probably removed in a later step to allow the completion of HR.

Supplementary information

Supplementary Figures

This file contains Supplementary Figs 1-2 - the uncropped blots and FACS gating strategy.

Reporting Summary

Rights and permissions

[Reprints and Permissions](#)

About this article



Check for
updates

Cite this article

Ouyang, J., Yadav, T., Zhang, JM. *et al.* RNA transcripts stimulate homologous recombination by forming DR-loops. *Nature* **594**, 283–288 (2021). <https://doi.org/10.1038/s41586-021-03538-8>

[Download citation](#)

- Received: 01 October 2020
- Accepted: 12 April 2021
- Published: 12 May 2021
- Issue Date: 10 June 2021
- DOI: <https://doi.org/10.1038/s41586-021-03538-8>

Further reading

- [**Repair of DNA Double-Strand Breaks in RNAPI- and RNAPII-Transcribed loci**](#)
 - E. Lesage
 - , T. Clouaire

◦ & G. Legube

DNA Repair (2021)

Comments

By submitting a comment you agree to abide by our [Terms](#) and [Community Guidelines](#). If you find something abusive or that does not comply with our terms or guidelines please flag it as inappropriate.

[Access through your institution](#)

[Change institution](#)

[Buy or subscribe](#)

Advertisement

This article was downloaded by **calibre** from <https://www.nature.com/articles/s41586-021-03538-8>

| [Section menu](#) | [Main menu](#) |

- Matters Arising
- [Published: 09 June 2021](#)

Perovskite decomposition and missing crystal planes in HRTEM

- [Yu-Hao Deng](#) ORCID: [orcid.org/0000-0002-8828-3820¹](https://orcid.org/0000-0002-8828-3820)

[Nature](#) volume 594, pages E6–E7 (2021) [Cite this article](#)

- 1276 Accesses
- 5 Altmetric
- [Metrics details](#)

Subjects

- [Quantum dots](#)
- [Structural properties](#)
- [Transmission electron microscopy](#)

[Matters Arising](#) to this article was published on 09 June 2021

The [Original Article](#) was published on 15 July 2015

arising from Ning, Z. et al. *Nature* <https://www.nature.com/articles/nature14563> (2015).

Access options

[Subscribe to Journal](#)

Get full journal access for 1 year

\$199.00

only \$3.90 per issue

[Subscribe](#)

All prices are NET prices.

VAT will be added later in the checkout.

Tax calculation will be finalised during checkout.

Rent or Buy article

Get time limited or full article access on ReadCube.

from \$8.99

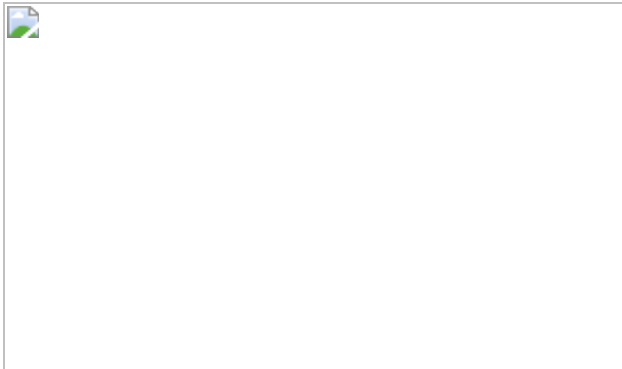
[Rent or Buy](#)

All prices are NET prices.

Additional access options:

- [Log in](#)
- [Access through your institution](#)
- [Learn about institutional subscriptions](#)

Fig. 1: Ball and stick models, simulated electron diffraction patterns of MAPbI₃, PbS and PbI₂.



Data availability

All data are available from the corresponding author upon reasonable request.

References

1. 1.

Ning, Z. et al. Quantum-dot-in-perovskite solids. *Nature* **523**, 324–328 (2015).

[ADS](#) [CAS](#) [Article](#) [Google Scholar](#)

2. 2.

Zhu, Y. et al. Direct atomic scale characterization of the surface structure and planar defects in the organic-inorganic hybrid $\text{CH}_3\text{NH}_3\text{PbI}_3$ by cryo-TEM. *Nano Energy* **73**, 104820 (2020).

[CAS](#) [Article](#) [Google Scholar](#)

3. 3.

Pham, H. T. et al. Insights into twinning formation in cubic and tetragonal multi-cation mixed-halide perovskite. *ACS. Mater. Lett.* **2**, 415–424 (2020).

[CAS](#) [Article](#) [Google Scholar](#)

4. 4.

Rothmann, M. U. et al. Direct observation of intrinsic twin domains in tetragonal $\text{CH}_3\text{NH}_3\text{PbI}_3$. *Nat. Commun.* **8**, 14547 (2017).

[ADS](#) [CAS](#) [Article](#) [Google Scholar](#)

5. 5.

Ding, J. et al. A self-powered photodetector based on a $\text{CH}_3\text{NH}_3\text{PbI}_3$ single crystal with asymmetric electrodes. *Cryst. Eng. Comm.* **18**, 4405–4411 (2016).

[CAS](#) [Article](#) [Google Scholar](#)

6. 6.

Dong, Q. et al. Electron-hole diffusion lengths $>175 \mu\text{m}$ in solution-grown $\text{CH}_3\text{NH}_3\text{PbI}_3$ single crystals. *Science* **347**, 967–970 (2015).

[ADS](#) [CAS](#) [Article](#) [Google Scholar](#)

7. 7.

Zhang, X. W. et al. Directly imaging the structure–property correlation of perovskites in crystalline microwires. *J. Mater. Chem. A* **7**, 13305–13314 (2019).

[CAS](#) [Article](#) [Google Scholar](#)

8. 8.

Hammond, C. *The Basics of Crystallography and Diffraction* (Oxford Univ. Press, 2001).

9. 9.

Fu, X. et al. Quantum confinement effects on charge-transfer between PbS quantum dots and 4-mercaptopuridine. *J. Chem. Phys.* **134**, 024707 (2011).

[ADS](#) [Article](#) [Google Scholar](#)

10. 10.

Chen, S. et al. Atomic scale insights into structure instability and decomposition pathway of methylammonium lead iodide perovskite. *Nat. Commun.* **9**, 4807 (2018).

[ADS](#) [Article](#) [Google Scholar](#)

11. 11.

Rothmann, M. U. et al. Microstructural characterisations of perovskite solar cells—from grains to interfaces: techniques, features, and challenges. *Adv. Energy Mater.* **7**, 1700912 (2017).

[Article](#) [Google Scholar](#)

12. 12.

Deng, Y. H. & Nest, L. G. Analysis of misidentifications in TEM characterization of organic–inorganic hybrid perovskite material. *J. Microsc.* <https://doi.org/10.1111/jmi.13000> (2021).

13. 13.

Li, Y. et al. Unravelling degradation mechanisms and atomic structure of organic–inorganic halide perovskites by cryo-EM. *Joule* **3**, 2854–2866 (2019).

[CAS](#) [Article](#) [Google Scholar](#)

14. 14.

Zhang, D. et al. Atomic-resolution transmission electron microscopy of electron beam–sensitive crystalline materials. *Science* **359**, 675–679 (2018).

[ADS](#) [CAS](#) [Article](#) [Google Scholar](#)

15. 15.

Rothmann, M. U. et al. Atomic-scale microstructure of metal halide perovskite. *Science* **370**, eabb5940 (2020).

[CAS](#) [Article](#) [Google Scholar](#)

[Download references](#)

Acknowledgements

I thank the original authors for discussions and anonymous reviewers for suggestions. I also appreciate encouragement from Y. Xiong. This friendly Matters Arising only aims to perfect the original paper and benefit the development of the academic community.

Author information

Affiliations

1. Department of Chemistry, Ghent University, Ghent, Belgium

Yu-Hao Deng

Authors

1. Yu-Hao Deng

[View author publications](#)

You can also search for this author in [PubMed](#) [Google Scholar](#)

Contributions

All findings, simulations, data analysis and writing in this paper were undertaken by Y.-H.D.

Corresponding author

Correspondence to [Yu-Hao Deng](#).

Ethics declarations

Competing interests

The authors declare no competing interests.

Additional information

Publisher's note Springer Nature remains neutral with regard to jurisdictional claims in published maps and institutional affiliations.

Rights and permissions

[Reprints and Permissions](#)

About this article



Check for
updates

Cite this article

Deng, YH. Perovskite decomposition and missing crystal planes in HRTEM. *Nature* **594**, E6–E7 (2021). <https://doi.org/10.1038/s41586-021->

03423-4

[Download citation](#)

- Received: 20 July 2020
- Accepted: 04 March 2021
- Published: 09 June 2021
- Issue Date: 10 June 2021
- DOI: <https://doi.org/10.1038/s41586-021-03423-4>

Comments

By submitting a comment you agree to abide by our [Terms](#) and [Community Guidelines](#). If you find something abusive or that does not comply with our terms or guidelines please flag it as inappropriate.

[Access through your institution](#)

[Change institution](#)

[Buy or subscribe](#)

Advertisement

This article was downloaded by **calibre** from <https://www.nature.com/articles/s41586-021-03423-4>

- Matters Arising
- [Published: 09 June 2021](#)

Reply to: Perovskite decomposition and missing crystal planes in HRTEM

- [Zhijun Ning¹ na1](#),
- [Xiwen Gong](#) [ORCID: orcid.org/0000-0003-4004-1299^{2,3,4,5,6} na1](#),
- [Riccardo Comin⁷ na1](#),
- [Grant Walters⁸](#),
- [Fengjia Fan^{9,10,11,12}](#),
- [Oleksandr Voznyy](#) [ORCID: orcid.org/0000-0002-8656-5074¹³](#),
- [Emre Yassitepe¹⁴](#),
- [Andrei Buin⁸](#),
- [Sjoerd Hoogland](#) [ORCID: orcid.org/0000-0002-3099-585X⁸](#) &
- [Edward H. Sargent](#) [ORCID: orcid.org/0000-0003-0396-6495⁸](#)

[Nature](#) volume 594, pages E8–E9 (2021) [Cite this article](#)

- 1008 Accesses
- 5 Altmetric
- [Metrics details](#)

Subjects

- [Materials for devices](#)
- [Nanoscale materials](#)

The [Original Article](#) was published on 09 June 2021

In our Letter published in 2015¹, we reported epitaxial growth of perovskite around PbS quantum dots. The quantum dot surface is passivated by the crystalline perovskite scaffolding without the need of conventional ligands, leading to a two-orders-of-magnitude enhancement in the photoluminescence quantum yield in infrared quantum dot films. This material provided efficient charge carrier transfer from the perovskite to the quantum dots, enabling sensitization.

Access options

Subscribe to Journal

Get full journal access for 1 year

\$199.00

only \$3.90 per issue

[Subscribe](#)

All prices are NET prices.

VAT will be added later in the checkout.

Tax calculation will be finalised during checkout.

Rent or Buy article

Get time limited or full article access on ReadCube.

from \$8.99

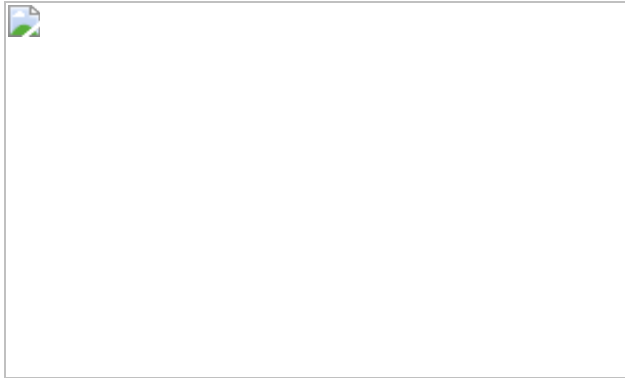
[Rent or Buy](#)

All prices are NET prices.

Additional access options:

- [Log in](#)
- [Access through your institution](#)
- [Learn about institutional subscriptions](#)

Fig. 1: TEM analysis of quantum dots in perovskite.



Data availability

The data within this paper and findings of this study are available from the corresponding author upon reasonable request.

References

1. 1.

Ning, Z. et al. Quantum-dot-in-perovskite solids. *Nature* **523**, 324–328 (2015).

[ADS](#) [CAS](#) [Article](#) [Google Scholar](#)

2. 2.

Deng, Y.-H. Perovskite decomposition and missing crystal planes in HRTEM. *Nature* <https://doi.org/10.1038/s41586-021-03423-4> (2021).

3. 3.

Chen, S. et al. Atomic scale insights into structure instability and decomposition pathway of methylammonium lead iodide perovskite. *Nat. Commun.* **9**, 4807 (2018).

[ADS](#) [Article](#) [Google Scholar](#)

4. 4.

Zhu, H. et al. Lead halide perovskite nanowire lasers with low lasing thresholds and high quality factors. *Nat. Mater.* **14**, 636–642 (2015).

[ADS](#) [CAS](#) [Article](#) [Google Scholar](#)

5. 5.

Gao, L. et al. Passivated single-crystalline $\text{CH}_3\text{NH}_3\text{PbI}_3$ nanowire photodetector with high detectivity and polarization sensitivity. *Nano Lett.* **16**, 7446–7454 (2016).

[ADS](#) [CAS](#) [Article](#) [Google Scholar](#)

6. 6.

Kollek, T. et al. Porous and shape-anisotropic single crystals of the semiconductor perovskite $\text{CH}_3\text{NH}_3\text{PbI}_3$ from a single-source precursor. *Angew. Chem. Int. Ed.* **54**, 1341–1346 (2015).

[CAS](#) [Article](#) [Google Scholar](#)

7. 7.

Son, D. Y. et al. Self-formed grain boundary healing layer for highly efficient $\text{CH}_3\text{NH}_3\text{PbI}_3$ perovskite solar cells. *Nat. Energy* **1**, 16081 (2016).

[ADS](#) [CAS](#) [Article](#) [Google Scholar](#)

8. 8.

Long, M. et al. Textured $\text{CH}_3\text{NH}_3\text{PbI}_3$ thin film with enhanced stability for high performance perovskite solar cells. *Nano Energy* **33**, 485–496 (2017).

[CAS](#) [Article](#) [Google Scholar](#)

9. 9.

Zhu, F. et al. Shape evolution and single particle luminescence of organometal halide perovskite nanocrystals. *ACS Nano* **9**, 2948–2959 (2015).

[CAS](#) [Article](#) [Google Scholar](#)

10. 10.

Fan, Z. et al. Layer-by-layer degradation of methylammonium lead tri-iodide perovskite microplates. *Joule* **1**, 548–562 (2017).

[CAS](#) [Article](#) [Google Scholar](#)

11. 11.

Jung, Y. K., Butler, K. T. & Walsh, A. Halide perovskite heteroepitaxy: bond formation and carrier confinement at the $\text{PbS}-\text{CsPbBr}_3$ interface. *J. Phys. Chem. C* **121**, 27351–27356 (2017).

[CAS](#) [Article](#) [Google Scholar](#)

12. 12.

Sytnyk, M. et al. Quasi-epitaxial metal–halide perovskite ligand shells on PbS nanocrystals. *ACS Nano* **11**, 1246–1256 (2017).

[CAS](#) [Article](#) [Google Scholar](#)

13. 13.

Zhang, X. et al. Inorganic CsPbI₃ perovskite coating on PbS quantum dot for highly efficient and stable infrared light converting solar cells. *Adv. Energy Mater.* **8**, 1702049 (2018).

[Article](#) [Google Scholar](#)

14. 14.

Liu, M. et al. Lattice anchoring stabilizes solution-processed semiconductors. *Nature* **570**, 96–101 (2019).

[ADS](#) [CAS](#) [Article](#) [Google Scholar](#)

15. 15.

Masi, S. et al. Chemi-structural stabilization of formamidinium lead iodide perovskite by using embedded quantum dots. *ACS Energy Lett.* **5**, 418–427 (2020).

[CAS](#) [Article](#) [Google Scholar](#)

16. 16.

Zhang, X. et al. PbS capped CsPbI₃ nanocrystals for efficient and stable light-emitting devices using p-i-n structures. *ACS Cent. Sci.* **4**, 1352–1359 (2018).

[CAS](#) [Article](#) [Google Scholar](#)

17. 17.

Peng, J., Chen, Y., Zhang, X., Dong, A. & Liang, Z. Solid-state ligand-exchange fabrication of CH₃NH₃PbI₃ capped PbS quantum dot solar cells. *Adv. Sci.* **3**, 1500432 (2015).

[Article](#) [Google Scholar](#)

[Download references](#)

Acknowledgements

The TEM characterization was supported by the Center for High-resolution Electron Microscopy (ChEM) at ShanghaiTech University. We thank Y. Yu, B. Yuan and K. Xu at ShanghaiTech University for the TEM measurement. We thank Y. Li at Stanford University for discussions.

Author information

Author notes

1. These authors contributed equally: Zhijun Ning, Xiwen Gong, Riccardo Comin

Affiliations

1. School of Physical Science and Technology, ShanghaiTech University, Shanghai, China

Zhijun Ning

2. Department of Chemical Engineering, University of Michigan, Ann Arbor, MI, USA

Xiwen Gong

3. Department of Materials Science and Engineering, University of Michigan, Ann Arbor, MI, USA

Xiwen Gong

4. Department of Electrical Engineering and Computer Science, University of Michigan, Ann Arbor, MI, USA

Xiwen Gong

5. Macromolecular Science and Engineering Program, University of Michigan, Ann Arbor, MI, USA

Xiwen Gong

6. Applied Physics Program, University of Michigan, Ann Arbor, MI, USA

Xiwen Gong

7. Department of Physics, Massachusetts Institute of Technology, Cambridge, MA, USA

Riccardo Comin

8. Department of Electrical and Computer Engineering, University of Toronto, Toronto, Ontario, Canada

Grant Walters, Andrei Buin, Sjoerd Hoogland & Edward H. Sargent

9. Hefei National Laboratory for Physical Sciences at the Microscale, University of Science and Technology of China, Hefei, China

Fengjia Fan

10. Department of Modern Physics, University of Science and Technology of China, Hefei, China

Fengjia Fan

11. CAS Key Laboratory of Microscale Magnetic Resonance, University of Science and Technology of China, Hefei, China

Fengjia Fan

12. Synergetic Innovation Center of Quantum Information and Quantum Physics, University of Science and Technology of China, Hefei, China

Fengjia Fan

13. Department of Physical and Environmental Sciences, University of Toronto Scarborough, Scarborough, Ontario, Canada

Oleksandr Voznyy

14. Department of Physics, University of Maranhão, São Luís, Brazil

Emre Yassitepe

Authors

1. Zhijun Ning

[View author publications](#)

You can also search for this author in [PubMed](#) [Google Scholar](#)

2. Xiwen Gong

[View author publications](#)

You can also search for this author in [PubMed](#) [Google Scholar](#)

3. Riccardo Comin

[View author publications](#)

You can also search for this author in [PubMed](#) [Google Scholar](#)

4. Grant Walters

[View author publications](#)

You can also search for this author in [PubMed](#) [Google Scholar](#)

5. Fengjia Fan

[View author publications](#)

You can also search for this author in [PubMed](#) [Google Scholar](#)

6. Oleksandr Voznyy

[View author publications](#)

You can also search for this author in [PubMed](#) [Google Scholar](#)

7. Emre Yassitepe

[View author publications](#)

You can also search for this author in [PubMed](#) [Google Scholar](#)

8. Andrei Buin

[View author publications](#)

You can also search for this author in [PubMed](#) [Google Scholar](#)

9. Sjoerd Hoogland

[View author publications](#)

You can also search for this author in [PubMed](#) [Google Scholar](#)

10. Edward H. Sargent

[View author publications](#)

You can also search for this author in [PubMed](#) [Google Scholar](#)

Contributions

X.G., Z.N., O.V. and E.H.S. designed and directed this study. Z.N. led the experimental work. X.G., Z.N., O.V. and E.H.S. wrote the manuscript. R.C., F.F., E.Y. and S.H. participated in discussions. All authors contributed to reviewing and commenting on the manuscript.

Corresponding author

Correspondence to [Edward H. Sargent](#).

Ethics declarations

Competing interests

The authors declare no competing interests.

Additional information

Publisher's note Springer Nature remains neutral with regard to jurisdictional claims in published maps and institutional affiliations.

Rights and permissions

[Reprints and Permissions](#)

About this article



Check for
updates

Cite this article

Ning, Z., Gong, X., Comin, R. *et al.* Reply to: Perovskite decomposition and missing crystal planes in HRTEM. *Nature* **594**, E8–E9 (2021).
<https://doi.org/10.1038/s41586-021-03424-3>

[Download citation](#)

- Published: 09 June 2021
- Issue Date: 10 June 2021
- DOI: <https://doi.org/10.1038/s41586-021-03424-3>

Comments

By submitting a comment you agree to abide by our [Terms](#) and [Community Guidelines](#). If you find something abusive or that does not comply with our

terms or guidelines please flag it as inappropriate.

[Access through your institution](#)

[Change institution](#)

[Buy or subscribe](#)

Associated Content

[Quantum-dot-in-perovskite solids](#)

- Zhijun Ning
- Xiwen Gong
- Edward H. Sargent

Nature Letter 15 Jul 2015

Advertisement

This article was downloaded by **calibre** from <https://www.nature.com/articles/s41586-021-03424-3>

| [Section menu](#) | [Main menu](#) |

Nature Outlook